



**GDAŃSK UNIVERSITY  
OF TECHNOLOGY**

Faculty of Electronics,  
Telecommunications and  
Informatics

Załącznik nr 1/2  
do Zarządzenia Rektora PG nr 5/2015 z 10 lutego 2015 r.

The author of the PhD dissertation: **Adrian Olejnik**

Scientific discipline: **Materials Engineering**

## **DOCTORAL DISSERTATION**

Title of PhD dissertation: **Electrochemical properties and structure of polydopamine – semiconductor interfaces**

Title of PhD dissertation (in Polish): **Właściwości elektrochemiczne i struktura złącz polidopamina – półprzewodnik**

Supervisor	Second supervisor
<i>signature</i>	<i>signature</i>
dr hab. eng. Robert Bogdanowicz, prof. PG	dr hab. eng. Katarzyna Siuzdak, prof. IMP PAN

## STATEMENTS

The author of the PhD dissertation: Adrian Olejnik

I, the undersigned, agree that my PhD dissertation entitled:

**Electrochemical properties and structure of polydopamine – semiconductor interfaces** may be used for scientific or didactic purposes.<sup>1</sup>

Gdańsk,.....

.....  
*signature of the PhD student*

Aware of criminal liability for violations of the Act of 4<sup>th</sup> February 1994 on Copyright and Related Rights (Journal of Laws 2006, No. 90, item 631) and disciplinary actions set out in the Law on Higher Education (Journal of Laws 2012, item 572 with later amendments),<sup>2</sup> as well as civil liability, I declare, that the submitted PhD dissertation is my own work.

I declare, that the submitted PhD dissertation is my own work performed under and in cooperation with the supervision of **dr hab. eng. Robert Bogdanowicz, prof. PG**, the second supervision of **dr hab. eng. Katarzyna Siuzdak, prof. IMP PAN**.

This submitted PhD dissertation has never before been the basis of an official procedure associated with the awarding of a PhD degree.

All the information contained in the above thesis which is derived from written and electronic sources is documented in a list of relevant literature in accordance with art. 34 of the Copyright and Related Rights Act.

I confirm that this PhD dissertation is identical to the attached electronic version.

Gdańsk,.....

.....  
*signature of the PhD student*

I, the undersigned, agree to include an electronic version of the above PhD dissertation in the open, institutional, digital repository of Gdańsk University of Technology, Pomeranian Digital Library, and for it to be submitted to the processes of verification and protection against misappropriation of authorship.

Gdańsk,.....

.....  
*signature of the PhD student*

---

<sup>1</sup> Decree of Rector of Gdansk University of Technology No. 34/2009 of 9<sup>th</sup> November 2009, TUG archive instruction addendum No. 8.

<sup>2</sup> Act of 27<sup>th</sup> July 2005, Law on Higher Education: Chapter 7, Criminal responsibility of PhD students, Article 226.



## Abstract:

Semiconductor electrochemistry is a rapidly developing branch of science devoted to understanding the processes at the interface between semiconductors and other materials. This field investigates physiochemical phenomena underlying the working principles of devices such as the solar cells, biosensors, batteries and supercapacitors. These devices are relevant for the most urgent problems of the XXI century, such as the energy crisis and implementation of the personalised medicine paradigm. Due to the complex nature of the phenomena occurring at semiconductor interfaces, fundamental and applied research is required to explore the possibilities to push forward the development of those devices.

**In this framework, the following thesis is devoted to modifications of titania nanotube (TNT) and boron-doped carbon nanowalls (B:CNW) model semiconductors with polydopamine (PDA) and its copolymers. The main research objective of the thesis is the fabrication of PDA coatings on B:CNWs and TNTs via electropolymerisation, followed by structural and electrochemical characterisations. The obtained composites are optimised towards applications in two strategies: ultrasensitive electrochemical sensing of neurotransmitters, and enhanced photocurrents.**

The thesis is a collection of four core publications with the dominant contribution of the author in each one. The character of the work is mostly experimental, supported by quantum chemistry calculations. The thesis begins with the outline of the research in the context of global problems in **Chapter 1**. Then, a comprehensive introduction to the PDA, PZ, B:CNW and TNT materials is presented in the associated literature contexts (**Chapter 2**). The specific research goals and hypotheses are presented in **Chapter 3**. The research methodology, including the experimental and computational techniques used in the thesis, is elaborated in **Chapter 4**. The results of the thesis in the form of a concise framework consisting of four core articles and their discussion are presented in **Chapter 5**. Finally, the conclusions and prospects for further research are proposed in **Chapter 6**.

## Keywords:

Polydopamine, structure, electropolymerisation, semiconductors, bulk heterojunction, charge transfer

## Streszczenie:

Elektrochemia półprzewodników to szybko rozwijająca się gałąź nauki poświęcona zrozumieniu procesów na interfejsie między półprzewodnikami a innymi materiałami. Dziedzina ta bada zjawiska fizykochemiczne leżące u podstaw zasad działania urządzeń takich jak ogniwa słoneczne, biosensory i superkondensatory. Urządzenia te są istotne dla najpilniejszych problemów XXI wieku, takich jak kryzys energetyczny i wdrażanie spersonalizowanej diagnostyki medycznej. Ze względu na złożony charakter zjawisk zachodzących na interfejsach półprzewodnikowych, wymagane jest prowadzenie badań podstawowych i stosowanych w celu zrozumienia mechanizmów, odpowiedzialnych za ich funkcjonowanie oraz przyczynienia się do dynamicznego przyspieszenia rozwoju tych urządzeń

**W tym kontekście, niniejsza praca doktorska poświęcona jest modyfikacjom dwóch powszechnie stosowanych półprzewodników na różnych etapach rozwoju technologicznego: nanorurek ditlenku tytanu (TNT) i nanościamek węglowych domieszkowanych borem (B:CNW) przy użyciu polidopaminy (PDA) i jej kopolimerów. Głównym celem badawczym pracy było wytworzenie powłok PDA na B:CNW i TNT poprzez elektropolimeryzację, a następnie ich strukturalna i elektrochemiczna charakterystyka. Otrzymane kompozyty zostały zoptymalizowane pod kątem zastosowań w dwóch kontekstach: elektrochemicznego wykrywania neuroprzekazników oraz poprawy generacji fotoprądu, co wskazuje na ogromne możliwości jakie daje modyfikacja struktury i morfologii w skali nano.**

Praca doktorska jest zbiorem czterech głównych publikacji, z dominującym wkładem Autora w każdej z nich. Charakter pracy jest głównie eksperymentalny, wspierany obliczeniami z zakresu chemii kwantowej. Praca rozpoczyna się od przedstawienia kontekstu badań w kontekście globalnych problemów w **Rozdziale 1**. Następnie, w **Rozdziale 2**, przedstawione jest wszechstronne wprowadzenie do materiałów PDA, PZ, B:CNW i TNT w kontekście literatury związanej. W **Rozdziale 3** przedstawiono szczegółowe cele badawcze i hipotezy. Metodologia badawcza, obejmująca techniki eksperymentalne i obliczeniowe używane w pracy, została opisana w **Rozdziale 4**. Wyniki pracy w formie zwięzłego opracowania składającego się z czterech głównych artykułów i ich dyskusji przedstawiono w **Rozdziale 5**. Ostatni **Rozdział 6**, poświęcono na wnioski z pracy oraz perspektywy dalszych badań.

## Słowa kluczowe:

Polidopamina, struktura, elektropolimeryzacja, półprzewodniki, złącze objętościowe, transfer ładunku

## List of core publications:

**Article 1: Olejnik, A., Ficek, M., Siuzdak, K., & Bogdanowicz, R. (2022).** Multi-pathway mechanism of polydopamine film formation at vertically aligned diamondised boron-doped carbon nanowalls. *Electrochimica Acta*, 409, 140000. <https://doi.org/10.1016/j.electacta.2022.140000>

(IF = 7.3, Points = 100)

- In **Article 1**, PDA synthesis protocols via electropolymerisation are proposed. PDA coatings are obtained on a B:CNW surface. Related reaction mechanisms are investigated via electrochemical techniques supported by quantum chemical calculations.

**Article 2: Olejnik, A., Ficek, M., Szkodo, M., Stanisławska, A., Karczewski, J., Ryl, J., Dołęga, A., Siuzdak, K. & Bogdanowicz, R. (2022).** Tailoring diffusional fields in zwitterion/dopamine copolymer electropolymerized at carbon nanowalls for sensitive recognition of neurotransmitters. *ACS Nano*, 16(8), 13183–13198. <https://doi.org/10.1021/acsnano.2c06406> (IF = 17.1, Points = 200)

- In **Article 2**, a state-of-the-art co-electropolymerisation protocol for obtaining a PDA\_PZ coating on a B:CNW surface is developed. Structural characterisation using the electron microscopy, nanoindentation and spectroscopic methods is performed. The material is applied for the electrochemical sensing of neurotransmitters.

**Article 3: Olejnik, A., Olbryś, K., Karczewski, J., Ryl, J., Bogdanowicz, R., & Siuzdak, K. (2023).** Band Gap Engineering toward Semimetallic Character of Quinone-Rich Polydopamine. *The Journal of Physical Chemistry C* 127(26), 12662–12677 <https://doi.org/10.1021/acs.jpcc.2c08804> (IF = 4.2, Points = 140)

- **Article 3** adapts the electropolymerisation protocol to obtain PDA layers on TNTs. Structural characterisation using electron microscopy, XPS, Raman and optical spectroscopy is performed. The material's photoelectrochemical properties are investigated, and the synthesis is optimised towards the highest photocurrents.

**Article 4: Olejnik, A., Polaczek, K., Szkodo, M., Stanisławska, A., Ryl, J., & Siuzdak, K. (2023).** Laser-induced graphitization of polydopamine on titania nanotubes. *ACS Applied Materials & Interfaces*, 15(45), 52921–52938. <https://doi.org/10.1021/acsnano.2c06406> (IF = 10.4, Points = 200)

- In **Article 4**, a PDA laser graphitisation state-of-the-art protocol is developed towards the further enhancement of photocurrents. After structural characterisation, the synthesis parameters are optimised towards the simultaneously highest photocurrents and charge transfer rates. The material is applied in the photoelectrochemical sensing of serotonin.



## Acknowledgements:

### Supervisors:

dr hab. eng. Robert Bogdanowicz, prof. PG

dr hab. eng. Katarzyna Siuzdak, prof. IMP PAN

### Collaborators, colleagues:

dr hab. eng. Jacek Ryl, prof. PG

dr hab. eng. Jakub Karczewski, prof. PG

prof. dr hab. eng. Anna Dołęga, prof. PG

dr hab. eng. Mirosław Sawczak, prof. IMP PAN

dr hab. Katarzyna Grochowska

mgr eng. Wiktoria Lipińska

dr eng. Łukasz Haryński

dr eng. Jakub Wawrzyniak

mgr eng. Krzysztof Polaczek

mgr eng. Karol Olbryś

dr eng. Mateusz Ficek

dr eng. Michał Sobaszek

dr eng. Bartłomiej Dec

dr hab. eng. Marek Szkodo, prof. PG

dr eng. Alicja Stanisławska

dr Zbigniew Karkuszewski

### Funding:

Ministry of Science and Higher Education project Diamentowy Grant DI2019 017649 '*Poly(zwitterionic) brushes on titania nanotubes for supercapacitor applications. Characterization of the structure, electrochemistry and nanomechanical properties of heterojunctions*', 217,800 PLN (project duration: 2021–2024)

National Science Centre PRELUDIUM 2022/45/N/ST5/00192 project '*Structure and photoelectrochemistry of the laser graphitized polydopamine on titania nanotubes*', 69,620 PLN (project duration: 2023–2024)

<b>1. BIRD'S EYE VIEW ON THE SCOPE OF THE THESIS .....</b>	<b>10</b>
1.1. Photosensitisation of metal oxide semiconductors.....	10
1.2. Electrochemical sensing .....	11
<b>2. INTRODUCTION .....</b>	<b>13</b>
2.1. Polydopamine (PDA).....	13
2.1.1. Overview of the structure of PDA .....	13
2.1.2. PDA Synthesis .....	13
2.1.3. Properties of PDA .....	14
2.1.4. Carbonisation of PDA and Laser-Induced Graphene (LIG) .....	18
2.2. Polyzwitterions (PZ).....	21
2.2.1. PZ chemical structure and synthesis .....	21
2.2.2. Antifouling property and hydration structure of zwitterions .....	23
2.2.3. Modification of surfaces with PZ.....	24
2.2.4. Mechanical and electrical properties of PZ.....	26
2.3. Boron-doped Carbon Nanowalls (B:CNW).....	27
2.3.1. Overview and synthesis of boron-doped carbon nanowalls .....	27
2.3.2. B:CNW properties .....	28
2.3.3. Electrochemical sensing on B:CNW.....	29
2.4. Hydrogenated titania nanotubes (TNT) .....	30
2.4.1. Overview of TNT .....	30
2.4.2. Fabrication of TNTs by anodisation .....	31
2.4.3. Bandgap engineering and photosensitisation of TNTs .....	32
2.4.4. Laser modifications of nanotubes .....	34
2.5. Research problem.....	36
<b>3. RESEARCH OBJECTIVES AND HYPOTHESES .....</b>	<b>38</b>
3.1. Objectives .....	38
3.2. Hypotheses .....	40
<b>4. RESEARCH METHODOLOGY .....</b>	<b>42</b>
4.1. Synthesis protocols .....	42
4.1.1. Synthesis of B:CNWs.....	42
4.1.2. Synthesis of hydrogenated TNTs .....	42
4.1.3. Electropolymerisation of dopamine on B:CNWs and hydrogenated TNTs.....	43
4.1.4. Co-electropolymerisation of dopamine and zwitterions on B:CNWs.....	43
4.1.5. Laser graphitisation of PDA deposited on TNTs .....	44
4.2. Experimental characterisation techniques .....	44
4.2.1. Scanning Electron Microscopy (SEM).....	44
4.2.2. X-ray Photoelectron Spectroscopy .....	47
4.2.3. FT-IR spectroscopy.....	49
4.2.4. Raman spectroscopy .....	51

4.2.5.	Optical diffuse reflectance spectroscopy .....	52
4.2.6.	Nanoindentation .....	56
4.2.7.	Electrochemical techniques .....	59
4.3.	Computational techniques in materials science and engineering .....	70
4.3.1.	Multiscale paradigm .....	70
4.3.2.	Computational chemistry methods .....	71
4.3.3.	Density Functional Theory .....	73
4.3.4.	Geometry optimisations and technical aspects .....	75
4.3.5.	Properties calculable from DFT .....	78
4.3.6.	Molecular dynamics and ReaxFF force fields .....	80
5.	RESULTS – LIST OF PUBLICATIONS .....	83
5.1.	Article 1: ‘Multi-pathway mechanism of polydopamine fil formation at vertically aligned diamondised boron-doped carbon nanowalls’ .....	85
5.2.	Article 2: ‘Tailoring diffusional fields in zwitterion/dopamine copolymer electropolymerized at carbon nanowalls for sensitive recognition of neurotransmitters’ .....	87
5.3.	Article 3: ‘Band gap engineering toward semimetallic character of quinone-rich polydopamine’ .....	90
5.4.	Article 4: ‘Laser-induced graphitization of polydopamine on titania nanotubes’ .....	94
6.	CONCLUSIONS AND FURTHER RESEARCH .....	97
6.1.	Conclusions .....	97
6.2.	Future directions of research.....	99
7.	LIST OF FIGURES.....	101
8.	LIST OF ABBREVIATIONS .....	105
8.1.	Compounds and materials: .....	105
8.2.	Techniques: .....	105
8.3.	Computational: .....	106
8.4.	Physical quantities .....	107
8.5.	Other.....	107
	CREDIT DEFINITIONS (ELSEVIER’S DEFINITION).....	108
	INVOLVEMENT IN RESEARCH PROJECTS .....	109
	CONFERENCES AND SCHOOLS .....	110

<b>LIST OF PUBLICATIONS .....</b>	<b>112</b>
-----------------------------------	------------

<b>OTHER ACHIEVEMENTS .....</b>	<b>116</b>
---------------------------------	------------

<b>LIST OF REFERENCES .....</b>	<b>118</b>
---------------------------------	------------

### **Remark on the quotes appearing at the beginning of chapters and subchapters**

\*Quotes of philosophers, poets, and other artists invoked in the thesis at the beginning of chapters and subchapters may not always be exact translations. Their main purpose is to inspire the reader and to indirectly express the emotional attachment of the author to the contents of the thesis.

In some cases, they are exact.

In some cases, they are deep learning translations of Polish versions of the text.

In some cases, they are cited from the author's memory (probably with errors).

In some cases, they are paraphrases trying to reflect the general intellectual heritage of the philosopher.

# 1. Bird's eye view on the scope of the thesis

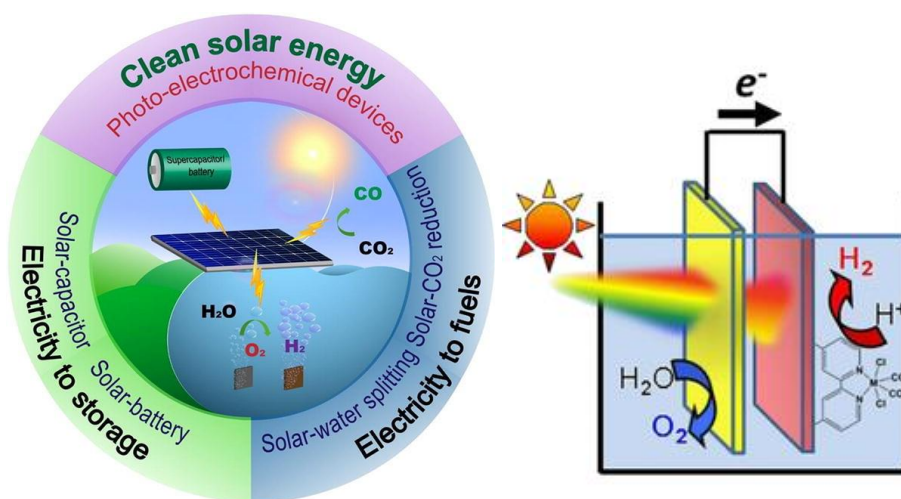
*Man spreads out. Man is the cancer of the earth.*

*Człowiek rozprzestrzenia się. Człowiek jest rakiem dla ziemi.*

**Emil Cioran** – Romanian pessimistic philosopher; 'The Trouble with Being Born' (1973)

## 1.1. Photosensitisation of metal oxide semiconductors

Reversing climate change and reducing environmental pollution are two of the greatest problems of modern science. Solving them requires multidimensional, long-term ventures, one of which is switching from conventional to renewable energy sources. According to this idea, manufacturing efficient and low-cost energy conversion and energy storage is an essential scientific objective. The objective of solar energy conversion is realised by various semiconductor devices, including solar cells and photoelectrochemical cells (**Figure 1**). While solar cells convert solar energy to generate voltage, photoelectrochemical cells utilise solar energy to conduct chemical reactions, such as water splitting, degrading pollutants, or synthesis of organic compounds.

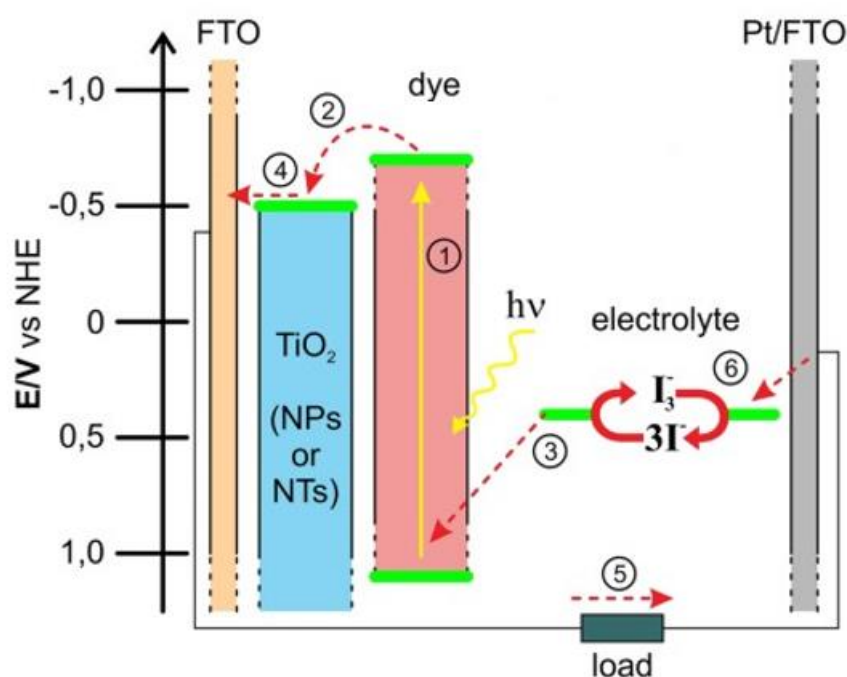


**Figure 1.** Solar energy conversion diagram (left)<sup>1</sup> and scheme of photoelectrochemical cell for water splitting (right)<sup>2</sup>.

Various types of solar cells have been developed, including silicon-based cells, dye sensitised solar cells (DSSC) and perovskite cells, each having their pros and cons and specific materials technologies. In the case of DSSCs, the most notable advantages include low production costs<sup>3,4</sup>, use of typically non-toxic, eco-friendly materials<sup>5</sup> and decent performance in indoor applications<sup>6,7</sup>. They consist of a transparent semiconductor photoanode, an electrolyte containing redox-active species, and a counter electrode (typically Pt). The photoanode is made of a metal oxide such as BiVO<sub>4</sub>, Fe<sub>x</sub>O<sub>y</sub> and TiO<sub>2</sub> with a photosensitiser on its surface. The working principle of the DSSC is shown in **Figure 2**. After irradiation of the photoanode, electrons of the photosensitiser are excited (1) and transferred to



the semiconductor (2) and then to the contact electrode (4). The absorbed solar energy is used to exert work in an external circuit (5). The electrons then return to the reference electrode through the external circuit (6), reduce the oxidation state of the redox marker on its surface and finally, after charge transfer to the photoanode, the circuit is closed (3).



**Figure 2.** Scheme of the dye sensitised solar cell<sup>8</sup>.

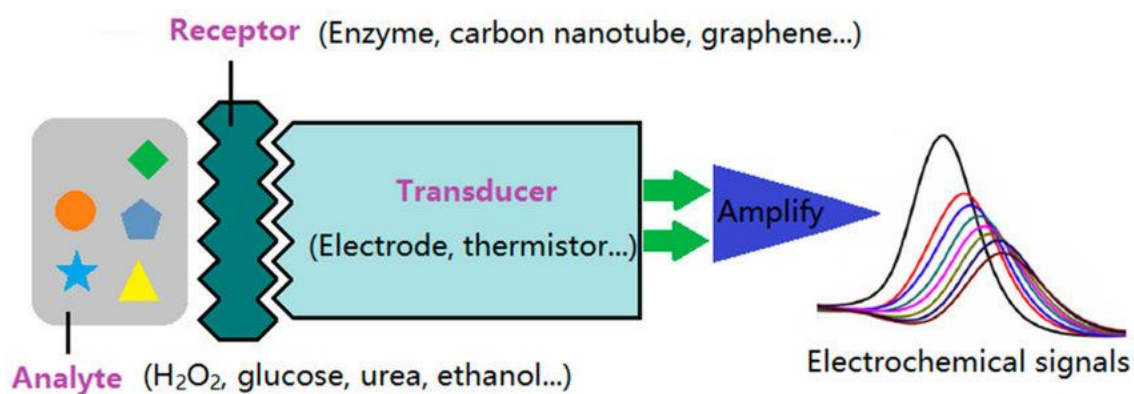
Despite their advantages, DSSCs exhibit lower conversion efficiencies than the other types of solar cells. That is because the metal oxide semiconductors constituting the photoanode typically exhibit wide bandgaps. This feature results in an absorption maximum in the UV range of the electromagnetic spectrum, hindering the photovoltage/photocurrent generation in the visible part and thus the device's performance. There are various strategies to overcome this problem, such as manipulation of the electrolyte's composition<sup>9</sup>, interfacial engineering<sup>10</sup>, and photosensitiser engineering<sup>11</sup>. Photosensitisers are typically thin layers of molecules, polymers or other semiconductors with smaller bandgaps than the substrate semiconductor. Improving the photosensitisation strategies is required to enhance the performance and improve the marketability of DSSCs. Besides solar cells, the same aspect is relevant for photoelectrochemical water splitting<sup>12</sup> and devices for photoelectrocatalytic degradation of pollutants<sup>13</sup>. In this context, the design of both the semiconductors and photosensitisers, and understanding of physiochemical processes on the related interfaces, are crucial for advancing the field.

## 1.2. Electrochemical sensing

To realise the paradigm of personalised diagnostics, there is an urgent need to develop electrochemical devices for sensing many biomarkers. These are chemical compounds relevant for the diagnostics and

management of common diseases such as glucose in diabetes<sup>14</sup>, or catecholamines in neurodegenerative disorders such as Alzheimer disease<sup>15</sup>. Sensing devices are also important for designing strategies for prolonging overall health and for building strategies for combating ageing in the general population. Stable, label-free and inexpensive (photo)electrochemical sensors with high temporal and special resolution are desirable for such biomedical applications, especially in the single-synapse sensing of neurotransmitters<sup>16</sup>.

Detailed goals in this field are diverse but linked through the need to develop materials for the core elements of the sensors, especially the main platform where electrochemical processes occur. Among the requirements that must be satisfied are a few general ones, such as the preserving the selectivity of the receptor (for a particular group of analytes), sensitivity (high signal-to-noise ratio), high stability and shelf-life, and ideally low cost (**Figure 3**). Understanding of the sensing mechanisms and analyte-surface interactions are curial elements necessary for developing new applicable devices. The multiscale paradigm, based on gathering data at the atomic scale, through the mesoscale to the macroscopic properties, is essential in this context.



**Figure 3.** Schematic diagram of the electrochemical sensing process<sup>17</sup>.

The general scope of the thesis falls within the framework defined by those two global research trends: photosensitisation and sensing. In both trends, understanding the fundamental semiconductor (photo)electrochemistry and careful materials engineering oriented towards a particular application is required to make progress. **Thus, this thesis is devoted to the modification of semiconductors with polydopamine (PDA)-based functional polymers and investigations of their electrochemical and photoelectrochemical properties.** In the following **Chapter 2**, a thorough literature review is given to introduce the materials used in the work. Specific research goals and hypotheses are defined in **Chapter 3**.

## 2. Introduction

### 2.1. Polydopamine (PDA)

*Entia non sunt multiplicanda praeter necessitate.*

*Entities must not be multiplied beyond necessity.*

*Nie należy mnożyć bytów ponad konieczność.*

**William Ockham** – English scholastic philosopher; (XIV century)

#### 2.1.1. Overview of the structure of PDA

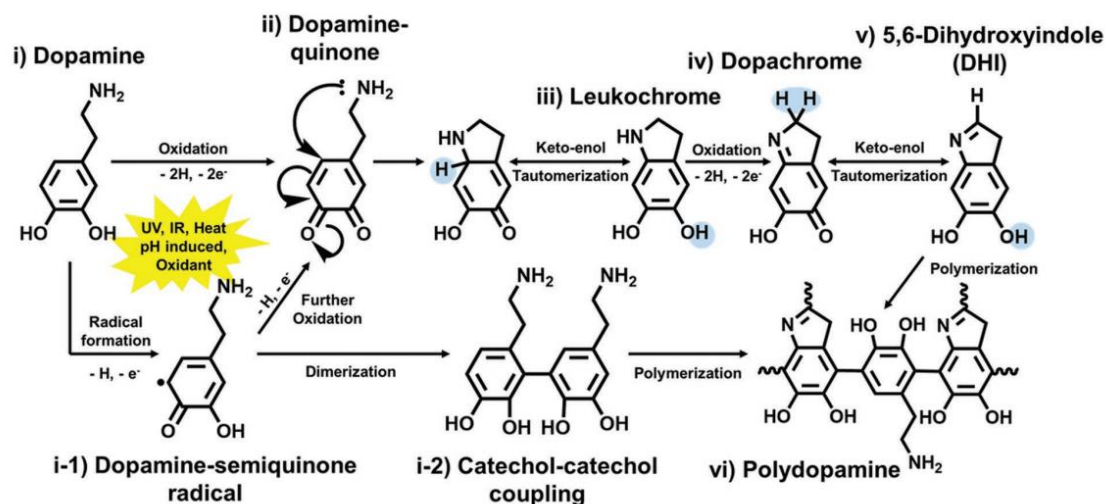
Melanins are biopolymers found in many organisms, including humans. They serve as pigments, adhesives and building blocks in skin, hair, and neural tissues<sup>18</sup>. Polydopamine (PDA) is an artificial melanin with a similar structure and properties to those of its natural analogues, exhibiting facile synthetic routes and a high propensity towards chemical and physical modifications.

In practice, PDA is everything obtained through the oxidative polymerisation of its monomer – dopamine. Elucidation of the chemical structure of PDA is a very complicated issue, described as a ‘never-ending story’ by the leaders of the field in 2013<sup>19</sup>. In general, a few tens of structural units can be found in PDA chains. Some of them are composed of single rings, such as dopamine-quinone, with a primary amine group, while the rest are double-ringed with or without  $\pi$ -conjugation, such as dihydroxyindole (DHI). It is reported that DHI is the most abundant unit in PDA, but PDA cannot be composed purely of DHI. PDA units can be in the state of catechols or quinones, and applying a potential can change their ratio, making PDA a prominent redox mediator. This property was utilised in the construction of electrochemical force microscopy tips<sup>20</sup> in the electroless reduction of metals for nanoparticle synthesis and in pseudocapacitors<sup>21</sup>. The polymeric nature of PDA was questioned for many years, but it was finally proven in 2018 using single-molecule atomic force microscopy<sup>22</sup>.

#### 2.1.2. PDA Synthesis

Two of the most common synthesis methods are self-polymerisation with oxygen and electropolymerisation on the surface of conductive materials<sup>23–26</sup> (**Figure 4**). Self-polymerisation is used most commonly due to its versatility and ability to create films on the surface of existing materials<sup>23,27,28</sup>, and to form free-standing structures such as nanoparticles or core-shell particles<sup>29–31</sup>. On the other hand, electropolymerisation is limited only to surface modifications of conductive substrates. However, the obtained films are thicker and more uniform with respect to the classic approach<sup>23,32,33</sup>. Therefore, in the works related to the thesis, electropolymerisation is used. There are

also more advanced synthesis protocols involving, for example, CVD synthesis<sup>34,35</sup>. The PDA obtained in this way exhibits a very large content of single-ringed structures capable of binding protons in an acidic solution, which was utilised for efficient, nonmetal hydrogen storage.



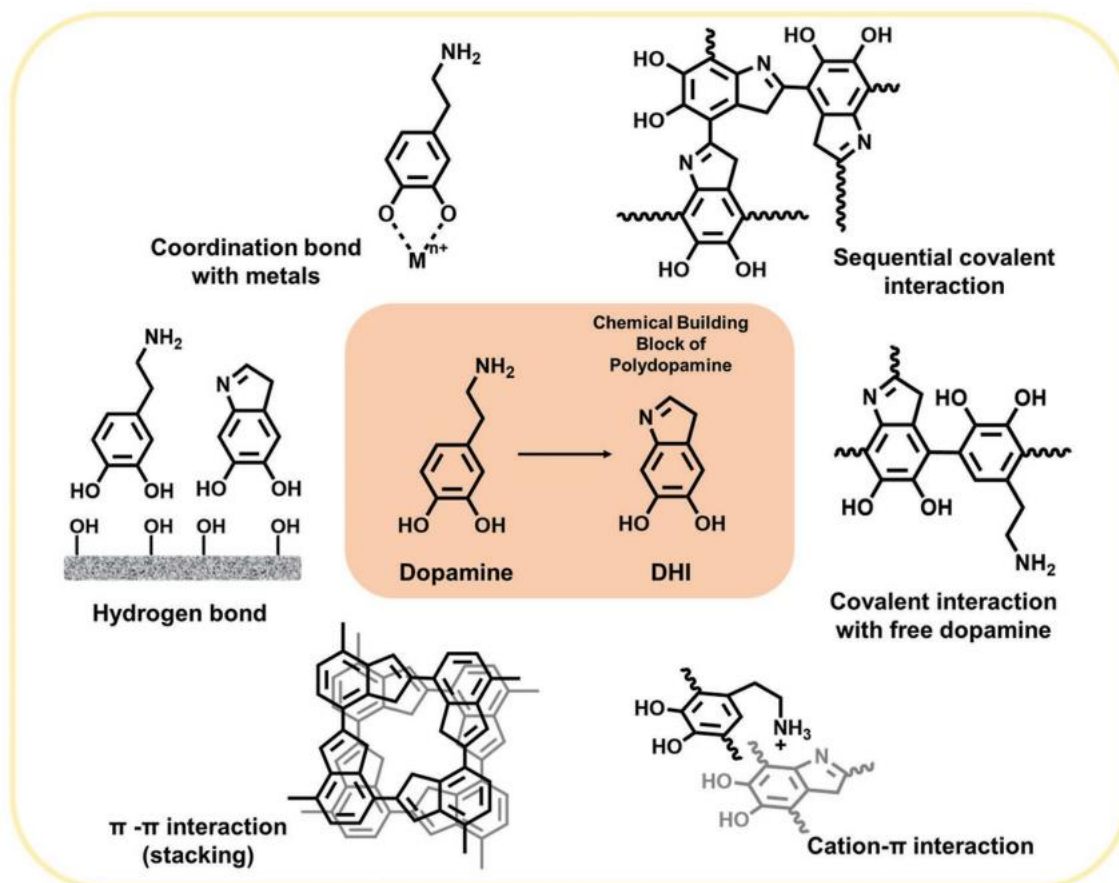
**Figure 4.** Two basic routes to synthesise polydopamine with the proposed reaction mechanism; Electropolymerisation route: i->iii->iv->v->vi; Oxidative polymerization route: i->i-1->i-2->vi<sup>36</sup>.

The widely accepted mechanism of electropolymerisation is shown in (**Figure 4**). First, the dopamine unit (DA) is oxidised to dopamine-quinone (DQ) through electron transfer, then a chemical step of Michael cyclisation occurs, and leukodopaminechrome (LDC) is formed. Next, a second electrochemical step leads to the transformation of LDC to dopaminechrome (DC). Finally, a second chemical step involving aromatisation of the second ring occurs, and a DHI unit is obtained<sup>23,37</sup>. Polymerisation then occurs via electrogenerated radicals, leading to the creation of covalent aryl-aryl linkages between the described structural units and different forms of cross-linking. It is noted that double-ringed molecules have a higher probability of taking part in the polymerisation process.

### 2.1.3. Properties of PDA

PDA is known as an excellent adhesive and binder for many materials. Its exceptional property originates from the interaction between catechol-quinone groups, aromatic rings, and aliphatic amines<sup>38</sup>. Moreover, structural units of the PDA can bind with themselves in different patterns, forming tetramers, octamers, cyclotetramers, or different aromatic adducts with different levels of covalent crosslinking. As a result, many intramolecular and intermolecular interactions can occur between units, such as hydrogen bonding with amines and catechols,  $\pi$ - $\pi$  stacking of aromatic rings,  $\pi$ -cation interactions and chelation of metals<sup>39</sup> (**Figure 5**). Following that, the structure-property relations are generally very complicated. For example, depending on the proportions of the structural units, the antioxidant activity<sup>40</sup>

and hydrophilicity<sup>36</sup> might vary significantly. Polydopamine rich in DA units with dangling amine groups can be applied for hydrogen electrosorption<sup>35</sup>, but polydopamine rich in DHI and IQ units has better photocatalytic properties<sup>41</sup>. Therefore, knowledge of the details of the electropolymerisation process is desired. To obtain a particular structure, it is essential to know the potential reactions that can occur and how to control their parameters to achieve the desired structure.

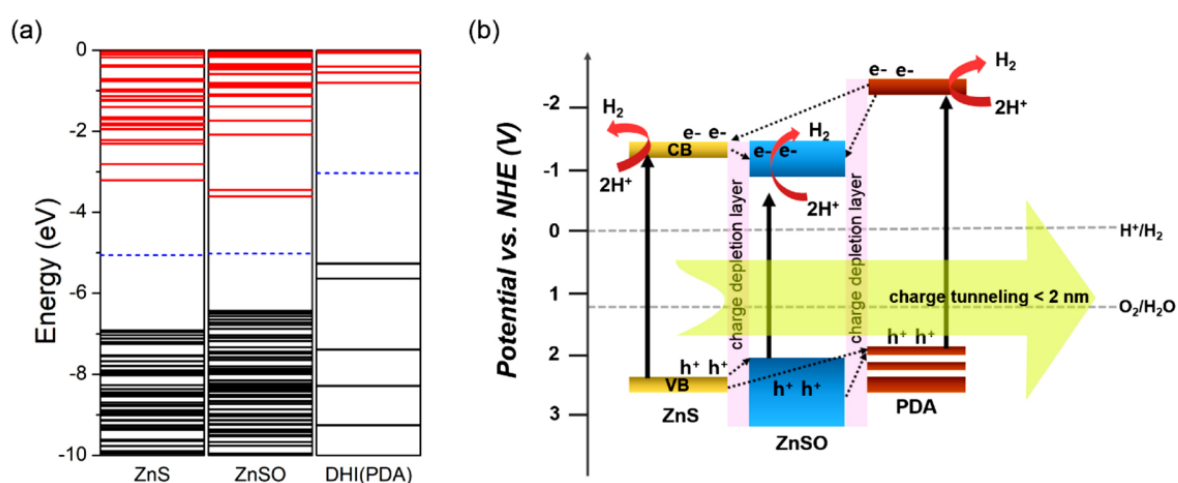


**Figure 5.** Intermolecular interactions of polydopamine<sup>36</sup>.

In terms of electrical properties, PDA was initially viewed as a semiconductive polymer, due to its increasing conductivities with temperature<sup>34,42</sup>. In this view, the charge transport mechanism would be dominated by polarons and bipolarons transferred along the pi-conjugated system by analogy to other similar polymers, such as polyaniline, polypyrrole, and poly(ethylene dioxythiophene). However, this perspective has been shown to be incorrect and ionic transport might play an even more important role in PDA's conductivity, especially in an aqueous environment<sup>43</sup>. According to this model, PDA structural units undergo a disproportionation dissociation, in which protons are released to the polymer matrix. Another aspect differentiating PDA from other semiconductive polymers is the nonvanishing dipole and multipole moments along the chains due to the presence of polar functional groups<sup>44</sup>. These electrostatic interactions increase the reactivity of PDA, enhancing its capability towards surface modifications, influencing the electronic structure locally. Presumably, such phenomena govern the

heat-dissipation mechanism in PDA and naturally occurring melanins, which is essential for the protective functions of skin in vertebrae, including humans<sup>45,46</sup>. Moreover, there is a notable tendency for PDA to create trap states for both electrons and holes, which might be beneficial for creating heterojunctions with other, inorganic semiconductors.

The electronic properties of such junctions can be very complex and difficult to predict. The problem is even more complicated because the electronic properties of PDA are also dependent on metal ions introduced to a greater or lesser extent during the synthesis<sup>47</sup>. In general, PDA can be used as a photosensitizer for  $\text{TiO}_2$ <sup>29,48–50</sup>. Similarly, in the case of  $\text{ZnO} \mid \text{PDA}$ , an enhancement of the recombination time and a minimisation of photocorrosion were observed<sup>28,51</sup>. In composition with  $\text{MoS}_2$ , PDA improves the capacitive responses and enhances the wettability<sup>52</sup>. On the other hand, an extraordinary structure of the  $\text{ZnS} \mid \text{PDA}$  heterojunctions, a doubly staggered band structure, was recently reported. The  $\text{ZnS}$  surfaces were coated with thin (1–4 nm) layers of PDA by oxidative polymerisation. Interestingly, at the interface, the PDA-induced  $\text{ZnS}_{1-x}\text{O}_x$  layer was registered by TEM measurements<sup>53</sup>. As a result, a unique alignment of energy levels was revealed by DFT calculations of the  $\text{ZnS} \mid \text{PDA}$  slab models (**Figure 6**). In this scheme, photoexcited electrons are trapped in the conduction band of the  $\text{ZnS}_{1-x}\text{O}_x$  and the holes are trapped in the valence band of the PDA. Effectively, this band structure makes it possible to explain the enhancement of the photocatalysis after PDA-coating and simultaneous active protection from photocorrosion.



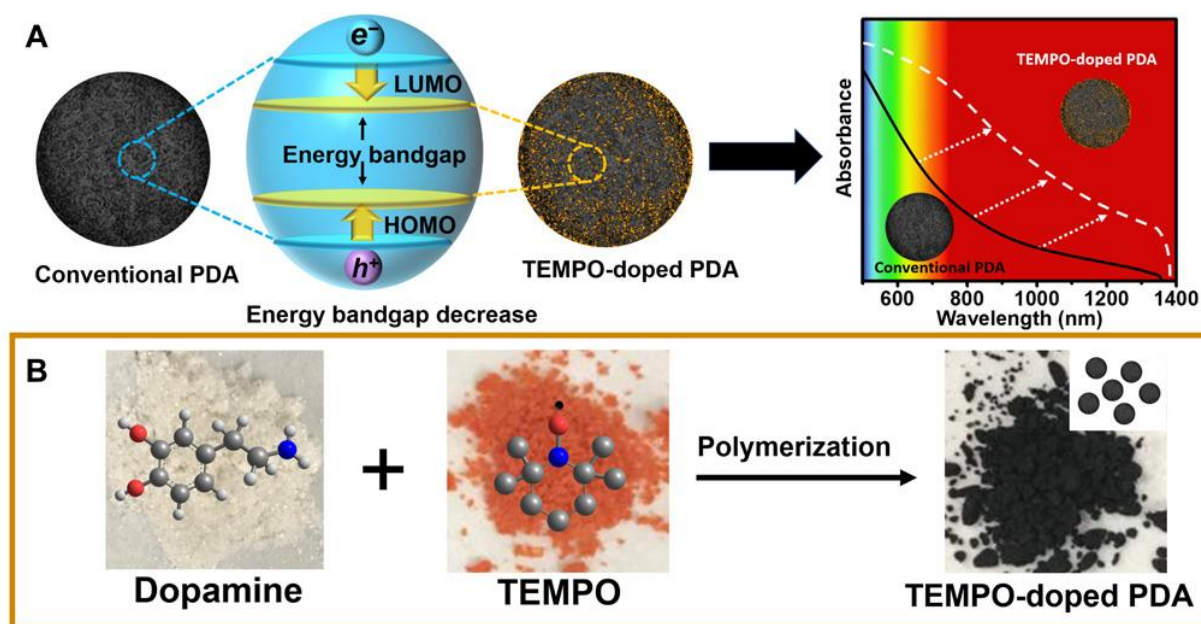
**Figure 6.** Doubly staggered band structure of the PDA (reprinted from<sup>53</sup>) (a) Electronic band structures of  $\text{ZnS}$ ,  $\text{ZnS}_{1-x}\text{O}_x$  ( $\text{ZnSO}$  in the scheme), and 5,6-dihydroxyindole (DHI). The black and red lines are the filled and unfilled states, respectively. (b) Schematic representation of the  $\text{ZnS}/\text{PDA}$  heterojunction and photocatalytic process considering charge carrier transfer<sup>53</sup>.

Moreover, in the same study, it was shown that the thickness of the PDA on the semiconductor surface is a crucial parameter determining its photocatalytic and photoelectrocatalytic performance. In particular, the material with the thinnest layer (1.2 nm) exhibited the highest yield in the hydrogen



evolution reaction and the highest photocurrents, as well as the highest reduction of the charge-transfer resistances. Although many applications and preliminary studies have been proposed, the electronic properties of PDA | semiconductor heterojunctions at the quantum mechanical level are still mostly unknown. Therefore, the modification of titania nanotubes with electropolymerised PDA planned in the thesis is anticipated to produce new knowledge on the electronic properties of PDA | semiconductor interfaces, or more generally redox polymer | semiconductor interfaces.

The optical spectrum of PDA can be controlled by inserting other molecules into its structure. A prominent example of this approach was performed in the study of Zou et al.<sup>54</sup> with 2,2,6,6-tetramethylpiperidine-1-oxyl (TEMPO) as a doping agent for free-standing PDA nanoparticles (see **Figure 7**). As a result of the modification, the energy bandgap of the PDA decreased from ca. 4.5 eV to ca. 2.2 eV, which was confirmed experimentally via UV-Vis spectra and DFT electronic structure calculations. Moreover, it was accompanied by electron delocalisation of the HOMO-LUMO orbitals for the same redox structure of PDA. These two effects lead to a significant increase in optical absorption in a NIR region, leading to a strong photothermal effect and excellent performance in solar desalination.

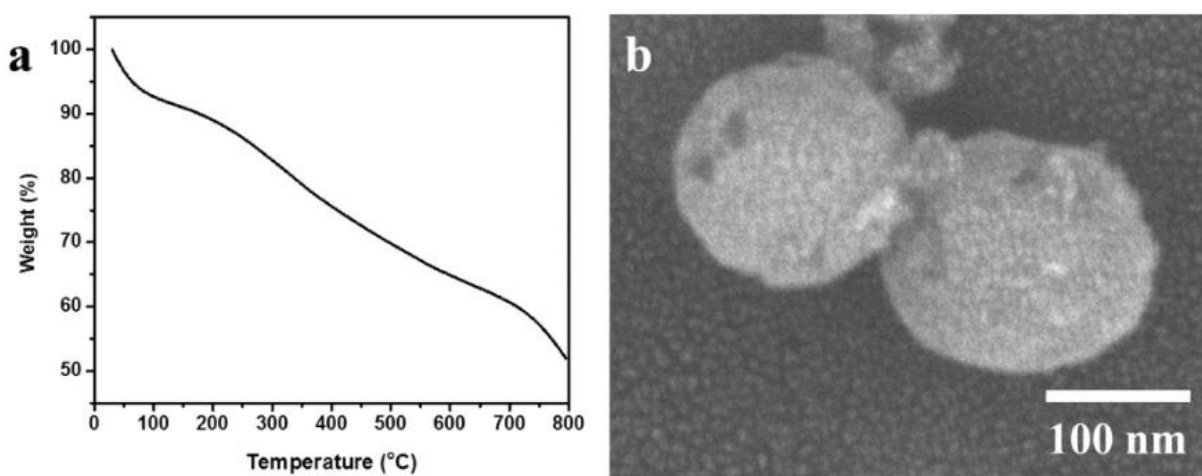


**Figure 7.** Synthesis and structure of TEMPO-PDA. (A) Schematic illustration of TEMPO-doped PDA with a narrower bandgap and improved light absorption ability compared to conventional PDA. (B) Polymerisation of dopamine and TEMPO, together with their molecular structures and powder photographs<sup>54</sup>.

Alternative routes of modifying PDA include forming PDA-based composites, e.g. with carbon nitride<sup>55</sup>, and applying other polymers similar to PDA, such as pheomelanins and pyomelanins<sup>56</sup>. Considering the described study, it is anticipated that modifying PDA with other agents than TEMPO can bring several new properties to PDA.

#### 2.1.4. Carbonisation of PDA and Laser-Induced Graphene (LIG)

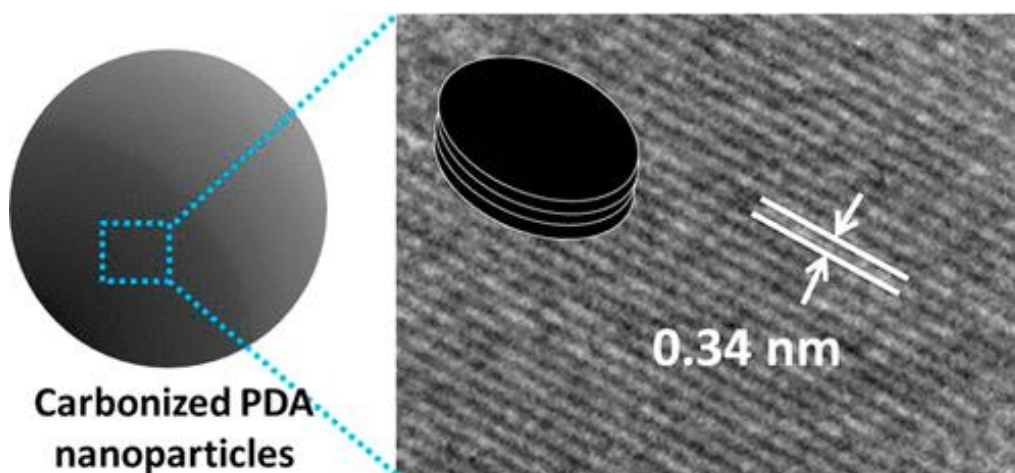
In general, nanocarbons, including graphite/graphene, can be synthesised from organic precursors such as polymers, resins and biomass. Those substrates can be transformed into nanocarbons via chemical and phase transitions activated by various stimuli. These approaches encompass a range of high-temperature and chemical treatments, including catalytic graphitisation/carbonisation/pyrolysis and hydrothermal treatment<sup>57</sup>. In the case of pyrolysis, a high temperature, inert atmosphere and catalysts, such as transition metals (Fe, Ni, Co)<sup>58</sup>, their salts and oxides<sup>59</sup>, boron compounds<sup>60</sup>, and carbon nanostructures<sup>61,62</sup>, are required. Despite efforts in designing catalysts, pyrolysis methods require temperatures exceeding 1,000°C, sometimes reaching up to 3,000°C, along with an inert atmosphere for efficient conversion<sup>57,58</sup>. In contrast to pyrolysis approaches, the hydrothermal process involves autoclaving pre-treated precursors at lower temperatures in alkaline or acidic environment<sup>57</sup>. However, the resulting carbonised product tends to be strongly disordered and oxidised, requiring an additional high-temperature step to transform it into crystalline nanocarbons, such as graphene. For instance, Chen et al. applied this methodology to wheat straw waste, requiring a high graphitisation temperature of 2,600°C for electrochemical applications, in particular in lithium-ion batteries<sup>63</sup>. PDA can also be used as a substrate for the synthesis of nanocarbons. The typical method for PDA graphitisation/carbonisation is purely thermal, with temperature values ranging between 700 and 1,000°C<sup>64–67</sup>. The resulting carbonised PDA exhibits the structure of nitrogen-doped graphite with varying levels of crystallinity and ordering, typically in the form of nanoparticles (**Figure 8** and **Figure 9**). Surprisingly, some studies report the calcination of PDA into amorphous carbon at a relatively low temperature of 500°C in a nitrogen flow<sup>68</sup>. Conversely, in certain carbon-carbon composites, the required temperatures can be as high as 3,000°C<sup>31,69</sup>.



**Figure 8.** a) Thermogravimetric curve for PDA carbonisation;  
b) SEM image of carbonised PDA nanoparticles<sup>70</sup>.



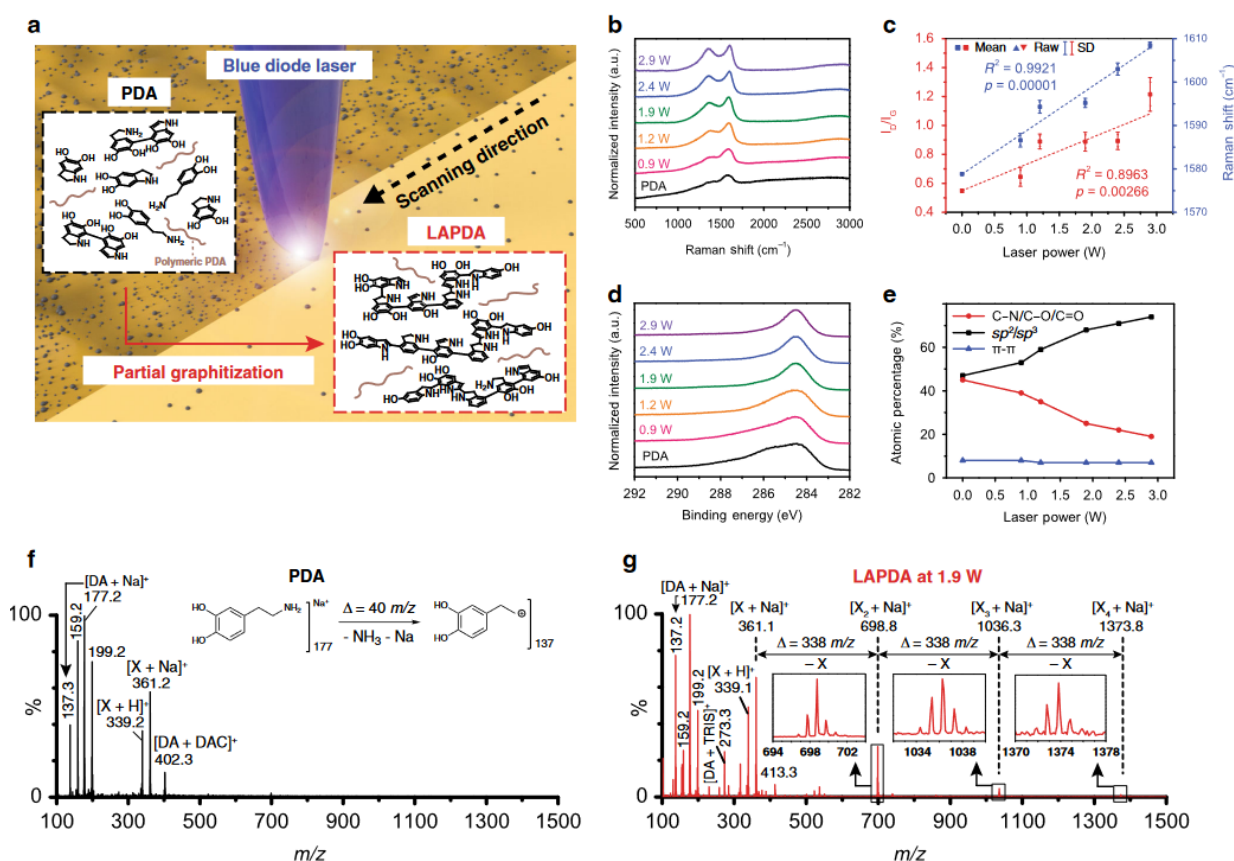
Nevertheless, graphitised PDA exhibits markedly larger thermal and electrical conductivity, the latter being important for electronic and electrochemical applications<sup>69</sup>. In the case of carbon-PDA composites, a higher PDA content leads to a higher degree of N-doping in the final structure<sup>31</sup>. It is typically less crystalline, although short-range ordering is preserved<sup>67</sup>. This higher N-doping is believed to be responsible for its greater electrical conductivity. Some authors report this enhancement over several orders of magnitude and describe the phenomenon as an irreversible insulation-to-conduction phase transition<sup>64</sup>. A side effect of the greater conductivity is the loss of the characteristic optical absorption bands. On the other hand, higher electron-phonon coupling (induced by the PDA) is responsible for higher thermal conductivity<sup>69</sup>. A non-trivial aspect of the PDA graphitisation is that it does not lose two of its properties – adhesiveness and pseudocapacitance – even despite the change in the electronic and optical properties<sup>64,66</sup>. This is most presumably due to the residual catechol and quinone groups not destroyed during the high-temperature treatment. The overall hydrophilicity is slightly reduced, though<sup>65</sup>.



**Figure 9.** HRTEM image of carbonised PDA nanoparticles and scheme of graphite-like stacking<sup>70</sup>.

Poor mechanical properties associated with high roughness and agglomeration present a significant obstacle to the application as a component of certain materials and devices. This issue is particularly pressing in the realm of electrochemical applications (sensing, supercapacitors, etc.)<sup>21</sup>. One potential solution is the abovementioned pyrolytic graphitisation of PDA. However, an alternative approach was proposed by Lee et al. in a 2020 paper published in Nature Communications<sup>71</sup>, which introduces the laser-graphitisation protocol for PDA (**Figure 10**). In this study, PDA was deposited onto quartz through standard oxidative polymerisation in Tris buffer. Subsequently, it was separated from the surface and subjected to treatment with a blue diode continuous laser with a power output of 1–2 W. The results demonstrated that partial graphitisation occurred, with covalent coupling between PDA units. This modification led to a remarkable 100-fold increase in scratch resistance and improvements to other mechanical parameters. The original high-roughness layer was transformed into a uniform 37-

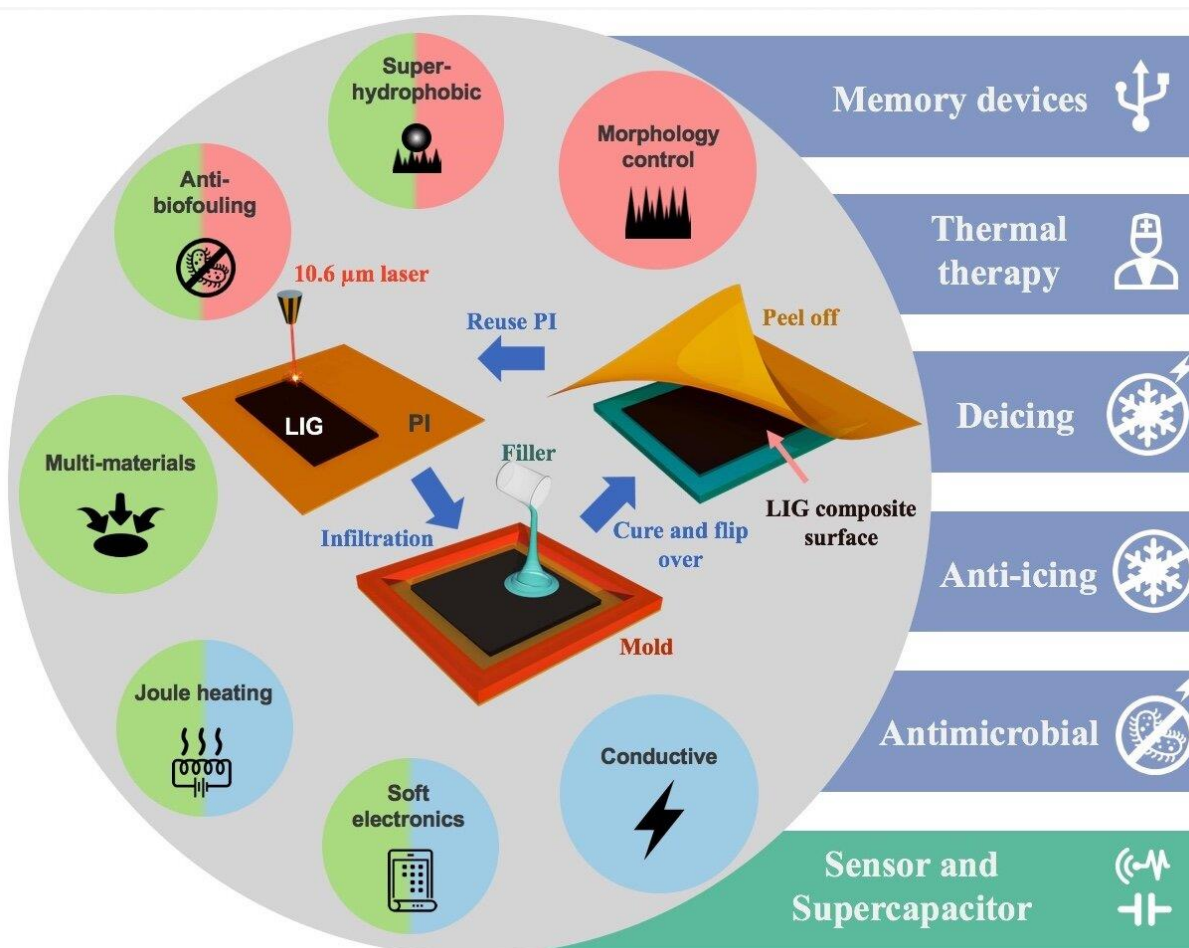
nm film devoid of agglomerated PDA nanoparticles. Importantly, the desirable properties of PDA, such as high adhesiveness and resistance to biofouling associated with the presence of catechol functionality, were preserved to the high extent.



**Figure 10.** Laser graphitisation of PDA; a) proof-of-concept graphics; b) Raman spectra; c) D/G Raman peaks ratio; d) XPs spectra in the carbon C1s region; e) atomic content as a function of the laser power; f–g) mass spectrometry results of pristine and laser graphitised PDA<sup>71</sup>.

The outcome of the laser graphitisation, abbreviated as lgPDA or LAPDA, can be categorised as a member of the broader group of materials, i.e. laser-induced graphene/graphite (**Figure 11**). The purpose of PDA lasing is to transform a weakly conducting  $\pi$ -conjugated organic polymer, such as polyether ether ketone (PEEK) or polyetherimide (PEI), into a carbon-based sheet with exceptional conductivity, typically N-doped graphene/graphite<sup>72–74</sup>. From an electrochemical standpoint, this treatment effectively enhances the charge transfer rates at the interface between the electrode and the electrolyte. In general, laser induced graphene (LIG) has a wide range of applications, including but not limited to electrochemical sensing, supercapacitors, electrocatalysis, and photodetectors<sup>75,76</sup>. A drawback of laser graphitisation that may limit its electrochemical applications is the increased hydrophobic behaviour in comparison to the initial polymer changing into the carbon phase. Additionally, if some parameters, e.g. fluence, are not optimised, the initial nanostructure might be strongly distorted or destroyed.

Given the current state-of-the-art, Laser-Induced Graphitisation emerges as an appealing, energy-efficient tool for PDA graphitisation, primarily due to the significantly lower energy dissipation. Moreover, an inert atmosphere is typically sufficient in contrast to pyrolysis or hydrothermal treatment<sup>77</sup>. This idea holds significant potential not only in enhancing PDA's mechanical properties and expanding its library of chemical structures, but also in elucidating its complex electronic structure.



**Figure 11.** Diagram of applications for laser induced graphene-based materials<sup>78</sup>.

## 2.2. Polyzwitterions (PZ)

*And this is the misery and the terror of the paradox, in human terms, it can never be comprehended.  
I to właśnie jest nędza i trwoga paradoksu, że paradoks, mówiąc po ludzku, nigdy nie daje się pojąć.*

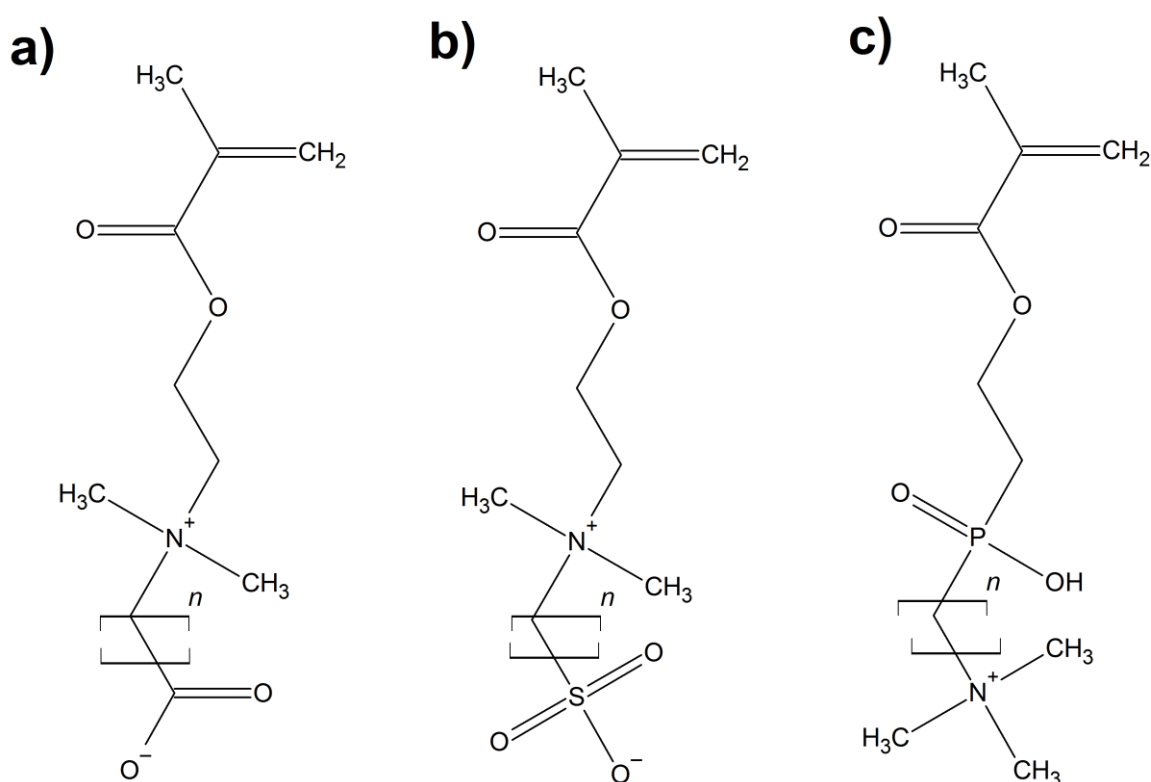
**Søren Kierkegaard** – Danish philosopher and theologian; ‘Fear and Trembling’ (1843)

### 2.2.1. PZ chemical structure and synthesis

Zwitterions are molecules containing both positively and negatively charged functional groups with zero net charge. They are frequently abundant in biochemistry, as most amino acids, choline derivatives, carnitine, some peptides, and polynucleotides are zwitterions<sup>79,80</sup>. From a materials science perspective, the most important subgroup is polyzwitterions (PZ). According to the terminology defined by

Laschewsky, polyzwitterions are polymers, which ‘bear, within their structural repeating unit, the same amount of cationic and anionic groups’<sup>81</sup>. Some authors distinguish strong PZs, where every unit has two oppositely charged ionic groups, and weak PZs, where only a portion of the units bear simultaneously two ionic groups<sup>82</sup>.

Three exemplary structures of synthetic monomers for PZ synthesis are given in **(Figure 12)**. It can be easily seen that these monomers are methacrylates possessing a C=C bond, which is susceptible to different types of polymerisations. Products of polymerisation include poly(carboxybetaine methacrylate) (PCBMA), poly(sulfobetaine methacrylate) (PSBMA) and poly(phosphoryl choline methacrylate) (PMPC).



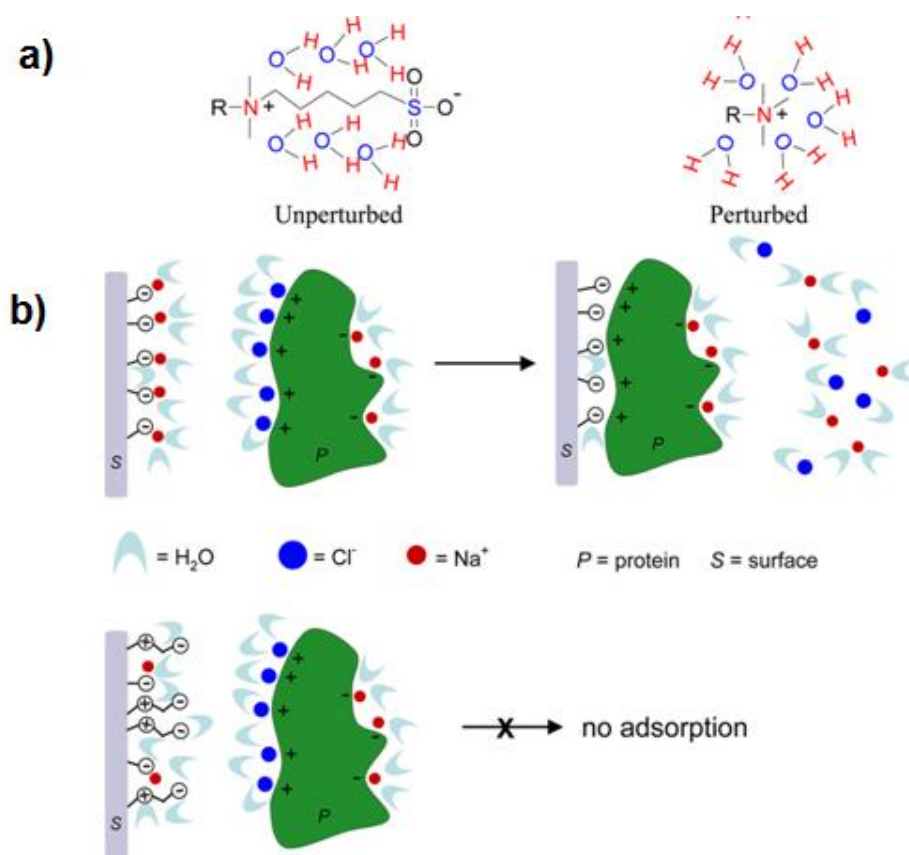
**Figure 12.** Three canonical monomers used for synthesis of polyzwitterions; a) carboxybetaine methacrylate (CBMA), b) sulfobetaine methacrylate (SBMA), c) phosphorylcholine methacrylate (MPC). Value of  $n$  is typically 1–3 methylene groups<sup>83</sup>.

Monomers can differ by the number of methylene groups that separate the cationic and anionic moieties (integer  $n$  in **Figure 12**), i.e. a spacer. The length of the spacer is crucial and determines the strength of the intermolecular interactions of poly(zwitterions)<sup>84</sup>, which consequently determine their physiochemical properties and application potential. The significantly most commonly studied PZs in the literature are PSBMA, PCBMA and PMPC, mainly due to the commercial availability of monomers<sup>80</sup>. However, there are increasing scientific efforts towards expanding the structural diversity of PZs, both in terms of their chemical structure and physical deposition strategies<sup>85</sup>. The molecular

structure of zwitterions is a source of their unique properties at both the microscopic and macroscopic levels. From a nanoscale perspective, they exhibit strong intramolecular and intermolecular electrostatic and van der Waals interactions (dipole and multipole), which dictate their macroscopic properties<sup>80,86</sup>.

### 2.2.2. Antifouling property and hydration structure of zwitterions

Zwitterions are commonly applied as a coating for different surfaces to increase their fouling resistance, i.e. their ability to resist the non-specific adsorption of biomolecules, typically proteins, and whole cells and microorganisms. This antifouling property of PZ is defined as the ability to reduce the adsorption of biomolecules (e.g. proteins) and whole cells onto their surface. This property opened up a vast area of applications involving biocompatible coatings<sup>87</sup>, membranes for ultrafiltration<sup>88</sup>, sensing of biomolecules<sup>89</sup> and many more. The detailed antifouling mechanism at a molecular level is a complicated issue and was thoroughly discussed by Schlenoff<sup>86</sup>. He included arguments based on perturbation of the hydrogen bond structure in the proximity of the PZ-coated surface (entropic contribution) and counterion release (enthalpic contribution). As PZs do not perturb the structure of hydrogen bonds in the solution and do not have counterions to be released, the free energy of protein adsorption is generally very high on PZ-coated surfaces (**Figure 13**). Because of the antifouling property, PZ is an excellent candidate as a coating for electrochemical sensors.

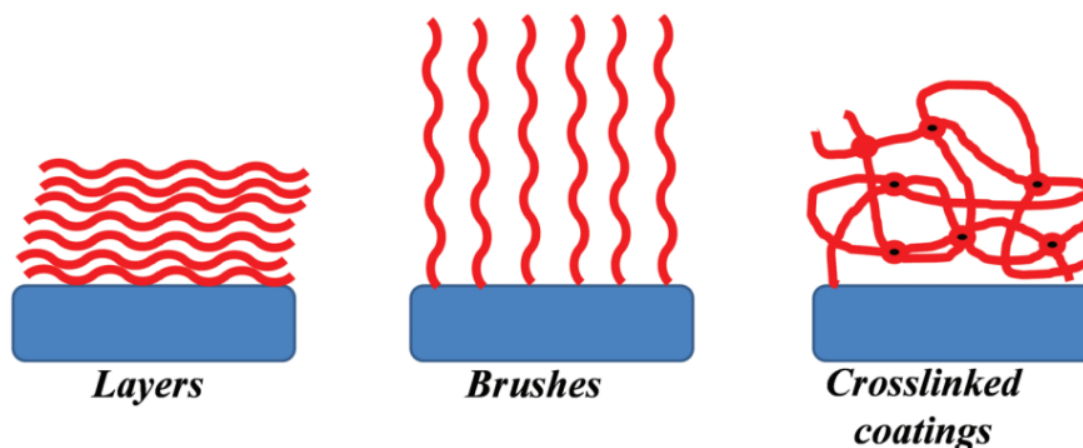


**Figure 13.** a) Zwitterions leaving the structure of hydrogen bonding in water unperturbed and b) antifouling mechanism on the molecular level involving a lack of counterion release<sup>86</sup>.



### 2.2.3. Modification of surfaces with PZ

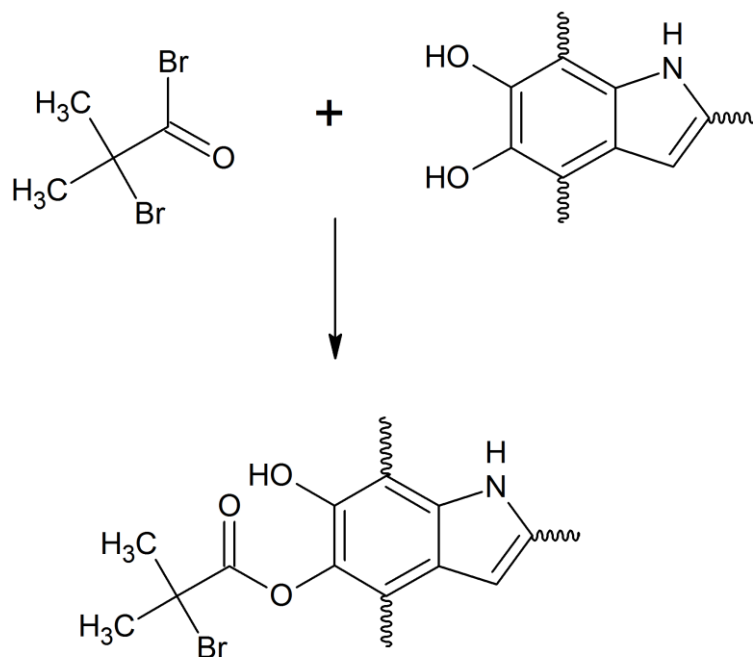
PZ exhibits different morphologies and topologies on modified surfaces (**Figure 14**). They typically include layers, brushes, and crosslinked coatings. Synthetic methods for the modification include layer-by-layer deposition by, e.g., evaporation of a solvent<sup>82</sup>, which is typically accompanied by other polymeric materials. Polyzwitterions in aqueous solutions tend to associate with polycations and polyanions, forming stable solvated structures. In this state, they gain the ability to physically adsorb onto a surface. In a study by Kharlampieva *et al.*<sup>82</sup>, PCBMAs were deposited by adsorption with polycation or polyanions from an aqueous solution on flat silica wafers. The whole process was carried out in a weakly acidic solution (pH = 4.5) to facilitate the adhesion of PCBMA. Therefore, multilayered films with thicknesses of 2 to 20 nm (measured by ellipsometry) were obtained, which represents progress in the field. Layers can consist of parallel chains or be crosslinked, for example via crosslinking agents or photopolymerisation<sup>90</sup>.



**Figure 14.** Simplified topologies of PZ-modified surfaces.

Although the layers are relatively easy to obtain, they have a certain window of stability in terms of pH (protonation or deprotonation of carboxylic groups) and salt concentration (antipolyelectrolyte effect), outside which they become soluble. Some of them are stable only at a very acidic pH<sup>91</sup> and some are stable in a neutral or weakly acidic pH (co-deposition with tannic acid)<sup>92</sup>, all depending on the structure of the co-deposited material.

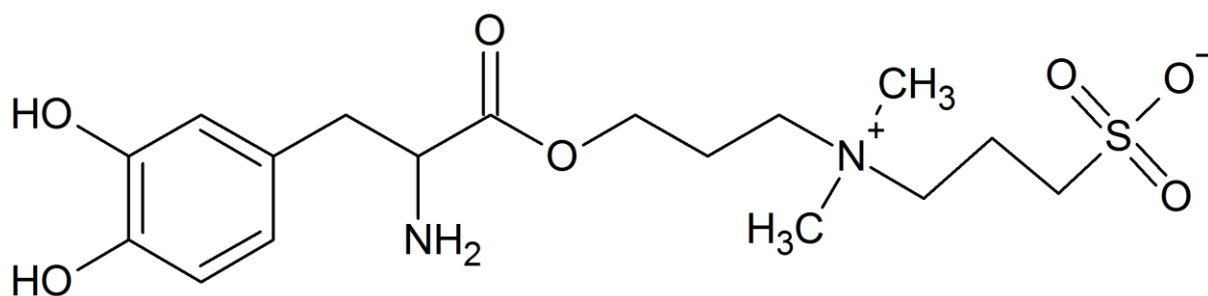
Another possible shape of the PZ deposited on the surface is brushes. However, one crucial requirement is a covalent attachment of the polymerisation initiators onto the desired surface. A very promising strategy for covalent attachment is employing polydopamine chemistry (**Figure 15**). In this approach, PDA is first deposited on the surface and then catechol groups of PDA are prone to nucleophilic addition/substitution, which can be utilised in the covalent attachment of initiators (e.g. bromoisobutyrate bromate BiBB). The brushes are synthesised by controlled polymerisation. A prominent example of such technique is Atom Transfer Radical Polymerisation (ATRP).



**Figure 15.** Covalent attachment of bromoisobutyrate bromide BiBB initiator (top left) to the surface of polydopamine (top right)<sup>83</sup>.

PDA can be utilised in the synthesis of crosslinked PZ coatings as well. Zhou *et al.* obtained copolymer cross-linked PDA / PSBMA membranes with enhanced antifouling properties and washing stability by simple one-pot deposition on a porous polypropylene substrate<sup>88</sup>. Simultaneous deposition of PSBMA and polymerisation of dopamine at a slightly alkaline pH led to stable porous polyelectrolytic membranes. Photopolymerisation is also a universal tool for obtaining cross-linked PZ hydrogels and electrolytes not only in free-standing form and as functional materials, e.g. biosensors<sup>89</sup>.

Increasing the structural diversity of zwitterionic monomers, polymers and materials is of paramount importance in the field. Yeon *et al.*<sup>93</sup> synthesised such a monomer based on a dopamine derivative and sulfobetaine (**Figure 16**). Then oxidative polymerisation was conducted using air oxygen in Tris buffered solution, ammonium persulfate and sodium periodate (NaIO<sub>4</sub>). The more oxidative the factor used, the faster the kinetics and thicker the films that were achieved from 1.1 to 40 nm. The presence of both catechol and primary ammonium groups abundant in the polymerised dopamine derivatives, leads to superior adhesion properties to various substrates. In a study by Yeon<sup>93</sup>, Ti/TiO<sub>2</sub>, stainless steel, and nylon surfaces were successfully coated with a polyelectrolytic dopamine derivative, indicating a high versatility of this synthesis approach. All coatings exhibited strong antifouling behaviours in the presence of a marine environment. A similar polymer was also used in protein binding applications<sup>94</sup>.



**Figure 16.** ZI dopamine monomer<sup>93</sup>.

In my thesis, different approaches to merging the properties of PDA and PZ are proposed. Considering that the purpose of the coatings is to change the electrochemical properties towards sensing or supercapacitance, the co-electropolymerisation technique is developed. According to the knowledge of the author, no such approach has been proposed to date. It is anticipated that co-electropolymerisation will be more suited to the electrochemical application due to the higher conductivity of the materials in comparison with organic chemistry routes.

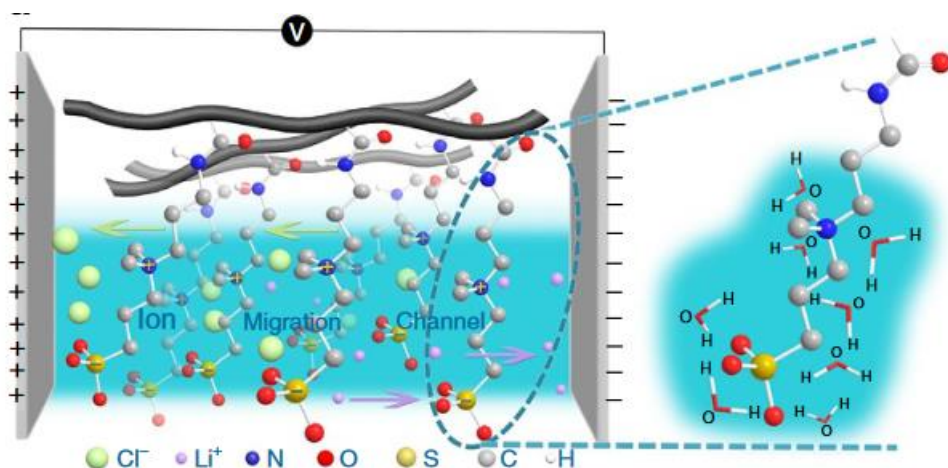
#### 2.2.4. Mechanical and electrical properties of PZ

Several interesting properties of zwitterated<sup>86</sup> materials were observed during tensile testing. Solvent-cast phosphine-based PZ exhibits a markedly higher tensile strength due to physical crosslinking than its polycation analogues, caused by attractive intermolecular interactions of the PZ<sup>95</sup>. Large dipole moments enforced by the molecular structure of the polymer lead to ionic associations that reinforce the mechanical structure of the material. The existence of those ionic aggregates was confirmed by SAXS (Small-Angle X-Ray Scattering). As a natural consequence of crosslinking, the elasticity of the polymer decreases, and the glass transition temperature  $T_g$  increases.

Another manifestation of the electrostatic interactions is the capability of PZ towards self-ordering when an external electric field is applied. This effect can be beneficial in energy storage applications, as the specific capacity of zwitterion-based supercapacitors is enhanced with respect to the analogous materials without zwitterions<sup>96,97</sup>.

In polyelectrolytes for PZ-based supercapacitors, this ordering led to the creation of fast transport channels of ions, as implemented by Peng *et al.*<sup>97</sup> (**Figure 17**). They worked on a zwitterionic gel electrolyte that can be used in graphene-based solid-state supercapacitors. In this case, poly(propylsulfonate dimethylammonium propylmethacrylamide) (PPDP) was used. A volume capacitance of  $300.8 \text{ F cm}^{-3}$  at  $0.8 \text{ A cm}^{-3}$  was achieved, and the authors claimed that this value is the best among previously reported ones for graphene-based solid-state supercapacitors (SCs).





**Figure 17.** a) Ion migration channels in PZ-based electrolytes; b) XANES spectrum of the PZ<sup>97</sup>.

Moreover, it should be underlined that capacitance retention at the level of 103% was maintained after 10,000 charge/discharge cycles. A similar approach was applied in the works of Ge and Liu<sup>98</sup>, Diao *et al.*<sup>99</sup>, and Hyeon *et al.*<sup>100</sup>. In the last example, the fabricated SC exhibited an ionic conductivity of 20 mS cm<sup>-1</sup> and a specific capacitance of 677 F g<sup>-1</sup>. In addition to supercapacitors, the application of PZ as electrolytes in lithium-ion batteries<sup>101,102,103</sup>, a vanadium redox flow battery<sup>104</sup>, and a Zn metal battery<sup>105</sup> are also reported.

### 2.3. Boron-doped Carbon Nanowalls (B:CNW)

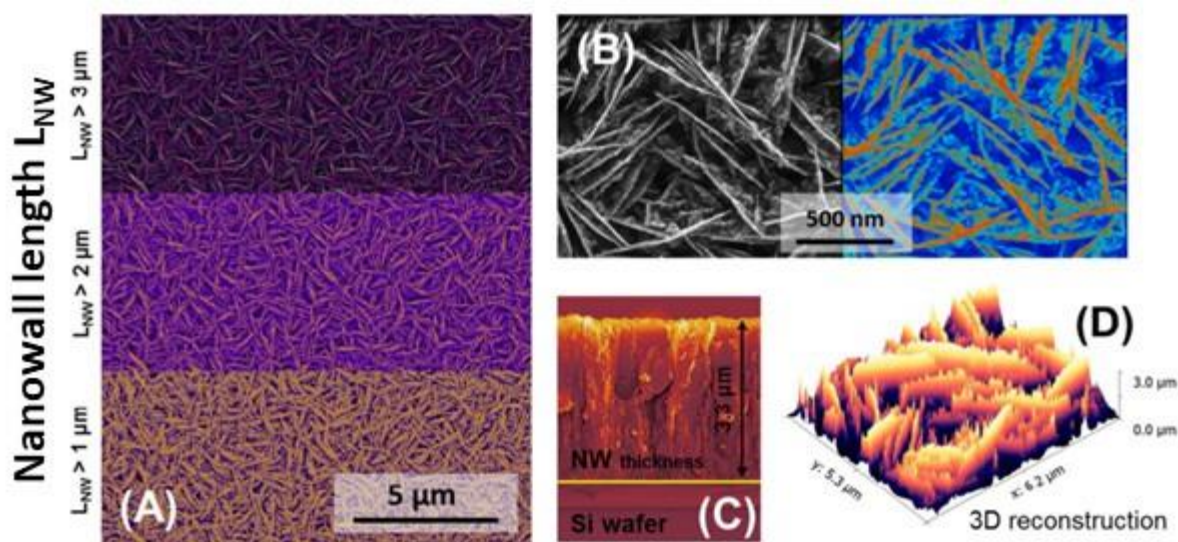
*A detail can only be understood against the background of the whole,  
and the explanation of the detail presupposes the explanation of the whole.*

*Szczegół można zrozumieć jedynie na tle całości,  
a wyjaśnienie szczegółu z góry zakłada wyjaśnienie całości.*

**Friedrich Schleiermacher** – German philosopher and theologian; (XVIII–XIX century)

#### 2.3.1. Overview and synthesis of boron-doped carbon nanowalls

Boron-doped carbon nanowalls (B:CNW) are carbon-based semiconductor electrodes synthesised during plasma-enhanced chemical vapour deposition (PE-CVD). While the pristine diamond nanostructures are insulators, the purpose of incorporating boron is p-doping of the carbon to enhance the overall conductivity. Nanowalls form a forest of vertically oriented graphene plates with a polycrystalline, fractal structure composed of both sp<sup>2</sup> and sp<sup>3</sup> phases. The presence of both phases is confirmed by the T, D, and G bands that can be found in the Raman spectra<sup>106</sup>. While sp<sup>2</sup> graphitic carbons provide  $\pi$ -conjugation, leading to a high surface conductivity, sp<sup>3</sup> diamond-like carbons tend to increase the catalytic properties of the electrode. Moreover, due to its fractal structure, B:CNW exhibits a very high electroactive surface area (EASA) (**Figure 18**).

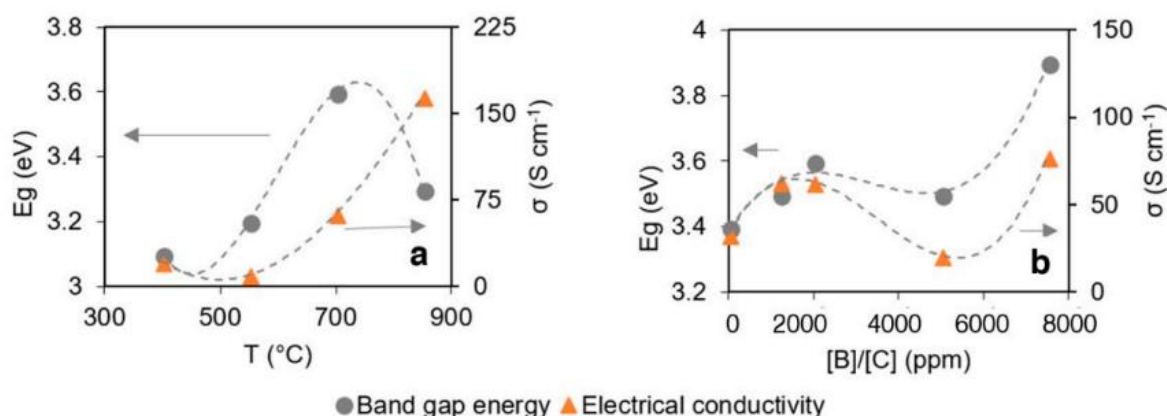


**Figure 18.** Morphology of B:CNW (A) nanowall length distribution, (B) top view with the nanowall pattern, (C) cross-sectional image and (D) three-dimensional reconstruction of the nanowall surface<sup>107</sup>.

The B:CNW growth mechanism is based on the joint chemistry of many species in plasma, not only limited to CN, CNH<sub>x</sub>, BH<sub>x</sub>, and CH<sub>x</sub> radicals<sup>106</sup>. Boron doping allows for formation of sharp-edged, flat, and up to 3 μm long carbon walls<sup>107</sup> with superior electrochemical performance ( $k^\circ = 1.1 \times 10^{-2} \text{ cm s}^{-1}$  and  $\Delta E = 85 \text{ mV}$ ). On the contrary, undoped CNW samples do not present highly developed maze-like structures with a high surface area that alters the fast kinetics at multiple redox centres ( $k^\circ = 3.7 \times 10^{-3} \text{ cm s}^{-1}$ ). Pristine CNWs revealed a significantly narrower electrochemical potential window in 0.5 M K<sub>2</sub>SO<sub>4</sub> electrolyte with pH = 7 (measured against an Ag | AgCl | 3 M KCl reference electrode) with irreversible oxidation (+0.83 V) and reduction peaks (−0.50 V)<sup>107</sup>.

### 2.3.2. B:CNW properties

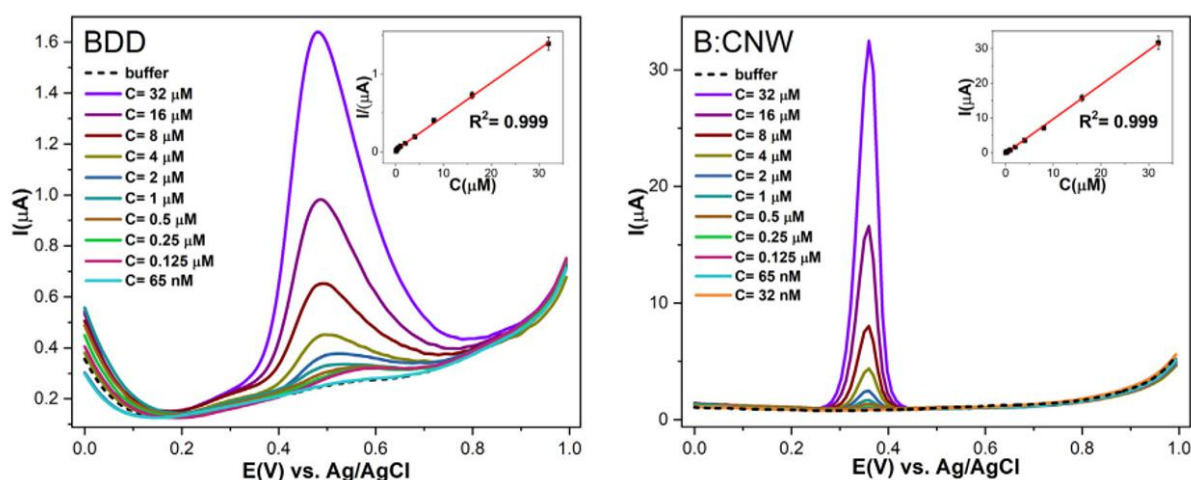
The bandgap of the nanowalls is a non-linear function of the temperature during synthesis and boron doping (**Figure 19**). In general, there is an optimum concentration of the dopant for which the gap is minimised. Moreover, for boron concentrations higher than  $2 \times 10^{20} \text{ atoms per cm}^3$ , a transition between p-type conducting CNW to semi metallic is observed, where the current is dominated by the temperature-independent carrier concentration with mainly nearest-neighbour hopping conduction<sup>106</sup>. Another crucial factor determining the electronic structure of the carbon nanostructures, including nanowalls, is surface terminations. DFT calculations have shown that both the nature of the functional groups, their density, geometric pattern, and the crystallographic plane on which they are attached are important determinants of the bandgap<sup>108</sup>. The surface of the nanowalls can be rich in functional groups involving ketones, alcohols, esters and carboxyl, as well as defect sites and unsaturated bonds, forming a set of unique electronic states relevant for bandgap engineering and electrocatalysis<sup>106</sup>.



**Figure 19.** Variations of the bandgap ( $E_g$ ) of boron-doped carbon nanowalls. (a) Optical bandgap ( $E_g$ ) and electrical conductivity ( $\sigma$ ) for B:CNW growth at 400 $^{\circ}C$ , 550 $^{\circ}C$ , 700 $^{\circ}C$ , and 850 $^{\circ}C$  at a ratio of 2,000 ppm [B]/[C]; (b) optical bandgap and electrical conductivity for B:CNW growth at 0, 2,000, 5,000, and 7,500 ppm [B]/[C] at 700 $^{\circ}C$ <sup>109</sup>.

### 2.3.3. Electrochemical sensing on B:CNW

Consequently, great potency of boron-doped carbon nanowalls in electrochemical sensing has been reported with superior performances of as-synthesised electrodes without further modifications. Due to the interplay between the  $sp^2$  and the  $sp^3$  phases and the high EASA with sharp edges, the kinetic constant of the redox reactions is higher with respect to boron-doped diamond and undoped nanowalls, resulting in higher currents from electroanalytical processes. In particular, paracetamol<sup>110</sup>, adenine and guanine DNA bases<sup>107</sup>, and nitroaromatic compounds<sup>111</sup> were detected with sensitivities and low detection limits comparable to other state-of-the-art carbon-based materials (**Figure 20**). However, no surface functionalisation with biomolecules was used prior to the detection.



**Figure 20.** Comparison of BDD (left) and B:CNW (right) in the electrochemical sensing of paracetamol via the difference pulsed voltammetry (DPV) technique<sup>110</sup>.

Additionally, B:CNWs can be coupled with titanium dioxide to produce several new properties. For example, transparent nanowalls grown on quartz were modified with a  $\text{TiO}_2$  layer by sol-gel deposition. In this junction, B:CNW facilitates the separation of photogenerated charges and directs the crystal structure of the  $\text{TiO}_2$  towards anatase. Effectively, this structure exhibits excellent performance towards the photocatalytic oxidation of nitrogen oxide (NO) in a plug-flow reactor<sup>112</sup>.

## 2.4. Hydrogenated titania nanotubes (TNT)

*What is good either was or will be, but never is.*

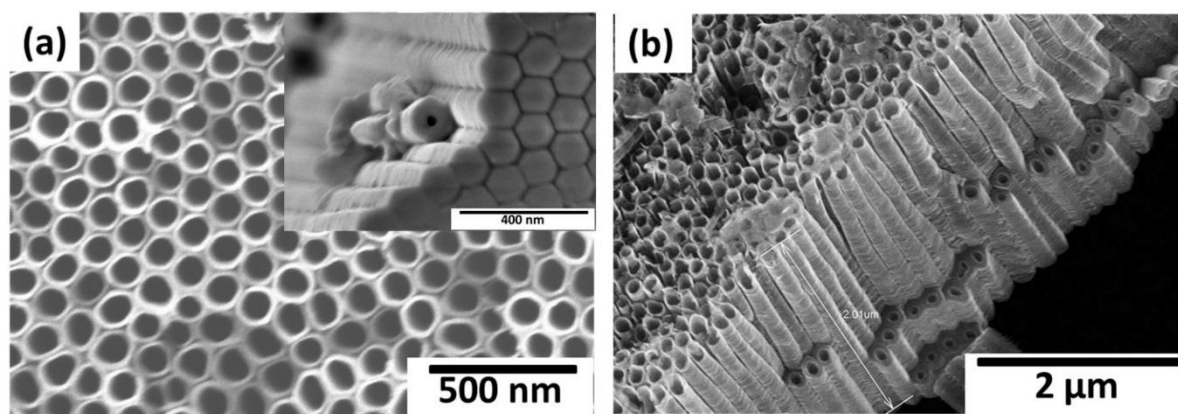
*To co dobre – albo było, albo będzie – ale nigdy nie jest.*

**Emil Cioran** – Romanian pessimistic philosopher; *The Evil Demiurge* (1967)

### 2.4.1. Overview of TNT

Titanium dioxide is a model n-type semiconductor with a wide range of applications in dye-sensitised solar cells, photocatalysis, photoelectrochemical water splitting and degradation of pollutants. Although they are hindered by the low electrical conductivity and high indirect bandgap (c.a. 3.1 eV<sup>113,114</sup>), it has a high propensity towards photosensitisation and surface modifications with other materials. Moreover, nanostructurisation enhances the surface area and alters the electronic structure, which are both beneficial for the abovementioned applications.

In particular, titania nanotubes are promising templates for photoelectrocatalysis and supercapacitors because of their large surface area and permanent connection to the Ti current collector<sup>115</sup>. The facile and inexpensive synthetic approach towards  $\text{TiO}_2$  nanomaterials involving anodisation results in high scalability and repeatability of the manufacturing.  $\text{TiO}_2$  can be found in three phases – anatase, rutile, and brookite – with different crystallographic systems. As formed, titania nanotubes are amorphous but can be easily crystallised thermally. The morphology of a nanotube array measured by scanning electron microscopy (SEM) is shown in **Figure 21**.



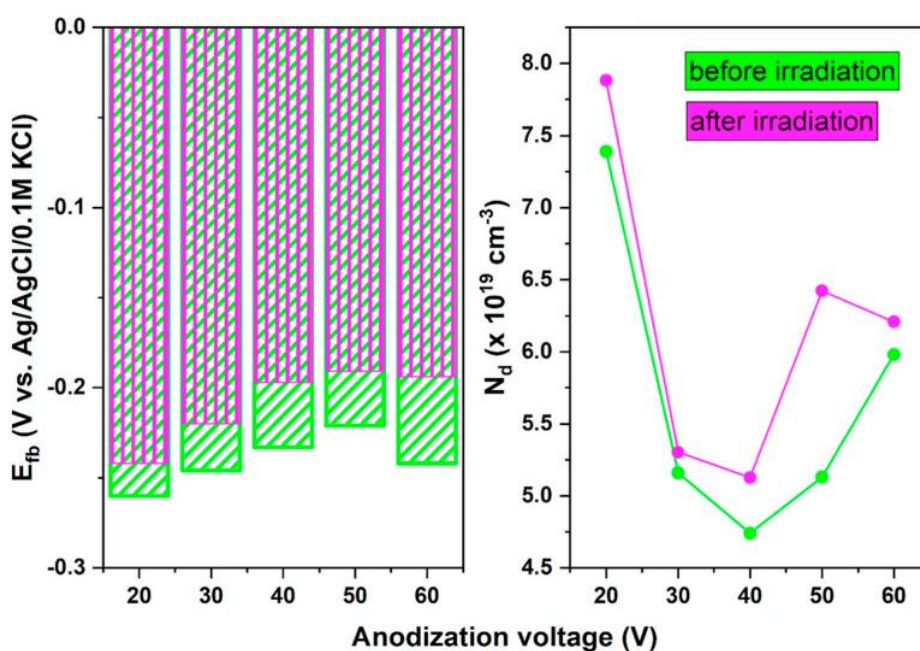
**Figure 21.** SEM images of a titania nanotube a) top view, b) side view<sup>116</sup>.



### 2.4.2. Fabrication of TNTs by anodisation

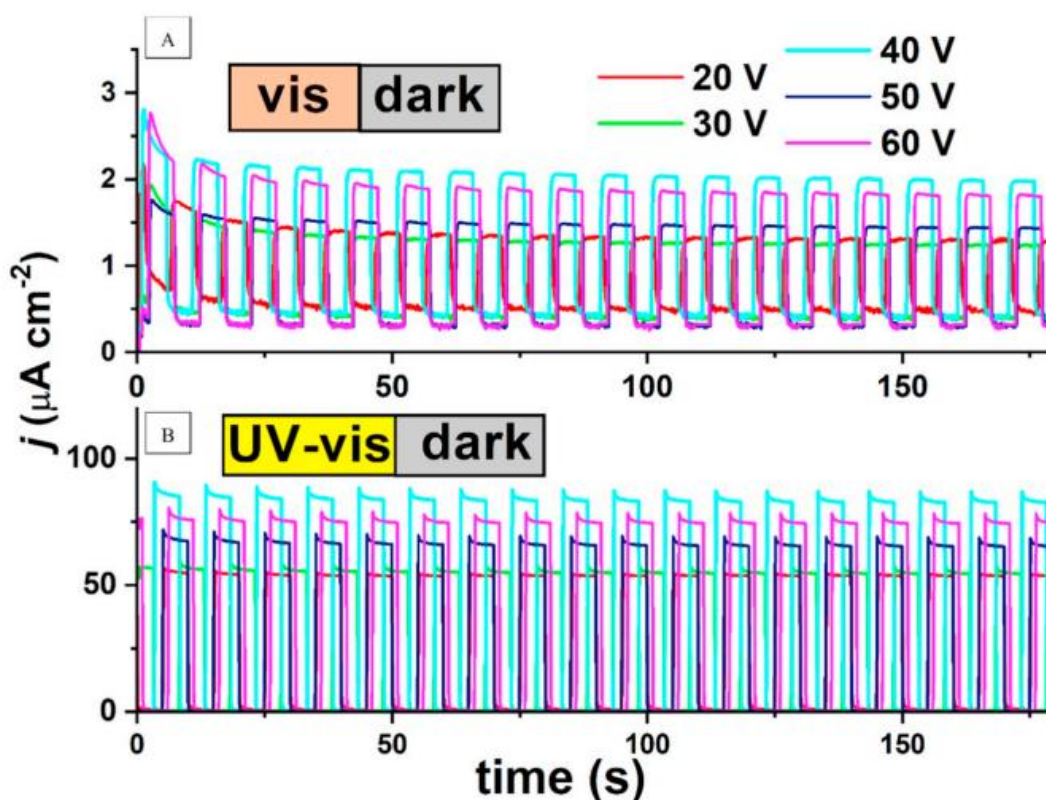
Anodisation is a process of oxidising titanium – an anode – to porous titanium dioxide. Typically, this process is carried out in a two-electrode setup where the cathode is a Pt mesh aligned parallel to the Ti plate. The product of the anodisation is porous  $\text{TiO}_2$  layers or nanotubes. Depending on the anodisation parameters, such as voltage profile, temperature, and electrolyte content, different morphologies can be obtained. As a first approach, electrolytes based on water and ethylene glycol were proposed and enabled the production of compact and tightly packed nanotubes. Later on, diethylene glycol (DEG) and dimethyl sulfoxide (DMSO) electrolytes were explored and lead to the formation of loosely spaced nanotubes. In general, increasing the anodisation time results in elongation of the nanotubes, however, in the case of loosely spaced nanotubes, it provides a minor effect. Similarly, voltage in the range between 10 V and 40 V also leads to increased lengths and diameter of the nanotubes. However, after crossing 50 V, the morphology resembles a sponge instead of nanotubes. Experiments performed at lower temperatures result in spongy layers, but at 40°C and above, loosely spaced nanotubes are created.

The anodisation voltage has a profound influence not only on their morphology but also on their physiochemical properties (**Figure 22** and **Figure 23**). In particular, there is a parabolic relation between the anodisation voltage, and the flat band potential and the charge carrier concentration, measured from EIS measurements and using the Mott-Schottky relation<sup>117</sup>.



**Figure 22.** Influence of the anodisation voltage on the physiochemical parameters of loosely spaced titania nanotubes. Dependence of the flat band potential (left panel) and charge carrier concentration (right panel)<sup>118</sup>.

As a result, the photocurrent density recorded for electrodes overgrown by nanotubes also varies with the anodisation voltage, with 40 V nanotubes being most photoactive during both UV and UV-VIS exposure. However, those relations are not straightforward because the maximum of the photocurrents roughly corresponds to the minimum of the charge carrier concentration, which seems to be contradictory. In other words, there are other phenomena, possibly involving surface states and defects, such as oxygen vacancies, that govern the experimentally observed relations.

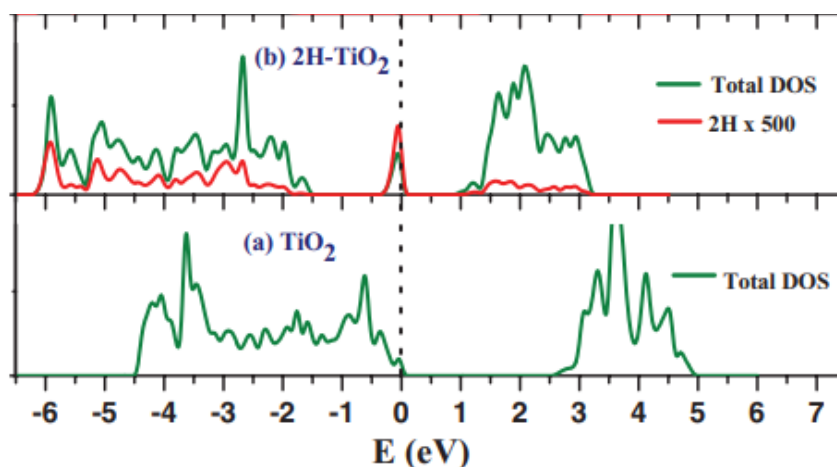


**Figure 23.** Influence of anodisation voltage on transient A) vis and B) UV-vis photocurrent response<sup>118</sup>.

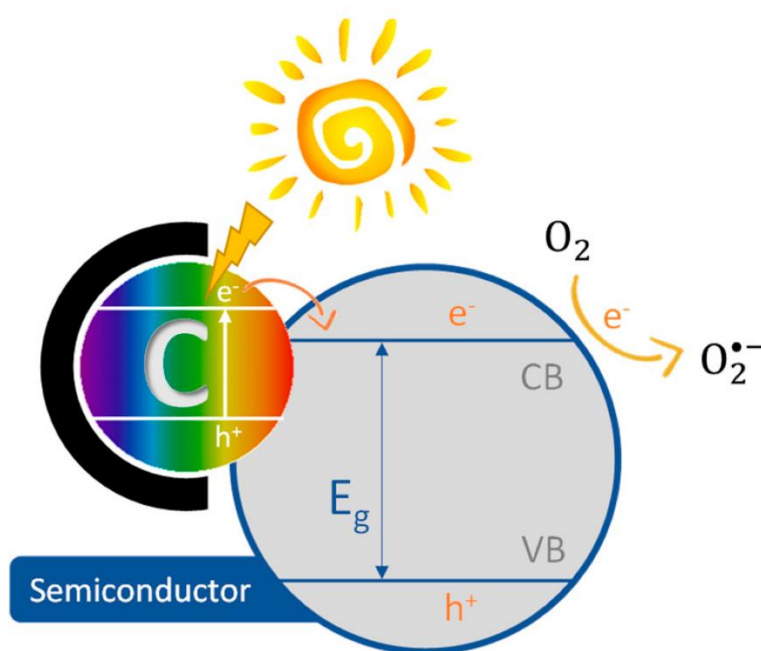
### 2.4.3. Bandgap engineering and photosensitisation of TNTs

Titania nanotubes have a wide bandgap and are poorly conductive, which significantly hinders their electrochemical applications. However, there are several ways to improve their conductivity by doping or hydrogenation (black titania)<sup>119–121</sup>. These include high-pressure treatment or annealing in a hydrogen atmosphere, as well as electrochemical reduction<sup>122</sup>. The last one is especially attractive, due to the simplicity and inexpensiveness of the process and the possibility of obtaining very high surface conductivities. Hydrogen atoms have been shown to penetrate into the unit cells of TiO<sub>2</sub>, altering the symmetry and injecting electrons into the conduction band<sup>123</sup>. Moreover, DFT calculations show that energy levels related to the hydrogen dopant are introduced inside the bandgap (**Figure 24**). A notable drawback of this method is the phenomenon of the trapped hydrogen atoms escaping, accompanied by conductivity losses over time. However, even after that, there are structural changes that lead to

a long-term increase in the conductivity, such as the permanent strain of surface crystallites, introducing point defects and changes of the symmetry towards  $\text{Ti}_2\text{O}_3$ <sup>124</sup>.



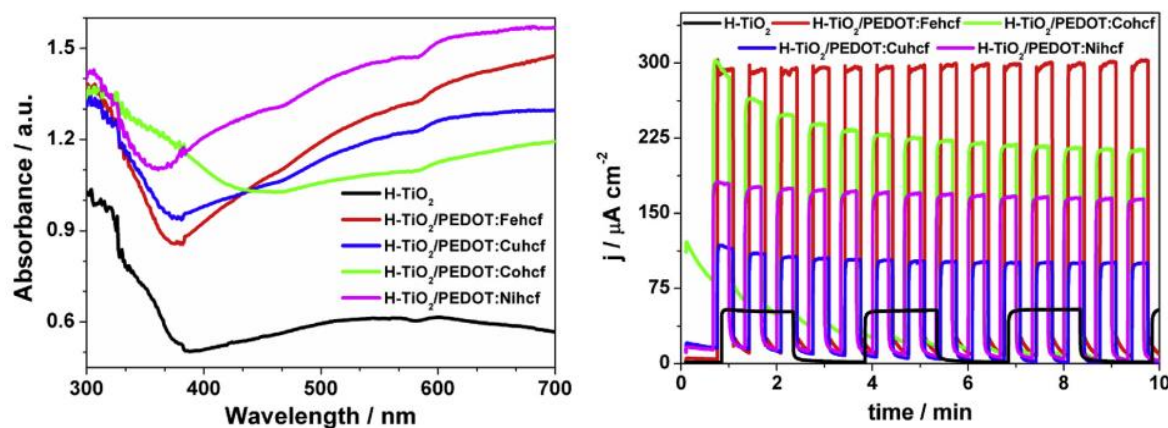
**Figure 24.** DOS calculations of pristine and hydrogenated  $\text{TiO}_2$ <sup>123</sup>.



**Figure 25.** Photosensitisation scheme for example  $\text{Au}_x - \text{GSH}$  photosensitiser<sup>134</sup>.

Titania nanotubes can also be doped with other elements, such as nitrogen<sup>125</sup>, iodine<sup>126</sup> and metal oxides, such as nickel, tungsten, chromium, and molybdenum oxides<sup>127–130</sup>, or photosensitised with molecules<sup>131,132</sup> and semi-conducting polymers, such as PSS:PEDOT (polystyrene sulfonate: poly(3,4-ethylenedioxythiophene)) and PDA<sup>29,48,133</sup>. Various modification routes can be also mixed. After these modifications, the obtained materials typically have increased absorption and photocurrent response. The reason underlying those changes is the small HOMO-LUMO gap of the photosensitiser

relative to the bandgap of the semiconductor (**Figure 25**). Strong electronic coupling between the electronic levels of the photosensitiser and the substrate – in other words, fast interfacial electron transfer kinetics – is desired. Considering the very promising results from the modification of TNTs with PSS:PEDOT (**Figure 26**), an analogous route with modified deposition parameters for PDA was performed in the thesis.



**Figure 26.** (Left) Optical absorption spectra and (right) transient photocurrent response of hydrogenated nanotubes modified with PEDOT and different hexacyanometalates<sup>135</sup>.

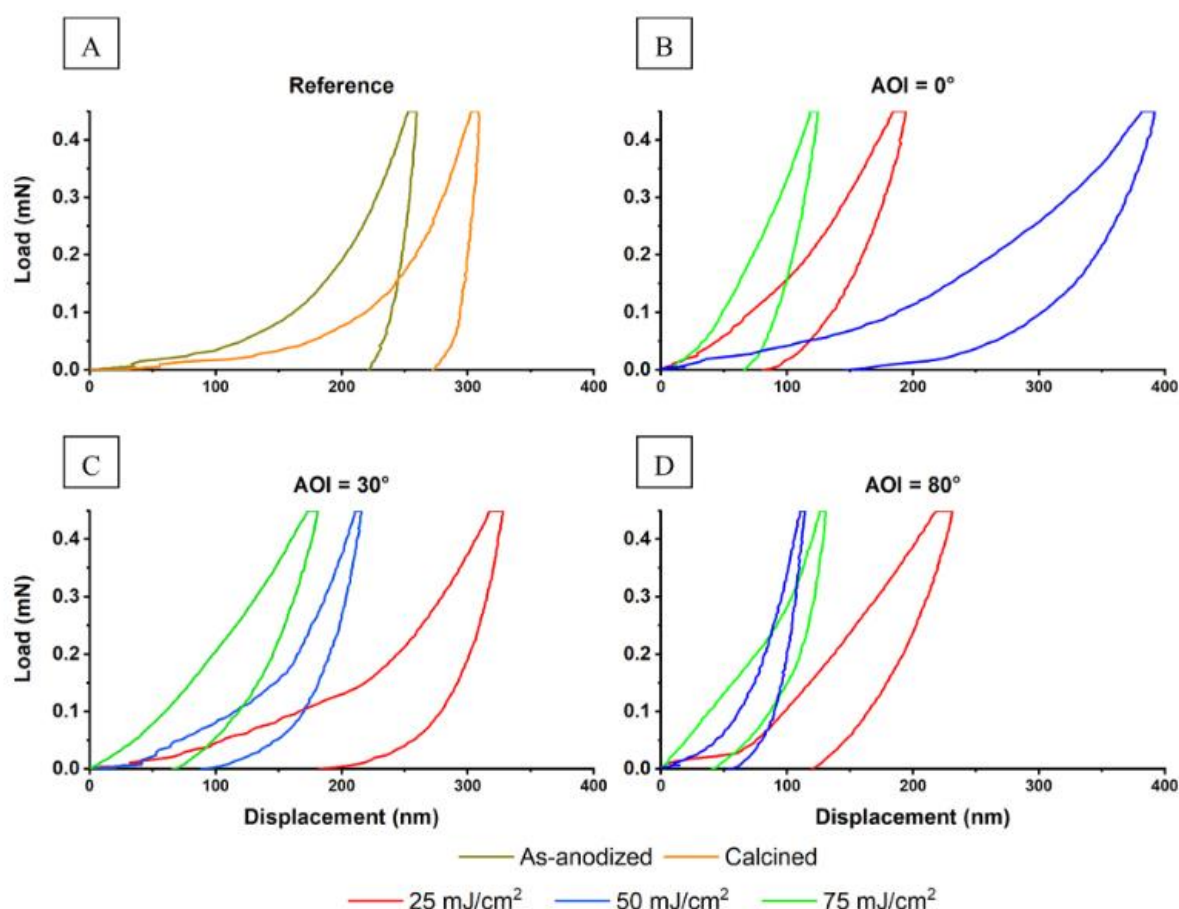
#### 2.4.4. Laser modifications of nanotubes

Another approach towards enhancing the optoelectronic properties of titania nanotubes is their laser modification. The process is based on irradiation of the TNT surface with a pulsed UV laser (typically nanosecond or picosecond pulses<sup>136</sup>) with a perpendicular or tilted direction of the beam<sup>137</sup>. If amorphous (as-anodised) nanotubes undergo the laser treatment, they can be partially crystallised after absorption of the light because of the thermal effect the arises. If TNTs are already crystallised by calcination, the crystal structure becomes disordered at the surface due to the interaction with the laser<sup>138</sup>. This is believed to cause bandgap narrowing and increasing the donor density, thus increasing the absorption in the visible part of the spectrum<sup>139</sup>.

Another aspect of the laser beam interaction with TNT is alteration of the morphology and nanomechanical properties. One example of the former is closing of the nanotubes so they form nanocapsules<sup>140</sup>. Proof of the former statement is given in **Figure 27**, which depicts nanoindentation experiments of such modified nanotubes. Depending on the laser fluence, the modified material exhibits altered hardness and stiffness, although the dependencies are not linear, suggesting multiple factors that determine the overall mechanical performance. The effects of the laser beam are also anisotropic, as the result is dependent on the indenter angle of incidence (AOI).

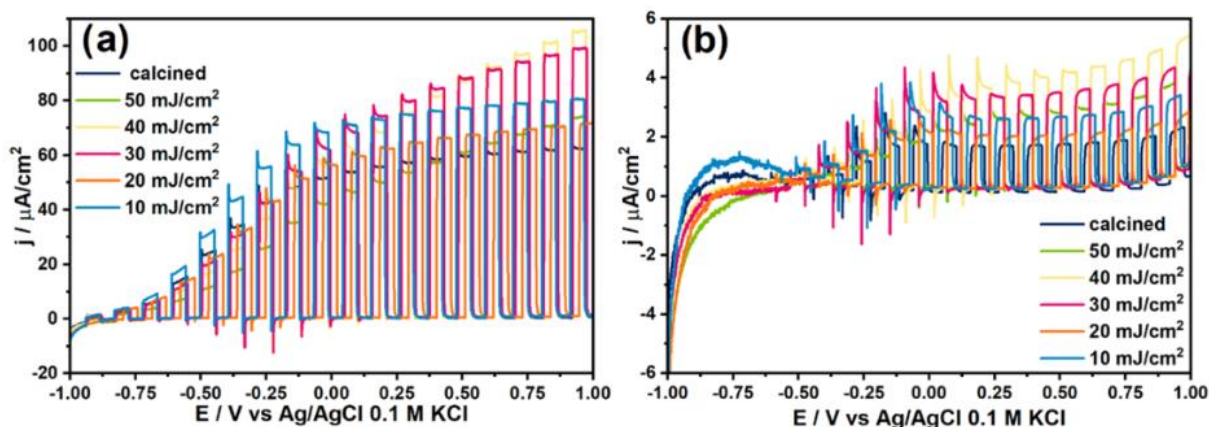


From a photoelectrochemical context, the outcome of such modifications is alteration of the flat band potential (**Figure 22**) and photocurrent generation in the visible range (**Figure 28**)<sup>139</sup>. The boost is strongly dependent on the laser wavelength, fluence and geometrical parameters of the initial TNTs. A higher photocurrent yield is typically observed when larger anodic polarisations of the electrodes are used. While the pristine TNTs exhibit a mild photocurrent-potential dependence, photocurrents of the laser-modified TNTs benefit more from anodic polarisation. Based on low-frequency impedance data, it is also inferred that, after irradiation, the number of deep trap states (ca. 1 V below the conduction band) decreases, while the shallow states remain.



**Figure 27.** Nanomechanical properties of TNTs modified with a laser beam with varying fluence and indenter angle of incidence<sup>141</sup>.

Those observations suggest that laser treatment changes the potential distribution across the space charge region in a complex way, nevertheless allowing a photocurrent increase. Despite this complexity, it is beneficial to find optimal laser wavelengths and fluences to maximise the photocurrent, which is crucial towards enhancement of the performance of photoelectrochemical devices.



**Figure 28.** Photoelectrochemical response in UV-vis (left) and vis (right) of TNT modified with various fluences of a Nd:YAG 355 nm laser<sup>142</sup>.

## 2.5. Research problem

The second semiconductor revolution is ongoing. This time, contrary to 1960, the scientific community has put the focus on nanoscale manipulations, introducing seemingly minor changes to the surface morphology, yet resulting in a profound alteration of the properties. Basing such research on the well-known semiconducting materials as a starting point makes it possible to provide them with new electronic and electrochemical properties, giving them new applications in micro/nano systems. These applications are in the ultrasensitive detection of molecules as well as supercapacitors, solar cells and photocatalytic cells, among others.

One of the most urgent objectives in the field is building bulk heterojunctions by connecting two surfaces with highly developed nanostructured areas. Although building interfaces is relatively easy for planar junctions, the problem is more complex at the nanoscale due to a morphology mismatch and various interactions at the molecular level, which can be either helpful or distorting. The challenge is to obtain a homogeneous bulk heterojunction, where one material is infiltrated to the base by another one and the effective area of contact is maximised. To achieve this goal, the two materials must be chemically compatible to create strong electronic coupling for efficient charge transfer.

Considering the abovementioned literature review related to the topic of the thesis, several intuitions can be extracted. On the one hand, B:CNW is a prominent platform for electrochemical sensing due to its high conductivity and surface area. On the other hand, PDA contains a large amount of functional groups with catalytic activity and capability of redox reactions. It may be possible to link these two properties and effectively boost the B:CNW performance if such a B:CNW\_PDA heterostructure can be successfully fabricated. Moreover, as PZ can provide excellent antifouling properties, which are

beneficial for sensing in biofluids, it may be beneficial to fabricate a mixed PDA\_PZ coating to extend the longevity of such electrodes in harsh environments.

On the one hand, TNT arrays are prominent n-type semiconductors due to their ease of synthesis, large surface area and tailorable properties. In spite of the large bandgap, they can be photosensitised to extend the photoactivity to the visible part of the spectrum. On the other hand, PDA is known for its photosensitisation capabilities and also has a largely tailorable structure. Thus, it may be possible to link those two properties towards developing an efficient photosensitisation strategy and extend the photoactivity of TNTs.

**Therefore, the main problem in the thesis is to elucidate the synthesis-structure-property relations for PDA-semiconductor bulk heterojunction interfaces in the context of electrochemical and photoelectrochemical applications.**

# 3. Research objectives and hypotheses

## 3.1. Objectives

*The aim of theoretical knowledge is truth, whereas the aim of practical knowledge is action.*

*Celem wiedzy teoretycznej jest prawda, a wiedzy praktycznej działanie.*

**Aristotle** – Ancient philosopher – Metaphysics (IV century B.C.)

In reference to the research problem posed above, the main objective of the thesis is proposed:

**The main research objective of the thesis is the fabrication of PDA coatings on B:CNW and TNT semiconductors via electropolymerization in aqueous media followed by structural and electrochemical characterisation towards applications in ultrasensitive electrochemical and photoelectrochemical sensing.**

A series of experiments involving the synthesis and modifications of B:CNW and TNT with PDA-based polymers are conducted throughout the thesis. The primary tool for the deposition of polymers is the electropolymerisation of dopamine and other precursors in an electrochemical three-electrode system. Exploration of the synthesis-structure-property relations is performed towards finding potential applications in electrochemical and photoelectrochemical contexts, as outlined in **Chapter 1**. The character of the work is mostly experimental, although computational physics and chemistry methods (DFT, ReaxFF MD) are used to support the results wherever necessary. Materials are characterised experimentally in terms of their molecular structure (XPS, FT-IR), morphology (SEM), mechanical properties (nanoindentation), as well as electrochemical (CV, EIS) and photoelectrochemical properties (transient photocurrents, IPCE action maps). The main objective of the thesis is split into the following specific objectives:

**Objective 1: Development of PDA and PZ electropolymerisation protocols for B:CNW and TNT surfaces.**

Tasks related to this objective include:

- Application of cyclic voltammetry to activate the surface and polymerise monomers on semiconductor surfaces.
- Exploration of the deposition parameters space (pH, potential windows) and their influence on the electrochemical properties, such as charge transfer rate and double layer capacitance.
- Studies of electropolymerisation mechanisms using voltammetric and impedimetric techniques supported by quantum chemical calculations.

Completion of this objective is crucial for the thesis, as it sets the foundations of the PDA synthesis protocol and description of the properties. Therefore, it enables the realisation of the further objectives.

### **Objective 2: Structural characterisation of B:CNW\_PDA\_PZ and TNT\_PDA composites.**

Tasks related to this objective include:

- Application of SEM to study the surface morphology of the composites, estimation of the PDA thickness.
- Application of the XPS and FT-IR techniques to verify the chemical composition of the obtained PDA and PDA\_PZ coatings.
- Influence of the coatings on the mechanical properties of the composites studied by nanoindentation.

Completion of the objective provides insight into the synthesis-structure-property relationships of the composites. Knowledge gained in this part facilitates further optimisations of the synthesis parameters towards electrochemical and photoelectrochemical applications.

### **Objective 3: Electrochemical properties of B:CNW\_PDA\_PZ and applications in electrochemical sensing.**

Tasks related to this objective include:

- Investigation of the charge transfer between redox markers and the semiconductor surface via voltametric and impedimetric techniques.
- Application of modified B:CNW electrodes in the non-enzymatic sensing of neurotransmitters.
- Influence of the coating on the sensing performance of the modified electrodes.

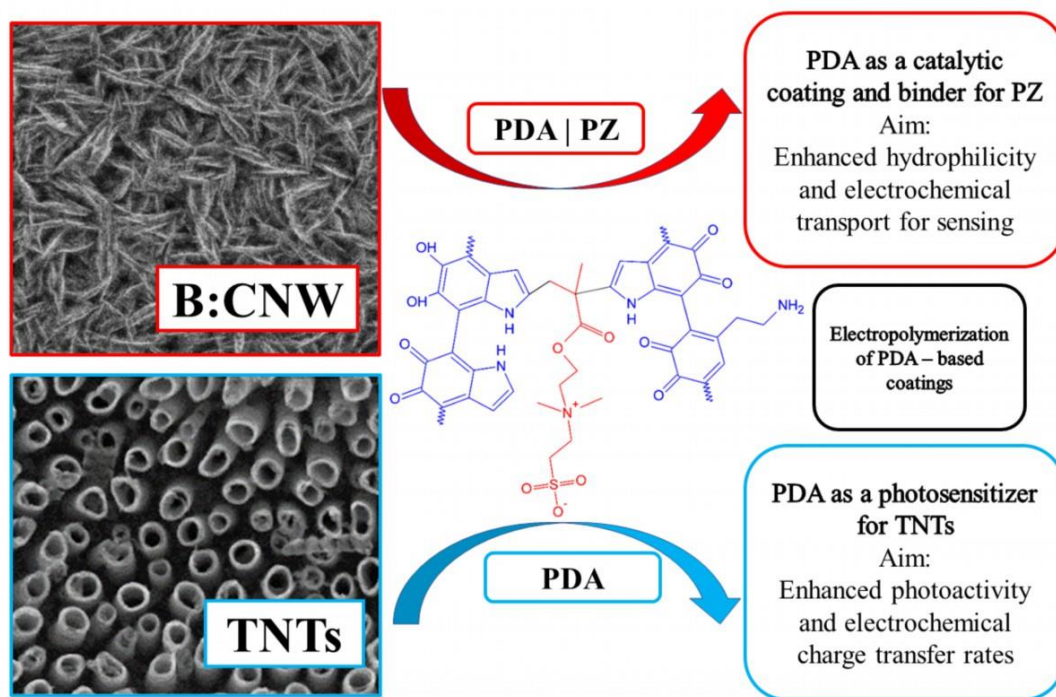
This task is aimed at resolving the potency of PDA towards applications in electrochemical sensing. It is also focused on uncovering the mechanisms of the sensing enhancement on various length scales, from molecular to macroscopic.

### **Objective 4: Photoelectrochemical properties of TNT\_PDA and optimisations towards efficient photosensitisation.**

Tasks related to this objective include:

- Investigation of the charge transfer between redox markers and the semiconductor surface via voltammetric and impedimetric techniques.
- Estimating the relations between the optical absorption, electrochemical properties and the ability of TNT\_PDA electrodes to generate a photocurrent.
- Development of a PDA laser graphitisation protocol.

This task is aimed at resolving the potency of the PDA towards applications in photoelectrochemistry as a photosensitizer. It is also focused on understanding the electronic properties and mechanisms of photocurrent enhancement and related nonlinear effects of TNT\_PDA. General concepts related to the research objectives are schematically presented in **Figure 29**. A detailed description of the research methodology is presented in the next **Chapter 4**.



**Figure 29.** Proof-of-concept diagram of the experiments proposed in the thesis.

### 3.2. Hypotheses

*I ask countless inappropriate questions. If only I could break through this forest.  
Stawiam niezliczone niestosowne pytania. Gdybym tylko zdołał przedrzeć się przez ten las.*

**Ludwig Wittgenstein** – German philosopher of language; (XX century)

In relation to the abovementioned problem and research goals, the following list of hypotheses is proposed:

**Hypothesis 1:** It will be possible to obtain a homogeneous layer of PDA on the surface of semiconductors via electropolymerisation protocols.

Premises for the formulation of the hypothesis:

- Due to the high surface area and conductivity of B:CNW, it will be possible to observe features of the PDA electropolymerisation mechanisms<sup>107</sup>.



- Hydrogenation of titania nanotubes will increase their surface conductivity, enabling charge transfer to the monomer and, in consequence, facilitate electropolymerisation<sup>123</sup>.

Evidences for **Hypothesis 1** can be found in **Articles 1 and 3** for B:CNW and TNT semiconductors, respectively. By implementing **Objectives 1 and 2**, PDA layers with variable chemistry have been obtained and characterised on B:CNW (**Articles 1 and 2**) and TNTs (**Articles 3 and 4**).

**Hypothesis 2: Application of the PDA-based coating to B:CNWs will significantly increase the sensitivity and selectivity of the electrode towards sensing catecholamine neurotransmitters.**

Premises for the formulation of the hypothesis:

- The presence of the PDA scaffold, which is rich in catechol/quinone groups, is expected to increase its specificity towards catecholamine neurotransmitters<sup>19</sup>.
- The presence of zwitterions inside the coating will increase the antifouling capabilities in the biofluids due to repulsion of the larger molecules in there<sup>89</sup>.

The whole of **Article 2** is devoted to verifying **Hypothesis 2** and achieve **Objective 3** by investigating PDA-based coatings on the surface of B:CNWs tailored towards electrochemical sensing applications.

**Hypothesis 3: Application of the PDA-based coating on TNTs will increase their capability towards photocurrent generation in the visible part of the spectrum.**

Premises for the formulation of the hypothesis:

- Considering the broad optical absorption spectrum of PDA, its presence on the surface of TNTs is expected to extend the photocurrent spectrum to the visible range<sup>56</sup>
- Laser graphitisation of PDA on the surface of nanotubes will increase the charge transfer rate through the electrode-electrolyte interface, thus further boosting the photocurrents<sup>76</sup>

The results of **Objective 4** are presented in **Articles 3–4**, which are focused on the photoelectrochemical properties of PDA-based coatings deposited on TNTs, providing strong evidence for **Hypothesis 3**.

#### **Contents of the thesis:**

The results of the thesis form a collection of four core publications with the dominant contribution of the author in each one. The thesis begins with the outline of the research in the context of global problems and the comprehensive literature review already presented in **Chapters 1 and 2**. Specific research goals and hypotheses were presented in the current **Chapter 3**. The research methodology, including the experimental and computational techniques used in the thesis, is elaborated in **Chapter 4**. The four core articles and their discussion are presented in **Chapter 5**. Finally, the conclusions and prospects for further research are proposed in **Chapter 6**.

## 4. Research methodology

The following chapter describes all the experimental and computational methodologies developed and used throughout the PhD thesis.

### 4.1. Synthesis protocols

*Die Grenzen meiner Sprache bedeuten die Grenzen meiner Welt.*

*The limits of my language define the limits of my world.*

*Granice mojego języka oznaczają granice mojego świata.*

**Ludwig Wittgenstein** – ‘Tractatus Logico-Philosophicus’ (1922)

#### 4.1.1. Synthesis of B:CNWs

B:CNW electrodes were manufactured on p-type (100) Si wafer plates utilising a microwave plasma-enhanced chemical vapour deposition system (SEKI Technotron AX5400S, Japan) as reported elsewhere<sup>143</sup>. The stage temperature was set to 700°C, while the microwave power was kept at 1300 W. The fabrication process was carried out at a pressure of 50 Torr in a gas mixture flow equal to 325 sccm. The CNW electrodes were boron-doped *in situ* utilising a diborane precursor ([B]/[C] ratio in the gas phase = 2000 ppm). The 6-hour process resulted in thick, vertically aligned carbon nanowall surfaces (d~3 µm) with a high content of diamond phase<sup>144</sup>. The Si wafers were cut into 5 x 20 mm pieces, serving as electrodes for electrochemical measurements. B:CNWs were used as substrate electrodes in **Article 1** and **Article 2**.

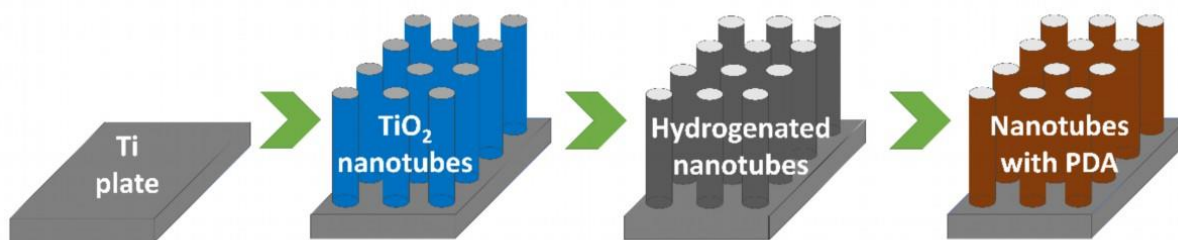
#### 4.1.2. Synthesis of hydrogenated TNTs

Two-electrode anodisation in ethylene glycol or diethylene glycol solution containing HF and NH<sub>4</sub>F was used to synthesise titania nanotubes according to protocols comprehensively described previously<sup>118,145</sup>. In that process, a piece of Ti foil served as an anode and Pt rectangular mesh as a cathode with an applied constant voltage (30–40 V). Both electrodes were placed in a cell equipped with the thermostatic jacket. After anodisation, the TiO<sub>2</sub> nanotube layers were calcined in a tube furnace at 450°C for 2 hours to convert the initially amorphous structure into crystalline phase. Immediately before electropolymerisation, two-electrode hydrogenation of TNT was performed in 0.5 M Na<sub>2</sub>SO<sub>4</sub> solution. In most of the experiments, the hydrogenation voltage was set to -4 V for 2–5 minutes. Synthesis of the nanotubes, development of the hydrogenation protocol, and the hydrogenations were developed and performed by me. TNTs were used as substrate electrodes in **Article 3** and **Article 4**.



#### 4.1.3. Electropolymerisation of dopamine on B:CNWs and hydrogenated TNTs

Electropolymerisation of dopamine on the surface of TNTs and B:CNWs was conducted in a three-electrode electrochemical cell with TNTs or B:CNWs as the working electrode, a platinum mesh as the counter electrode, and Ag | AgCl | 3 M KCl as the reference electrode. The electrolyte contained 1X Tris buffer and different amounts of dopamine monomer, typically 5 mM, and was purged with Argon, so the layer was obtained mostly during electrogenerated radicals, without the influence of oxygen radicals. Electropolymerisations were performed using the cyclic voltammetry method described in **4.2.7.2 section** in varying pH conditions (in the range of 3–12) and potential windows. In the case of TNTs, the process was performed immediately after hydrogenation to maintain the conductivity boost. Moreover, the supporting electrolyte contained an additional 0.5 M Na<sub>2</sub>SO<sub>4</sub> to further enhance the conductivity. A synthesis protocol was developed and performed by the author, details of which are described in **Articles 1 and 3** (below, **Figure 30**) and used in all four articles.



**Figure 30.** Synthesis of titania nanotubes covered with PDA (TNT\_PDA composite)<sup>146</sup>.

#### 4.1.4. Co-electropolymerisation of dopamine and zwitterions on B:CNWs

Simultaneous electrodeposition of dopamine and zwitterionic sulfobetaine methacrylate on the surface of carbon nanowalls was performed in a setup similar to pristine PDA electropolymerisation. The synthesis protocol was developed and performed by the author; details of which are shown in **Article 2**. Briefly, the most crucial difference is the presence of an additional 500 mM of SBMA zwitterionic monomer in the solution, yielding a 100:1 molar ratio of the PDA:PZ monomers in the solution. This amount was the highest possible and limited by the solubility and the overall viscosity. Moreover, in the solution containing both monomers, more strict control of the pH was required, as the acidic SBMA monomer became dominant. To maintain the neutrality, NaOH was added to the solution and subsequently measured with a pH-meter until the pH reached 7.

#### 4.1.5. Laser graphitisation of PDA deposited on TNTs

After electropolymerisation on the surface of titania nanotubes, PDA was graphitised using a pulsed laser beam. Several parameters, including the fluence, wavelength, and substrate nanotubes geometries, were optimised to obtain the best material for the photoelectrochemical sensing. The two optimisation criteria were high charge transfer kinetics and high photocurrent generation capability of the laser-treated structure compared to the unmodified one. Details of the optimisation are elucidated in **Article 4**. Briefly, two wavelengths of the nanosecond, pulsed Nd:YAG laser were tested – 532 nm and 365 nm – in the range of fluences between 30 and 120 mJ cm<sup>-2</sup>. A motorised table was used to define a geometric pattern on the electrode that undergoes modification with variable velocities. The protocol was performed on both adjacent and loosely spaced nanotube geometries with pre-optimised lengths and diameters to maximise the photocurrent of the initial TNT\_PDA structures. The author's original contribution is the application of a pulsed laser to graphitise the PDA and perform PDA graphitisation on the semiconductor substrate.

#### 4.2. Experimental characterisation techniques

*Tak nas Panie obdarzasz, wždy nam zawsze mało –  
Za nic mamy – co mamy, więcej by się chciało.*

*Thus, you grace us, Lord, yet we always want more –  
We value not what we have, always wishing for  
more.*

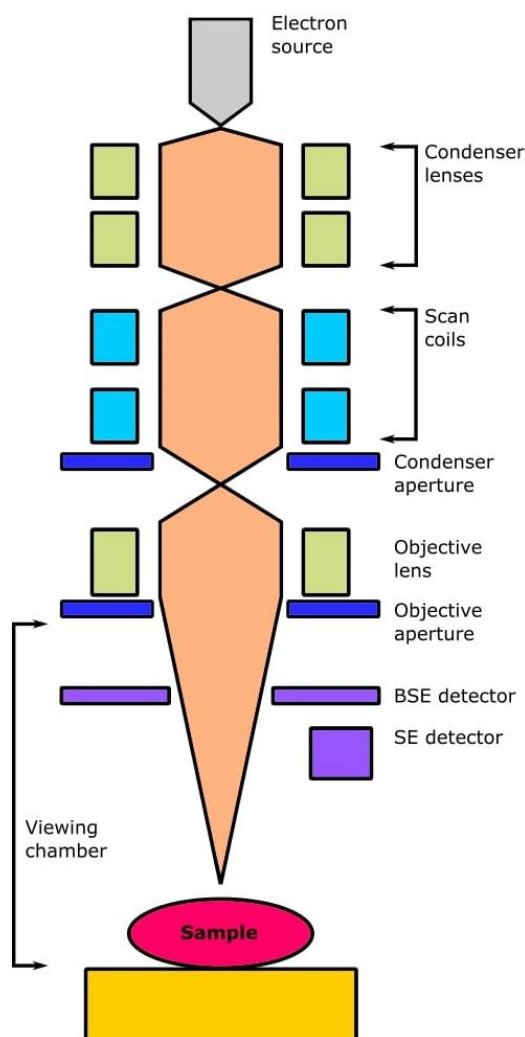
**Jacek Kaczmarski** – Polish poet and bard; 'Jan Kochanowski' (2000)

##### 4.2.1. Scanning Electron Microscopy (SEM)

In general, Scanning Electron Microscopy (SEM) is a powerful technique for high-resolution imaging of surfaces and bulk materials and biological samples at the micro-to-nanoscale. Central to SEM is the utilisation of a focused beam of primary electrons directed onto the specimen surface via dedicated optics in a sufficiently high vacuum. Primary electrons can be generated by several approaches, such as field emission, and are accelerated towards the specimen by the electric field, penetrating its surface and initiating various interactions with the sample (**Figure 31**).

On striking the specimen, primary electrons can undergo transmission, or elastic or inelastic scattering, yielding other electrons and X-Rays as information sources for detection (**Figure 32**). Transmission does not happen in SEM. With inelastic scattering, low-energy secondary electrons are emitted. This

interaction occurs within the topmost atomic layers of the specimen (ca. 1 nm) and is used for topography analysis, which is used to visualise the surface features.

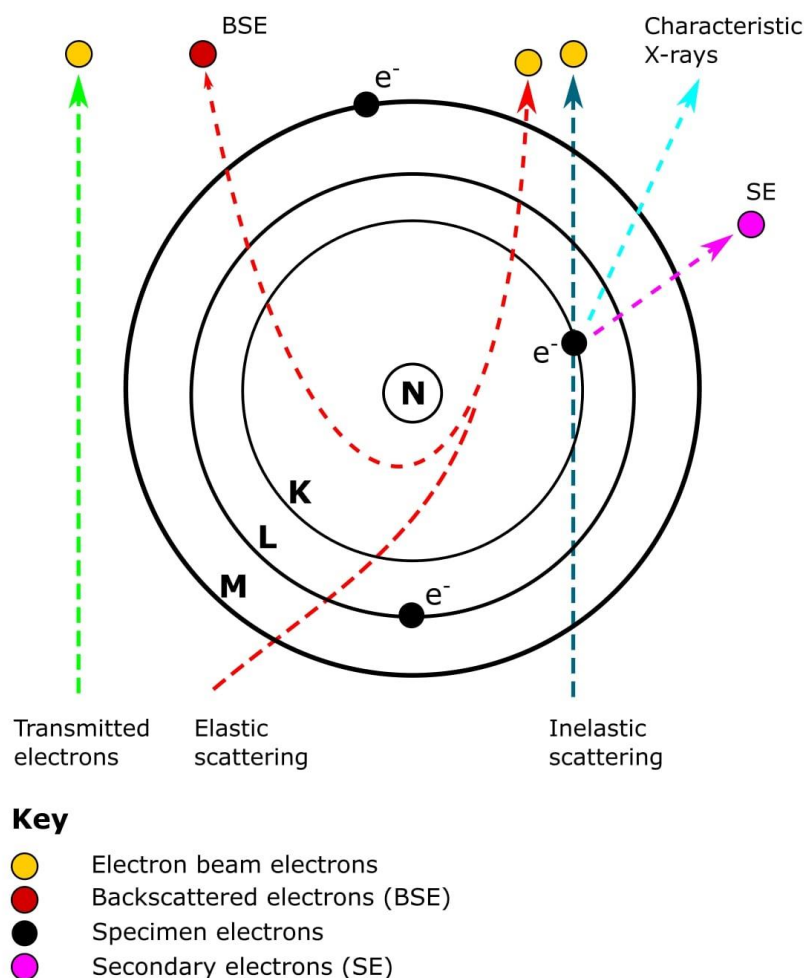


**Figure 31.** Schematic diagram of the construction of a scanning electron microscope<sup>147</sup>.

With elastic scattering, high-energy backscattered electrons are emitted. These electrons are generated within deeper parts of the sample (down to several nm) and their kinetic energy depends on the atomic numbers of the matter within the sample. Thus, this information can be used to generate contrast and distinguish various phases.

Complementing the imaging capabilities of SEM, Energy Dispersive X-Ray Analysis (EDX) makes it possible to probe the elemental composition of the specimen<sup>148</sup>. As primary electrons interact with the surface atoms, inner-shell electrons are ejected, leading to the emission of characteristic X-rays. The energy of those X-rays corresponds to the differences between the inner-shell electronic levels. Based on the values of this energy, the chemical composition of the surface can be mapped. Besides the characteristic X-rays, electron-electron X-ray Bremsstrahlung radiation is also formed during SEM

experiments as a by-product of inelastic scattering. However, it does not carry information relevant to the chemical composition.



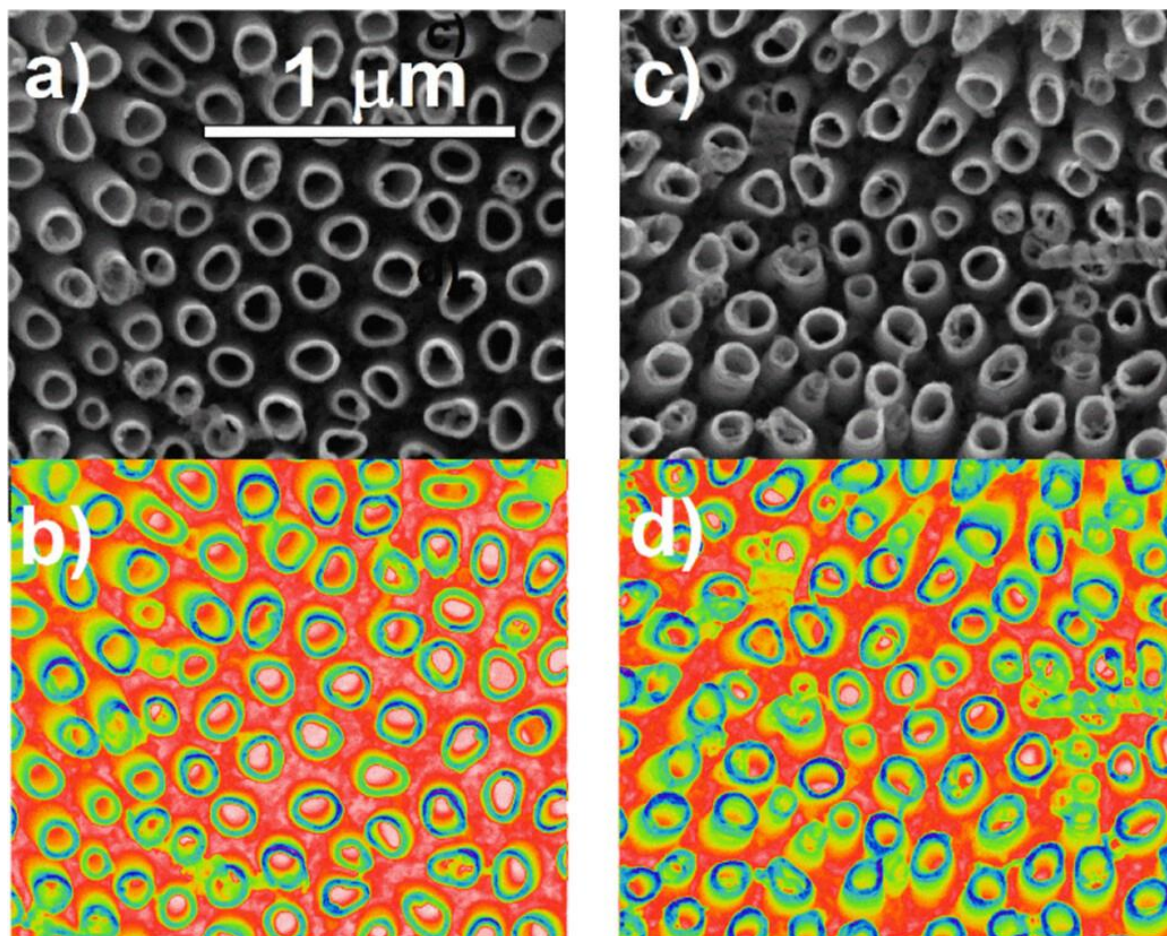
**Figure 32.** Interactions of the SEM primary electrons with electrons in the specimen's atoms<sup>147</sup>.

In the following thesis, SEM is used to investigate the morphology of the B:CNW and TNT samples before and after all modifications. It was one of the tools for confirming the presence of the deposited coating and the topography of the whole composites (**Article 2** and **Article 3**). In particular, the PDA thickness,  $D_{PDA}$ , deposited onto the TNT could be estimated through a comparison of the thickness of the nanotube walls before,  $W_{TNT\_PDA}$ , and after,  $W_{TNT}$ , modification according to the simple equation:

$$D_{PDA} = \frac{W_{TNT\_PDA} - W_{TNT}}{2} \quad \text{Equation 1}$$

Estimating thickness of the PDA is crucial, as this parameter dictates many properties of the PDA, such as the charge transfer kinetics and capability of photocurrent generation (**Article 3**). Example figures for TNT\_PDA structures are given in **Figure 33**. Images of the fabricated samples were obtained using

an FE-SEM Quanta FEG 250 (FEI) with an ET secondary electron detector. The author's contribution is the analysis and interpretation of the SEM images.



**Figure 33.** SEM images of the loosely-spaced titania nanotubes at two different colour palettes a–b) before and c–d) after electropolymerisation of the PDA<sup>146</sup>.

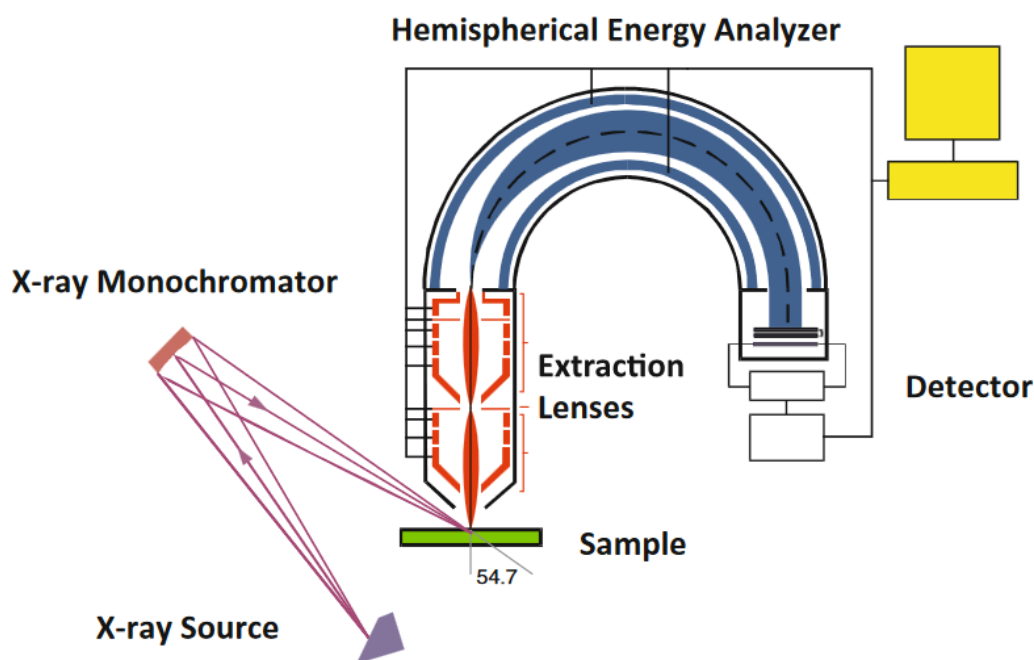
#### 4.2.2. X-ray Photoelectron Spectroscopy

In general, XPS operates by irradiating a sample with X-ray photons, typically monochromatic, and collecting electrons ejected from the inner atomic shells. The process is performed under ultra-high vacuum conditions to prevent interactions between X-rays and the gaseous environment. The kinetic energy and number of the emitted photoelectrons are then measured, e.g. by a hemispherical energy analyser, and analysed by a detector (**Figure 34**). The obtained information on the kinetic energy is then used to estimate the binding energies.

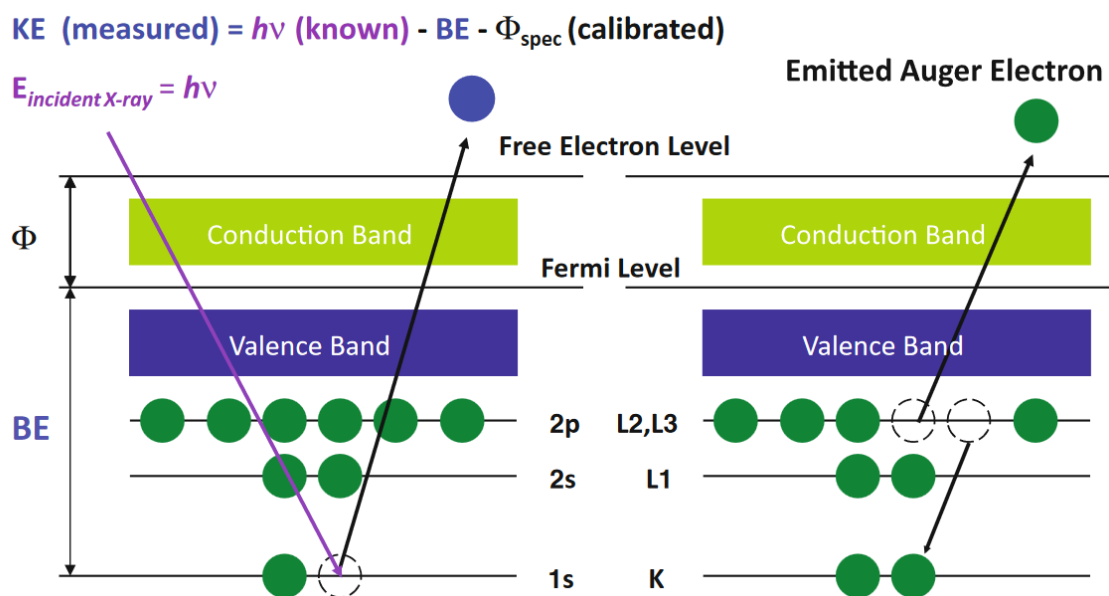
The measured kinetic energy can be decomposed into the initial monochromatic X-ray photon energy, which is known, the binding energy, and the work function specific for each material, which can be subtracted during calibration. The most chemically relevant quantity is the binding energy. Each atom type is associated with a different set of binding energies corresponding to X-ray excitations from



various levels, e.g. C1s, N1s, Ti2p or S2p orbitals (**Figure 35**). Fine structure levels can be also distinguished in high-resolution measurements, e.g. Ti 2p 1/2 and Ti 2p 3/2. Different oxidation states also correspond to different binding energies. Besides the emission of photoelectrons from inner shells, Auger emission of electrons with lower kinetic energy is also possible. The essence of the Auger process is the interaction of the initially ejected inner-shell electron with another electron located higher on the energy scale. As a result, the latter electron is ejected and measured.



**Figure 34.** Schematic of the XPS experimental setup<sup>149</sup>.

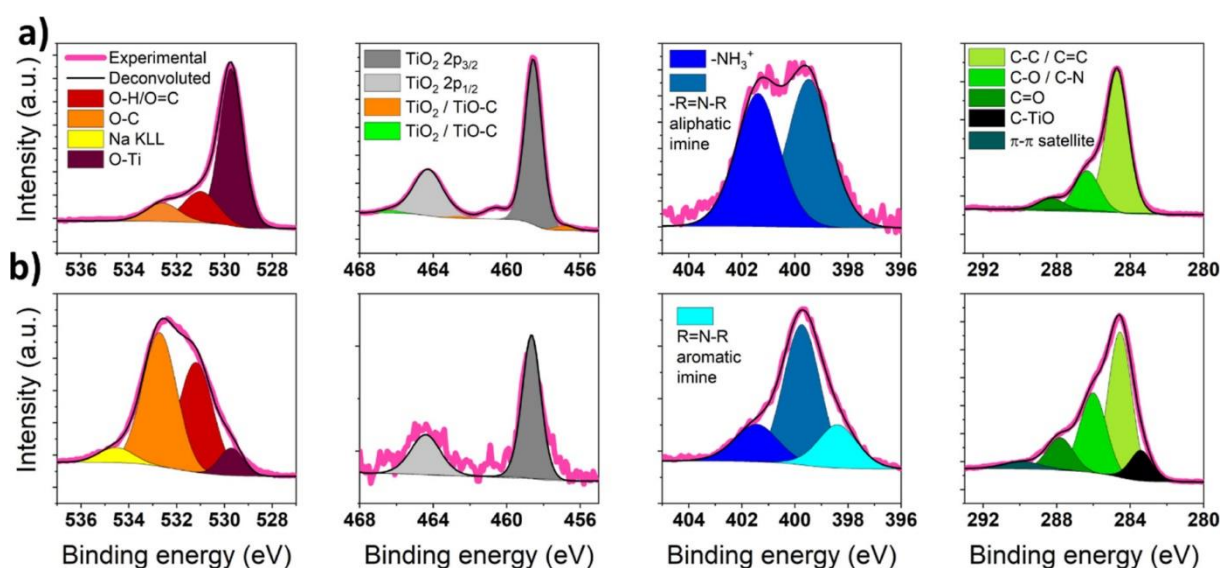


**Figure 35.** Interaction of X-ray photon with inner-shell electrons of the specimen<sup>149</sup>.



Overall, the XPS spectrum exhibits a set of peaks corresponding to each type of atom in a particular oxidation state. By analysing the positions and intensities of these peaks, it is possible to deduce the chemical composition and oxidation states of the elements present in the material.

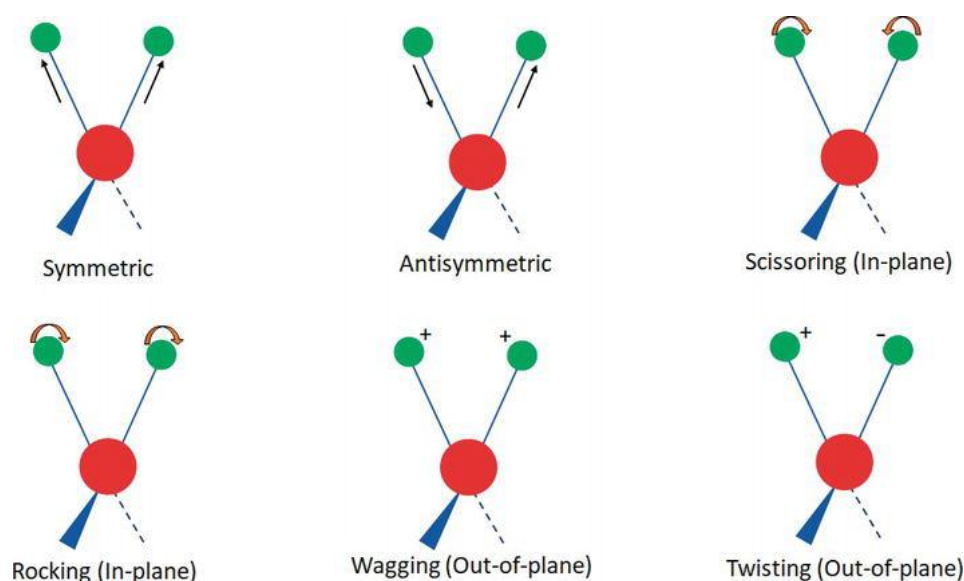
In the thesis, the X-ray photoelectron spectroscopy (XPS) technique is employed to elucidate the chemical structure of the B:CNW (**Article 2**) and TNT (**Article 3**) substrates before and after PDA-related modifications. Examples of XPS spectra illustrating the difference between the PDA synthesised in acidic (pH = 5.7) and alkaline (pH = 9.1) conditions are given in **Figure 36**. The XPS information is used in assessing the effect of laser graphitisation and IgPDA-substrate interactions (**Article 4**). The author's contribution is the analysis and interpretation of the XPS spectra.



**Figure 36.** High-resolution XPS spectra of TNT\_PDA with dopamine polymerised in (a) acidic pH=5.7 and (b) alkaline pH=9.1<sup>146</sup> environments.

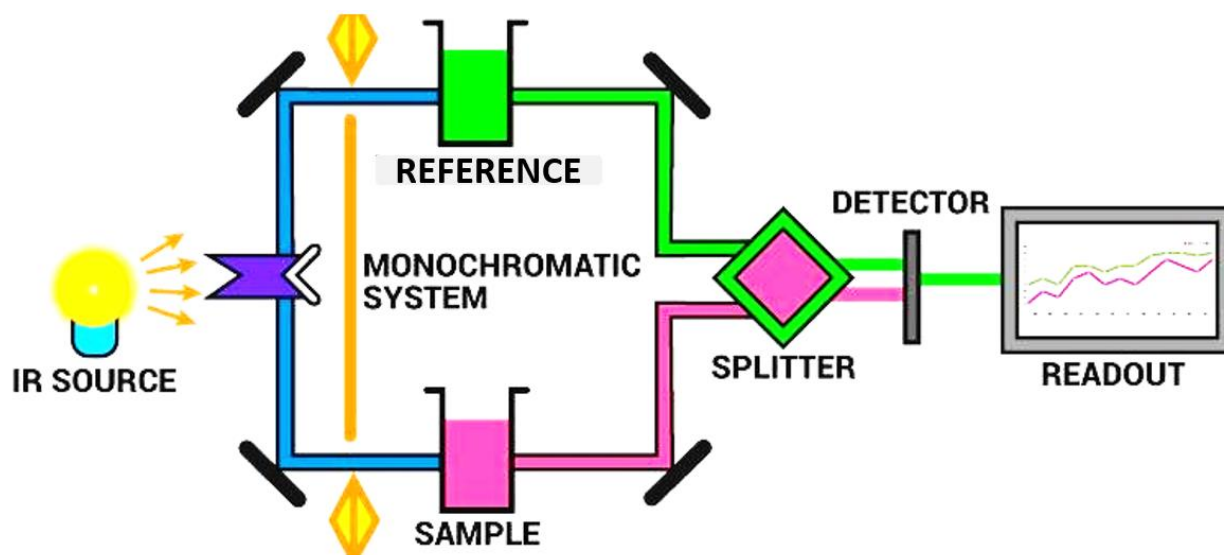
#### 4.2.3. FT-IR spectroscopy

As a type of absorption spectroscopy in the infrared region of the electromagnetic spectrum, FT-IR captures information on molecular vibrations. The most rudimentary forms of vibrations include stretching (along the bond), in-plane bending and out-of-plane bending (**Figure 37**). When IR photons interact with a sample, they selectively excite vibrations of the matching energy. The absorption of IR radiation induces changes in the dipole moment of the molecule, resulting in characteristic absorption bands corresponding to specific vibrational modes. Energies (wavenumbers) of vibrational modes are specific for each type of chemical group, e.g. O-H, C-H (aliphatic), C-H (aromatic). Thus, FT-IR can be used to identify and analyse the chemical composition of functional groups.



**Figure 37.** Examples of molecular vibrational modes<sup>150</sup>.

The experimental setup for a classical IR measurement consists of the source, monochromator, optics and detectors (**Figure 38**). The default configuration is designed for liquids, although solids can be studied by implementing an attenuated total reflection (ATR) add-on. In an FT-IR experiment, a broad spectrum of IR radiation is directed onto the sample. The resulting transmitted or reflected light is then interfered with a reference beam using a Fourier-transform interferometer. This process generates an interferogram, from which the complete infrared spectrum is reconstructed through Fourier transform.



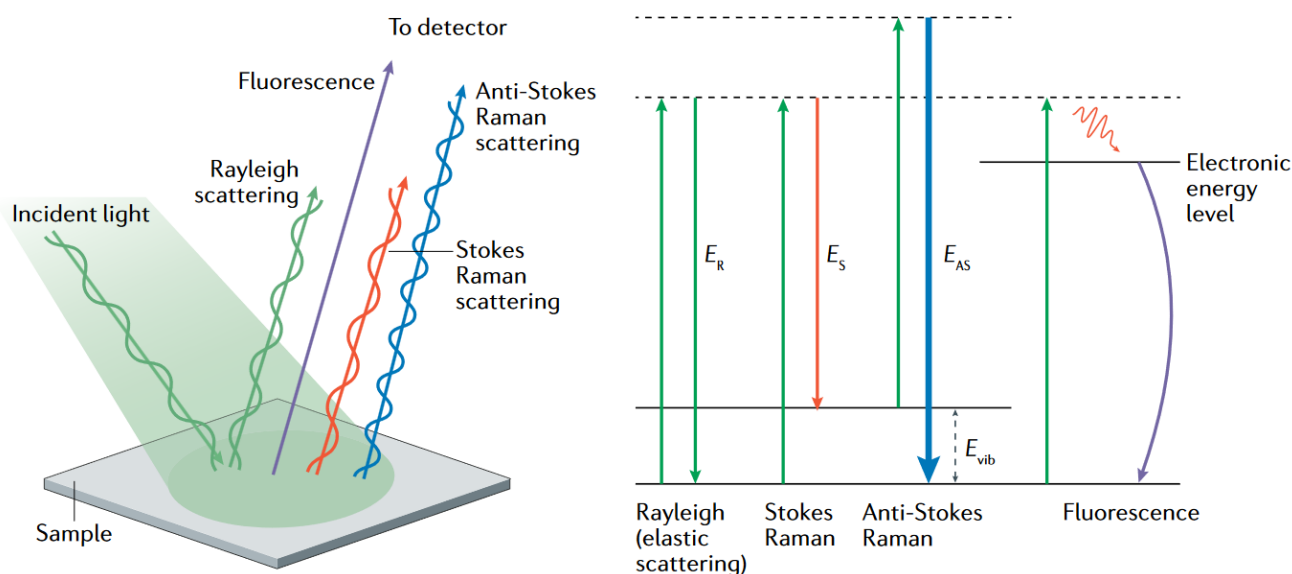
**Figure 38.** Experimental setup for IR absorption spectroscopy experiment<sup>151</sup>.

The FT-IR spectra of the electrodes were used to investigate the chemical structure of the PDA-related coatings. It is one of the tools confirming the presence of zwitterionic units inside the PDA\_PZ copolymer synthesised in **Article 2**. Spectra were recorded using a Nicolet iS50 FTIR spectrometer equipped with an attenuated total reflectance (ATR) accessory ATR Special Quest. Spectra were

recorded within the 4,000–400  $\text{cm}^{-1}$  wave number range. Analysis of the data was performed using the OMNIC software. The author's contribution was the collection, analysis and interpretation of the FT-IR spectra.

#### 4.2.4. Raman spectroscopy

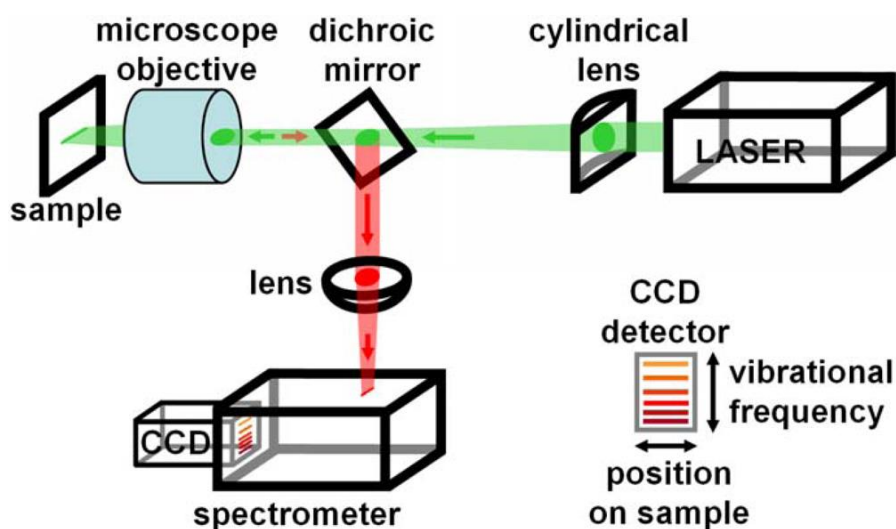
Similarly to FT-IR, Raman is a vibrational spectroscopy, but instead of absorption, it utilises inelastic (Raman) scattering of the light in contact with the sample. High input power densities in the form of a laser are required to capture Raman scattering from gases, solutions, or solid surfaces. Depending on the characteristic frequencies of the vibrational modes, signals with various Raman shifts appear in the spectrum. In general, when an incoming photon is scattered, it is excited to a virtual electronic-vibrational level, and when relaxed, it emits another photon of lower or higher energy (Figure 39). The majority of Raman scattered photons have lower energy than the incident photons – Stokes transitions. In the other less probable case, anti-Stokes signals can be registered. Besides Raman scattering, the fluorescence signal is also collected during the experiment, which can be useful for detecting fluorescent molecules and pose indirect inferences on their structure.



**Figure 39.** Schematic of possible interactions of the light with the sample during a Raman experiment<sup>152</sup>.

Typical experimental setup for Raman spectroscopy measurements includes the laser source (e.g. 532 nm or 785 nm), microscope, diffraction gratings and associated optics. The choice of the laser source depends on the optical properties of the studied material (position of the absorption bands) and the goal of the experiment, which determines the Raman bands that should be analysed in detail. Light scattered from the sample is directed to a spectrometer equipped with a CCD detector and diffraction gratings corresponding to the proper wavelength of the laser (Figure 40). Manipulating the magnification of the microscope used during the experiment makes it possible to investigate various sample areas.

Depending on the laser's intensity and the optical parameters of the sample, various penetration depths can be achieved. Thus, information on the material's structure can be gathered from different thicknesses in the Z direction (parallel to the beam) up to several microns. Provided the setup contains a motorised table, X-Y scanning (in the direction perpendicular to the beam) is possible during the measurement. Thus, areal maps of particular features extracted from Raman signals can be obtained. For example, distribution of the anatase signal across the X and Y coordinates of the sample can provide information on the surface homogeneity of the nanotube crystallisation.



**Figure 40.** Experimental setup for Raman spectroscopy experiment<sup>153</sup>.

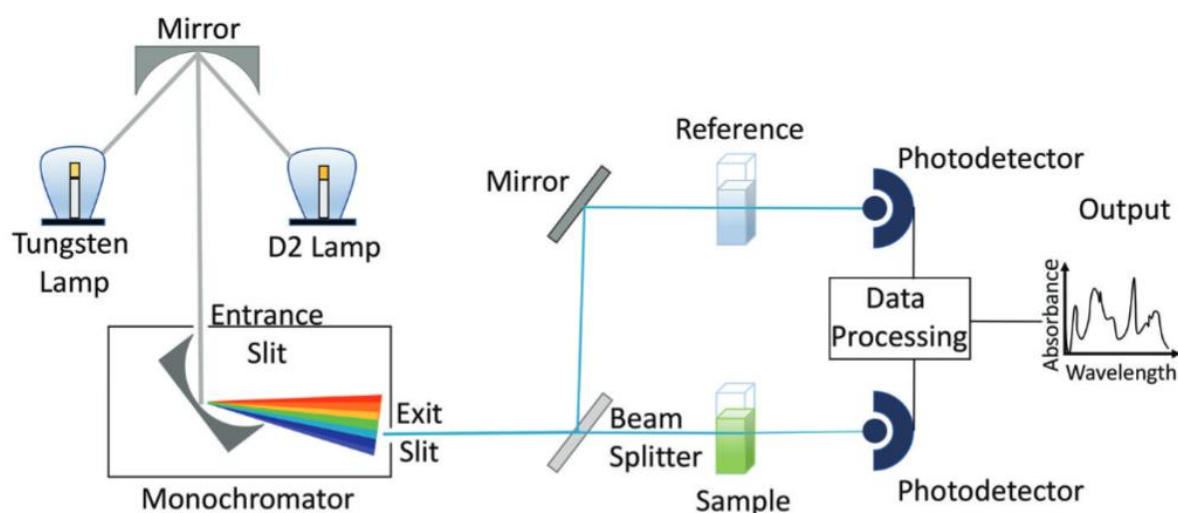
In this work, Raman spectroscopy was used to investigate the  $sp^2/sp^3$  phase contents on the surface of modified B:CNWs and TNTs and as a tool to verify the presence of polymers. As the PDA and related polymers exhibited strong fluorescence<sup>154</sup>, comparison of the fluorescence background signal was a viable tool for achieving this goal (**Article 3** and **Article 4**). Both the B:CNW<sup>106</sup> and TNT<sup>135</sup> substrates possess their own characteristic Raman signals – G/D graphitic bands and anatase/rutile, respectively. Quenching those signals after depositing the polymers is another indirect tool for investigation. Raman spectroscopy can be also used to track the degree of graphitisation after laser treatment of the PDA, because after graphitisation, the G/D band ratio increases<sup>155</sup>. Thus, registering the G/D band ratio for various lasing parameters can be used to deduce the optimal conditions for graphitisation. Measurements were performed using an InVia Renishaw Raman microscope equipped with a 512 nm laser source. The author's contribution was collection, analysis, and interpretation of the Raman spectra.

#### 4.2.5. Optical diffuse reflectance spectroscopy

In general, optical absorption spectroscopy is performed by a spectrophotometer equipped with UV and visible light sources, a monochromator and proper optics (**Figure 41**). Per analogy to FT-IR, photodetectors capture the light transmitted out of the sample and the reference. Transmittance is

obtained as the ratio between the sample intensity  $I$  and the reference intensity  $I_0$ . Absorption coefficient  $\alpha$  is related to the transmittance  $T$  and absorbance  $A$  by the Lambert-Beer law:

$$A = \alpha l = \log \frac{I_0}{I} = \log \left( \frac{1}{T} \right) \quad \text{Equation 2}$$

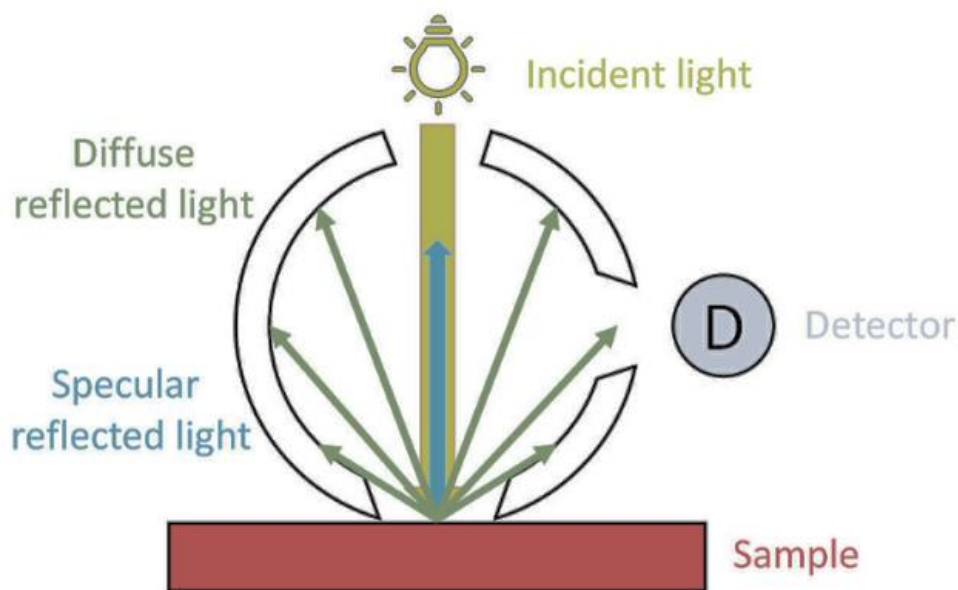


**Figure 41.** Example experimental setup for optical absorption spectroscopy experiment; D2 is a deuterium lamp emitting UV light and there is a tungsten lamp emitting a broad spectrum from the UV to IR parts of the electromagnetic spectrum<sup>156</sup>.

If the specimen is not transparent, using an integrating sphere is required to investigate its optical absorption spectra. An example geometry for this type of measurement is given in **Figure 42**. Reflected light can be divided into specular and diffuse – the latter is collected by the integrating sphere and used as the data source for the reflectance spectrum. Then, the Kubelka-Munk ( $F(R)$ ) relation can be used to extract the data on absorptivity from reflectance  $R$  according to the formula<sup>157</sup>:

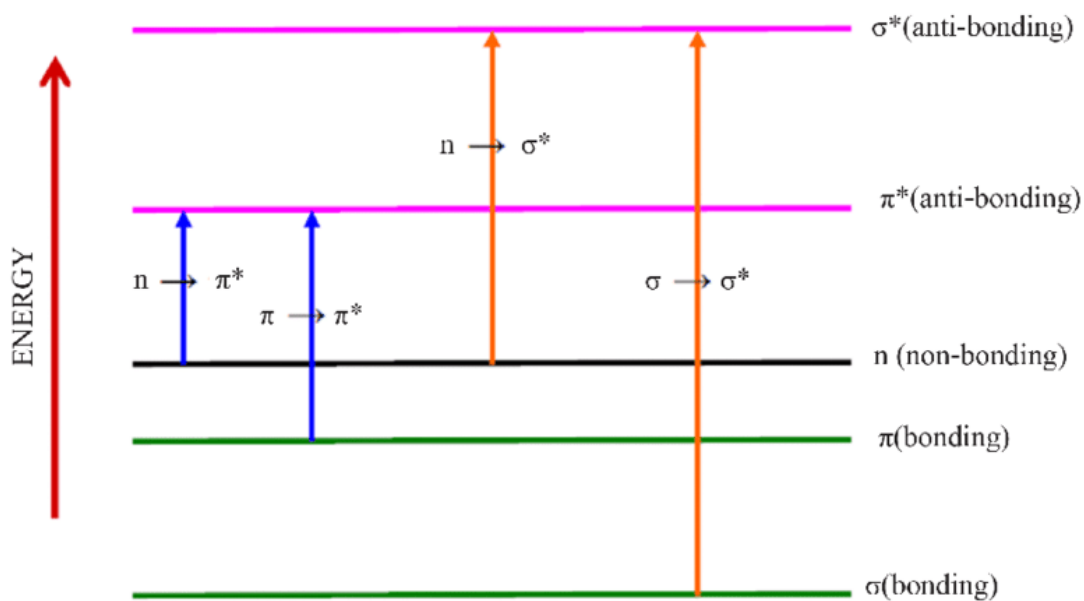
$$F(R) = \frac{(1 - R)^2}{2R} \quad \text{Equation 3}$$

Due to the assumptions of the flat surface and constant refractive index – imposed in the derivation of the  $F(R)$  relation – interpreting the  $F(R)$  data of nanomaterials needs to be performed with caution<sup>158</sup>. Although comparing the absolute values between different materials can be strongly misleading, a differential analysis of the same material before and after modification is typically devoid of large errors. Thus, the analysis remains rather qualitative.



**Figure 42.** Schematic diagram of the integration sphere used in diffuse reflectance measurements<sup>159</sup>.

In contrast to the FT-IR spectrum, the wavelength range used in the UV-vis spectroscopy corresponds to the optical transitions between electronic energy levels. For molecules (in solutions), these are transitions between sigma-bonding, pi-bonding or non-bonding orbitals, as shown in **Figure 43**. Provided the sample does not exhibit large spin-orbit coupling, all transitions are singlet-singlet, and the excited electron relaxes back to the ground state via radiative (fluorescence) or non-radiative (heat dissipation) pathways. Photochemical phenomena related to the spin-orbit coupling such as singlet-triplet transitions, intersystem crossings, delayed fluorescence and phosphorescence are not the subject of this work.



**Figure 43.** Electronic transitions in UV – vis spectroscopy for a molecule<sup>160</sup>.

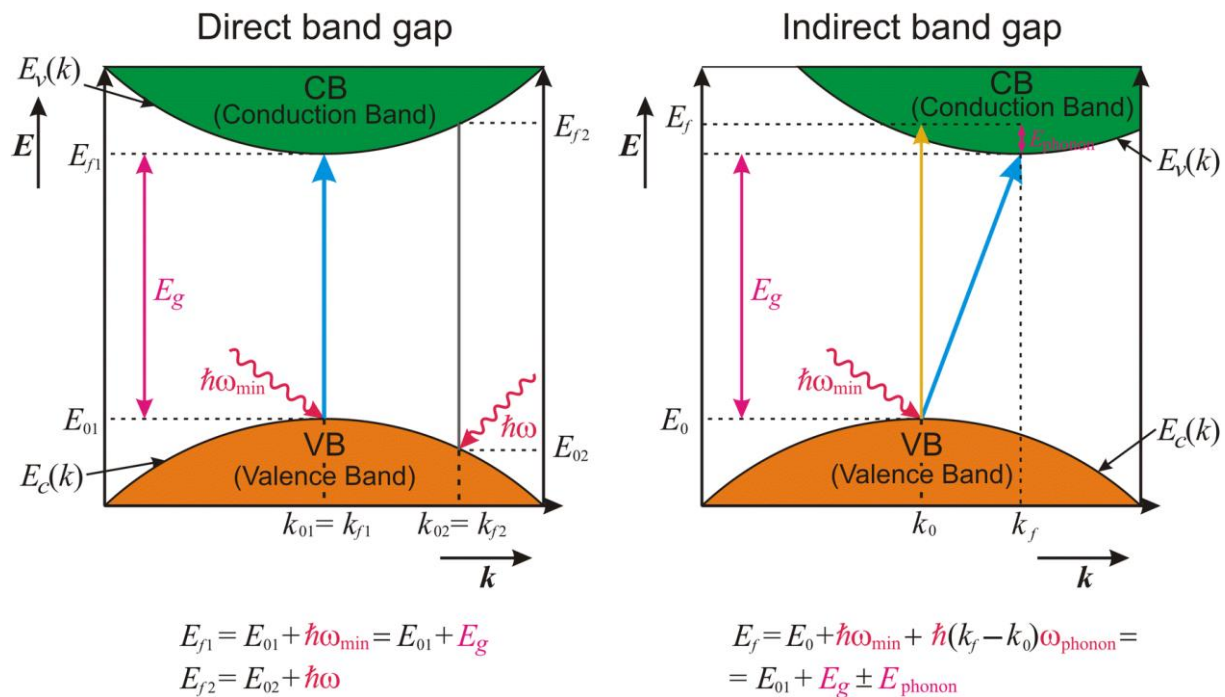


In the case of solid samples, the band structure perspective applies, and electronic transitions occur between valence (VB) and conduction (CB) bands. In semiconductors, the Fermi level is located somewhere between those bands, depending on the doping density, temperature and surface chemistry. Intraband transitions (excitations within the same band) in metals and plasmonic nanostructures are not the subject of this work.

Optical transition can be direct or indirect. In the case of direct transition, the photon (typically from the UV-vis range) is absorbed without generating a phonon, provided that its energy is larger than the bandgap. The transition can be from the VB edge or levels below (see **Figure 44**). After absorption, the excited electron relaxes to the CB edge (emitting vibrations) and then relaxes back to the edge of the VB (emitting photon). In direct semiconductors, direct transition is always of the highest probability and others can be neglected.

For indirect transition, a phonon is generated upon absorption to compensate for the change of the crystal momentum. Relaxation to the CB edge occurs the same way as in the direct case, although the CB-to-VB transition requires another photon. Therefore, the time constant of this process is several orders of magnitude longer. This scenario is beneficial in DSSCs because the photogenerated carriers can survive longer before annihilation and have a chance of reaching the contacts.

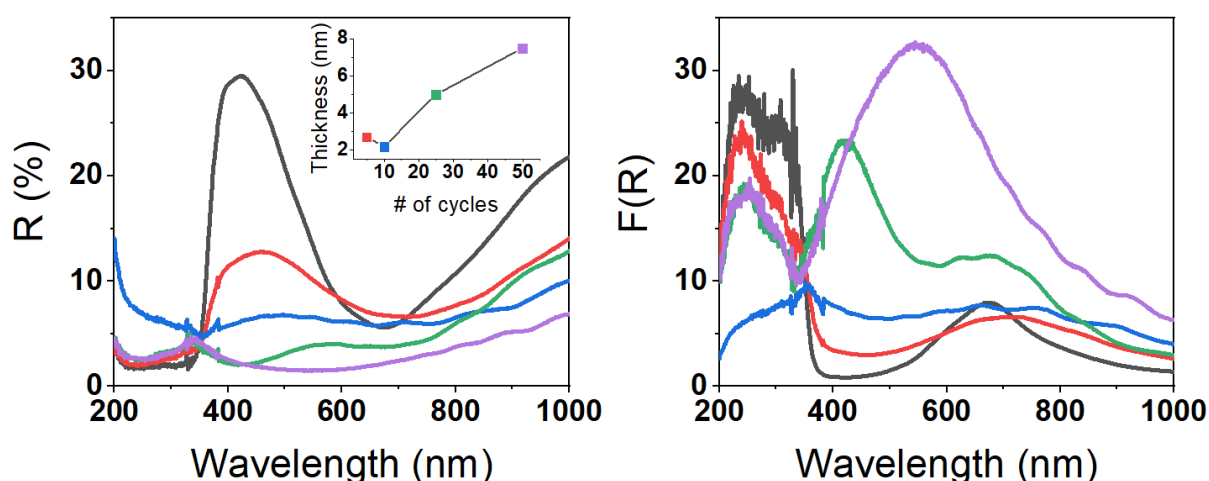
For indirect semiconductors, when the energy is greater than the bandgap ( $E_0$ ) but smaller than  $E_f$  (see **Figure 44**), the indirect transition is the only possible action. However, when the photon energy exceeds  $E_f$ , direct transition can become dominant for the indirect semiconductor.



**Figure 44.** Optical transitions in UV-vis spectroscopy for a solid semiconductor<sup>161</sup>.

For bulk semiconductors, the bandgap can be estimated from the reflectance spectra in several ways, including the Tauc or Cody methods<sup>162–164</sup>. Provided several conditions are satisfied and the studied transition is known, the same methods can be applied to nanostructured materials. For semiconducting polymers (such as PEDOT, polyaniline, and perhaps PDA), both the molecular and the band structure perspectives can be applied. Answering the question of which is more accurate depends on the chain length, interactions between chains and the long-range order within the polymer. Therefore, estimating the bandgap of such materials – and their composites with other materials – needs to be performed rather with caution.

Example diffuse reflectance plots and the associated Kubelka-Munk function for the TNT\_PDA structures with varying PDA thicknesses are given in **Figure 45**. As the TNT\_PDA samples are not transparent, UV-vis spectroscopy measurements were performed in reflectance mode (**Article 3**). The optical properties were investigated using a Perkin Elmer Lambda 35 UV-vis spectrometer equipped with a diffuse reflectance accessory and integrating sphere. The author's contribution is collection, analysis and interpretation of the optical spectra.

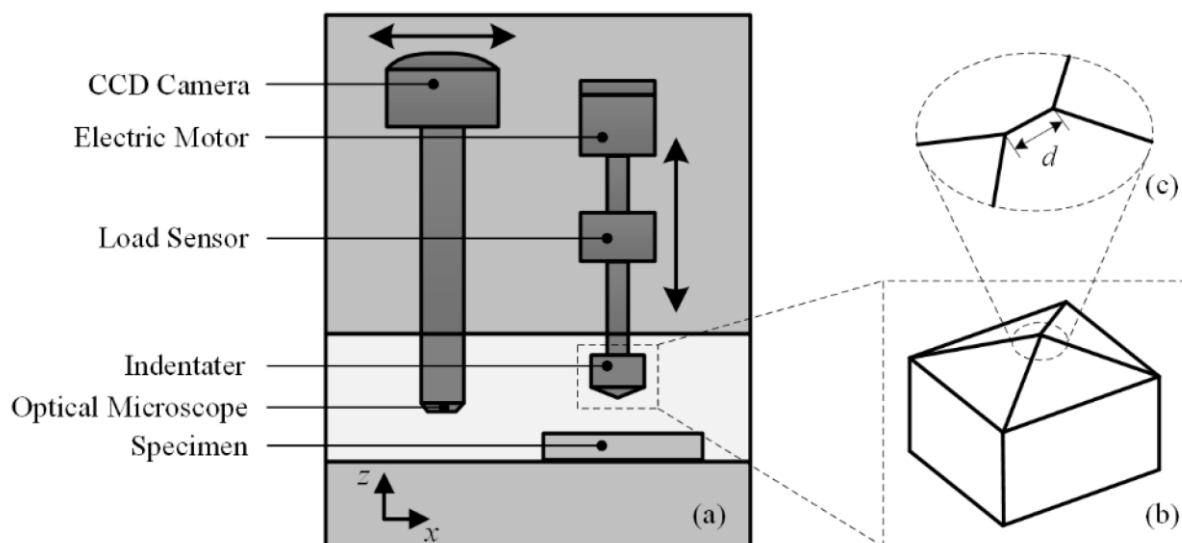


**Figure 45.** Reflectance (left) and Kubelka-Munk (right) spectra of TNT\_PDA materials with variable PDA thicknesses; inset shows the relation between the number of PDA electropolymerisation cycles against the thickness<sup>146</sup>.

#### 4.2.6. Nanoindentation

The nanoindentation method involves measuring the depth and force during the controlled indentation of a sharp tip into a material. Various mechanical properties, such as hardness, elastic modulus, and deformation behaviour, can be obtained at the sub-micron level. Nanoindentation instruments typically consist of a diamond or Berkovich-shaped indenter attached to a load sensor. The associated motorised table and optical microscope allow X-Y scanning of the material's surface and performing the

measurement in several places (**Figure 46**). The sample is typically in the form of a thin film, coating, or small bulk specimen.

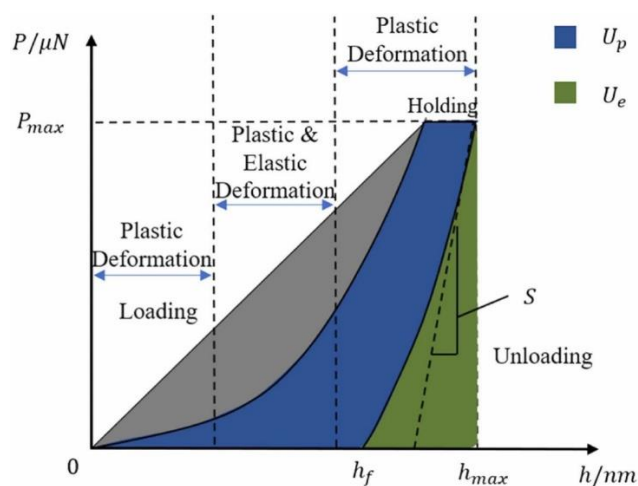


**Figure 46.** a) Schematic of the nanoindentation experimental setup, b) geometry of the example indenter, c) magnification of the indenter tip and its characteristic parameter,  $d^{165}$ .

Force and displacement data are continuously recorded with nanometre-scale precision during both the loading and unloading phases (**Figure 47**). Hardness is calculated by dividing the applied force by the contact area. The elastic modulus is derived from the slope of the initial linear portion of the unloading curve. It quantifies the material's ability to deform under stress and recover upon unloading. Analysing the load-displacement curve provides information about the material's deformation mechanisms, including swelling, the ratio of elastic to plastic deformation, and cracks.

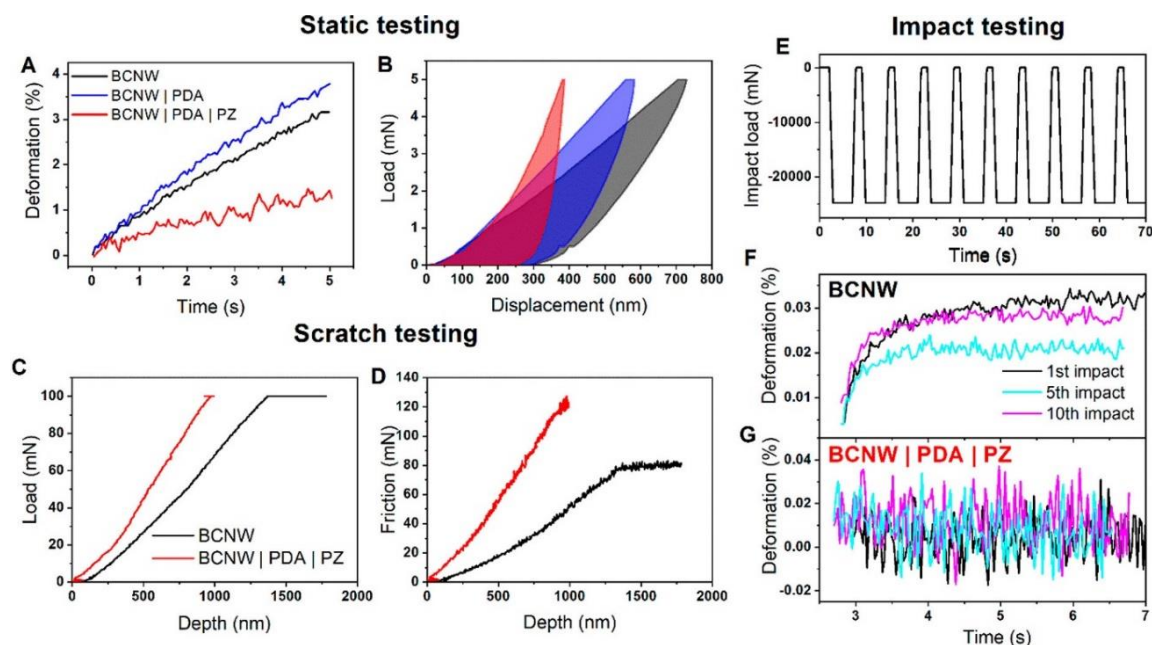
Those aspects are important for assessing the influence of the PDA and PZ coatings on the mechanical characteristics of the modified B:CNW and PDA electrodes. In particular, it is beneficial to verify the influence of the coating on the mechanical properties of the whole composite and establish correlations between the chemical structures and other properties (photoelectrochemical, electrical).

Besides the single measurements, there are several modifications, such as multi-load experiments, scratch testing and impact testing. In contrast to conventional nanoindentation, the impact loading method introduces a rapid application of force and continuous measurement of the deformation. Typically, several impact cycles are conducted consecutively. In the scratch testing mode, the indenter penetrates vertically into the sample and then horizontal forces are applied. The lateral load and friction are then measured against the vertical penetration depth. Higher friction indicates better scratch resistance of the sample.



**Figure 47.** Exemplar load-displacement curve obtained during the nanoindentation process<sup>166</sup>.

Nanoindentations were performed to elucidate the effect of the PDA-related coatings applied on the B:CNWs (**Article 2**) and TNTs (**Article 4**). Indentations were conducted mostly using a Berkovich indenter at room temperature with thermal drift correction. The hardness and Young's modulus were calculated using the Oliver-Pharr method. Besides single indentations, multiple impulse, impact testing and scratch experiments were also performed. During the experiment, data on acoustic emission and friction were also collected and correlated with other properties of the coatings. Example data are given in **Figure 48**. The author's contribution is participation in the analysis and interpretation of the nanoindentation data.



**Figure 48.** Nanoindentation studies of B:CNW\_PDA\_PZ. (A) Deformation velocity curves; (B) corresponding load–displacement curves; (C) load measured in the scratch test; (D) force of friction measured in the scratch test; (E) load profile applied during impact testing; (F) first, fifth, and tenth impact response of pristine B:CNWs; (G) first, fifth, and tenth impact response of B:CNWs functionalised with a copolymer PDA\_PZ coating<sup>167</sup>.

## 4.2.7. Electrochemical techniques

### 4.2.7.1. Experimental setups

In this thesis, electrochemical experiments were performed in the three-electrode configuration with a potentiostat. The studied materials were the working electrodes (WE) and their properties were investigated. The current flows between the WE and counter electrode (CE), which is typically a highly conductive material with a high surface area, such as Pt mesh. The reference electrode (REF) is a junction, which should have a well-defined standard potential and should not conduct the current during the experiment (typically Ag | AgCl | 3 M KCl). The use of REF makes it possible to control the WE potential by driving current through the potentiostat circuits. In reality, the current that flows through the WE is the sum of the potentiostat's influence and the effect of the WE's polarisation. The latter is measured and interpreted in terms of physiochemical processes, such as reactions, adsorption/desorption, polymerisation, etc. If the current is measured at an arbitrary time, it is a transient current. If the current is measured at the constant potential and time approaching infinity (equilibration), it is a steady state current. All processes involving the electrode-electrolyte charge transfers and concentration changes of charged species in the vicinity of the interface result in electronic or ionic current flow. The photocurrent is the difference between the current flowing during the illumination of the electrode and when the electrode is kept in the dark, which is called a dark current. It can be non-zero when the light shines on the semiconductor, which is capable of optical absorption and charge separation. Every charge that manages to reach the contact contributes to the photocurrent.

In this thesis, several techniques were used: cyclic voltammetry (CV), chronoamperometry (CA), electrochemical impedance spectroscopy (EIS) and difference pulsed voltammetry (DPV). Electrochemical properties were tested using Autolab PGStat 302N and Biologic SP-150 potentiostats-galvanostats. Characterisation was performed in different electrolytes, in pristine supporting electrolytes, such as Na<sub>2</sub>SO<sub>4</sub> and Tris buffer, and also in the presence of standard redox couples, such as ferro/ferricyanides(II)/(III) and hexaammineruthenium(II)/(III).

The photoelectrochemical properties were tested on three stations. The first one was an Autolab PGStat 302N potentiostat coupled with a solar light simulator (Xe lamp 150W, LOT-Oriel). The irradiation intensity was set to 100 mW cm<sup>-2</sup>, and the calibration was carried out using a silicon solar cell (Rera). A UV filter (Schott GG420) was applied to obtain only the visible part of the solar spectrum. The second one was a photoelectric spectrometer equipped with a solar simulator (Xe lamp), Czerny-Turner monochromator allowing wavelength sweep from 200 nm to 1100 nm and a potentiostat (Instytut Fotonowy). The third and final one was a photoelectric spectrometer equipped with several diode sources of variable intensities and a potentiostat (Instytut Fotonowy). In the measurements performed during the characterisation, 373, 398, 424, 455, and 524 nm LEDs were used.

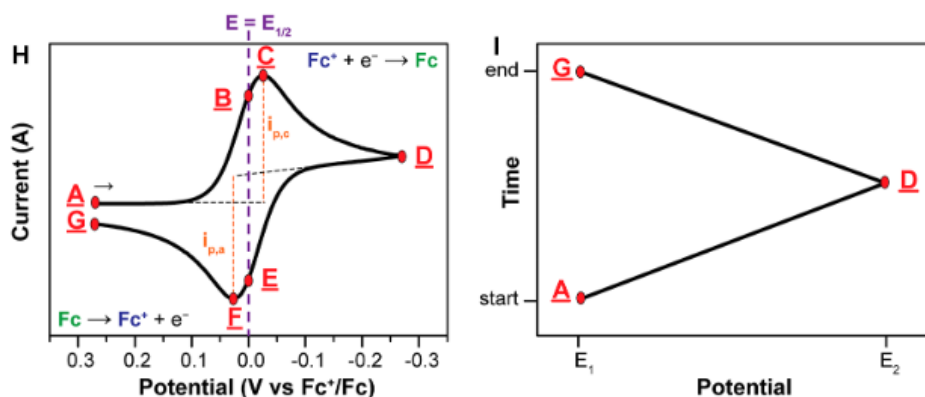
All electrochemical and photoelectrochemical experiments presented in the thesis were performed by the author, including data analysis and interpretation.

#### 4.2.7.2. Cyclic voltammetry

Cyclic voltammetry consists of alternating forward and reverse potential sweeps that are linear with time. The differential of the potential to time is called the scan rate. The anodic/cathodic polarisation direction drives oxidation/reduction reactions, both resulting in the current flow and current increase at the potential region of the faradaic reaction. If the reaction is associated with diffusion of the electroactive species, the current (density) is proportional to the square root of the scan rate according to the Randles-Sevcik equation. In this case, the typical duck-shaped curves are registered – examples can be seen in **Figure 49**<sup>168</sup>:

$$j = A \sqrt{\frac{dE}{dt}} \quad \text{Equation 4}$$

where A is the Randles-Sevcik slope proportional to the concentration and to the square root of the diffusion constant D, and E is the electrode potential. The slope of the current-scan rate function can vary depending on the reaction's reversibility. The difference between the peak potentials in the forward and reverse scans (peak-to-peak separation) provides information about the reaction kinetics. A larger separation indicates slower kinetics.



**Figure 49.** Left: exemplar plot of the CV plot of the redox couple with a single electron transfer reaction; Right: time-potential profile during the forward and backward scan of the CV experiment;  $E_2 > E_1$ ; Fc+/Fc is the ferrocene redox couple standard potential<sup>169</sup>.

Every process studied experimentally consisted of a series of elementary processes – transports, adsorptions, chemical reactions and charge transfers. Transport can occur in the form of diffusion (concentration gradient), migration (electric potential gradient) or convection (external force or velocity field). If there is no external mechanical force and the conductivity of the solution is sufficiently high



(due to the supporting electrolyte), diffusion is dominant. If the slowest process is diffusion and the kinetics is fast, the overall process is diffusion-controlled. If the opposite is true, the process is kinetically controlled. The scan rate often determines which process is controlling the overall rate. If the reaction is surface-bound or the dominant transport is migration, instead of Randles-Sevcik behaviour, the current is proportional to the scan rate:

$$j = B \frac{dE}{dt} \quad \text{Equation 5}$$

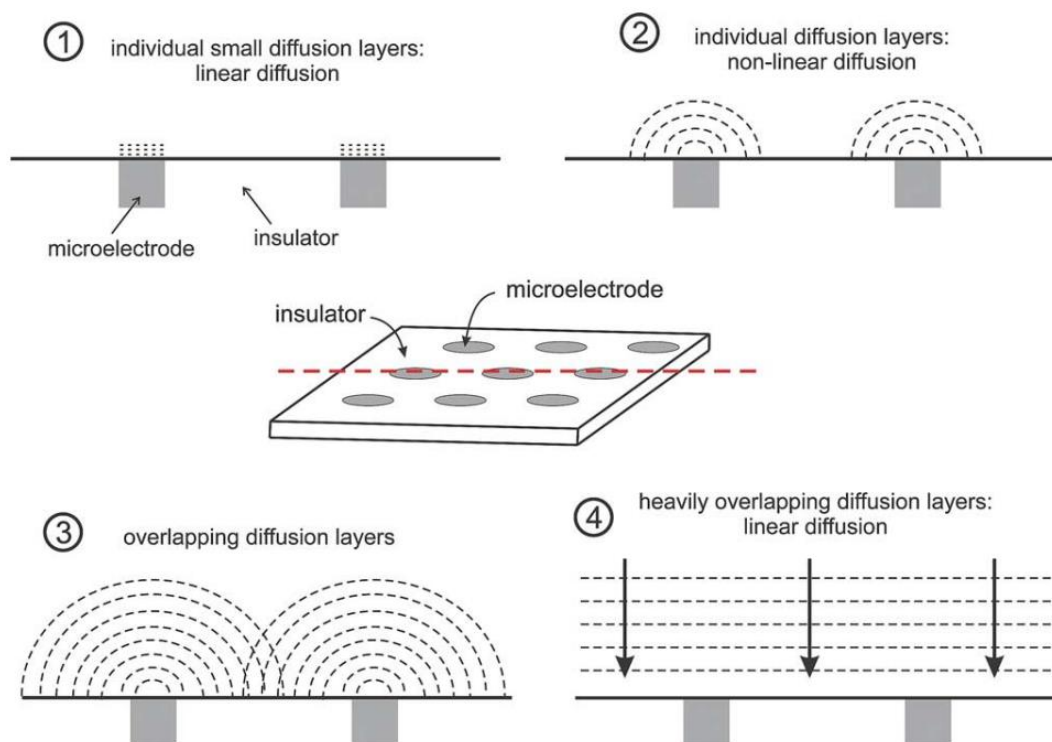
where B is a constant proportional to the surface concentration of the species<sup>168</sup>. If the dominant transport route is convection (which is the case for the RDE method), the steady-state current is independent of the scan rate.

One of the applications of the CV method in the thesis (in all **Articles 1–4**) is electropolymerisation of PDA and PZ coatings on the surface of B:CNW and TNT electrode materials, as described in **Section 4.1.3**. The co-electropolymerisation of PDA and PZ on B:CNW developed in **Article 2** was also performed using the CV method. Moreover, it was used to investigate the PDA electropolymerisation mechanisms in varying pH and potential windows in **Article 1**. The window from –500 mV to +1000 mV corresponded to the full spectrum of monomer reactions. In this series of experiments, depositions were performed until the three subsequent CV curves were identical. Typically, 50 CV cycles were recorded to meet this criterion. The influence of the solution's pH (ranging from 3 to 12) and the potential window in which the CV scans were recorded on the properties of the obtained PDA layer were significant.

Another way of utilising the CV method is measurements in an electrolyte containing a redox couple (ferro/ferricyanides (II)/(III) or hexaammineruthenium (II)/(III)). The purpose of these experiments is to describe the charge transfer kinetics between the redox marker of the obtained PDA or PDA\_PZ film, reflecting the electrochemical activity of the studied material. This adaptation of the CV method is used in **Article 1**, **Article 2** and **Article 3** for assessing the properties of the PDA coating electropolymerised in different conditions and in **Article 4** to establish the influence of the laser graphitisation parameters.

In **Article 2**, a CV in the presence of a redox marker was used in an extended approach to study the shape of the diffusion field in the vicinity of the modified B:CNW electrodes. In general, there are several types of CV shapes that correspond to different geometries of the concentration field  $C(x,y,z,t)$  during the electrochemical reactions (**Figure 50**). The general theory developed for the flat electrodes corresponds to the well-known duck-shaped CVs or Case 4 (see **Figure 50**) with heavily overlapping diffusion layers. The gradient of the concentration increase is perpendicular to the surface at every point of the space and points out of the surface where the reaction occurs. Isolines of the concentration are also parallel to the surface. If the surface is structured as a microelectrode array (Case 2 or 3), the shape

of the concentration gradient becomes spherical at each array component. As a result, the shape of the CV becomes more sigmoidal diffusion and the concentration profile is spherical. The curvature of the concentration field depends on the spacing between the array components, kinetic constant, and diffusion tensor. In the limiting case of infinitely spaced microelectrodes, the CV shape is again duck-shape and the diffusion is linear, as the electrode surface is flat.



**Figure 50.** Diffusion field distribution cases with respect to various spacings between microelectrodes in the array<sup>170</sup>.

In experiments performed in **Article 2**, CV curves with variable scan rates were recorded in the presence of either ferrocyanides(II)/(III) and hexaammineruthenium(II)/(III). Randles-Sevcik plots were established and fitted according to the generalised equation, as follows:

$$j = A \sqrt{\frac{dE}{dt}} + B \frac{dE}{dt} + j_{ss} \quad \text{Equation 6}$$

where the first term is analogous to the standard Randles-Sevcik  $A \sqrt{\frac{dE}{dt}}$ , the second term is analogous to the surface-bound process  $B \frac{dE}{dt}$ , and the last  $j_{ss}$  term is a steady-state current contribution to the overall current. A higher  $j_{ss}$  is associated with a higher curvature of the diffusion field<sup>171</sup>.

Another utilisation of the CV method in **Article 2** is the investigation of dopamine electrochemical detection mechanisms on the surface of B:CNW\_PDA\_PZ electrodes. In this case, CVs were performed

with varying pH values and scan rates. In the former case, the aim was to verify the presence of proton-coupled electron transfer. In the latter case, current-scan rate plots in the linear and log-log scale were prepared to establish whether the reaction was determined by the surface species.

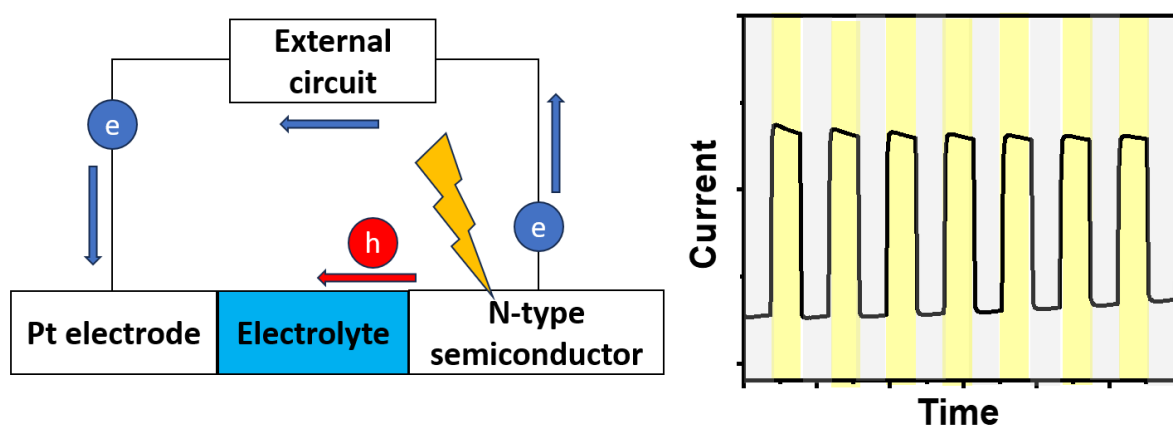
Finally, in **Article 3** and **Article 4**, the CV method was also used as one of the tools to confirm the deposition of PDA on the surface of titania nanotubes, as in such cases, the capacitive currents increased. Moreover, it was used to prepare the surface prior to the photoelectrochemical measurements.

#### 4.2.7.3. Chronoamperometry in chopped light/dark conditions

In a standard CA method, a constant potential step is applied, and the current is measured. If there is a reaction occurring at the surface, the current response follows the Cottrell equation<sup>172</sup>:

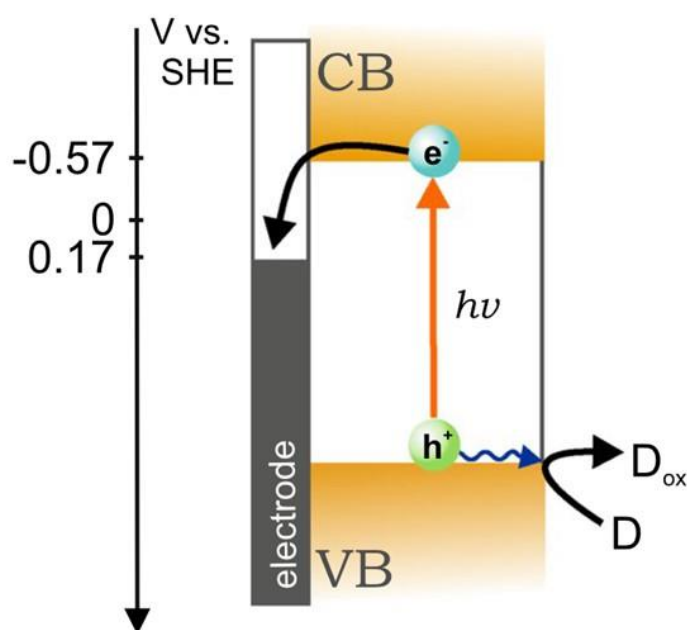
$$j = \frac{C_c}{\sqrt{t}} \quad \text{Equation 7}$$

where  $C_c$  is a constant proportional to the concentration of electroactive species and to the square root of the diffusion constant. However, the light stimulus can be superimposed on the standard CA, yielding a chopped dark/light CA. If the underlying semiconductor electrode is capable of generating a photocurrent, it will appear during the periods when the working electrode is exposed to light and the overall result will have a shape approximately of the rectangular wave depicted in **Figure 51**. In the case of an n-type semiconductor, the photocurrent is anodic (by convention, positive). In the case of a p-type semiconductor, the photocurrent is cathodic (by convention, negative). The shape of the stairs contains information on the number and magnitudes of time constants in the system. It is a function of the applied potential, light intensity, its wavelength, electrode preconditioning and electrolyte contents, e.g. the presence of a hole or electron scavenger.



**Figure 51.** Left: simplified diagram illustrating the photocurrent direction and value; Right: exemplar chopped dark/light CA result.

A brief explanation of why the photocurrent flows is given in **Figure 52**. Due to the finite conductivity of the semiconductor, a space-charge region forms on the semiconductor-electrolyte interface. In this region, there is an electric field and associated capacitance that, in the case of an n-type semiconductor, points the positive charge in the direction of the electrolyte. After optical absorption, the excited electron is separated from the hole in the space charge region. The hole moves towards the electrolyte and can oxidise molecules such as water or cause an ionic current in the electrolyte. The electron moves to the contact and can be collected. Both can recombine in various ways before reaching their final destination. If the circuit is closed, the photocurrent has flown.



**Figure 52.** Diagram of the photocurrent generation in the TiO<sub>2</sub> n-type semiconductor<sup>173</sup>.

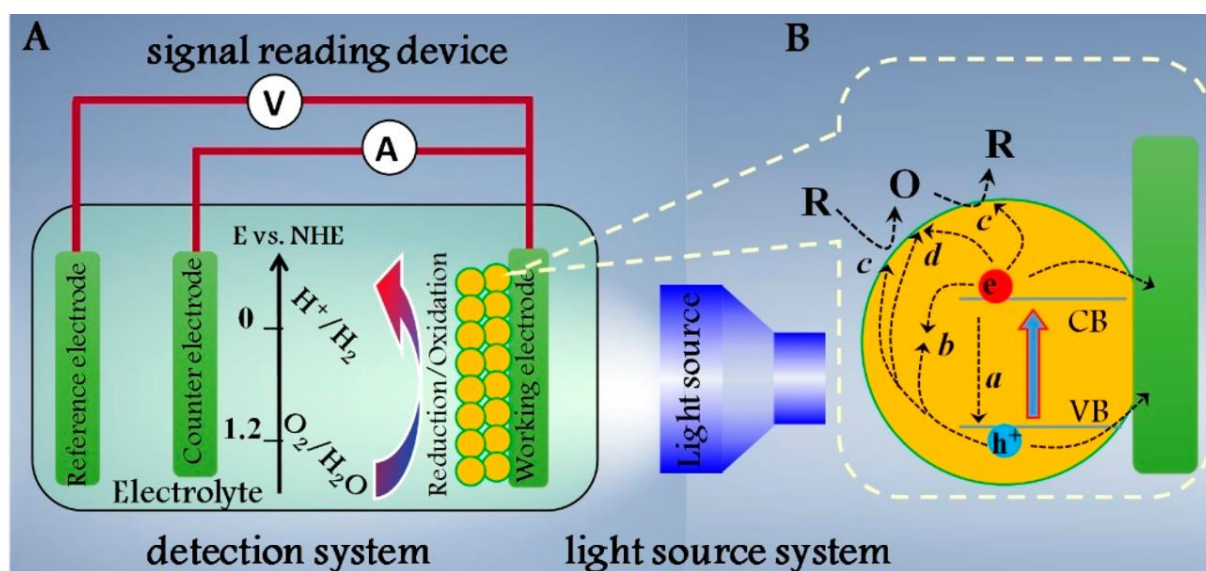
In **Article 3** and **Article 4**, the chopped dark/light CA is used to investigate the influence of the PDA and its graphitised variant, IgPDA, (**section 4.1.5**) on the photocurrent generation of modified TNT electrodes. In these works, the PDA deposition and graphitisation parameters are optimised towards the highest photocurrents and the fastest charge transfer kinetics. Moreover, in **Article 3**, it was used for the long-term testing of the photoelectrochemical performance.

The CA method is also used during the quantum efficiency measurements performed by the photoelectric spectrometers. This type of investigation makes it possible to estimate the incident photon-to-current efficiency (IPCE) ratio for varying polarisation conditions and wavelengths according to the equation:

$$IPCE = \frac{j}{P} \hbar \omega \quad \text{Equation 8}$$

where  $j$  is the photocurrent,  $P$  is the incident light intensity,  $\omega$  is the frequency, and  $h$  is the reduced Planck's constant. In **Article 3** and **Article 4**, quantum efficiencies of photocurrent generation were recorded for a range of wavelengths (typically between 200 and 700 nm) along with potential windows (typically between +100 mV to +800 mV). The purpose was to investigate the influence of the PDA synthesis parameters and laser graphitisation parameters on the IPCE.

In **Article 4**, dark/light CA is used for proof-of-concept studies of the non-enzymatic photoelectrochemical sensing of serotonin. It was implemented with a photoelectric spectrometer with the light source being a 373 nm LED with  $2 \text{ mW cm}^{-2}$  intensity and a constant potential of +100 mV vs Ag/AgCl. In this type of detection, the target molecule is oxidised on the surface of an n-type semiconductor. In this process, photogenerated holes are utilised to overcome the activation energy barrier for that oxidation. This is beneficial when the target molecule has an oxidation potential higher than the oxygen evolution threshold or is unavailable for other reasons (e.g. dark oxidation results in a toxic product). Schemes associated with this process are given in **Figure 53**.



**Figure 53.** A) Scheme of photoelectrochemical cell; B) Scheme of photoexcitation process utilised for sensing<sup>174</sup>.

Finally, in **Article 2**, the CA method without light is also used as a supporting tool for establishing the curvature of the diffusion field, complementary to the CV method described in **Section 4.2.7.2**. In this context, CA curves were recorded in the presence of ferro/ferricyanides in various potentials and fitted to the formula:

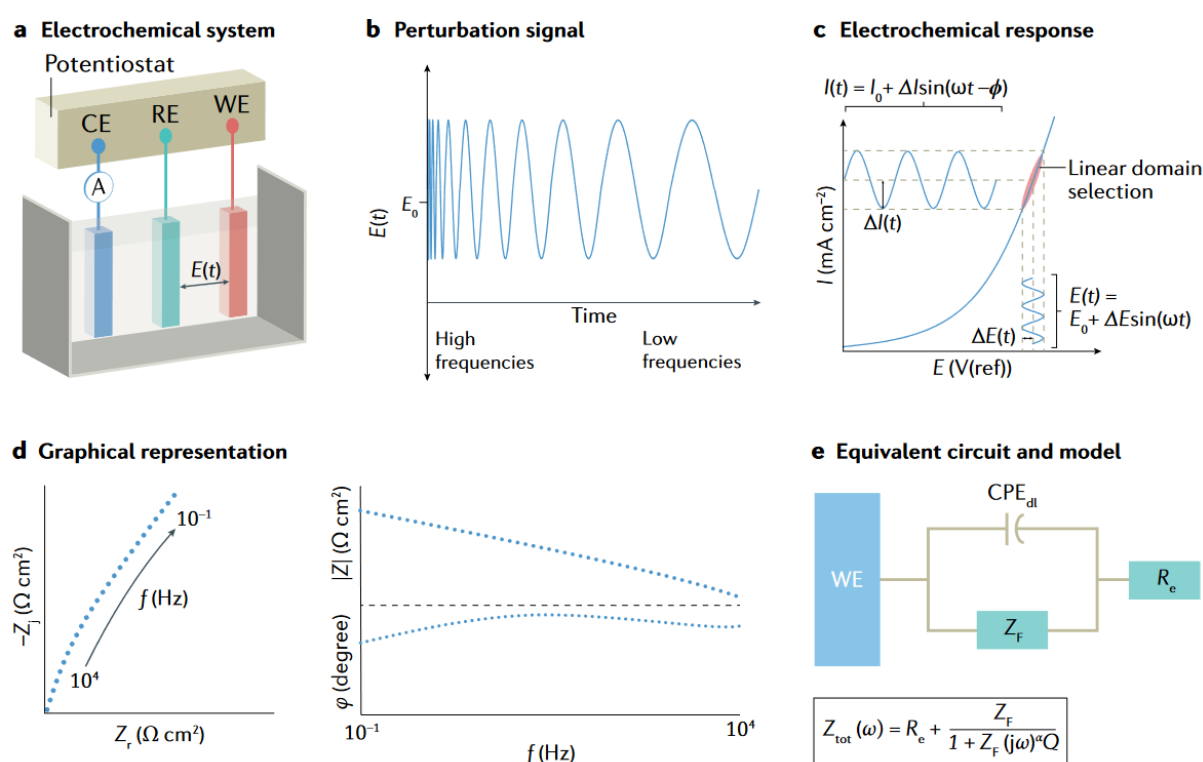
$$j = j_0 \exp\left(-\frac{t}{t_0}\right) + \frac{C_c}{\sqrt{t}} + j_{ss} \quad \text{Equation 9}$$

where the first term corresponds to the double layer discharge with the time constant  $t_0$  and the pre-exponential factor  $j_0$ , the second term is analogous to the Cottrell equation, and the last term is a

steady-state current contribution, analogous to the last term in the generalised Randles-Sevcik equation discussed above.

#### 4.2.7.4. Electrochemical Impedance Spectroscopy

EIS involves the application of a small amplitude alternating current (AC) signal over a range of frequencies to the three-electrode electrochemical cell (a) (**Figure 54**). This AC signal perturbs the system, inducing time-dependent responses that are recorded for analysis (b). Typically, high frequencies (typically up to 100 kHz) are applied first and then the frequency is reduced (typically down to 100 mHz)<sup>175</sup>. Per analogy to CV, EIS can be performed in various electrolytes depending on the measurement purpose.



**Figure 54.** Overview of electrochemical impedance spectroscopy; a) three-electrode system; b) sinusoidal input signal; c) linear approximation; d) Nyquist and Bode plots; e) exemplar Randles equivalent circuit<sup>176</sup>.

EIS was initially developed for linear and time invariant (LTI) systems. In those systems, the input signal is in linear relation with the output signal and the system does not change with time. In practice, this means that the sample does not have any hysteresis and two consecutive measurements should give the same result. Moreover, a single sine input will result in a single sine output with altered magnitude and phase difference  $\varphi$ . Thus, the transfer function (impedance –  $Z$ ) can be calculated as follows:

$$Z = \frac{L[U]}{L[j]} = \frac{|U|}{|j|e^{-i\varphi}} = |Z|e^{i\varphi} = X - iY \quad \text{Equation 10}$$



where  $L$  is the operator of the Laplace transform for the voltage or current. For each frequency, there is a separate impedance value. As a complex number, impedance can be decomposed into its real (resistive –  $X$ ) and imaginary (capacitive –  $Y$ ) parts or the phase and magnitude. The result is presented in the form of  $X$ -frequency,  $Y$ -frequency, phase-frequency (Bode), amplitude-frequency or  $X$ - $Y$  (Nyquist) projections.

Unfortunately, most processes in electrochemistry violate both conditions of the LTI principle. An example is the exponential Butler-Volmer equation linking the current and potential for a single electron transfer. In the field, there is a commonly used attempt to solve the problem by using a sufficiently small input perturbation ( $C$ ). An equivalent circuit (EC) is typically used to interpret the results. This involves nonlinear fitting (e.g. via the Levenberg-Marquardt algorithm) the experimental data to a circuit model that mimics the electrochemical processes occurring in the system. There are several rudimentary elements in each circuit, such as solution resistance  $R_s$  and charge transfer resistance  $R_{ct}$ , which is inversely proportional to the charge transfer rate<sup>175</sup>,  $k^0$ :

$$R_{ct} = \frac{RT}{n^2 F^2 k^0 [C]} \quad \text{Equation 11}$$

where  $n$  is the number of electrons transferred during the redox process,  $[C]$  is the concentration of electroactive compound,  $F$  is the Faraday constant,  $R$  is the universal gas constant, and  $T$  is the temperature. Basic capacitive elements include double layer capacitance  $C_{dl}$  and constant phase element CPE, the impedance of which is defined as:

$$Z_{CPE} = \frac{1}{Q(j\omega)^n} \quad \text{Equation 12}$$

where  $Q$  is the magnitude of the CPE element, and  $n$  is the number related to the homogeneity of the electrode and equal to 1 for an ideal capacitor. The impedance of the basic Warburg diffusion element,  $A_w$ , is defined as:

$$A_w = \frac{RT}{2n^2 F^2 \sqrt{D} C_{ox}} \quad \text{Equation 13}$$

A comprehensive list of these elements can be found in the literature<sup>175</sup>. In general, slower timescales (below 10 Hz) correspond to the transport (diffusion/migration) in the electrolyte, and higher timescales (below 10 kHz) are typically interfacial electron transfers and double-layer charging.

In **Article 1**, the EIS method is used complementarily to CV to investigate the mechanisms of PDA electropolymerisation. In this context, EIS spectra were recorded at various potentials for the B:CNW electrode in the pristine buffer and the buffer containing the monomer. The purpose of this experiment was to verify the electrode impedance in potential ranges corresponding to various redox reactions of

the monomers in the PDA synthesis. This made such investigations critical to assessing which reactions at which potentials are critical for forming the polymerised PDA layer.

Moreover, in **Article 1**, **Article 2**, and **Article 3**, EIS was used to verify the influence of the PDA on the charge transfer characteristics of the B:CNW and TNT electrodes. In **Article 3**, large-amplitude stimuli were applied to explore the nonlinear behaviour of the TNT\_PDA electrodes. The dependencies of the charge transfer resistance and impedance magnitudes on the stimulus magnitude and PDA thickness were important for understanding the electrical properties of the PDA. In **Article 4**, EIS was used to investigate the influence of the lasing parameters on the charge transfer occurring in the modified material. In all those experiments, redox markers were present in solution.

If the studied electrode is a semiconductor, the Mott-Schottky method can be used for obtaining the position of its flat band potential,  $E_{fb}$ , and donor density,  $N_d$ . The flat band potential is such potential that the space-charge region of the semiconductor is exactly zero<sup>177</sup>. The experiment is a series of EIS measurements performed for various electrode potentials in a high-frequency regime. The electrolyte typically contains inorganic salts but does not contain any source of redox species. At each potential, a single impedance point is taken, and its imaginary part is recalculated to the inverse squared capacitance,  $C$ , according to the formula<sup>175</sup>:

$$\frac{1}{C^2} = \frac{1}{2q\epsilon\epsilon_0 N_d} \left( E - E_{fb} - \frac{kT}{e} \right) \quad \text{Equation 14}$$

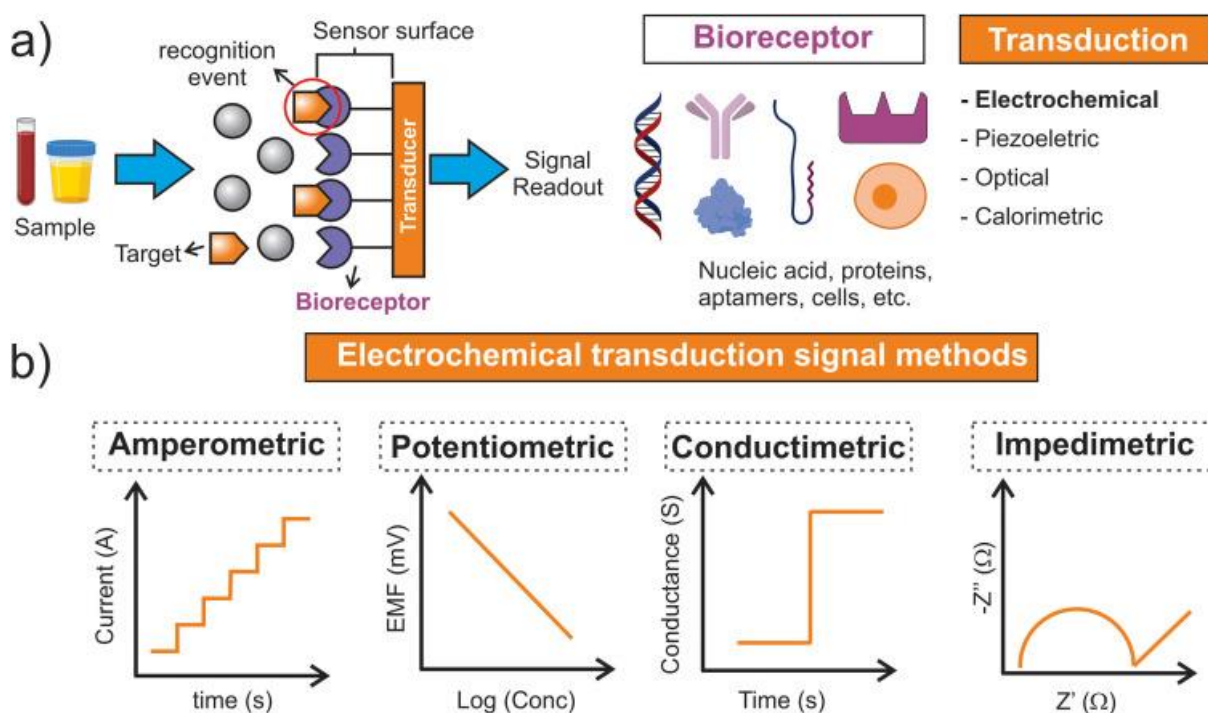
where  $\epsilon$  and  $\epsilon_0$  are the electrical permittivity of the medium and vacuum, respectively,  $q$  is the elementary charge,  $k$  is the Boltzmann constant,  $T$  is the temperature, and  $e$  is the elementary charge. The intercept is the flat band potential, i.e. the single potential at which the space charge region of the semiconductor is non-existent. The slope is positive for n-type and negative for p-type semiconductors and corresponds to the inverse of the donor density. The equation is based on several assumptions, the most important of which is flatness of the surface. Considering that this assumption is not satisfied for most of the electrodes used in electrochemistry, especially nanomaterials<sup>178</sup>, it should be used with caution. Similarly to the K-M method in optical spectroscopy, the comparative approach is advised, as absolute values of donor densities can be misleading.

In **Article 3**, the Mott-Schottky method it is applied for calculating the flat band potential of pristine and PDA-modified TNTs<sup>117</sup>. In fact, this type of measurements has shown that the TNT\_PDA material does not exhibit a typical slope and flat band potential characteristic for a semiconductor.

#### 4.2.7.5. *Difference pulsed voltammetry*

There are various methods of performing electrochemical sensing experiments. The first criterion is the mechanism of detection (**Figure 55**), which can be electrocatalytic, i.e. the direct oxidation/reduction

of the target molecule occurring at the electrode surface. Alternatively, the target molecule can react with some receptor (enzyme, aptamer, molecularly imprinted polymer, etc.), which alters the charge transfer between the electrode and the redox mediator or nanostructured charge transporter<sup>179</sup>. Information readout in these scenarios is amperometric, voltammetric, potentiometric, coulometric or impedimetric. Among these methods, difference pulsed voltammetry (DPV) stands as a prominent tool for electrocatalytic non-enzymatic sensing. In this technique, the waveform is a series of potential rectangular impulses with manipulable shapes. The baseline of each pulse is higher with each pulse so that the potential is effectively swept through the desired window. The current difference between the pulse and its baseline is recorded as a function of the potential.



**Figure 55.** A) General concepts behind electrochemical sensing – recognition, transduction, signal readout; b) sensing signal transduction using various electrochemical techniques<sup>179</sup>.

As a result of the pulsed character in the DPV method, high sensitivities and better temporal resolutions of the signals can be obtained. This feature is relevant for the detection of low-concentration analytes, such as neurotransmitters in biofluids. Therefore, in the thesis in **Article 2**, the electrochemical sensing of dopamine is performed on B:CNW\_PDA\_PZ electrodes in an electrocatalytic scheme using DPV. Measurements are performed in varying concentrations of the analyte in 1 X Tris buffer solution and bovine serum albumin. The latter is used to simulate the environment of biochemical fluids. Additionally, sensing tests in the presence of various interference compounds, multiple sensing tests of the same electrode and repetitive testing over several days are conducted to verify the applicability of the material in the harsh media of biofluids full of different interfering species.

### 4.3. Computational techniques in materials science and engineering

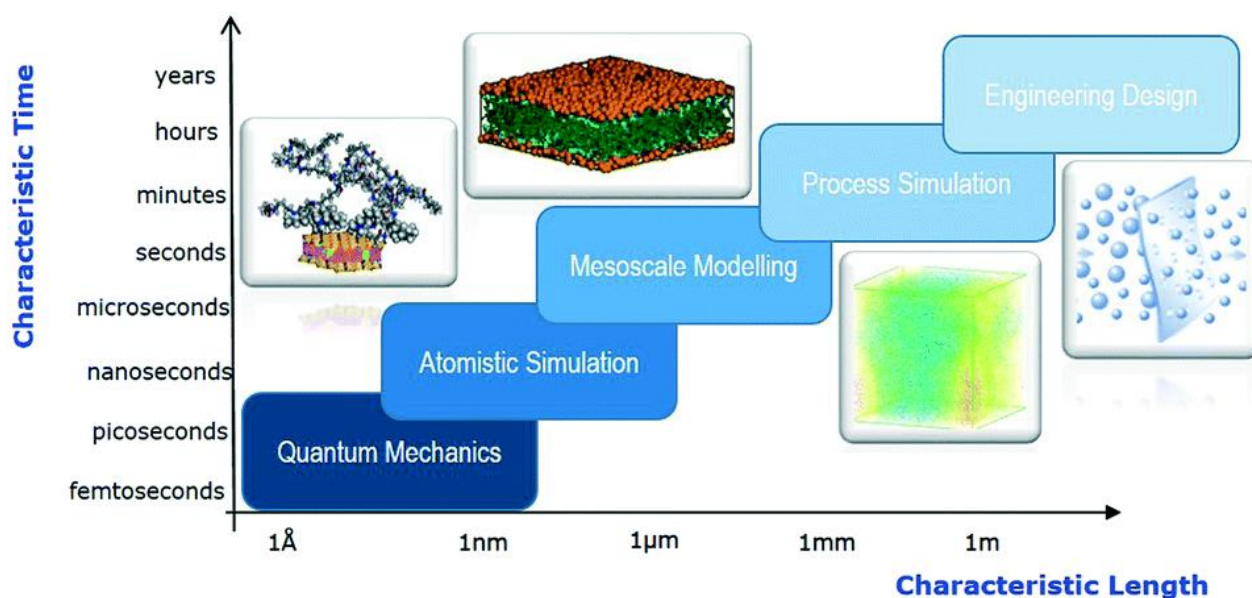
*The definition of a thing and the proof of its existence are two different and eternally separate things;  
the first tells us what is thought, the second that such a thing exists.*

*Definicja rzeczy a dowód jej istnienia są to dwie różne i wiecznie różne rzeczy;  
pierwsza mówi nam, co się myśli, druga że coś takiego jest.*

**Arthur Schopenhauer** – German, pessimistic philosopher; his PhD thesis (1813)

#### 4.3.1. Multiscale paradigm

Physiochemical properties of materials can be modelled on various length and time scales depending on the purposes of the researcher. This multi-scale paradigm is illustrated in **Figure 56**<sup>180</sup>. At the most macroscopic end of this diagram, classical mechanics and electrodynamics are used in various computational flavours. Computed quantities include strains, stresses, fluid flows and macroscopic dynamics of large (1 m scale) for objects such as turbines and engines. At the most microscopic end, there are approaches aimed at obtaining information at the atomic scale (1 nm scale) and computing basic physical quantities from the first principles of quantum mechanics (QM). In the intermediate regime, there are various molecular dynamics (MD) and mesoscale modelling approaches, which utilise information obtained by QM to propagate classical dynamics. In this thesis, several QM and MD methods are incorporated to support the experimental investigations.



**Figure 56.** Multiscale modelling paradigm in materials science. Characteristic length and time correspond to the sizes of the simulation boxes and times of the trajectories for the system investigated with each method<sup>180</sup>.

### 4.3.2. Computational chemistry methods

Computational quantum chemistry serves as a fundamental framework for understanding the electronic structure of molecules and solids. The main objective is to calculate equilibrium structures and their properties (electronic, thermal, etc.) from the first principles of QM. At its core lies the solution to the many-body Schrödinger equation, which describes the quantum state of a system composed of interacting electrons and nuclei<sup>181</sup>. The associated many-body Hamiltonian  $\hat{H}$  is a sum consisting of the following terms:

$$\hat{H} = \hat{T}_n + \hat{T}_e + \hat{V}_{nn} + \hat{V}_{en} + \hat{V}_{ee} \quad \text{Equation 15}$$

where  $\hat{T}_n$  and  $\hat{T}_e$  are kinetic energy operators for nuclei and electrons, respectively, and  $\hat{V}_{nn}$ ,  $\hat{V}_{en}$ , and  $\hat{V}_{ee}$  are potential energy operators for nuclei-nuclei repulsion, electron-nuclei attraction and electron-electron repulsion, respectively. The many-body Schrödinger equation is then:

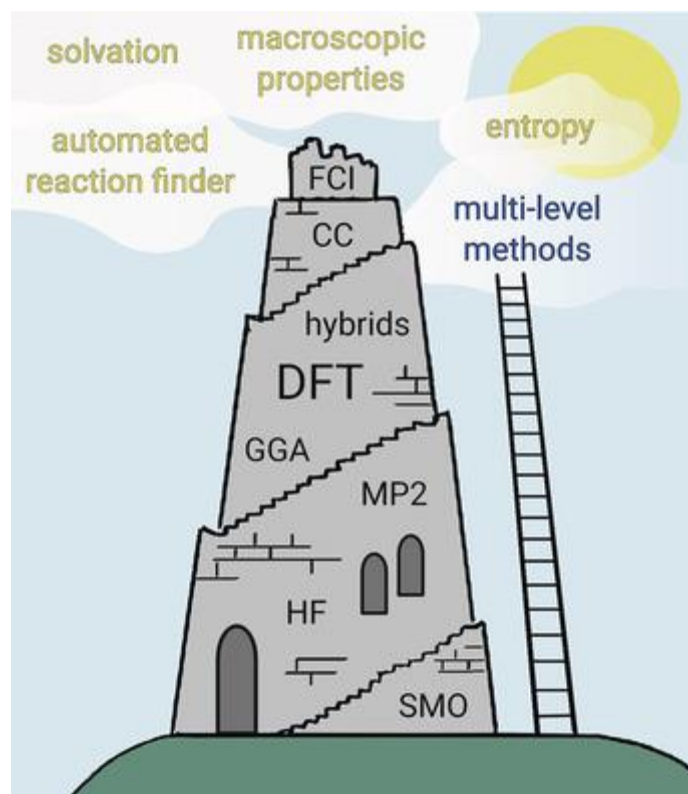
$$\hat{H}\Psi(r_1, r_2, \dots, r_n, R_1, R_2, \dots, R_N) = E\Psi(r_1, r_2, \dots, r_n, R_1, R_2, \dots, R_N) \quad \text{Equation 16}$$

where  $\Psi(r_1, r_2, \dots, r_n, R_1, R_2, \dots, R_N)$  is the many-body wavefunction, dependent on the positions of electrons  $r_n$  and the position of the nuclei  $R_N$ . However, solving the many-body Schrödinger equation is impossible analytically and extensively demanding from a computational view (typically, exponential  $O(\exp(n))$  scaling). Therefore, various approximation methods have been developed to solve this equation and predict molecular properties with variable accuracies and computational costs. The landscape of those methods is schematically depicted in **Figure 57**<sup>182</sup>.

The most rudimentary approach is the Hartree-Fock (HF) method. In this approximation, electrons are treated as independent particles subject to an average potential generated by other electrons. This is a ground state theory. It is computationally cheap, but no longer used due to its poor accuracy in most problems. It provides a starting point for more advanced methods, though.

One possible improvement of the HF method is the Møller-Plesset (MP) perturbation theory, which introduces corrections to the electron-electron interaction. As a result, the description of the dynamic electron correlation effects is improved. It has a small niche of applications in some areas of quantum chemistry but is not widely used due to its exponential scaling.

DFT is a widely used method that approaches the many-body problem by focusing on the electron density rather than the wavefunction. It introduces an exchange-correlation functional to approximate the electron-electron interaction. Due to linear or superlinear scaling, it makes it possible to study larger systems, but it is still a ground state theory. While computationally less demanding, DFT still requires careful selection of the functionals for accurate results. DFT is the primary tool used in the thesis and will be described further in more detail.

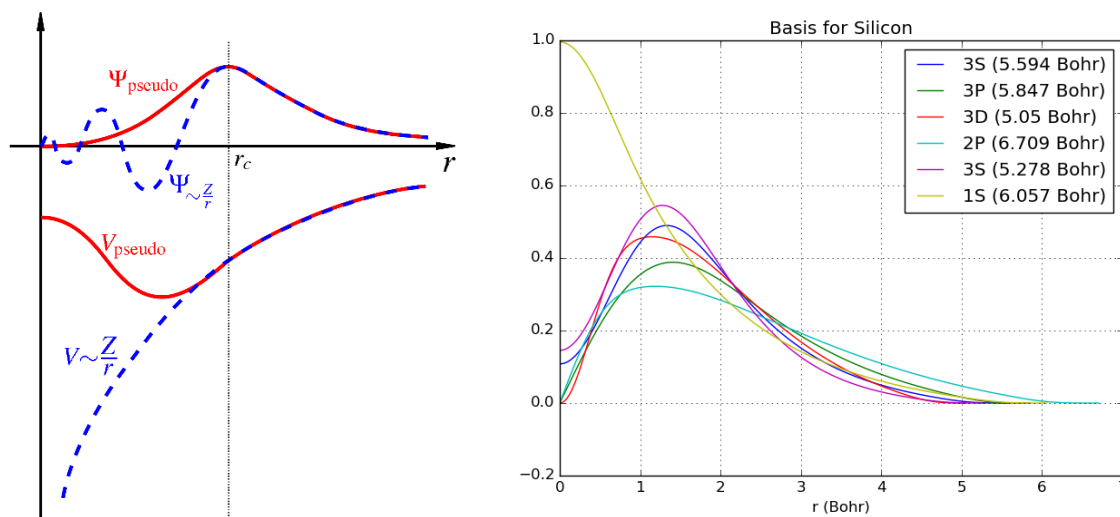


**Figure 57.** Landscape of the quantum chemistry methods<sup>182</sup>.

Among the high-accuracy and high-computational cost methods are the couple cluster (CC) and configuration interaction (CI) theories. Both methods build on the Hartree-Fock reference state and include electron excitations that capture electron correlations more comprehensively than DFT. CCSD (Coupled Cluster with Single and Double excitations) is a commonly employed variant of CC, and CISD (Configuration Interaction with Single and Double excitations) is a typically used variant of CI.

With each method, the ultimate object is to solve for the molecular orbitals. The accuracy of the calculations is always influenced by the choice of the basis set, which represents the mathematical functions used to describe those orbitals. Increasing the size and flexibility of the basis set generally leads to more accurate results but also generates higher computational cost (**Figure 58**). A fruitful approach to reducing the computational cost is utilising pseudopotentials. The main idea is to use a full basis set to describe only the valence electrons and substitute the core electrons basis set with empirical potentials. In this case, empirical means that the parameters of the pseudopotentials can be estimated based on computations at the more accurate levels of theory or experimental results or directly from experiments. In most chemical problems, it is a reasonable choice, provided that a sufficient number of electrons are counted as valence.



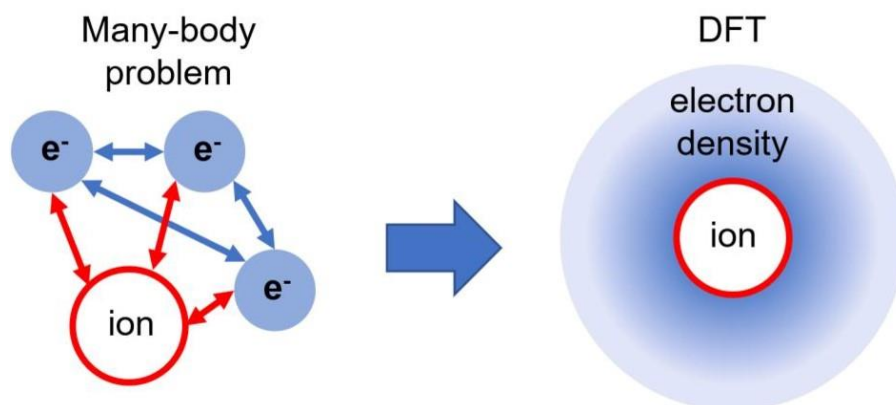


**Figure 58.** General concepts of the pseudopotential (left)<sup>183</sup> and the basis set (right)<sup>184</sup> used in quantum chemistry calculations.

### 4.3.3. Density Functional Theory

The groundbreaking concept within DFT is focusing on the electron density rather than the many-electron wavefunction<sup>181</sup>, which greatly reduces the computational scaling even to linear  $O(n)$  or superlinear  $O(n \cdot \log n)$  scaling. This concept is schematically depicted in **Figure 59**. Density functional means that the energy of the system depends on electron density as a functional. The function is considered here as a map from number to number, while the functional is a map from function to number. According to the Hohenberg-Kohn theorems, those two descriptions are equivalent in the ground state. Instead of the Schrodinger equation, the central object to solve in DFT is the Kohn-Sham equation. It takes the form:

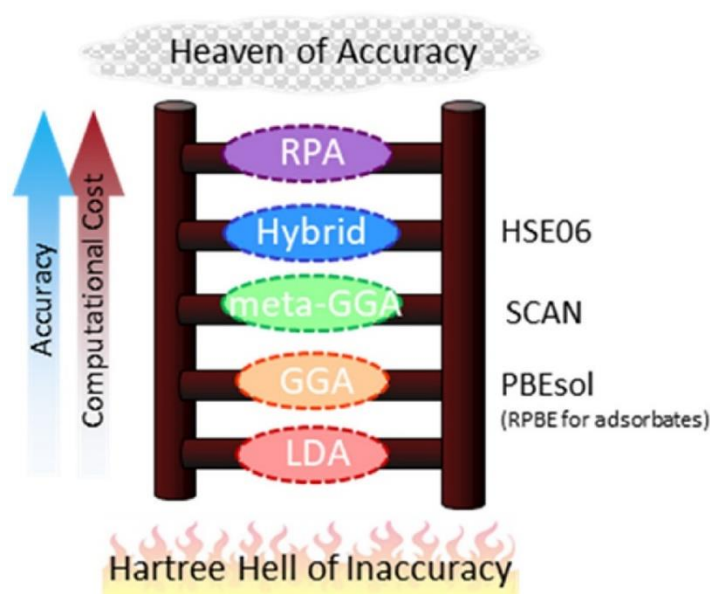
$$[\hat{T} + \widehat{v_{eff}}]\phi(r) = [\hat{T} + \widehat{v_{ext}} + \widehat{v_{coul}} + \widehat{v_{xc}}]\phi(r) = \varepsilon\phi(r) \quad \text{Equation 17}$$



**Figure 59.** Schematic idea differentiating the many-body problem in most quantum chemistry approaches and the electron density problem in DFT<sup>185</sup>.

where  $\phi(r)$  are Kohn-Sham orbitals,  $\hat{T}$  is the kinetic energy operator,  $\widehat{v_{eff}}$  is the effective potential energy operator, consisting of external field of nuclei  $\widehat{v_{ext}}$ , coulombic electron-electron repulsion  $\widehat{v_{coul}}$  and exchange correlation term correcting for the quantum behaviour of the electrons  $\widehat{v_{XC}}$ , and finally,  $\varepsilon$  are energies (Kohn-Sham eigenvalues). The Kohn-Sham equation is a non-interacting system whose electron density mirrors the real interacting system. While formally a single-electron equation, the Kohn-Sham orbitals collectively approximate the true electronic density of the interacting system.

The most problematic term in the Kohn-Sham equation is the effective potential. It consists of several terms, one of which  $-\widehat{v_{XC}}$  is related to the exchange-correlation (XC) functional. This object is responsible for the level of accuracy of the physical description of the DFT result and is generally unknown. Therefore, it must be designed from other arguments and intuitions. There are many XCs in the literature with varying accuracies and computational costs, as depicted in **Figure 60**.



**Figure 60.** Hierarchy of the exchange-correlation functionals used in DFT<sup>186</sup>.

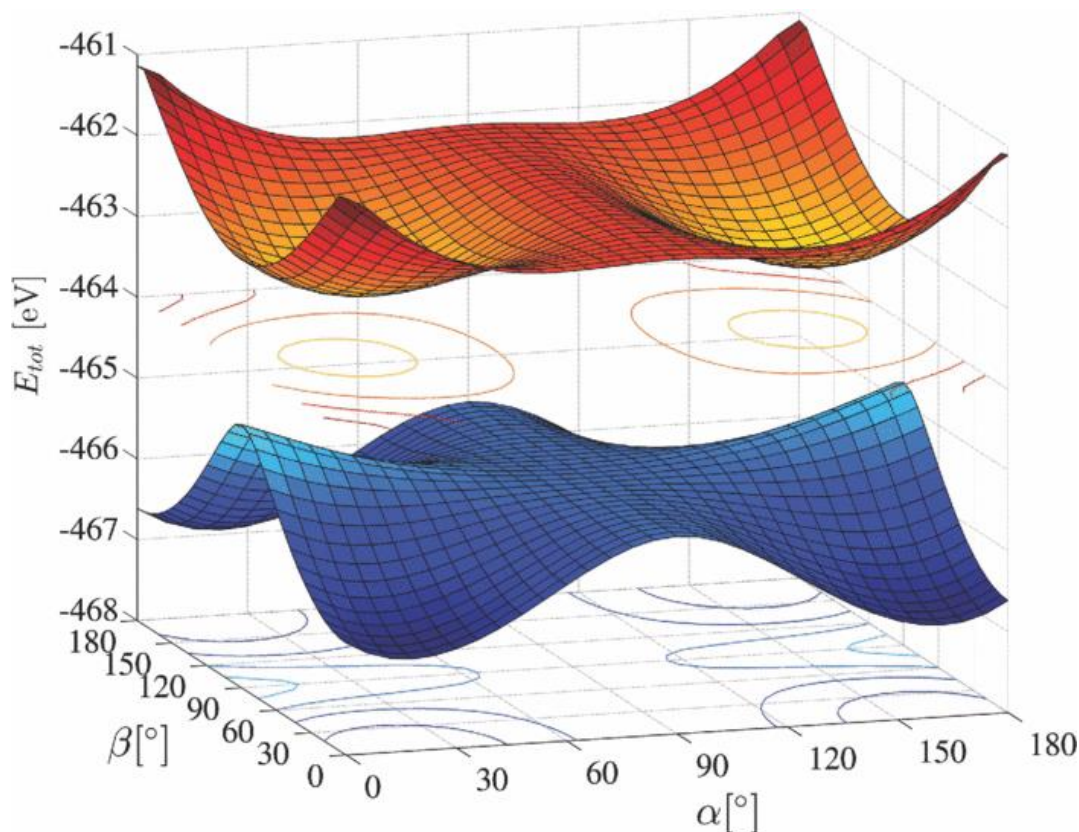
The Local Density Approximation is the simplest exchange-correlation functional, assuming a uniform electron density within a local region. While computationally most efficient, LDA struggles with accurately describing systems with a significant electron correlation. GGA (General Gradient Approximation) represents a substantial improvement over LDA by incorporating information about the gradient of the electron density. It considers both local and non-local electron density variations, enhancing the accuracy in describing molecular structures and interactions. Popular GGAs include the Perdew-Burke-Ernzerhof (PBE) functional and its variants. Meta-GGA functionals go beyond GGAs by incorporating information about the kinetic energy density, which improves the accuracy in describing molecular properties in some systems. Functional SCAN is the most widely used in this category. Hybrid functionals combine Hartree-Fock exchange with a fraction of the

exchange-correlation energy from GGA or LDA. Examples include the Becke 3-parameter Lee-Yang-Parr (B3LYP) functional, sometimes considered as a gold standard for chemistry-oriented calculations. Finally, random phase approximation (RPA) functionals use the perturbation theory corrections to further improve the description of the electron-electron correlation, which is relevant for accurate chemical results.

In general, GGAs at the PBE level of theory are applied in the thesis as a compromise between accuracy and the ability to simulate larger systems. With this choice, however, it is necessary to make further approximations, such as the DFT- $\frac{1}{2}$  correction correcting the bandgap<sup>187</sup> and the DFT-D3 correction correcting the van der Waals interactions<sup>188</sup>.

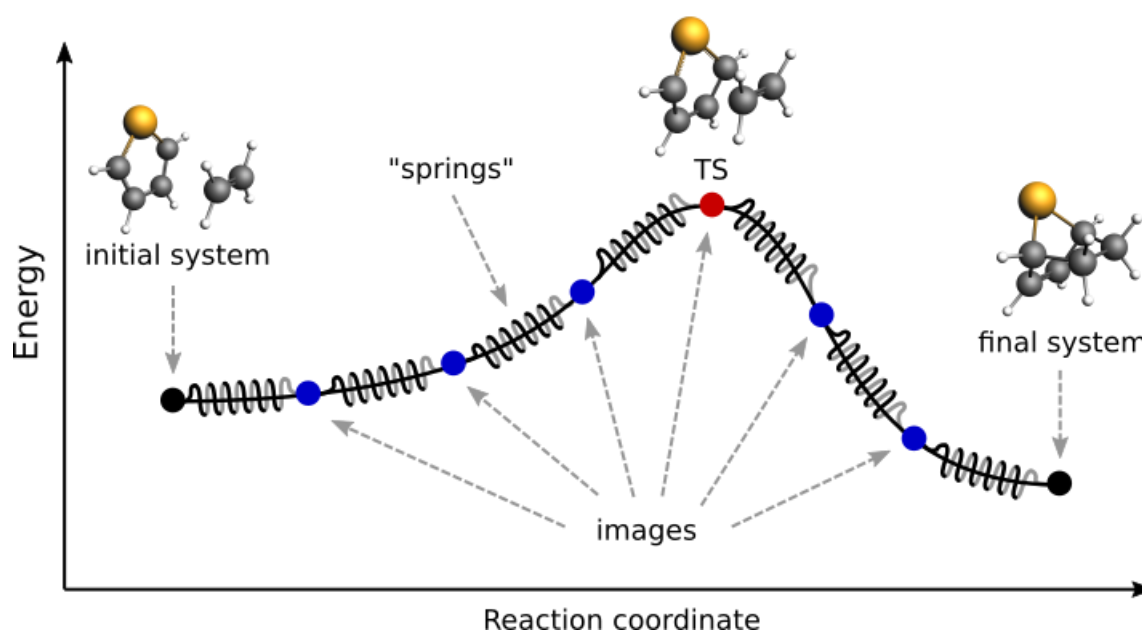
#### 4.3.4. Geometry optimisations and technical aspects

To begin the calculations of any property of the DFT, one needs to find the optimised geometry of the studied system. In general, the molecule ground state energy depends strongly on the geometry characteristics, such as the bond lengths, bond angles, and dihedral angles. Technically, energy is a multidimensional function of all those characteristics called potential energy surface (PES)<sup>181</sup>. Each electronic state, i.e. ground state (the realm of DFT), and every excited state has its own PES (an example for a two-dimensional system is shown in **Figure 61**).



**Figure 61.** Example of two-dimensional potential energy surface<sup>189</sup>.

The minima on the PES correspond to optimised molecular geometries and are targets of geometry optimisation algorithms. In the context of solids, the minima correspond to the equilibrium crystallographic parameters. The curvatures of the PES correspond to the vibrational frequencies that can be registered using the FT-IR and Raman techniques. The maxima on the PES correspond to transition states and are relevant for studies of chemical reactions (an example of such an optimisation for a single-reaction coordinate – one dimension – is given in **Figure 62**). In this context, the energy barriers for the reactions and reaction pathways can be studied.

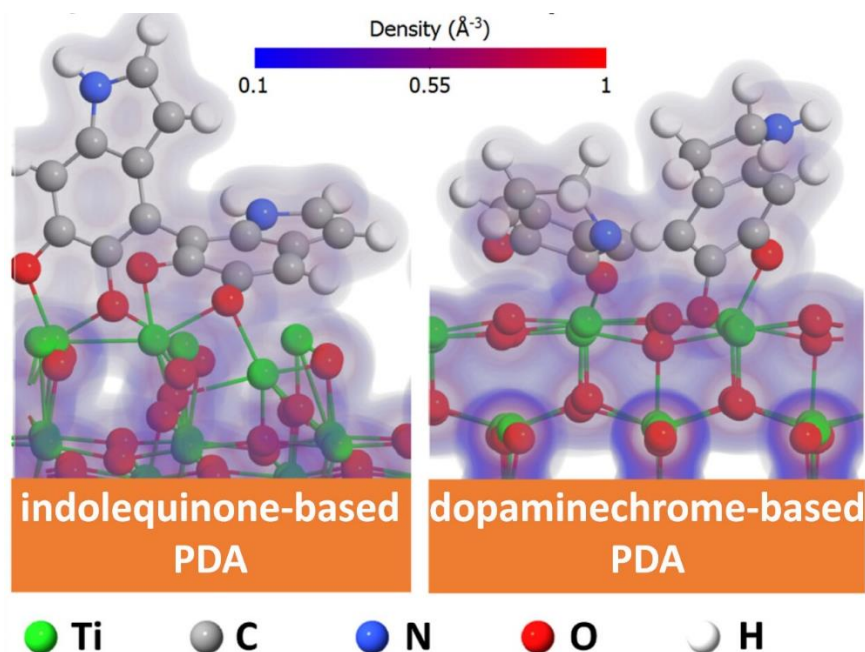


**Figure 62.** Example of geometry optimisations to reactants, products and transition state<sup>190</sup>.

Geometry optimisation algorithms have a particular use in studies of the adsorption of a molecule on a surface. In general, a single molecule can be adsorbed in many geometries in many positions on a surface with varying adsorption energies. This energy is defined as the following free-energy difference:

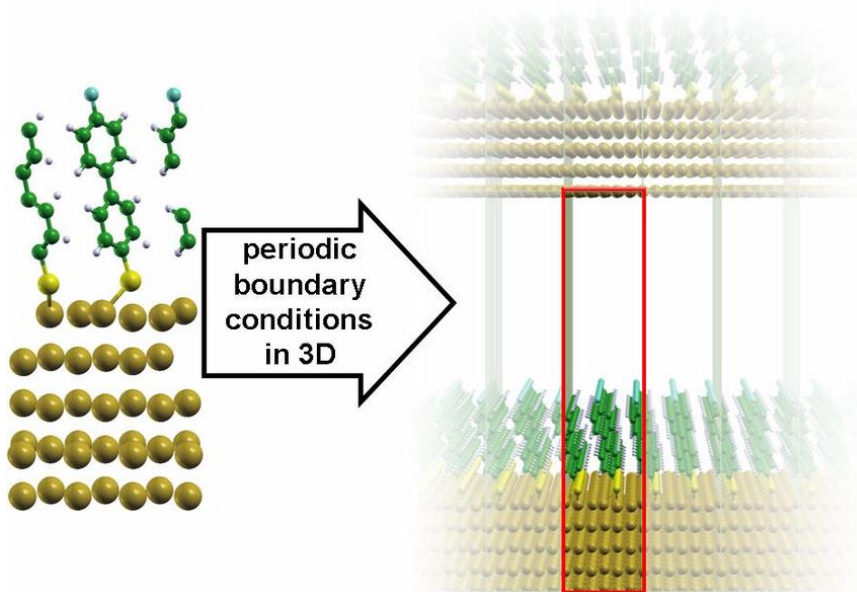
$$G_{ads} = G_{slab-molecule} - G_{slab} - G_{molecule} \quad \text{Equation 18}$$

The alternative quantity being exactly the negative of the adsorption energy is the surface binding energy. In other words, various adsorption geometries form a PES, and the minima on this PES correspond to the lowest energy configurations. Example binding energies are shown in **Figure 63**, where the b) configuration has the optimal (most probable) geometry. Per analogy to the molecular scenario, the highest adsorption energy (lowest binding energies) configurations can be considered as transition states in surface catalytic reactions. Adsorption simulations were used in the thesis in **Article 2** and **Article 3**.



**Figure 63.** Adsorption geometries of two different PDA fragments on anatase (101) surfaces with electron density maps<sup>146</sup>.

The final technical remark on the surface calculation with DFT or other methods is the necessity of using the slab model and available boundary conditions. A slab is a three-dimensional cell of atoms with full periodicity in two dimensions and reasonably large vacuum space above the surface in the third dimension. In this dimension, one can also use the periodic boundary conditions (as in **Figure 64**) or other types depending on the aim of the computations. Nevertheless, the purpose of the top vacuum is to simulate the surface behaviour by minimising artificial cell-to-cell interactions.

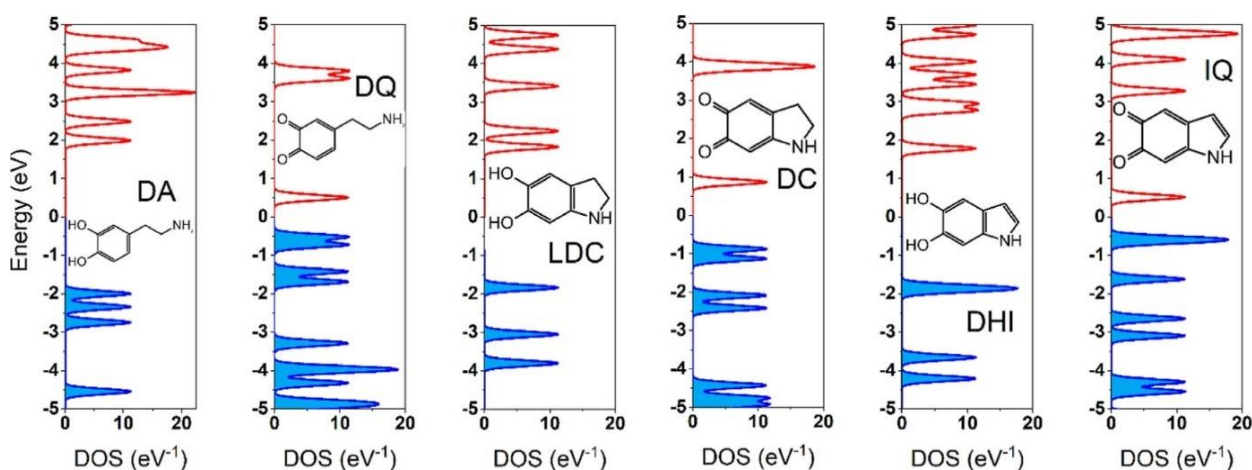


**Figure 64.** Illustration of the slab model and periodic boundary conditions ideas<sup>191</sup>.



#### 4.3.5. Properties calculable from DFT

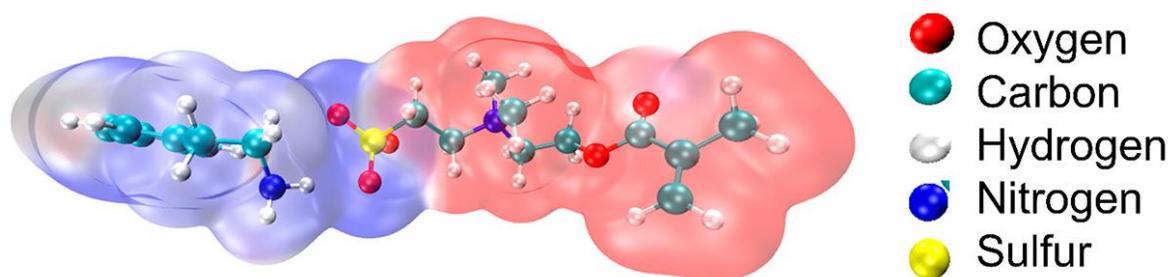
One of the most fundamental outcomes of the DFT calculations is the orbitals, their energies, and electronic populations. Alternatively, one can look at this outcome in the form of the density of states (DOS), i.e. the number of available orbitals per given energy (**Figure 65**). In solid systems, orbitals are populated according to the Fermi-Dirac distribution, where the Fermi level corresponds to the half-occupancy. The intuition is that any orbital above the Fermi level is likely unoccupied, and any orbital below is occupied most of the time. From the DOS plots, it is possible to infer whether the larger system is more like a molecule (discrete levels) or like an infinite solid (levels form bands). Depending on the Fermi level position, the studied system can be classified as a semiconductor or metal, and forbidden energy gaps can be obtained. Comparison of the DOS in the vicinity of the Fermi level for various materials can be used to screen for the optimal catalytic or electrical properties and assist experimental investigations in those contexts. This approach was used in **Article 3** to study the electronic structure of the PDA structural units alone and in junction with the  $\text{TiO}_2$  substrate.



**Figure 65.** Schematic diagrams of the Density of States plots for several subunits of PDA. Fermi level is located at 0 eV, blue bands are occupied and red are unoccupied<sup>146</sup>.

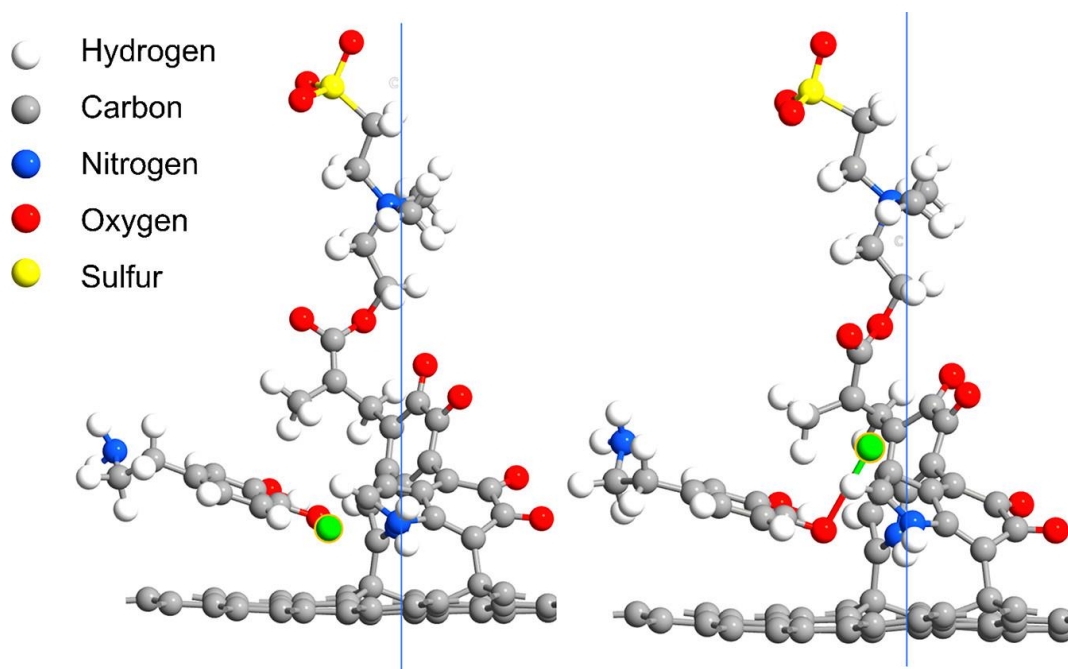
Another relevant category of results is 3D maps of properties such as the electrostatic potential (ESP), an example of which is shown in **Figure 66**. It can be obtained from the DFT-calculated electron density by solving the classical Poisson's equation. As a result, a two-colour map of the surface charge distribution is produced. Information on this distribution can be used for assessing the chemical reactivity of a molecule, investigating the catalytically active sites on the complex surface and elucidating the charge transfer characteristics. This approach was used in **Article 2** for the investigation of PDA\_PZ interactions.





**Figure 66.** Example of electrostatic surface potential (ESP) map illustrating interactions between the PDA subunit and zwitterionic molecule<sup>167</sup>.

In this thesis, DFT algorithms are used for geometry optimisation of the molecular structures of PDA and PZ structural units and the surfaces they adsorb onto. Their adsorption geometries and energetics on model TiO<sub>2</sub> and B:CNW surfaces are investigated to elucidate intermolecular interactions between those compounds. Electronic structure investigations of the optimised structures are then performed, including molecular orbital analysis, and density of states calculations with the DFT+ $\frac{1}{2}$  correction for the bandgap<sup>187</sup>. In particular, electron density maps and molecular ESP<sup>192</sup> are helpful for visualising the results. A specific example of the DFT application in **Article 2** is the elucidation of the interaction between the catecholamine analyte and the surface modified with a model PDA\_PZ molecule, as shown in **Figure 67**. Overall, DFT techniques support experimental results by providing additional insights into the mechanisms of the macroscopic processes at the molecular level.

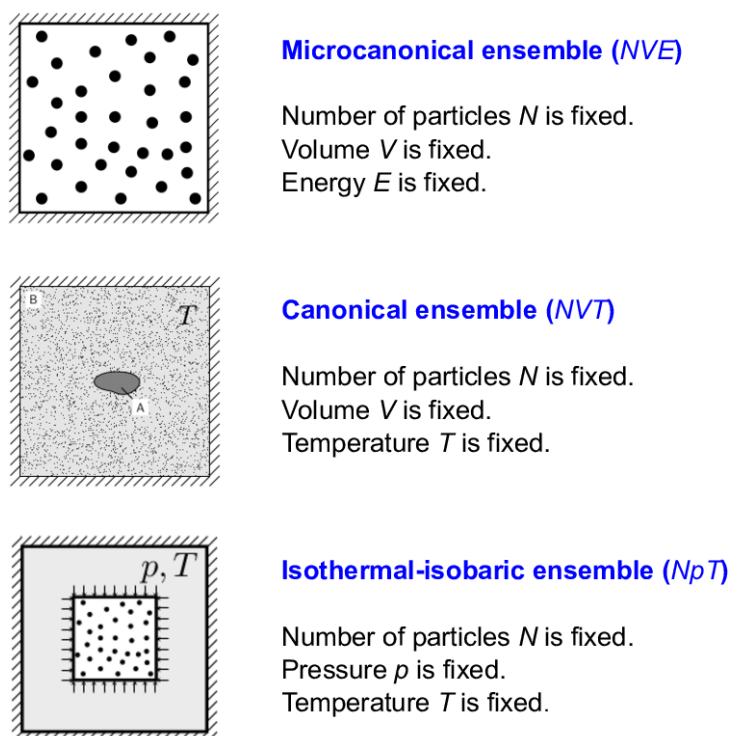


**Figure 67.** Left panel: preoptimised geometry of dopamine adsorbed on a carbon surface coated with PDA\_PZ and the formation of a molecular pocket for dopamine; Right panel: DFT full optimisation of the adsorbed dopamine and geometry illustrating the stabilisation of the transition state in the dopamine-dopamine quinone oxidation reaction; the green atom is hydrogen abstracted from the catechol group<sup>167</sup>.

Most of the calculations are performed at the general gradient approximation (GGA) level with the Perdew-Burke Ernzerhof (PBE) functional. For systems with a larger number of atoms, effective core potentials are used, such as Fritz-Haber Institute (FHI) pseudopotentials or pseudo Dojo<sup>193</sup>, as implemented in the Quantum ATK Synopsis<sup>184</sup> license provided by the Department of Metrology and Optoelectronics at the Gdansk University of Technology. All DFT calculations included in the thesis were performed, analysed and interpreted by the author.

#### 4.3.6. Molecular dynamics and ReaxFF force fields

The main objective of molecular dynamics (MD) is to calculate the temporal evolution of solid, surface or molecular systems. Trajectories of particles can be obtained either by solving the Schrödinger equation (full quantum dynamics) or Newton's classical equation (classical dynamics) for the series of time steps in the range of 1 fs<sup>181</sup>. Due to high computational load of the former approach, it is reserved for relatively small systems or relatively small time evolutions. In the realm of classical dynamics, interatomic forces can be calculated using quantum methods (ab initio MD) or with a predefined set of parameters. The classical MD allows orders of magnitude lower computational costs than ab initio MD, but the result is strongly dependent on the choice of those parameters. Nevertheless, the main aim of the MD is to calculate various structural, dynamic and thermodynamic properties from the trajectory. There are three most basic statistical ensembles that the MD calculations can be subjected to (**Figure 68**).



**Figure 68.** Statistical ensembles used in molecular dynamics<sup>194</sup>.

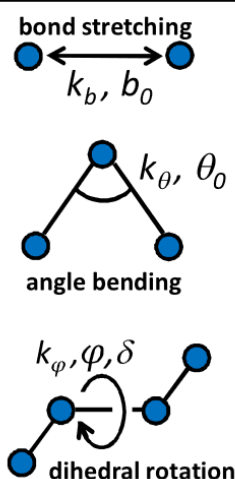
In the case of NVE, Newton's equations are solved for each time step in a fixed box, typically with periodic boundary conditions. In NVT, the temperature is held constant by a thermostat (e.g. Berendsen or Nosé-Hoover), which inputs or withdraws energy from the system to maintain the desired constant temperature. In NpT, both the pressure and temperature are kept constant by a barostat and a thermostat. The size of the box is adjusted by the barostat so that a constant pressure is maintained. Barostats and thermostats are purely mathematical procedures allowing the trajectory to propagate.

As mentioned above, a fully classical MD calculation requires a set of input parameters describing the interactions between the atoms, such as the bond force constants, angle force constants, dihedral force constants, improper dihedral force constants, van der Waals and terms electrostatic (Coulombic) interactions. Collectively, those parameters form a force field (FF) (an example of such quantities is given in **Figure 69**). In the force field file, every pair and triplet of atoms must be written to reflect their interactions in the trajectory. Particular values for each pair/triplet can vary depending on the purpose of the force field, even for the same set of atoms (e.g. C-C interactions will be different in a FF devoted to hydrocarbons and different in carbon nanostructures).

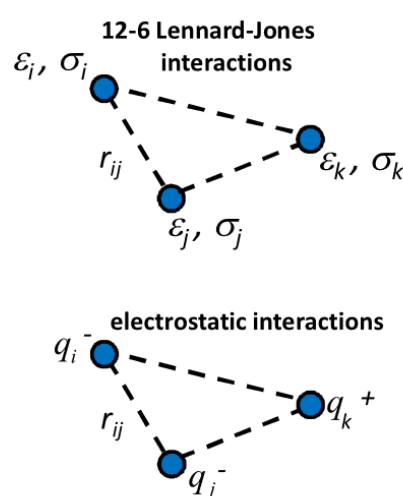
### Force Field Equation

$$\begin{aligned}
 PE = & \sum k_b (b - b_o)^2 \\
 & + \sum_{\text{angle}} k_\theta (\theta - \theta_o)^2 \\
 & + \sum_{\text{dihed}} k_\varphi [1 + \cos(n\varphi - \delta)] \\
 & + \sum_{L-J} 4\epsilon_{ij} \left[ \left( \frac{\sigma_{ij}}{r_{ij}} \right)^{12} - \left( \frac{\sigma_{ij}}{r_{ij}} \right)^6 \right] \\
 & + \sum_{\text{Coulomb}} \frac{q_i q_j}{4\pi\epsilon_o r_{ij}}
 \end{aligned}$$

### Bonded Terms



### Nonbonded Terms



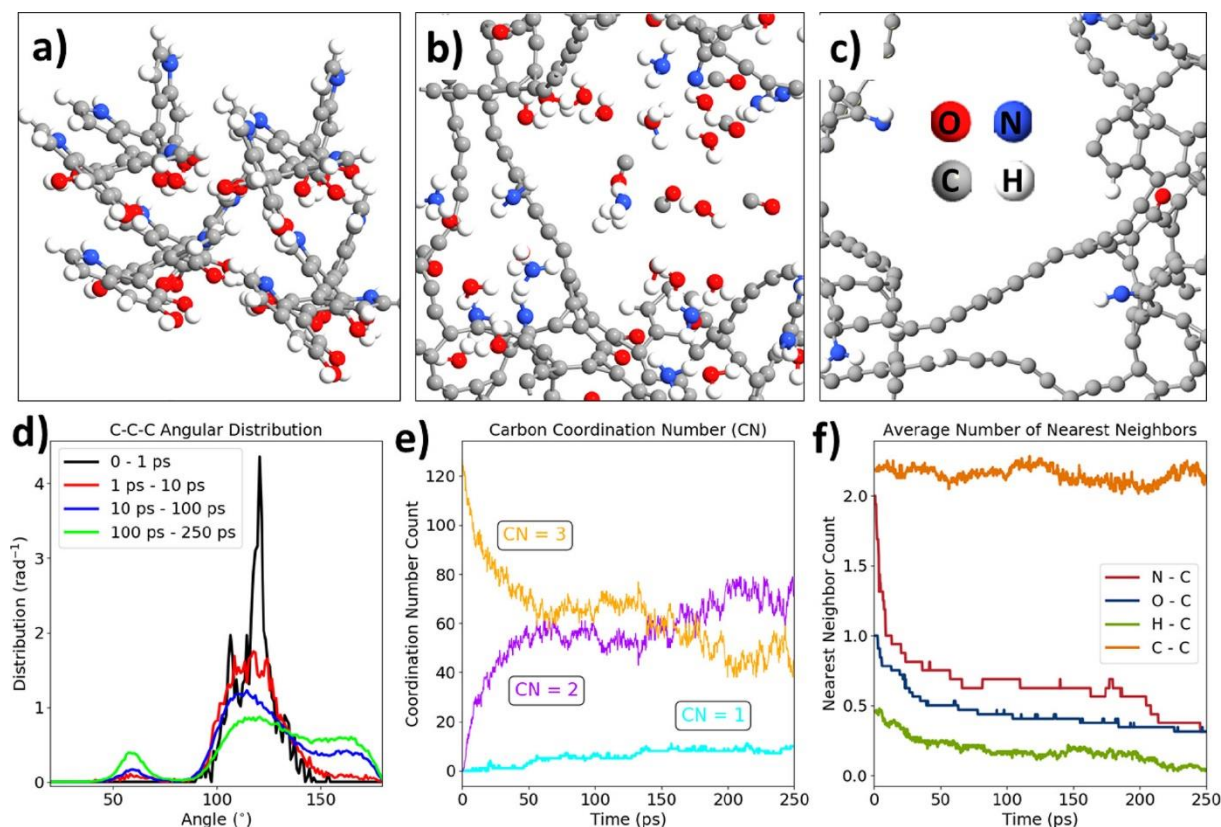
**Figure 69.** Components of the typical force field for classical dynamics<sup>195</sup>.

Force field parameters can be obtained (trained) experimentally or using QM-based computations. A very promising approach in this research area is the application of machine learning algorithms to resolve the force field accuracy to mimic the quantum accuracy<sup>196</sup>.

In standard classical MD force fields, the bonds between atoms are fixed and chemical reactions cannot be modelled this way. To make this possible within classical MD, reactive force fields have been developed. Among them, the ReaxFF group solves the problem by introducing additional components responsible for breaking and forming bonds (penalty terms). Unfortunately, in most cases, a force field

trained for a particular type of atoms and application does not yield a correct result for different applications. In this context, correct result means the result that aligns with chemical intuition and possesses sufficiently low error compared to experiments and calculations at the more accurate levels of theory. Moreover, developing such a type of FF for a system containing a large number of atom types can be extremely laborious.

Nevertheless, ReaxFF simulations can be very promising in the modelling of many physiochemical processes. One that is particularly relevant for the subject of the thesis is polymer graphitisation. During this simulation, the laser action is substituted as increased temperature. Propagation of the system at the nanosecond timescale with the proper ReaxFF yields the evolution of various gases and transformation of the polymer stack into a single N-doped graphene sheet and by products. In the thesis (**Article 4**), this protocol is adapted for the graphitisation of PDA model molecules (**Figure 70**). Such a simulation was also performed for several LIG substrates such as PEEK in the work of Vashisth et al.<sup>197</sup> All ReaxFF calculations included in the thesis were performed, analysed and interpreted by the author.



**Figure 70.** ReaxFF molecular dynamics of the early graphitisation stage: (a) initial geometry of the system (4 DHI tetramers); (b, c) geometry of the whole system and the carbon backbone after 250 ps of annealing at 3000 K; (d) angular distribution function for several periods of the trajectory; (e) evolution of the carbon coordination number; and (f) evolution of the carbon nearest neighbour number projected onto N, O, H, and C atoms (1.8 Å cutoff)<sup>155</sup>.

## 5. Results – List of publications

*Jest z tego pieniądz na przehulanie...  
Nie ma na dzieci, dom i ogródek!*

*The money from it is enough to squander away...  
Although it is insufficient for kids, a home, and a  
garden!*

**Przemysław Gintrowski** – Polish poet and bard – ‘Kuglarze’ (1993)

In this chapter, the results of the studies conducted in the thesis are presented in the form of four core articles related to the PhD thesis and connected with the research objectives outlined in **Chapter 3**.

In **Article 1**, the PDA electropolymerisation protocols are applied to obtain PDA coatings on a B:CNW surface. Related reaction mechanisms are investigated via electrochemical techniques supported by quantum chemical calculations (**Objective 1**). The role of the author in the investigations was conducting the electropolymerisation on the B:CNW electrodes, and performing all electrochemical experiments and DFT calculations. All the conceptual work and development of the methodology behind the investigations (such as the methodology for studying the electrodeposition mechanisms) also belong to the author. Data analysis for all the results was performed by the author.

In **Article 2**, a state-of-the-art co-electropolymerisation protocol for obtaining a PDA\_PZ coating on a B:CNW surface was developed. Structural characterisation using the SEM, XPS, FT-IR and nanoindentation methods was performed to elucidate the structure of the deposited polymer (**Objective 2**). The material was applied for electrochemical sensing of neurotransmitters in biofluid-mimicking media (**Objective 3**). Diffusion field formalism and DFT calculations were used to explain the behaviour observed in the electrochemical experiments and improvements in the sensing performance. The role of the author in the investigations was conducting the electropolymerisation on the B:CNW electrodes, recording the FT-IR spectra, and performing all electrochemical characterisations and sensing experiments, as well as DFT calculations. All the conceptual work and development of the methodology behind the investigations (such as the development of co-electropolymerisation protocol and application of the diffusion field description to explain the observed results) also belong to the author. The author performed all the data analyses for the electrochemical and DFT investigations and participated significantly in the analysis of the FT-IR, XPS, SEM and nanoindentation results.



Based on prior knowledge, **Article 3** adapts the electropolymerisation protocol to obtain PDA layers on TNTs (**Objective 1**). Structural characterisation using SEM, XPS, Raman spectroscopy and optical spectroscopy was performed to estimate the synthesis-structure-property relationships (**Objective 2**). The material's photoelectrochemical properties were investigated, and the synthesis optimised towards the highest photocurrents (**Objective 4**). Nonlinear impedance spectroscopy and quantum chemical calculations were utilised to explain the influence of the PDA on the observed properties. The role of the author in the investigations was conducting the electropolymerisations on the TNTs, recording the Raman and optical spectra, performing the majority of the electrochemical and photoelectrochemical characterisations, as well as all DFT calculations. All the conceptual work and development of the methodology behind the investigations (such as the methodology for studying the structure-property relations and application of nonlinear electrochemical impedance spectroscopy) also belong to the author. Data analysis for all the results was primarily performed by the author.

Finally, in **Article 4**, a state-of-the-art PDA laser graphitisation protocol was developed. SEM, XPS, Raman and nanoindentation measurements were involved in the structural characterisation and estimation of the degree of graphitisation (**Objective 2**). The material was extensively studied in terms of the photocurrent generation mechanisms and further applied in the photoelectrochemical sensing of serotonin (**Objective 4**). The role of the author in the investigations was conducting the electropolymerisation on the TNTs, performing the laser graphitisation, recording the Raman spectra, performing approximately half of the electrochemical and photoelectrochemical characterisations, as well as all ReaxFF and DFT calculations. All the conceptual work and development of the methodology behind the investigations (such as development of the graphitisation protocol and the idea to use the material in photoelectrochemical sensing) also belong to the author. Data analysis for all the results was predominately performed by the author.

With all articles from the list, the author is the main contributor to the paper. The role of the author in the data visualisation and curation, manuscript preparation and preparation of the responses to the reviewers during peer review is dominant.

The chosen articles form a concise line of research. This line originates from the synthesis of the PDA and elucidating its structure and properties. Then, through the various optimisations and development of the state-of-the-art protocols, the fine-tuning of the electrochemical and photoelectrochemical properties is achieved. The resulting materials are aimed at achieving the highest application potential in the non-enzymatic sensing of neurotransmitters. Evidence for **Hypothesis 1** is included in **Articles 1 and 3**, where homogeneous PDA coatings were obtained on B:CNWs and TNTs, respectively. Evidence for **Hypothesis 2** is contained in **Article 2**, which is devoted to the electrochemical sensing



of the modified B:CNWs. **Hypothesis 3** is evidenced in **Articles 3 and 4**, which are devoted to the photoelectrochemical properties of the modified TNTs.

In the following subsections, **Articles 1–4** are discussed in more detail. Most of the results presented in the articles were gathered and processed by the author, with precise annotations given in the CRediT statements below each paper.

### **5.1. Article 1: ‘Multi-pathway mechanism of polydopamine fil formation at vertically aligned diamondised boron-doped carbon nanowalls’**

**Olejnik, A., Ficek, M., Siuzdak, K., & Bogdanowicz, R. (2022).** Multi-pathway mechanism of polydopamine film formation at vertically aligned diamondised boron-doped carbon nanowalls. *Electrochimica Acta*, 409, 140000. <https://doi.org/10.1016/j.electacta.2022.140000>. (**IF = 7.3, Points = 100**)

Several methods of obtaining PDA are discussed in the Introduction section of the thesis, including mostly oxidative polymerisation and electropolymerisation. PDA can be electropolymerised using potentiodynamic waveforms (e.g. by CV) on various surfaces, typically metals, but rarely semiconductors. The content of the electrolyte and its pH is different among the literature and the common problems are the stability and homogeneity of the obtained film. Therefore, the challenge is to create a coating that is stable over time and homogeneously distributed over the surface. Elucidating the influence of the pH on the electrochemical properties of the obtained films is also beneficial. Moreover, the shape of the CV curves, and the number and potentials of the current signals differ significantly depending on the substrate. These outcomes suggest the strong influence of the substrate on the mechanism of reactions and deposition of the polymer, which has not yet been clearly articulated in the associated literature. Although the main reactions involved in the formation of PDA during electropolymerisation are already known, there seems to be a very weak connection between the proposed chemical models and the actually observed current signals. Therefore, the challenge is to concisely link the observed signals during the synthesis with the occurring chemical processes.

The main novelty of this article is the investigation of the mechanism of dopamine electropolymerisation on the surface of boron-doped carbon nanowalls in potentiodynamic conditions. A series of fundamental monomer transformations, including redox reactions, are described and thoroughly investigated by electrochemical techniques. This article addresses **Hypothesis 1** and **Objective 1**, which are devoted to the development of electropolymerisation protocols:

**Hypothesis 1: It will be possible to obtain a homogeneous layer of PDA on the surface of semiconductors via electropolymerisation protocols.**

### **Objective 1: Development of PDA and PZ electropolymerisation protocols for B:CNW and TNT surfaces.**

Synthesis of the PDA was performed in different values of the pH (between 3 and 12) and potential windows. The elaborated methodology of electrochemical techniques, including voltammetry and impedance spectroscopy, was developed to estimate the potential window of the bottleneck reaction responsible for the creation of the PDA. Based on the literature and results, the mechanism of electropolymerisation was proposed and supported by DFT calculations of the reaction energies and electron density distributions. Six PDA structural units and all the chemical and electrochemical reactions transforming into each other were used to explain the shape of the voltammetric signals recorded during the electropolymerisation scans.

Despite the main reaction occurring at the potential range between +100 mV and +400 mV, a wide potential window from –500 mV to +1000 mV is required to achieve full deposition of the PDA on the surface of the nanowalls. Full deposition is understood as full coverage of the surface of the nanowalls with PDA, which is achievable by electropolymerisation. The experimental manifestation of the full coverage is appearance of several consecutive cycles of deposition after some time period.

The electropolymerisation pH plays a major role in determining the electrochemical properties of the B:CNW\_PDA surfaces. The properties under investigation were the CV- and EIS-derived parameters, such as charge transfer resistance  $R_{CT}$  and CPE constants. After polymerisation at pH 3, no significant change in the properties of the B:CNW after the PDA deposition protocol was observed. In the pH range of 4–6, the double layer capacitance slightly increased. At a neutral pH of 7, a significant increase of the charge transfer rate was seen. pH values of 8 and higher resulted in a less conductive PDA layer with the highest values of the charge transfer resistance. However, all the voltammetric signals included in the mechanisms were only observed at a pH of 7.

In the context of the PhD thesis, this work confirmed **Hypothesis 1**, as the PDA layers were obtained via electropolymerisation methods. It also contributes to the realisation of **Objective 1**, as the PDA electropolymerisation protocol was implemented on a B:CNW electrode. The work underlying this article was also a milestone for all the remaining articles, as it provided an understanding of the interactions between the surface of the B:CNWs and the PDA coating. The results served as inspiration to exploit these interactions and develop the state-of-the-art PDA\_PZ co-electropolymerisation protocol in **Article 2** and adapt the PDA electropolymerisation process to the deposition on the TNT substrate in **Article 3**. Additionally, during this work, the author gathered experience in the application of quantum chemistry tools for supporting experimental results.

**The author's contribution to Article 1 was the following:**

Conceptualisation:	All major ideas associated with the study;
Methodology:	Experimental methodology of studying electropolymerisation mechanisms;
Formal analysis:	All electrochemical experiments and DFT calculations; Formulation of major conclusions and inferences in the paper;
Investigation:	Synthesis of the PDA on B:CNWs and application of the developed protocols; Conducting all electrochemical experiments and DFT calculations;
Resources:	In part (through Diamentowy Grant DI2019 017649);
Data curation:	Electrochemical and DFT data collection and management;
Writing Original draft:	Leading role;
Writing Review & edit:	Leading role;
Visualisation:	Almost all the figures in the paper;
Project administration:	In part (Diamentowy Grant);
Funding:	In part (through Diamentowy Grant);

**5.2. Article 2: 'Tailoring diffusional fields in zwitterion/dopamine copolymer electropolymerized at carbon nanowalls for sensitive recognition of neurotransmitters'**

**Olejniak, A.,** Ficek, M., Szkodo, M., Stanisławska, A., Karczewski, J., Ryl, J., Dołęga, A., Siuzdak, K. & Bogdanowicz, R. (2022). Tailoring diffusional fields in zwitterion/dopamine copolymer electropolymerized at carbon nanowalls for sensitive recognition of neurotransmitters. *ACS Nano*, 16(8), 13183–13198. <https://doi.org/10.1021/acsnano.2c06406>. (IF = 17.1, Points = 200)

As discussed in the Introduction section of the thesis, there are several ways to alter the properties of PDA by modifications with other chemical compounds. Typically, modified PDA is obtained by mixing the dopamine monomer with some other agent during oxidative polymerisation protocols, and the copolymer is obtained. However, such copolymerisations are rarely reported when the driving force for the PDA deposition is the electrode anodic potential (i.e. electrodepositions). Therefore, the challenge is to explore the possibilities of merging PDA with other molecules to imbue it with new properties (e.g. electronic or electrochemical in the context of the thesis). Another route of modifications is to graft some chemical entity after the PDA polymerisation or change the composition of the functional groups via organic modifications. An example of such an entity is zwitterionic molecules giving the surface superhydrophilic properties, which are valuable for several applications elaborated in the Introduction section. Moreover, as-obtained carbon nanostructures are typically highly hydrophobic, which can

hinder their electrochemical utilisation in aqueous environments. Therefore, the challenge accepted in Article 2 was to develop the protocol for merging PDA with zwitterions using copolymerisation driven by the anodic potential, i.e. co-electropolymerisation.

The first aim of this work was the development of the dopamine/zwitterions co-electropolymerisation protocol towards modification of B:CNW electrodes and the application of these electrodes to the non-enzymatic, electrochemical detection of neurotransmitters. There are several aspects to the scientific novelty in this work:

- Introduction of the PDA\_PZ co-electropolymerisation protocol.
- Characterisation of the B:CNW\_PDA\_PZ composite using the microscopic, spectroscopic, nanoindentation and electrochemical methods.
- Application of the B:CNW\_PDA\_PZ material in the electrochemical sensing context and observation of the superior performance.
- Application of the diffusion field paradigm and computational methods of quantum chemistry to explain the observed electrochemical properties and the sensing mechanisms.

This article addresses two of the hypotheses posed in the thesis:

**Hypothesis 1: It will be possible to obtain a homogeneous layer of PDA on the surface of semiconductors via electropolymerisation protocols.**

**Hypothesis 2: Application of the PDA-based coating to B:CNWs will significantly increase the sensitivity and selectivity of the electrode towards sensing catecholamine neurotransmitters.**

This article contributes to the realisation of three objectives:

**Objective 1: Development of PDA and PZ electropolymerisation protocols for B:CNW and TNT surfaces.**

**Objective 2: Structural characterisation of B:CNW\_PDA\_PZ and TNT\_PDA composites.**

**Objective 3: Electrochemical properties of B:CNW\_PDA\_PZ and applications in electrochemical sensing.**

In general, PDA\_PZ coatings are synthesised on the surface of B:CNWs using the state-of-the-art co-electropolymerisation protocol described in **Section 4.1.4** and in the current paper. FT-IR and XPS investigations confirmed the incorporation of SBMA zwitterionic molecules into the PDA matrix during electropolymerisation. This observation confirms **Hypothesis 1** and contributes to the realisation of **Objective 1**, stating that the mixed PDA\_PZ coatings can also be obtained on the surface of B:CNWs. Nanomechanical testing showed increased hardness and scratch resistance after successful modification

with polymers. The SEM technique made it possible to observe variable coating thicknesses depending on the electrolyte composition. After deposition of the coatings, the water contact angle decreased significantly from the 123° of the pristine B:CNW to 34° for the B:CNW\_PDA and further to 13° for the B:CNW\_PDA\_PZ materials. These structural characterisations contribute to the realisation of **Objective 2** as they made it possible to estimate the influence of the PDA and PDA\_PZ coatings on the physical properties, chemistry, and morphology of the polymers.

Standard electrochemical techniques (EIS, CV in the presence of redox probes) and the formalism describing the distribution of diffusion fields were used to investigate the properties of the pristine and modified B:CNW electrodes. Contrary to the pure PDA modification, incorporating zwitterions into the coating did not decrease the charge transfer rate or redox reaction currents significantly after polymerisation. After modifications, the electrode exhibited a shift of the diffusion field geometry towards microelectrode-array-like behaviour. This behaviour was magnified when the redox pair originating from dissolved hexaammineruthenium salt reacted according to the OSET (Outer Sphere Electron Transfer) mechanism.

The second aim of this work was to apply the obtained electrodes towards the electrochemical sensing of the neurotransmitter dopamine using the DPV technique. The reaction fundamental to sensing is a proton-coupled oxidation of the dopamine molecule, which was confirmed by the CV curves registered under various pH conditions. Although the sensing performance of the B:CNWs themselves is already prominent, the modification lead to 4-fold increase in the sensitivity and a 5-fold decrease in the limit of detection towards the target analyte, to 89 nM. Both changes are beneficial in the application perspective and occur only when both PZ and PDA are present in the coating. The obtained value of sensitivity towards dopamine equal to  $14.3 \mu\text{A cm}^{-2} \mu\text{M}^{-1}$  was comparable to the state-of-the-art electrodes reported in the 2022 literature measured in similar concentration ranges.

The presence of the coating over the B:CNWs gave the material partial selectivity without any biomolecule. Moreover, the electrode was stable in the concentrated bovine serum – mimicking the biofluid environment – after up to 100 measurement cycles. Although the amperometric response of the electrode decreased over several days of exposure, 75% of the initial response was preserved. These results confirm the idea that the modified material inherited the antifouling properties of the PZ introduced during electropolymerisation.

Overall, experiments in this article fully realise **Objective 3** of the thesis, showing a significant change in the electrochemical properties after the deposition of the PDA-based coatings and utilisation of the modified materials in the sensing applications. **Hypothesis 2** is also confirmed, because the sensing performance was indeed enhanced after deposition of the optimised PDA\_PZ copolymer.

Finally, DFT calculations were used to investigate the mechanism of sensing enhancement by the PDA\_PZ mixed coating. ESP (Electrostatic Surface Potential) maps point to the suggestion that zwitterionic SMBA molecules might be capable of the molecular recognition of the analyte and facilitate its transport along the coating via electrostatic interactions. On the other hand, the PDA adsorbed onto the carbon surface might form a pocket for the PDA monomer and facilitate the hydrogen abstraction, which is a step in the fundamental sensing reaction. This can also be interpreted as electrocatalytic enhancement of the oxidation, manifested as a higher current density for the same concentration, i.e. greater sensitivity.

**The author's contribution to Article 2 was the following:**

Conceptualisation:	All major ideas associated with the study
Methodology:	State-of-the-art PDA-PZ co-electropolymerisation protocol; Implementation of the diffusion field formalism; Methodology for studying PDA-PZ interactions; Application of quantum chemistry methods;
Formal analysis:	All electrochemical experiments and DFT calculations; Formulation of the major conclusions and inferences in the paper; Participation in the analysis of the FT-IR, XPS, SEM and nanomechanical results;
Investigation:	Synthesis of the PDA-PZ coatings and application of the developed protocols; Conducting all electrochemical experiments and DFT calculations; Participation in conducting the FT-IR experiments;
Resources:	In part (through Diamentowy Grant DI2019 017649)
Data curation:	Electrochemical and DFT data collection and management
Writing Original draft:	Leading role
Writing Review & edit:	Leading role
Visualisation:	Almost all the figures in the paper
Project administration:	In part (Diamentowy Grant)
Funding:	In part (through Diamentowy Grant)

### **5.3. Article 3: 'Band gap engineering toward semimetallic character of quinone-rich polydopamine'**

**Olejnik, A., Olbryś, K., Karczewski, J., Ryl, J., Bogdanowicz, R., & Siuzdak, K. (2023).** Band Gap Engineering toward Semimetallic Character of Quinone-Rich Polydopamine. *The Journal of Physical Chemistry C*. 127(26), 12662–12677 <https://doi.org/10.1021/acs.jpcc.2c08804> (IF = 4.2, Points = 140)



Various routes towards the photosensitisation of metal oxide semiconductors towards increasing their photocurrents in the visible range are thoroughly discussed in the Introduction section. One of them is the deposition of a conductive or semiconductive polymer on the surface of a high-bandgap semiconductor, such as titania, with a high absorption coefficient in the visible range. The challenge is to tailor the chemical structure and synthesis routes to maximise the visible photocurrents, which is beneficial for photocatalytic or photovoltaic applications. PDA is a known photosensitiser and is capable of increasing both the absorption and photocurrents of the base semiconductor. However, the only synthetic route to obtain PDA-semiconductor composites reported so far is via standard oxidative polymerisation. There is also a large inconsistency in the literature in terms of the effectiveness of this approach and the mechanisms that govern the enhancements. Moreover, the thickness and chemical structure of the PDA itself seems to have a profound role, but this was not investigated thoroughly yet. Therefore, the challenge was to fabricate a PDA coating – ideally uniform – on the surface of a semiconductor, such as titania, to verify the synthesis-structure-property relationships. Mechanistic studies of the photocurrent generation are also beneficial and can shed light on the photophysics of the PDA-semiconductor interfaces in general.

This article concerns the photoelectrochemical properties of hydrogenated titania nanotubes modified with polydopamine via electropolymerisation. The scientific novelty of this work can be divided into several points:

- Synthesis of TNT\_PDA composites using electrochemical hydrogenation of TNTs followed by PDA electropolymerisation.
- Optimisation of the TNT morphology and PDA synthesis parameters towards the highest photocurrents.
- Observation of the increased optical absorption in the visible part of the electromagnetic spectrum and 20× photocurrent enhancement.
- Observation of non-trivial, semi-metallic electrical characteristics of the PDA synthesised in alkaline conditions.
- Postulating the hypothesis of the semi-metallic nature of the alkaline-synthesised PDA derived via the following techniques: EIS including Mott-Schottky, CV and nonlinear EIS in the presence of redox markers, Raman and optical spectroscopies, photocurrent spectroscopy and density functional theory calculations.

This article addresses the following hypotheses:

**Hypothesis 1: It will be possible to obtain a homogeneous layer of PDA on the surface of semiconductors via electropolymerisation protocols.**

**Hypothesis 3: Application of the PDA-based coating on TNTs will increase their capability towards photocurrent generation in the visible part of the spectrum.**

This article contributes to the realisation of the following research objectives:

**Objective 1: Development of PDA and PZ electropolymerisation protocols for B:CNW and TNT surfaces.**

**Objective 2: Structural characterisation of B:CNW\_PDA\_PZ and TNT\_PDA composites.**

**Objective 4: Photoelectrochemical properties of TNT\_PDA and optimisations towards efficient photosensitisation.**

Thanks to the knowledge on the polymerisation mechanism gathered in **Article 1**, the electropolymerisation procedure was adapted to the TNT substrates and performed for various nanotube geometries. SEM images confirmed the presence of PDA on inner and outer walls of the nanotubes with thicknesses ranging from 2 nm to 7 nm. Signals characteristic of PDA structural units were present on the XPS spectra. Raman spectra revealed D and G bands characteristic for nanocarbons, and UV-vis spectroscopy showed enhanced absorption of the visible light compared to the pristine nanotubes. Thus, **Hypothesis 1** is fully confirmed and **Objective 1** fully realised on TNT substrates.

Both the morphology, the chemical structure and properties of the obtained PDA strongly depend on the electropolymerisation pH and the number of polymerisation cycles. PDA synthesised in acidic conditions is thinner and does not lead to significant a boost in the optical absorption and photocurrent, thus rendering it ineffective as a photosensitiser. On the other hand, PDA synthesised in a mildly alkaline environment strongly enhances the visible absorption and photocurrents. DFT calculations suggest that this is due to quinone-like units in the PDA chains responsible for the introduction of the electronic energy levels inside the bandgap of the TiO<sub>2</sub>.

The geometry of the nanotubes also plays a fundamental role in the photosensitisation as longer nanotubes and with a bigger diameter exhibit a higher propensity towards photosensitisation. In the optimised synthesis parameters for both the TNTs and PDA, the photocurrent enhancement exclusively in the visible range is 20× compared to the pristine nanotubes. This response is stable after 9 days of measurements. This observation undoubtedly confirms **Hypothesis 3**.

Another crucial factor determining the photoelectrochemical performance is the PDA thickness related to the number of electropolymerisation cycles. In general, thicker PDA provides higher optical absorption across a broad spectrum of the visible light, but it needs to be sufficiently thin (up to 7 nm) to maintain high photocurrents. This is also confirmed by the quantum efficiency action maps showing increased IPCE in the visible range (400–500 nm) from 0% to 10% for a 5 nm PDA layer. The quantum

efficiency in the UV range is slightly reduced, though. The discussed structural and physical characterisations of TNT\_PDA composites synthesised with various parameters with techniques (SEM, XPS, Raman and Optical spectroscopies) contribute to the realisation of **Objective 2**.

The electrochemical response of the TNT-PDA electrode in the Mott-Schottky measurement exhibits metallic behaviour, in contrast to the n-type semiconductor behaviour of the pristine TNTs. This effect is the same regardless of the PDA electropolymerisation pH. Moreover, after the deposition of the PDA, the material acquires the ability to oxidise the molecules of the ferro/ferricyanide redox couple, which is impossible for a wide bandgap n-type semiconductor, such as TiO<sub>2</sub>. These aspects, coupled with the optical and structural properties, lead to the suggestion that electropolymerised PDA behaves as a set of distributed redox mediators mimicking a metallic character, rather than as a semiconducting polymer. Those electrochemical investigations coupled with the photocurrent and IPCE measurements contribute to the realisation of **Objective 4** of the thesis.

**The author's contribution to Article 3 was the following:**

Conceptualisation:	All major ideas associated with the study
Methodology:	Optimisation of electropolymerisation protocol; Methodology towards studying TNT_PDA composites; Application of quantum chemistry methods;
Validation:	Validation of investigations performed by KO;
Formal analysis:	Most of the photoelectrochemical, optical and Raman spectroscopy results; All DFT calculations; Participation in the analysis of the XPS and SEM results; Formulation of the major conclusions and inferences in the paper;
Investigation:	Participation in the synthesis of the TNT_PDA composites; Participation in the photoelectrochemical, optical and Raman experiments; All DFT calculations;
Resources:	In part (through Diamentowy Grant DI2019 017649)
Data curation:	Electrochemical, Raman, optical and DFT data collection and management
Writing Original draft:	Leading role
Writing Review & edit:	Leading role
Visualisation:	All the figures in the paper
Project administration:	In part (Diamentowy Grant)
Funding:	In part (through Diamentowy Grant)

#### 5.4. Article 4: ‘Laser-induced graphitization of polydopamine on titania nanotubes’

**Olejniak, A., Polaczek, K., Szkodo, M., Stanisławska, A., Ryl, J., & Siuzdak, K. (2023).** Laser-induced graphitization of polydopamine on titania nanotubes. *ACS Applied Materials & Interfaces*, 15(45), 52921–52938. <https://doi.org/10.1021/acsami.3c11580> (IF = 10.4, Points = 200)

Organic polymers can be transformed into carbon nanostructures using various treatments, such as thermal annealing or catalytic graphitisation. The most important aim of this process is to transform the material from an insulating to a conducting state, preferably in an inexpensive manner. PDA can also be considered as a reagent in such a process. PDA is beneficial due to the large amount of polar functional groups, which might be preserved during the graphitisation and can thus retain its high adhesiveness. There are several chemical entities capable of being transformed into graphite/graphene via laser treatment, such as polyimide. There is only a single work that achieves the goal of obtaining laser-induced graphite from PDA as a source. The PDA was obtained via the standard protocol and a continuous blue diode laser was used for the treatment. The challenge accepted in **Article 4** was to obtain laser induced graphene from polydopamine that is already deposited on the surface of the TNT semiconductor.

This article concerns the development of the protocol towards pulsed laser graphitisation of PDA deposited on the surface of titania nanotubes. The scientific novelty of this article can be captured in the following features:

- Verification of the PDA laser graphitisation protocol using a pulsed Nd:YAG laser, and the PDA electropolymerised on the surface of TNTs beforehand.
- Optimisation of the lasing parameters towards the highest photocurrents in the visible light spectrum and the highest charge transfer rates simultaneously.
- Molecular dynamics simulations of the PDA graphitisation using ReaxFF.
- Application of the laser graphitised TNT\_PDA electrodes to the photoelectrochemical sensing of serotonin.

This article was focused on further enhancement of the visible photocurrents and thus pushing forward **Hypothesis 3:**

**Hypothesis 3: Application of the PDA-based coating on TNTs will increase their capability towards photocurrent generation in the visible part of the spectrum.**

Two objectives of the thesis are realised in this article:

**Objective 2: Structural characterisation of B:CNW\_PDA\_PZ and TNT\_PDA composites.**

#### **Objective 4: Photoelectrochemical properties of TNT\_PDA and optimisations towards efficient photosensitisation.**

Two laser wavelengths of the Nd:YAG laser were used to graphitise PDA: 532 nm and 365 nm, the former corresponding to absorption solely by the PDA, the latter being absorbed both by the PDA and the substrate TNTs. It is possible to perform the laser modification in a predefined geometric pattern if needed. The morphology of the nanotubes slightly changed after the PDA deposition and laser graphitisation – nanotube coronas are locally ‘glued’ together. A crucial signature of the PDA graphitisation is the decreased fluorescence signal and increased G/D band ration captured in the Raman spectroscopy data. The XPS spectra show several symptoms of PDA graphitisation that were dependent on the laser wavelength used. The greatest effect of the laser graphitisation on the nanomechanical properties was increased hardness; the other parameters, such as the elastic work, stiffness and creep rate, did not differ between the pristine and graphitised PDA coating. Additionally, the water contact angle increased after the treatment, indicating a higher hydrophobicity, which is expected after the transformation of a hydrophilic polymer into graphite/graphene. Those structural characterisations make **Objective 2** fully realised.

A set of ReaxFF molecular dynamics calculations was conducted to investigate the possibility of PDA laser graphitisation in the nanosecond timescale. During the simulation, several PDA molecules were transformed into a single, defected graphene sheet terminated by hydrogen. Small gas molecules evolved from the polymer during the process, which can be seen in the frames extracted from the simulation.

The laser parameters, including wavelength, fluence and motorised table speed (number of laser pulses per area), were screened with respect to photoelectrochemical properties of the resulting materials. Based on the photocurrent generation capability and the charge transfer rate estimated from the CV and EIS experiments, optimal parameters were chosen and used in the further characterisation experiments.

These characterisations included photocurrent action maps for various electrode potentials and wavelengths as well as quantum efficiency measurements. After PDA deposition, The TNTs gained the ability to generate photocurrents from the 400–500 nm wavelengths, but the maximum still resided in the UV spectrum, as in the case of pristine nanotubes. After subsequent graphitisation, the maximum was shifted to the visible (ca. 400 nm). Interestingly, these materials exhibited photoelectrochemical nonlinearities, i.e. the photocurrent was not linear with respect to the light intensity. The presented photoelectrochemical investigations fully confirm **Hypothesis 3** and complete **Objective 4**.

Finally, TNT\_IgPDA structures were applied as platforms for the non-enzymatic photoelectrochemical sensing of serotonin as a proof-of-concept study. High sensitivities ( $809 \text{ nA cm}^{-2} \text{ nM}^{-1}$ ) and relatively

low detection limits (0.2 nM) were achieved and were comparable to the state-of-the-art materials reported in the field in 2023.

**The author's contribution to Article 4 was the following:**

Conceptualisation:	All major ideas associated with the study
Methodology:	State-of-the art pulsed laser PDA graphitisation protocol; Optimisation of laser parameters; Methodology of studying TNT_IgPDA composites; Application of quantum chemistry methods;
Validation:	Validation of investigations performed by KP;
Formal analysis:	Most of the photoelectrochemical, optical and Raman spectroscopy results All DFT and ReaxFF calculations; Participation in the analysis of the nanoindentation, XPS and SEM results; Formulation of the major conclusions and inferences in the paper;
Investigation:	Participation in the synthesis of the TNT_IgPDA composites; Participation in the photoelectrochemical, optical and Raman experiments; All DFT and ReaxFF calculations;
Resources:	In part (through Diamentowy Grant DI2019 017649 and NCN PRELUDIUM 2022/45/N/ST5/00192)
Data curation:	Electrochemical, Raman, optical and DFT data collection and management
Writing Original draft:	Leading role
Writing Review & edit:	Leading role
Visualisation:	All the figures in the paper
Project administration:	Full (Diamentowy Grant and PRELUDIUM)
Funding:	In part (through Diamentowy Grant and PRELUDIUM)





# Multi-pathway mechanism of polydopamine film formation at vertically aligned diamondised boron-doped carbon nanowalls

Adrian Olejnik<sup>a,b</sup>, Mateusz Ficek<sup>a</sup>, Katarzyna Siuzdak<sup>b</sup>, Robert Bogdanowicz<sup>a,\*</sup>

<sup>a</sup> Department of Metrology and Optoelectronics, Faculty of Electronics, Telecommunications and Informatics, Gdańsk University of Technology, Narutowicza 11/12 St., Gdańsk 80-233, Poland

<sup>b</sup> Centre for Plasma and Laser Engineering, The Szevalski Institute of Fluid-Flow Machinery, Polish Academy of Sciences, Fiszerka 14 St., Gdańsk 80-231, Poland

## ARTICLE INFO

### Keywords:

Polydopamine  
Electropolymerisation  
Carbon nanowalls  
Electrochemical impedance spectroscopy  
Constant phase element

## ABSTRACT

Boron-doped carbon nanowall (B:CNW) electrodes were used as a platform for studying the electropolymerisation of dopamine. Due to the unique properties of B:CNW, including the fast charge-transfer kinetics and high surface conductivity, a high degree of reversibility of redox reactions was achieved. Three separated redox peaks were observed on voltammograms and attributed to three fundamental reactions in the dopamine polymerisation mechanism: dopamine/dopamine quinone, leukodopaminechrome/dopaminechrome, and dihydroxyindole/indolequinone. The mechanism was also supported by the density functional theory calculations of the single point energy of the polydopamine structural units. Moreover, the electrochemical impedance spectroscopy experiments strongly suggest that the majority of the epolymerisation occurs only in the narrow range of potentials between +0.0 and +0.4 V vs. the silver chloride reference electrode. The concept of a resistor-like CPE element is introduced to facilitate the description of the electrochemical properties of B:CNW electrodes in a neutral electrolyte. Further, it is shown that electropolymerisation differs significantly as a function of pH. In acidic environments (pH 3–6) mostly the dopamine/dopamine quinone reaction can be seen, whereas in a more alkaline pH (8–10), the leukodopaminechrome/dopaminechrome reaction becomes dominant. The dihydroxyindole/indolequinone redox pair is seen only in a short pH interval between 7 and 8. Additionally, the kinetics of polymerisation is significantly boosted when the pH is more than 7. Together, these results provide insight into the complexity of the formation of polydopamine and can assist in better controlling the properties of electropolymerised dopamine films.

## 1. Introduction

Polydopamine (PDA) is a synthetic bioinspired polymer formed during the oxidative polymerisation of dopamine. It possesses a few interesting capabilities such as exceptionally high adhesiveness and biocompatibility as well as the versatility of coating practically any material [1]. Due to its properties, it has attracted a significant amount of scientific attention over the last decade, and a vast spectrum of applications has been proposed. They concern the energy storage field, such as anodes for lithium and sodium-ion batteries [2], supercapacitors [3], photo- [4] and electrocatalysis [5], the environmental protection field, such as water filtration [6], oil-water separation [7], and biomedical applications such as antibacterial coatings [8], and drug delivery and cancer therapy [9]. A recent interesting example of a novel PDA application was given by Daboss et al. [10], where it functions as a

redox switch for electrochemical atomic force microscopy. Polydopamine can also be used for molecular imprinting [11] of small molecules such as ethanolamine [12] and large biomolecules such as antibody epitopes [13], most commonly for applications in electrochemical sensing.

Polydopamine is typically synthesised on the surface of various materials using electropolymerisation (ePDA) or oxidative polymerisation under UV–Vis–IR light illumination, temperature [14], or oxidative agents such as NaIO<sub>4</sub> in the form of films or nanoparticles [15]. Electropolymerisation is preferable to dip coating due to the faster kinetics [16], and because thicker and more homogeneous films can be obtained [17]. Although it has one name, PDA is a set of polymers having different chemical structures. There are over 150 pathways of electron transfer during the electropolymerisation process, and a few tens of structural units have been discovered using various experimental methods, making

\* Corresponding author.

E-mail address: [rbogdan@eti.pg.edu.pl](mailto:rbogdan@eti.pg.edu.pl) (R. Bogdanowicz).

<https://doi.org/10.1016/j.electacta.2022.140000>

Received 16 December 2021; Accepted 30 January 2022

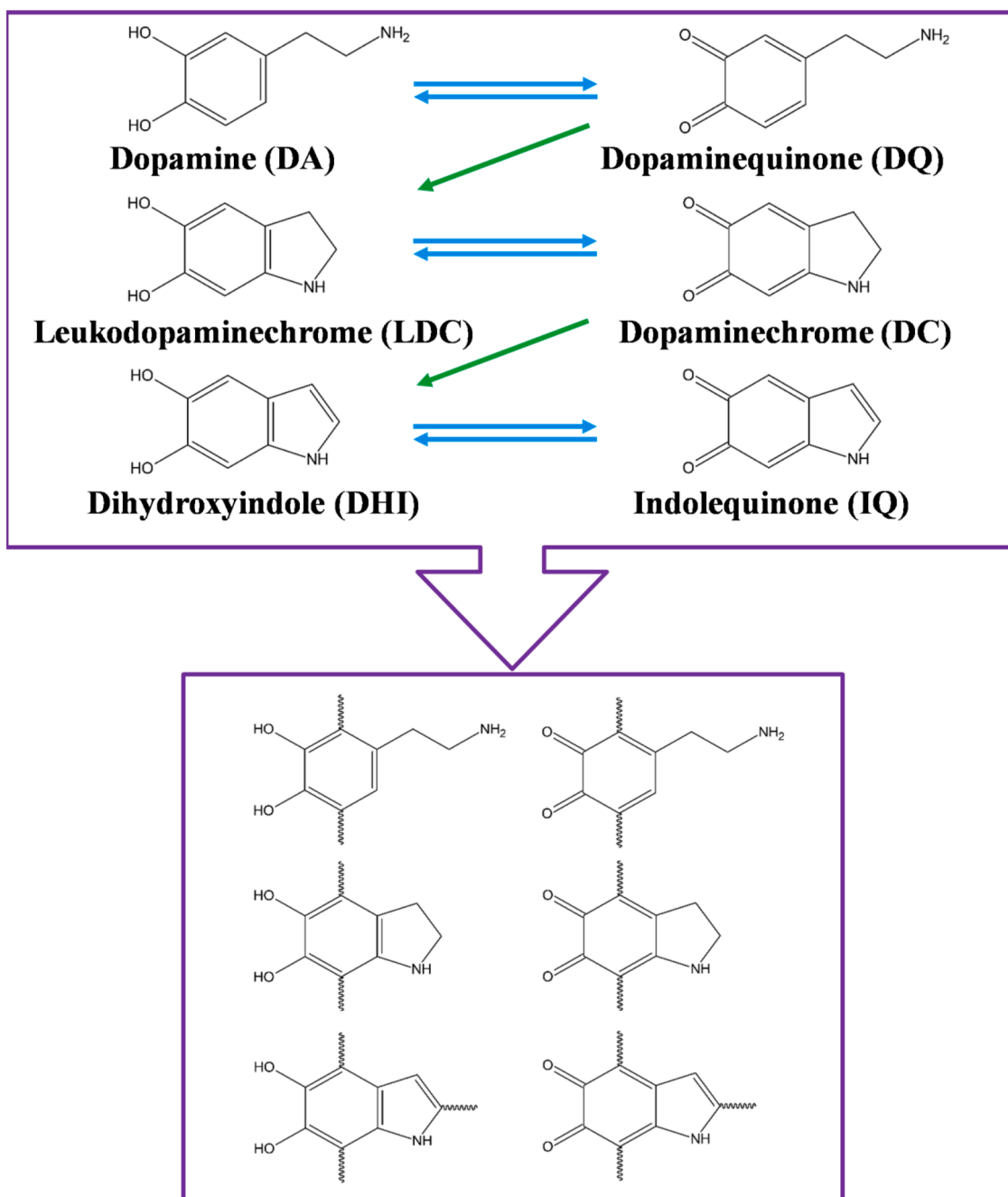
Available online 2 February 2022

0013-4686/© 2022 Elsevier Ltd. All rights reserved.

the investigation a never-ending story [18].

The widely accepted mechanisms of ePDA formation are shown in Fig. 1. There are six typical compounds [19],[20] involved, i.e. dopamine (DA) which can be oxidised to dopamine quinone (DQ). DQ then undergoes isomerisation via the Michael reaction to form leukodopaminechrome (LDC), which can be further oxidised to dopaminechrome (DC) during subsequent charge transfer. This compound can undergo a second isomerisation to dihydroxyindole (DHI), which can be oxidised to indolequinone (IQ). In principle, each of those molecules can be incorporated into the polymeric structure of PDA via covalent bonds [18], however, double-ringed molecules have a higher probability of taking part in the polymerisation process. Moreover, DHI can lead to a crosslinking reaction, because it has three carbon atoms that are prone to linking with other structural units.

The exceptional properties of PDA originate from the interplay between catechol-quinone groups, aromatic rings, and aliphatic amines [21]. Following that, the structure-property relations are generally very complicated. For example, depending on the proportions of structural units, the antioxidant activity [22] and hydrophilicity [14] might vary significantly. Polydopamine rich in DA units with dangling amine groups can be applied for hydrogen electrosorption [23], but polydopamine rich in DHI and IQ units has better photocatalytic properties [24]. Therefore, knowledge regarding the details of the electropolymerisation process is desired. To obtain a particular structure, one needs to know at which potentials reactions occur, and how to control their parameters to achieve the desired structure. Despite the large variety of works published on the electrosynthesis of PDA, those issues are not obvious and still require systematic studies.



**Fig. 1.** Potential chemical (green arrows) and electrochemical (blue arrows) reactions of dopamine indicating possible structural units of the polymer [18],[20] (For interpretation of the references to color in this figure legend, the reader is referred to the web version of this article.).

High-surface-area boron-doped carbon nanowall (B:CNW) electrodes are diamond-rich vertically orientated few-layer graphene sheets [25] grown on a substrate. The B:CNW surfaces reveal a tunable bandgap, high conductivity, superior wear behaviour, and unique electrochemical performance [26],[27]. In principle, B:CNW exhibits a high standard rate constant ( $k^0$ ), and a low peak-to-peak separation value ( $\Delta E$ ) for the oxidation and reduction processes of the  $[\text{Fe}(\text{CN})_6]^{3-/4-}$  redox system [28]. Due to these properties, B:CNW electrodes have been successfully applied for rapid-response ultrasensitive sensing [27–29], electrochemical oxidative treatment of landfill leachates [30], and supercapacitors [31]. The authors have also demonstrated low friction coefficients and large wear endurance [32]. Next, Pierpaoli et al. [33] showed that B:CNWs' properties could be predicted by autonomous advanced image-analysis methods by Fractal Analysis for specifically assembled electrochemical devices. Recently, Hejaziet al. [34] reported that boron-doped carbon nanowalls considerably enhance the electrochemical properties of carbon fibres while maintaining their mechanical properties, stability, and biocompatibility, when used for neural interfacing.

In this work, dopamine electropolymerisation on B:CNW electrodes using cyclic voltammetry and electrochemical impedance spectroscopy is investigated. The particular focus is on the determination of the dominating electrochemical reactions leading to the creation of polydopamine. We also discuss the possibility of obtaining different PDA structures depending on the pH of the monomer-containing solution. Firstly, we observe exceptional characteristics of the dopamine polymerisation on B:CNWs. We show that in contrast to some works, polymerisation occurs only in a narrow potential range between +0.0 and +0.4 V vs. Ag | AgCl | 0.1 M KCl electrode. We also apply a constant phase element to describe the inhomogeneous distribution of the resistance occurring on the surface of the B:CNW electrodes. The overall analysis of the electropolymerisation of dopamine in different conditions is supported by density functional theory (DFT) calculations of the equilibrium geometry and free energy of the structural units of polydopamine.

## 2. Experimental

### 2.1. Reagents

10 X Tris Buffer was obtained from Santa Cruz Biotechnology and diluted 10 times prior to the measurements, dopamine hydrochloride was purchased from Sigma-Aldrich, KCl,  $\text{K}_3\text{Fe}(\text{CN})_6$  and  $\text{K}_4\text{Fe}(\text{CN})_6$ , were obtained from Chempur, and the deionised water used in the experiment was provided by a Hydrolab HLP-5p system.

### 2.2. Boron-doped carbon nanowall (B:CNW) fabrication

B:CNW electrodes were fabricated on p-type (100) Si wafer plates utilising a microwave plasma-enhanced chemical vapour deposition system (SEKI Technotron AX5400S, Japan) as reported elsewhere [25]. The temperature of the stage was set to 700 °C, while the microwave power was kept at 1300 W. The fabrication process was conducted at a pressure of 50 Torr in a  $\text{H}_2/\text{CH}_4/\text{N}_2$  gas mixture flow equal to 325 sccm. The CNW electrodes were boron-doped *in-situ* utilising a diborane precursor ( $[\text{B}]/[\text{C}]$  ratio in the gas phase = 2000 ppm). The 6 h process resulted in thick, vertically aligned carbon nanowall surfaces ( $d \sim 3 \mu\text{m}$ ) with a high content of the diamond phase [33].

### 2.3. Electropolymerisation of dopamine

50 CV (Cyclic Voltammetry) cycles were used for all electropolymerisation experiments with a 20 mV/s scan rate and at the potential range from –0.5 V to +1.0 V vs. The solution consisted of 1X Tris and 5 mM dopamine (pH = 7.4) and was purged with Argon 15–20 min before starting the deposition. Different pH values of solutions were

established by adding 1 M HCl or 1 M NaOH to the 1X Tris solution. An MP-103 handheld potentiometric pH metre was used to control the pH value.

### 2.4. Electrochemical characterisation

All voltammetric and impedance measurements were performed using a BioLogic SP-150 potentiostat-galvanostat in a standard three-electrode configuration at room temperature. Ag | AgCl | 0.1 M KCl was used as the reference electrode and a platinum mesh as the counter electrode, respectively. The geometric surface areas of the working electrodes were 0.5–1 mm<sup>2</sup>.

Two types of Potentiostatic Electrochemical Impedance Spectroscopy (pEIS) experiments were performed, i.e. potential scanning pEIS and single-potential pEIS. The aim of scanning pEIS was to verify the response from different redox reactions of dopamine before completion of the electropolymerisation on the B:CNW electrodes. The potential range was from –0.5 V to 1.0 V with 0.1 V spacing and starting from –0.5 V. The polarisation time before each step was 1 min. The single-sine amplitude was 5 mV and the frequency ranged from 10 kHz to 100 mHz. The solution was 1 X Tris with and without added dopamine providing its final concentration of 5 mM. The single-potential pEIS step aimed to verify the general properties of the PDA coatings obtained during electropolymerisation on B:CNW in solutions of different pHs. Spectra were recorded in 1 M KCl and 5 mM  $\text{K}_3\text{Fe}(\text{CN})_6 / \text{K}_4\text{Fe}(\text{CN})_6$ . The formal potential of the redox reaction, i.e. +0.28 V vs Ag | AgCl | 0.1 M KCl, and the polarisation time of 5 min, were set. The single-sine amplitude was equal to 10 mV, and the applied frequencies covered the range from 10 kHz to 100 mHz. The impedance data were fit through a complex nonlinear least squares (CNLS) procedure based on the proposed electric equivalent circuit (EEC) using the Powell algorithm embedded in the EIS Spectrum Analyser software [35].

### 2.5. DFT computations

Atomic structures of PDA units were designed using a builder tool provided by Atomistic ToolKitQuantumwise (ATK, Synopsys, USA) as reported in [36]. The optimised geometries and electron density iso-surfaces of various dopamine structure units present in PDA were obtained using the density functional theory (DFT) approach in the Linear Combination of Atomic Orbitals (LCAO) method [37]. The General Gradient Approximation (GGA) level of the theory and the Perdew–Burke–Ernzerhof (PBE) functional were applied as implemented in the ATK package. Pseudo-Dojo norm-conserving pseudopotentials with an ultra-basis set were chosen for geometry optimisation and electron density calculations [38]. The free energies of the isomerisation were computed according to formulas (1–2). They are based upon subtracting single point energies of geometry optimized molecules so that the total energy difference is obtained. This value is total isomerization energy. This approach is analogous to the one reported in [39], however, the enthalpy-energy corrections are not included for simplicity.

$$E_{\text{iso1}} = E_{\text{LDC}} - E_{\text{DQ}} \quad (1)$$

$$E_{\text{iso2}} = E_{\text{DHI}} - E_{\text{DC}} \quad (2)$$

## 3. Results and discussion

### 3.1. Electropolymerisation on B:CNW

The morphology and characterisation of the substrate materials, i.e. boron-doped carbon nanowalls, were thoroughly described in our previous papers [27],[40]. The electropolymerisation of dopamine on B:CNW electrodes using cyclic voltammetry is presented in Fig. 2.

Three separated redox peaks with current densities gradually decreasing with the consecutive cycles to less than 20  $\mu\text{A cm}^{-2}$  after 50

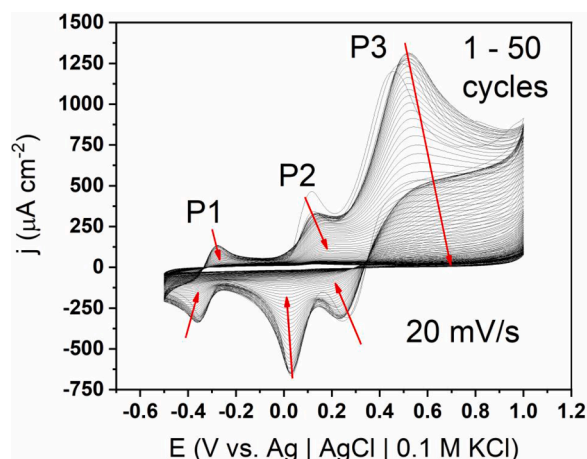


Fig. 2. Electropolymerisation of 5 mM dopamine on B:CNW electrodes in 1 X Tris (pH = 7.4).

cycles can be seen. Those CV shapes and a high level of reversibility are exceptional amongst the already published works. This unique character of the PDA formation was enabled by two properties of B:CNW: high surface conductivity due to boron doping, and high charge transfer rates due to the interplay between the  $sp^2$  and  $sp^3$  phases compared to, e.g. glassy carbon electrodes [27],[40]. Despite the molecular mechanism of PDA formation being generally known, the shape and the number of peaks in the CV curves are strictly dependant on the substrate material [48]. Literature data describing the attributions of dopamine oxidation reactions to the CV peaks depending on the substrate material for PDA coating is given in Table 1. The notation used to describe the peaks in the cited works is changed to (P1, P2, P3) as displayed in Fig. 2. The potentials of the reference electrodes are shifted to the silver chloride. P1 can be interpreted either as the reaction of LDC to DC or as the DC/IQ. In some works, however, it is either not present in the CV curves or not assigned to any reaction. The correlation between the assignment and the type of substrate material can hardly be noticed. P2 is most typically assigned to the LDC/DC reaction accompanied with DHI polymerisation to form PDA regardless of the substrate, except in the case of electrochemically reduced graphene oxide (ERGO), where it is ascribed to the DA/DQ reaction. Moreover, in the case of nitinol stents, there are no peaks other than P1, and P2 takes the form of a plateau and is ascribed to DHI polymerisation. The highest level of agreement in the literature is for the case of P3, and the DA/DQ reaction is the most common choice. Although there are cases where it is not present (ERGO) or, presently, no reactions are assigned (e.g. carbon nano-onions). Polymerisation is considered to happen at either all three peaks

depending on the substrate material.

Considering the unique character of the dopamine oxidation on B:CNW electrodes, depicted in Fig. 2, a set of depositions in narrower potential windows was performed. Resulting CV characteristics are given in Fig. 3a–d). In the most cathodic range from  $-0.5$  to  $-0.1$  V (i.e. in the area of P1) there is basically only capacitive behaviour. In contrast to the full window, the P1 peak current is diminished to the fraction of  $\mu A$ . Therefore P1 could be manifested only if the reaction undergoing at P2 and P3 had already proceeded. In the middle potential window from  $-0.1$  V to  $+0.25$  V P2 is manifested, but oxidation currents are higher than reduction currents. In other words oxidation at P2 is irreversible. Moreover, in contrast to the full-window treatment, currents do not decay after 50 cycles. In the slightly anodic range from  $+0.25$  V to  $+0.6$  V there is a quasireversible redox reaction at P3 and current densities gradually decrease with cycling. This behaviour is similar to the full-window deposition case and therefore, the most probable scenario is that the polymerization starts from the reactions undergoing at P3 (which is DA to DQ oxidation). For completeness, also the last deep anodic treatment was performed. In this region no peaks are present and the current is settled constantly after a few cycles.

For a more thorough investigation of dopamine oxidation, CV and EIS measurements after exposure to dopamine were performed in presence of ferrocyanide redox pair (Fig. 3e, f). There are only small differences between electrochemical properties of electrodes after exposure to either window in comparison to the oxidation at the full window. The change of voltammetric current is marginal for smaller windows, while for a full window it is straightforward. The same conclusions could be derived from the EIS spectra and values of impedance. Every element in the Randles equivalent circuit has an almost identical value to that of pure (blank) B:CNW without exposure (see Table S3 for detailed information), except the case of full-window exposure. In this special situation, charge transfer resistance increases from  $2$  to  $108 \Omega$   $cm^2$ , and Warburg coefficient increases from  $30$  to  $142 \Omega$   $cm^2$   $s^{1/2}$  indicating the formation of a layer onto the electrode surface. To summarize, if the polymerisation is to proceed, smaller potential windows are not sufficient. A wide window including all three peaks is required.

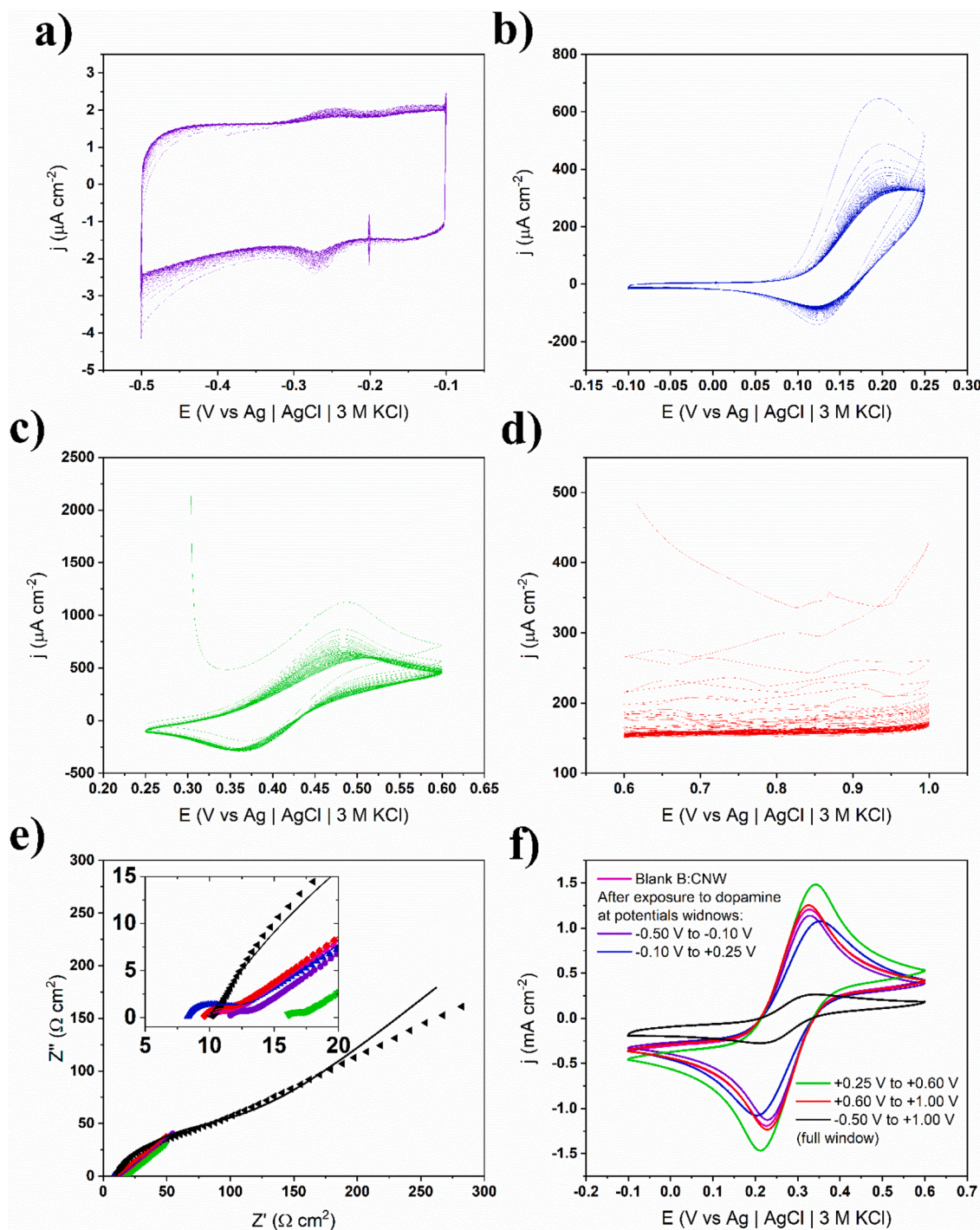
Next, the investigation of dopamine electropolymerisation on B:CNW was performed by EIS at different potentials in two solutions: 1 X Tris without and with 5 mM dopamine (see Figs 4 and 5). Regardless of the applied potential, the EIS spectrum has an analogous shape. It consists of a high-radius semicircle at low and moderate frequencies, indicating a double-layer capacitance with some real resistance. There is also an almost straight line at higher frequencies, corresponding to the diffusion impedance. The spectrum only curves down into a semicircle at high anodic potentials, indicating the presence of some redox reaction, possibly connected to oxidation of the B:CNW surface or the evolution of oxygen [27].

Table 1

Assignment of dopamine oxidation reactions to the CV peaks depending on the substrate material for the PDA coating.

Electrode	Reaction at P1	Reaction at P2	Reaction at P3	Solution pH	Refs.
Screen Printed carbon electrode (SPCE)	Not assigned	LDC/DC	DA/DQ	Britton-Robinson buffer (pH = 7.0)	Kanyong et al.[41]
Gold electrode, 316 L stainless steel	Not present in CV curves	LDC/DC	DA/DQ	Tris-Buffered Saline (pH = 7.4)	Wang et al.[17]
Electrochemically reduced graphene oxide (ERGO)	DC/IQ	DA/DQ	Not present in CV curves	Phosphate Buffered Saline (pH = 7.2)	Kumar et al.[42]
Gold electrode	DHI polymerisation	Not assigned	Not present in CV curves	Phosphate Buffer (pH = 7.0)	D'Alvise et al.[16]
Carbon nano-onions	Not present in CV curves	DHI polymerisation	Not assigned	Phosphate Buffer (pH = 6.5)	Gardonaet al.[43]
Nitinol stents	Not assigned	DHI polymerisation in the form of a plateau	Tris-Buffered Saline (pH = 7.4)	Aguilar et al.[44]	
Glassy carbon electrode	LDC/DC	Not present in CV curves	DA/DQ	Citrate-Phosphate Buffer (pH = 7.0)	Almeida et al.[20], [45]
Boron doped carbon nanowalls (B:CNW) (current work)	DHI/IQ	LDC/DC+DHI polymerisation	DA/DQ	Tris-Buffered Saline (pH = 7.4)	–





**Fig. 3.** (a)–(d) Electrooxidation of dopamine on B:CNW in 1 X Tris (pH = 7.4) in narrow potential windows. (e), (f) CV curves and EIS spectra of electrodes after exposure to dopamine recorded in presence of 5 mM  $K_3Fe(CN)_6$  /  $K_4Fe(CN)_6$  in 1 M KCl (pH = 7). Dotted lines are experimental values and solid lines are fitted. Colors in subfigures (a)–(d) correspond to the same colors in (e), (f).

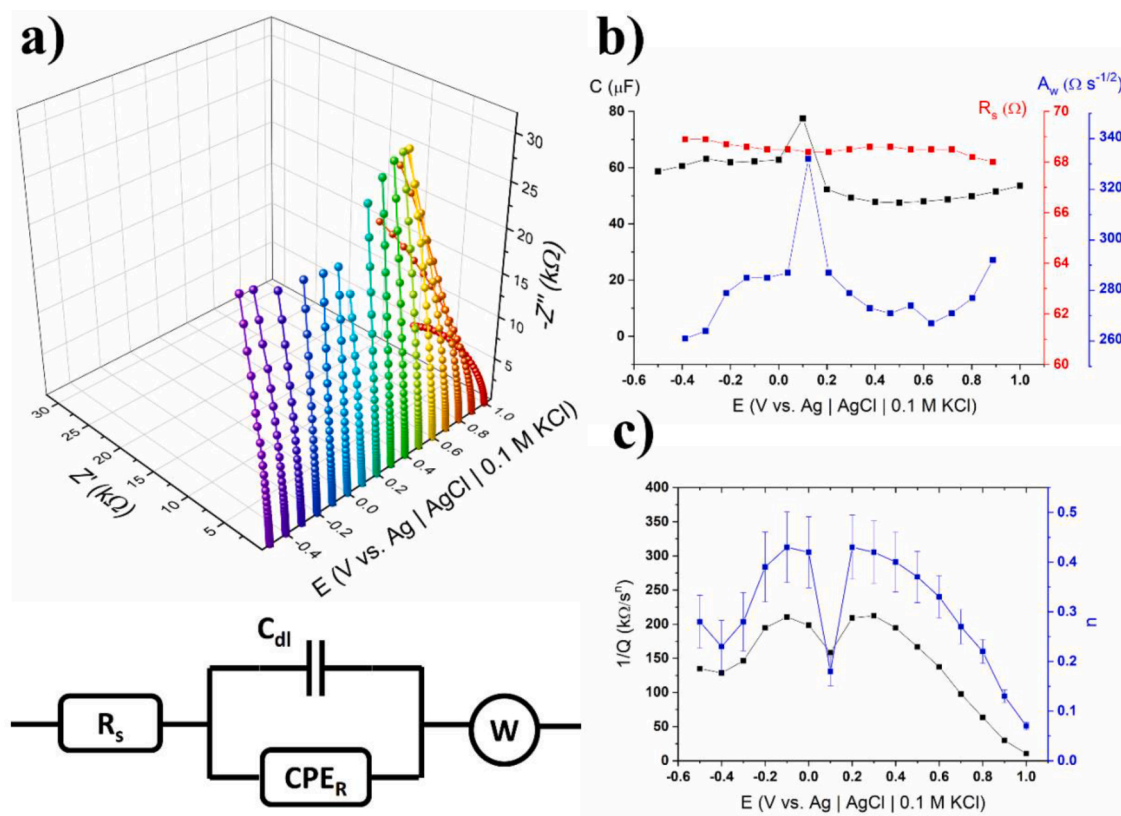
A constant phase element (CPE) is a commonly used element in an equivalent circuit in liquid electrolyte electrochemistry. Its impedance is given by Eq. (3) [49]:

$$Z_{CPE} = \frac{1}{Q(j\omega)^n} \quad (3)$$

where  $j$  is an imaginary unit, and  $\omega$  is a frequency in rad/s. Both exponent  $n$  and  $Q$  are fitted during the Complex Non-linear Least Squares (CNLS) procedure and are used for the interpretation of impedance data. The CPE reflects the non-ideal characteristics of the double-layer

resulting from the inhomogeneity or roughness of the material surface [46],[49]. During double-layer charging-discharging, diffusion processes also contribute to the overall impedance. Therefore,  $n = 1$  for the ideal capacitor, and is less than one for non-ideal, typically 0.8–0.95. Although there are works that report  $n$  values even below 0.7 [50–52], it does not necessarily imply the low quality of the impedance data.

Obviously, once  $n = 0$ , the CPE becomes an ideal resistor. Per analogy to the standard concept of a capacitor-like CPE, i.e. double-layer capacitance coupled with diffusion, we propose that a resistor-like CPE could be used to model the charge transfer resistance coupled with



**Fig. 4.** (a) pEIS spectra of B:CNW electrode in 1 X Tris (pH = 7.4) with equivalent circuit used for this material (b) changes of double-layer capacitance  $C_{dl}$  (black dots), solution resistance  $R_s$  (red dots) and Warburg coefficient  $A_w$  (blue dots) (c) changes of resistor-like  $CPE_R$  modulus (black dots) and  $CPE_R$  exponent (blue dots) with respect to potential (For interpretation of the references to color in this figure legend, the reader is referred to the web version of this article.).

diffusion. This approach allowed the simplification of the equivalent circuit describing B:CNW electrodes. Non-zero  $n$ -values for pure B:CNW also reflect a fractal nanostructure of B:CNW, where diffusion processes are very complex and presumably cannot be described by simple Warburg elements due to non-Fickian transport [33], but a resistor-like CPE provides a reasonably accurate fitting with negligible relative errors for all elements (up to 2%) and small errors for the  $n$  value of a resistor-like CPE (10–20%).

In general, the elements of the equivalent circuits used for fitting EIS spectra have the following meaning.  $R_s$  is straightforwardly a solution resistance. The capacitor in Fig. 4 ( $C_{dl}$ ), as well as capacitor-like CPE in Fig. 5 (CPEs), simply describe the process of double-layer charging. Resistor-like CPE ( $CPE_R$ ) is mostly connected to the resistance of adsorption and/or charge transfer in the redox reaction of terminal functional groups on the surface of carbon nanowalls. The Warburg impedance is intertwined with this reaction and represents the diffusion of hydroxyl ions to the surface. The subject of termination was thoroughly studied in other work, where we showed that this process is reversible to some extent [53].

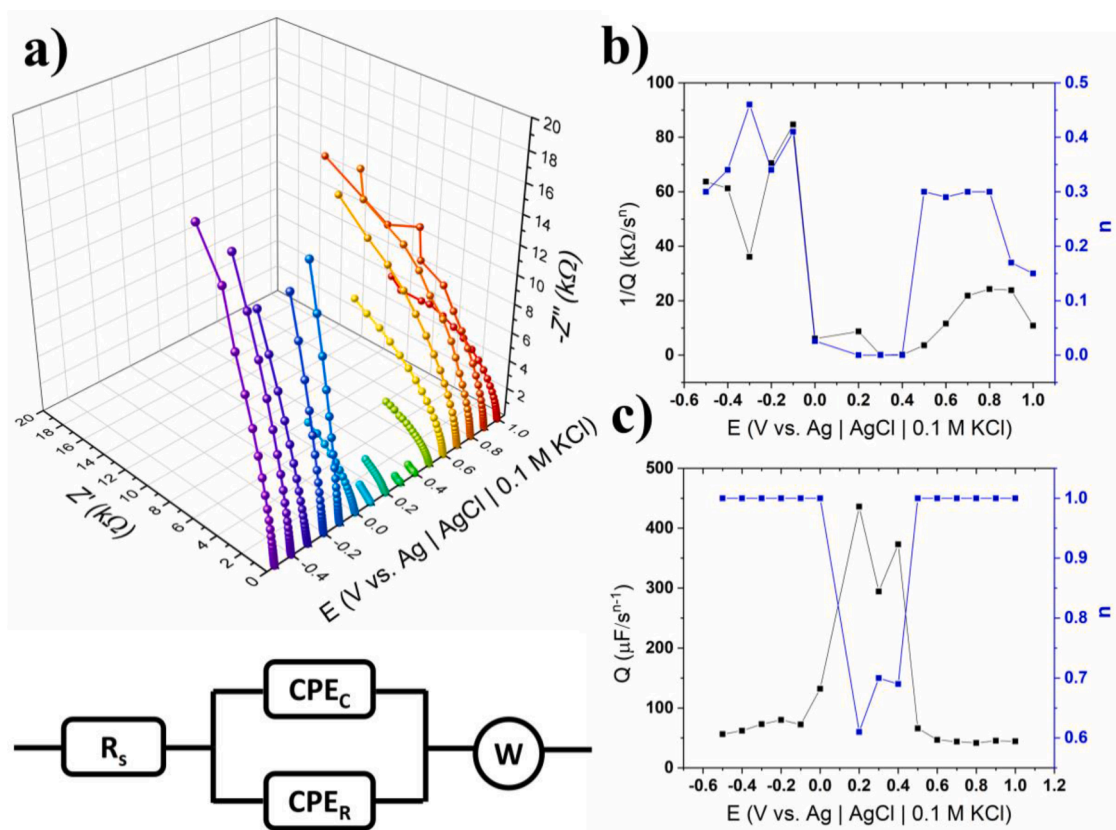
While the equivalent circuit elements corresponding to the double-layer capacitance, the diffusion impedance, and the electrolyte resistance do not change significantly while varying the potential, the resistor-like CPE does (Fig. 4c). In cathodic and moderately anodic potentials up to +0.6 V, it represents a resistor with a large resistance of more than 100 kΩ, and  $n = 0.3$ –0.4. This behaviour seems reasonable because no redox reaction occurs within this potential range. However, at higher anodic potentials close to the oxygen evolution reaction, the resistance decreases to a few kΩ, and the  $n$  value also decreases to zero, indicating that the CPE becomes a resistor, which is also feasible because a redox process occurs at this potential range.

A similar multiple pEIS experiment was performed for a B:CNW electrode in 1X Tris buffer solution containing 5 mM of dopamine. In

contrast to the dopamine-free solution, there are strong differences both in the shape of the EIS spectrum, and values of the equivalent circuit elements with the respect to the potentials. Firstly, at the lowest cathodic potentials (P1), the EIS data resemble the data from Fig. 4a in the case where no dopamine was introduced to the solution. In other words, no signal from the redox reaction at P1 was registered during the experiments. This suggests that the process at P1 can occur only if other processes at P2 and P3 also take place. Similar behaviour is observed in Fig. 3a during deposition of PDA in small potential windows. Secondly, at the potentials extending from 0.0 to +0.4 V, there is a strong decrease in both the real and imaginary parts of the impedance accompanied by significant changes in the values of the CPE elements. Thirdly, at the highest anodic potential, the shape of the EIS spectra again resembles the data from Fig. 4 describing a B:CNW electrode without dopamine in the solution. Data from Fig. 3d describing deposition in the most anodic windows stay in accordance with this fact. Generally one can conclude that the formation of PDA layer (and possibly other surface-bounded processes) occurs only in the range from 0.0 to +0.4 V vs. Ag | AgCl | 0.1 M KCl electrode.

Sweeping of the polarisation potential is accompanied by changes in both of the constant phase elements. The resistor-like CPE in the area of P1 is similar as in the pure 1 X Tris solution, i.e. the  $n$  value is between 0.3 and 0.4 while the resistance fits the kΩ range. When the applied potential approaches the electropolymerisation region, the  $n$  value drops to almost zero, meaning that the circuit resembles a Randles circuit, and the resistance decreases to less than 1 kΩ, indicating the charge transfer kinetics. Lastly in the area of P3, the  $n$  value increases to 0.3 again, and the resistance increases. The capacitive element ( $CPE_C$ ), on the other hand, exhibits an  $n$  value close to 1 for the whole range of potentials except for the region of polymerisation (P2), where it decreases to 0.7. Moreover, the value of  $Q$  increases in this region, suggesting the formation of a polymer on the surface. The electrolyte





**Fig. 5.** (a) pEIS spectra of B:CNW electrode in 1 X Tris (pH = 7.4) and 5 mM of dopamine with the scheme of the equivalent circuit used for this material (b) changes of resistor-like  $CPE_R$  modulus (black dots) and  $CPE_R$  exponent (blue dots) (c) changes of capacitor-like  $CPE_C$  modulus (black dots) and  $CPE_C$  exponent (blue dots) with respect to potential (For interpretation of the references to color in this figure legend, the reader is referred to the web version of this article.).

resistance and Warburg impedance are almost the same for all potentials (see Fig. S1).

### 3.2. Electropolymerisation on B:CNW as a function of pH

Polydopamine has different chemical structures and properties depending on the solution's pH [54]. To verify those effects in the case of dopamine electropolymerised on B:CNW, a series of electrochemical syntheses were performed in both acidic and alkaline solutions (Fig. 6). Considering the environment of pH 3, there is only one quasi reversible redox peak at the potential +0.48 V, most probably corresponding to the oxidation of DA to DQ (Fig. 1). This reaction is well-studied in the literature and is commonly used during the sensing of dopamine [55], [56]. The amperometric signal of both oxidation and reduction peaks does not decay in time after 50 cycles, suggesting that no polymerisation or activation of the electrode happened. In a less acidic environment (i.e. pH 4 and 6), two additional small redox peaks are located at -0.3 V and +0.15 V, i.e. at similar positions as in a neutral pH (Fig. 2). In this case, the peaks decrease during cycling, meaning that the electrode surface is being blocked either by the accumulation of oxidation products or by electropolymerisation [57]. In a neutral and slightly alkaline pH starting from 8, one can see that two smaller peaks grow. Moreover, the current density of all three redox peaks drop significantly lower values before reaching 50 cycles, and a characteristic resistor-like baseline is also created. Those observations suggest that polymerisation occurred in pH 7 and 8. For an even higher pH, e.g. 9, the current density drops even faster, and after 1 cycle, it decreases to less than  $1 \mu A cm^{-2}$ , indicating a very fast polymerisation.

The decay of the reduction peaks in an alkaline pH might be caused by the consumption of oxidation products in subsequent chemical reactions [47], suggesting that the chemical steps in Fig. 1 are much more

likely to occur in an alkaline pH. Conversion of DQ to LDC (Fig. 1) can be described as Michael cyclisation. This reaction happens via the carbanion path, and is faster in an alkaline pH [19]. Considering that DHI and IQ derivatives are more likely to polymerise than DA and DQ, electropolymerisation is less likely in acidic conditions, therefore the PDA coating is formed only in a neutral and alkaline pH.

The general electrochemical properties of ePDA formed in solutions of different pHs are given in Fig. 7. One can see that the CV curves recorded in the presence of a ferrocyanide redox pair at pH 3, 4 and 6 exhibit both reduction and oxidation peaks. Although the current density is decreased, those curves indicate that in an acidic pH, the formation of a coating is not complete [14].

On the other hand, in a neutral and alkaline pH, a significant drop in the current density of the redox peaks indicates a full coating of the surface by ePDA. Similar conclusions can be withdrawn from the EIS spectra presented in Fig. 7c and d. In an acidic pH, one can see semi-circles at moderate frequency ranges and generally low values of impedance, and a straight Warburg line at low frequencies. This behaviour resembles pure B:CNW, and is further confirmed by the similarities of the equivalent circuit elements, i.e. the charge transfer resistances are of the same order of magnitude (Table S1). However, in a neutral and alkaline pH, there are more than 10 times higher values of both the real and imaginary impedance, and the semicircles have vanished. The spectra consist of a single curved line corresponding to the charging of a double-layer combined with diffusion. The equivalent circuits and values of their elements are given in Tables S1 and S2 in an acidic and alkaline pH PDA, respectively. The charge transfer resistance is significantly higher than for a pure B:CNW electrode, and two Warburg elements are required for a reasonable fitting of the low-frequency data. An increase of the capacitive currents (Fig. 7e and f) of the PDA-modified electrodes in pH 4 and higher is another argument

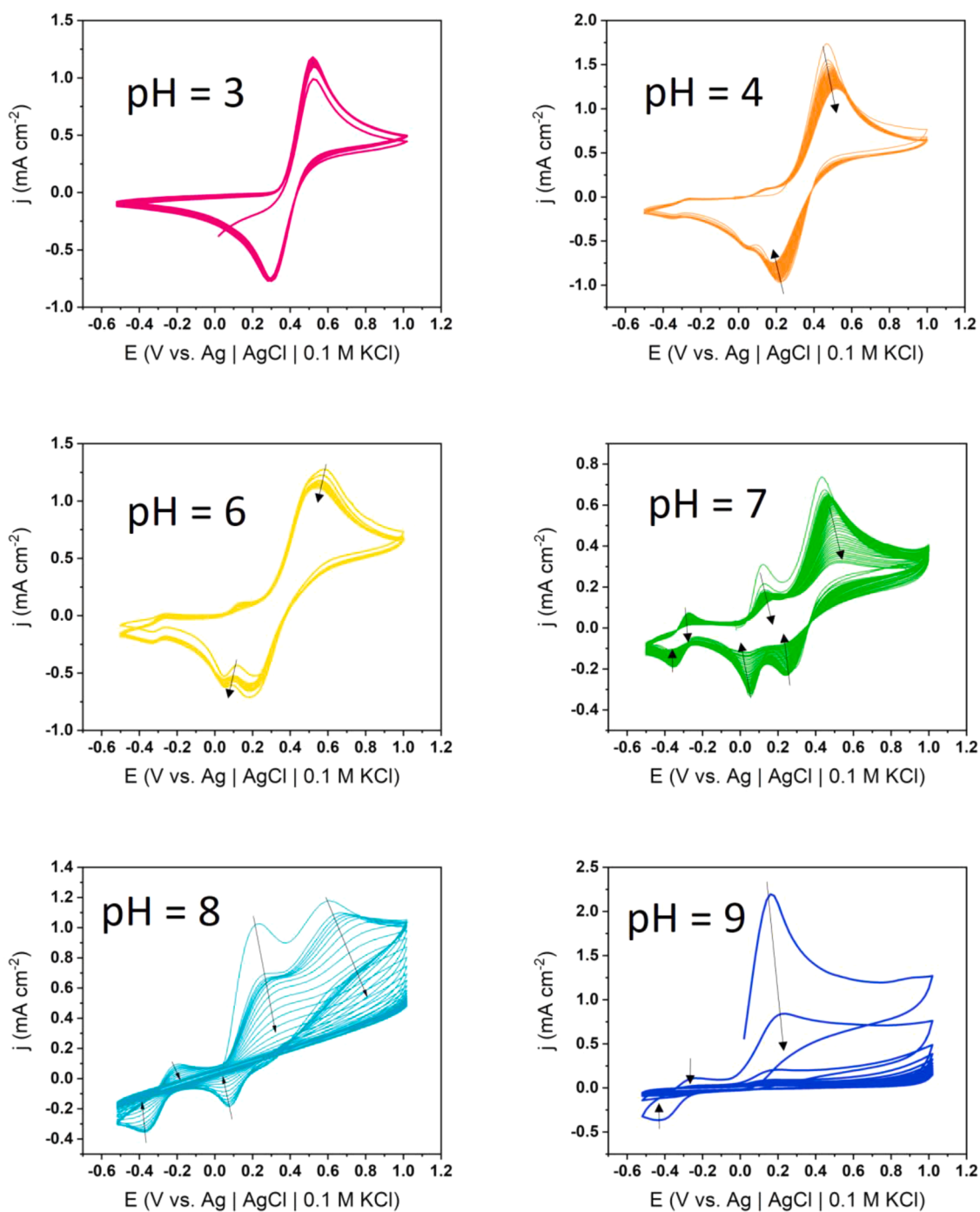


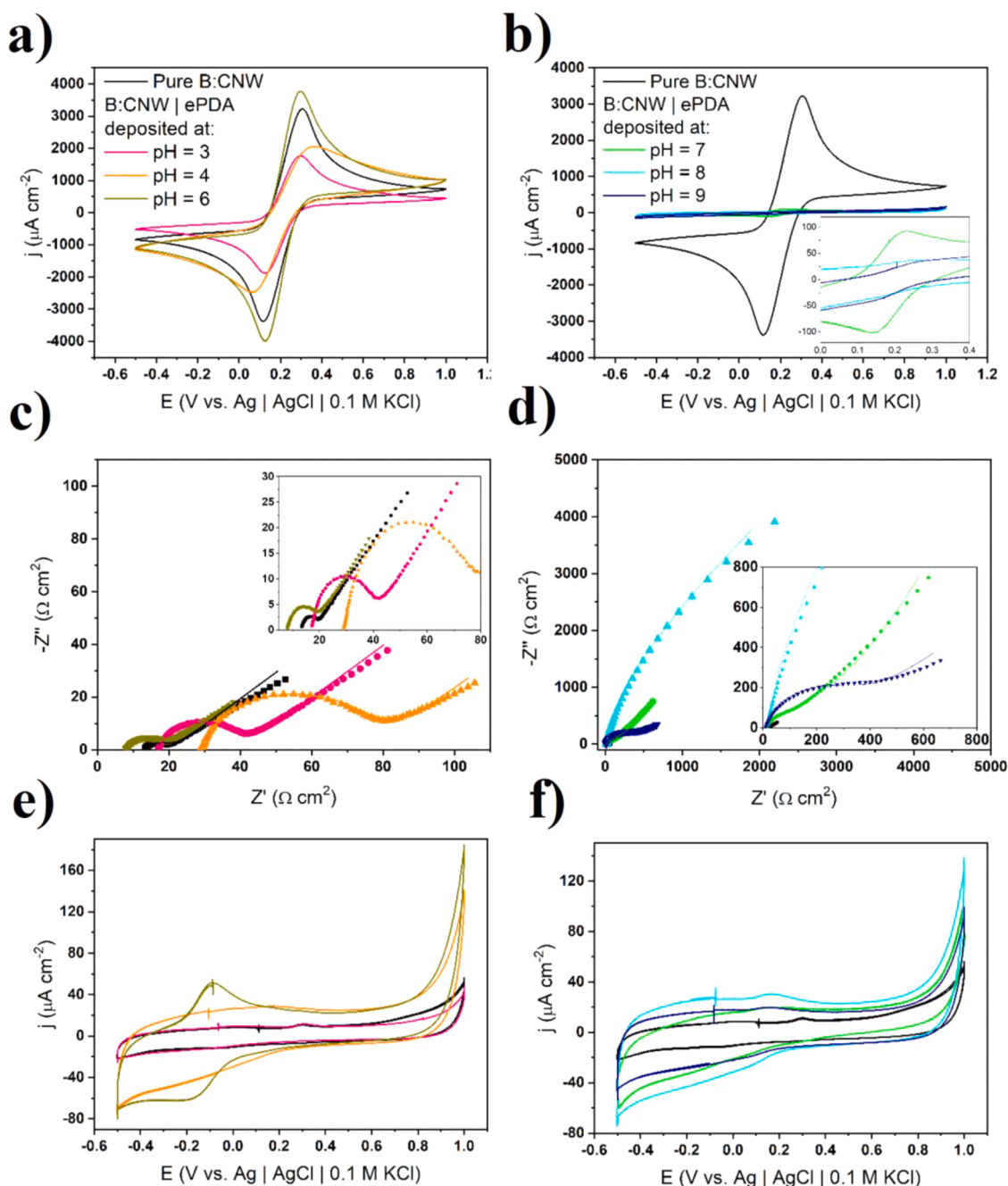
Fig. 6. Electrodeposition of polydopamine on B:CNW in different pHs in 1X Tris. Arrows indicate the direction of CV changes with ongoing cycles.

supporting the formation of the coating. Oxidation or reduction peaks are observed in the voltammograms, possibly corresponding to catechol-quinone redox pairs in the PDA structure. In particular, the coating formed in pH 6 exhibits an oxidation and reduction peak at  $-0.1$  V. In the case of PDA formed in an alkaline pH (8 and 9), another small oxidation peak at  $+0.2$  V is also present. It suggests that the formed polymer can be oxidised and reduced with no signs of degradation. Similar conclusions were obtained in the work of Dabosset al. [10], where redox responses were assigned to the quinone-catechol redox pairs of PDA.

### 3.3. DFT structure optimisation and single-point energy calculations of PDA units

DFT structure optimisation was performed for six possible units present in dopamine to support electrochemical measurements investigating the electropolymerised dopamine. The implications from the electron density isosurfaces and the isomerisation energy calculations supported the interpretation of electrochemical signals appearing in the CV curves.

Isosurface graph structures of six possible PDA structural units are presented in Fig. 8. An important observation is that all of the three quinone forms have less electron density accumulated in the aromatic ring than the corresponding catechol forms. Therefore, they seem to be



**Fig. 7.** (a), (b) CV curves (c), (d) potentiostatic EIS spectra of B:CNW | ePDA electrodes electropolymerised in different pHs. Measurement solution was 5 mM  $\text{K}_3\text{Fe}(\text{CN})_6$  /  $\text{K}_4\text{Fe}(\text{CN})_6$  in 1 M KCl. Dotted lines are experimental values and solid lines are fitted (e), (f) CV curves registered in 1 X Tris.

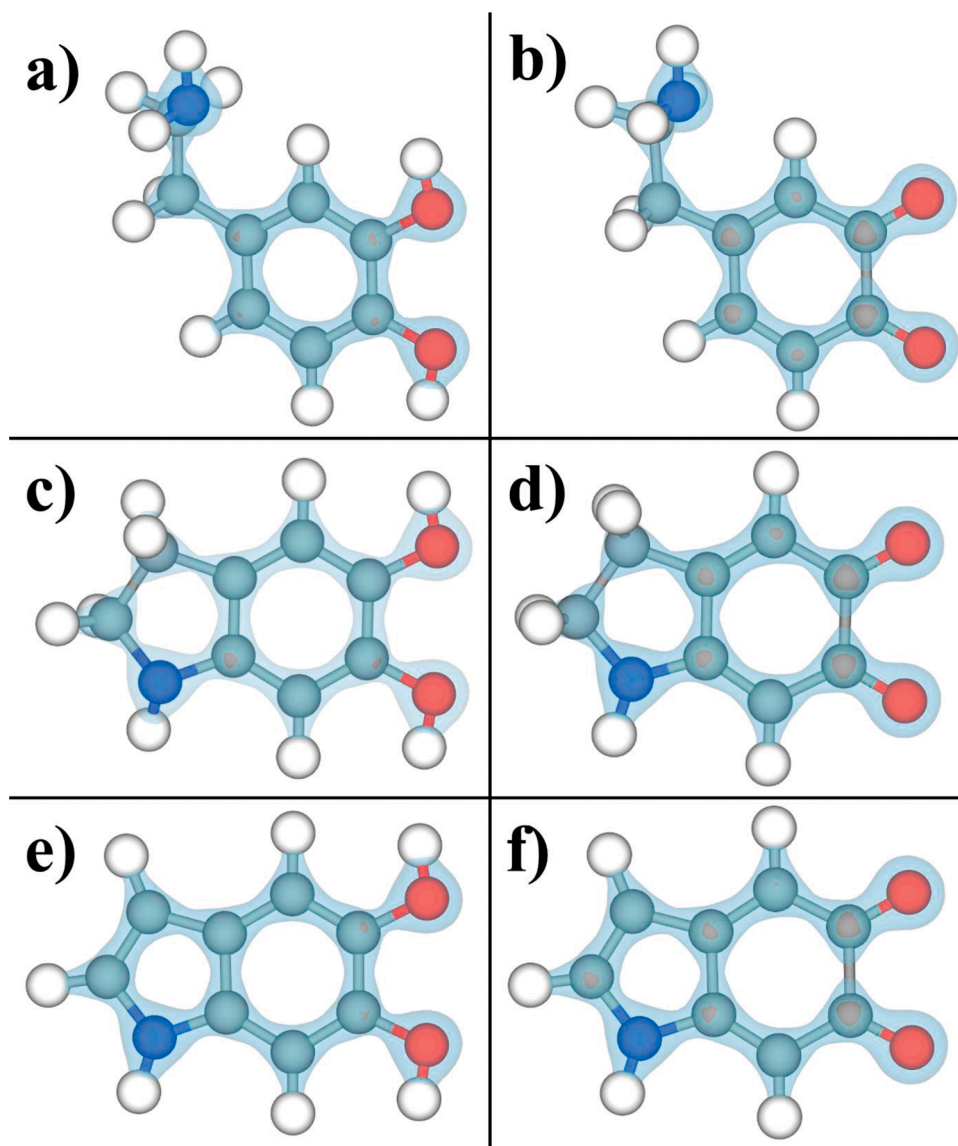
less likely to contribute to the polymerisation reaction, which is based on oxidation, i.e. withdrawing of electrons. Moreover, in the phenyl ring DA unit, there is a higher electron density in the vicinity of the 2nd and 4th carbon atoms than on the 5th, suggesting that polymerisation occurs in the 2 and 4 positions. Another observation is that depending on the oxidation state of the atoms in the five-membered rings, the electron density is accumulated at different carbon atoms, which suggests different sites for crosslinking of ePDA. These observations support the existence of the variety of structures proposed in the literature [18].

The energy of the first isomerisation (Michael cyclisation) is equal to  $-118$  kJ/mol, while the second equals  $-72$  kJ/mol. Therefore, one can state that catechol forms (LDC and DHI) are more stable than quinone ones (DQ and DC). Further, more free energy is released in the first isomerisation than in the second, meaning that in the second transition,

a smaller thermodynamic driving force occurs. Therefore, a more alkaline pH is required. This is in agreement with the experimental data (Fig. 6) showing that at a higher pH, the P2 associated with electropolymerisation (which requires the presence of double-ringed structures) has a higher current density than the corresponding P2 in a lower pH.

Resuming our investigations into electrochemistry and DFT, P3 can be associated mainly with the oxidation of DA to DQ, which is the dominating reaction in an acidic pH (e.g. pH = 3). When the pH becomes more alkaline, P1 and P2 emerge, indicating that DQ is transformed to LDC via Michael cyclisation and can therefore be oxidised to DC at the potential where P2 arises. P1 can be attributed to the oxidation of DHI to IQ, which is supported by the following arguments.

Firstly, Huynh et al. [58] showed that the standard potential of



**Fig. 8.** DFT-optimised structures of possible six structural units in ePDA (a) DA (b) DQ (c) DHI (d) IQ (e) LDC (f) DC. Blue area indicates electron density isosurface  $1.5 e^-/\text{\AA}^3$ . Legend for atoms: grey – carbon, navy blue – nitrogen, red – oxygen, white – hydrogen (For interpretation of the references to color in this figure legend, the reader is referred to the web version of this article.).

quinone redox pairs decreases when aromatic rings are substituted with electron-donating groups in the series  $-\text{CH}_3$ ,  $-\text{OCH}_3$ , aliphatic ring, aromatic ring. The same interpretation could be applied to the structures studied here because DA has the least substituted ring, LDC has an aliphatic adjacent ring, and DHI has an adjacent aromatic ring. It is then expected that the standard potential of quinone pairs should have a similar trend as in the work of Huynh. Therefore, the DHI/IQ redox reaction should have the lowest value of the standard potential. Secondly, the reduction and oxidation peaks both decreased with the scan number in a similar way during the CV experiment (see Fig. 2), suggesting the product of the reaction (IQ) is not consumed in further chemical steps. That is in agreement with the fact that IQ does not undergo any further chemical transitions, in contrast to DQ and DC. Moreover, considering that quinone forms are less prone to electropolymerisation than catechol ones (Fig. 8), it is not expected that polymerisation occurs at the potential of P1. This is also experimentally confirmed via a detailed analysis of both CV and EIS data (see Figs. 3–5).

#### 4. Conclusions

The electropolymerisation of dopamine on B:CNW exhibiting exceptional mechanism was studied in detail. CV and EIS investigations showed that electropolymerisation occurs mainly at a narrow range of potentials from 0.0 to +0.4 V and the wide (−0.5 to 1.0 V) window is required for the PDA layer formation. A resistor-like CPE element was used to model the inhomogeneity of the resistance on the surface of a B:CNW electrode leading to a decrease in the number of elements in the equivalent circuit.

An ePDA coating is formed in a pH ranging from 4 to 11, but the current densities of the redox peaks vanish only at a neutral or alkaline pH, indicating completeness of polymerisation. The pseudocapacitive peaks were recorded for polydopamine-modified electrode materials, indicating a different chemical structure of the catechol-quinone redox couples. Electrochemical investigations along with DFT computations allowed three charge transfer reactions of PDA monomers to be assigned to the three quasi-reversible redox peaks observed in voltammograms. These transitions are DHI/IQ at −0.35 V, LDC/DC at +0.15 V, and DA/DQ at +0.5 V. DFT optimised structures. Moreover, the calculated free



energies suggest that catechol units are more likely polymerised than quinone forms, while the polymerisation occurs faster in the more alkaline solutions.

## Declaration of Competing Interest

The authors declare no conflict of interest.

## Funding statement

This work was funded by the Polish Ministry of Science and Higher Education via Diamantowy Grant DI2019 017649, and the Polish National Science Centre via Sonata Bis 6 2016/22/E/ST7/00102 and Sonata-BIS 2017/26/E/ST5/00416. The research leading to these results has received funding from the Norway Grants 2014–2021 via the National Centre for Research and Development (NOR/POLNOR/UP-TURN/0060/2019).

## Supplementary materials

Supplementary material associated with this article can be found, in the online version, at doi:10.1016/j.electacta.2022.140000.

## References



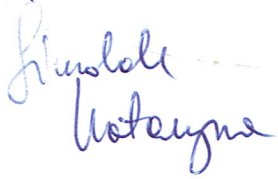

- J. Tan, Z. Xie, Z. Zhang, Y. Sun, W. Shi, D. Ge, Dopamine modified polyaniline with improved adhesion, dispersibility, and biocompatibility, *J. Mater. Sci.* 53 (2018) 447–455, <https://doi.org/10.1007/s10853-017-1520-9>.
- T. Sun, Z. Li, H. Wang, D. Bao, F. Meng, X. Zhang, A biodegradable polydopamine-derived electrode material for high-capacity and long-life lithium-ion and sodium-ion batteries, *Angew. Chem. Int. Ed.* 55 (2016) 10662–10666, <https://doi.org/10.1002/anie.201604519>.
- Y. Zheng, S. Lu, W. Xu, G. He, Y. Cheng, T. Yu, Y. Zhang, The fabrication of graphene/polydopamine/nickel foam composite material with excellent electrochemical performance as supercapacitor electrode, *J. Solid State Chem.* 258 (2018) 401–409, <https://doi.org/10.1016/j.jssc.2017.11.006>.
- J.H. Kim, M.K. Joshi, J. Lee, C.H. Park, C.S. Kim, Polydopamine-assisted immobilization of hierarchical zinc oxide nanostructures on electrospun nanofibrous membrane for photocatalysis and antimicrobial activity, *J. Colloid Interface Sci.* 513 (2018) 566–574, <https://doi.org/10.1016/j.jcis.2017.11.061>.
- K. Qu, Y. Zheng, S. Dai, S.Z. Qiao, Graphene oxide-polydopamine derived N, S-codoped carbon nanosheets as superior bifunctional electrocatalysts for oxygen reduction and evolution, *Nano Energy* 19 (2016) 373–381, <https://doi.org/10.1016/j.nanoen.2015.11.027>.
- Y. Lv, Y. Du, W.Z. Qiu, Z.K. Xu, Nanocomposite membranes via the codeposition of polydopamine/polyethyleneimine with silica nanoparticles for enhanced mechanical strength and high water permeability, *ACS Appl. Mater. Interfaces* 9 (2017) 2966–2972, <https://doi.org/10.1021/acsami.6b13761>.
- Z. Xu, Fabrication of polydopamine-coated superhydrophobic fabrics for oil/water separation and self-cleaning, *Appl. Surf. Sci.* 9 (370) (2016) 243–251.
- L. Su, Y. Yu, Y. Zhao, F. Liang, X. Zhang, Strong antibacterial polydopamine coatings prepared by a shaking-assisted method, *Sci. Rep.* 6 (2016) 24420, <https://doi.org/10.1038/srep24420>.
- Z. Xu, K. Miyazaki, T. Hori, Fabrication of polydopamine-coated superhydrophobic fabrics for oil/water separation and self-cleaning, *Appl. Surf. Sci.* 370 (2016) 243–251, <https://doi.org/10.1016/j.apsusc.2016.02.135>.
- S. Daboss, J. Lin, M. Godejohann, C. Kranz, Redox switchable polydopamine-modified AFM-SECM probes: a probe for electrochemical force spectroscopy, *Anal. Chem.* 92 (2020) 8404–8413, <https://doi.org/10.1021/acs.analchem.0c00995>.
- P. Palladino, F. Bettazzi, S. Scarano, Polydopamine: surface coating, molecular imprinting, and electrochemistry-successful applications and future perspectives in (bio)analysis, *Anal. Bioanal. Chem.* 411 (2019) 4327–4338, <https://doi.org/10.1007/s00216-019-01665-w>.
- L.C. Almeida, T. Frade, R.D. Correia, Y. Niu, G. Jin, J.P. Correia, A.S. Viana, Electrosynthesis of polydopamine-ethanolamine films for the development of immunosensing interfaces, *Sci. Rep.* 11 (2021) 2237, <https://doi.org/10.1038/s41598-021-81816-1>.
- T. Khumsap, S. Bamrungsap, V.T. Thu, L.T. Nguyen, Epitope-imprinted polydopamine electrochemical sensor for ovalbumin detection, *Bioelectrochemistry* 140 (2021), 107805, <https://doi.org/10.1016/j.bioelechem.2021.107805>.
- H.A. Lee, E. Park, H. Lee, Polydopamine and its derivative surface chemistry in material science: a focused review for studies at KAIST, *Adv. Mater.* 32 (2020), <https://doi.org/10.1002/adma.201907505>, 1907505.
- X. Han, F. Tang, Z. Jin, Free-standing polydopamine films generated in the presence of different metallic ions: the comparison of reaction process and film properties, *RSC Adv.* 8 (2018) 18347–18354, <https://doi.org/10.1039/C8RA02930J>.
- T. Marchesi D'Alvise, S. Harvey, L. Hueske, J. Szelwicka, L. Veith, T.P.J. Knowles, D. Kubiczek, C. Flaig, F. Port, K. Gottschalk, F. Rosenau, B. Graczykowski, G. Fytas, F.S. Ruggeri, K. Wunderlich, T. Weil, Ultrathin polydopamine films with phospholipid nanodiscs containing a glycoprotein domain, *Adv. Funct. Mater.* 30 (2020), 2000378, <https://doi.org/10.1002/adfm.202000378>.
- J. Wang, B. Li, Z. Li, K. Ren, L. Jin, S. Zhang, H. Chang, Y. Sun, J. Ji, Electropolymerization of dopamine for surface modification of complex-shaped cardiovascular stents, *Biomaterials* 35 (2014) 7679–7689, <https://doi.org/10.1016/j.biomaterials.2014.05.047>.
- J. Liebscher, R. Mrówczyński, H.A. Scheidt, C. Filip, N.D. Hádade, R. Turcu, A. Bende, S. Beck, Structure of polydopamine: a never-ending story? *Langmuir* 29 (2013) 10539–10548, <https://doi.org/10.1021/la4020288>.
- E. Chalmers, H. Lee, C. Zhu, X. Liu, Increasing the conductivity and adhesion of polypyrrole hydrogels with electropolymerized polydopamine, *Chem. Mater.* 32 (2020) 234–244, <https://doi.org/10.1021/acs.chemmater.9b03655>.
- L.C. Almeida, R.D. Correia, A. Marta, G. Squillaci, A. Morana, F. La Cara, J. P. Correia, A.S. Viana, Electrosynthesis of polydopamine films - tailored matrices for laccase-based biosensors, *Appl. Surf. Sci.* 480 (2019) 979–989, <https://doi.org/10.1016/j.apsusc.2019.03.015>.
- M. Alfieri, L. Panzella, S. Oscurato, M. Salvatore, R. Avolio, M. Errico, P. Maddalena, A. Napolitano, M. d'Ischia, The chemistry of polydopamine film formation: the amine-quinone interplay, *Biomimetics* 3 (2018) 26, <https://doi.org/10.3390/biomimetics3030026>.
- S. El Yakhli, M.L. Alfieri, Y. Arntz, M. Eredia, A. Ciesielski, P. Samorì, M. d'Ischia, V. Ball, Oxidant-dependent antioxidant activity of polydopamine films: the chemistry-morphology interplay, *Colloids Surf. A* 614 (2021), 126134, <https://doi.org/10.1016/j.colsurfa.2021.126134>.
- H. Coskun, A. Aljabour, T. Greunz, M. Kehr, D. Stifter, P. Stadler, Electrochemical hydrogen storage in amine-activated polydopamine, *Adv. Sust. Syst.* 5 (2021), <https://doi.org/10.1002/advs.202000176>, 2000176.
- Y. Kim, E. Coy, H. Kim, R. Mrówczyński, P. Torruella, D.-W. Jeong, K.S. Choi, J. H. Jang, M.Y. Song, D.-J. Jang, F. Peiro, S. Jurga, H.J. Kim, Efficient photocatalytic production of hydrogen by exploiting the polydopamine-semiconductor interface, *Appl. Catal. B* 280 (2021), 119423, <https://doi.org/10.1016/j.apcatb.2020.119423>.
- Y. Zhao, Preparation and characterization of vertically columnar boron doped diamond array electrode, *Appl. Surf. Sci.* 6 (303) (2014) 419–424.
- S. Wang, X. Ji, Y. Ao, J. Yu, Vertically aligned N-doped diamond/graphite hybrid nanosheets epitaxially grown on B-doped diamond films as electrocatalysts for oxygen reduction reaction in an alkaline medium, *ACS Appl. Mater. Interfaces* 10 (2018) 29866–29875, <https://doi.org/10.1021/acsami.8b06101>.
- K. Siuzdak, M. Ficek, M. Sobaszek, J. Ryl, M. Gnyba, P. Niedziałkowski, N. Malinowska, J. Karczewski, R. Bogdanowicz, Boron-enhanced growth of micron-scale carbon-based nanowalls: a route toward high rates of electrochemical biosensing, *ACS Appl. Mater. Interfaces* 9 (2017) 12982–12992, <https://doi.org/10.1021/acsami.6b16860>.
- A. Dettlaff, P. Jakóbczyk, M. Ficek, B. Wilk, M. Szala, J. Wojtas, T. Ossowski, R. Bogdanowicz, Electrochemical determination of nitroaromatic explosives at boron-doped diamond/graphene nanowall electrodes: 2,4,6-trinitrotoluene and 2,4,6-trinitroanisole in liquid effluents, *J. Hazard. Mater.* 387 (2020), 121672, <https://doi.org/10.1016/j.jhazmat.2019.121672>.
- M. Brodowski, M. Kowalski, M. Skwarecka, K. Pałka, M. Skowicki, A. Kula, T. Lipiński, A. Dettlaff, M. Ficek, J. Ryl, K. Dziąbłowska, D. Nidzworski, R. Bogdanowicz, Highly selective impedimetric determination of Haemophilus influenzae protein D using maze-like boron-doped carbon nanowall electrodes, *Talanta* 221 (2021), 121623, <https://doi.org/10.1016/j.talanta.2020.121623>.
- M. Pierpaoli, P. Jakóbczyk, M. Sawczak, A. Łuczkiwicz, S. Fudala-Książek, R. Bogdanowicz, Carbon nanoarchitectures as high-performance electrodes for the electrochemical oxidation of landfill leachate, *J. Hazard. Mater.* 401 (2021), 123407, <https://doi.org/10.1016/j.jhazmat.2020.123407>.
- D. Banerjee, K.J. Sankaran, S. Deshmukh, M. Ficek, G. Bhattacharya, J. Ryl, D. M. Phase, M. Gupta, R. Bogdanowicz, I.N. Lin, A. Kanjilal, K. Haenen, S.S. Roy, 3D hierarchical boron-doped diamond-multilayered graphene nanowalls as an efficient supercapacitor electrode, *J. Phys. Chem. C* 123 (2019) 15458–15466, <https://doi.org/10.1021/acs.jpcc.9b03628>.
- R. Rani, K. Panda, N. Kumar, K.J. Sankaran, R. Pandian, M. Ficek, R. Bogdanowicz, K. Haenen, I.N. Lin, Triboenvironment dependent chemical modification of sliding interfaces in ultrananocrystalline diamond nanowall film: correlation with friction and wear, *J. Phys. Chem. C* 122 (2018) 945–956, <https://doi.org/10.1021/acs.jpcc.7b10992>.
- M. Pierpaoli, M. Ficek, P. Jakóbczyk, J. Karczewski, R. Bogdanowicz, Self-assembly of vertically oriented graphene nanostructures: multivariate characterisation by Minkowski functionals and fractal geometry, *Acta Mater.* 214 (2021), 116989, <https://doi.org/10.1016/j.actamat.2021.116989>.
- M.A. Hejazi, W. Tong, A. Stacey, S.H. Sun, M. Yunzab, A. Almasi, Y.J. Jung, H. Meffin, K. Fox, K. Edalati, A. Nadarajah, S. Prawer, M.R. Ibbotson, D.J. Garrett, High fidelity bidirectional neural interfacing with carbon fiber microelectrodes coated with boron-doped carbon nanowalls: an acute study, *Adv. Funct. Mater.* 30 (2020), <https://doi.org/10.1002/adfm.202006101>, 2006101.
- In A.S. Bondarenko, G.A. Ragoisha, A.L. Pomerantsev, *Progress in Chemometrics Research*, In, Nova Science Publishers, New York, 2005, pp. 89–102. Ed.; (the program is available online at <http://www.abc.chemistry.bsu.by/vi/analyser/>, (n. d.).
- S. Smidstrup, et al., *QuantumATK: An integrated platform of electronic and atomic-scale modelling tools*, *J. Phys.: Condens. Matter* 32 (2020), 015901.

- [37] J.M. Soler, E. Artacho, J.D. Gale, A. García, J. Junquera, P. Ordejón, D. Sánchez-Portal, The SIESTA method for ab initio order- N materials simulation, *J. Phys. Condens. Matter* 14 (2002) 2745–2779, <https://doi.org/10.1088/0953-8984/14/11/302>.
- [38] M.J. van Setten, M. Giantomassi, E. Bousquet, M.J. Verstraete, D.R. Hamann, X. Gonze, G.-M. Rignanese, The PseudoDojo: training and grading a 85 element optimized norm-conserving pseudopotential table, *Comput. Phys. Commun.* 226 (2018) 39–54, <https://doi.org/10.1016/j.cpc.2018.01.012>.
- [39] S. Grimme, M. Steinmetz, M. Korth, How to compute isomerization energies of organic molecules with quantum chemical methods, *J. Org. Chem.* 72 (2007) 2118–2126, <https://doi.org/10.1021/jo062446p>.
- [40] M. Sobaszek, K. Siuzdak, J. Ryl, M. Sawczak, S. Gupta, S.B. Carrizosa, M. Ficek, B. Dec, K. Darowicki, R. Bogdanowicz, Diamond phase (sp<sup>3</sup>-C) rich boron-doped carbon nanowalls (sp<sup>2</sup>-C): physicochemical and electrochemical properties, *J. Phys. Chem. C* 121 (2017) 20821–20833, <https://doi.org/10.1021/acs.jpcc.7b06365>.
- [41] P. Kanyong, S. Rawlinson, J. Davis, Fabrication and electrochemical characterization of polydopamine redox polymer modified screen-printed carbon electrode for the detection of guanine, *Sens. Actuators B* 233 (2016) 528–534, <https://doi.org/10.1016/j.snb.2016.04.099>.
- [42] D.R. Kumar, S. Kesavan, T.T. Nguyen, J. Hwang, C. Lamiel, J.-J. Shim, Polydopamine@electrochemically reduced graphene oxide-modified electrode for electrochemical detection of free-chlorine, *Sens. Actuators B* 240 (2017) 818–828, <https://doi.org/10.1016/j.snb.2016.09.025>.
- [43] J.C. Zuaznabar-Gardona, A. Frago, A wide-range solid state potentiometric pH sensor based on poly-dopamine coated carbon nano-onion electrodes, *Sens. Actuators B* 273 (2018) 664–671, <https://doi.org/10.1016/j.snb.2018.06.103>.
- [44] L.E. Aguilar, B. Tumurbaatar, A. Ghavaminejad, C.H. Park, C.S. Kim, Functionalized non-vascular nitinol stent via electropolymerized polydopamine thin film coating loaded with bortezomib adjunct to hyperthermia therapy, *Sci. Rep.* 7 (2017) 9432, <https://doi.org/10.1038/s41598-017-08833-x>.
- [45] L.C. Almeida, R.D. Correia, G. Squillaci, A. Morana, F. La Cara, J.P. Correia, A. S. Viana, Electrochemical deposition of bio-inspired laccase-polydopamine films for phenolic sensors, *Electrochim. Acta* 319 (2019) 462–471, <https://doi.org/10.1016/j.electacta.2019.06.180>.
- [46] A.J. Bard, L.R. Faulkner, *Electrochemical Methods: Fundamentals and Applications*, 2nd ed., Wiley, New York, 2001.
- [47] R.G. Compton, E. Kätelhön, K.R. Ward, E. Laborda, *Understanding Voltammetry: Simulation of Electrode Processes*, 2nd ed., World Scientific (Europe), 2020 <https://doi.org/10.1142/q0246>.
- [48] S. Li, H. Wang, M. Young, F. Xu, G. Cheng, H. Cong, Properties of electropolymerized dopamine and its analogues, *Langmuir* 35 (2019) 1119–1125, <https://doi.org/10.1021/acs.langmuir.8b01444>.
- [49] A. Lasia, *Electrochemical Impedance Spectroscopy and Its Applications*, Springer, New York, 2014.
- [50] T. Jänsch, J. Wallauer, B. Roling, Influence of electrode roughness on double layer formation in ionic liquids, *J. Phys. Chem. C* 119 (2015) 4620–4626, <https://doi.org/10.1021/jp512617j>.
- [51] S.P. Sah, Corrosion of 304 stainless steel in carbonates melt – a state of enhanced dissolution of corrosion products, *Corros. Sci.* 169 (2020), 108535, <https://doi.org/10.1016/j.corsci.2020.108535>.
- [52] C. Man, C. Dong, Z. Cui, K. Xiao, Q. Yu, X. Li, A comparative study of primary and secondary passive films formed on AM355 stainless steel in 0.1 M NaOH, *Appl. Surf. Sci.* 427 (2018) 763–773, <https://doi.org/10.1016/j.apsusc.2017.08.151>.
- [53] J. Ryl, L. Burczyk, R. Bogdanowicz, M. Sobaszek, K. Darowicki, Study on surface termination of boron-doped diamond electrodes under anodic polarization in H<sub>2</sub>SO<sub>4</sub> by means of dynamic impedance technique, *Carbon* 96 (2016) 1093–1105, <https://doi.org/10.1016/j.carbon.2015.10.064>.
- [54] M. Salomäki, L. Marttila, H. Kivelä, T. Ouvinen, J. Lukkari, Effects of pH and oxidants on the first steps of polydopamine formation: a thermodynamic approach, *J. Phys. Chem. B* 122 (2018) 6314–6327, <https://doi.org/10.1021/acs.jpcc.8b02304>.
- [55] R.P. Bacil, L. Chen, S.H.P. Serrano, R.G. Compton, Dopamine oxidation at gold electrodes: mechanism and kinetics near neutral pH, *Phys. Chem. Chem. Phys.* 22 (2020) 607–614, <https://doi.org/10.1039/C9CP05527D>.
- [56] D.N. Oko, S. Garbarino, J. Zhang, Z. Xu, M. Chaker, D. Ma, D. Guay, A.C. Tavares, Dopamine and ascorbic acid electro-oxidation on Au, AuPt and Pt nanoparticles prepared by pulse laser ablation in water, *Electrochim. Acta* 159 (2015) 174–183, <https://doi.org/10.1016/j.electacta.2015.01.192>.
- [57] A.M. Abdel-Aziz, H.H. Hassan, I.H.A. Badr, Glassy carbon electrode electromodification in the presence of organic monomers: electropolymerization versus activation, *Anal. Chem.* 92 (2020) 7947–7954, <https://doi.org/10.1021/acs.analchem.0c01337>.
- [58] M.T. Huynh, C.W. Anson, A.C. Cavell, S.S. Stahl, S. Hammes-Schiffer, Quinone 1 e<sup>-</sup> and 2 e<sup>-</sup> / 2 H<sup>+</sup> reduction potentials: identification and analysis of deviations from systematic scaling relationships, *J. Am. Chem. Soc.* 138 (2016) 15903–15910, <https://doi.org/10.1021/jacs.6b05797>.



**CReditS table for Article 1:**

**Olejniak, A., Ficek, M., Siuzdak, K., & Bogdanowicz, R. (2022).** Multi-pathway mechanism of polydopamine film formation at vertically aligned diamondised boron-doped carbon nanowalls. *Electrochimica Acta*, 409, 140000. <https://doi.org/10.1016/j.electacta.2022.140000>.

Author	CRedit author statement	Signature
Adrian Olejniak	<b>Conceptualisation:</b> Full <b>Methodology:</b> Leading role <b>Formal analysis:</b> Leading role <b>Investigation:</b> Leading role <b>Resources:</b> In part <b>Data curation:</b> Full <b>Writing Original draft:</b> Leading role <b>Writing Review &amp; edit:</b> Leading role <b>Visualisation:</b> Full <b>Project administration:</b> In part (DG) <b>Funding:</b> In part	
Mateusz Ficek	<b>Methodology:</b> In part <b>Formal analysis:</b> In part <b>Investigation:</b> In part	
Katarzyna Siuzdak	<b>Validation:</b> In part <b>Resources:</b> In part <b>Writing Original draft:</b> In part <b>Writing Review &amp; edit:</b> In part <b>Supervision:</b> In part	
Robert Bogdanowicz	<b>Methodology:</b> In part <b>Validation:</b> In part <b>Resources:</b> In part <b>Writing Original draft:</b> In part <b>Writing Review &amp; edit:</b> In part <b>Supervision:</b> Leading role <b>Project administration:</b> In part <b>Funding:</b> In part	

# Tailoring Diffusional Fields in Zwitterion/Dopamine Copolymer Electropolymerized at Carbon Nanowalls for Sensitive Recognition of Neurotransmitters

Adrian Olejnik, Mateusz Ficek, Marek Szkodo, Alicja Stanisławska, Jakub Karczewski, Jacek Ryl, Anna Dołęga, Katarzyna Siuzdak, and Robert Bogdanowicz\*



Cite This: *ACS Nano* 2022, 16, 13183–13198



Read Online

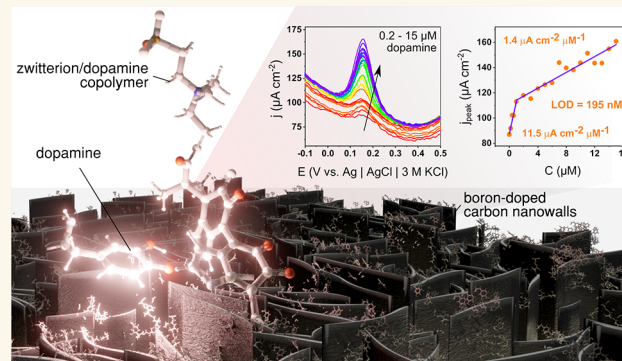
ACCESS |

Metrics & More

Article Recommendations

Supporting Information

**ABSTRACT:** The importance of neurotransmitter sensing in the diagnosis and treatment of many psychological illnesses and neurodegenerative diseases is non-negotiable. For electrochemical sensors to become widespread and accurate, a long journey must be undertaken for each device, from understanding the materials at the molecular level to real applications in biological fluids. We report a modification of diamondized boron-doped carbon nanowalls (BCNWs) with an electropolymerized polydopamine/polyzwitterion (PDA/PZ) coating revealing tunable mechanical and electrochemical properties. Zwitterions are codeposited with PDA and noncovalently incorporated into a structure. This approach causes a specific separation of the diffusion fields generated by each nanowall during electrochemical reactions, thus increasing the contribution of the steady-state currents in the amperometric response. This phenomenon has a profound effect on the sensing properties, leading to a 4-fold enhancement of the sensitivity ( $3.1$  to  $14.3 \mu\text{A cm}^{-2} \mu\text{M}^{-1}$ ) and a 5-fold decrease of the limit of detection ( $505$  to  $89 \text{ nM}$ ) in comparison to the pristine BCNWs. Moreover, as a result of the antifouling capabilities of the incorporated zwitterions, this enhancement is preserved in bovine serum albumin (BSA) with a high protein concentration. The presence of zwitterion facilitates the transport of dopamine in the direction of the electrode by intermolecular interactions such as cation- $\pi$  and hydrogen bonds. On the other hand, polydopamine units attached to the surface form molecular pockets driven by hydrogen bonds and  $\pi$ - $\pi$  interactions. As a result, the intermediate state of dopamine-analyte oxidation is stabilized, leading to the enhancement of the sensing properties.



**KEYWORDS:** polydopamine, zwitterions, coelectropolymerization, carbon nanowalls, nanoindentation, sensing, diffusion fields

## INTRODUCTION

The number of patients with mental illnesses and neurodegenerative diseases is rapidly increasing all over the world. Many of these diseases are associated with dysfunctions in dopaminergic transmission centers in the brain. In particular, a deficiency in the substantia nigra is typical in Parkinson's disease and leads to motor dysfunctions such as tremors.<sup>1</sup> Attention deficit disorder (ADD) is associated with dysregulation of noradrenaline metabolism in the locus coeruleus and dopaminergic transmission in the mesolimbic and mesocortical pathways, which cause impairment of executive functions, memory, and concentration.<sup>2,3</sup> On the other hand, the long-standing hypothesis of schizophrenia involves excessive firing

of dopaminergic neurons in the stratum, leading to positive symptoms such as paranoia.<sup>4</sup>

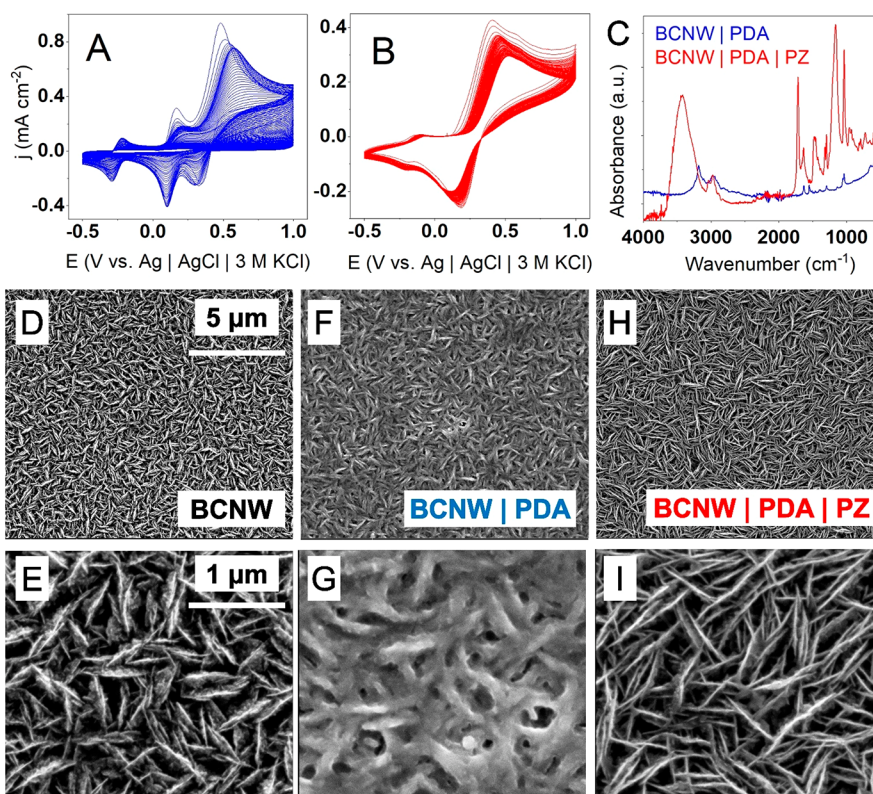
Engineering directed medical therapies as well as understanding the neurological and metabolic background of those diseases requires precise and inexpensive tools for in situ measurements of dopamine concentrations in the synaptic

Received: June 29, 2022

Accepted: July 14, 2022

Published: July 22, 2022





**Figure 1.** (A, B) Electropolymerization of polydopamine (PDA) and a hybrid PDA/PZ coating on boron-doped carbon nanowalls (BCNWs); (C) FTIR spectrum of deposited coatings; SEM pictures of BCNWs (D, E), BCNW/PDA (F, G), and BCNW/PDA/PZ (H, I) electrodes.

clefts and interstitial fluid of neural tissue.<sup>5</sup> The most potent advantage of the electrochemical sensors of neurotransmitters and neuromodulators is their very high temporal (time) resolution compared to fluorescent sensors.<sup>5</sup> Moreover, this method of sensing does not require the introduction of carefully engineered viral vectors (e.g., adenoviruses) capable of expressing the desired fluorescent markers into the tissue.

However, the most critical drawback of electrochemical sensors is their relatively low temporal (spatial) resolution,<sup>5</sup> which unfortunately does not allow precise imaging of single-neuron transmission and modulation. A potential solution to this problem is the fabrication of sensitive microelectrodes that are able to accomplish this task.<sup>6</sup> Therefore, it is essential to fabricate miniaturizable electrode materials with a very high affinity toward sensing a specific molecule, i.e., high sensitivity and selectivity, low limit of detection, and the ability to resist biofouling.

Polyzwitterions (PZs) are polymers possessing two ionized functional groups in each structural unit: one positive and one negative.<sup>7</sup> They are well-known due to their antifouling properties,<sup>8–12</sup> i.e., their ability to resist the adsorption of various biomolecules and to prevent the creation of biofilm on their surface. The antifouling mechanisms are generally complicated. Briefly, due to dipole–dipole and dipole–multipole interactions, the zwitterion-coated surface has a high level of hydration with a low ion concentration in the double layer. In this case, the adsorption of a protein is thermodynamically unfavorable, because there is neither entropic gain through counterion release nor enthalpic gain through reduction of the contact surface area.<sup>10,12</sup> Therefore, polyzwitterions are potent candidates for coatings for biosensors.

Dopamine can be polymerized on various surfaces using oxidative polymerization or electropolymerization.<sup>13–17</sup> The structure of the resulting polydopamine (PDA) consists of several chemically different structural units arranged in covalently or noncovalently cross-linked chains.<sup>18,19</sup> Among these, there are single-ringed dopamine (DA) and dopamine quinone (DQ) units containing the primary amine group as well as double-ringed dihydroxyindole (DHI) and indole quinone (IQ) units with aromatic carbon atoms capable of forming aryl–aryl cross-links.<sup>19,20</sup> PDA has a set of very useful properties due to its capability of forming strong hydrogen bonds and  $\pi$ – $\pi$  and  $\pi$ –cation interactions with various molecules.<sup>18,21</sup> It makes PDA a superior adhesive promoting agent,<sup>22</sup> complexation agent for chelating metal ions,<sup>23,24</sup> template for molecular imprinting,<sup>25</sup> and a functional ingredient of stimuli (pH, temperature, electric field, mechanical) responsive coatings<sup>26</sup> and supercapacitors.<sup>27</sup>

In this work, zwitterionic sulfobetaine methacrylate (SBMA) is incorporated into the PDA matrix utilizing a one-step electropolymerization strategy. Analogous chemistry was applied for the synthesis of antifouling membranes<sup>28</sup> and thermoresponsive hydrogels<sup>29</sup> by means of oxidative polymerization. However, according to our best knowledge, the synthesis of hybrid PDA/PZ thin films by means of electropolymerization has not yet been reported. The platform electrodes for modifications are chemical vapor deposition (CVD)-synthesized boron-doped carbon nanowalls (BCNWs). They constitute a fractal structure<sup>30</sup> of diamondized, vertically oriented sheets of graphene.<sup>31</sup> The structural features of the bare BCNW and functionalized BCNW/PDA/PZ electrodes are investigated via scanning electron microscopy (SEM), Fourier transform infrared (FTIR) spectroscopy, and X-ray photo-



electron spectroscopy (XPS) as well as nanomechanical testing. We have manifested the significant potency of BCNW electrodes in electrochemical sensing,<sup>31–33</sup> attributed to the fast charge transfer kinetics and surface conductivity resulting from the interplay between  $sp^3$  and  $sp^2$  phases.

BCNWs can be thought of as an array of micro(nano) electrodes. There are several cases describing the electrochemical response depending on the topology of the diffusion fields. In particular, Case 3 is an array with partially overlapping diffusion fields and Case 4, with completely overlapping diffusion fields resulting in a response almost identical to that of an ideally planar electrode.<sup>34,35</sup> Electrochemical investigations supported by density functional theory (DFT) computations show that pristine the BCNW exhibits Case 4 behavior, but application of the PDA/PZ coating shifts it to Case 3. Finally, we show that this phenomenon is responsible for enhancement of the electrode sensing properties in a neutral environment and in bovine serum solution.

## RESULTS AND DISCUSSION

**Synthesis and Chemical Structure of PDA/PZ Coatings.** The B:CNW growth mechanism is based on the joint chemistry of many species in plasma, not only limited to  $CN^-$ ,  $HyCNH_x$ ,  $BH-x$ , and  $CH+x$  radicals.<sup>36</sup> Boron doping allows for the formation of sharp-edged, flat, and up to 3  $\mu m$  long carbon walls<sup>31</sup> with superior electrochemical performance ( $k^0 = 1.1 \times 10^{-2} \text{ cm s}^{-1}$  and  $\Delta E = 85 \text{ mV}$ ). On the contrary, undoped CNW samples do not present highly developed maze-like structures with high surface area impairing fast kinetics at the multiple redox centers ( $k^0 = 3.7 \times 10^{-3} \text{ cm s}^{-1}$ ). Pristine CNWs revealed a significantly narrower electrochemical potential window with irreversible oxidation (+0.83 V) and reduction peaks (−0.50 V).<sup>31</sup>

Both the PDA and PDA/PZ coatings were electropolymerized in argon-purged 1× Tris buffer (pH 7.4) containing 5 mM dopamine with or without an excess of 500 mM SBMA monomer. Significant differences between the deposition processes can be observed on cyclic voltammograms depending on the presence of the additional zwitterionic monomer (Figure 1A,B). In the case of sole dopamine solution, three quasi-reversible redox peaks are present, centered at −0.3, +0.1, and +0.5 V. Investigations from our previous work<sup>37</sup> show that the peaks correspond to the redox couples as follows: the far cathodic peak to dihydroxyindole (DHI)–indole quinone (IQ), the middle one to leukodopaminechrome (LDC)–dopaminechrome (DC), and the last anodic one to dopamine (DA)–dopamine quinone (DQ), respectively. The current densities of each peak gradually decrease with consecutive cyclic voltammetry (CV) scans until very small currents (i.e., several  $\mu A$ ) are reached. However, when zwitterionic monomer is introduced to the electrolyte (to a large extent, 500 mM), the deposition characteristics are altered. First, only two redox couples can be seen at −0.15 and +0.35 V, and second, they are shifted with respect to those in pure PDA deposition voltammograms.

Intermolecular electrostatic and  $\pi$ –cation interactions between PZ and PDA are responsible for the shift of the leftmost DHI/IQ peak toward more anodic potentials. Electrostatically positive  $N(CH_3)_4$  groups can interact with the aromatic rings of the PDA, which leads to the withdrawal of the electron cloud from the ring.<sup>38</sup> Therefore, further oxidation of DHI to IQ is energetically more favorable, and the peak shifts from −0.25 to −0.15 V. Partial justification of those

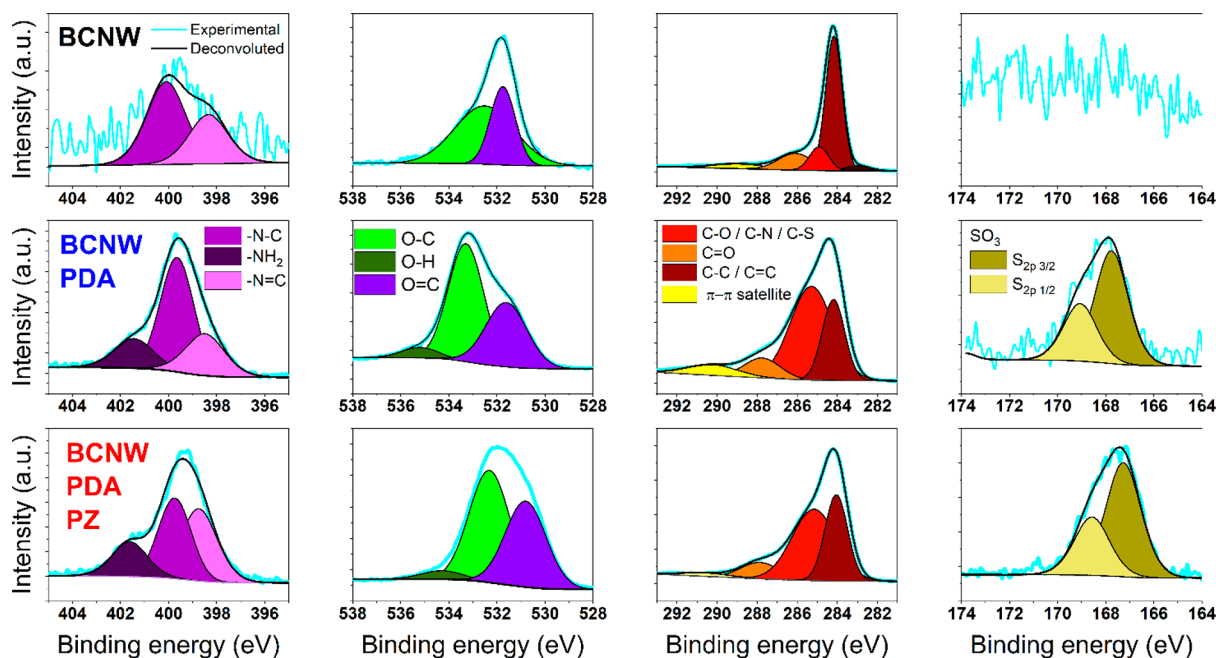
phenomena are provided with the FT-IR spectra and ESP calculations (see further answers). It is foreseen that zwitterions could act catalytically for the DC isomerization to DHI. However, the detailed mechanism of this catalysis is unknown to us. Presumably, the intermolecular interaction between PDA and PZ leads to the stabilization of the quinone–methide intermediate, which occurs in living organisms (as described in ref 39) and also is predicted from quantum chemical calculations<sup>40</sup> (DFT B3LYP). This hypothesis would also explain the lack of the middle CV peaks corresponding to the LDC/DC pair in comparison to the pure PDA electropolymerization as all the DC would quickly isomerize to DHI.

Moreover, the current magnitudes are two times smaller but do not decay as fast with consecutive scans. This observation indicates that the hybrid coating is more conductive than PDA, which has the utmost importance in sensing applications. Higher conductivity could originate from the increased concentration of ionic charge carriers (generated via autoprotonation of dopamine or sulfonate groups<sup>41</sup> or from an external solution) in the region between zwitterionic structural units.<sup>42</sup>

Additionally, a further study of the electrodeposition CV curves for varying PZ content was performed to verify the effect of PZ on the electropolymerization mechanism. At the lowest PZ content, they (Figure S2A,B) strongly resemble pristine PDA curves. In those cases, three pairs of redox peaks are present and the current gradually diminishes with consecutive cycling until 50  $\mu A \text{ cm}^{-2}$  is reached. However, for higher PZ contents starting from a 5:100 ratio (Figure S2C,D), currents do not plummet to very small values after 50 cycles. Simultaneously, the second oxidation peak corresponding to the LDC  $\rightarrow$  DC reaction is smaller in comparison to others. It presumably originates from the higher contribution of  $\pi$ –cation interactions catalyzing chemical steps in the mechanism. Nevertheless, both CV curves and electrochemical impedance spectroscopy (EIS) spectra clearly indicate that, after deposition, the electrochemical activity is higher with increasing PZ content (Figure S2E,F). Low-rate CVs for the 5:100 PDA/PZ ratio show both oxidation and reduction peaks, but the oxidation peaks are flattened for higher rates. Moreover, Randles slope ( $H$ ) rises with increasing PZ content, but the linearity is weaker for lower ratios. From those results, it can be inferred that the kinetics of charge transfer is generally slower at lower PZ contents. Therefore, choosing the highest possible PZ content limited by solubility (5:500) is optimal for maximizing the sensing performance of the material.

Insight into the structure of the PDA and PDA/PZ deposited on the BCNW can be obtained by the SEM inspection given in Figure 1D–I. Each picture displays vertically aligned graphite sheets confirming the structure of the nanowalls. Interestingly, the walls seem to be thicker after PDA deposition but thinner after hybrid coating. This second observation suggests that the incorporation of zwitterionic units into the polymer chains alters the interactions of PDA with the electron beam and ultimately the electrical properties of the surface.

The thickness of the coating was measured using AFM recorded at the edge of pristine and coated BCNW (Figure S3A–C). Then, several topography scans were conducted on the BCNW area of the specimen and on the BCNW/PDA or BCNW/PDA/PZ area. Each point on the histograms (Figure S3D,E) corresponds to the average of the single topography scan. When one calculates the average of those points for



**Figure 2.** High resolution XPS spectra of BCNW, BCNW/PDA, and BCNW/PDA/PZ electrodes in the nitrogen, oxygen, carbon, and sulfur energy regions.

pristine and coated BCNW and subtracts the values, the thickness of the hybrid PDA/PZ coating could be obtained, and it is equal to 51 nm. The thickness of the PDA solely was equal to 6 nm; however, this value is in the experimental error and, therefore, gives only a rough approximation.

The chemical structure of the coatings was investigated by FTIR attenuated total reflection (ATR) spectroscopy (Figure 1C). While the signals of the BCNW/PDA electrodes are very weak and difficult to interpret, a spectrum of BCNW/PDA/PZ exhibits a well-pronounced series of absorption peaks. Considering the differences in signal intensities and clearness, one can anticipate that the zwitterionic units constitute a large portion of the hybrid coating structure. First, a broad medium band between 3200 and 3700  $\text{cm}^{-1}$  corresponds to OH stretching vibrations of water adsorbed on the surface or absorbed into the structure.<sup>43</sup> Hydroxyl groups of the PDA units also fall into this wavenumber range.<sup>44</sup> Second, there are several small bands at ca. 3100–2800  $\text{cm}^{-1}$  corresponding to the C–H stretching modes. They can originate from both aromatic (3100–3000  $\text{cm}^{-1}$ ) and aliphatic (3000–2800  $\text{cm}^{-1}$ ) C–H bonds of the PDA<sup>44</sup> and SBMA units.<sup>45</sup> Third, a band at 1720  $\text{cm}^{-1}$  corresponds to C=O stretching vibrations of carbonyls in quinone-rich units of PDA<sup>46</sup> or SBMA methacrylate parts.<sup>45</sup> The low intensity band at 1650  $\text{cm}^{-1}$  could correspond to C=C stretching modes in some indole rings in the PDA<sup>47</sup> or unreacted adsorbed methacrylates.<sup>48</sup> The small band at 1450  $\text{cm}^{-1}$  is likely to be due to O–H deformation or C–N stretching vibrations.

The evidence supporting the idea of the zwitterion being incorporated into the coating includes two typical strong bands: a relatively broad one at 1160  $\text{cm}^{-1}$  corresponding to S–O stretching and one at 1030  $\text{cm}^{-1}$  related to C–O stretching modes.<sup>45</sup> The signals in this range are significantly higher than in the case of pure PDA. The most probable origins of the variety of small bands in the range of 720–960  $\text{cm}^{-1}$  are different modes of C–H groups such as bending, scissoring, and possibly C–S stretching.<sup>49</sup> Those fingerprint

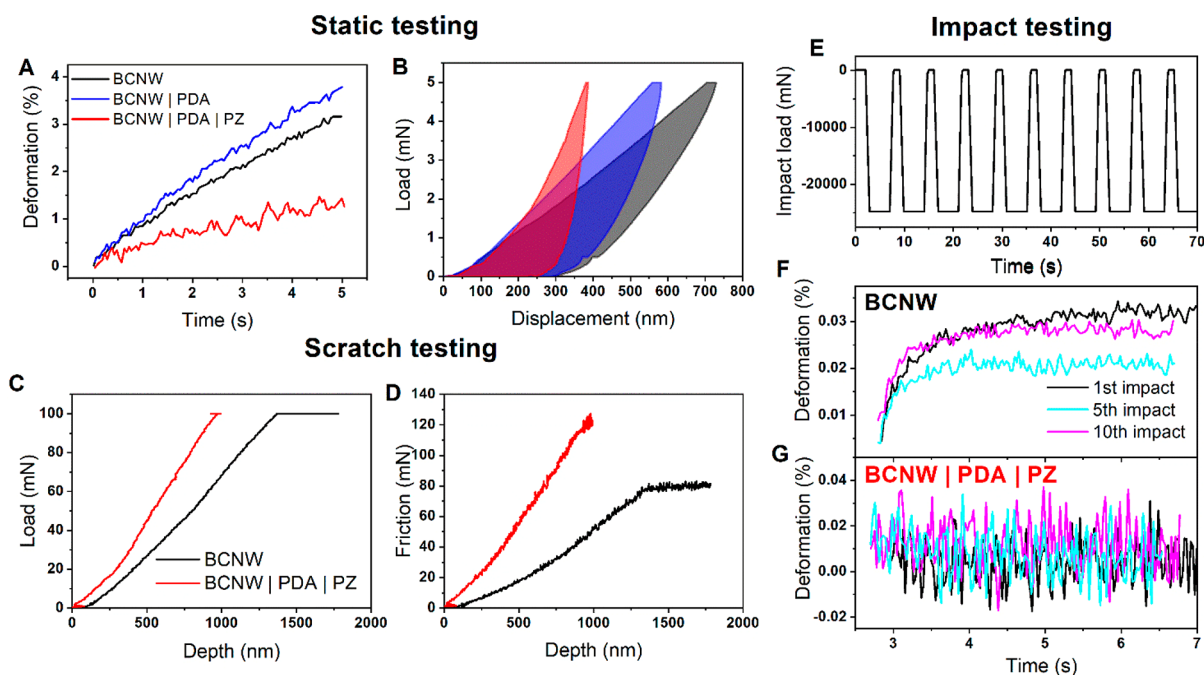
bands occur only in the hybrid coating and therefore should come only from zwitterionic components of the coating. A similar set of bands, although slightly shifted, was observed in our previous work in a hybrid Nafion-co-PZ coating for glucose sensing applications.<sup>50</sup>

These bands are also visible on the sample of the pristine PZ coating (Figure S1). Generally, there are no substantial differences in the whole range of the spectrum except the C–H bond region (inset). Several C–H bands in the range between 2750 and 3150  $\text{cm}^{-1}$  are diminished and shifted after deposition of the PZ. Considering that most of the C–H bonds are present in PZ, not PDA, these results suggest noncovalent  $\pi$ –cation interactions between tetraalkylammonium groups of PZ and aromatic rings of the PDA. Moreover, those changes support the fact that PDA undergoes cyclization to the indolequinone double-ringed units.

Another piece of evidence of the incorporation of zwitterions into the coating is the drastic decrease of the water contact angle from 123° for the pristine BCNW to 13° for the functionalized electrode. It is non-negotiable that the high level of acquired hydrophilicity must stem from surface modification with zwitterions.<sup>10,12,43,51</sup>

For further analysis of the chemical structure of the coatings, high resolution XPS spectra of bare and functionalized BCNW electrodes are provided in Figure 2. The nitrogen area of the spectra clearly shows that, in pristine BCNW, only trace amounts of nitrogen are present as a result of the 5% nitrogen in the plasma during CVD.<sup>31</sup> They contribute to 0.57 atomic % in the form of N–C bonds at 400 eV and N=C bonds at 398 eV. However, after the deposition of the PDA or hybrid PDA/PZ coating, a notable increase was recorded, including the emergence of a third component at 401.5 eV, which was attributed to N–H bonds. Their presence comes from the primary and secondary amines commonly found in each structural unit of PDA. A similar set of peaks was observed in works in both freestanding PDA and PDA as a coating.<sup>52–54</sup> In the oxygen region, the pristine BCNW spectrum consists of





**Figure 3.** Nanindentation studies of BCNW before and after electrodeposition of coatings. (A) Deformation velocity curves; (B) corresponding load–displacement curves; (C) load measured in the scratch test; (D) force of friction measured in the scratch test; (E) load profile applied during impact testing; (F) first, fifth, and 10th impact response of pristine BCNWs; (G) first, fifth, and 10th impact response of BCNWs functionalized with a hybrid PDA/PZ coating.

two deconvoluted components at 531.5 and 533 eV associated with C=O and C–O surface bonds, respectively. In our previous work, we showed that C–O bonds on the BCNW surface come in several variations, such as C–O–C and C–OH. The variety of C–O chemistries might explain the high fwhm of the C–O peak.<sup>31</sup> After electropolymerization, an additional component is manifested at ca. 535 eV, originating from O–H bonds, presumably from residual water absorbed into the PDA and catechol groups. Narrowing of the C–O peak is a consequence of the fact that, in functionalized electrodes, the XPS signal originates from the C–O bonds of catechol and methacrylate groups rather than from the surface bonds of the BCNW that are far below the organic layer and do not interact with Ar<sup>+</sup> ions during measurement. Finally, a slight increase of the C=O peak area and decrease of the O–H peak area can be observed for BCNW/PDA/PZ in comparison to that for BCNW/PDA. These two observations strongly suggest a higher oxidation state of the structural units in the hybrid coating compared to the pristine PDA.

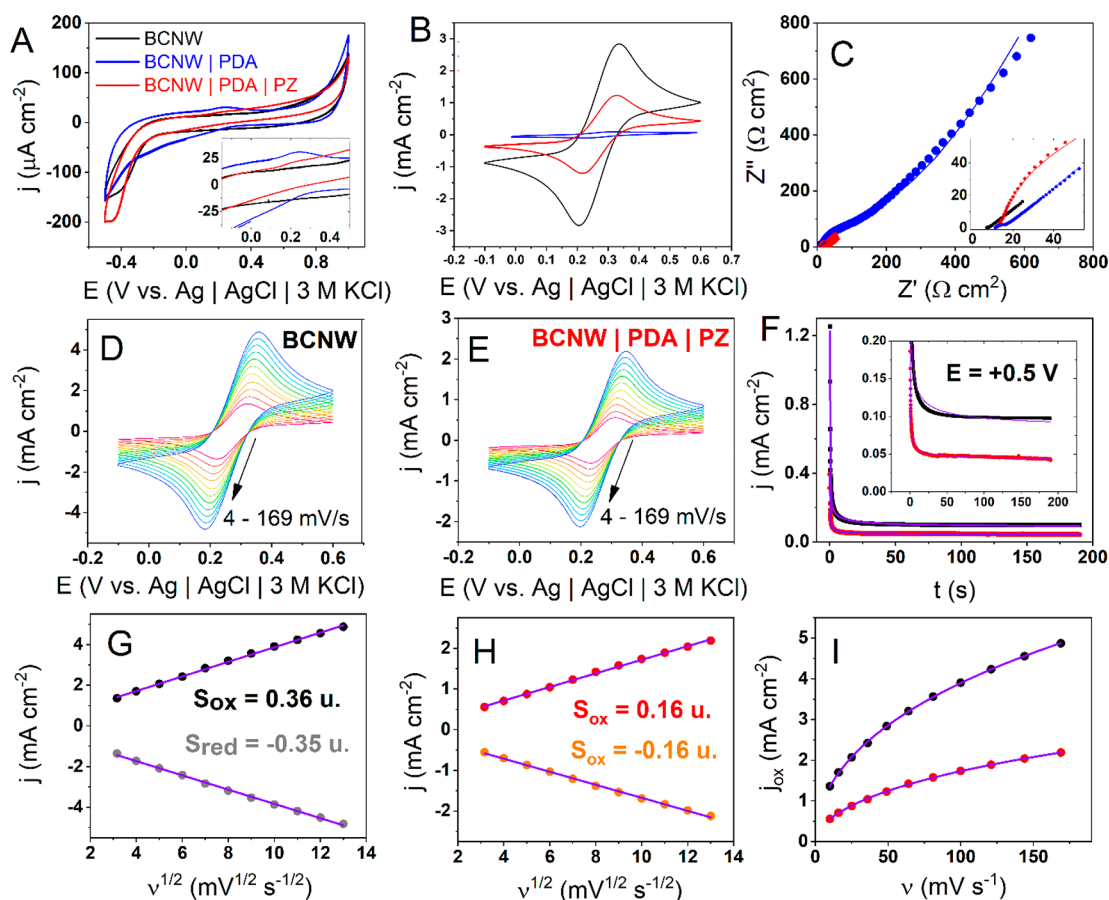
Carbon parts of the XPS spectra reveal five components for bare BCNW and four components for functionalized BCNW. The differentiating peak is located at 283 eV and originates from C–B bonds. This signal vanishes after the modifications as a result of the finite penetration depth of the X-rays through the polymers. The four remaining peaks can be attributed to C–C bonds (284 eV), C–O and C–N bonds (285 eV), C=O bonds (287–288 eV), and a broad signal of  $\pi$ – $\pi$  satellite distortions at 289–292 eV.<sup>55,56</sup> It can be clearly seen that the C–O and C–N content rises after polymerizations, staying in agreement with the chemistry of PDA. Additionally, two deconvoluted peaks attributed to C–O and C=O shift from 285 to 286 eV and from 286.5 to 288 eV, respectively. The reason is that, in functionalized electrodes, the XPS signal is gathered from the incorporated C–O catechol and C–N amines, rather than from surface C–O–C bonds. Moreover, in

the case of the BCNW/PDA/PZ, there is also a possible contribution of C–S bonds of the sulfobetaine unit in this range.<sup>57–59</sup> In the hybrid coating, the signal corresponding to the  $\pi$ – $\pi$  satellite peak plummets, presumably because SBMA units constitute a large portion of the coating. Since they have  $\pi$  bonds only in methacrylate groups, PZ does not contribute to the conjugated system of  $\pi$  bonds and the  $\pi$ – $\pi$  signal is diminished.

The pristine BCNW does not contain sulfur compounds. However, XPS investigations show that PDA contains some number of sulfates, most probably originating from trace amounts of sulfates in the Tris buffer. In the case of PDA/PZ, those signals are amplified due to the presence of sulfonate groups in the SBMA monomers incorporated into the structure.

Several conclusions were drawn from the FTIR and XPS investigations. First, polydopamine is deposited onto the surface of the nanowalls, and SBMA zwitterions are incorporated into the PDA structure, most probably through noncovalent bonding involving  $\pi$ –cation interactions. A similar structure was proposed recently by Zhang et al.<sup>29</sup> in the PDA/PSBMA composite, where PDA served as a noncovalent cross-linker. In the next section, nanomechanical studies are conducted to verify this hypothesis more rigorously.

**Nanomechanical Properties.** The AFM-estimated thickness of the PDA/PZ coating is equal to 51 nm and that of the PDA coating is only 6 nm. However, the second value is in the range of the experimental error and, therefore, is only approximate. For a better understanding of the relationships between the chemistry and surface properties of the functionalized BCNW, nanindentation studies were performed in static, scratch, and impact modes (Figure 3). The load–displacement curves show that the pristine BCNW has the lowest stiffness and hardness, which increases after electropolymerization (see the calculated mechanical properties



**Figure 4.** Electrochemical properties of pristine and functionalized BCNW electrodes. Comparison of CV curves recorded at 50 mV/s scanning speed (A) in 1× Tris buffer; (B) in 5 mM ferrocyanide solution; (C) EIS spectra (dots are experimental data, and lines are fitted data); (D, E) CV curves with different scan rates; (F) chronoamperograms registered at +0.5 V; (G, H) Randles–Ševčík plots,  $S_{ox}$  and  $S_{red}$  are slopes obtained through linear fitting and units (u) are  $\text{mA cm}^{-2} \text{mV}^{-1/2} \text{s}^{1/2}$ ; (I) nonlinear fitting of current–scan rate dependence; electrolyte for panels B–I was 5 mM  $\text{K}_3\text{Fe}(\text{CN})_6$  + 5 mM  $\text{K}_4\text{Fe}(\text{CN})_6$  + 1 M KCl; EIS spectra were fitted according the Randles circuit, i.e.,  $R(R(QW))$ ,  $Q$  is the constant phase element, and  $W$  is the Warburg element.

collected in Table S1). Pure PDA increases the Young's modulus ca. 2 times, while hybrid PDA/PZ increases it up to 7.3 times. Moreover, the slope of the time–deformation curves is the lowest among the tested electrodes, indicating the increase of the rigidity of the nanowalls by PDA/PZ. Lastly, the final depth of the indenter in this experiment is the smallest, i.e., 376 nm in comparison to 698 nm for pristine BCNW, and the contribution of plastic deformation during the indent is the highest for the hybrid coating. These observations strongly suggest that the hybrid coating has more cross-links in the polydopamine backbone than PDA. They are presumably caused by electrostatic interactions between amphiphilic PZ molecules and  $\pi$ –cation interactions. It stands in agreement with the anticipated method of the incorporation of zwitterionic monomers into the coating during electropolymerization.<sup>28</sup>

The effect of increased hardness is also manifested in scratch tests (Figure 3C–D). For the plain BCNW, the desired 100 mN load is achieved at the depth ca. 1.35  $\mu\text{m}$ , while in the case of BCNW/PDA/PZ, it is only 0.85  $\mu\text{m}$ . Moreover, the friction force of the modified BCNW increases faster with the depth and reaches up to ca. 130 mN, which is almost two times higher with respect to the plain BCNW. Those observations indicate that modification with PDA/PZ reinforces the structure of the BCNW and increases the resistance against

scratches.<sup>60</sup> This feature is beneficial for biosensors working in fluid-flow conditions, where abrasion and wear through fluid friction could cause damage over time.

Impact testing reveals several important correlations between the mechanical properties and structure of the functionalized BCNW electrodes. The bare BCNW exhibits a swelling behavior after each impact, which is seen in Figure 3F as the large plateau of the deformation accompanied by smaller oscillations around the plateau. Additionally, after the first impact, the value of the plateau decreases from 0.03% to 0.02% at the fifth impact and the deformation velocity decreases to nearly zero, suggesting permanent distortion of the nanowalls. However, at the 10th impact, the plateau increases again and the deformation velocity is slightly larger than zero, which might be associated with relaxation through the fracture mechanism.<sup>61</sup> A significantly different impact response is manifested by the functionalized BCNW (only BCNW/PDA/PZ is shown, but the response for BCNW/PDA is identical). Instead of the swelling, there are oscillations around the axis of zero deformation regardless of the number of impacts. The interpretation of this behavior is that after coating the BCNW, the inner spaces between the walls are smaller or diminished completely so that there is no place for swelling. In other words, the nanowalls are forced to oscillate between their equilibrium positions because the coating changed the

geometry and precluded the swelling. This observation provides further confirmation that PDA and PZ cause a profound alteration of BCNW surface properties, which is also revealed in the electrochemical performance.

**Electrochemical Properties.** Cyclic voltammograms (CVs) of the pristine and functionalized BCNW electrodes in neutral (1× Tris) electrolyte are shown in Figure 4A. In the case of BCNWs, no significant currents from redox reactions can be observed in the window from −0.2 to +0.6 V; only capacitive currents ( $\pm 20 \mu\text{A cm}^{-2}$ ) are present in this range. The PDA-functionalized electrode exhibits oxidation and reduction waves originating from redox reactions of catechol/quinone pairs that are abundant in most of the structural units of PDA.<sup>16,62</sup> However, those currents are significantly smaller for the BCNW/PDA/PZ electrode. This observation stands in agreement with the FTIR and XPS investigations, because a large number of molecules in the PDA/PZ coating are zwitterionic units, not PDA, and they do not possess reactive catechol/quinone redox pairs.

Investigations of the processes occurring at the electrode/electrolyte interface were performed by measurements in a solution containing a 5 mM ferrocyanide redox pair. CV curves for pristine and functionalized BCNW electrodes are given in Figure 4B. For the unmodified BCNW, a pair of well-shaped, symmetric redox peaks with roughly  $3 \text{ mA/cm}^2$  current densities can be observed. The high electrochemical activity stems from the structure of nanowalls and was thoroughly studied in our previous works.<sup>31,36</sup> Briefly, due to boron doping, they have high surface conductivity, and due to the interplay between the  $\text{sp}^2$  and  $\text{sp}^3$  phases, high charge transfer rates are achieved.

After electrodeposition of PDA solely, there is a significant loss in the redox response of ferrocyanides; current densities plummet to less than  $0.1 \text{ mA/cm}^2$ , presumably due to adsorption of nonconductive products of dopamine oxidation. Interestingly, when a hybrid PDA/PZ coating is deposited, the decrease in the redox response of the ferrocyanides is smaller (40% of the bare BCNWs) and two redox peaks are preserved. This supports the hypothesis posed in previous sections that PDA/PZ results in higher surface conductivity than pure PDA.

A similar corollary can be drawn from the EIS measurements presented in Figure 4C and Table S2. In the case of pure PDA, both the real and imaginary impedances are significantly higher with respect to the pure BCNW. More precisely, there is a huge (80×) increase in charge transfer resistance  $R_{\text{ct}}$  and Warburg element magnitude  $A_w$  (14×), indicating the formation of a coating with low conductivity. However, in the case of the hybrid coating, the changes in impedance data are rather mild (3× increase of charge transfer resistance and 2× increase of the Warburg element magnitude), indicating the formation of the coating, but have less blocking than PDA solely. The kinetic constant  $k^0$  can be calculated on the basis of the charge transfer resistance from the equation:<sup>63</sup>

$$R_{\text{ct}} = \frac{RT}{n^2 F^2} \frac{1}{\alpha k_{\text{red}} C_{\text{ox}}(0) + (1 - \alpha) k_{\text{ox}} C_{\text{red}}(0)} \approx \frac{RT}{n^2 F^2 k^0 C_{\text{ox}}} \quad (1)$$

where  $R$  is the gas constant,  $T$  is the temperature,  $F$  is the Faraday constant,  $n$  is the number of electrons involved in the reaction ( $n = 1$ ),  $\alpha$  is the charge transfer coefficient,  $k_{\text{red}}$  and  $k_{\text{ox}}$  are kinetic constants of the reduction and oxidation semi-

reactions in the redox couple, and finally  $C_{\text{ox}}(0)$  and  $C_{\text{red}}(0)$  are the surface concentrations of the redox active species. The simplification is based on the fact that  $\alpha \approx 1/2$ ,  $C_{\text{ox}}(0) \approx C_{\text{red}}(0)$ , and  $k_{\text{red}} \approx k_{\text{ox}}$  due to the high degree of symmetry between oxidation and reduction. Similarly, the apparent diffusion coefficient  $D$  can be calculated from the value of the Warburg element according to eq 1:<sup>63</sup>

$$A_w = \frac{RT}{n^2 F^2} \frac{1}{\sqrt{D_{\text{ox}} C_{\text{ox}}(0)} + \sqrt{D_{\text{red}} C_{\text{red}}(0)}} \approx \frac{RT}{2n^2 F^2 \sqrt{D} C_{\text{ox}}} \quad (2)$$

where  $D_{\text{ox}}$  and  $D_{\text{red}}$  are diffusion constants of the oxidized and reduced agent of the redox (ferrocyanide) couple. The simplification is based again on the symmetry between reduction and oxidation mass transport so that  $C_{\text{ox}}(0) \approx C_{\text{red}}(0)$  and  $D_{\text{ox}} \approx D_{\text{red}} \approx D$ . Lastly, the averaged double layer capacitance  $C_{\text{dl}}$  can be computed using the Brug formula (eq 3):<sup>64</sup>

$$C_{\text{dl}} = Q_0^{1/\alpha} \left[ \frac{1}{R_s} + \frac{1}{R_{\text{ct}}} \right]^{1/(1-\alpha)} \quad (3)$$

where  $R_s$  is the solution resistance,  $Q_0$  is the magnitude of the CPE element, and  $n$  is the CPE exponent. It is easy to see that after deposition of PDA both the kinetic constant and diffusion coefficient plummet, but in the case of coelectropolymerization of PDA/PZ, the changes are moderate. Interestingly, the double layer capacitance is very similar for all three electrodes. Therefore, the modification does not influence this parameter of the electrode. When one considers that only the hybrid coating is more relevant from the sensing point of view, only this electrode will be subjected to further investigations.

CVs of the bare BCNW and BCNW/PDA/PZ recorded with different scan rates are shown in Figure 4D–E along with the Randles–Sevcik plots (Figure 4G–H). There is a high degree of symmetry between the oxidation and reduction currents in the whole range of scan rates, and the shapes of the quasi-reversible peaks are similar for both electrodes. However, the polymerized electrode currents are ca. 2 times lower in magnitude. Similarly, the Randles–Sevcik slopes are equal to 0.36 and  $0.16 \text{ mA cm}^{-2} \text{ mV}^{-1/2} \text{ s}^{1/2}$  for bare and coated BCNW, respectively, suggesting a roughly 50% reduction of the active surface area after electropolymerization. Interestingly, at the lowest scan rate, i.e.,  $9 \text{ mV/s}$ , the peak-to-peak separation is equal to  $90 \text{ mV}$  for pristine BCNW and  $80 \text{ mV}$  for BCNW/PDA/PZ. In other words, the PDA/PZ coating leads to a mild decrease of both the apparent diffusion and kinetic constants (EIS results, Table S2), but the overall reversibility is increased. Nevertheless, it is still a mixed diffusion/kinetics-controlled process. The hypothesis explaining this behavior is as follows. The PDA/PZ coating decreases the active surface area of the electrode and induces specific changes in the surface geometry. As a result, the shape of the diffusion field around the nanowalls is shifted from heavily overlapped to moderately overlapped diffusion layers. In other words, the behavior of the BCNW after modification changes toward a microelectrode array, leading to the creation of a steady-state response.<sup>34,35</sup>

Several additional experiments were conducted to support this hypothesis. First, chronoamperometry measurements in the presence of 5 mM ferrocyanides were performed at the oxidative potential equal to  $+0.5 \text{ V}$  so that the stationary state was obtained after about 1 min (Figure 4F). The resulting



experimental curves for BCNW and BCNW/PDA/PZ were fitted using the modified version of the standard Cottrell equation<sup>65</sup> (eq 4):

$$j = j_0 \exp\left(-\frac{t}{t_0}\right) + \frac{C_C}{\sqrt{t}} + j_s \quad (4)$$

where the exponential term describes the decay of current related to discharge of the double layer,  $j_0$  is a pre-exponential constant,  $t_0$  is the time constant of the capacitor discharge, and  $C_C$  is a Cottrell constant, proportional to the concentration of the electroactive species and the square root of the diffusion constant. For the purpose of this discussion, the most important is the last term, i.e., the steady-state current  $j_s$ , which is the asymptotic current density when time approaches infinity. The physiochemical interpretation of this object is related to the geometry of the diffusion field in the vicinity of the electrode. In the case of a flat electrode, it equals zero, but for spherical or cylindrical electrodes, it is nonzero and dependent on the geometric parameters such as the electrode radius.<sup>34,65</sup>

Analogous behavior is observed for arrays of micro/nanoelectrodes and is captured by a theory of diffusive cases.<sup>34,35</sup> If diffusion fields of electroactive antennas are separated, the steady-state current is nonzero. The greater the confinement of the fields, the higher the current amplification. This phenomenon is a valuable factor for electroanalysis because the steady-state current is more sensitive to trace amounts of analytes and independent of time.<sup>35</sup> Simply,  $j_s$  is an indicator of the field geometry and can be used as a guide to distinguish between diffusion cases. Specific values of the parameters obtained through nonlinear fitting are gathered in Table 1. The curves are very well fitted with  $\chi^2$  less than  $3 \times$

**Table 1. Resulting Values of the Nonlinear Fitting to the Experimental Chronoamperometric Curves According to Eq 4<sup>a</sup>**

fitted parameter	BCNW	BCNW/PDA/PZ
$j_0$ [mA cm <sup>-2</sup> ]	1.64 (1.2%)	0.40 (1.0%)
$t_0$ [s]	0.27 (1.1%)	0.29 (1.0%)
$C_C$ [s <sup>1/2</sup> ]	0.18 (0.5%)	0.06 (0.6%)
$j_s$ [mA cm <sup>-2</sup> ]	0.08 (0.3%)	0.04 (0.2%)
$j_s/C_C$ [mA cm <sup>-2</sup> s <sup>-1/2</sup> ]	<b>0.44</b>	<b>0.67</b>
$\chi^2$ [10 <sup>-6</sup> ]	30.3	2.1

<sup>a</sup>Standard errors are given in brackets.

$10^{-5}$  and standard errors less than 2% each. There is one crucial difference between the pristine and functionalized BCNWs. Although the  $j_s$  value decreases after modification, the ratio between steady-state current  $j_s$  and the Cottrell current is greater and equal to 0.67 mA cm<sup>-2</sup> s<sup>-1/2</sup> compared to 0.44 mA cm<sup>-2</sup> s<sup>-1/2</sup> before modification. This almost 2-fold increase suggests that the contribution of the steady-state current to the overall current is higher in the case of the PDA/PZ functionalized electrode. Furthermore, the discharge time constant  $t_0$  is similar between the two electrodes, confirming the EIS results that the double layer capacitance is similar between the pristine and functionalized BCNWs.

Another piece of information about the structure of diffusional fields can be drawn from the nonlinear fitting of the current density vs scan rate dependence (Figure 4I). Two functions were fitted according to the following eq 5:

$$j = A \sqrt{\frac{dE}{dt}} + B \frac{dE}{dt} + j_{ss} \quad (5)$$

where  $A$  is a constant related to the diffusive current proportional to the square root of the scan rate,  $B$  is a capacitive/adsorptive component of the current proportional to the linear scan rate, and finally  $j_{ss}$  is a measure of current independent of the scan rate. A similar equation is used to determine the capacitive and faradaic contribution in the fields of batteries and supercapacitors.<sup>66–69</sup> The current is scan rate independent only when the steady state is reached, which happens in a rotating disk electrode experiment with a high angular frequency of rotations.<sup>65</sup> Therefore,  $j_{ss}$  is another element indicating the contribution of the steady-state current to the overall current. The parameters obtained by nonlinear fitting are gathered in Table 2. It can be observed that  $j_{ss}$  is

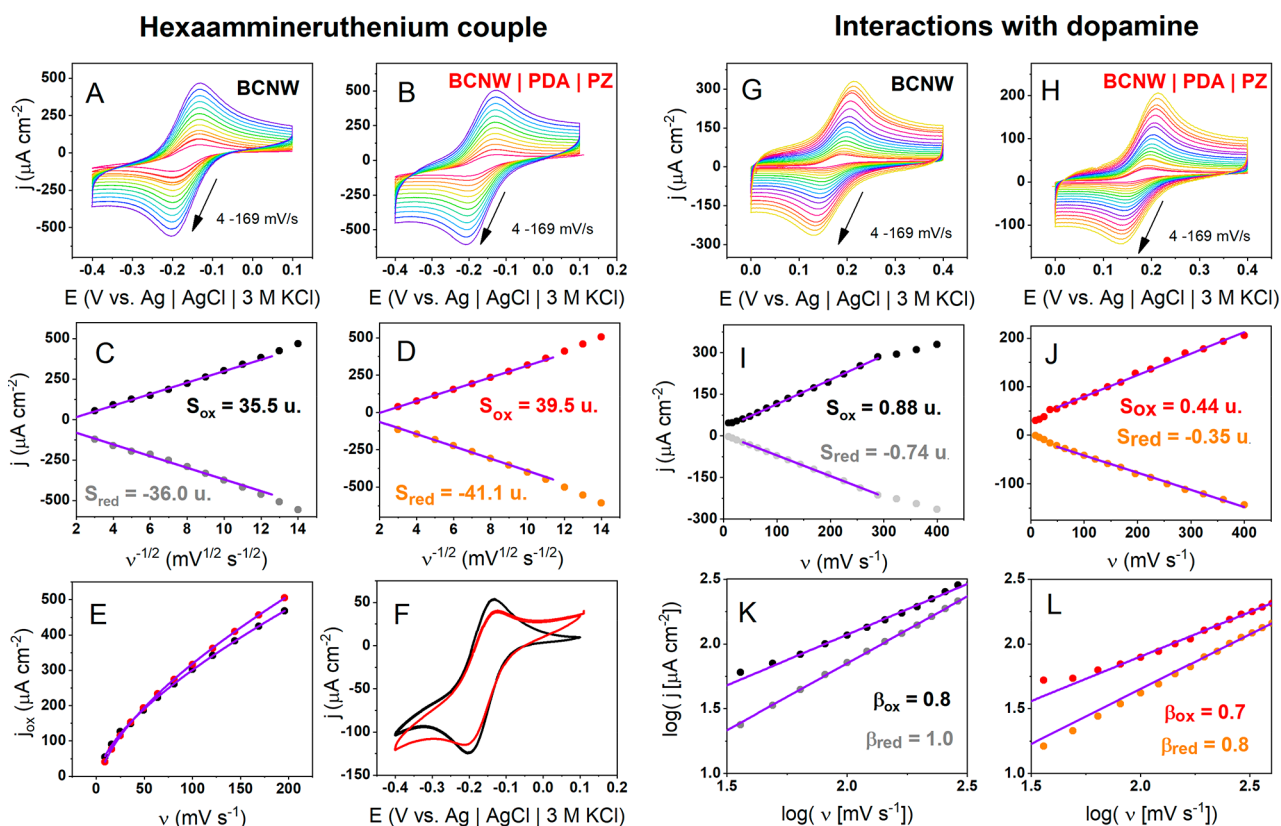
**Table 2. Resulting Values of the Nonlinear Fitting to the Experimental Chronoamperometric Curves According to Eq 5<sup>a</sup>**

fitted parameter	BCNW	BCNW/PDA/PZ
$j_{ss}$ [mA cm <sup>-2</sup> ]	0.034 (9.7%)	0.063 (37.2%)
$A$ [mA cm <sup>-2</sup> mV <sup>-1/2</sup> s <sup>1/2</sup> ]	0.43 (2.1%)	0.20 (3.0%)
$B$ [mA cm <sup>-2</sup> mV <sup>-1</sup> s]	−0.0045 (12.4%)	−0.0020 (18.6%)
$\chi^2$	$2.5 \times 10^{-4}$	$1.2 \times 10^{-4}$

<sup>a</sup>Standard errors are given in brackets.

equal to 34  $\mu\text{A cm}^{-2}$  for the pristine BCNW electrode and 63  $\mu\text{A cm}^{-2}$  for the BCNW/PDA/PZ electrode, which is again almost two times the increase of the steady-state current after modification. An additional argument supporting the validity of this nonlinear fitting approach is the similarity between the estimated  $A$  values (0.43 and 0.20 mA cm<sup>-2</sup> mV<sup>-1/2</sup> s<sup>1/2</sup>) and the same values calculated via fitting according to the Randles–Ševčík formula (Figure 4G–H) (0.36 and 0.16 mA cm<sup>-2</sup> mV<sup>-1/2</sup> s<sup>1/2</sup>, respectively). The component  $B$  associated with the surface-bound reactions is close to zero and negligible in this case.

Considering the above-discussed results, the hypothesis of altering the diffusional field geometry by the PDA/PZ coating becomes an interesting idea, leading to several outcomes that may be fruitful in sensing applications. However, several additional experiments were performed to present more arguments supporting this approach. Electrochemical measurements of the pristine and functionalized BCNW electrodes in the presence of the hexammineruthenium redox couple are presented in Figure 5A–F. Both electrodes exhibit two redox peaks, increasing with the scan rate. However, in contrast to ferrocyanide peak separations, they do not increase with the scan rate and are equal to 71 mV for BCNW and 65 mV for BCNW/PDA/PZ, which is a value very close to the theoretical 60 mV for an ideally reversible, purely diffusion-controlled system.<sup>65</sup> This reduction of peak separation is attributed to the fact that the hexammineruthenium couple has a lower reorganization energy than the ferrocyanide couple and therefore can be treated as an OSET (outer sphere electron transfer) redox pair.<sup>70</sup> The Randles–Ševčík slope obtained from the oxidation peaks of the CV curves is equal to 35.5  $\mu\text{A cm}^{-2}$  mV<sup>-1/2</sup> s<sup>1/2</sup> for pristine BCNW and 39.5  $\mu\text{A cm}^{-2}$  mV<sup>-1/2</sup> s<sup>1/2</sup> for BCNW/PDA/PZ. Considering the almost pure diffusion control (in contrast to the mixed control of ferrocyanides), it is another suggestion that the surface of BCNW/PDA/PZ



**Figure 5.** (A–F) Electrochemical properties of BCNW and BCNW/PDA/PZ in solutions containing a hexaammineruthenium redox pair and in dopamine: (A, B) CV curves with different scan rates; (C, D) Randles-Ševčík plots; units (u) of the slopes are  $\mu\text{A cm}^{-2} \text{ mV}^{-1/2} \text{ s}^{1/2}$ ; (E) nonlinear fitting of current–scan rate dependence; (F) comparison of CV curves for pristine and functionalized BCNW; (G–L) interactions of pristine and functionalized BCNW with dopamine; (G, H) CV curves with different scan rates; (I, J) linear current–scan rate dependencies; (K, L) log–log plots for current–scan rate dependencies.

provides a more microelectrode-like geometry of diffusional fields for redox reactions, resulting in higher current densities. Asymmetries between the oxidation and reduction slopes can be attributed to the presence of nonzero background currents at the cathodic part of the potential window (see Figure 2A).

Analogous nonlinear fitting experiments for current vs scan rate dependence were also performed for the hexaammineruthenium pair (Figure 5E). In this case, there are no significant differences in the curves and in the fitting parameters. However, if we compare the cyclic voltammograms for the pristine and functionalized electrodes registered at very low scan rates (4 mV/s), an interesting difference can be seen. While the current density magnitudes are roughly the same for both, the BCNW/PDA/PZ electrodes exhibit a higher current after exceeding the peak potential, so that the overall CV shape is close to sigmoidal. When one considers the theory of microelectrode arrays and diffusion cases mentioned above, the microelectrode-like behavior of the BCNW/PDA/PZ is also suggested.

A similar methodology was applied to verify the interactions of dopamine with the surface of the pristine and the functionalized BCNW electrodes. Figure 5G,H shows CV curves registered at different scan rates. Two quasi-reversible redox peaks of the catechol/quinone redox couple are manifested, and their current density and peak separation increase with the scan rate. However, this reaction is surface-confined because this relationship is linear,<sup>34,71</sup> in contrast to the quadratic relationship for classical redox couples (Figure 5I,J). There is also a 50% reduction in the slope (from 0.88 to

0.44  $\mu\text{A cm}^{-2} \text{ mV}^{-1} \text{ s}$ ) after modification, which is a similar behavior to the ferrocyanide couple. These observations strongly suggest that dopamine–dopamine quinone redox reactions are inner-sphere electron transfer (ISET), confirming the well-described mechanism.<sup>17,72</sup> Lastly, log–log plots of the current density vs scan rate were calculated according to eq 6:<sup>68,73</sup>

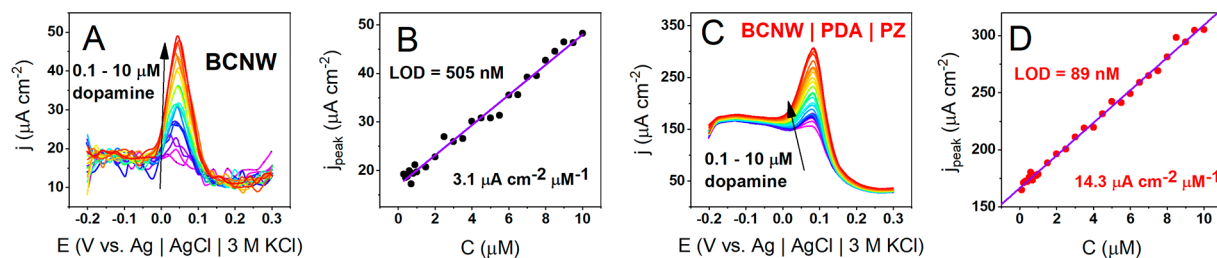
$$j = j_0 \left( \frac{dE}{dt} \right)^\beta \quad (6)$$

Exponent  $\beta$  is an alternative tool for estimating the contributions of different types of current (capacitive/absorptive, diffusive, and steady state). In the case of bare BCNW, it is equal to 0.8 for oxidation and 1.0 for reduction, indicating that there is a primary capacitive/adsorptive component. Values close to 1.0 explain the linear dependence observed in Figure 5I,J. However, for BCNW/PDA/PZ, there is a notable decrease in the exponents for both oxidation (0.7) and reduction (0.8). Considering that the exponent for the processes in the steady state is equal to zero, the lowered value for the functionalized electrode is another clue suggesting shifts in the diffusional fields toward microelectrode-like behavior.

**Influence of Diffusion Field Shift on the Sensing Properties of BCNW/PDA/PZ.** Considering a high potency of BCNW toward sensing and the specific electrochemical properties acquired after modification with PDA/PZ, a set of dopamine sensing experiments was conducted. This particular choice of analyte was motivated by the fact that the



## Enhancement of sensing properties by PDA | PZ coating



## Interference and stability of BCNW | PDA | PZ in bovine serum

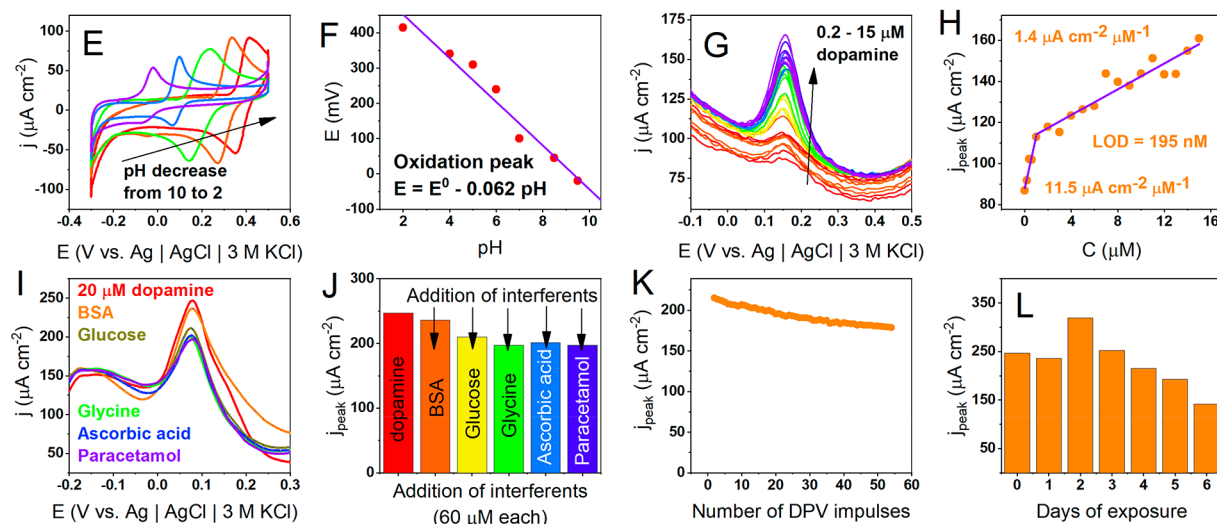


Figure 6. (A–D) DPV current response of pristine BCNW and BCNW/PDA/PZ in increasing concentrations of dopamine; (A, C) DPV curves in 1x Tris; (B, D) calibration curves in 1x Tris; (E–L) sensing properties of BCNW/PDA/PZ in bovine serum; (E) dopamine oxidation in different pHs; (F) dependence of oxidation potential peak on the pH; (G) DPV curve in BSA; (H) calibration curves in BSA; (I) DPV curves in BSA in the presence of interferents (red, dopamine; orange, BSA, green–yellow, glucose; green, glycine; blue, ascorbic acid; violet, paracetamol); (J) bar plot of current densities in the presence of interferents; (K) stability of the response in the subsequent 55 DPV cycles in BSA; (L) long-term stability test in BSA.

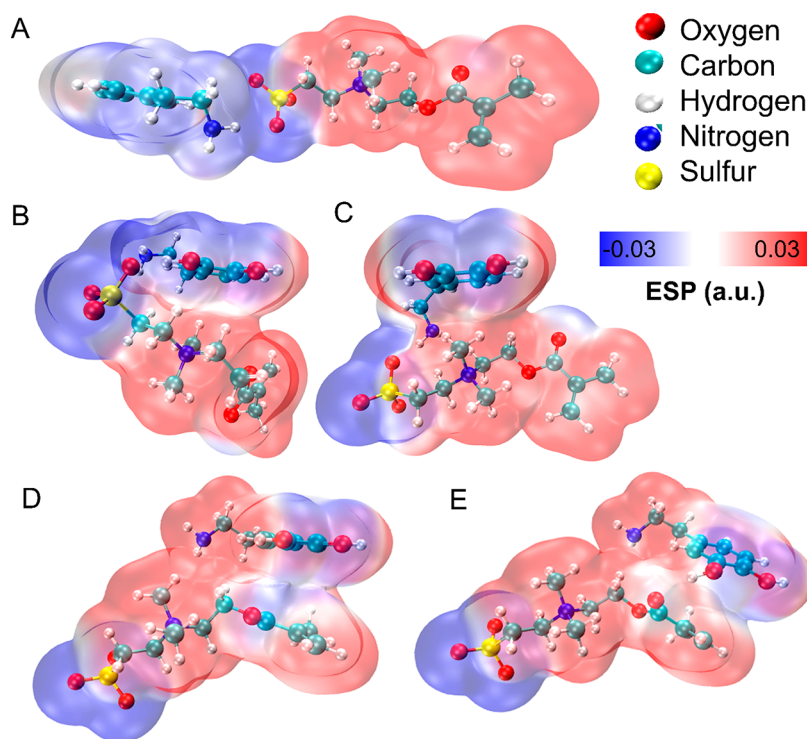
Table 3. Comparison of the Sensing Properties of Different Electrodes toward Dopamine Electrooxidation in Neutral Media

material	electrochemical method/solution pH	sensitivity [ $\mu\text{A cm}^{-2} \mu\text{M}^{-1}$ ]	linear range [ $\mu\text{M}$ ]	LOD [nM]	reference
CdSe/CdS quantum dots on graphite	DPV/pH = 11	0.05	0.5–15	96	80
N-doped porous carbon	DPV/pH unknown	4.64	30–90	2.74	81
			200–400		
CNTs@nanoporous carbon	DPV/pH = 3.0		0.5–49	20	82
Ni-MOF/glassy carbon	DPV/pH = 7.2	0.07	2–10	60	83
laser-induced graphene from biomass	DPV/pH = 7.2	4.39	5–40	3400	84
bioassisted AgNP	DPV/pH = 7.2	0.27	10–100	100	85
AgNPs/CuO	CV/pH = 7.5	3.00	0.04–10	7	86
aptamer IMIP/AuNPS/GC	DPV/pH = 7.2	0.7	0.05–10	47	87
Fe <sub>3</sub> O <sub>4</sub> @SiO <sub>2</sub> –laccase–GCE	DPV/pH = 6.0	0.23	1.5–75	177	88
exopolysaccharide/laccase/MWCNTs/GCE	SWV/pH = 6.0	0.58	3–38.5	127	89
MoS <sub>2</sub> –laccase@Nafion–carbon paper	CA/pH = 6.0	0.34	0.1–0.5	10	90
DNA/PAMAM/MWCNT–chitosan/Au	DPV/pH = 7.4	0.3	0.2–10	30	91
polypyrrole/MWCNT/GCE	DPV/pH = 7.0	0.09	0.6–100	60	92
BCNW	DPV/pH = 7.4	3.1	1–10	505	this work
BCNW/PDA/PZ	DPV/pH = 7.4	14.3	0.7–20	89	this work

polydopamine moieties linked to the carbon surface could increase the selectivity via the creation of hydrogen and electrostatic interactions with a chemically similar analyte, dopamine. This mechanism is commonly utilized for molecular imprinting applications with PDA as the template,<sup>25</sup> e.g., in the

detection of proteins,<sup>74</sup> nitroaromatic explosives<sup>75</sup> and insecticides.<sup>76</sup>

Difference pulse voltammetry was used for dopamine detection. Figure 6A–D shows a comparison of the sensing properties between the plain and PDA/PZ functionalized



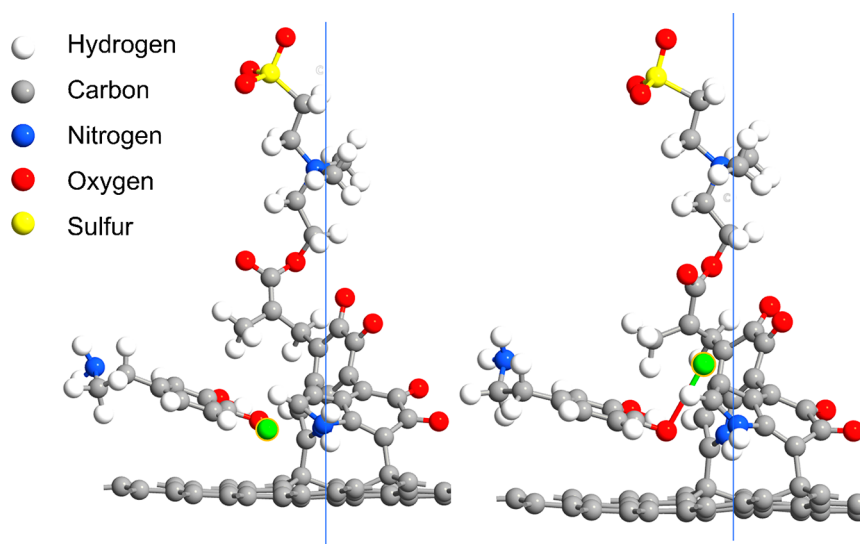
**Figure 7.** Simulation of intramolecular mechanisms underlying enhancement of the BCNW/PDA/PZ sensing capabilities. (A–E) Series of optimized geometries and electrostatic surface potential maps illustrating the intermolecular interactions between dopamine that facilitate transport of the analyte toward the surface.

BCNW in 1× Tris buffer solution. In the case of both electrodes, a set of characteristic current pulses is observed with magnitudes that linearly increase with the dopamine concentration. Although the CV measurements showed dopamine oxidation onset at +0.17 V, the peaks on the DPV curves are located at +0.05 V, which is a standard behavior.<sup>65</sup> However, while a pristine BCNW electrode exhibits a symmetric current pulse, BCNW/PDA/PZ increased the current plateau at potentials lower than the pulse. In other words, zwitterionic modification reduces the onset of the dopamine oxidation potential. Simultaneously, the slope of the calibration curve is 4.6 times higher, while the limit of detection decreases from 505 to 89 nM. Moreover, the linear range is slightly widened in both lower and higher concentrations (see Table 3). A comparison of those values with several recently published dopamine-sensitive materials leads to the conclusion that the BCNW/PDA/PZ electrode exhibits superior sensitivity while maintaining a solid compromise with the limit of detection (LOD) and linear range. The improvement of the three described sensing parameters is explained by the fact that the application of a hybrid PDA/PZ coating on BCNW leads to shifts in the diffusional fields toward more microelectrode-like behavior. Due to the higher contribution of the steady-state current, the increase of the current response is attributed to dopamine oxidation and an amplification of the signal at lower concentrations is observed. Furthermore, zwitterions are known to improve the transport of different charged molecules by forming ionic transport channels.<sup>77–79</sup> It is therefore anticipated that surface zwitterions in BCNW/PDA/PZ play a supporting role in the enhancement of dopamine sensing. This issue will be revisited in the next section, including theoretical

DFT investigations of zwitterion–dopamine intermolecular interactions.

The sensing of dopamine on the BCNW/PDA/PZ electrodes is possible in a wide pH range from 2 to 10 (Figure 6E). In more alkaline solutions, the amperometric signal is quenched, presumably because of the adsorption of different oxidation products, leading to the loss of PDA/PZ conductivity. Furthermore, the dependence of the reaction potential on the pH exhibits slopes equal to 0.062 V/pH units (close to the theoretical 0.059 V/pH units), indicating that the dopamine oxidation is proton-coupled (Figure 6F).

Further investigations include dopamine sensing in an environment reflecting body fluid conditions, particularly in bovine serum with a high albumin concentration (2 wt %). Dopamine oxidation DPV peaks are still present and increase with the concentration of dopamine. However, the prepeak current plateau plummets in contrast to that of the 1× Tris buffer solution, and the calibration curve has a different shape (Figure 6H). Two linear ranges of 200–1000 nM and 1–15  $\mu\text{M}$  are present with 11.5 and 1.4  $\mu\text{A cm}^{-2} \mu\text{M}^{-1}$  sensitivities, respectively. The first sensitivity value is very close to the slope measured in 1× Tris. This behavior suggests a transition to a different sensing mechanism,<sup>93</sup> presumably due to interactions of dopamine with proteins. In higher dopamine concentrations, it can spontaneously bind to tryptophan and tyrosine residues of albumins by hydrogen bonding (DA–albumin).<sup>94,95</sup> As a result, the chemical moiety being sensed in BSA is not pure DA but DA–albumin. According to the standard theory of voltammetry, the current–concentration slope depends on the electroactive surface area, diffusion coefficients, and kinetic parameters.<sup>65</sup> Therefore, the sensitivity decreases with higher dopamine concentrations either due to blocking of the surface by DA–albumin or due to transport



**Figure 8.** Left panel: Dreiding preoptimized geometry of the dopamine adsorbed on the carbon surface coated with PDAlPZ and formation of the molecular pocket for dopamine; Right panel: DFT full optimization of the adsorbed dopamine and geometry illustrating the stabilization of the transition state in the dopamine–dopamine quinone oxidation reaction; the green atom is hydrogen abstracted from the catechol group.

inhibition by the albumin adjoint. Regardless of the mechanism change, at a lower concentration range, the limit of detection remains very low, 195 nM.

Dopamine sensing was tested for interference by several other electroactive, physiologically abundant compounds such as glucose, glycine, ascorbic acid, and paracetamol. Interferents were subsequently added to the electrolyte in 3 times higher amounts than dopamine, i.e., 60  $\mu$ M. Despite the significant excess of interferent, dopamine oxidation pulses were observed (Figure 6I) in a similar potential range. The current density dropped (16%) after the addition of glucose, although the other interferents seemed to not significantly influence the dopamine signal. Additionally, two stability tests were performed in BSA solution. The first included 55 subsequent DPV pulses (Figure 6K), and the second included a continuous exposure to BSA containing dopamine and interferents for a week (Figure 6L). After 55 pulses, the current density at the peak decreased (17%), but the overall sensing capability was not altered. Long-term exposure showed that the amperometric response was maintained for 5 days ( $254 \pm 39 \mu\text{A cm}^{-2}$ ) and started to decrease after the sixth day. This behavior can be ascribed to the protective role of zwitterion preventing the adsorption of albumins.<sup>8,12,59</sup>

**Intermolecular Interaction between Zwitterion and Dopamine.** This section is devoted to the elucidation of the intermolecular interactions between the zwitterion (SBMA) incorporated into the PDA structure and the analyte, dopamine (DA). Particular focus is put into finding the molecular mechanism explaining the experimentally observed shifts in the diffusion fields after application of the PDAlPZ coating. Therefore, a series of geometry optimizations was performed for different spatial arrangements along the zwitterion molecule and electrostatic surface potential maps (ESPs) are plotted for each step. The idea was to simulate the transport of dopamine analyte toward the electrode in the presence of zwitterion (Figure 7).

The initial contact (Figure 7A) of the two molecules starts by forming a bond of 3.14 Å length between the primary amine of DA and the sulfonate group of SBMA. The next step

involves a rigid rotation of dopamine accompanied by breaking of the sulfonate–amine bond and creation of the  $\pi$ –cation interaction between tertiary amine and the aromatic ring (Figure 7B). Alternatively, dopamine can undergo a rotation along the alkyl chain also resulting in  $\pi$ –cation interactions (Figure 7C). The distance between the methyl carbon and the phenyl ring is equal to 3.61 Å, indicating a relatively strong affinity toward these groups.<sup>96</sup> Either way, a translation toward the polyzwitterion alkyl chain is thermodynamically favored.

The next step of the dopamine transport is breaking of the as-formed bonds and forming the  $\pi$ – $\pi$  interaction between the phenyl ring and the  $\pi$  electrons of the methacrylate group (Figure 7D). This distance is equal to 3.68 Å, which indicates a very strong  $\pi$ – $\pi$  interaction; however, the changes of the ESP values are rather mild.<sup>97</sup> At the last step, as the dopamine is translated further, another hydrogen bond is formed between the catechol and methacrylate oxygens with a length of 2.84 Å (Figure 7E).

Finally, dopamine is adsorbed onto the surface of the BCNW coated with PDAlPZ. Results of preoptimization using the Dreiding force field show that polydopamine units attached to the carbon surface create a specific environment for the dopamine–analyte consisting of several hydrogen bonds and  $\pi$ – $\pi$  interactions (Figure 8, left panel). In this geometry, a molecular host for dopamine oxidation is formed. In fact, this phenomenon is similar to the molecular imprinting studies, where PDA serves as a template.<sup>25,75,76,87</sup> Instead of imprinting a protein or nitroaromatic explosive for detection in a PDA matrix, the PDA itself is the template for dopamine sensing. Another corollary confirming this statement can be drawn from analysis of the DFT-optimized molecular pocket (Figure 8, right panel). After full optimization, a hydrogen atom from the catechol group (marked as green) is abstracted from the dopamine and transported toward one of the DHI units of polydopamine.

In the standard dopamine electrooxidation mechanism utilized for sensing,<sup>83–85</sup> dopamine gets oxidized to the dopamine quinone, and this reaction is coupled with the abstraction of two protons (see Figure 6E). The following



DFT calculations strongly suggest that the transition state of this reaction (i.e., the moiety with only one abstracted hydrogen atom) is stabilized by intermolecular interactions induced by the pocket. In other words, dopamine oxidation is thermodynamically easier when electropolymerized PDA is present on the surface. It is believed that both transport facilitation by PZ and the formation of the molecular host by PDA explain the above-mentioned enhancement of the dopamine sensing parameters of the BCNW/PDA/PZ electrode.

## CONCLUSIONS

In summary, zwitterions can be incorporated in the structure of PDA by coelectropolymerization with dopamine on the BCNW surface. FTIR and XPS studies suggest that it most probably occurs through noncovalent electrostatic and  $\pi$ -cation interactions, and it leads to a higher physical cross-linking density than in pure polydopamine. Nanoindentation studies show that the hybrid coating exhibits enhanced stiffness, hardness, and the resistance of BCNW against scratches, reflected by a higher cross-linking density.

The functionalized BCNW electrode has promising capabilities for the detection of dopamine. Although the application of pure PDA causes quenching of the electron transfer, the hybrid coating only mildly changes the kinetic constant, and the high electrochemical activity of the BCNW substrate is maintained. In particular, BCNW/PDA/PZ exhibits up to 5 times the enhancement of sensitivity and 5 times reduced LOD after modification with PDA/PZ. This improvement is ascribed to the shifts of diffusional fields toward more microelectrode-like behavior. A large set of electrochemical experiments, directed toward examination of steady-state currents using different redox mediators and polarization conditions, support this hypothesis. Moreover, DFT calculations showed that zwitterions facilitate the transport of dopamine to the electrode via a chain of subsequent intermolecular interactions. It is composed of several hydrogen bonds and cation- $\pi$  and  $\pi$ - $\pi$  interactions. The PDA anchored to the surface, on the other hand, creates an environment that stabilizes the transition state between the dopamine and dopamine quinone, a molecular pocket. These phenomena are believed to be another mechanism explaining the enhanced sensing parameters. Additionally, zwitterions protect the electrode against interference and support the stability of the signal during several days of continuous exposure to the albumins in bovine serum.

## METHODS

**Boron-Doped Carbon Nanowall (BCNW) Fabrication.** BCNW electrodes were manufactured on p-type (100) Si wafer plates utilizing a microwave plasma-enhanced chemical vapor deposition system (SEKI Technotron AX5400S, Japan) as reported elsewhere.<sup>98</sup> The stage temperature was set to 700 °C, while the microwave power was kept at 1300 W. The fabrication process was carried out at a pressure of 50 Torr in a gas mixture flow equal to 325 sccm. The CNW electrodes were boron-doped in situ utilizing a diborane precursor ( $[B]/[C]$  ratio in the gas phase = 2000 ppm). The 6 h process resulted in thick vertically aligned carbon nanowall surfaces ( $d \sim 3 \mu\text{m}$ ) with a high content of the diamond phase.<sup>30</sup>

**Electropolymerization of Dopamine and PZ Coelectropolymerization.** 50 voltammetry cycles were used for all electropolymerization experiments with a 20 mV/s scan rate and at the potential range from -0.5 to +1.0 V vs. Ag/AgCl/3 M KCl. In the case of pure PDA deposition, the solution consisted of 1× Tris and 5 mM

dopamine and was purged with argon 15–20 min before starting the deposition. In the case of coelectropolymerization, 500 mM SBMA monomer was also added. The pH for deposition was adjusted to 7.2 by adding 1 M NaOH. An MP-103 hand-held potentiometric pH meter was used to control the pH value.

## ASSOCIATED CONTENT

### Supporting Information

The Supporting Information is available free of charge at <https://pubs.acs.org/doi/10.1021/acsnano.2c06406>.

Figure S1, the comparison of FT-IR spectra registered for pure PZ and BCNW coated with PDA/PZ; Figure S2, electropolymerization CV curves and electrochemical studies for PDA/PZ deposited with variable PDA/PZ ratios in the electrolyte; Figure S3, AFM images of BCNW, BCNW/PDA, and BCNW/PDA/PZ with histograms used for estimation of the coating thickness; Tables S1 and S2, detailed values of the nanomechanical properties and physiochemical quantities obtained via nonlinear fitting of EIS data, respectively; more thorough description of the methods used throughout the manuscript: data on reagents, SEM inspection, XPS and FT-IR spectroscopic measurements, nanoindentation methodology, electrochemical characterization, and DFT computational details (PDF)

## AUTHOR INFORMATION

### Corresponding Author

Robert Bogdanowicz — Department of Metrology and Optoelectronics, Faculty of Electronics, Telecommunications and Informatics, Gdańsk University of Technology, 80-233 Gdańsk, Poland; [orcid.org/0000-0002-7543-2620](https://orcid.org/0000-0002-7543-2620); Phone: +48-58-347-15-03; Email: [rbogdan@eti.pg.edu.pl](mailto:rbogdan@eti.pg.edu.pl); Fax: +48 58-347-18-48

### Authors

Adrian Olejnik — Department of Metrology and Optoelectronics, Faculty of Electronics, Telecommunications and Informatics, Gdańsk University of Technology, 80-233 Gdańsk, Poland; Centre for Plasma and Laser Engineering, The Szwedzki Institute of Fluid-Flow Machinery, Polish Academy of Sciences, 80-231 Gdańsk, Poland

Mateusz Ficek — Department of Metrology and Optoelectronics, Faculty of Electronics, Telecommunications and Informatics, Gdańsk University of Technology, 80-233 Gdańsk, Poland; [orcid.org/0000-0003-2334-9697](https://orcid.org/0000-0003-2334-9697)

Marek Szkodo — Institute of Manufacturing and Materials Technology, Faculty of Mechanical Engineering and Ship Technology, Gdańsk University of Technology, 80-233 Gdańsk, Poland

Alicja Stanisławska — Institute of Manufacturing and Materials Technology, Faculty of Mechanical Engineering and Ship Technology, Gdańsk University of Technology, 80-233 Gdańsk, Poland

Jakub Karczewski — Institute of Nanotechnology and Materials Engineering and Advanced Materials Center, Gdańsk University of Technology, 80-233 Gdańsk, Poland

Jacek Ryl — Institute of Nanotechnology and Materials Engineering and Advanced Materials Center, Gdańsk University of Technology, 80-233 Gdańsk, Poland; [orcid.org/0000-0002-0247-3851](https://orcid.org/0000-0002-0247-3851)

Anna Dołęga – Department of Inorganic Chemistry, Faculty of Chemistry, Gdańsk University of Technology, 80-233 Gdańsk, Poland; [orcid.org/0000-0003-0509-2285](https://orcid.org/0000-0003-0509-2285)

Katarzyna Siuzdak – Centre for Plasma and Laser Engineering, The Szwalski Institute of Fluid-Flow Machinery, Polish Academy of Sciences, 80-231 Gdańsk, Poland; [orcid.org/0000-0001-7434-6408](https://orcid.org/0000-0001-7434-6408)

Complete contact information is available at:  
<https://pubs.acs.org/10.1021/acsnano.2c06406>

## Funding

This work was funded by the Polish Ministry of Science and Higher Education through Diamontowy Grant DI2019 017649. R.B. and M.F. gratefully acknowledge financial support from the Foundation for Polish Science co-financed by the European Union under the European Regional Development Fund, project POIR.04.04.00-00-1644/18.

## Notes

The authors declare no competing financial interest.

## REFERENCES

- (1) Fearnley, J. M.; Lees, A. J. AGEING AND PARKINSON'S DISEASE: SUBSTANTIA NIGRA REGIONAL SELECTIVITY. *Brain* **1991**, *114* (5), 2283–2301.
- (2) Chandler, D. J.; Waterhouse, B. D.; Gao, W.-J. New Perspectives on Catecholaminergic Regulation of Executive Circuits: Evidence for Independent Modulation of Prefrontal Functions by Midbrain Dopaminergic and Noradrenergic Neurons. *Front. Neural Circuits* **2014**, *8*, 1.
- (3) Castellanos, F. X.; Proal, E. Large-Scale Brain Systems in ADHD: Beyond the Prefrontal–Striatal Model. *Trends Cogn. Sci.* **2012**, *16* (1), 17–26.
- (4) Stahl, S. M. Beyond the Dopamine Hypothesis of Schizophrenia to Three Neural Networks of Psychosis: Dopamine, Serotonin, and Glutamate. *CNS Spectr.* **2018**, *23* (3), 187–191.
- (5) Leopold, A. V.; Shcherbakova, D. M.; Verkhusha, V. V. Fluorescent Biosensors for Neurotransmission and Neuromodulation: Engineering and Applications. *Front. Cell. Neurosci.* **2019**, *13*, 474.
- (6) Shen, M.; Qu, Z.; DesLaurier, J.; Welle, T. M.; Sweedler, J. V.; Chen, R. Single Synaptic Observation of Cholinergic Neurotransmission on Living Neurons: Concentration and Dynamics. *J. Am. Chem. Soc.* **2018**, *140* (25), 7764–7768.
- (7) International Union of Pure and Applied Chemistry. IUPAC - zwitterionic compounds/zwitterions (Z06752); <https://goldbook.iupac.org/terms/view/Z06752> (accessed 2021-03-23); DOI: 10.1351/goldbook.Z06752.
- (8) Baggerman, J.; Smulders, M. M. J.; Zuilhof, H. Romantic Surfaces: A Systematic Overview of Stable, Biospecific, and Antifouling Zwitterionic Surfaces. *Langmuir* **2019**, *35* (5), 1072–1084.
- (9) Liu, C.; Lee, J.; Ma, J.; Elimelech, M. Antifouling Thin-Film Composite Membranes by Controlled Architecture of Zwitterionic Polymer Brush Layer. *Environ. Sci. Technol.* **2017**, *51* (4), 2161–2169.
- (10) Schlenoff, J. B. Zwitterion: Coating Surfaces with Zwitterionic Functionality to Reduce Nonspecific Adsorption. *Langmuir* **2014**, *30* (32), 9625–9636.
- (11) Nitzel, A. E.; De Hoe, G. X.; Tirrell, M. V. Expanding the Structural Diversity of Polyelectrolyte Complexes and Polyzwitterions. *Curr. Opin. Solid State Mater. Sci.* **2021**, *25* (2), 100897.
- (12) Laschewsky, A.; Rosenhahn, A. Molecular Design of Zwitterionic Polymer Interfaces: Searching for the Difference. *Langmuir* **2019**, *35* (5), 1056–1071.
- (13) Li, S.; Wang, H.; Young, M.; Xu, F.; Cheng, G.; Cong, H. Properties of Electropolymerized Dopamine and Its Analogues. *Langmuir* **2019**, *35* (5), 1119–1125.
- (14) Wang, J.; Li, B.; Li, Z.; Ren, K.; Jin, L.; Zhang, S.; Chang, H.; Sun, Y.; Ji, J. Electropolymerization of Dopamine for Surface Modification of Complex-Shaped Cardiovascular Stents. *Biomaterials* **2014**, *35* (27), 7679–7689.
- (15) Aguilar, L. E.; Tumurbaatar, B.; Ghavaminejad, A.; Park, C. H.; Kim, C. S. Functionalized Non-Vascular Nitinol Stent via Electropolymerized Polydopamine Thin Film Coating Loaded with Bortezomib Adjunct to Hyperthermia Therapy. *Sci. Rep.* **2017**, *7* (1), 9432.
- (16) Almeida, L. C.; Frade, T.; Correia, R. D.; Niu, Y.; Jin, G.; Correia, J. P.; Viana, A. S. Electrosynthesis of Polydopamine-Ethanolamine Films for the Development of Immunosensing Interfaces. *Sci. Rep.* **2021**, *11* (1), 2237.
- (17) Almeida, L. C.; Correia, R. D.; Marta, A.; Squillaci, G.; Morana, A.; La Cara, F.; Correia, J. P.; Viana, A. S. Electrosynthesis of Polydopamine Films - Tailored Matrices for Laccase-Based Biosensors. *Appl. Surf. Sci.* **2019**, *480*, 979–989.
- (18) Liebscher, J.; Mrówczyński, R.; Scheidt, H. A.; Filip, C.; Hädade, N. D.; Turcu, R.; Bende, A.; Beck, S. Structure of Polydopamine: A Never-Ending Story? *Langmuir* **2013**, *29* (33), 10539–10548.
- (19) Delparastan, P.; Malollari, K. G.; Lee, H.; Messersmith, P. B. Direct Evidence for the Polymeric Nature of Polydopamine. *Angew. Chem.* **2019**, *131* (4), 1089–1094.
- (20) Alfieri, M.; Panzella, L.; Oscurato, S.; Salvatore, M.; Avolio, R.; Errico, M.; Maddalena, P.; Napolitano, A.; d'Ischia, M. The Chemistry of Polydopamine Film Formation: The Amine-Quinone Interplay. *Biomimetics* **2018**, *3* (3), 26.
- (21) Jin, Z.; Yang, L.; Shi, S.; Wang, T.; Duan, G.; Liu, X.; Li, Y. Flexible Polydopamine Bioelectronics. *Adv. Funct. Mater.* **2021**, *31* (30), 2103391.
- (22) Chalmers, E.; Lee, H.; Zhu, C.; Liu, X. Increasing the Conductivity and Adhesion of Polypyrrole Hydrogels with Electropolymerized Polydopamine. *Chem. Mater.* **2020**, *32* (1), 234–244.
- (23) Lee, H. A.; Park, E.; Lee, H. Polydopamine and Its Derivative Surface Chemistry in Material Science: A Focused Review for Studies at KAIST. *Adv. Mater.* **2020**, *32* (35), 1907505.
- (24) Wang, Z.; Zou, Y.; Li, Y.; Cheng, Y. Metal-Containing Polydopamine Nanomaterials: Catalysis, Energy, and Theranostics. *Small* **2020**, *16* (18), 1907042.
- (25) Palladino, P.; Bettazzi, F.; Scarano, S. Polydopamine: Surface Coating, Molecular Imprinting, and Electrochemistry—Successful Applications and Future Perspectives in (Bio)Analysis. *Anal. Bioanal. Chem.* **2019**, *411* (19), 4327–4338.
- (26) Yang, P.; Zhu, F.; Zhang, Z.; Cheng, Y.; Wang, Z.; Li, Y. Stimuli-Responsive Polydopamine-Based Smart Materials. *Chem. Soc. Rev.* **2021**, *50* (14), 8319–8343.
- (27) Yang, L.; Guo, X.; Jin, Z.; Guo, W.; Duan, G.; Liu, X.; Li, Y. Emergence of Melanin-Inspired Supercapacitors. *Nano Today* **2021**, *37*, 101075.
- (28) Zhou, R.; Ren, P.-F.; Yang, H.-C.; Xu, Z.-K. Fabrication of Antifouling Membrane Surface by Poly(Sulfobetaine Methacrylate)/Polydopamine Co-Deposition. *J. Membr. Sci.* **2014**, *466*, 18–25.
- (29) Zhang, C.; Zhou, Y.; Han, H.; Zheng, H.; Xu, W.; Wang, Z. Dopamine-Triggered Hydrogels with High Transparency, Self-Adhesion, and Thermoresponse as Skinlike Sensors. *ACS Nano* **2021**, *15* (1), 1785–1794.
- (30) Pierpaoli, M.; Ficek, M.; Jakóbczyk, P.; Karczewski, J.; Bogdanowicz, R. Self-Assembly of Vertically Orientated Graphene Nanostructures: Multivariate Characterisation by Minkowski Functionals and Fractal Geometry. *Acta Mater.* **2021**, *214*, 116989.
- (31) Siuzdak, K.; Ficek, M.; Sobaszek, M.; Ryl, J.; Gnyba, M.; Niedziałkowski, P.; Malinowska, N.; Karczewski, J.; Bogdanowicz, R. Boron-Enhanced Growth of Micron-Scale Carbon-Based Nanowalls: A Route toward High Rates of Electrochemical Biosensing. *ACS Appl. Mater. Interfaces* **2017**, *9* (15), 12982–12992.
- (32) Dettlaff, A.; Jakóbczyk, P.; Ficek, M.; Wilk, B.; Szala, M.; Wojtas, J.; Ossowski, T.; Bogdanowicz, R. Electrochemical Determination of Nitroaromatic Explosives at Boron-Doped Diamond/



Graphene Nanowall Electrodes: 2,4,6-Trinitrotoluene and 2,4,6-Trinitroanisole in Liquid Effluents. *J. Hazard. Mater.* **2020**, 387, 121672.

(33) Niedzialkowski, P.; Cebula, Z.; Malinowska, N.; Białobrzaska, W.; Sobaszek, M.; Ficek, M.; Bogdanowicz, R.; Anand, J. S.; Ossowski, T. Comparison of the Paracetamol Electrochemical Determination Using Boron-Doped Diamond Electrode and Boron-Doped Carbon Nanowalls. *Biosens. Bioelectron.* **2019**, 126, 308–314.

(34) Compton, R. G.; Kätelhön, E.; Ward, K. R.; Laborda, E. *Understanding Voltammetry: Simulation of Electrode Processes*, 2nd ed.; World Scientific: London, 2020; DOI: 10.1142/q0246.

(35) Pumera, M., Ed. *Nanomaterials for Electrochemical Sensing and Biosensing*; Pan Stanford Publishing: Singapore, 2014.

(36) Sobaszek, M.; Siuzdak, K.; Ryl, J.; Sawczak, M.; Gupta, S.; Carrizosa, S. B.; Ficek, M.; Dec, B.; Darowicki, K.; Bogdanowicz, R. Diamond Phase ( $\text{Sp}^3$ -C) Rich Boron-Doped Carbon Nanowalls ( $\text{Sp}^2$ -C): Physicochemical and Electrochemical Properties. *J. Phys. Chem. C* **2017**, 121 (38), 20821–20833.

(37) Olejnik, A.; Ficek, M.; Siuzdak, K.; Bogdanowicz, R. Multi-Pathway Mechanism of Polydopamine Film Formation at Vertically Aligned Diamondised Boron-Doped Carbon Nanowalls. *Electrochim. Acta* **2022**, 409, 140000.

(38) Dougherty, D. A. The Cation- $\pi$  Interaction. *Acc. Chem. Res.* **2013**, 46 (4), 885–893.

(39) Sugumaran, M. Reactivities of Quinone Methides versus O-Quinones in Catecholamine Metabolism and Eumelanin Biosynthesis. *Int. J. Mol. Sci.* **2016**, 17 (9), 1576.

(40) Salomäki, M.; Marttila, L.; Kivelä, H.; Ovinen, T.; Lukkari, J. Effects of PH and Oxidants on the First Steps of Polydopamine Formation: A Thermodynamic Approach. *J. Phys. Chem. B* **2018**, 122 (24), 6314–6327.

(41) Kharlampieva, E.; Izumrudov, V. A.; Sukhishvili, S. A. Electrostatic Layer-by-Layer Self-Assembly of Poly(Carboxybetaine)s: Role of Zwitterions in Film Growth. *Macromolecules* **2007**, 40 (10), 3663–3668.

(42) Mostert, A. B.; Powell, B. J.; Pratt, F. L.; Hanson, G. R.; Sarna, T.; Gentle, I. R.; Meredith, P. Role of Semiconductivity and Ion Transport in the Electrical Conduction of Melanin. *Proc. Natl. Acad. Sci. U. S. A.* **2012**, 109 (23), 8943–8947.

(43) Liang, B.; Zhang, G.; Zhong, Z.; Huang, Y.; Su, Z. Superhydrophilic Anti-Icing Coatings Based on Polyzwitterion Brushes. *Langmuir* **2019**, 35 (5), 1294–1301.

(44) Luo, H.; Gu, C.; Zheng, W.; Dai, F.; Wang, X.; Zheng, Z. Facile Synthesis of Novel Size-Controlled Antibacterial Hybrid Spheres Using Silver Nanoparticles Loaded with Poly-Dopamine Spheres. *RSC Adv.* **2015**, 5 (18), 13470–13477.

(45) Lalani, R.; Liu, L. Synthesis, Characterization, and Electrospinning of Zwitterionic Poly(Sulfobetaine Methacrylate). *Polymer* **2011**, 52 (23), 5344–5354.

(46) An, T.; Lee, N.; Cho, H.-J.; Kim, S.; Shin, D.-S.; Lee, S.-M. Ultra-Selective Detection of  $\text{Fe}^{2+}$  Ion by Redox Mechanism Based on Fluorescent Polymerized Dopamine Derivatives. *RSC Adv.* **2017**, 7 (49), 30582–30587.

(47) Touqeer, T.; Mumtaz, M. W.; Mukhtar, H.; Irfan, A.; Akram, S.; Shabbir, A.; Rashid, U.; Nehdi, I. A.; Choong, T. S. Y.  $\text{Fe}_3\text{O}_4$ -PDA-Lipase as Surface Functionalized Nano Biocatalyst for the Production of Biodiesel Using Waste Cooking Oil as Feedstock: Characterization and Process Optimization. *Energies* **2020**, 13 (1), 177.

(48) Xiang, T.; Wang, R.; Zhao, W.-F.; Sun, S.-D.; Zhao, C.-S. Covalent Deposition of Zwitterionic Polymer and Citric Acid by Click Chemistry-Enabled Layer-by-Layer Assembly for Improving the Blood Compatibility of Polysulfone Membrane. *Langmuir* **2014**, 30 (18), 5115–5125.

(49) Crowder, G. A. The C-S Stretching Frequency in Thiol Acids and Esters. *Appl. Spectrosc.* **1972**, 26 (4), 486–487.

(50) Olejnik, A.; Karczewski, J.; Dołęga, A.; Siuzdak, K.; Cenian, A.; Grochowska, K. Simple Synthesis Route for Fabrication of Protective Photo-crosslinked Poly(Zwitterionic) Membranes for Application in

Non-enzymatic Glucose Sensing. *J. Biomed. Mater. Res. B Appl. Biomater.* **2022**, 110 (3), 679–690.

(51) Li, D.; Wei, Q.; Wu, C.; Zhang, X.; Xue, Q.; Zheng, T.; Cao, M. Superhydrophilicity and Strong Salt-Affinity: Zwitterionic Polymer Grafted Surfaces with Significant Potentials Particularly in Biological Systems. *Adv. Colloid Interface Sci.* **2020**, 278, 102141.

(52) Liu, T.; Kim, K. C.; Lee, B.; Chen, Z.; Noda, S.; Jang, S. S.; Lee, S. W. Self-Polymerized Dopamine as an Organic Cathode for Li- and Na-Ion Batteries. *Energy Environ. Sci.* **2017**, 10 (1), 205–215.

(53) Batul, R.; Bhawe, M.; Mahon, P. J.; Yu, A. Polydopamine Nanosphere with In-Situ Loaded Gentamicin and Its Antimicrobial Activity. *Molecules* **2020**, 25 (9), 2090.

(54) Han, X.; Zhang, L.; Li, C. Preparation of Polydopamine-Functionalized Graphene- $\text{Fe}_3\text{O}_4$  Magnetic Composites with High Adsorption Capacities. *RSC Adv.* **2014**, 4 (58), 30536–30541.

(55) Gardella, J. A.; Ferguson, S. A.; Chin, R. L.  $\pi^* \leftarrow \pi$  Shakeup Satellites for the Analysis of Structure and Bonding in Aromatic Polymers by X-Ray Photoelectron Spectroscopy. *Appl. Spectrosc.* **1986**, 40 (2), 224–232.

(56) Zhu, H.; Sun, X.; Yang, H.; Pang, Y.; Ta, S.; Wang, L.; Zhu, H.; Zhang, Q. Polydopamine-Derived Nitrogen-Doped Carbon-Coated NiS Nanoparticles as a Battery-Type Electrode for High-Performance Supercapacitors. *Ceram. Int.* **2021**, 47 (7), 9332–9341.

(57) Sivashanmugan, K.; Liu, P.-C.; Tsai, K.-W.; Chou, Y.-N.; Lin, C.-H.; Chang, Y.; Wen, T.-C. An Anti-Fouling Nanoplasmonic SERS Substrate for Trapping and Releasing a Cationic Fluorescent Tag from Human Blood Solution. *Nanoscale* **2017**, 9 (8), 2865–2874.

(58) Cao, Q.; Wu, S.; Wang, L.; Shi, X.; Li, G. Effects of the Morphology of Sulfobetaine Zwitterionic Layers Grafted onto a Silicone Surface on Improving the Hydrophilic Stability, Anti-Bacterial Adhesion Properties, and Biocompatibility. *J. Appl. Polym. Sci.* **2018**, 135 (44), 46860.

(59) Yandi, W.; Nagy, B.; Skallberg, A.; Uvdal, K.; Zimmermann, R.; Liedberg, B.; Ederth, T. Polyampholytic Poly(AEMA-*co*-SPMA) Thin Films and Their Potential for Antifouling Applications. *ACS Appl. Polym. Mater.* **2021**, 3 (11), 5361–5372.

(60) Xiao, K.; Li, J.; Wu, X.; Liu, H.; Huang, C.; Li, Y. Nanoindentation of Thin Graphdiyne Films: Experiments and Molecular Dynamics Simulation. *Carbon* **2019**, 144, 72–80.

(61) Soifer, Ya. M.; Verdyan, A.; Kazakevich, M.; Rabkin, E. Edge Effect during Nanoindentation of Thin Copper Films. *Mater. Lett.* **2005**, 59 (11), 1434–1438.

(62) Daboss, S.; Lin, J.; Godejohann, M.; Kranz, C. Redox Switchable Polydopamine-Modified AFM-SECM Probes: A Probe for Electrochemical Force Spectroscopy. *Anal. Chem.* **2020**, 92 (12), 8404–8413.

(63) Lasia, A. *Electrochemical Impedance Spectroscopy and Its Applications*; Springer: New York, 2014.

(64) Brug, G. J.; van den Eeden, A. L. G.; Sluyters-Rehbach, M.; Sluyters, J. H. The Analysis of Electrode Impedances Complicated by the Presence of a Constant Phase Element. *J. Electroanal. Chem. Interfacial Electrochem.* **1984**, 176 (1–2), 275–295.

(65) Bard, A. J.; Faulkner, L. R. *Electrochemical Methods: Fundamentals and Applications*, 2nd ed.; Wiley: New York, 2001.

(66) Da Rocha, M.; Dunn, B.; Rougier, A. Faradaic and/or Capacitive: Which Contribution for Electrochromism in NiO Thin Films Cycled in Various Electrolytes? *Sol. Energy Mater. Sol. Cells* **2019**, 201, 110114.

(67) Augustyn, V.; Simon, P.; Dunn, B. Pseudocapacitive Oxide Materials for High-Rate Electrochemical Energy Storage. *Energy Environ. Sci.* **2014**, 7 (5), 1597.

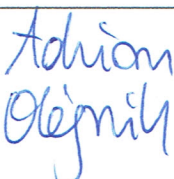

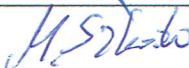
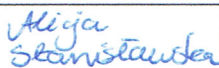



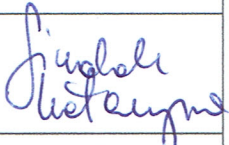

(68) Wang, J.; Polleux, J.; Lim, J.; Dunn, B. Pseudocapacitive Contributions to Electrochemical Energy Storage in  $\text{TiO}_2$  (Anatase) Nanoparticles. *J. Phys. Chem. C* **2007**, 111 (40), 14925–14931.

(69) Giannuzzi, R.; Scarfiello, R.; Sibillano, T.; Nobile, C.; Grillo, V.; Giannini, C.; Cozzoli, P. D.; Manca, M. From Capacitance-Controlled to Diffusion-Controlled Electrochromism in One-Dimensional Shape-Tailored Tungsten Oxide Nanocrystals. *Nano Energy* **2017**, 41, 634–645.

- (70) Fan, F.-R. F.; Gould, E. S. Electron Transfer through Organic Structural Units. XVII. Reductions of Pentaaminecobalt(III) Complexes with Hexaammineruthenium(II). Partition of the Reduction of Carboxylatocobalt(III) Complexes into Outer- and Inner-Sphere Paths. *Inorg. Chem.* **1974**, *13* (11), 2647–2651.
- (71) Elgrishi, N.; Rountree, K. J.; McCarthy, B. D.; Rountree, E. S.; Eisenhart, T. T.; Dempsey, J. L. A Practical Beginner's Guide to Cyclic Voltammetry. *J. Chem. Educ.* **2018**, *95* (2), 197–206.
- (72) Bacil, R. P.; Chen, L.; Serrano, S. H. P.; Compton, R. G. Dopamine Oxidation at Gold Electrodes: Mechanism and Kinetics near Neutral pH. *Phys. Chem. Chem. Phys.* **2020**, *22* (2), 607–614.
- (73) Li, K.; Wang, X.; Li, S.; Urbankowski, P.; Li, J.; Xu, Y.; Gogotsi, Y. An Ultrafast Conducting Polymer@MXene Positive Electrode with High Volumetric Capacitance for Advanced Asymmetric Supercapacitors. *Small* **2020**, *16* (4), 1906851.
- (74) Han, W.; Han, X.; Liu, Z.; Zhang, S.; Li, Y.; Lu, J.; Chen, J.; Ou, L.; Fu, G. Facile Modification of Protein-Imprinted Polydopamine Coatings over Nanoparticles with Enhanced Binding Selectivity. *Chem. Eng. J.* **2020**, *385*, 123463.
- (75) Leibl, N.; Duma, L.; Gonzato, C.; Haupt, K. Polydopamine-Based Molecularly Imprinted Thin Films for Electro-Chemical Sensing of Nitro-Explosives in Aqueous Solutions. *Bioelectrochemistry* **2020**, *135*, 107541.
- (76) Miao, J.; Liu, A.; Wu, L.; Yu, M.; Wei, W.; Liu, S. Magnetic Ferroferric Oxide and Polydopamine Molecularly Imprinted Polymer Nanocomposites Based Electrochemical Impedance Sensor for the Selective Separation and Sensitive Determination of Dichlorodiphenyltrichloroethane (DDT). *Anal. Chim. Acta* **2020**, *1095*, 82–92.
- (77) Mo, F.; Chen, Z.; Liang, G.; Wang, D.; Zhao, Y.; Li, H.; Dong, B.; Zhi, C. Zwitterionic Sulfobetaine Hydrogel Electrolyte Building Separated Positive/Negative Ion Migration Channels for Aqueous Zn-MnO<sub>2</sub> Batteries with Superior Rate Capabilities. *Adv. Energy Mater.* **2020**, *10* (16), 2000035.
- (78) Li, L.; Zhang, L.; Guo, W.; Chang, C.; Wang, J.; Cong, Z.; Pu, X. High-Performance Dual-Ion Zn Batteries Enabled by a Polyzwitterionic Hydrogel Electrolyte with Regulated Anion/Cation Transport and Suppressed Zn Dendrite Growth. *J. Mater. Chem. A* **2021**, *9* (43), 24325–24335.
- (79) Peng, X.; Liu, H.; Yin, Q.; Wu, J.; Chen, P.; Zhang, G.; Liu, G.; Wu, C.; Xie, Y. A Zwitterionic Gel Electrolyte for Efficient Solid-State Supercapacitors. *Nat. Commun.* **2016**, *7* (1), 11782.
- (80) de França, C. C. L.; Meneses, D.; Silva, A. C. A.; Dantas, N. O.; de Abreu, F. C.; Petroni, J. M.; Lucca, B. G. Development of Novel Paper-Based Electrochemical Device Modified with CdSe/CdS Magic-Sized Quantum Dots and Application for the Sensing of Dopamine. *Electrochim. Acta* **2021**, *367*, 137486.
- (81) Kasturi, P. R.; Aparna, T. K.; Arokiyanathan, A. L.; Lakshmiipathi, S.; Sivasubramanian, R.; Lee, Y. S.; Selvan, R. K. Synthesis of Metal-Free Nitrogen-Enriched Porous Carbon and Its Electrochemical Sensing Behavior for the Highly Sensitive Detection of Dopamine: Both Experimental and Theoretical Investigation. *Mater. Chem. Phys.* **2021**, *260*, 124094.
- (82) Wu, F.-H.; Ren, M.-J.; Wang, M.; Sun, W.-B.; Wu, K.-L.; Cheng, Y.-S.; Yan, Z. One-Dimensional Nitrogen Doped Porous Carbon Nano-Array Arranged by Carbon Nanotubes for Electrochemical Sensing Ascorbic Acid, Dopamine and Uric Acid Simultaneously. *Nanotechnology* **2021**, *32* (25), 255601.
- (83) Huang, Z.; Zhang, L.; Cao, P.; Wang, N.; Lin, M. Electrochemical Sensing of Dopamine Using a Ni-Based Metal-Organic Framework Modified Electrode. *Ionic* **2021**, *27* (3), 1339–1345.
- (84) Mahmood, F.; Sun, Y.; Wan, C. Biomass-Derived Porous Graphene for Electrochemical Sensing of Dopamine. *RSC Adv.* **2021**, *11* (25), 15410–15415.
- (85) Memon, R.; Memon, A. A.; Nafady, A.; Sirajuddin; Sherazi, S. T. H.; Balouch, A.; Memon, K.; Brohi, N. A.; Najeeb, A. Electrochemical Sensing of Dopamine via Bio-Assisted Synthesized Silver Nanoparticles. *Int. Nano Lett.* **2021**, *11* (3), 263–271.
- (86) Li, Y.-Y.; Kang, P.; Wang, S.-Q.; Liu, Z.-G.; Li, Y.-X.; Guo, Z. Ag Nanoparticles Anchored onto Porous CuO Nanobelts for the Ultrasensitive Electrochemical Detection of Dopamine in Human Serum. *Sens. Actuators B Chem.* **2021**, *327*, 128878.
- (87) Shen, M.; Kan, X. Aptamer and Molecularly Imprinted Polymer: Synergistic Recognition and Sensing of Dopamine. *Electrochim. Acta* **2021**, *367*, 137433.
- (88) Li, Z.; Zheng, Y.; Gao, T.; Liu, Z.; Zhang, J.; Zhou, G. Fabrication of Biosensor Based on Core-Shell and Large Void Structured Magnetic Mesoporous Microspheres Immobilized with Laccase for Dopamine Detection. *J. Mater. Sci.* **2018**, *53* (11), 7996–8008.
- (89) Coelho, J. H.; Eisele, A. P. P.; Valezi, C. F.; Mattos, G. J.; Schirmann, J. G.; Dekker, R. F. H.; Barbosa-Dekker, A. M.; Sartori, E. R. Exploring the Exocellular Fungal Biopolymer Botryosphaeran for Laccase-Biosensor Architecture and Application to Determine Dopamine and Spironolactone. *Talanta* **2019**, *204*, 475–483.
- (90) Rubio-Govea, R.; Hickey, D. P.; García-Morales, R.; Rodríguez-Delgado, M.; Domínguez-Rovira, M. A.; Minter, S. D.; Ornelas-Soto, N.; García-García, A. MoS<sub>2</sub> Nanostructured Materials for Electrode Modification in the Development of a Laccase Based Amperometric Biosensor for Non-Invasive Dopamine Detection. *Microchem. J.* **2020**, *155*, 104792.
- (91) Liu, X.; Peng, Y.; Qu, X.; Ai, S.; Han, R.; Zhu, X. Multi-Walled Carbon Nanotube-Chitosan/Poly(Amidoamine)/DNA Nanocomposite Modified Gold Electrode for Determination of Dopamine and Uric Acid under Coexistence of Ascorbic Acid. *J. Electroanal. Chem.* **2011**, *654* (1–2), 72–78.
- (92) Kan, X.; Zhou, H.; Li, C.; Zhu, A.; Xing, Z.; Zhao, Z. Imprinted Electrochemical Sensor for Dopamine Recognition and Determination Based on a Carbon Nanotube/Polypyrrole Film. *Electrochim. Acta* **2012**, *63*, 69–75.
- (93) Olejnik, A.; Karczewski, J.; Dołęga, A.; Siuzdak, K.; Grochowska, K. Insightful Analysis of Phenomena Arising at the Metal/Polymer Interphase of Au-Ti Based Non-Enzymatic Glucose Sensitive Electrodes Covered by Nafion. *Coatings* **2020**, *10* (9), 810.
- (94) Li, J.; Duan, H.; Wei, W.; Luo, S. Spectrometric Investigations on the Binding of Dopamine to Bovine Serum Albumin. *Phys. Chem. Liq.* **2012**, *50* (4), 453–464.
- (95) Zhang, Q.; Ni, Y.; Kokot, S. Binding Interaction of Dopamine with Bovine Serum Albumin: A Biochemical Study. *Spectrosc. Lett.* **2012**, *45* (2), 85–92.
- (96) Mahadevi, A. S.; Sastry, G. N. Cation- $\pi$  Interaction: Its Role and Relevance in Chemistry, Biology, and Material Science. *Chem. Rev.* **2013**, *113* (3), 2100–2138.
- (97) Hunter, C. A.; Sanders, J. K. M. The Nature of  $\pi$ - $\pi$  Interactions. *J. Am. Chem. Soc.* **1990**, *112* (14), 5525–5534.
- (98) Zhao, Y.; Yu, H.; Quan, X.; Chen, S.; Zhao, H.; Zhang, Y. Preparation and Characterization of Vertically Columnar Boron Doped Diamond Array Electrode. *Appl. Surf. Sci.* **2014**, *303*, 419.

**CReditS table for Article 2:**

**Olejniak, A., Ficek, M., Szkodo, M., Stanisławska, A., Karczewski, J., Ryl, J., Dołęga, A., Siuzdak, K. & Bogdanowicz, R. (2022).** Tailoring diffusional fields in zwitterion/dopamine copolymer electropolymerized at carbon nanowalls for sensitive recognition of neurotransmitters. *ACS Nano*, 16(8), 13183–13198. <https://doi.org/10.1021/acsnano.2c06406>.

Author	CRedit author statement	Signature
Adrian Olejnik	<b>Conceptualisation:</b> Full <b>Methodology, Formal analysis, Investigation, Data curation, Writing Original draft, Writing Review &amp; edit, Visualisation:</b> Leading role <b>Project administration, Funding, Resources:</b> In part (DG)	
Mateusz Ficek	<b>Methodology, Formal analysis, Investigation:</b> In part	
Marek Szkodo	<b>Validation, Methodology, Formal analysis, Investigation, Data curation, Writing Original draft, Writing Review &amp; edit:</b> In part	
Alicja Stanisławska	<b>Methodology, Formal analysis, Investigation:</b> In part	
Jakub Karczewski	<b>Methodology, Formal analysis, Investigation:</b> In part	
Jacek Ryl	<b>Validation, Methodology, Formal analysis, Investigation, Data curation, Writing Original draft, Writing Review &amp; edit:</b> In part	
Anna Dołęga	<b>Validation, Methodology, Formal analysis, Investigation:</b> In part	
Katarzyna Siuzdak	<b>Validation, Resources, Writing Original draft, Writing Review &amp; edit, Supervision:</b> In part	
Robert Bogdanowicz	<b>Methodology, Validation, Resources, Visualisation, Writing Original draft, Writing Review &amp; edit, Funding, Project administration:</b> In part, <b>Supervision:</b> Leading role	



# Band Gap Engineering toward Semimetallic Character of Quinone-Rich Polydopamine

Adrian Olejnik, Karol Olbryś, Jakub Karczewski, Jacek Ryl, Robert Bogdanowicz,\* and Katarzyna Siuzdak



Cite This: *J. Phys. Chem. C* 2023, 127, 12662–12677



Read Online

ACCESS |



Metrics & More

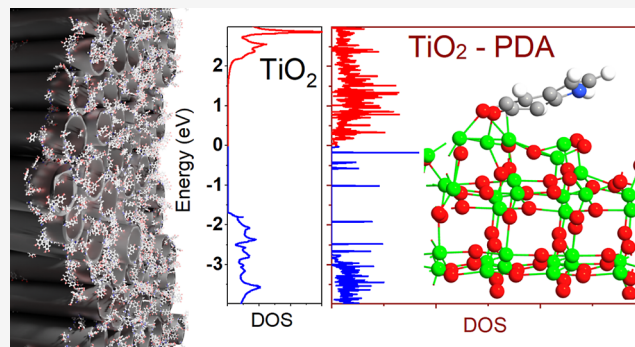


Article Recommendations



Supporting Information

**ABSTRACT:** Semiconductor/melanin interfaces have received increasingly more attention in the fields of photocatalysis and applied electrochemistry because of their facile synthesis, unique electrical properties, and strong capability toward photosensitization. In this work, we describe the electropolymerization of quinone-rich polydopamine (PDA) on the surface of hydrogenated TiO<sub>2</sub> nanotubes with enhanced photoactivity in the visible spectrum. PDA is deposited uniformly on the nanotube walls, and the chemical structures of the resulting PDA layer strongly depend on the pH of the supporting electrolyte. The film thickness varies in the range of 2–8 nm depending on the number of electropolymerization cycles. Optical and electrochemical experiments coupled with density functional theory simulations revealed strong evidence of a semimetallic character of the junction with a broad distribution of midgap surface states induced by PDA. As a result of the nanotube modification, a 20-fold increase in the photocurrent response is observed. Quantum efficiency measurements show that the enhancement occurs mainly at wavelengths between 500 and 550 nm. Additionally, nonlinear electrochemical impedance spectroscopy experiments strongly suggest that, in the TiO<sub>2</sub>/PDA junction, PDA behaves as a set of redox mediators distributed at the surface rather than as a semiconducting polymer. This concept might be crucial for understanding the electronic properties of semiconductor/melanin junctions.



## 1. INTRODUCTION

Living organisms utilize melanins for several biological purposes, including pigmentation, adhesives, and as a building component of different tissues. Depending on the chemical structure and cellular functions, they can be divided into eumelanins, pyromelanins, pheomelanins, neuromelanins, and allomelanins.<sup>1,2</sup> The elucidation of the structure of melanin is generally a complicated issue and attracts significant attention among the community of chemists and material scientists.<sup>3–5</sup> A gold-standard synthetic eumelanin is polydopamine (PDA), which is a name for everything that is a product of oxidative polymerization of dopamine. The chemistry of PDA involves several tens of different structural units with many functional groups, such as catechol, quinone, indole, and amine. It is believed that the most abundant monomer of PDA is 5,6-dihydroxyindole (DHI) and its oxidized analogue indolequinone (IQ), which are double-ringed,  $\pi$ -conjugated molecules.<sup>2,6–8</sup> Additionally, some double-ringed units in the PDA chain can be hydrogen-saturated and thus not fully  $\pi$ -conjugated, such as leukodopaminechrome (LDC) and dopaminechrome (DC). It has also been shown that a minority of single-ringed units such as dopamine-quinone (DQ) and unchanged dopamine (DA) are also present in PDA.<sup>6</sup>

Although the presence of polymeric chains in PDA has been questioned for a long time, Delparastan et al. in 2018 used single-

molecular force microscopy to provide direct evidence of the polymeric nature of PDA.<sup>9</sup> It is generally accepted that the structural units are connected by aryl–aryl linkages and covalent crosslinks. Moreover, hydrogen bonds and physical stacking of rings governed by  $\pi$ – $\pi$ ,  $\pi$ –cation, and electrostatic interactions also contribute to the structure.<sup>6,8,10</sup> The ratio between units of PDA and the degree of crosslinking can be controlled by the choice of deposition method, solvent, buffer pH, and other polymerization parameters.<sup>2,3,11,12</sup>

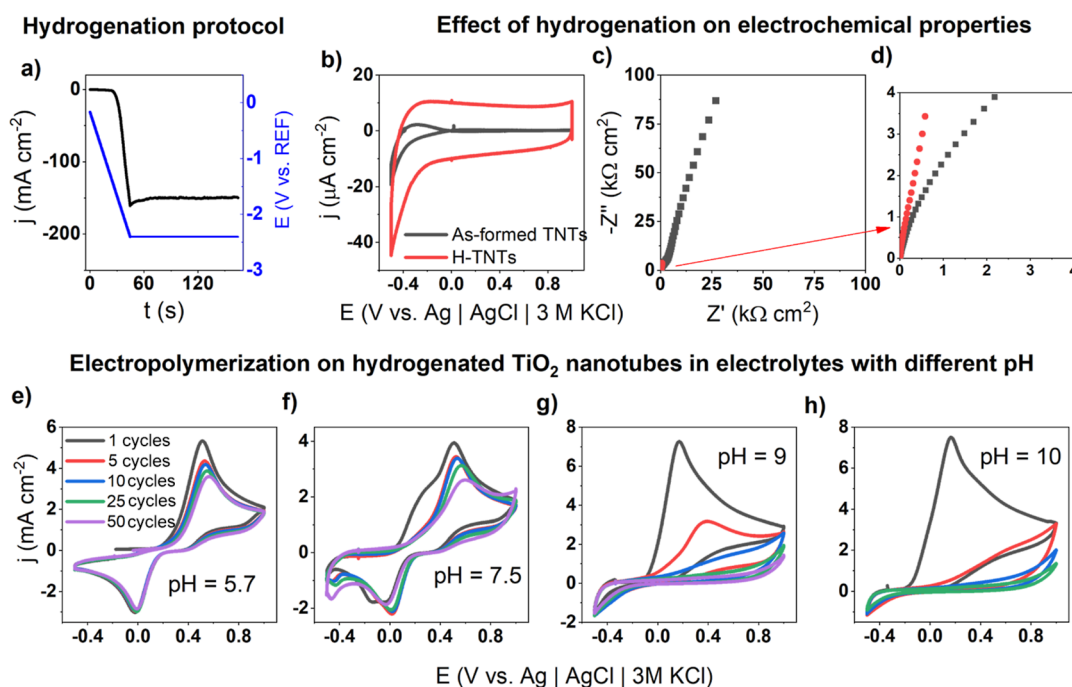
PDA has especially strong prospects due to its simplicity of polymerization onto practically any surface and the high malleability of its electrical and optical properties through manipulation of energy levels in the  $\pi$ -conjugated systems.<sup>3,13</sup> The presence of redox active sites involving catechol/quinone pairs in PDA can be utilized in many areas of electrochemistry, such as supercapacitors,<sup>14</sup> catalysis,<sup>15</sup> and probes in chemical force microscopies.<sup>16</sup> Due to the wide variety of intermolecular

Received: December 16, 2022

Revised: June 7, 2023

Published: June 24, 2023





**Figure 1.** Hydrogenation of TNTs and electropolymerization of dopamine. (a) Potential program and current response of nanotubes during hydrogenation; (b–d) CV curves and EIS spectra of as-prepared and hydrogenated nanotubes (supporting electrolyte: 0.5 M Na<sub>2</sub>SO<sub>4</sub>); (e–h) CV curves registered during electropolymerization with 5 mM dopamine in electrolytes of different pH of 5.7, 7.5, 9.0, and 10.0 (supporting electrolyte: 1 × Tris + 0.5 M Na<sub>2</sub>SO<sub>4</sub>).

interactions, PDA is known as a prominent adhesive and as a binder for many composite materials.<sup>3</sup> Moreover, it is composed only of highly abundant nonmetal atoms, which is beneficial for sustainable, green chemistry solutions.<sup>4</sup> However, in recent years, researchers have focused on further expansions of the variety of these structures by introducing new monomers,<sup>1</sup> with copolymerization agents<sup>17,18</sup> or as a template for molecular imprinting of biomolecules.<sup>19</sup>

The molecular mechanisms underlying the electronic properties of melanins, including PDA, are complicated and not fully understood yet. Traditionally, eumelanins were considered amorphous semiconductors due to the characteristic dependence of the conductivity on temperature.<sup>12,20</sup> However, Mostert et al. showed in 2012 that this view is incorrect.<sup>21</sup> Based on EPR measurements, they showed that the disproportionation reactions—especially in DHI carboxylic acid (DHI-CA) units—lead to the creation of protons and hydroxyl ion radicals as ionic charge carriers. In addition to polaronic-based charge transport in  $\pi$ -conjugated systems, there is also a strong component of ionic conduction. Furthermore, in a thorough study using picosecond/femtosecond fluorescence spectroscopy, PDA structural units were shown to differ in terms of the capability of proton transfer.<sup>22</sup> For example, the rates of these processes are up to 1000 times slower for DHI compared to its carboxylated analogue, which explains the higher conductivity of DHI-CA.

In addition to the electronic properties of PDA itself, an area actively exploited nowadays is PDA semiconductor junctions. Kim et al. explored the PDA/ZnS interface using photoelectrochemical experiments and density functional theory (DFT).<sup>23</sup> In that study, it was shown that, after PDA deposition, some ZnS surface regions are oxidized to ZnSO, leading to changes in the local band structure. As a result, a doubly staggered band alignment is created. On the one hand, ZnSO

lowers the band gap and the capability of trapping photoexcited electrons for catalysis; on the other hand, PDA can accept holes from the valence band (VB) and thus prevent photocorrosion (acting as a reversible hole scavenger). A similar effect was observed a decade earlier in EPR studies by Dimitrijevic et al. on the TiO<sub>2</sub>/PDA interface.<sup>24</sup> They showed the localization of holes on PDA, which prevents the oxidation of water and the creation of free radicals. At the same time, however, dopamine did not affect the reductive ability of photogenerated electrons in the TiO<sub>2</sub> conduction band. In other words, the recombination of holes with electrons is suppressed because of the unique staggered band alignment.

Guan et al. reported that PDA can also be used as a binder integrating multicomponent sulfides on TiO<sub>2</sub> nanowires.<sup>25</sup> They showed that the thickness of the PDA layer is a crucial factor in determining the magnitude of the boost in photoactivity and electrochemical properties. Specifically, 1 nm-thick PDA is too thin to efficiently enhance absorption, while 3 nm produces optimal photosensitization. However, layers thicker than 3 nm impede the charge transfer kinetics by shielding active sites, thus limiting the electrochemical performance, presumably due to the longer distance for the charge carrier tunneling. In another work, core-shell TiO<sub>2</sub>@PDA nanoparticles exhibited the highest photocatalytic enhancement with 1 nm-thick PDA.<sup>26</sup> These investigations suggest that the optimal thickness for photosensitization is strongly dependent on the geometry of the substrate material.

In this work, we report on experimental and computational investigations of the electronic structure of PDA and report for the first time a semimetallic character of the PDA semiconductor interface. Both experiments and DFT calculations of the density of states (DOS) show that quinone-rich, electropolymerized PDA exhibits highly populated midgap states and a high propensity toward photosensitization. When deposited on



hydrogenated loosely spaced titania nanotubes (TNTs), it results in a 2000% enhancement of photocurrents, mainly in the visible spectrum after PDA modification as well as unique electrochemical behavior in the presence of ferrocyanides. Based on these observations, we propose a model in which PDA is treated as a set of distributed redox mediators, rather than as an organic semiconductor, with high explanatory power for other interfaces involving PDA.

## 2. MATERIALS AND METHODS

**2.1. Reagents.** 10× Tris buffer was obtained from Santa Cruz Biotechnology and diluted 10 times prior to the measurements, dopamine hydrochloride was purchased from Sigma-Aldrich, and the deionized water used in the experiment was provided by a Hydrolab HLP-5p system. A titanium plate (99.7% purity) was obtained from Strem Chemicals.  $\text{Na}_2\text{SO}_4$ , acetone, ethanol, diethylene glycol, HCl, NaOH,  $\text{K}_3[\text{Fe}(\text{CN})_6]$ ,  $\text{K}_4[\text{Fe}(\text{CN})_6]$ , and  $\text{NH}_4\text{F}$  were provided by Chempur.

**2.2. Synthesis of Loosely Spaced TNTs.** The titania nanotube synthesis was reported previously elsewhere.<sup>27,28</sup> Prior to anodization, the titanium plate was ultrasonically cleaned in acetone, ethanol, and subsequently water. Single-step anodization of the titanium plate was performed in an electrolyte containing diethylene glycol/water/HF (69/5/1 vol %) and 9.4 mM  $\text{NH}_4\text{F}$ . The anodization voltage was 30 or 40 V (as indicated in the text), the polarization time was 2 h, and the temperature was 40 °C. After anodization, the TNTs were rinsed with ethanol and dried in an air stream. Finally, the plates were calcined in a tube furnace (Nabertherm) at 450 °C for 2 h.

**2.3. Hydrogenation of  $\text{TiO}_2$  Nanotubes and Electropolymerization of Dopamine.** All electrochemical experiments, including the hydrogenation and electropolymerization of dopamine, were performed using a Biologic SP-150 potentiostat–galvanostat. Unless stated otherwise, the working electrode was hydrogenated pure or modified TNTs, the counter electrode was a platinum mesh, and the reference electrode was Ag/AgCl/3 M KCl. All potentials in the study are expressed with respect to this reference electrode. The geometric surface areas of the working electrodes were between 0.5 and 1 mm<sup>2</sup>, and all currents were transformed to current densities.

Hydrogenation of TNTs was performed in an argon-purged 0.5 M  $\text{Na}_2\text{SO}_4$  solution through the following protocol. First, linear sweep voltammetry (LSV) with a 100 mV/s rate was used for cathodic polarization up to −2.4 V. Then, a constant potential equal to −2.4 V was applied for 2 min (Figure 1a).

Electropolymerization of dopamine on hydrogenated TNT electrodes was carried out potentiodynamically in an argon-purged solution of 0.5 M  $\text{Na}_2\text{SO}_4$  containing 1× Tris buffer, immediately after hydrogenation. The pH of the solution was adjusted by adding 1 M HCl or 1 M NaOH to the desired values, i.e., 5.7, 7.5, 8.5, 9.0, or 10.0. An MP-103 handheld potentiometric pH meter was used to control the pH value. The number of cyclic voltammetry (CV) cycles was 5, 10, 25, or 50 with a 20 mV/s scan rate in the range from −0.5 to +1.0 V.

**2.4. SEM Inspection and Measurement of the PDA Film Thickness.** The surface morphology of the electrodes was investigated by means of a Quanta FEG 250 (FEI) Schottky field-emission scanning electron microscope equipped with a secondary ET electron detector with a beam accelerating voltage of 10 kV. The thickness of the PDA layer ( $d_{\text{PDA}}$ ) was estimated by measuring the wall thickness of the PDA-modified nanotubes

( $W_{\text{TNT|PDA}}$ ), subtracting the thickness of the unmodified nanotubes ( $W_{\text{TNT}}$ ), and then dividing it by 2 (eq 1)

$$d_{\text{PDA}} = \frac{W_{\text{TNT|PDA}} - W_{\text{TNT}}}{2} \quad (1)$$

Measured values were averaged over at least 100 points.

**2.5. X-ray Photoelectron Spectroscopy.** X-ray photoelectron spectroscopy (XPS) studies were carried out on an ESCALAB 250Xi multispectroscopy (Thermo Fisher Scientific) operating with an Al  $K\alpha$  X-ray source. The spot size was 650  $\mu\text{m}$ , and the pass energy through the hemispherical analyzer was 20 eV. Throughout the measurement, the samples were flooded with low-energy electrons and low-energy  $\text{Ar}^+$  ions to assure charge compensation, with a final peak calibration at adventitious carbon C 1s (284.8 eV). The obtained spectra were analyzed and deconvoluted using the Advantage v5.9921 software (Thermo Fisher Scientific).

**2.6. Diffuse Reflectance, UV + Vis, and Raman Spectroscopy.** Diffuse reflectance spectra were collected with a PerkinElmer Lambda 35 (PerkinElmer, Waltham, MA, USA) dual-beam spectrophotometer in the range of 200–1000 nm with a scanning speed of 60 nm/min.

The Kubelka–Munk (KM) functions  $F(R)$  were calculated on the reflectance  $R$  data according to eq 2<sup>29</sup>

$$F(R) = \frac{(1 - R)^2}{2R} \quad (2)$$

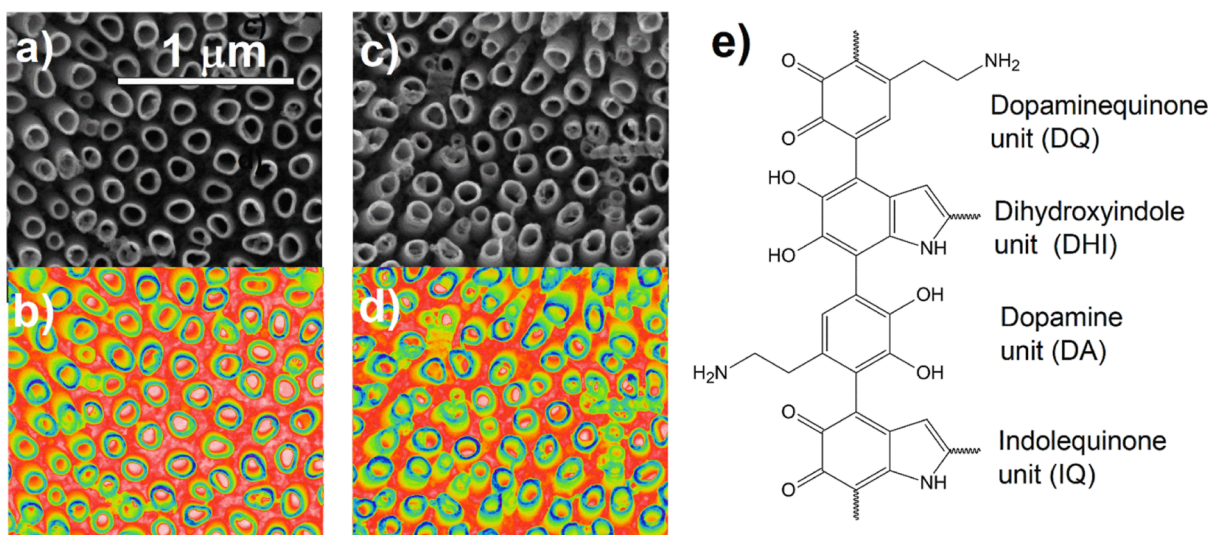
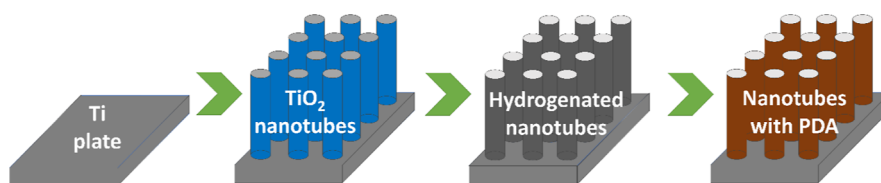
Raman spectroscopy measurements were conducted using a confocal micro-Raman spectrometer (inVia, Renishaw, Wotton-under-Edge, Gloucestershire, UK) with an argon-ion laser source emitting at 514 nm and operating with a power of 10 mW.

**2.7. Incident Photon Conversion Efficiency.** Quantum efficiency maps were measured with a photoelectric spectrometer for quantum efficiency measurements (Instytut Fotonowy, Poland). The wavelength range was set from 600 to 200 nm, and a measurement point was taken every 25 nm. The photoresponse regarding the wavelength was recorded in the potential range between −200 and 1000 mV, and the spacing between points was 200 mV. The illumination source was calibrated using a silicon reference cell.

**2.8. Electrochemical and Photoelectrochemical Characterization.** The effects of hydrogenation on the properties of TNTs were verified in a 0.5 M  $\text{Na}_2\text{SO}_4$  electrolyte with CV with a 50 mV/s scan rate, as well as electrochemical impedance spectroscopy (EIS) at open circuit potential and a 10 mV amplitude of stimulating single-sine potential waves. The frequency range for this experiment was 100 kHz–100 mHz (96 points per decade), and the electrode was preconditioned for 3 min before EIS measurement to preserve equilibrium.

Photoelectrochemical tests were performed in a 0.5 M  $\text{Na}_2\text{SO}_4$  electrolyte using LSV with a scan rate of 20 mV/s or using chronoamperometry (CA) at a potential of +0.3 V. As a light source, a xenon lamp equipped with AM 1.5 and UV cutoff (GG40, Schott) filters was used. The irradiation intensity was established to be 100 mW/cm<sup>2</sup> using a Si reference cell (Rera). The EIS measurements used for Mott–Schottky were performed at potentials ranging from −0.5 to +1.0 V with a 1 min polarization time at each step and a 10 mV sine amplitude. The inverse squared capacitance was calculated from the impedance data at a 1 kHz frequency.

## Scheme 1. Experimental Procedure to Obtain Loosely Spaced TNT Covered with PDA



**Figure 2.** SEM images with different color contrasts of (a–b) pure nanotubes and (c–d) nanotubes with deposited PDA at pH = 7.5; (e) fragments of the molecular structure of PDA.

The semimetallic properties of the TNT/PDA junction were established by CV and EIS experiments in an electrolyte containing 5 mM  $K_4[Fe(CN)_6]$  and 5 mM  $K_3[Fe(CN)_6]$  with a 1 M KCl supporting electrolyte. Prior to each EIS measurement, the working electrode was polarized to +0.260 V for 1 min. The amplitudes of the voltage stimulus were 10, 100, 200, 300, or 500 mV, and the frequency range was 100 kHz–100 mHz.

**2.9. DFT Computations.** Molecular structures of anatase surfaces and PDA units were designed using a builder tool provided by Atomistix ToolKit Quantumwise (ATK, Synopsys, USA) as reported in ref 30. DFT computations were performed using the Perdew–Burke–Ernzerhof (PBE) functional within the generalized gradient approximation implemented in the package. The linear combination of the atomic orbital method<sup>31</sup> with the medium ATK basis set and PseudoDojo norm-conserving pseudopotentials were applied.<sup>32</sup> The adsorption geometry and intermolecular interactions between dopamine structural units and  $TiO_2$  were investigated by geometry optimizations and calculating electron density maps in optimized structures. A preoptimization using a Dreiding force field was used to facilitate several geometry optimizations.<sup>33</sup> The DOS was calculated with a  $7 \times 7 \times 1$   $A^3$   $k$ -point mesh and a density mesh cutoff of 125 Ha and using half-occupation (DFT–1/2) correction.<sup>34</sup> The DOS spectra of isolated monomers, dimers, and trimers of PDA were computed for the optimized structures using multipole boundary conditions (single  $k$ -point). Adsorption simulations were performed using slab models of anatase  $TiO_2$  cleaved along the (101) crystallographic plane of an anatase unit cell and containing 30 atoms of Ti each (5 layers of Ti atoms). This plane was chosen because it is one of the most abundant planes in the experimental XRD spectrum and electron diffraction pat-

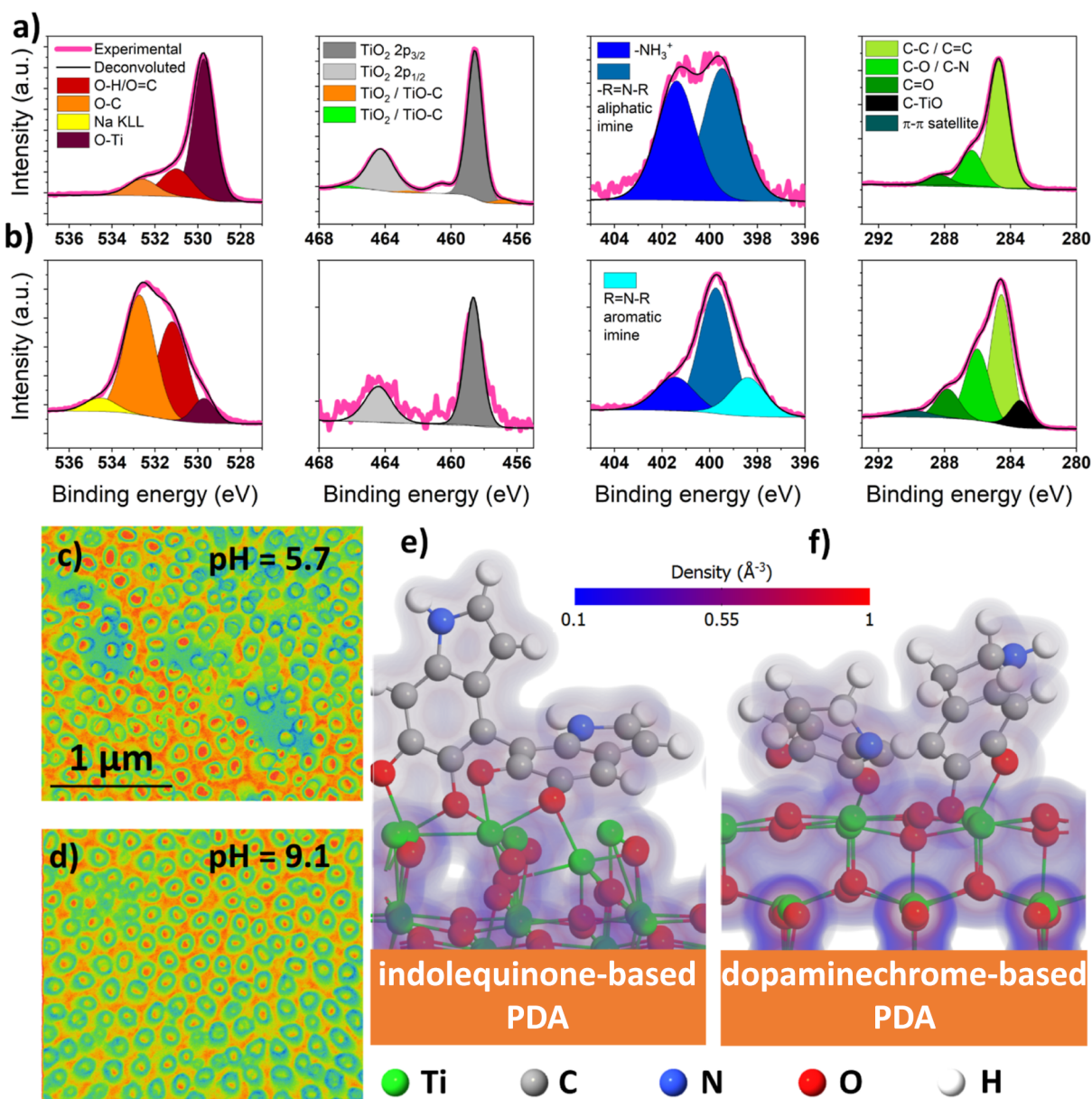
tern.<sup>35,36</sup> The symmetry-reduced body-centered tetragonal unit cell of anatase used for preparing the slab was taken from the Quantum ATK database, having a size of  $3.79 \times 3.79 \times 9.51$  Å. The final supercell used for adsorption models throughout the paper was  $11.35 \times 10.23 \times 36.09$  Å with 28 Å of vacuum. Prior to adsorption, the molecule of the PDA monomer/dimer/trimer was placed 5 Å above the surface and relaxed. DOS spectra were calculated based on Kohn–Sham orbitals calculated for the last frame of geometry optimization.

### 3. RESULTS AND DISCUSSION

**3.1. Hydrogenation of TNTs and Electropolymerization of Dopamine.** The overall synthetic procedure is shown in Scheme 1. Prior to enhancement of the surface conductivity, TNTs were electrochemically hydrogenated according to the protocol depicted in Figure 1a. This process has been shown to lead to the incorporation of hydrogen atoms into the surface layer of  $TiO_2$  unit cells, introducing several energy levels within the energy gap and increasing the electronic populations inside the conduction band.<sup>37–39</sup> As a result, a significant increase in capacitive currents is observed in both the cathodic and the anodic branches (Figure 1b). Moreover, the real and imaginary parts of the impedance are significantly decreased (Figure 1c,d), indicating an enhancement of both the surface conductivity of the nanotubes and template and the double-layer capacitance.

Subsequently, the hydrogenated nanotubes were subjected to electropolymerization of dopamine in a 0.5 M  $Na_2SO_4$  electrolyte buffered with 1× Tris and the pH adjusted to different levels, i.e., 5.7, 7.5, 9.0, and 10.0. Due to the fact that the electrochemical steps of PDA electropolymerization are proton-coupled<sup>40</sup> and the chemical steps are base-catalyzed,<sup>7,41</sup> significant pH dependence of the PDA structure and properties



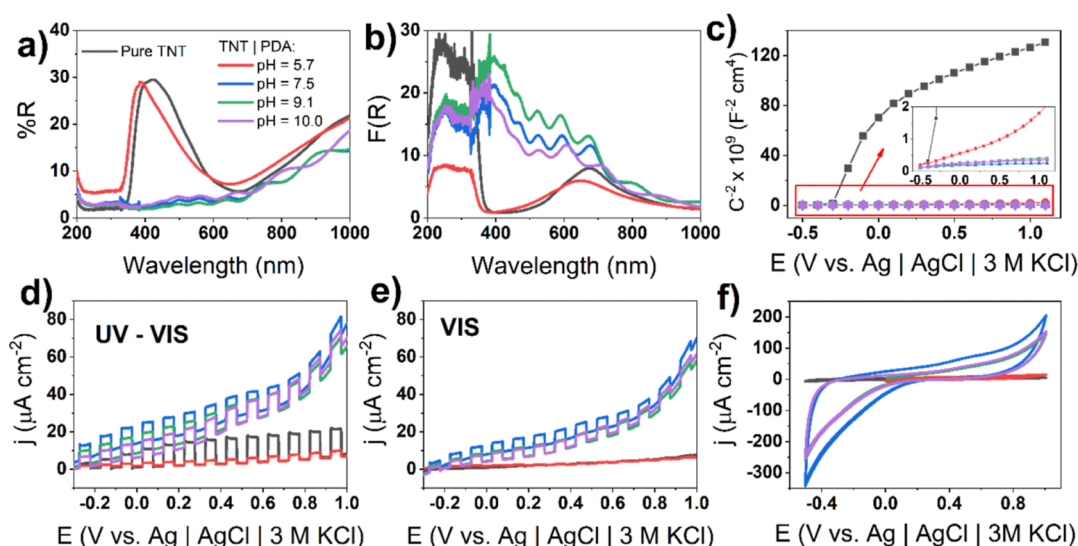


**Figure 3.** High-resolution XPS spectra of TNT/PDA with dopamine polymerized in (a) acidic pH (5.7) and (b) alkaline pH (9.1); SEM pictures of TNT/PDA with dopamine polymerized in (c) acidic pH (5.7) and (d) alkaline pH (9.1); DFT-optimized geometry of PDA adsorption on anatase  $\text{TiO}_2$  slabs (101) along with electron density maps; PDA is modeled as a dimer of (e) IQ or (f) DC monomers.

is expected. At a slightly acidic pH, there is only one pair of redox peaks, with a gradually decreasing current density corresponding to the DA/DQ pair.<sup>17,42,43</sup> These signals lie at the potentials at 0.0 and +0.5 V, and the oxidative currents are higher, suggesting irreversibility of the oxidation. Under neutral conditions (7.5 pH), an additional signal at +0.25 V is manifested but only in the first cycle. In our previous work, we indicated that, during PDA electrodeposition, LDC/DC redox pair reactions are mainly observed in this potential range.<sup>42</sup> The shapes of the CV curves at this pH are in agreement with analogous experiments reported in the literature.<sup>44,45</sup> At a more alkaline pH between 9 and 10, there is only one complex oxidation peak between 0.0 and +0.8 V superimposed of several redox reactions, presumably of the LDC/DC and DHI/IQ pairs. Additionally, the current density decay is faster in alkaline pH and plummets to several  $\mu\text{A cm}^{-2}$  after 25 cycles. In an even more alkaline pH of 11 and above, the PDA coating is not formed, most probably due to delamination

of the PDA layered structure in the presence of hydroxyl ions.<sup>46,47</sup>

Two different color contrasts of the SEM images were used to show changes in the morphology of the TNTs after electropolymerization (Figure 2a–d). In general, as-formed nanotubes have a wall thickness of  $27.7 \pm 5.9$  nm. However, after modification, this value is on average  $38.6 \pm 6.9$  nm. This indicates the formation of the layer on both the inner and outer walls of the nanotubes with an approximate thickness of  $5.5 \pm 1.0$  nm. Visually, it is especially pronounced with the orange–green contrast of the SEM pictures. Tilted nanotubes are thickened not only at the corona but also along the shaft. It is a strong clue that PDA covers a large area of the nanotubes from the bottom to the top. Similar coverages were obtained with photo-electropolymerization of dopamine on  $\text{TiO}_2$  nanorods.<sup>48</sup> Moreover, a set of SEM pictures of various areas of the sample at



**Figure 4.** Comparison of optical and photoelectrochemical properties of 30 V TNT/PDA heterojunctions polymerized at different pH (50 CV cycles of polymerization); (a) reflectance spectra; (b) KM functions; (c) Mott–Schottky plot inset showing the range of low  $C^{-2}$  values; chopped dark–light LSV scans with a 20 mV/s scan rate, (d) illumination with a UV–vis light source, (e) vis light source, and (f) CV scans; the electrolyte for electrochemical experiments was 0.5 M  $\text{Na}_2\text{SO}_4$ .

different magnifications are presented to support this effect (Figures S1–S3).

**3.2. XPS Studies of PDA Deposited on TNTs.** Besides morphology, there are major differences in the chemical structure of TNT/PDA junctions depending on the pH used for electropolymerization (Figure 3a,b). First, in the oxygen part of the spectrum, three peaks are present for acidic PDA (TNT/a-PDA), which correspond to O–Ti (530 eV), C–O–H (531 eV), and O–C (533 eV) bonds, respectively. A significant increase in signals corresponding to C–O and O–H bonds—compared to the pristine nanotubes<sup>27,49,50</sup>—suggests the formation of PDA consisting mostly of catecholic units such as DA, LDC, and DHI. This is in agreement with the overall reaction scheme, where the presence of  $\text{H}^+$  ions shifts the reaction toward catecholic products (eq 3)



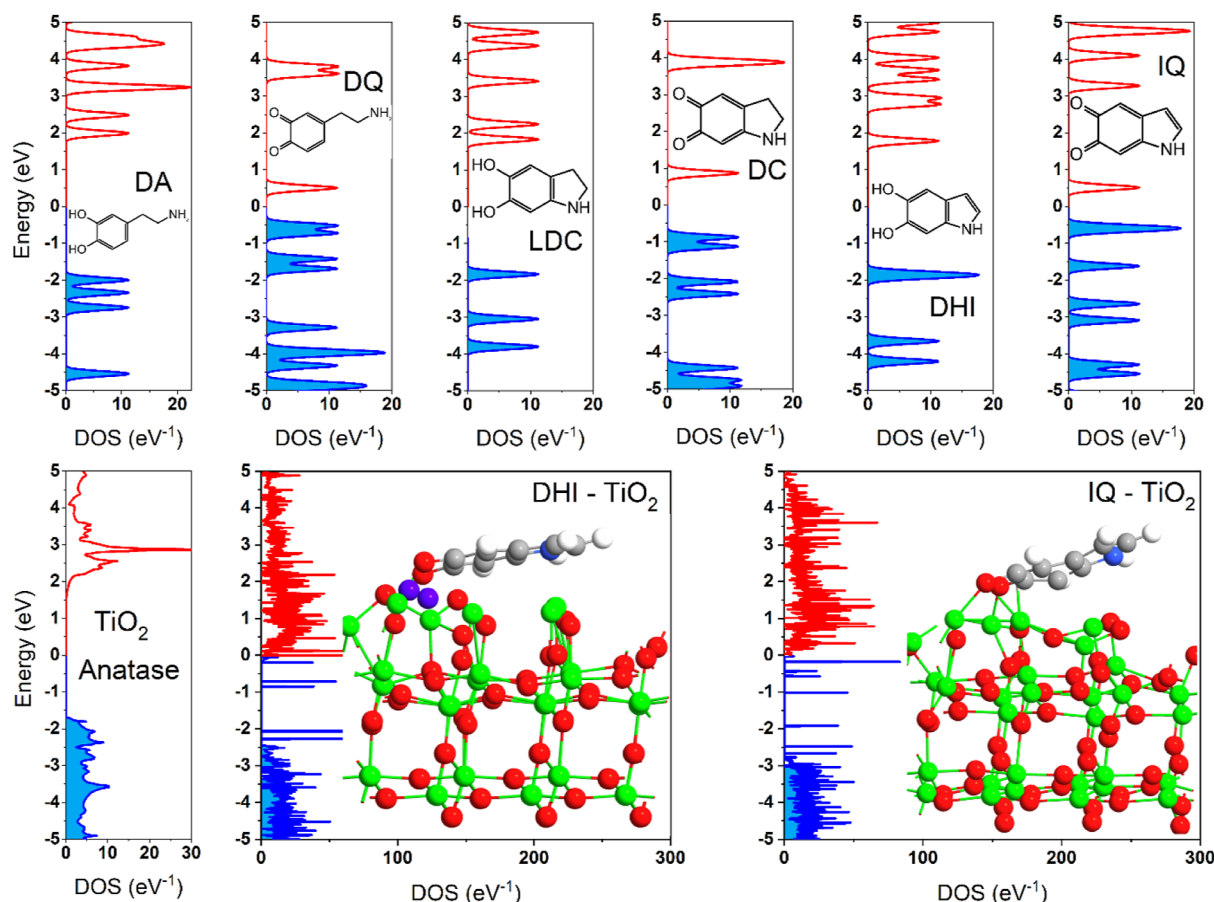
where R stands for the ring of the PDA units. However, the basic PDA (TNT/b-PDA) exhibits an additional peak at 535 eV corresponding to C=O bonds. This suggests the presence of a strong contribution of quinone-containing units such as DQ, DC, and IQ in the structure.

The titanium region shows six peaks for TNT/a-PDA and only two for TNT/b-PDA. All signals are characteristic of pristine TNTs<sup>27,49,50</sup> but are notably smaller for TNT/b-PDA. This is justified by the higher coverage of the nanotubes in b-PDA, which leads to quenching of the XPS signal. The quantitative data of the atomic surface composition is given in Table S1. It is easy to see that the total contribution of Ti in acidic PDA is 16.41%, while it equals only 0.33% in case of basic PDA. On the other hand, the total carbon content for b-PDA is twice as high and the nitrogen content is tripled. Considering that the XPS signal originates from approx. 1–5 nm beneath the surface, the anticipated cause of the weaker Ti 2p signal in an alkaline environment is the larger thickness of the PDA coating and higher degree of uniformity. In terms of morphology, a-PDA is found in the form of islands and several nanotubes remain bare, while b-PDA uniformly covers the walls of most of the nanotubes.

Detailed studies and discussions on the uniformity of PDA on different length scales can be found in the Supporting Information. SEM images with numerous magnifications and contrasts recorded on different areas of the TNT\_bPDA sample are displayed in Figures S1–S3, revealing uniformly distributed PDA across the surface. Furthermore, Raman maps of the ratio of the G, D, and A bands at micrometer and millimeter scales (Figures S4–S7) were studied. The G-to-A band map showed that over 80% of the sample areas exhibit a ratio of 3.4 to 4.5, while the G-to-D map exhibited a 1.4 ratio across 98% of the surface, both implying the phase uniformity of PDA. Several islands deviating from the average ratios indicate that the uniformity is not perfect, although it can be considered satisfactory for the proposed photoelectrochemical investigations. Next, uniformity analyses were supported by spatially and spectrally resolved photocurrent maps (Figure S8) and macroscopic images of the TNT\_bPDA samples (Figure S9). Therefore, uniformly coated PDA hinders the signal from the  $\text{TiO}_2$  substrate and leads to the increased signal of carbon and nitrogen. Quantitative results for oxygen are inconclusive in this context because both PDA and  $\text{TiO}_2$  contain oxygen atoms in different electronic environments.

Examination of the nitrogen region of the XPS spectra reveals two peaks for TNT/a-PDA located at 399 and 401 eV, attributed to  $\text{R}=\text{N}-\text{R}$  aliphatic imine and  $\text{R}-\text{NH}_3^+$  groups, respectively. Alternatively, the 399 eV signal could originate from  $\text{R}-\text{NH}-\text{R}$  aliphatic groups of LDC and DC units, which are suspected to be dominant in TNT/a-PDA.<sup>11,42</sup> An additional peak at 398 eV, observed only for TNT/b-PDA, was attributed to the  $\text{R}=\text{N}-\text{R}$  aromatic imine or aromatic  $\text{R}-\text{NH}-\text{R}$  amine, both of which are known to be present in the structure of alkaline-based PDA.<sup>3</sup> This is strong evidence that a-PDA contains more aliphatic amines/imines than b-PDA, indicating the higher content of DHI and IQ conjugated units in b-PDA, which was reflected in computational models.

Lastly, three peaks are found in the carbon region for TNT/a-PDA, attributed to C–C and C=C bonds, collectively, at 284 eV, C–O and C–N bonds at 286 eV, as well as C=O bonds at 289 eV. On the other hand, TNT/b-PDA exhibits two additional



**Figure 5.** DOS spectra for six different structural units of PDA: dopamine (DA), DQ, LDC, DC, DHI, and IQ; for pristine bulk anatase; for anatase with adsorbed DHI and anatase with adsorbed IQ. The Fermi energy is at zero; filled states are marked in blue and empty in red. The surface used for adsorption is anatase (101), and the atom colors are the same as in Figure 3.

peaks at 283 and 291 eV, attributed to C–TiO bonds and  $\pi$ – $\pi$  shakeup satellite peaks, respectively. A higher share of the C=O peak for TNTIPDA suggests a higher content of quinone forms and the presence of  $\pi$ – $\pi$  shakeup satellite peaks, which provides additional evidence of the strong contribution of  $\pi$ -conjugated DHI and IQ units in b-PDA but not in a-PDA.

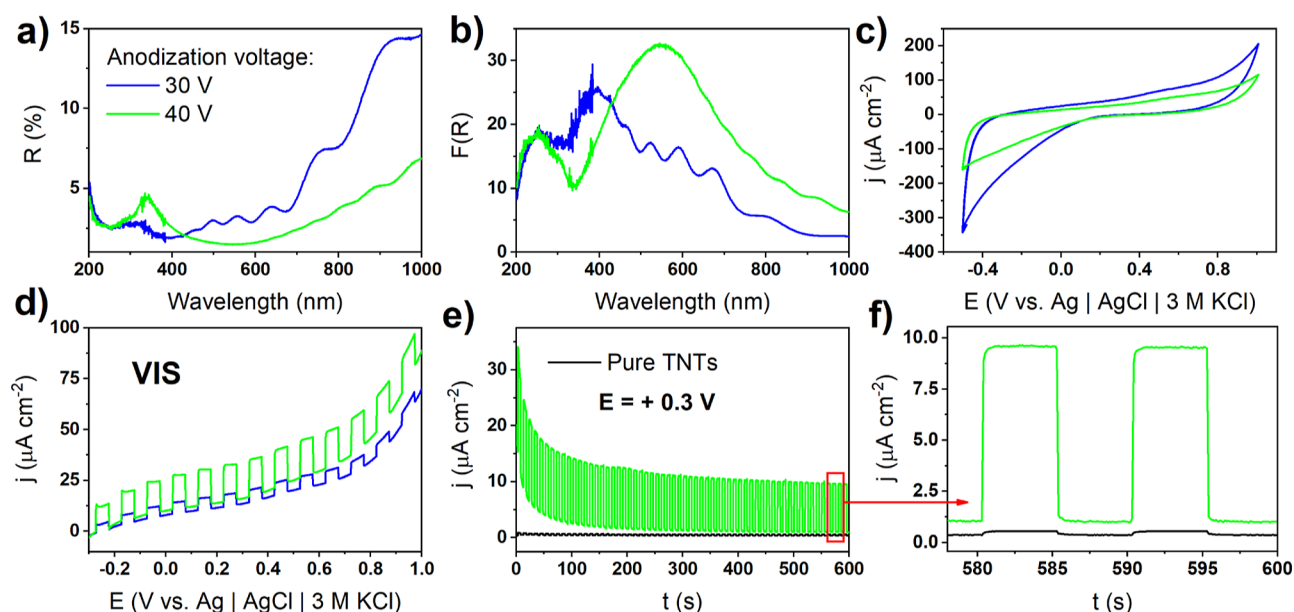
The unique nature of C–TiO bonds can be justified by DFT calculations of the PDA adsorption on the surface of TiO<sub>2</sub> (Figure 3e,f). In this simulation, two types of PDA dimers (indolequinone IQ–IQ and DC–DC dopaminechrome) were relaxed on the surface of anatase (101). IQ–IQ can be considered as a model for b-PDA and DC–DC for a-PDA because the registered electropolymerization CV curves and data from the literature indicate that these units are expected to dominate in PDA obtained in alkaline solutions.<sup>11,42</sup> After optimization, several Ti–O–C surface bonds can be found for both types of PDA, and the high overlap of the electron densities strongly suggests their relatively strong character. In general, PDA subunits attain an equilibrium position so that the surface Ti atom lies below the ring. There is a strong overlap in electron densities between adjacent Ti and C atoms with lengths of 2.41–2.64 Å for IQ–IQ and 2.35–2.38 Å for DC–DC structures, suggesting nontrivial surface Ti–C bonding. These lengths are smaller than for typical  $\pi$ – $\pi$  interactions (on the order of 3 Å and higher) but larger than in the case of typical C–C covalent bonds (1.8 Å and lower). Therefore, the binding energy of the abovementioned Ti–C bond is anticipated to be smaller than C–C. As a result, such a

molecular arrangement of PDA subunits might explain the atypical peak at the carbon part of the XPS spectrum at 283 eV. Moreover, such a bond might be the origin of interactions described as Ti–O–C in Ti 2p spectra. These observations suggest that the DC–DC type of PDA has a slightly stronger affinity toward the surface of anatase, but Ti–C bonds are present in both types.

In general, XPS studies indicate that PDA electropolymerized under slightly alkaline conditions exhibits a higher content of quinones and conjugated units such as IQ involving R=N–R imines and R–NH–R amines compared to PDA synthesized in a slightly acidic environment.

**3.3. Influence of Electropolymerization pH and Nanotube Geometry on Optical and Photoelectrochemical Properties of TNTIPDA Heterojunctions.** The pH of the electropolymerization solution plays a tremendous role in tailoring the adsorption and chemistry of PDA. Figure 4 indicates that it also has a significant effect on the optical and photoelectrochemical properties of the TNTIPDA junctions. UV–vis reflectance spectroscopy data, as well as KM function plots (Figure 4a,b), clearly show that pristine nanotubes exhibit a pronounced absorption edge that starts at ca. 380 nm in the UV region followed by a broad band in the visible and near-infrared (NIR) range (500–900 nm). Subsequent spectra of TNTIPDA polymerized at pH = 5.7 resemble pristine PDA to a large extent, with a notable reduction in the absorption intensity at the band edge (Figure 4b). However, when the pH of electropolymerization was neutral or slightly alkaline, the





**Figure 6.** Comparison of the optical and photoelectrochemical properties of TNT/PDA heterojunctions with different nanotube dimensions resulting from various anodization voltages. Polymerization of dopamine was performed in pH = 8.5 and with 50 CV cycles; (a) reflectance spectra; (b) KM functions; (c) CV scans; (d) chopped dark–light LSV scans with 20 mV scan and visible-range light source; (e) chopped dark–light CA curves; (f) inset at a steady state; 0.5 M  $\text{Na}_2\text{SO}_4$  was used as an electrolyte.

emergence of several peaks is observed in the visible and NIR range, with a simultaneous decrease of the absorption edge. The origin of these peaks is either from the presence of discrete energy levels introduced into the system through electropolymerization<sup>15</sup> or the geometry-dependent scattering observed in several works.<sup>51,52</sup> Moreover, the enhancement of the spectral signal in the visible range is larger compared to the other works reporting modification of  $\text{TiO}_2$  with PDA.<sup>48,53</sup>

The described effects also have a profound influence on the photoelectrochemical activity (Figure 4d,e). LSV curves recorded under cyclic dark–light exposure during polarization show that there is an increase in photocurrents after modification of pure nanotubes in the potential range from  $-0.2$  to  $+1.0$  V. This improvement is observed only when PDA is polymerized at a pH of 7.5 or greater. Interestingly, the magnitude of the photocurrents is almost equal in either UV–vis or solely vis conditions. In other words, pristine nanotubes have poor photoactivity in visible light and decent photoactivity in UV–vis, while TNT/PDA structures have roughly the same photoactivity regardless of the UV component. These observations agree well with the presence of peaks in the KM functions in the visible range. This is therefore another strong clue that absorption bands in the visible range stem from discrete energy levels of PDA and, in turn, cause enhancement of photocurrents.

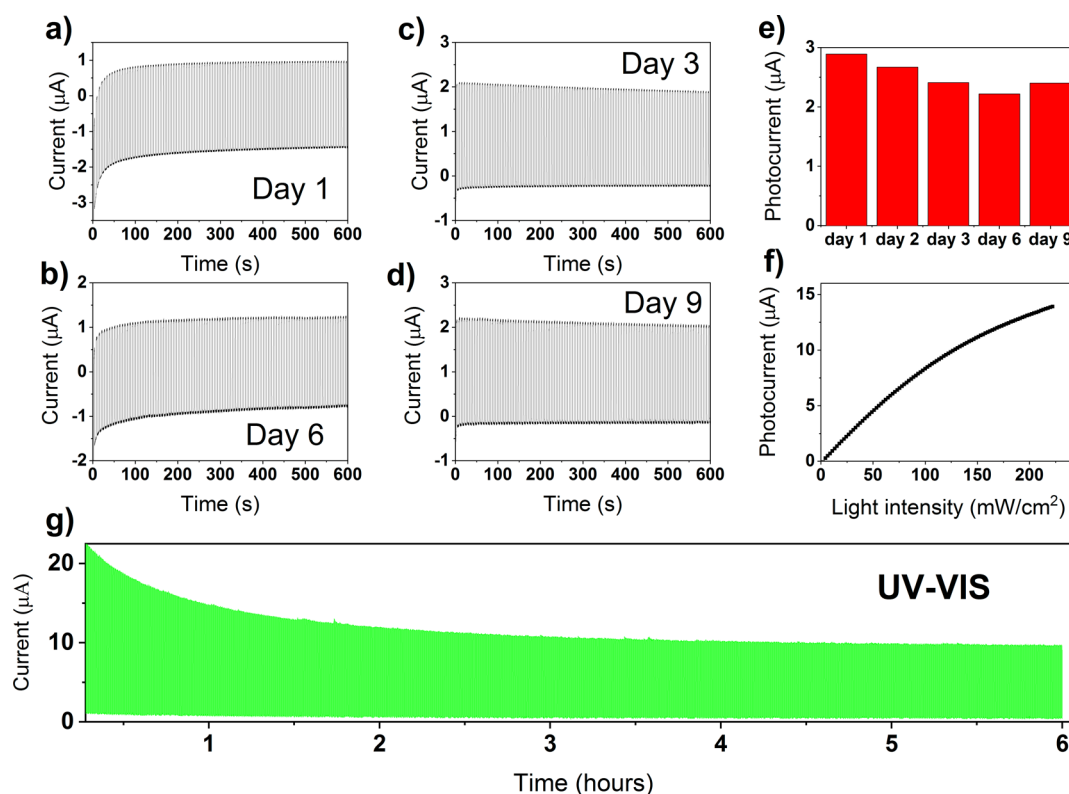
Additionally, the application of a PDA layer causes an increase in the background (dark) currents. A comparison of CV curves registered under dark conditions (Figure 4f) shows that these currents are mostly capacitive, which has been reported in the literature.<sup>54</sup> Additionally, the Faradaic currents of the quinone–catechol redox reactions are also notable at  $+0.5$  and  $-0.2$  V.<sup>42</sup> To compare the electrical properties of pure nanotubes with those modified with PDA, Mott–Schottky plots (Figure 4c) were constructed. Surprisingly, after electropolymerization, there is no change in the inverse squared capacitance  $C^{-2}$  with the electrode potential, which is a characteristic effect for a semiconductor.<sup>55</sup> Therefore, the flat-band potential does not

exist for TNT/PDA structures. The hypothesis is that the application of PDA on  $\text{TiO}_2$  nanotubes shifts the surface electrical properties from an n-type semiconductor to a semimetal. Interestingly, although PDA deposited at pH 5.7 does not cause significant changes in the optical properties and photocurrents, it still shifts the electrical character of the TNT/PDA heterojunction (Figure 4c, red curve).

The relations observed in the UV–vis spectra and electrochemistry can be better understood through the analysis of the DOS plots of different PDA structural units (Figure 5). First, the HOMO–LUMO gap is equal to 3.4–3.8 eV for catecholic units (DA, LDC, and DHI) and there are only slight differences between them.<sup>56</sup> Considering that the XPS spectra coupled with the electrochemistry and DFT adsorption simulations showed that a-PDA consists mainly of catecholic units, its high HOMO–LUMO gap is responsible for the negligible effects on the UV–vis characteristics (Figure 4a–c) and reduced photoactivity. However, quinone structural units (DQ, DC, and IQ) exhibit significantly smaller gaps, ranging from 0.7 to 1.4 eV, which consequently lead to enhancement of the absorption and photoactivity. A similar effect was also observed in the work of Zou et al.<sup>15</sup>

Moreover, when PDA structural units are adsorbed on the surface of anatase (101), the density of surface states changes remarkably. The DOS of pristine anatase exhibits well-separated conduction and VBs with a ca. 3.5 eV gap. However, when the PDA unit is adsorbed on its surface, several states are formed between the bands and the type of adsorbent strongly determines their number, position on the energy scale, and electronic population. In particular, the IQ- $\text{TiO}_2$  junction exhibits a larger contribution of intraband states. Additionally, more states in the conduction band and near its edge are populated with electrons, which is another argument for a semimetallic character of the TNT/PDA junction and for the observed photosensitization effects.<sup>47</sup>

A crucial factor influencing the optical and photoelectrochemical properties of TNT/PDA structures is the geometry of



**Figure 7.** (a–d) Transient photocurrents of the TNT\_bPDA sample registered during 9 days; (e) photocurrent change during the course of measurements; (f) intensity profile of the photocurrent—100% intensity equals to  $2.2 \text{ mA cm}^{-2}$  power density; (g) transient photocurrents measured continuously during the 6 h exposure to the mixed UV–vis light. All measurements were performed in a three-electrode configuration with 0 V vs AgCl polarization.

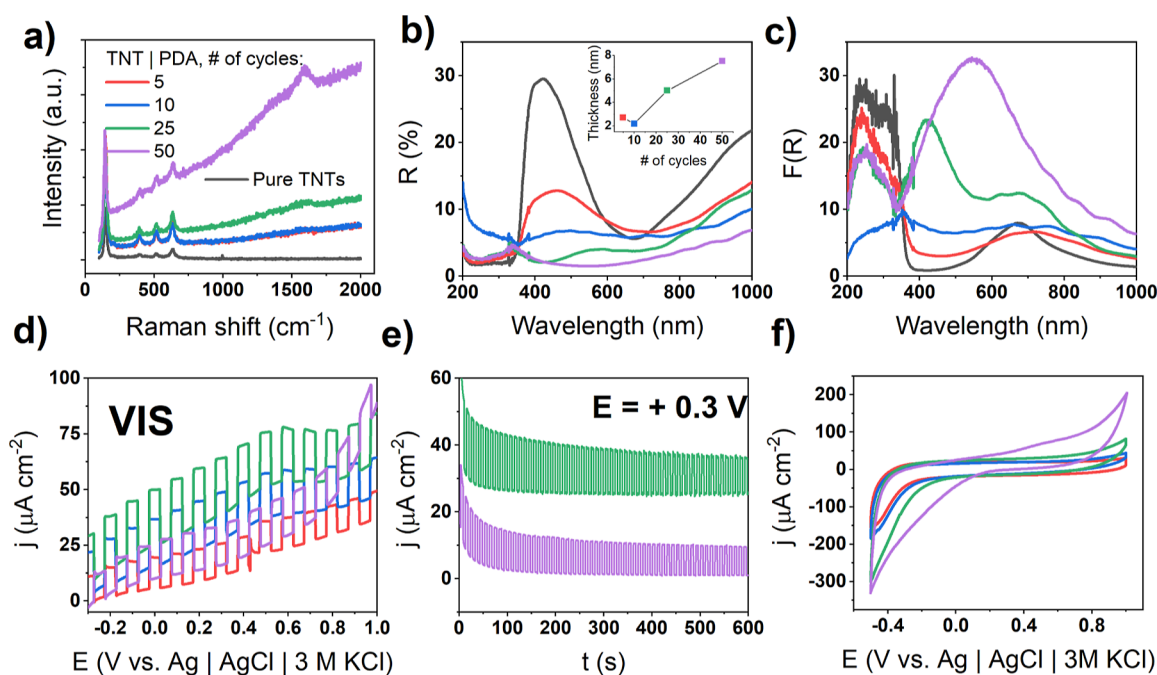
the nanotubes. Manipulation of the anodization voltage is a versatile tool to adjust the nanotube dimensions. In particular, 30 V TNTs have a 700 nm length and a 110 nm diameter, while 40 V TNTs have a 1100 nm length and 160 nm diameter on average.<sup>27</sup> Considering the promising photosensitization capabilities of PDA, the geometry of the nanotubes was optimized to obtain the highest photocurrents in the visible range. The reflectance spectra of TNT|PDA with different TNT geometries, but the same route of PDA deposition, are given in Figure 6a (30 V are represented as blue and 40 V as green curves). For this comparison, the electropolymerization pH was optimized to 8.5 and the number of polymerization cycles was 50. The optical spectra and KM functions show clearly that 40 V TNT|PDA junctions—with wider and longer nanotubes—have higher absorption in the visible range. Additionally, instead of several small absorption bands, there is a single, wide band centered at ca. 550 nm, presumably originating both from changes in the electronic structure and the geometry-dependent scattering.<sup>51,52</sup> The issue of deconvolution of these two effects will be discussed further on the basis of IPCE spectra.

The LSV curves registered during the dark–light cycling (Figure 6d) indicate that 40 V TNT|PDA exhibit photocurrents 3 times higher than 30 V TNT|PDA in the visible range. This fact correlates with the higher absorption edge (lower reflectance). Prolonged potentiostatic polarization at a potential of +0.3 V (Figure 6e) shows that the TNT|PDA exhibits decay of dark current according to the Cottrell equation (i.e., inversely proportional to time), but after ca. 8 min, a steady state is achieved. The PDA modification increases photocurrents by ca. 20 times compared to pristine TNTs. In the steady state (Figure 6f), a magnification from 0.5 to 10  $\mu\text{A cm}^{-2}$  is observed. This

effect, attributed to the absorption by discrete levels of PDA, is greater than previously observed in the literature for  $\text{TiO}_2$ |PDA junctions.<sup>48</sup> Presumably, the key factor explaining the difference is hydrogenation before PDA deposition. Although this information is insufficient to conclude that PDA is stable after UV light exposure, another set of studies have been performed to verify this issue and have been exhaustively discussed in the Supporting Information. In brief, XPS and SEM pictures recorded after 100 cycles of UV exposure strongly suggest that no major changes in morphology and surface chemistry can be detected (Figures S10 and S11). Moreover, TNT\_bPDA retains its optical properties and capability of photocurrent generation at a constant level even after 9 days of measurements and 6 h of continuous polarization and UV–vis exposure (Figures S12, S13, and 7).

Another difference between the electrochemical properties of TNT|PDA depending on the nanotube geometry was noticed. The CV results in Figure 6c show that the capacitive currents of 30 V TNT|PDA are noticeably higher than those of 40 V TNT|PDA. However, in the LSV curves in Figure 6d, the relationship is the opposite and the dark capacitive currents of 30 V TNT|PDA are smaller. Moreover, the dark capacitive currents of 40 V TNT|PDA increase faster with applied potential than those of 30 V TNT|PDA. This behavior suggests that there could be some photoinduced charging of 40 V TNT|PDA leading to the increase of capacitive currents.<sup>57</sup> Presumably, during light exposure, ionic excited states (e.g., anionic radicals) are created in the PDA layer, and thus, the surface charge is generated, which does not decay in the second timescale of the experiment.

The stability of photocurrents was assessed using various methods. Initially, the transient photocurrents of a single sample



**Figure 8.** Comparison of optical and photoelectrochemical properties of 40 V TNT/PDA heterojunctions with different thicknesses of PDA; (a) Raman spectra and (b) reflectance spectra (inset shows the relationship between the number of polymerization cycles and thickness of PDA measured by SEM); (c) KM functions; (d) chopped dark–light LSV scans with a 20 mV scan and visible-range light source; (e) chopped dark–light CA curves for 25 times cycled and 50 times cycled TNT/PDA; (f) CV scans; 0.5 M  $\text{Na}_2\text{SO}_4$  was used as an electrolyte.

were measured over a span of 9 days while exposing it to UV light from an LED with an intensity of  $2.2 \text{ mW}/\text{cm}^2$ . Each day was analyzed separately, as depicted in Figure 7a–f. It is evident from the results that the TNT\_bPDA sample maintains a relatively stable photocurrent response. This suggests that the sample does not experience significant degradation when stored or repeatedly exposed to UV light, electrolytes, or oxygen. Additionally, the response of the TNT\_bPDA sample to a combination of UV–vis light was examined during a 6 h transient measurement, as shown in Figure 7g. Over time, a Cottrellian decay of the total current is observed, affecting the photocurrents in the initial 2 h. However, after this initial period, the response stabilizes and remains mostly unchanged for the following 4 h.

**3.4. Influence of PDA Thickness on Optical and Photoelectrochemical Properties of TNT/PDA Heterojunctions.** The thickness of PDA depends on many factors such as the solvent, ionic environment, and synthetic approach,<sup>11,12,58,59</sup> which have a profound role in the properties of the semiconductor/PDA heterojunctions.<sup>23,25</sup> In our work, the thickness of the PDA electropolymerized in  $\text{TiO}_2$  is almost linearly dependent on the number of CV cycles during electropolymerization with the limiting value of ca. 8 nm (inset in Figure 8b). Similar behavior was observed in the work of Kund et al.<sup>59</sup> Diffuse reflectance spectra and KM functions show that as the PDA thickens, absorption in the visible range is more pronounced and the band-to-band absorption edge plummets (Figure 8b,c).

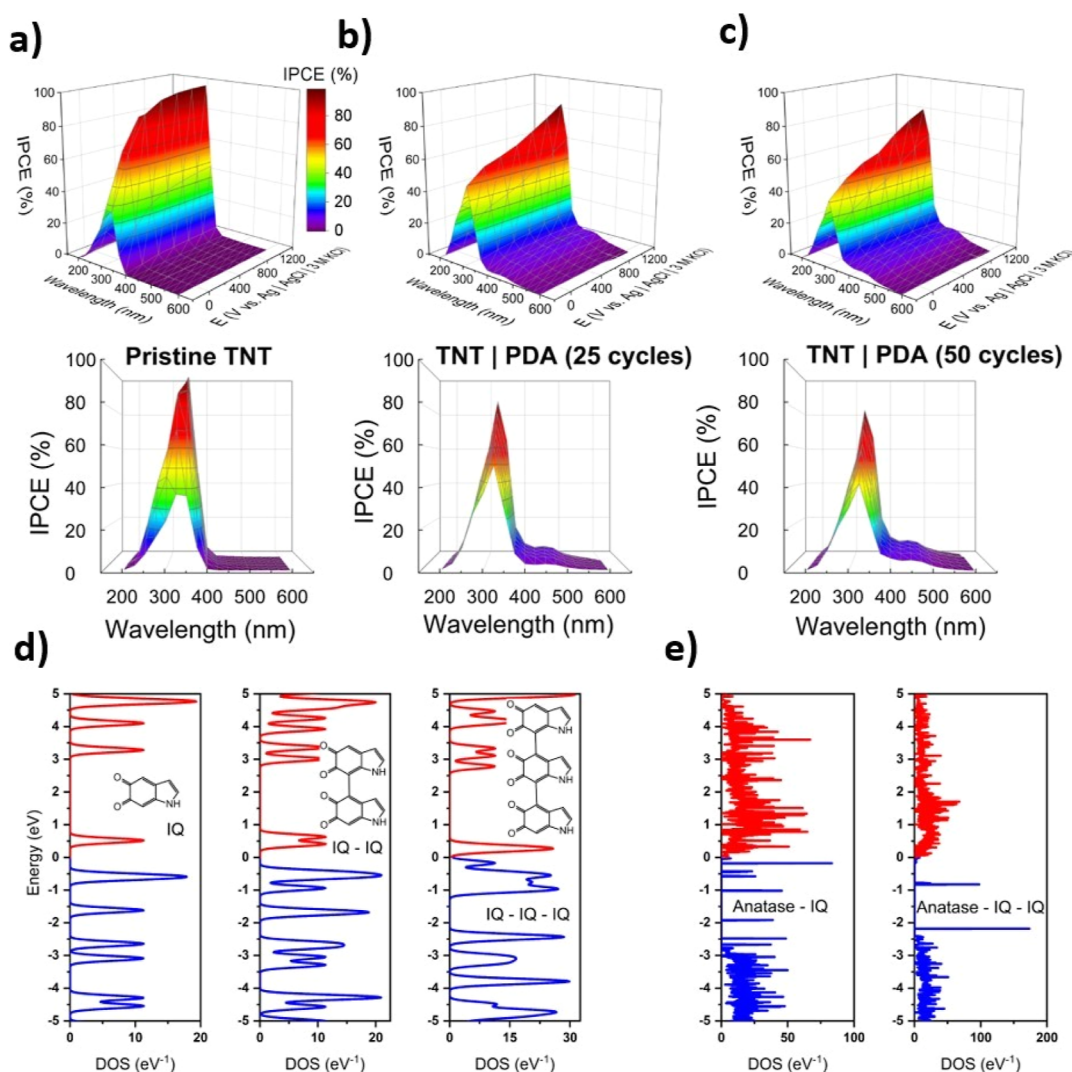
Raman spectra show several characteristic bands of anatase for both pristine TNT and all TNT/PDA samples.<sup>27,50</sup> However, with the increasing PDA thickness, additional D and G bands of  $\text{sp}^2$  rings emerge and the relative intensity with respect to anatase signals drastically increases (Figure 8a). The observed D and G bands are especially pronounced for the thickest PDA layer, with

a significant increase of the baseline, indicating fluorescence<sup>60</sup> (see the Raman maps shown in Figures S4–S7).

The magnitude of photocurrents in the visible range is the smallest for 5-cycled PDA ( $13 \mu\text{A cm}^{-2}$ ), which then increases (to  $30 \mu\text{A cm}^{-2}$ ) for 25-cycled TNT/PDA and slightly decreases for 50-cycled TNT/PDA ( $25 \mu\text{A cm}^{-2}$ ). On the one hand, the photocurrent baseline is twice as high for 25-cycled TNT/PDA with respect to 50-cycled TNT/PDA, and on the other hand, dark CV currents show that the capacitive currents are higher for the thickest PDA (Figure 8d–f). This increase again suggests a photocharging effect in the PDA layer with a 5 nm thickness with nonvanishing charges in the timescale of the experiment.<sup>57</sup>

Enhancement of the photocurrent response by PDA was further confirmed by quantum efficiency measurements (Figure 9a–c). The IPCE map registered for pristine TNTs exhibits a characteristic band edge starting at 400 nm with a maximum at 350 nm (80% efficiency) for a wide range of polarizations (0–1200 mV vs  $\text{Ag}/\text{AgCl}/3 \text{ M KCl}$ ). Zero efficiency is observed for wavelengths longer than 410 nm. The magnitude of the IPCE maximum remains almost constant regardless of the applied potential. However, when TNT/PDA structures are considered, an additional small IPCE band emerges in the whole visible spectrum, with a maximum at 450 nm reaching 9% IPCE for the 25-cycled sample and 14% for the 50-cycled sample. The presence of this peak explains the photocurrent enhancement after the application of the PDA coating. These enhancements in the visible region can be observed in detail on the transient photocurrent plots recorded for different wavelengths and several samples, strongly suggesting that the phenomenon is universal to the proposed PDA modification. Furthermore, the IPCE maximum for the  $\text{TiO}_2$  band edge is smaller for TNT/PDA and increases with the applied anodic potential. Presumably, because PDA covers the nanotube walls, most of the photon absorption occurs inside the PDA layer, so band-to-band transitions are quenched. Additionally, oxidation of PDA leads





**Figure 9.** Comparison of quantum efficiency maps of 40 V TNT/PDA heterojunctions with different thicknesses of PDA, (a) pure TNTs, (b) 25-cycled TNT/PDA, (c) 50-cycled TNT/PDA, (d) DOS spectra of the isolated PDA monomer (IQ), dimer (IQ–IQ), and trimer (IQ–IQ–IQ); (e) DOS spectra of the PDA monomer and dimer adsorbed on the anatase (101) surface.

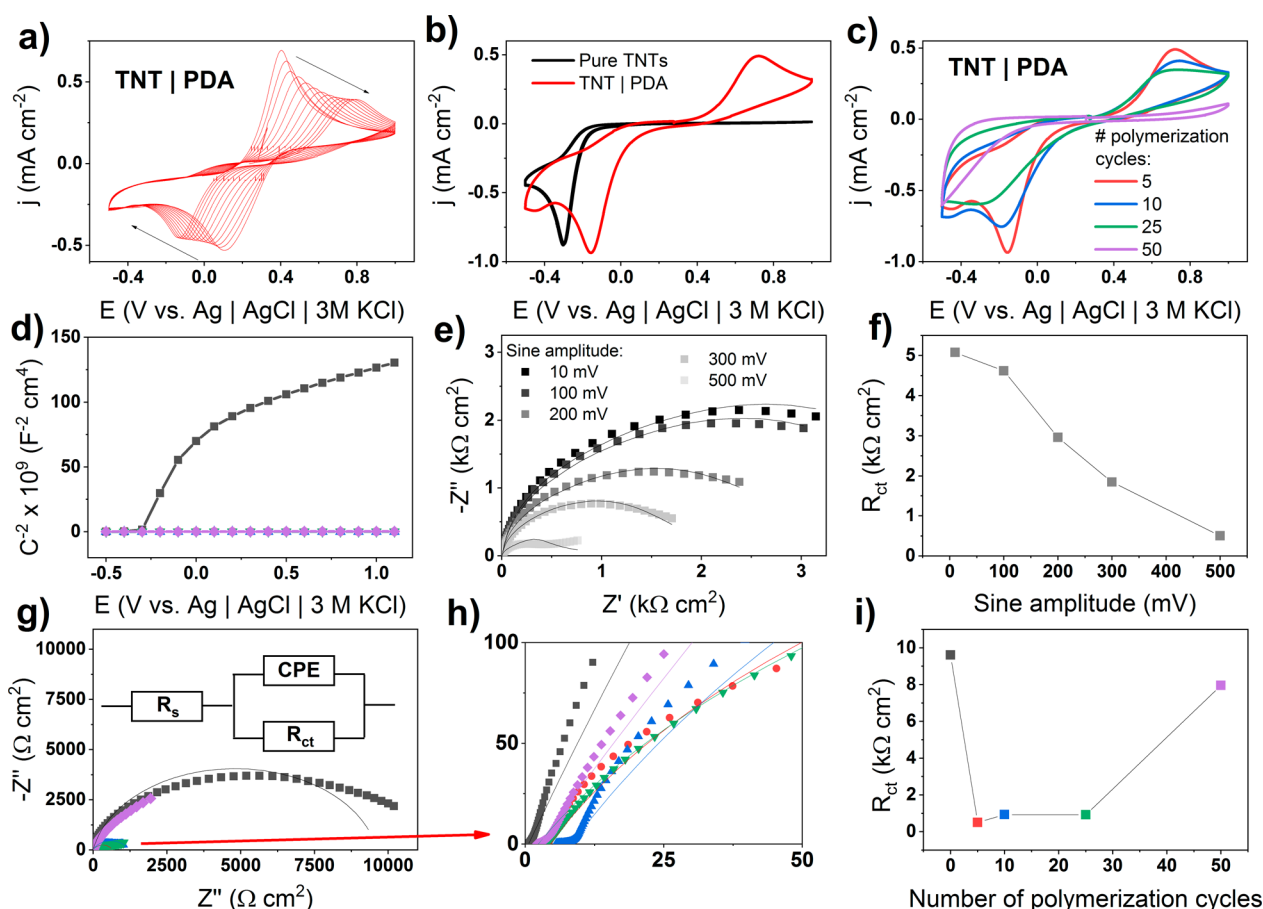
to the increased contribution of quinone units, which have a lower HOMO–LUMO gap (Figure 5), so the absorption rate is higher, and therefore, the IPCE is higher. The thickest PDA layer (TNT/PDA 50 cycles) results in a higher magnitude of the IPCE in the visible part of the spectrum, which correlates well with the changes observed in the reflectance spectra (Figure 8b,c).

DFT-based DOS spectra of PDA with variable chain lengths were computed for further elucidation of its thickness-dependent photoelectrochemical properties (Figure 9d). It is easy to see that the HOMO–LUMO gap decreases from 0.7 eV for one unit of PDA to basically 0.0 eV for three units of PDA. This is because the density contributions from  $\pi$  orbitals of the conjugated system overlap. This behavior would explain the experimentally observed fact that a larger amount of polymerization cycles during PDA synthesis leads to greater enhancement of optical absorption (Figure 8b,c). As shown in Figure 5, when PDA units are adsorbed on the anatase surface, several intraband energy levels emerge and the edges of the conduction and VBs are smeared out. Interestingly, single-unit PDA introduces up to 8 intraband states, while double-unit PDA introduces only two states, but their electronic population is

markedly higher (Figure 9e). Moreover, the energy distance between the most highly populated intraband state and the conduction band of the anatase equals 2.2 eV, which corresponds to a 550 nm wavelength—almost exactly at the onset of the IPCE band for TNT/PDA structures. Therefore, IPCE analysis in conjunction with DFT calculations gives strong evidence that intraband states introduced by the PDA increase the photoactivity of TNT/PDA in the visible range.

### 3.5. Semimetallic Character of the TNT/PDA Interface.

So far, several sets of data, including reflectance spectra, Mott–Schottky plots, DFT analysis, and quantum efficiency maps, have suggested that the TNT acquires a semimetallic character after modification with PDA. This section focuses on an in-depth analysis of the properties of this interface by employing the electrochemistry of ferrocyanides in a standard and nonlinear approach. Figure 10a shows the first 10 cyclic voltammograms of TNT/PDA when exposed to a 5 mM solution of ferrocyanides. The first cycle consists of two symmetric redox peaks located at +0.15 and +0.35 V. Although the peak separation is 200 mV, and therefore the reaction is irreversible, this curve resembles the response characteristic of metallic surfaces, such as gold and platinum.<sup>61</sup> However, with



**Figure 10.** Investigations of the electrical and electrochemical properties of the TNT/PDA heterojunction; (a) 10 subsequent CV cycles (50 mV/s rate) of TNT/PDA in 5 mM ferrocyanides; (b) comparison of ferrocyanide response of TNTs and TNT/PDA after stabilization; comparison of (c) ferrocyanide response and (d) Mott–Schottky plots for TNT/PDA with different thicknesses of PDA; (e) NL-EIS spectra of TNT/PDA recorded in 5 mM ferrocyanides with different amplitudes of stimulating single-sine voltage; (f) nonlinear relationship between charge-transfer resistance and amplitude of stimulating voltage; (g–i) comparison of EIS spectra for TNT/PDA with different thicknesses of PDA and the relationship between charge-transfer resistance and thickness of PDA [supporting electrolyte was always 0.5 M Na<sub>2</sub>SO<sub>4</sub>; the equivalent circuit for all fitting was the one depicted in (g)].

consecutive cycling, the peak separation increases, and the symmetry is lost—the reduction peaks are slightly larger. After ca. 10 cycles, the CV curves are stabilized with a peak separation equal to ca. 850 mV.

The ferrocyanide response of pure TNT consists only of the reduction peak at  $-0.33$  V (Figure 10b) as TiO<sub>2</sub> is an n-type semiconductor with a wide band gap and an oxidation peak is expected. However, after PDA modification, this peak is shifted toward more positive potentials and an oxidation peak is also present. These data further strongly suggest that the PDA introduced a set of energy levels associated with surface midgap states, effectively changing the character of the titania surface toward semimetallic while preserving the capability of photocurrent generation through the separation of charge carriers in the space charge region of TiO<sub>2</sub>. The hypothesis is that the quinone catechol redox pairs abundant in the PDA chain play a crucial role as redox mediators that enable charge transfers in the energy range inside the band gap.<sup>16,62,63</sup> In other words, even in dark conditions, holes of the VB migrate to the surface states of the TNT and oxidize catechols to quinones. These quinones are then capable of oxidizing ferrocyanides, which was energetically impossible for direct oxidation by VB holes. Consecutive cycling increases the potential difference between the ferrocyanide peaks (Figure 10a) presumably due to depletion of surface

states—fewer surface states occupied by holes lead to less oxidation of catechols and a higher energetic barrier for the oxidation of Fe(II) to Fe(III).

Figure 10c shows differences in the response for various thicknesses of PDA. 5-Cycled, 10-cycled, and 25-cycled samples have similar responses with a notable decrease in the magnitude of the redox peaks with the PDA thickness. However, for a 50-cycle sample, the redox response is completely diminished. The hypothesis explaining this phenomenon is that when the PDA thickness reaches a certain threshold (in this case, 8 nm), electron transfer processes are quenched; i.e., electrons can no longer tunnel through the PDA layer. This behavior was observed frequently in other works, but the limiting thickness is dependent on the substrate semiconductor material.<sup>23,25,54</sup> In other words, regardless of the hole oxidizing the catechol on the TNT side of the PDA, the electron from the Fe(II) cannot tunnel through the other side of the PDA to complete the reaction. Therefore, the Fe(II) stays reduced and there are no oxidation current peaks on the CV curves. Interestingly, the Mott–Schottky analysis shows that all TNT/PDA interfaces exhibit a semimetallic character regardless of the thickness of PDA (Figure 10d). Supposedly, while the ferrocyanide response involves charge transfer and tunneling of the electrons, the Mott–Schottky analysis utilizes information mostly about the



double-layer structure. Therefore, there is no upper limit in the tunneling distance, and the double-layer structure of TNTIPDA remains semimetallic regardless of the thickness.

For further investigation of the TNTIPDA electrical properties, EIS was employed in the nonlinear potential regime (NL-EIS). In this setup, very high amplitudes of the potential stimulus were applied purposely, so the higher-order effects would occur.<sup>64</sup> The equivalent circuit for fitting was the Randles circuit with a constant-phase element (CPE), i.e.,  $R(CPE, R)$ , in Figure 10g. The fitting procedure was conducted using open-source EIS spectrum analyzer software.<sup>65</sup>

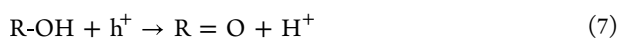
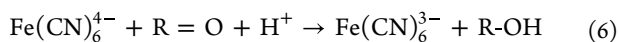
Figure 10e shows the NL-EIS first harmonic spectra registered in 5 mM ferrocyanides for a 10-cycled electrode (2 nm-thick PDA) with different sine amplitudes of 10 to 500 mV. Before each NL-EIS measurement, the TNTIPDA specimen was polarized for 3 min at the formal potential of the ferrocyanide redox pair. It is easy to see that the sizes of the semicircles are gradually decreasing with the amplitude. The explanation is that higher amplitudes allow the potential to sweep to the vicinity of the oxidation and reduction peaks (see Figure 10b). As a result, with higher amplitudes, more Faradaic current is registered, and thus, the polarization resistance is lowered. Inevitably, charge-transfer resistance also decreases with amplitude, almost linearly in the wide range of potentials (Figure 10f and Table S1). According to the Butler–Volmer theory, a Faradaic current for a single reaction during strong oxidative polarization is given by eq 4<sup>61</sup>

$$I = FADk^0 \exp\left(\frac{(1 - \alpha)nF}{RT}\eta\right) = I^0 \exp(A\eta) \quad (4)$$

where  $F$  is the Faraday constant,  $A$  is the electrode surface,  $D$  is the diffusion coefficient of ferrocyanides,  $k^0$  is the kinetic constant,  $\alpha$  is the Butler–Volmer charge transfer coefficient,  $R$  is the universal gas constant, and  $\eta$  is the overpotential. In this theory, the differential charge-transfer resistance is given by eq 5<sup>61</sup>

$$R_{ct} = \frac{d\eta}{dI} = \frac{\exp(-A\eta)}{I^0 A} = \frac{1}{I^0 A} \left( 1 - A\eta + \frac{(A\eta)^2}{2} - \frac{(A\eta)^3}{6} + \dots \right) \quad (5)$$

Considering that the experimental potential amplitude was up to 0.5 V, which is a strong oxidation polarization, this equation is valid. The linear term is negative, which represents a decrease in the charge-transfer resistance with applied positive potential, which is observed in the experiment. However, the expected dependence of the charge-transfer resistance is exponential and not linear. Therefore, two sources of nonlinearity must be present in the experimental system, so the higher-order terms in the Taylor expansion can cancel out, leaving a linear dependence. The first of them is the oxidation of ferrocyanides. Based on the chemistry of PDA, the second source is hypothesized to be catechol/quinone reactions that are localized across the PDA chain.<sup>15,66</sup> The following simplified mechanism of the ferrocyanide electrochemistry on the TNTIPDA surface is proposed in eqs 6 and 7



First, there is a proton-coupled chemical step, and the electron is transferred from ferrocyanide to quinone. As a result, quinone-PDA is transformed into catechol-PDA. Then, there is an electrochemical step that involves hole transfer from the VB to the catechol-PDA, effectively regenerating quinone-PDA. The anodic current registered during the voltammetry of TNTIPDA presumably comes from the reduction of quinones by Fe(II) being oxidized, and the cathodic current comes from the oxidation of catechols by Fe(III) being reduced.

With regard to the experimentally and theoretically discussed properties, we propose an alternative view of the electrochemistry of PDA semiconductor interfaces. In this model, the PDA structural units behave as a set of spatially distributed redox mediators or as an electroactive polymer, rather than as a semiconductive polymer. This viewpoint explains why a slight change in the thickness of PDA leads to huge differences in the electrical and electrochemical properties of the TNTIPDA junction in our work (see Figure 8c–f). If the layer of redox mediators is too high, the electron cannot tunnel, and all currents are diminished. However, the absorption observed in UV–vis spectroscopy remains high because of the low HOMO–LUMO gap of each quinone unit of PDA. This model is also in agreement with recently published computational work by Matta et al., who showed localized dipole moments across the PDA octamers included by catechol/quinone pairs, leading to the entrapment of electrons and holes.<sup>66</sup>

Finally, high-voltage sine-amplitude (500 mV) NL-EIS spectra were collected for TNTIPDA samples with different PDA thicknesses (Figure 10g–i). In the case of pure TNTs, there is a huge semicircle, and the charge-transfer resistance is equal to 10 kΩ cm<sup>2</sup>. This behavior is because only the reduction of ferrocyanides can occur on this material. However, for the 5-cycled, 10-cycled, and 25-cycled TNTIPDA samples, the semicircles are smaller and there is a tremendous decrease in the charge-transfer resistance down to ca. 0.5 kΩ cm<sup>2</sup> (Table S2). Moreover, in the case of the 50-cycled sample, both the size of the semicircle and  $R_{ct}$  increase once again. These observations support the previously introduced idea that smaller thicknesses of PDA (5 nm) facilitate charge transfer, while bigger thicknesses (8 nm) quench the charge transfer.

In contrast to the  $R_{ct}$  variations, the  $Q$  values of the CPE elements remain constant regardless of the sinus amplitude. In other words, the structure of the double layer does not contain significant electrical nonlinearities. It should be acknowledged that the quality of the fit in the low-frequency region is getting poorer, which is typical behavior in nonlinear EIS experiments.<sup>64</sup> In summary, there are several pieces of evidence suggesting the semimetallic character of the designed TNTIPDA junctions. The presence of both oxidation and reduction peaks on the CV curves for ferrocyanide electrochemistry was observed, while TiO<sub>2</sub> is an n-type semiconductor and should exhibit only a reduction peak. The missing flat-band potential and potential-dependent capacitance were registered during the Mott–Schottky analysis. The double layer is the only source of the capacitance and space charge region characteristic for semiconductors that was not observed or was negligible. We recorded additional absorption bands on optical spectroscopy in the visible range analogously to those observed in plasmonic metallic nanoparticles.<sup>67</sup> Furthermore, an additional band revealed on the IPCE action map in the visible range strongly suggests the presence of midgap states capable of both electronic excitation and separation of excitons.<sup>68</sup> However, the electric

field required for the separation was not induced in the space charge layer but rather by the intermolecular interactions. Lastly, the conducted DFT calculations of the  $\text{TiO}_2$ –PDA interfaces supported the concept of occupied midgap states since the Fermi level crosses those states located at the bottom of the conduction band similarly as it crosses the occupied band in the case of metals. It is worth noting that the semimetallic properties of PDA within the TNT–PDA composite could be confirmed through measurements of its electrical characteristics at varying temperatures. However, due to the temperature sensitivity of the synthesized PDA and its thermal decomposition at 175 °C, it was impossible to construct an effective Arrhenius plot (refer to Figure S14 in the Supporting Information file). Ultraviolet photoelectron spectroscopy (UPS) is another possible complementary technique to investigate the semimetallicity issue. However, this method requires high vacuum conditions that could potentially alter the morphology of the entire structure, including both the PDA coating and the nanotubes underneath. Furthermore, while PDA is stable when exposed to near-UV light, which is relevant for photoelectrochemical applications, it remains uncertain whether far-UV light would maintain the surface chemistry. As a result, the use of UPS for the TNT–PDA material under investigation is debatable.

#### 4. CONCLUSIONS

In this work, PDA was deposited uniformly on the surface of hydrogenated TNTs through potentiodynamic electropolymerization. The chemical structure of the resulting PDA layer and its adsorption geometry on the surface of  $\text{TiO}_2$  at both molecular and micrometer scales are highly dependent on the pH used for the electropolymerization. Several structure–property relationships were established:

- After PDA modification, a set of localized midgap states are introduced into the DOS spectrum of  $\text{TiO}_2$  and a significant portion of these states is occupied, leading to the semimetallic properties of the TNT/PDA junctions.
- XPS studies and DFT analyses indicate that the alkaline-based PDA exhibits more conjugated quinone units with a lower HOMO–LUMO gap than catecholic units compared to acid-based PDA, leading to higher absorption in the visible range.
- Up to a 20× increase in the photocurrent response of TNTs is observed, and the IPCE maps indicate that the enhancement occurs mainly in the visible range.
- Electrochemical investigations of the TNT/PDA junctions also suggest the semimetallic character of the material because both oxidation and reduction peaks are present on the ferrocyanide voltammograms, and the Mott–Schottky plot does not exhibit the flat-band potential.

The study proposes a cheap and facile strategy for photosensitization of metal oxide semiconductors with PDA. On top of that, both experimental and theoretical results strongly suggest the semimetallic character of the modified material in which PDA serves as a set of surface-distributed redox mediators rather than a semiconductive polymer. This viewpoint opens up a new perspective for understanding the general properties of polymer semiconductor junctions instead of the standard picture of the p–n junction. Consequently, in the long term, this perspective might be helpful in improving the performance of various photoelectrochemical devices.

#### ■ ASSOCIATED CONTENT

##### Supporting Information

The Supporting Information is available free of charge at <https://pubs.acs.org/doi/10.1021/acs.jpcc.2c08804>.

Quantitative analysis of the XPS data of TNT\_PDA samples; EIS equivalent circuit parameters obtained from fitting the spectra presented in Figure 9; additional SEM images with different magnifications and areas on the sample; Raman maps and data elucidating the issue of PDA uniformity; transient photocurrents of four different TNT\_b-PDA samples using monochromatic illumination; data connected to the issue of PDA stability, including SEM, XPS, FT-IR, optical, and FT-IR measurements of TNT\_PDA before and after exposure to UV light; and two-point probe measurements of the TNT-bPDA electrical properties (PDF)

#### ■ AUTHOR INFORMATION

##### Corresponding Author

Robert Bogdanowicz – Department of Metrology and Optoelectronics, Faculty of Electronics, Telecommunications and Informatics, Gdańsk University of Technology, 80-233 Gdańsk, Poland; [orcid.org/0000-0002-7543-2620](https://orcid.org/0000-0002-7543-2620); Email: [rbogdan@eti.pg.edu.pl](mailto:rbogdan@eti.pg.edu.pl)

##### Authors

Adrian Olejnik – Department of Metrology and Optoelectronics, Faculty of Electronics, Telecommunications and Informatics, Gdańsk University of Technology, 80-233 Gdańsk, Poland; Centre for Plasma and Laser Engineering, The Szwedzki Institute of Fluid-Flow Machinery, Polish Academy of Sciences, 80-231 Gdańsk, Poland; [orcid.org/0000-0002-1807-8995](https://orcid.org/0000-0002-1807-8995)  
Karol Olbrys – Faculty of Chemistry, Gdańsk University of Technology, 80-233 Gdańsk, Poland  
Jakub Karczewski – Institute of Nanotechnology and Materials Engineering and Advanced Materials Center, Gdańsk University of Technology, 80-233 Gdańsk, Poland  
Jacek Ryl – Institute of Nanotechnology and Materials Engineering and Advanced Materials Center, Gdańsk University of Technology, 80-233 Gdańsk, Poland; [orcid.org/0000-0002-0247-3851](https://orcid.org/0000-0002-0247-3851)  
Katarzyna Siuzdak – Centre for Plasma and Laser Engineering, The Szwedzki Institute of Fluid-Flow Machinery, Polish Academy of Sciences, 80-231 Gdańsk, Poland; [orcid.org/0000-0001-7434-6408](https://orcid.org/0000-0001-7434-6408)

Complete contact information is available at: <https://pubs.acs.org/doi/10.1021/acs.jpcc.2c08804>

##### Notes

The authors declare the following competing financial interest(s): Elements of this work are submitted as a patent proposal to the Polish Patent Office #P.442200. No other financial interests or personal relationships are declared.

#### ■ ACKNOWLEDGMENTS

This work was financially supported by the Polish Ministry of Science and Higher Education through Diamentowy grant DI2019 017649. R.B. acknowledges the funding from the National Science Centre, Poland, under the OPUS call in the Weave programme (project number: 2021/43/I/ST7/03205).

## REFERENCES

- (1) Aguilar-Ferrer, D.; Szweczyk, J.; Coy, E. Recent Developments in Polydopamine-Based Photocatalytic Nanocomposites for Energy Production: Physico-Chemical Properties and Perspectives. *Catal. Today* **2022**, 397–399, 316–349.
- (2) Cao, W.; Zhou, X.; McCallum, N. C.; Hu, Z.; Ni, Q. Z.; Kapoor, U.; Heil, C. M.; Cay, K. S.; Zand, T.; Mantanona, A. J.; et al. Unraveling the Structure and Function of Melanin through Synthesis. *J. Am. Chem. Soc.* **2021**, 143, 2622–2637.
- (3) Lee, H. A.; Park, E.; Lee, H. Polydopamine and Its Derivative Surface Chemistry in Material Science: A Focused Review for Studies at KAIST. *Adv. Mater.* **2020**, 32, 1907505.
- (4) Ryu, J. H.; Messersmith, P. B.; Lee, H. Polydopamine Surface Chemistry: A Decade of Discovery. *ACS Appl. Mater. Interfaces* **2018**, 10, 7523–7540.
- (5) Huang, Q.; Chen, J.; Liu, M.; Huang, H.; Zhang, X.; Wei, Y. Polydopamine-Based Functional Materials and Their Applications in Energy, Environmental, and Catalytic Fields: State-of-the-Art Review. *Chem. Eng. J.* **2020**, 387, 124019.
- (6) Liebscher, J.; Mrówczyński, R.; Scheidt, H. A.; Filip, C.; Hädäde, N. D.; Turcu, R.; Bende, A.; Beck, S. Structure of Polydopamine: A Never-Ending Story? *Langmuir* **2013**, 29, 10539–10548.
- (7) Abdel-Aziz, A. M.; Hassan, H. H.; Badr, I. H. A. Glassy Carbon Electrode Electromodification in the Presence of Organic Monomers: Electropolymerization versus Activation. *Anal. Chem.* **2020**, 92, 7947–7954.
- (8) d'Ischia, M.; Napolitano, A.; Ball, V.; Chen, C.-T.; Buehler, M. J. Polydopamine and Eumelanin: From Structure–Property Relationships to a Unified Tailoring Strategy. *Acc. Chem. Res.* **2014**, 47, 3541–3550.
- (9) Delparastan, P.; Malollari, K. G.; Lee, H.; Messersmith, P. B. Direct Evidence for the Polymeric Nature of Polydopamine. *Angew. Chem.* **2019**, 131, 1089–1094.
- (10) Hong, S.; Na, Y. S.; Choi, S.; Song, I. T.; Kim, W. Y.; Lee, H. Non-Covalent Self-Assembly and Covalent Polymerization Co-Contribute to Polydopamine Formation. *Adv. Funct. Mater.* **2012**, 22, 4711–4717.
- (11) Della Vecchia, N. F.; Luchini, A.; Napolitano, A.; D'Errico, G.; Vitiello, G.; Szekely, N.; d'Ischia, M.; Paduano, L. Tris Buffer Modulates Polydopamine Growth, Aggregation, and Paramagnetic Properties. *Langmuir* **2014**, 30, 9811–9818.
- (12) Coskun, H.; Aljabour, A.; Uiberlacker, L.; Strobel, M.; Hild, S.; Cobet, C.; Farka, D.; Stadler, P.; Sariciftci, N. S. Chemical Vapor Deposition - Based Synthesis of Conductive Polydopamine Thin-Films. *Thin Solid Films* **2018**, 645, 320–325.
- (13) Jin, Z.; Yang, L.; Shi, S.; Wang, T.; Duan, G.; Liu, X.; Li, Y. Flexible Polydopamine Bioelectronics. *Adv. Funct. Mater.* **2021**, 31, 2103391.
- (14) Yang, L.; Guo, X.; Jin, Z.; Guo, W.; Duan, G.; Liu, X.; Li, Y. Emergence of Melanin-Inspired Supercapacitors. *Nano Today* **2021**, 37, 101075.
- (15) Zou, Y.; Chen, X.; Yang, P.; Liang, G.; Yang, Y.; Gu, Z.; Li, Y. Regulating the Absorption Spectrum of Polydopamine. *Sci. Adv.* **2020**, 6, No. eabb4696.
- (16) Daboss, S.; Lin, J.; Godejohann, M.; Kranz, C. Redox Switchable Polydopamine-Modified AFM-SECM Probes: A Probe for Electrochemical Force Spectroscopy. *Anal. Chem.* **2020**, 92, 8404–8413.
- (17) Almeida, L. C.; Frade, T.; Correia, R. D.; Niu, Y.; Jin, G.; Correia, J. P.; Viana, A. S. Electrosynthesis of Polydopamine-Ethanolamine Films for the Development of Immunosensing Interfaces. *Sci. Rep.* **2021**, 11, 2237.
- (18) Olejnik, A.; Ficek, M.; Szkodo, M.; Stanisławska, A.; Karczewski, J.; Ryl, J.; Dołęga, A.; Siuzdak, K.; Bogdanowicz, R. Tailoring Diffusional Fields in Zwitterion/Dopamine Copolymer Electropolymerized at Carbon Nanowalls for Sensitive Recognition of Neurotransmitters. *ACS Nano* **2022**, 16, 13183–13198.
- (19) Leibl, N.; Duma, L.; Gonzato, C.; Haupt, K. Polydopamine-Based Molecularly Imprinted Thin Films for Electro-Chemical Sensing of Nitro-Explosives in Aqueous Solutions. *Bioelectrochemistry* **2020**, 135, 107541.
- (20) Jastrzebska, M. M.; Isotalo, H.; Paloheimo, J.; Stubb, H. Electrical Conductivity of Synthetic DOPA-Melanin Polymer for Different Hydration States and Temperatures. *J. Biomater. Sci., Polym. Ed.* **1996**, 7, 577–586.
- (21) Mostert, A. B.; Powell, B. J.; Pratt, F. L.; Hanson, G. R.; Sarna, T.; Gentle, I. R.; Meredith, P. Role of Semiconductivity and Ion Transport in the Electrical Conduction of Melanin. *Proc. Natl. Acad. Sci. U.S.A.* **2012**, 109, 8943–8947.
- (22) Corani, A.; Huijser, A.; Gustavsson, T.; Markovitsi, D.; Malmqvist, P.-Å.; Pezzella, A.; d'Ischia, M.; Sundström, V. Superior Photoprotective Motifs and Mechanisms in Eumelanins Uncovered. *J. Am. Chem. Soc.* **2014**, 136, 11626–11635.
- (23) Kim, Y.; Coy, E.; Kim, H.; Mrówczyński, R.; Torruella, P.; Jeong, D.-W.; Choi, K. S.; Jang, J. H.; Song, M. Y.; Jang, D. J.; et al. Efficient Photocatalytic Production of Hydrogen by Exploiting the Polydopamine-Semiconductor Interface. *Appl. Catal., B* **2021**, 280, 119423.
- (24) Dimitrijevic, N. M.; Saponjic, Z. V.; Rabatic, B. M.; Poluektov, O. G.; Rajh, T. Effect of Size and Shape of Nanocrystalline TiO<sub>2</sub> on Photogenerated Charges. An EPR Study. *J. Phys. Chem. C* **2007**, 111, 14597–14601.
- (25) Guan, P.; Bai, H.; Li, C.; Ge, Y.; Xu, D.; Chen, B.; Xia, T.; Fan, W.; Shi, W. Integrated Heterostructure of PDA/Bi-AgIn<sub>5</sub>S<sub>8</sub>/TiO<sub>2</sub> for Photoelectrochemical Hydrogen Production: Understanding the Synergistic Effect of Multilayer Structure. *Adv. Mater. Interfaces* **2018**, 5, 1701574.
- (26) Mao, W.-X.; Lin, X.-J.; Zhang, W.; Chi, Z.-X.; Lyu, R.-W.; Cao, A.-M.; Wan, L.-J. Core–Shell Structured TiO<sub>2</sub>@polydopamine for Highly Active Visible-Light Photocatalysis. *Chem. Commun.* **2016**, 52, 7122–7125.
- (27) Wawrzyniak, J.; Grochowska, K.; Karczewski, J.; Kupracz, P.; Ryl, J.; Dołęga, A.; Siuzdak, K. The Geometry of Free-Standing Titania Nanotubes as a Critical Factor Controlling Their Optical and Photoelectrochemical Performance. *Surf. Coat. Technol.* **2020**, 389, 125628.
- (28) Wawrzyniak, J.; Karczewski, J.; Kupracz, P.; Grochowska, K.; Coy, E.; Mazikowski, A.; Ryl, J.; Siuzdak, K. Formation of the Hollow Nanopillar Arrays through the Laser-Induced Transformation of TiO<sub>2</sub> Nanotubes. *Sci. Rep.* **2020**, 10, 20235.
- (29) Vargas, W. E.; Niklasson, G. A. Applicability Conditions of the Kubelka–Munk Theory. *Appl. Opt.* **1997**, 36, 5580.
- (30) Atomistix Toolkit Version 2019.03, Synopsys QuantumWise A/S ([www.quantumwise.com](http://www.quantumwise.com)).
- (31) Soler, J. M.; Artacho, E.; Gale, J. D.; García, A.; Junquera, J.; Ordejón, P.; Sánchez-Portal, D. The SIESTA Method for Ab Initio Order- N Materials Simulation. *J. Phys.: Condens. Matter* **2002**, 14, 2745–2779.
- (32) van Setten, M. J.; Giantomassi, M.; Bousquet, E.; Verstraete, M. J.; Hamann, D. R.; Gonze, X.; Rignanese, G.-M. The PseudoDojo: Training and Grading a 85 Element Optimized Norm-Conserving Pseudopotential Table. *Comput. Phys. Commun.* **2018**, 226, 39–54.
- (33) Mayo, S. L.; Olafson, B. D.; Goddard, W. A. DREIDING: A Generic Force Field for Molecular Simulations. *J. Phys. Chem.* **1990**, 94, 8897–8909.
- (34) Ferreira, L. G.; Marques, M.; Teles, L. K. Slater Half-Occupation Technique Revisited: The LDA-1/2 and GGA-1/2 Approaches for Atomic Ionization Energies and Band Gaps in Semiconductors. *AIP Adv.* **2011**, 1, 032119.
- (35) Wawrzyniak, J.; Karczewski, J.; Coy, E.; Iatsunskyi, I.; Ryl, J.; Gazda, M.; Grochowska, K.; Siuzdak, K. Spectacular Oxygen Evolution Reaction Enhancement through Laser Processing of the Nickel-Decorated Titania Nanotubes. *Adv. Mater. Interfaces* **2021**, 8, 2001420.
- (36) Wawrzyniak, J.; Karczewski, J.; Kupracz, P.; Grochowska, K.; Załęski, K.; Pshyk, O.; Coy, E.; Bartmański, M.; Szkodo, M.; Siuzdak, K. Laser-Assisted Modification of Titanium Dioxide Nanotubes in a Tilted Mode as Surface Modification and Patterning Strategy. *Appl. Surf. Sci.* **2020**, 508, 145143.
- (37) Szkodo, M.; Trzciński, K.; Rysz, J.; Gazda, M.; Siuzdak, K.; Lisowska-Oleksiak, A. Electrodes Consisting of PEDOT Modified by



Prussian Blue Analogues Deposited onto Titania Nanotubes – Their Highly Improved Capacitance. *Solid State Ionics* **2017**, *302*, 197–201.

(38) Raghunath, P.; Huang, W. F.; Lin, M. C. Quantum Chemical Elucidation of the Mechanism for Hydrogenation of TiO<sub>2</sub> Anatase Crystals. *J. Chem. Phys.* **2013**, *138*, 154705.

(39) Siuzdak, K.; Szkoda, M.; Lisowska-Oleksiak, A.; Karczewski, J.; Ryl, J. Highly Stable Organic–Inorganic Junction Composed of Hydrogenated Titania Nanotubes Infiltrated by a Conducting Polymer. *RSC Adv.* **2016**, *6*, 33101–33110.

(40) Amiri, M.; Amali, E.; Nematollahzadeh, A.; Salehniya, H. Poly-Dopamine Films: Voltammetric Sensor for PH Monitoring. *Sens. Actuators, B* **2016**, *228*, 53–58.

(41) Chalmers, E.; Lee, H.; Zhu, C.; Liu, X. Increasing the Conductivity and Adhesion of Polypyrrole Hydrogels with Electropolymerized Polydopamine. *Chem. Mater.* **2020**, *32*, 234–244.

(42) Olejnik, A.; Ficek, M.; Siuzdak, K.; Bogdanowicz, R. Multi-Pathway Mechanism of Polydopamine Film Formation at Vertically Aligned Diamondised Boron-Doped Carbon Nanowalls. *Electrochim. Acta* **2022**, *409*, 140000.

(43) Almeida, L. C.; Correia, R. D.; Marta, A.; Squillaci, G.; Morana, A.; La Cara, F.; Correia, J. P.; Viana, A. S. Electrosynthesis of Polydopamine Films - Tailored Matrices for Laccase-Based Biosensors. *Appl. Surf. Sci.* **2019**, *480*, 979–989.

(44) Li, S.; Wang, H.; Young, M.; Xu, F.; Cheng, G.; Cong, H. Properties of Electropolymerized Dopamine and Its Analogues. *Langmuir* **2019**, *35*, 1119–1125.

(45) Wang, J.; Li, B.; Li, Z.; Ren, K.; Jin, L.; Zhang, S.; Chang, H.; Sun, Y.; Ji, J. Electropolymerization of Dopamine for Surface Modification of Complex-Shaped Cardiovascular Stents. *Biomaterials* **2014**, *35*, 7679–7689.

(46) Klosterman, L.; Ahmad, Z.; Viswanathan, V.; Bettinger, C. J. Synthesis and Measurement of Cohesive Mechanics in Polydopamine Nanomembranes. *Adv. Mater. Interfaces* **2017**, *4*, 1700041.

(47) Loget, G.; Yoo, J. E.; Mazare, A.; Wang, L.; Schmuki, P. Highly Controlled Coating of a Biomimetic Polymer in TiO<sub>2</sub> Nanotubes. **2016**, arXiv:1610.04184. <https://doi.org/10.48550/ARXIV.1610.04184>.

(48) Guo, Z.; Wang, G.; Fu, H.; Wang, P.; Liao, J.; Wang, A. Photocatalytic Degradation of Methylene Blue by a Cocatalytic PDA/TiO<sub>2</sub> Electrode Produced by Photoelectric Polymerization. *RSC Adv.* **2020**, *10*, 26133–26141.

(49) Kupracz, P.; Grochowska, K.; Karczewski, J.; Wawrzyniak, J.; Siuzdak, K. The Effect of Laser Re-Solidification on Microstructure and Photo-Electrochemical Properties of Fe-Decorated TiO<sub>2</sub> Nanotubes. *Materials* **2020**, *13*, 4019.

(50) Haryński, Ł.; Grochowska, K.; Karczewski, J.; Ryl, J.; Rysz, J.; Siuzdak, K. Free-Standing TiO<sub>2</sub> Nanotubes Decorated with Spherical Nickel Nanoparticles as a Cost-Efficient Electrocatalyst for Oxygen Evolution Reaction. *RSC Adv.* **2021**, *11*, 219–228.

(51) Tesler, A. B.; Altomare, M.; Schmuki, P. Morphology and Optical Properties of Highly Ordered TiO<sub>2</sub> Nanotubes Grown in NH<sub>4</sub>F/o-H<sub>3</sub>PO<sub>4</sub> Electrolytes in View of Light-Harvesting and Catalytic Applications. *ACS Appl. Nano Mater.* **2020**, *3*, 10646–10658.

(52) Chiarello, G. L.; Zuliani, A.; Ceresoli, D.; Martinazzo, R.; Selli, E. Exploiting the Photonic Crystal Properties of TiO<sub>2</sub> Nanotube Arrays To Enhance Photocatalytic Hydrogen Production. *ACS Catal.* **2016**, *6*, 1345–1353.

(53) Sun, X.; Yan, L.; Xu, R.; Xu, M.; Zhu, Y. Surface Modification of TiO<sub>2</sub> with Polydopamine and Its Effect on Photocatalytic Degradation Mechanism. *Colloids Surf., A* **2019**, *570*, 199–209.

(54) Wang, Q.; Jia, F.; Song, S.; Li, Y. Hydrophilic MoS<sub>2</sub>/Polydopamine (PDA) Nanocomposites as the Electrode for Enhanced Capacitive Deionization. *Sep. Purif. Technol.* **2020**, *236*, 116298.

(55) Gelderman, K.; Lee, L.; Donne, S. W. Flat-Band Potential of a Semiconductor: Using the Mott–Schottky Equation. *J. Chem. Educ.* **2007**, *84*, 685.

(56) Kim, H.; Kim, G. Adsorption Properties of Dopamine Derivatives Using Carbon Nanotubes: A First-Principles Study. *Appl. Surf. Sci.* **2020**, *501*, 144249.

(57) Ambrico, M.; Vecchia, N. F. D.; Ambrico, P. F.; Cardone, A.; Cicco, S. R.; Ligonzo, T.; Avolio, R.; Napolitano, A.; d'Ischia, M. A Photoresponsive Red-Hair-Inspired Polydopamine-Based Copolymer for Hybrid Photocapacitive Sensors. *Adv. Funct. Mater.* **2014**, *24*, 7161–7172.

(58) Li, H.; Marshall, T.; Aulin, Y. V.; Thenuwara, A. C.; Zhao, Y.; Borguet, E.; Strongin, D. R.; Ren, F. Structural Evolution and Electrical Properties of Metal Ion-Containing Polydopamine. *J. Mater. Sci.* **2019**, *54*, 6393–6400.

(59) Kund, J.; Daboss, S.; D'Alvise, T. M.; Harvey, S.; Synatschke, C. V.; Weil, T.; Kranz, C. Physicochemical and Electrochemical Characterization of Electropolymerized Polydopamine Films: Influence of the Deposition Process. *Nanomaterials* **2021**, *11*, 1964.

(60) Yang, P.; Zhang, S.; Chen, X.; Liu, X.; Wang, Z.; Li, Y. Recent Developments in Polydopamine Fluorescent Nanomaterials. *Mater. Horiz.* **2020**, *7*, 746–761.

(61) Bard, A. J.; Faulkner, L. R. *Electrochemical Methods: Fundamentals and Applications*, 2nd ed.; Wiley: New York, 2001.

(62) Song, J.; Liu, H.; Lei, M.; Tan, H.; Chen, Z.; Antoshin, A.; Payne, G. F.; Qu, X.; Liu, C. Redox-Channeling Polydopamine-Ferrocene (PDA-Fc) Coating To Confer Context-Dependent and Photothermal Antimicrobial Activities. *ACS Appl. Mater. Interfaces* **2020**, *12*, 8915–8928.

(63) Kanyong, P.; Rawlinson, S.; Davis, J. Fabrication and Electrochemical Characterization of Polydopamine Redox Polymer Modified Screen-Printed Carbon Electrode for the Detection of Guanine. *Sens. Actuators, B* **2016**, *233*, 528–534.

(64) Fasmin, F.; Srinivasan, R. Review—Nonlinear Electrochemical Impedance Spectroscopy. *J. Electrochem. Soc.* **2017**, *164*, H443–H455.

(65) Bondarenko, A. S.; Ragoisha, G. A. *Progress in Chemometrics Research*; Pomerantsev, A. L., Ed.; Nova Science Publishers: New York, 2005; pp 89–102. the program is available online at: <http://www.abc.chemistry.bsu.by/vi/Analyser/>.


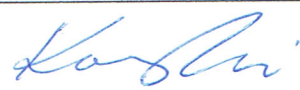


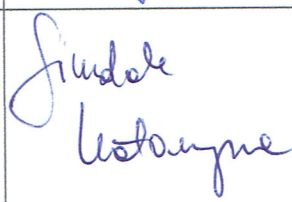
(66) Matta, M.; Pezzella, A.; Troisi, A. Relation between Local Structure, Electric Dipole, and Charge Carrier Dynamics in DHICA Melanin: A Model for Biocompatible Semiconductors. *J. Phys. Chem. Lett.* **2020**, *11*, 1045–1051.

(67) Boken, J.; Khurana, P.; Thatai, S.; Kumar, D.; Prasad, S. Plasmonic Nanoparticles and Their Analytical Applications: A Review. *Appl. Spectrosc. Rev.* **2017**, *52*, 774–820.

(68) Liu, B.; Zhao, X.; Yu, J.; Parkin, I. P.; Fujishima, A.; Nakata, K. Intrinsic Intermediate Gap States of TiO<sub>2</sub> Materials and Their Roles in Charge Carrier Kinetics. *J. Photochem. Photobiol., C* **2019**, *39*, 1–57.

**CReditTs table for Article 3:**

**Olejniak, A., Olbryś, K., Karczewski, J., Ryl, J., Bogdanowicz, R., & Siuzdak, K. (2023).** Band Gap Engineering toward Semimetallic Character of Quinone-Rich Polydopamine. *The Journal of Physical Chemistry C*. 127(26), 12662–12677 <https://doi.org/10.1021/acs.jpcc.2c08804>

Author	CReditT author statement	Signature
Adrian Olejnik	<b>Conceptualisation: Full</b> <b>Methodology, Formal analysis,</b> <b>Investigation, Data curation, Writing</b> <b>Original draft, Writing Review &amp; edit,</b> <b>Visualisation: Leading role</b> <b>Project administration, Funding</b> <b>Validation, Resources: In part</b>	
Karol Olbryś	<b>Methodology, Formal analysis,</b> <b>Investigation: In part</b>	Unable to get the signature: person not findable
Jakub Karczewski	<b>Methodology, Formal analysis,</b> <b>Investigation: In part</b>	
Jacek Ryl	<b>Validation, Methodology, Formal analysis,</b> <b>Investigation, Data curation, Writing</b> <b>Original draft, Writing Review &amp; edit: In</b> <b>part</b>	
Robert Bogdanowicz	<b>Validation, Resources, Data curation,</b> <b>Writing Original draft, Writing Review &amp;</b> <b>edit, Supervision: In part</b>	
Katarzyna Siuzdak	<b>Methodology, Validation, Resources,</b> <b>Visualisation, Writing Original draft,</b> <b>Writing Review &amp; edit, Funding, Project</b> <b>administration: In part</b> <b>Supervision: Leading role</b>	



# Laser-Induced Graphitization of Polydopamine on Titania Nanotubes

Adrian Olejnik,\* Krzysztof Polaczek, Marek Szkodo, Alicja Stanisławska, Jacek Ryl, and Katarzyna Siuzdak



Cite This: *ACS Appl. Mater. Interfaces* 2023, 15, 52921–52938



Read Online

ACCESS |



Metrics & More



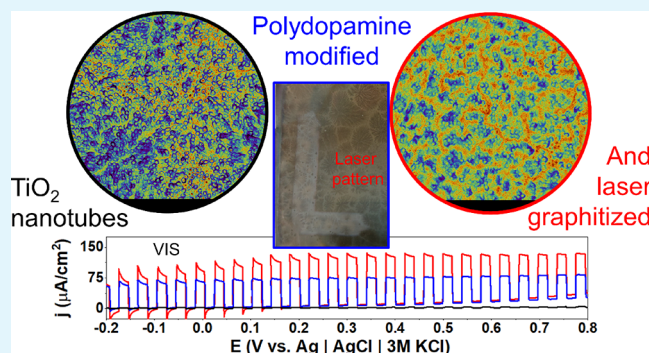
Article Recommendations



Supporting Information

**ABSTRACT:** Since the discovery of laser-induced graphite/graphene, there has been a notable surge of scientific interest in advancing diverse methodologies for their synthesis and applications. This study focuses on the utilization of a pulsed Nd:YAG laser to achieve graphitization of polydopamine (PDA) deposited on the surface of titania nanotubes. The partial graphitization is corroborated through Raman and XPS spectroscopies and supported by water contact angle, nanomechanical, and electrochemical measurements. Reactive molecular dynamics simulations confirm the possibility of graphitization in the nanosecond time scale with the evolution of  $\text{NH}_3$ ,  $\text{H}_2\text{O}$ , and  $\text{CO}_2$  gases. A thorough exploration of the lasing parameter space (wavelength, pulse energy, and number of pulses) was conducted with the aim of improving either electrochemical activity or photocurrent generation. Whereas the 532 nm laser pulses interacted mostly with the PDA coating, the 365 nm pulses were absorbed by both PDA and the substrate nanotubes, leading to a higher graphitization degree. The majority of the photocurrent and quantum efficiency enhancement is observed in the visible light between 400 and 550 nm. The proposed composite is applied as a photoelectrochemical (PEC) sensor of serotonin in nanomolar concentrations. Because of the suppressed recombination and facilitated charge transfer caused by the laser graphitization, the proposed composite exhibits significantly enhanced PEC performance. In the sensing application, it showed superior sensitivity and a limit of detection competitive with nonprecious metal materials

**KEYWORDS:** polydopamine, graphitization, laser-induced graphene, titania nanotubes, photoelectrochemistry, intensity-modulated photovoltage spectroscopy, IPCE



## 1. INTRODUCTION

Polydopamine (PDA) and melanin-based materials represent a vast research topic in electrochemistry photochemistry, surface science, and electronics with many promising applications in each field.<sup>1–3</sup> Despite its intrinsically rich chemistry<sup>4–6</sup>—associated with the amine–catechol–quinone interplay—and possibilities for various physical structures including  $\pi$ – $\pi$  stacking,  $\pi$ -cation, or aryl–aryl linking<sup>6–8</sup> there are still numerous procedures for altering its structure on various levels. Those procedures can include monomer alteration at the synthesis level (adrenaline, noradrenaline, L-DOPA, tyrosine derivatives, and more)<sup>9–11</sup> or direct modification of functional groups including amination, carboxylation,<sup>12</sup> and recently also N-methylation.<sup>13</sup> Alternatively, it is possible to include other chemical entities inside the PDA matrix such as transition metals<sup>14,15</sup> or organic molecules during the course of either oxidative or electropolymerization.<sup>16–18</sup> Proposed modifications are aimed at an incredibly vast scope of applications such as supercapacitors,<sup>19</sup> protection from photo-corrosion,<sup>20</sup> generation of fluorescence,<sup>21</sup> flexible electronics,<sup>2</sup>

and biomedicine including biosensing; PDA can act as an element of the organic layer onto the electrode<sup>18,22</sup> or as an imprinted polymer.<sup>23</sup>

One of the most serious problems limiting applications is poor mechanical properties associated with high roughness and agglomeration. This problem is especially urgent in the field of electrochemical applications<sup>19</sup> and colorimetric sensing.<sup>24</sup> An idea for improvement in this area was proposed in a *Nature Communications* paper in 2020<sup>25</sup> via the laser-graphitization protocol of the PDA. In this work, PDA was deposited on quartz using standard oxidative polymerization in Tris buffer. Then, it was detached from the surface and treated with a blue diode continuous laser with 1–2 W power. Through XPS and

**Received:** August 5, 2023

**Revised:** October 17, 2023

**Accepted:** October 17, 2023

**Published:** November 2, 2023



Raman measurements, it was evidenced that partial graphitization occurs with covalent coupling between the PDA units. The modification resulted in a 100-fold increase in scratch resistance, which was a higher value than quartz and TiO<sub>2</sub> reference parameters. The initial high-roughness layer was changed to a uniform 37 nm film without agglomerated PDA nanoparticles. More importantly, however, the most desired properties of PDA such as high adhesiveness and biofouling resistance associated with the catechol functionality were preserved.

The laser-graphitized PDA (lgPDA) can be considered a member of the laser-induced graphene/graphite (LIG) class of materials, which is prominent for electronic and electrochemical applications.<sup>26–28</sup> In general, the purpose of the LIG-ation is to change the weakly conducting  $\pi$ -conjugated organic polymer such as polyether(ether–ketone) or poly(etherimide) into a highly conductive carbon-based sheet, typically N-doped graphene/graphite. From an electrochemical point of view, such a treatment facilitates charge transfer at the electrode/electrolyte interface. In general, LIG finds many applications including electrochemical sensing, supercapacitors, electrocatalysis, and photodetectors.<sup>29,30</sup>

Besides laser treatment, there are several other approaches for synthesis of graphite/graphene and other nanocarbons from organic precursors, such as polymers, resins, or biomass. These include various high-temperature and chemical treatments, but for simplicity, they can be divided into catalytic graphitization/carbonization/pyrolysis and hydrothermal treatment.<sup>31</sup>

There are two distinguishable trends in the related literature. The first one is aimed at biomass conversion toward cheap and large-scale production of nanocarbons. In this space, reduction of the graphitization temperature, high output, simplicity, and stability of the fabrication method are highly appreciated.

Development of graphitization catalysts and dispersion agents for precursors<sup>32</sup> allows progress in the field. There are many types of catalysts including transition metals (Fe, Ni, Co),<sup>33</sup> their salts and oxides,<sup>34</sup> boron compounds,<sup>35</sup> and carbon nanostructures.<sup>36,37</sup> Among them, iron-catalyzed graphitization is an exemplary solution for carbonization of various kinds of precursors, and many protocols are already developed.<sup>38</sup> Despite the efforts, the pyrolysis methods require temperatures above 1000 °C and even up to 3000 °C and an inert atmosphere for efficient conversion.<sup>31,33</sup>

In contrast to the pyrolysis approaches, hydrothermal process is based on autoclaving the pretreated precursors at lower temperatures in alkaline or acidic environments.<sup>31</sup> However, the carbonized product is typically strongly disordered and oxidized and requires another high-temperature step to transform into crystalline nanocarbons, such as graphene. For example, Chen et al. applied such methodology for wheat straw waste.<sup>39</sup> The temperature required for graphitization was as high as 2600 °C to achieve a quality sufficient for electrochemical applications.

The second trend in the graphitization literature is focused on the modification of functional nanomaterials. In this space, fine-tuning of the electrical, thermal, and mechanical properties toward various applications is highly desired. Almost all of the work concerning PDA and its electrochemical applications falls into this category. The typical method of PDA graphitization/carbonization is purely thermal and requires temperature values between 700 and 1000 °C.<sup>40–43</sup> The resulting carbonized PDA possesses the structure of nitrogen-doped

graphite with varying levels of crystallinity and ordering. Surprisingly, one work reports the calcination of PDA to amorphous carbon at relatively low 500 °C in a nitrogen flow.<sup>44</sup> On the other hand, in some carbon–carbon composites, temperatures as high as 3000 °C are required.<sup>45,46</sup>

Thus, the current graphitization state of the art renders LIG-ation as an appealing, energy-efficient alternative because of the markedly lower energy dissipation. An ambient atmosphere is typically also sufficient.<sup>47</sup> Surprisingly though, according to the best knowledge of the authors, there have been no further realizations of the PDA laser modifications or LIG-ation in the literature since the *Nature Communications* paper in 2020. This idea is strongly potent not only in the context of PDA mechanical properties and expanding its library of chemical structures but also for elucidation of its complicated electronic structure.

PDA can be synthesized in the form of a free-standing film<sup>48</sup> or nanoparticles<sup>46,49</sup> as an element in composition with different materials (metals, semiconductors, organics).<sup>50</sup> In the seminal paper<sup>25</sup> describing laser graphitization of the PDA for the first time, PDA was in the form of a film. However, laser treatment of the PDA bound to some surface has not been studied yet, and the influence of such treatment on various properties of this composite material is unknown. Moreover, the electronic structure of the PDA–substrate composite will be clearly altered by laser treatment with various parameters.

In particular, PDA–semiconductor interfaces represent an especially interesting subgroup of the PDA–substrate composites due to nontrivial electrical and electrochemical properties.<sup>51–54</sup> In general, PDA can be viewed as an amorphous semiconductor (due to temperature dependence of the conductivity) with the ionic component of the conduction.<sup>50</sup> On the other hand, in contact with other semiconductors, it acts as a photosensitizer or another semiconductor depending on the film thickness.<sup>51,54,55</sup>

In our previous work, we have shown the alternative picture to think of quinone-rich PDA as a semimetallic entity. Such PDA electropolymerized on the surface of titania nanotubes leads to 20-fold photocurrent enhancement through photosensitization as it behaves as a net of spatially distributed redox mediators in electrochemical experiments with redox mediators.<sup>56</sup>

In this work, electropolymerized PDA is modified using a pulsed Nd:YAG laser with 365 and 532 nm wavelengths and varying pulse parameters. Titania nanotubes are chosen as a substrate for PDA deposition (prelaser graphitization) for several reasons. First, TiO<sub>2</sub> is a well-studied semiconductor with a high band gap and is prone to photosensitization with dyes or PDA.<sup>54,56,57</sup> Second, nanotubes exhibit nanomicroscopic morphology resulting in a high PDA loading. Therefore, it is a reasonable platform to study the PDA–semiconductor interactions. Partial graphitization is confirmed by several techniques, including XPS, Raman scattering, nanoindentation, water contact angle, and electrochemical measurements. Graphitization is modeled on the molecular level by a reactive molecular dynamics approach. Wavelength-resolved photoelectrochemistry and quantum efficiency measurements are employed to elucidate the mechanism of enhanced absorption and photocurrent generation in the visible range.

## 2. MATERIALS AND METHODS

**2.1. Hydrogenation of TiO<sub>2</sub> Nanotubes and Electropolymerization of Dopamine.** The list of chemicals and protocol for titania

nanotube (TNT) synthesis can be found in the SI file. All electrochemical experiments, including the hydrogenation and electropolymerization of dopamine, were performed by using a Biologic SP-150 potentiostat–galvanostat.

Unless stated otherwise, the working electrode was hydrogenated TNT (pure or modified), the counter electrode was a platinum mesh, and the reference electrode was Ag/AgCl/3 M KCl. All potentials in this article are expressed with respect to this reference electrode. The geometric surface areas of the working electrodes were between 0.5 and 1 cm<sup>2</sup>.

Hydrogenation of titania nanotubes was performed in an argon-purged 0.5 M Na<sub>2</sub>SO<sub>4</sub> solution through the following protocol. First, linear sweep voltammetry (LSV) with a 100 mV/s rate was used for cathodic polarization up to −5 V. Then, a constant potential equal to −5 V was applied for 2 min.

Electropolymerization of dopamine on hydrogenated TNT electrodes was carried out potentiodynamically in an argon-purged solution of 0.5 M Na<sub>2</sub>SO<sub>4</sub> containing 1× Tris buffer immediately after hydrogenation. The pH of the solution was adjusted by adding 1 M HCl or 1 M NaOH to the desired values, i.e., 5.7, 7.5, 8.5, 9.0, or 10.0. An MP-103 handheld potentiometric pH meter was used to control the pH value. The number of CV cycles was 5, 10, 25, or 50 with a 20 mV/s scan rate in the range from −0.5 to +1.0 V.

## 2.2. Laser Modification of the PDA-Modified Nanotubes.

Laser modification of samples aimed at PDA graphitization was performed using Nd:YAG (QSmart 850 Quantel) pulsed nanosecond laser using second (532 nm) and third (365 nm) harmonics. The pulse frequency was set to 10 Hz, and energy fluences varied between 30 and 120 mJ/cm<sup>2</sup> abbreviated as F30, F60, F90, and F120. Beam homogenizers for both wavelengths were used to maintain a flat profile of the light intensity during exposure. Electrodes were lasered in the programmed rectangular shape of a ca. 1 cm<sup>2</sup> area using the motorized table. The variable velocity of the table allows a variable number of laser pulses the sample is exposed to. In particular, speeds S200, S100, S50, and S25 correspond to 200, 100, 50, and 25 cm/h, respectively. Given that the spot for the 365 nm modification is a square with a 2.6 mm side, these would correspond to 4.6, 9.2, 18.4, and 36.8 pulses, respectively, for each point on the sample. Analogously, for the spot used for 532 nm modification, these would correspond to 6.4, 12.8, 25.6, and 51.2 pulses per sample point on average. All treatments were performed in a vacuum of 10<sup>−4</sup> mbar to mitigate the possible influence of oxygen and carbon dioxide present in the air.

**2.3. SEM Inspection and Measurement of the PDA Film Thickness.** The surface morphology of the electrodes was investigated using a Quanta FEG 250 (FEI) Schottky field-emission scanning electron microscope (SEM) equipped with a secondary ET electron detector with a beam accelerating voltage of 10 kV. The thickness of the PDA layer ( $d_{\text{PDA}}$ ) was estimated by measuring the wall thickness of the PDA-modified nanotubes ( $W_{\text{TNTIPDA}}$ ) and then subtracting the thickness of the unmodified nanotubes ( $W_{\text{TNT}}$ ) and dividing by 2 (eq 1):

$$d_{\text{PDA}} = \frac{W_{\text{TNTIPDA}} - W_{\text{TNT}}}{2} \quad (1)$$

**2.4. Nanoindentation.** The nanoindentation test was performed on the surface of TNT nanotubes as well as nanotubes with dopamine deposited on them (TNT\_PDA) and dopamine modified with laser (TNT\_IgPDA). The tests were conducted by using a Berkovich indenter with a maximum load of 0.4 mN. The loading rate of the indenter was 0.1 mN/s. Once the maximum load was reached, it was maintained for 5 s, and then the load was removed at a rate of 0.1 mN/s. The subsequent measurements were taken at the same location, with the described cycle repeated 10 times. After each cycle, the hardness and stiffness of the surface were determined using the Oliver–Pharr method.<sup>58</sup>

The elastic properties of the surface were also characterized by the elastic work during the unloading of the indenter. This work was calculated as the area under the unloading curve of the indenter, i.e., under the curve  $P = f(h)$ , where  $P$  is the indenter load and  $h$  is its

displacement in the tested material. Both hardness and stiffness, as well as the elastic work, were calculated by using the NanoTest Vantage nanoindenter software.

In each load cycle, the creep rate of the nanotubes at a constant maximum load was also determined. The creep rate was calculated based on the  $\Delta h/h = \varepsilon = f(t)$  curve, where  $\Delta h$  is the depth of penetration increment of the indenter at a constant maximum load and  $t$  is the time at a constant maximum load. The creep rate  $d\varepsilon/dt$  was determined for a steady-state condition in which  $\Delta h/h$  was a linear function of time  $t$ .

**2.5. Electrochemical and Photoelectrochemical Characterization.** Photoelectrochemical tests were performed in 0.5 M Na<sub>2</sub>SO<sub>4</sub> electrolyte using linear square voltammetry (LSV) with a scan rate of 20 mV/s or using chronoamperometry (CA) at a potential of +0.3 V. As a light source, a xenon lamp equipped with AM 1.5 and UV cutoff (GG40, Schott) filters were used. The irradiation intensity was established to be 100 mW/cm<sup>2</sup> using a Si reference cell (Rera).

Photocurrent action maps were measured with a photoelectric spectrometer for quantum efficiency measurements (Instytut Fotonowy, Poland) equipped with a solar simulator, Czerny–Turner monochromator, and potentiostat. The illumination source was calibrated by using a silicon photodiode to calculate light intensities. The wavelength range was set from 200 to 700 nm, and the potential range was set from 100 to 800 mV vs Ag/AgCl/3 M KCl reference electrode. Measurement points were taken with 25 nm and 50 mV steps.

External quantum efficiencies of photocurrent generation (or IPCE = incident photon to current efficiencies) were calculated for several wavelengths (373, 398, 424, 455, and 524 nm) and with variable light intensities using LED illumination sources. The standard formula was applied:

$$\text{IPCE} = \frac{j}{P} \hbar\omega \quad (2)$$

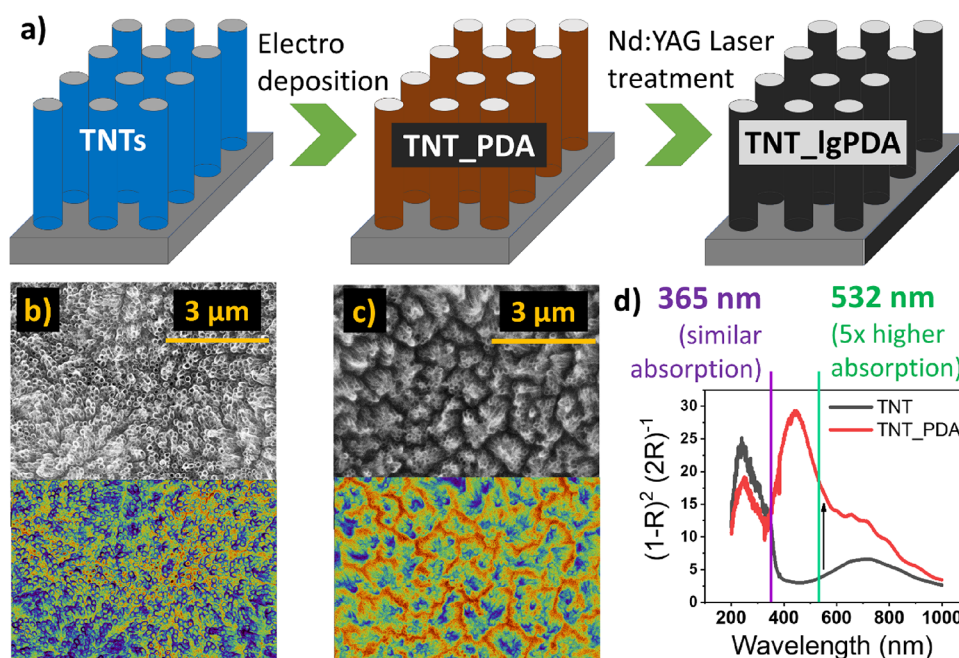
where  $j$  is the photocurrent,  $P$  is light intensity, and  $\hbar\omega$  is photon energy.

Intensity modulated photocurrent/photovoltage spectroscopy (IMPS/IMVS) experiments were performed on a dedicated device provided by the Instytut Fotonowy equipped with a revolver containing several LEDs with adjustable AC and DC components of the illumination and a potentiostat.

IMPS measurements were carried out with 373 and 424 nm LED wavelengths with variable AD and DC components indicated in the text. The sample was polarized with a + 500 mV anodic bias (with respect to the Ag/AgCl/3 M KCl reference electrode). The applied frequency range was 100 mHz–10 kHz, and for each frequency, two measurement points were registered. IMVS measurements were carried out with 373 nm LED with 0.2 mW/cm<sup>2</sup> AC and 1 mW/cm<sup>2</sup> DC components of the illumination in open circuit conditions.

**2.6. ReaxFF Simulation of PDA Graphitization.** Molecular structures of PDA units were designed using a builder tool provided by Atomistix ToolKit Quantumwise (ATK, Synopsys, USA) as reported in ref 59. The process of PDA graphitization was simulated using a reactive force field (ReaxFF) molecular dynamics (MD) approach.<sup>60,61</sup> The initial structure for the MD trajectory was a DFT-optimized set of four PDA tetramers based on DHI units. The density of molecules was set to 0.6 g/cm<sup>3</sup> with periodic boundary conditions similarly as proposed in a previous work<sup>62</sup> devoted to laser graphitization of other analogous polymers. An NVT Nosé–Hoover thermostat with 0.25 fs time step and three elements in Nosé–Hoover chains were used for generating MD trajectories up to 4 ns. Gases evolving throughout the simulation were kept in the box. Temperatures of 2000, 3000, and 4000 K were tested, but results are only presented for 3000 K because no significant temperature dependence on the final structure was observed. Analysis of MD trajectories was performed with an analyzer tool available in the ATK package as implemented.<sup>63</sup> The resulting IgPDA structure was then used for DFT calculations of the band structure and density of states; details can be found in the SI file.





**Figure 1.** (a) Synthesis of the laser graphitized polydopamine (IgPDA) on titania nanotubes (TNT). (b) SEM inspection of the pristine TNT. (c) After electropolymerization of PDA, two false-color contrasts of the same images are shown. (d) Kubelka–Munk functions obtained from diffuse reflectance data of pristine and PDA-modified TNTs with denoted wavelengths of the Nd:YAG laser used for treatment.

## 2.7. Photoelectrochemical (PEC) Detection of Serotonin.

Photoelectrochemical (PEC) sensing experiments were conducted using the cell and light sources identical to those in the case of the IMPS and quantum efficiency measurements. The light source was a 373 nm LED with 2 mW/cm<sup>2</sup> light intensity switched on/off during the chronoamperometric polarization equal to +100 mV.

Prior to the main sensing experiment, the sample was preconditioned in several ways. First, five CV cycles were applied in the range between −0.2 and +0.8 V and 100 mV/s scan rate. The purpose was to achieve surface reconstruction and remove all the residual currents that could potentially interfere with the proper analyte signal. Second, the gradual light exposure, i.e., 0.5, 1, 1.5, and 2 mW/cm<sup>2</sup>, was applied at −100 mV (it is ca. an open circuit potential). Third, the sample was polarized to +100 mV and held for 20 s until the second, analogous, gradual light exposure was applied. The current response of the final step at +100 mV and 2 mW/cm<sup>2</sup> is shown and used for construction of calibration curves. Limits of detection were calculated according to ref 64 as three standard deviations divided by the slope of the linear range.

The sample chosen for this experiment was TNT\_IgPDA<sub>365</sub> synthesized using 365 nm laser, 60 mJ/cm<sup>2</sup> fluence, and S25 table speed. The surface area exposed to light was equal to 0.785 cm<sup>2</sup>.

## 3. RESULTS AND DISCUSSION

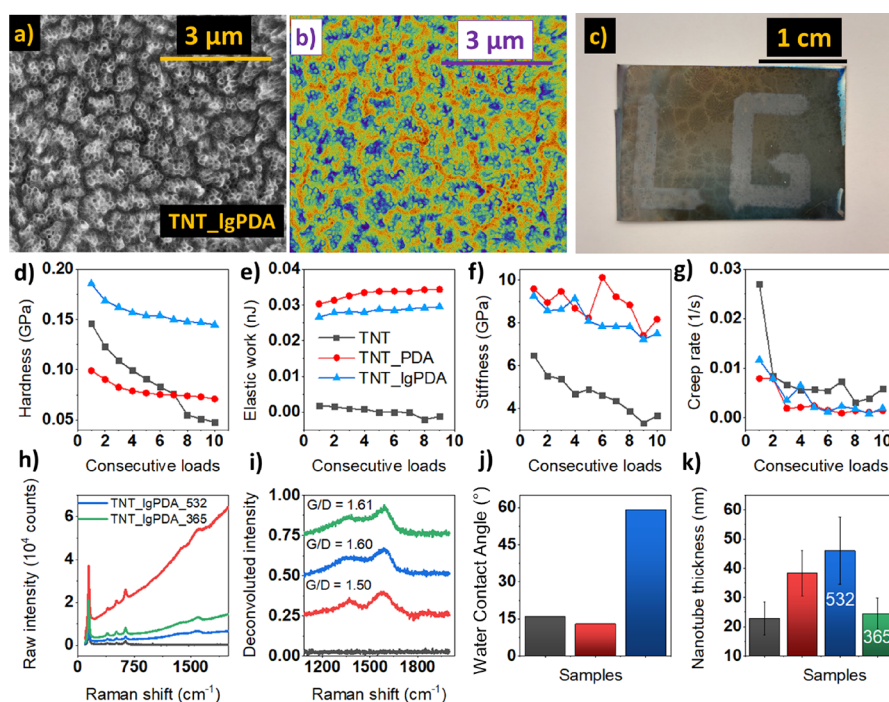
**3.1. General Synthesis Protocol for the Laser Graphitized Polydopamine (IgPDA) on the Surface of Titania Nanotubes (TNTs).** In general, the synthesis protocol adopted in the following study involved the anodization of titanium foil to obtain crystalline titania nanotubes (TNTs) with various geometries. Then, TNTs were electrochemically hydrogenated, and polydopamine (PDA) was deposited on them by electropolymerization of dopamine according to the procedure described in our previous works.<sup>16,65</sup> An exemplary CV curve of electropolymerization can be found in Figure S1 with characteristic redox peaks originating from reactions of the PDA structural units. The resulting TNT\_PDA heterostructure was modified by the nanosecond pulsed Nd:YAG laser using two wavelengths, i.e., 532 and 365 nm (second and

third harmonics), to obtain the final laser-graphitized polydopamine (IgPDA). The protocol is schematically presented in Figure 1a with SEM images acquired for the pristine (Figure 1b) and PDA-modified nanotubes (Figure 1c). Chosen wavelengths are based on the optical spectroscopy data of the TNTs and TNT\_PDA so that the 532 nm pulse is targeting mostly the absorption by the PDA, whereas the 365 nm pulse should interact both with the TNTs and the PDA (see the Kubelka–Munk function in Figure 1d).

**3.2. Optimization of TNT and PDA Synthesis Parameters prior to Laser Graphitization.** Several geometries of titania nanotubes were synthesized to screen for the optimal template for laser treatment. In terms of spacing between TNTs, adjacent and loosely spaced nanotubes were prepared in ethylene glycol and diethylene glycol, respectively, and in terms of their length, varying anodization times were applied between 15 min and 2 h. SEM images of the adjacent nanotubes are shown in Figure 1b,c, and those of loosely spaced nanotubes are shown in Figure S2a–d. After the deposition of polydopamine, nanotube walls thicken in both cases, and their coronas are slightly aggregated in the adjacent case. Those phenomena are visually easier to grasp by using the spectral contrast applied to SEM images.

There is also a tendency of TNT\_PDA based on longer and adjacent nanotubes to exhibit larger values of the current integral during CV sweeps of electropolymerization, indicating higher surface area and the amount of the PDA deposited (Figure S3a). Moreover, higher vis-photocurrent enhancement due to the PDA presence is observed for the longest nanotubes prepared during 2 h anodization (Figure S3d). TiO<sub>2</sub> samples obtained during anodization time exceeding 2 h have the property of the morphology switching from nanotubes to a spongy layer after PDA deposition (Figure S4).

It is known that there exists a large variability of the PDA structure and properties depending on the electropolymerization parameters.<sup>9,22,65,66</sup> Therefore, the influence of the



**Figure 2.** Physical properties of the TNT\_lgPDA heterostructure: (a, b) SEM image in two contrasts; (c) macroscopic picture of the laser graphitized sample; (d–g) series of multiloading nanoindentation results for hardness, elastic work of deformation, stiffness, and creep rate, respectively; (h) comparison of raw Raman signals for pristine (TNT), PDA-modified (TNT\_PDA), and laser graphitized samples (TNT\_lgPDA\_532, TNT\_lgPDA\_365); (i) corresponding rescaled Raman signals after subtraction of the fluorescence; (j) water contact angles; and (k) thicknesses of nanotube walls withdrawn from SEM images (images and corresponding statistics can be found in Figures S2 and S7, respectively).

number of polymerization cycles and the applied pH on the vis-photocurrents and electrochemical performance has been briefly tested for the studied set of TNT\_PDA samples (Figure S3). Is it easy to see that longer cycling up to 50 potentiodynamic cycles yields higher photocurrents and lower capacitive background accompanied by higher electroactivity expressed as a smaller distance between ferrocyanide redox peaks. Furthermore, PDA obtained at pH = 7.5 exhibits the same two properties in contrast to its more alkaline variants. The latter does not even exhibit clear ferrocyanide redox peaks and has a higher capacitive background current. This behavior stands in line with the literature reports suggesting lower electroactivity of other similar polymers such as *o*-phenylenediamine<sup>67–69</sup> synthesized in alkaline pH. Although this property might be beneficial in terms of, e.g., constructing molecular imprinted polymers (MIP) for sensing, for photoelectrochemical studies, the charge transfer rate and photocurrent generation are most important.

Therefore, for laser graphitization, adjacent and long (2 h anodization) nanotubes as well as PDA obtained during 50 cycles with solution pH = 7.5 are chosen for laser graphitization and further photoelectrochemical studies. Unless stated otherwise, TNT and PDA abbreviations correspond to those particular samples throughout the paper.

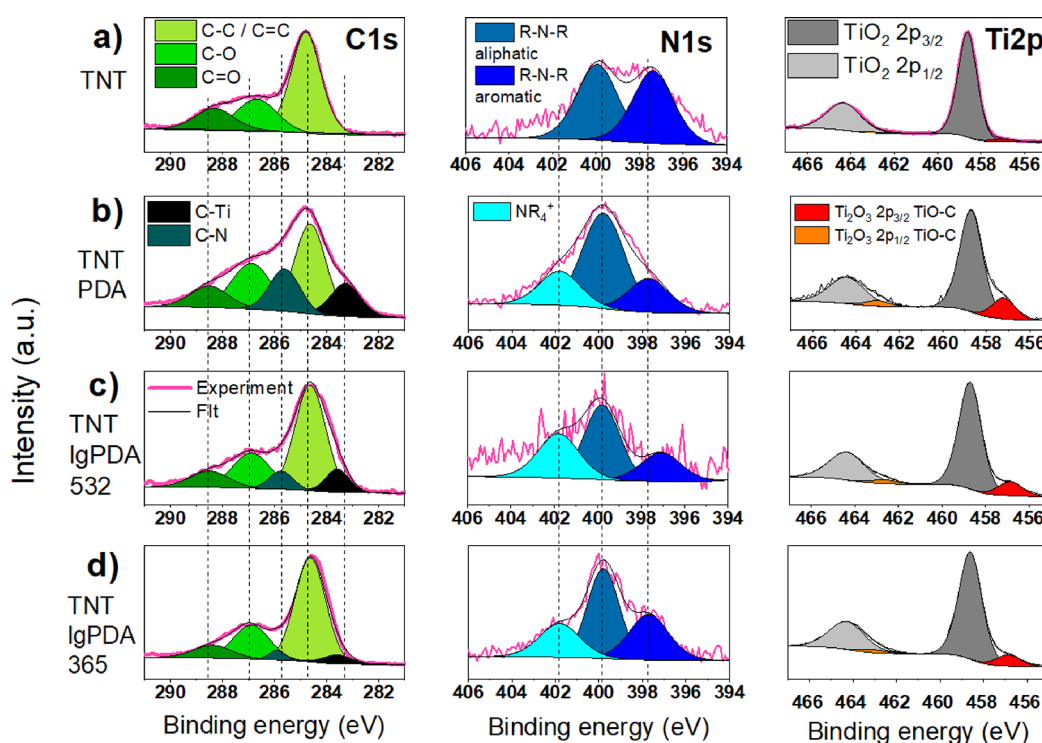
**3.3. Physical Properties of the TNT\_lgPDA Heterostructures.** SEM images of the TNT\_lgPDA structure are given in Figure 2a and are almost identical to the as-formed TNT\_PDA electrode, indicating that laser graphitization does not alter the morphology significantly. This behavior is preserved also for loosely spaced TNTs (Figure S2) using both 532 and 365 nm wavelengths. On the other hand, the macroscopic image of the sample allows easy distinction

between the modified and unmodified areas. With the application of the motorized table, spatially selective laser graphitization “lg” is enabled (Figure 2b). It was noted, however, that the treatment via 365 nm with higher fluences (above 90 mJ/cm<sup>2</sup>) leads to a significant distortion of the nanotubes themselves (Figure S5).

Considering that graphitization significantly changes the mechanical properties of the PDA,<sup>25</sup> a series of repetitive nanoindentation experiments have been performed to validate if the surface-deposited PDA exhibits the same behavior (Figures 2c–f). It is easy to see that hardness of the TNT\_lgPDA heterostructure is highest among studied samples, and its decay with consecutive loading is slower with respect to pristine nanotubes. Elastic work during indentation is markedly elevated for both pristine and laser-treated PDA, indicating that the higher energy is required for the deformation to occur. A similar trend is observed also for stiffness (Young’s modulus). Last, the creep rate (i.e., the slope of the deformation with respect to time during the indentation) is decreased after modification with either PDA or lgPDA. Detailed data on each multiloading experiment including load–displacement curves and deformation–time curves can be found in Figure S6. In summary, the phenomenon of increased hardness after laser modification has been replicated in the case of surface-deposited PDA. However, its influence on other mechanical properties seems to be negligible in the studied system. Presumably, the PDA itself causes major changes to the TNT electrode mechanical characteristics compared to the subsequent laser treatment.

A clear indication of the presence of PDA on the surface of TNTs is the Raman scattering measurement. In comparison to pristine TNTs, after PDA deposition, a significant increase in





**Figure 3.** High-resolution XPS spectra in the carbon (C 1s), nitrogen (N 1s), and titanium (Ti 2p) regions: (a) pristine TNTs (titania nanotubes), (b) TNT\_PDA (TNT covered with polydopamine), (c) TNT\_lgPDA\_532 (TNT\_PDA graphitized using 532 nm laser), and (d) TNT\_lgPDA\_365 (TNT\_PDA graphitized using 365 nm laser).

**Table 1.** Quantitative Data from the XPS Experiment Depicted in Figure 3

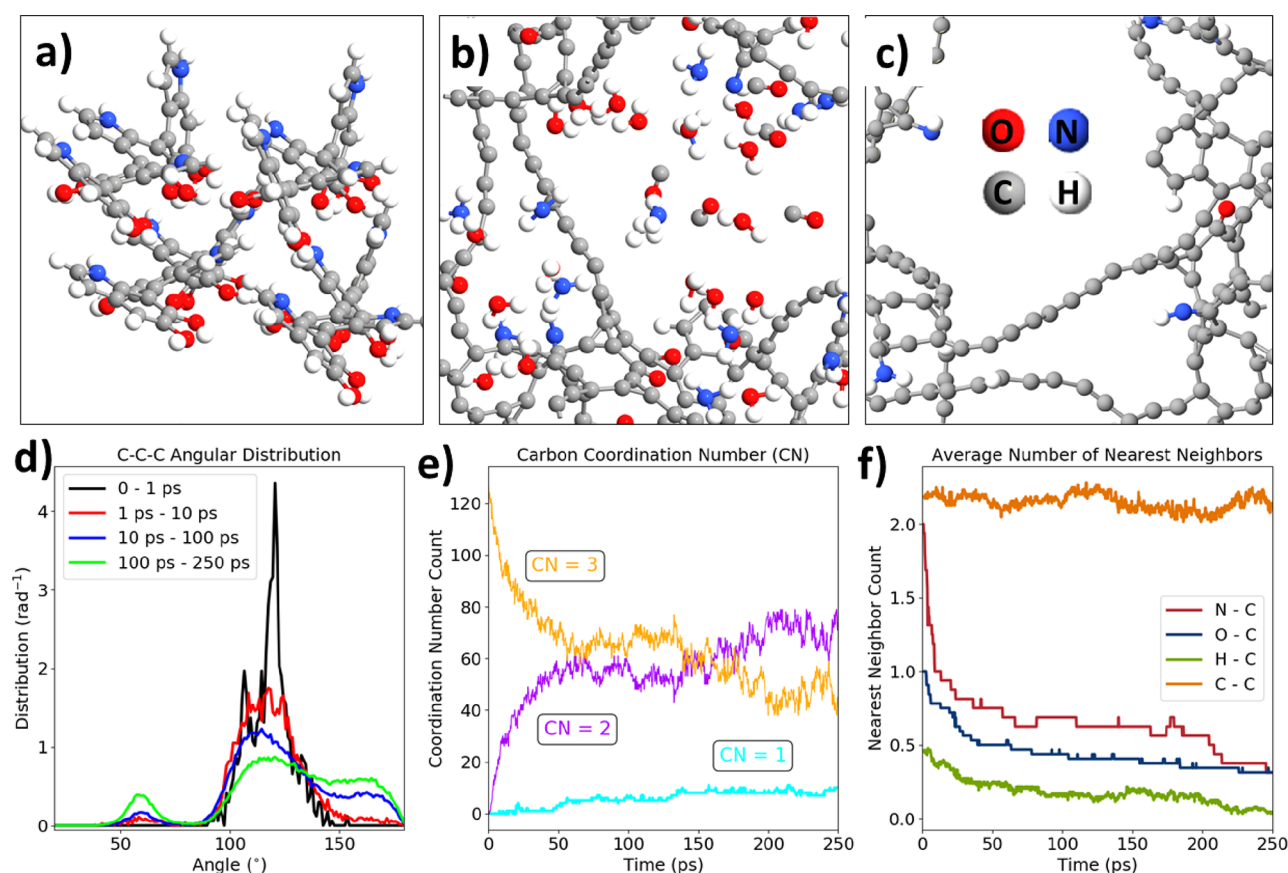
chemical group	TNT	TNT_PDA	TNT_PDA_532	TNT_PDA_365
C–C/C=C	14.55	25.01	20.62	30.43
C–O	5.88	16.36	8.41	11.6
C=O	3.94	7.63	4.12	4.78
C–Ti		9.15	3.55	2.44
C–N		11.66	2.72	1.45
<b>total C</b>	<b>24.37</b>	<b>69.81</b>	<b>39.42</b>	<b>50.7</b>
<b>total O</b>	<b>52.22</b>	<b>20.77</b>	<b>39.60</b>	<b>34.38</b>
R–N–R aliphatic	1.66	4.09	1.05	1.59
R–N–R aromatic	1.58	1.45	0.48	1.04
NR <sup>4+</sup>		1.46	0.74	0.79
<b>total N</b>	<b>3.24</b>	<b>7.00</b>	<b>2.27</b>	<b>3.42</b>
Ti 2p <sub>3/2</sub> TiO <sub>2</sub>	19.47	2.02	16.38	10.32
Ti 2p <sub>3/2</sub> Ti <sub>2</sub> O <sub>3</sub>	0.7	0.41	2.32	1.17
<b>total Ti</b>	<b>19.54</b>	<b>2.43</b>	<b>18.70</b>	<b>11.49</b>

the fluorescence is observed accompanied by the emergence of D and G bands at regions around 1350 and 1650  $\text{cm}^{-1}$ , respectively (Figure 2h). There are also notable changes after laser treatment regardless of the wavelength used, namely, a decrease in the fluorescence signal and an elevation of the G band. The latter can be seen more clearly when the fluorescence baseline is subtracted, and raw Raman data are rescaled (Figure 2i). It can be assumed that the G/D band ratio is a measure of the graphitization degree and will be used in this context throughout the rest of the paper. This ratio is increased from 1.50 to 1.60 after laser treatment, strongly suggesting that graphitization indeed occurred.

Moreover, the water contact angle is also markedly increased from about 15° of pristine TNTs and TNT\_PDA to about 60° (Figure 2j). Although the surface remains hydrophilic, the increased water contact angle is another indirect symptom of

graphitization. Considering increased hydrophobicity after laser treatment, this solution could be used to facilitate PDA loading of hydrophobic molecules into some porous materials through interactions with lgPDA. That is because even after graphitization, some catechol functionalities still remain.<sup>40</sup> This could be of strong interest in the fields of wastewater treatment or in colorimetric sensing.<sup>24</sup>

Finally, the thickness of the deposited coating can be roughly estimated from the SEM pictures by comparing the nanotube wall thickness before and after modifications (Figure 2k). It is easy to see that after PDA electropolymerization, there is a 2-fold increase of the thickness up to ca. 40 nm, indicating a 7.7 nm thickness of the PDA. The coating thickens even more to 11.5 nm after laser treatment using a 532 nm wavelength, suggesting the occurrence of the swelling phenomenon. On the other hand, the thickness plummets to



**Figure 4.** ReaxFF molecular dynamics of the early graphitization stage: (a) initial geometry of the system (4 DHI tetramers); (b, c) geometry of the whole system and the carbon backbone after 250 ps of the annealing at 3000 K; (d) angular distribution function for several periods of the trajectory; (e) evolution of the carbon coordination number; and (f) evolution of the carbon nearest neighbor number projected onto N, O, H, and C atoms (1.8 Å cutoff).

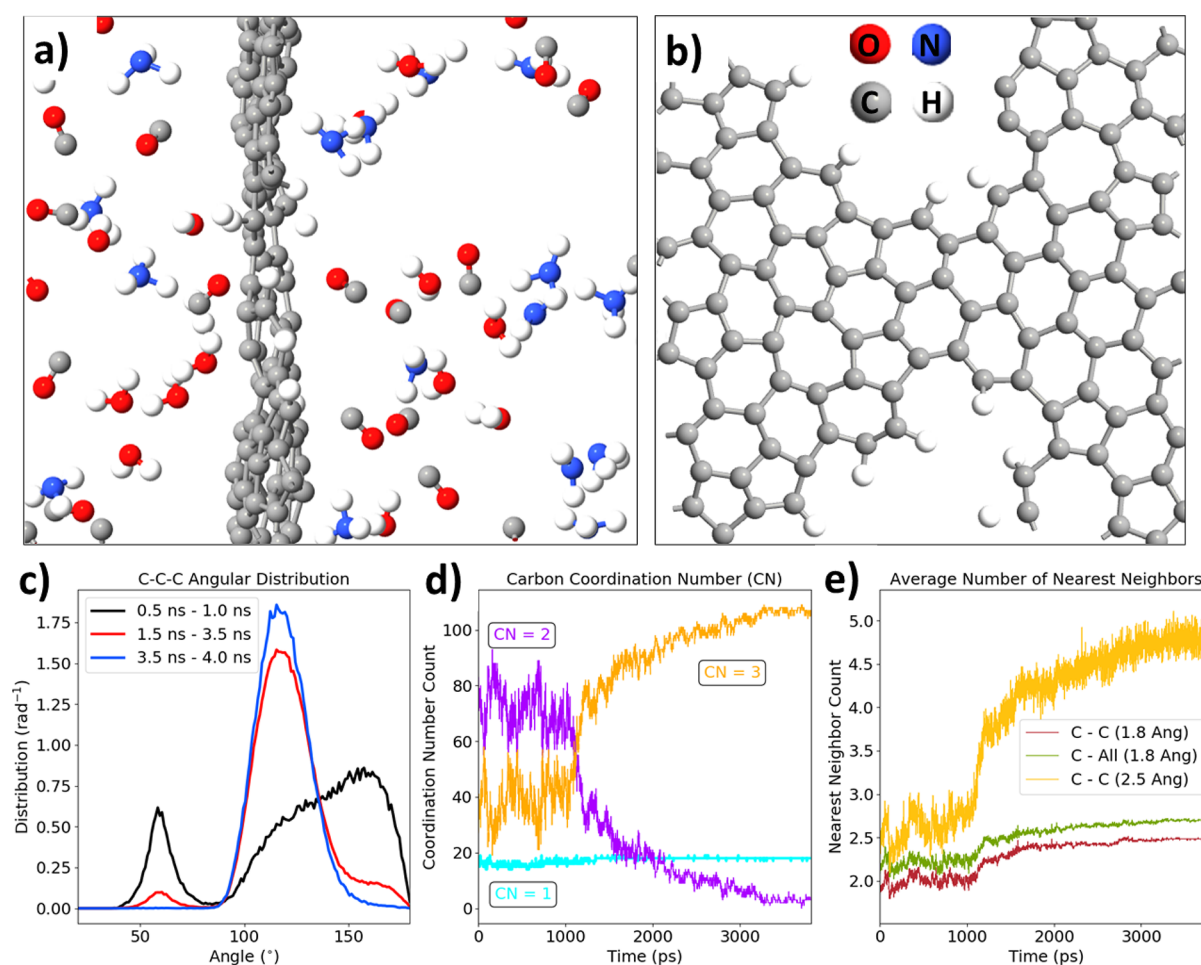
1.1 nm after 365 nm exposure, suggesting that a large part of the PDA is either evaporated or incorporated into the TNT structure after the process.

**3.4. XPS Measurements of the TNT\_IgPDA.** To investigate the changes in surface chemistry after each modification step, a series of high-resolution XPS measurements were performed (Figure 3 and Table 1). In general, besides the Ti 2p doublet, there are nonzero carbon and nitrogen signals even on the pristine TiO<sub>2</sub> nanotubes (24 and 3%, respectively). They most probably originate from the electrolyte used during anodization and adventitious carbon layer formation under atmospheric exposure.

Overall, after electropolymerization, the atomic carbon and nitrogen contents are increased to 70 and 7%, respectively, confirming the presence of the PDA, whereas the titanium content is reduced from 20 to 11%. Moreover, two new peaks emerge at the carbon spectrum at 283.3 and 285.7 eV associated with C–Ti and C–N bonds, respectively. The former can be interpreted as a noncovalent interaction of the PDA structural units with the surface layer of the TiO<sub>2</sub> rather than the formation of titanium carbides. This statement has been elucidated in our previous work and supported by DFT calculations.<sup>56</sup> The latter is a direct consequence of introducing PDA, which contains C–N bonds of different order, depending on the oxidation state of each unit. Such bonds are also reported on the nitrogen spectrum at 397.8, 399.9, and 401.8 eV associated with aromatic (imine) R–N–R groups, aliphatic R–N–R groups, and tetraalkylammonium (NR<sub>4</sub><sup>+</sup>)

groups, respectively.<sup>56,70–72</sup> However, one should consider that noisy N 1s spectra of TNT IgPDA 532, originating from the low N concentration, affect deconvolution certainty. Additionally, another doublet appeared on the Ti spectrum corresponding to the TiO–C interaction parallel to the data on the C spectrum.

Laser modification of the PDA using 532 nm wavelength yields a reduction of the carbon and nitrogen contents to 40 and 2%, respectively. This outcome strongly indicates that a significant portion of those PDA constituents has been either evaporated or incorporated into deeper atomic layers of the material. However, the general structures of carbon, nitrogen, and titanium spectra are preserved. It is to be noted though that the proportion of the C–C bond content to other types of carbon bonds is increased and the maximum of the C–Ti peak is shifted to larger binding energies. The former suggests that more carbon atoms within the surface layer are bonded to other carbons and nothing else. The latter indicates stronger binding of the organic layer to the titania surface. Both changes could be interpreted as symptoms of graphitization. Over the nitrogen spectrum, a notable decrease of the aliphatic R–N–R group content with respect to others is observed, strongly suggesting a higher level of conjugation characteristic for the sp<sup>2</sup> phase rather than sp<sup>3</sup>. Similar tendencies are observed in the case of the 365 nm modification, although the carbon and nitrogen contents did not plummet as much (to 51 and 3%, respectively).



**Figure 5.** ReaxFF molecular dynamics of the late graphitization stage: (a) final geometry of the system after 4 ns of annealing at 3000 K; (b) top view of the resulting graphene plane; (c) angular distribution function for several periods of the trajectory; (d) evolution of the carbon coordination number; and (e) evolution of the carbon nearest neighbors calculated with different cutoffs (1.8 or 2.5 Å).

Overall, these observations support the statement that graphitization occurred in the case of both the 532 and 365 nm laser exposures, and presumably, a smaller amount of the PDA evaporated in the 365 nm case.

**3.5. ReaxFF Molecular Dynamics Studies of the Laser Graphitization Mechanism.** There have been several mechanisms developed to explain the formation of nanocarbons from different organic precursors during thermal or laser treatment.

From the macroscopic thermodynamic perspective, thermal graphitization can be viewed as series of phase transition of the precursor and colling back to the stable graphitic phase (dissolution–precipitation).<sup>33,73</sup> This process can be catalytically enhanced by the presence of metal, which is capable of forming a solid solution with a carbon source, effectively reducing temperatures of phase transitions. Intermediate carbide formation can also contribute to this catalytic effect.

From the nanoscopic perspective, particles of metal catalysts (e.g., Fe, Ni, Co) facilitate the formation of the planar carbon from the  $sp^3$ -rich sources leading to the formation of graphite/graphene around particles. Then, “planarization” of the carbon propagates away from the catalyst. This can be clearly seen on the TEM images.<sup>38,73</sup>

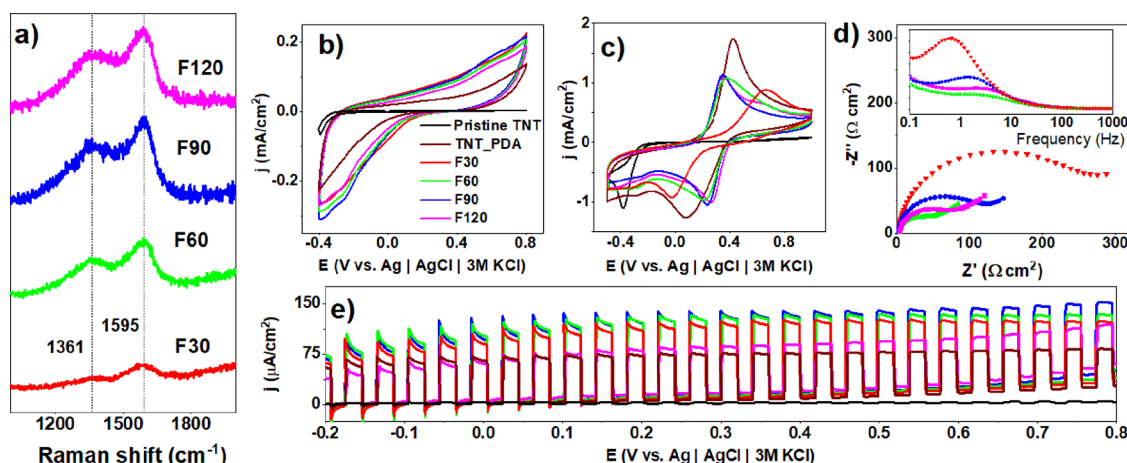
In the case of lasers operating in the IR range, e.g.,  $CO_2$  (10.6  $\mu m$ ), organic matter is initially converted to the amorphous carbon during the photothermal process followed

by phase transition to graphite/graphene upon subsequent lasing.<sup>47</sup> This mechanism seems to be general for both saturated and unsaturated precursors being  $\pi$ -conjugated or not. That is because the laser interacts with vibrational modes of C–C bonds that are abundant in any organics. Addition of metal catalysts prior to graphitization can also make this mechanism more feasible.<sup>74</sup> In essence, the IR laser graphitization mechanism is very similar to the standard thermal (furnace) treatments.

On the other hand, the mechanism of UV or vis laser graphitization is based on photochemical conversion, where chemical bonds break directly as a result of optical excitations without the local temperature rising.<sup>29</sup> In this case, the organic precursor must possess optical absorption bands (typically associated with a  $\pi$  conjugated structure), and the laser power/fluence needs to cross a certain threshold. Details of this mechanism are the least known for any polymer and require further research combining experimental and theoretical approaches.

As an attempt to support the ideas of the PDA graphitization occurring in the current experiments, a series of molecular dynamics (MD) simulations of this process have been performed using reactive force field ReaxFF.<sup>60</sup> The scheme of simulations was adapted from the work in other polymers prone to form laser-induced graphene/graphite.<sup>62</sup>





**Figure 6.** Optimization of laser fluence for TNT\_lgPDA modified using a 532 nm wavelength. Effect of the laser fluence on (a) Raman spectra, (b) CV curves in the dark (0.5 M Na<sub>2</sub>SO<sub>4</sub>), (c) CV curves in the presence of ferrocyanides and ferricyanides (5 mM Fe(CN)<sub>6</sub><sup>3−</sup>/5 mM Fe(CN)<sub>6</sub><sup>4−</sup>), (d) corresponding EIS spectra, and (e) photocurrent–potential dependence in the visible part of the solar spectrum (0.5 M Na<sub>2</sub>SO<sub>4</sub>). F30–F120 values correspond to the range of laser fluences between 30 and 120 mJ/cm<sup>2</sup>.

In general, an initial model of the PDA consisted of four linear tetramer geometry optimized in the periodic boundary conditions. The density of molecules was set to 0.6 g/cm<sup>3</sup> to maintain similar conditions as in a previous work,<sup>62</sup> which was equal to 0.8 g/cm<sup>3</sup>. A smaller density was taken to maintain sufficient free space for the flat graphene formation. During the first 250 ps of the NVT-MD, the initial stacked structure of tetramers begins to rupture with C–C, C–N, and C–O bonds breaking (Figure 4a,b). Then, the evolution of CO, H<sub>2</sub>, H<sub>2</sub>O, and NH<sub>3</sub> gaseous products occurs. At the same time, the sp<sup>2</sup> ringed carbon structures partially unfold and temporarily form sp chain-like entities (Figure 4c).

This initial loss of the ring structure can be seen on the angular distribution functions (Figure 4d) depicting the number of C–C–C bond angles per angle. Initially, most of the carbon atoms formed between 100 and 140° angles corresponding to five-membered and six-membered rings. As the trajectory progresses though, there are C–C–C fragments formed with 60 and 175° with the main 120° contribution plummeting. Second, the time evolution of the carbon coordination numbers (Figure 4e) shows a significant increase of the two-coordinated carbon in exchange with a decrease of the three-coordinated carbons. Thus, the shift from sp<sup>2</sup> to sp during the initial phases of graphitization is justified. Moreover, there is a notable rise in the contribution of singly coordinated carbons corresponding to the evolution of CO gas. The gas evolution can also be tracked by the analysis of the nearest neighbor counts for C–N, C–O, and C–H bonds (Figure 4f). In general, the number of C–N, C–O, and C–H bonds rapidly declines throughout the first 100 ps, whereas the number of C–C bonds oscillates between values of 2.0 and 2.4. Thus, the gas evolution is restricted mostly to the time scale of 100 ps.

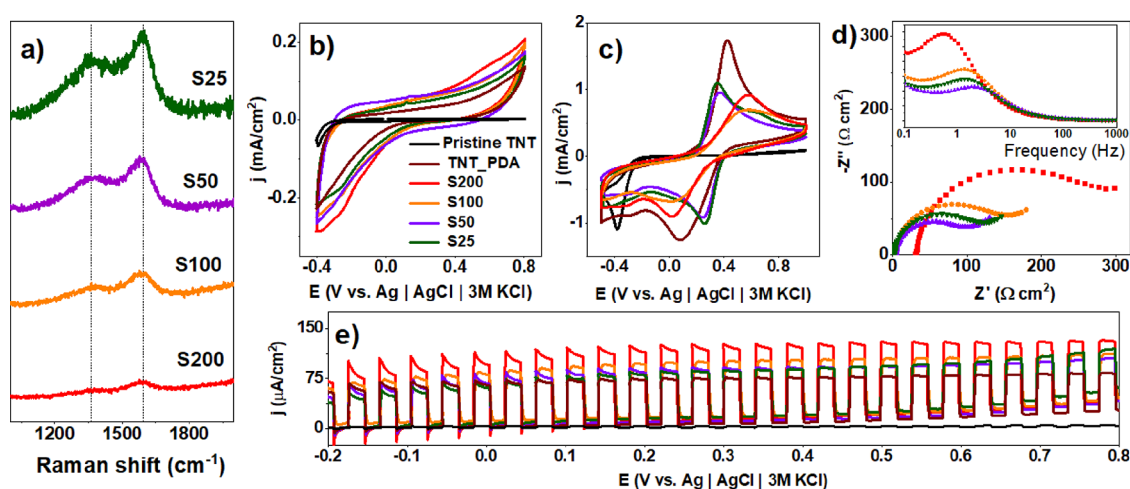
The latter part of the graphitization is mostly condensation of the unfolded structure into the sp<sup>2</sup> graphene-like structure, which is achieved after 4 ns simulation in total (Figure 5a,b). The final lgPDA molecule is equivalent to a slightly twisted defect graphene with hydrogen terminations. The folding back process is captured on the angular distribution functions in Figure 5c. Most of the folding occurs between 1 and 3 ns, and after 3.5 ns, all carbon atoms not evolved to the gas phase constitute a single graphitic molecule, and all C–C–C angles

are 120 ± 20°. The evolution of the carbon coordination number shows the opposite trend with respect to the initial part of the trajectory (compare Figure 5d with Figure 4e). An increase of the three-coordinated carbon numbers in exchange for two-coordinated ones corroborates the folding back process into the sp<sup>2</sup> phase. The nearly constant value of the singly coordinated carbons confirms that the gas evolution does not occur after 1 ns of simulation. Finally, Figure 5e shows that there is a steep rise in the number of carbon neighbors being equal to 2.5 for the 1.8 Å cutoff and 5 for the 2.5 Å cutoff. Those values are greater with respect to those of the pristine PDA (ca. 2). Moreover, almost all neighbors of carbons are other carbons, indicating the graphitization process.

Considering the ReaxFF results, the experimental time of the pulse equal to 8 ns is sufficient for graphitization to occur. The temperature of the NVT thermostat seems not to play a significant role in determining either the final structure or the chemistry of the evolved gases, provided that the bonds are broken during the initial 250 ps. The threshold for this to occur is 2000 K for the applied force field and thermostat parameters (results not shown). Therefore, regardless of the actual initial temperature inside the material after the laser pulse, it is anticipated that the graphitization should occur for a wide range of lasing parameters including energy density, wavelength, and number of pulses.

Furthermore, the final structure of the computed lgPDA was withdrawn from the box and DFT optimized. Then, the band structure and density of states were calculated and compared to those of the pristine DHI tetramer before graphitization (Figure S14a,b). In general, the twisted structure of the hydrogenated graphene is preserved upon the DFT optimization with hydrogen atoms terminating some of the defected areas. The band structure does not exhibit Dirac cone characteristics for ideal graphite;<sup>75</sup> the gap at the Gamma point is open, corroborating the defected structure (Figure S14c). However, there is still a nonzero density of electronic states at the Fermi level indicating that there are some occupied states in the Brillouin zone making the effective electronic band gap equal to zero, in contrast to the DHI tetramer (Figure S14d and e). In the case of zero effective band gap, photocurrent generation would be hindered because of the lack of exciton separation.<sup>76</sup> Although a partially





**Figure 7.** Optimization of the laser table speed for TNT\_IgPDA modified using a 532 nm wavelength. Effect of the laser fluence on (a) Raman spectra, (b) CV curves in the dark (0.5 M  $\text{Na}_2\text{SO}_4$ ), (c) CV curves in the presence of ferrocyanides and ferricyanides (5 mM  $\text{Fe}(\text{CN})_6^{3-}$ /5 mM  $\text{Fe}(\text{CN})_6^{4-}$ ), (d) corresponding EIS spectra, and (e) photocurrent–potential dependence in the visible part of the solar spectrum (0.5 M  $\text{Na}_2\text{SO}_4$ ). S25–S200 values correspond to the range of motorized table speed between 25 and 200 cm/h.

graphitized PDA structure with a nonzero band gap could act as an enhancer of the  $\text{TiO}_2$  absorption in the visible range, the fully graphitized one is expected to inhibit its photocurrent generation. On the other hand, zero band gap scenarios should facilitate electrochemical reactions, making the surface act as a metal compared to pure titania.

**3.6. Influence of the Laser Fluence and Pulse Number on the Properties of the TNT\_IgPDA.** Besides the laser wavelength, two other crucial parameters, the energy of the pulse (fluence) and the number of pulses, can strongly influence both the physical and chemical structure of the TNT\_IgPDA material. The latter parameter was manipulated indirectly by changing the speed of the motorized table during the laser exposure; higher speeds are equivalent to a smaller number of pulses. Results in Figure 6 thoroughly describe the influence of those parameters on the Raman spectra and electrochemical and photoelectrochemical properties in the case of the 532 nm exposure.

In general, intensities of D and G bands increase with the fluence of the laser beam used for sample treatment (Figure 6a). Considering the rapid increase in both intensities at 60  $\text{mJ}/\text{cm}^2$  with respect to 30  $\text{mJ}/\text{cm}^2$ , the former can be associated with the energy threshold required for graphitization. Regardless of this, all coatings slightly increase the capacitive background current with respect to the pristine PDA (Figure 6b).

Moreover, ferrocyanide redox currents are decreased, but the potential difference between them is shrunken (Figure 6c) except for the sample treated with 30  $\text{mJ}/\text{cm}^2$  fluence. This decrease indicates that after graphitization using 532 nm wavelength, the reversibility of the surface reactions and thus the charge transfer rate has been enhanced. A similar trend is present in the EIS data (Figure 6d), with decreasing impedance magnitudes when the fluence is greater than 30  $\text{mJ}/\text{cm}^2$ . Compared with the nongraphitized PDA, the decrease is 2 orders of magnitude from 10  $\text{k}\Omega$  to 100  $\Omega$  (Figure S8). Moreover, characteristic time constants of the graphitized samples (2–5 Hz range) are smaller with respect to the nongraphitized PDA and 30  $\text{mJ}/\text{cm}^2$  sample (0.8–0.9 Hz range). These trends strongly suggest that graphitized samples exhibit higher surface conductivity and charge transfer rates

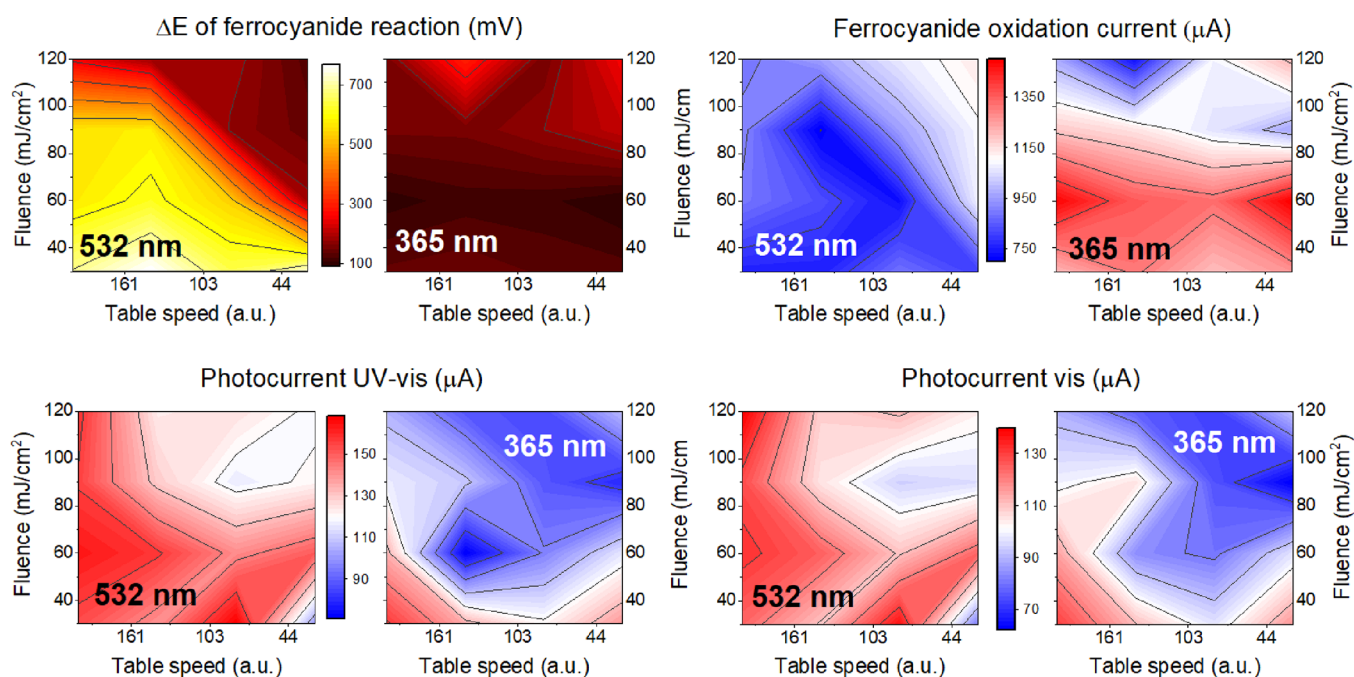
inherent to carbon-based surfaces. Therefore, it is anticipated that graphitization shifts the electronic structure of the PDA toward being more metallic.

Surprisingly though, vis-photocurrents are also increased as a consequence of graphitization (Figure 6e) across the wide window of polarization. Here, 30–90  $\text{mJ}/\text{cm}^2$  fluences provide enhancement, whereas 120  $\text{mJ}/\text{cm}^2$  does not. It suggests that too high of a fluence might cause too high of a degree of graphitization and metallic character. This in turn could plummet the electric field inside the space charge layer of the semiconductor and thus inhibit the capability of exciton separation and the photocurrent generation.<sup>76</sup>

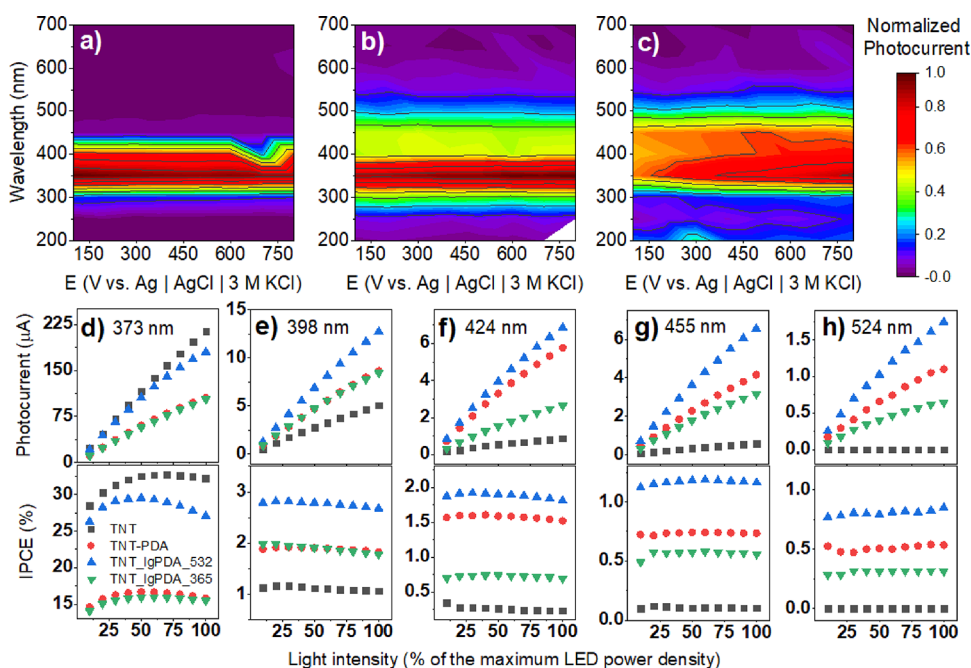
Exactly inverse trends can be captured with the speed of the table. Slower speeds corresponding to the higher number of pulses provide a gradual rise of both D and G Raman band intensities (Figure 7a). Similarly, capacitive background currents increase, (Figure 7b) and ferrocyanide redox peak current decreases (Figure 7c). Potential differences between peaks also decrease after graphitization provided the speed is less than 100 cm/h (S100), indicating a higher charge transfer rate and larger value of the characteristic time constant (Figure 7d). Additionally, Figure 7e shows that the vis-photocurrent enhancements are the most prominent only for samples modified with the highest laser table speed.

Such an outcome is in line with various literature showing the necessity of multiple lasing cycles for the efficient LIG-ation and enhanced electrical properties.<sup>47,77</sup> This feature seems to be general and not limited for PDA.<sup>29</sup>

Analogous optimizations of laser parameters have been performed in the case of the 365 nm exposure, as depicted in Figure S9. Briefly, all symptoms of graphitization i.e., higher G band intensities and lower photocurrents, are obtained by higher fluence and slower table speed. However, electrochemical performance in the presence of ferrocyanides seems not to be altered significantly either by the fluence or the table speed. Presumably, the 365 nm laser interacting mostly with nanotubes enhances the reaction reversibility through charge transfer facilitation between IgPDA and nanotubes to a higher extent than modifications of the PDA itself. These properties are generally also reproduced when the laser graphitization is performed on the PDA deposited on the loosely spaced



**Figure 8.** Contour maps illustrating the influence of laser wavelength, fluence, and number of pulses on various properties of the TNT\_IgPDA including the (a) potential difference between ferrocyanide redox peaks; (b) currents at the oxidation maximum; and (c) photocurrents in the UV–vis and (d) vis parts of the solar spectrum. The right direction at each map points to a higher number of pulses, and the top direction points to a higher fluence. The left panes of each doublet correspond to the 532 nm, and the right panels correspond to the 365 nm modifications.



**Figure 9.** Photoelectrochemical properties of the TNT\_IgPDA. Normalized photocurrent action maps for (a) pristine TNTs, (b) TNT\_PDA, and (c) TNT\_IgPDA modified with 532 nm, 60 mJ/cm<sup>2</sup> laser. (d–h) Photocurrent and quantum efficiency dependencies of the studied samples on the monochromatic light intensity for several wavelengths: 373, 398, 424, 455, and 524 nm. One hundred percent of the LED power density is equal to 2.2 1.6, 1.3, 1.9, and 0.7 mW for all diodes, respectively.

nanotubes (Figure S10) instead of adjacent ones described throughout the text.

**3.7. Optimization of Lasing Parameters on TNT\_IgPDA Photoelectrochemical Properties.** In the context of the ferrocyanide experiment, two parameters are crucial for estimating electrochemical activity: separation between redox peaks and the current value of the oxidation

peaks. The former reflects the reversibility of the charge transfer reaction because the basal TiO<sub>2</sub> n-type semiconductor is not expected to generate an oxidation peak due to the large band gap and deficiency of the density of states during anodic polarization. Those parameters alongside photocurrents are plotted as contour color maps in Figure 8 for 532 and 365 nm

modifications with various laser fluences and numbers of pulses.

In general, the redox peak separation ( $\Delta E$ ) varies significantly with lasing parameters. The first observed trend is that the 365 nm modification results in overall higher electrochemical reversibility ( $\Delta E$  being in the order between 90 and 180 mV) compared to the 532 nm modification (100–750 mV span). For the 532 nm modification, where the laser is believed to interact mostly with the PDA layer, higher fluence and number of pulses lead to a significant reduction of  $\Delta E$  (Figure 8a). Heuristically, this outcome suggests that the higher degree of graphitization improves reversibility. On the other hand, there is less variability in terms of the fluence and pulse number within the 365 nm results. Presumably, the interaction of the laser with nanotubes leads to a higher graphitization degree through thermal effects and heat dissipation rather than photochemical changes. Moreover, the magnitude of the ferrocyanide oxidation peak is markedly greater for the 3 $\omega$  modified samples (up to 1.4 mA compared to 0.8 mA for 532 nm on average, Figure 8b). Higher currents are observed when the material was irradiated with lesser fluences (30 and 60 mJ/cm<sup>2</sup>), presumably because higher fluences strongly distort the geometry of nanotubes beneath PDA (as reported in refs 78,79), thus reducing electroactive surface area.

In terms of the photocurrents, the relationships are almost the opposite because the 532 nm modification results in higher photocurrent under both vis and UV–vis irradiations (Figure 8 and dc). In the case of both wavelengths, lesser fluence and a smaller number of pulses correspond to greater photocurrents. In other words, if laser modification is too intense, the photocurrent yield plummets. There is an inverse dependence that the laser modification leads to higher electrochemical activity, ultimately yielding lower photocurrents and vice versa. To estimate the photosensitization mechanism, samples chosen for further photoelectrochemical investigations are the ones with the highest photocurrents. The parameters are the following: 60 mJ/cm<sup>2</sup> in the case of the 532 nm exposure and 30 mJ/cm<sup>2</sup> in the case of the 365 nm exposure. In both cases, the fastest table speed was chosen, corresponding to the smallest number of pulses the sample is exposed to.

**3.8. Wavelength-Resolved Photocurrents and Quantum Efficiencies of the TNT\_lgPDA.** To further elucidate the photoelectrochemical properties of the TNT\_lgPDA heterostructure, a series of wavelength-resolved photocurrent measurements were performed (Figure 9). In Figure 6a, an action map of the normalized positive photocurrent shows that the main ability of the photocurrent generation occurs for the 300–420 nm range for the pristine nanotubes with the maximum at 350 nm. When the PDA is electropolymerized, this range is extended and covers the wavelengths between 260 and 540 nm with the minimum still at 350 nm. Finally, after the laser treatment, the photocurrent is generated for 300 to 550 nm, but the maximum is shifted to 400 nm, which is visible light. Moreover, whereas the pristine TNT and TNT\_PDA do not exhibit significant variations of the photocurrent with the electrode polarization, it is notable in the case of the TNT\_lgPDA (compare with Figures 6 and 7 and S9).

In general, there are several requirements for efficient photocurrent generation: photon absorption, exciton separation in the space-charge region, fast transport, and slow recombination. The stronger polarization required for the efficient separation suggests that the laser-graphitized electrode

exhibits a weaker electric field in the space charge region, yet the photocurrents after modification are higher in magnitude. Therefore, intensity-modulated photocurrent–photovoltage spectroscopy IMPS/IMVS experiments have been performed to investigate the transport and recombination kinetics.

First, at the 373 nm illumination, the characteristic transport frequency is equal to 13–14 Hz for the samples modified with PDA and lgPDA compared to the 35 Hz of the pristine TNTs (Figure S11). There is also another characteristic frequency at ca. 700 Hz present only at the pristine TNTs. Those two frequencies presumably originate from two different electron transport pathways on the way to the terminal. This outcome suggests that modification with PDA—either graphitized or not—suppresses the transport component of the photocurrent generation requirements.

Moreover, in the regime of high frequencies over 1 kHz, the real part of the photocurrent becomes negative only for the modified samples. This “negative resistance” phenomenon might be associated with nonlinear effects of intensity-dependent transport or influence of localized surface states.<sup>80,81</sup> This behavior is magnified even more in the experiment performed with 424 nm illumination when photocurrents are 1 order of magnitude less (Figure S12).

However, an advantageous attribute of graphitization can be captured in IMVS experiments (Figure S13) performed with 373 nm illumination. In particular, there is a recombination characteristic frequency at 0.15 Hz for the pristine TNT, which is reduced after PDA deposition to 0.04 Hz and even further after graphitization to the value of 0.02 Hz. The last value corresponds to the 4 s characteristic time of recombination. In conclusion, the anticipated mechanism of the photocurrent enhancement induced by the PDA and further graphitization is hindering the recombination.

Furthermore, photocurrent–light intensity (I–P) profiles are given for five different wavelengths (373, 398, 424, 455, and 524 nm) in Figure 9d–h with the corresponding values of the quantum efficiency (IPCE). I–P profiles are slightly nonlinear for all wavelengths in all cases for both pristine and modified electrodes. In the case of the 373 nm laser, photocurrents of the pristine TNT are comparable with the TNT\_lgPDA treated with the 532 nm laser, and their IPCE value lies between 25 and 30%. It is to be noted that the IPCE varies quite significantly with the light intensity for this wavelength, most presumably due to nonlinear effects for the small intensities. However, at all the other wavelengths, photocurrents and quantum efficiencies exhibited by the TNT\_lgPDA are several times higher compared to the pristine TNT. There is also a clear advantage of the 532 nm over the 365 nm exposure even for the optimized samples.

**3.9. Photoelectrochemical Sensing of Serotonin.** TNT\_lgPDA composite can be considered as a member of the broad semiconductor–nanocarbon composite family. These materials are capable of photocurrent generation and have decent conductivity and charge transfer kinetics,<sup>82–84</sup> although not as fast as, e.g., precious metals and alloys. In this context, the spectrum of possible applications of the TNT\_lgPDA composite is spanned by several areas such as photoelectrochemical water splitting,<sup>85</sup> removal of pollutants including antibiotics,<sup>86</sup> and photoelectrochemical sensing (PEC).<sup>87</sup> This subsection of results presents brief, proof-of-concept results showing the high propensity of the TNT\_lgPDA toward PEC sensing of ultralow concentrations of serotonin in a neutral environment.



In general, serotonin was chosen because of the structural similarity to the PDA, which might facilitate amperometric detection.<sup>16</sup> There are many important aspects in the field of neurotransmitter electrochemical sensing, such as spatial and temporal resolution, high selectivity, and long-term stability.<sup>88</sup> However, for simplicity, the purpose here is to show how the graphitized PDA enables detection with a very low (below 1 nM) limit of detection without the support of any precious metals.

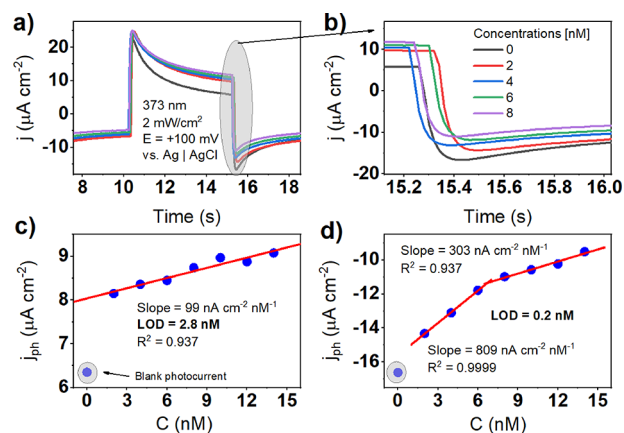
The mechanism of PEC detection is believed to be surface oxidation of the analyte by the photogenerated holes.<sup>89,90</sup> In other words, the analyte acts as a hole scavenger.<sup>84,91,92</sup> In this case, n-type semiconductors are used, and the photocurrent increase in the presence of analyte is also positive.<sup>93,94</sup> However, there are n-type based PEC sensing materials, where the photocurrent decreases upon the addition of analyte.<sup>90,95</sup> On the other hand, p-type semiconductors exhibit reverse trends and negative photocurrents.<sup>96,97</sup>

The sensing performance strongly depends on many factors such as the position of the Fermi level, tendency to Fermi level pinning, distribution of trap states, and experimental parameters.<sup>83,92,98</sup> Nevertheless, the general intuition is that because of the excess energy of the photogenerated electrons, the interfacial charge transfer should be faster. Thus, the detection performance should in principle be better in the PEC experiments compared with the plain electrochemistry. Moreover, the signal-to-noise ratio is also typically smaller because the stimulus signal (light) is different from the collection signal (polarization).<sup>82,94</sup>

The pristine titania nanotubes do not show any affinity toward the serotonin oxidation either in dark conditions or after vis illumination in the desired concentration range (data not shown). The proposed TNT\_lgPDA\_365 composite in the dark conditions also does not exhibit any sign of serotonin oxidation (however, the background capacitive current is reduced upon serotonin adsorption, see Figure S15a).

On the other hand, when the light is applied, there is a notable increase in the photocurrent response upon the addition of serotonin in the nM concentration range (Figure 10). This happens both in the case of transient chopped light on/off as well as during continuous, potentiodynamic experiments (Figure S15). In the former case, photocurrent is calculated as the difference between the quasi-steady-state current during illumination (15 s at Figure 10a) and the current just before illumination (10 s at Figure 10a). The resulting calibration curve in Figure 10c shows a rapid increase of the photocurrent after addition of 2 nM compared to the blank 1× Tris solution and then a roughly linear increase until 16 nM. The calculated limit of detection (LOD) is equal to 2.8 nM; however, the rapid increase of the photocurrent after the first portion strongly suggests that its true value should be smaller. Moreover, the linearity is far from perfect.

Interestingly, when the dark current right after the light-off switch is taken as the main signal, the limit of detection is improved by 1 order of magnitude (200 pM), and two well-defined linear ranges emerge instead of one (Figure 10b,d). It shows, on the one hand, the complexity of the PEC sensing mechanism and, on the other hand, the very prominent behavior toward ultralow concentration detection. It is to be noted that a relatively small overpotential (+100 mV with respect to the ca. −100 mV of the OCP) is required for the effective PEC sensing and further anodic polarization does not improve the performance (results not shown). The sensing



**Figure 10.** Photoelectrochemical chronoamperometric sensing of serotonin in 0.1× Tris (pH = 7.2) solution using TNT\_lgPDA\_365 nm: (a) shape of the photocurrent response; (b) magnification of the dark current just after switching off the light; (c) calibration curve plotted using photocurrent data; and (d) calibration curve plotted using dark current just after switching off the light. Polarization was equal to 0.1 V against Ag|AgCl |3 M KCl reference electrode. The light source was set to 373 nm LED with an intensity of 2 mW cm<sup>−2</sup>.

mechanism is even more complicated for higher concentrations of the analyte (Figure S15c,f). After exceeding ca. 16 nM, the photocurrent still increases, but the linearity is lost because of the current saturation of unknown origin. Moreover, the shape of the photocurrent response step changes markedly for some particular values of concentration.

According to the literature overview performed by the authors, there is no PEC sensor of serotonin published yet. However, there are some related works involving dopamine. Table 2 contains a comparison of the sensing performance against the plain electrochemical sensing of serotonin and the PEC sensing of dopamine. A more comprehensive discussion can be found in the review.<sup>99</sup> The most prominent aspect of the TNT\_lgPDA composite in comparison to other state-of-the-art materials is the lack of precious metals involved in the synthesis. Moreover, the fabrication protocol is simpler relative to other reports, and the material has only two constituents: titania nanotubes and graphitized PDA. Nevertheless, its limit of detection in a neutral (pH = 7.2) environment being equal to 200 pM is strongly competitive, and the sensitivity (defined as the slope of the linear range) is superior to all the other materials. The width of this range, related to the PEC sensing mechanisms, is to be improved though and requires more fundamental understanding of the photophysics of the detection. This is, however, in general not well understood in the literature.

**3.10. Discussion of Advantages and Disparities of the Laser Graphitization Protocol.** Overall, the main advantages of laser graphitization over other graphitization methods, including high temperature treatment, are its speed, possibility of pattern formation, and relatively low energy expenditure. In principle, a single sample can be graphitized in less than a minute compared to thermal treatments requiring several hours (of course, the increment of graphitized surface area with lasing time depends on the spot size, which is adjustable). Adjustability of laser parameters enables tailoring of the morphology, porosity, and hydrophilicity of the obtained carbonized material.<sup>30</sup> Moreover, in the case of PDA and other polymers (or even biomass components), temperatures



**Table 2. Comparison of Various Materials for the Electrochemical and Photoelectrochemical Detection of Neurotransmitters<sup>a</sup>**

material	analyte	method and environment	limit of detection [nM]	linear ranges	sensitivity (slope) [nA cm <sup>-2</sup> nM <sup>-1</sup> ]	ref
CNTs-Cu <sub>2</sub> O-CuO@Pt	serotonin	CA (0.1 M PBS, pH = 7.4)	3	100 nM–2.5 mM	0.2	100
AuNPs@rGO/pTBA-Pd (C <sub>2</sub> H <sub>4</sub> N <sub>2</sub> S <sub>2</sub> ) <sub>2</sub> /NF	serotonin	SWV (0.1 M PBS, pH = 7.4)	2.5	500 nM–200 μM	0.04	101
PEDOTNTs/rGO/AgNPs/GCE	serotonin	DPV (0.1 M PBS, pH = 8)	0.1	400 nM–44 μM	46	102
Ag/PPy/Cu <sub>2</sub> O/GCE	serotonin	DPV (0.1 M PBS, pH = 7.2)	12.4	10 nM–200 μM	0.08	103
Zn CNs-MWCNTs/H-Cu <sub>2</sub> O/CdTe QDs/GCE	dopamine	CA-PEC (0.1 M PBS, pH = 7.0)	0.3	1 nM–100 nM	unknown (logarithmic scaling)	104
BiPO <sub>4</sub> /BiOCl/g-C <sub>3</sub> N <sub>4</sub>	dopamine	CA-PEC (0.1 M PBS, pH = 7.0)	23	50 nM–10 μM	0.7	105
TNT_IgPDA	serotonin	CA-PEC (0.1× Tris, pH = 7.2)	0.2	2–68–16	809 303	this work

<sup>a</sup>CNTs = carbon nanotubes; rGO = reduced graphene oxide; pTBA = poly[2,2:5,2-terthiophene-3-(*p*-benzoic acid)]; PEDOT = poly(ethylene dioxythiophene); GCE = glassy carbon electrode; MWCTNs = multiwalled CNTs; QDs = quantum nanodots; SWV = square wave voltammetry; DPV = difference pulsed voltammetry, CA = chronoamperometry.

required for carbonization are above 700 °C.<sup>31</sup> Thus, a lot of energy is dissipated during furnace operation, in contrast to the laser treatment. Finally, the laser can enable formation of geometric patterns with the area graphitized selectively.

There are, however, disadvantages of the proposed method including the expensiveness of the laser device and optics as well as the necessity of lasing parameter fine-tuning. On the other hand, furnaces for thermal treatment can also be costly, especially because the presence of a vacuum or inert gas atmosphere is obligatory for PDA (and other polymers) carbonization. Despite the relatively high initial cost of the laser equipment, it is compensated over time due to large energy losses during thermal treatment. In the case of laser treatment, the presence of an inert gas or vacuum is not obligatory.<sup>29,47</sup>

In the opinion of the authors, the most problematic issue in the proposed method is the fine-tuning of the parameters. Although it was achieved in this study for titania nanotubes and PDA, each different pair of substrate and polymer would presumably require a different set of parameters for optimization toward electrochemical or photoelectrochemical performance. This optimization for novel pairs might be associated with relatively high costs and in the case of some pairs not even achievable due to nonspecific surface interactions.

Interestingly, fluences used for PDA graphitization in this work are in the range of 30–120 mJ/cm<sup>2</sup>. On the other hand, typical values for other polymers are markedly higher. Athanasios et al.<sup>77</sup> used Nd:YAG 1064 nm laser to synthesize turbostratic graphene from biomass for supercapacitor applications. The fluence required for graphitization was more than 3 J/cm<sup>2</sup> with the optimal value for electrochemical performance equal to 34 J/cm<sup>2</sup>. Fluence as large as 3 J/cm<sup>2</sup> would cause full ablation of the PDA from the surface of TNTs. In other work, Duy et al. calculated the critical fluence of 5 J/cm<sup>2</sup> for polyimide (PI).<sup>106</sup> In the case of continuous lasers,<sup>107</sup> the critical power was estimated to 2 W for PI and similarly to 1 W for the PDA in the seminal *Nature Communications* paper.<sup>25</sup> Therefore, the possibility of PDA graphitization with significantly lower fluences is very promising. Of course, it raises the question of the physical origin of such an effect. On the one hand, it strongly suggests the catalytic effect of the TNTs toward PDA graphitization. On the other hand, it might be associated with the intrinsic

propensity of the PDA toward graphitization. Further research is required to answer those questions and as a result develop applications.

#### 4. CONCLUSIONS

In this work, laser-graphitized polydopamine is obtained on the surface of titania nanotubes via dopamine electropolymerization and subsequent pulsed laser treatment with 365 and 532 nm wavelengths. Partial graphitization is confirmed by Raman and XPS spectroscopies and supported by the water contact angle and electrochemical measurements. An increase in the PDA hardness irradiation was reproduced. Reactive molecular dynamics simulations have shown that graphitization is possible within the several nanosecond pulse time scale and CO, H<sub>2</sub>O, and NH<sub>3</sub> gases evolve during the process. PDA tetramers are linked together into a single, slightly twisted carbon backbone with several defects and H terminations.

Whereas the 532 nm laser pulses interact mostly with PDA coating and graphitization through photochemical changes, the 365 nm pulses are absorbed by both PDA and the substrate nanotubes, leading to graphitization through both photochemical and thermal effects. As a result, the electrochemical activity is higher for 365 nm samples, but photocurrents are smaller. Although PDA already leads to the enhancement of the photocurrent and electrochemical activity of the titania nanotubes, after laser exposure, those are improved even more. Most of the photocurrent and quantum efficiency enhancement is observed in the visible light between 400 and 550 nm, and the boost is more prominent in the case of the 532 nm exposure. The anticipated mechanism of the photocurrent increase by laser modification is through slowing surface recombination rather than speeding up the charge transfer kinetics.

#### ■ ASSOCIATED CONTENT

##### Data Availability Statement

The dataset underlying this work is openly available in Zenodo repository under the following persistent link: <https://zenodo.org/records/10017804>.

##### Supporting Information

The Supporting Information is available free of charge at <https://pubs.acs.org/doi/10.1021/acsami.3c11580>.

Materials and methods—supplementary: reagent synthesis of titania nanotubes (TNTs), X-ray photoelectron

spectroscopy, diffuse reflectance UV–vis spectroscopy, Raman spectroscopy, and density functional theory calculation of the IgPDA electronic structure; results—supplementary: CV curves for dopamine electropolymerization on adjacent titania nanotubes, SEM images of the IgPDA on the surface of loosely spaced nanotubes, optimization of nanotube synthesis and PDA deposition parameters prior to graphitization, supplementary data on the physical properties of the TNT\_IgPDA heterostructure, supplementary electrochemical and photoelectrochemical measurements for IgPDA deposited on adjacent and loosely spaced nanotubes, supplementary photoelectrochemical IMPS and IMVS measurements of the TNT\_IgPDA system, and supplementary XPS quantitative data DFT calculations of the graphitized PDA electronic structure Supplementary serotonin sensing measurements (PDF)

## AUTHOR INFORMATION

### Corresponding Author

**Adrian Olejnik** – Department of Metrology and Optoelectronics, Faculty of Electronics, Telecommunications and Informatics, Gdańsk University of Technology, Gdańsk 80-233, Poland; Centre for Plasma and Laser Engineering, The Szevalski Institute of Fluid-Flow Machinery, Polish Academy of Sciences, Gdańsk 80-231, Poland; [orcid.org/0000-0002-1807-8995](https://orcid.org/0000-0002-1807-8995); Email: [aolejnik@imp.gda.pl](mailto:aolejnik@imp.gda.pl)

### Authors

**Krzysztof Polaczek** – Centre for Plasma and Laser Engineering, The Szevalski Institute of Fluid-Flow Machinery, Polish Academy of Sciences, Gdańsk 80-231, Poland; Department of Biomedical Chemistry, Faculty of Chemistry University of Gdansk, Gdańsk 80-308, Poland

**Marek Szkodo** – Institute of Manufacturing and Materials Technology, Faculty of Mechanical Engineering and Ship Technology, Gdańsk University of Technology, Gdańsk 80-233, Poland

**Alicja Stanisławska** – Institute of Manufacturing and Materials Technology, Faculty of Mechanical Engineering and Ship Technology, Gdańsk University of Technology, Gdańsk 80-233, Poland

**Jacek Ryl** – Institute of Nanotechnology and Materials Engineering and Advanced Materials Center, Gdańsk University of Technology, Gdańsk 80-233, Poland; [orcid.org/0000-0002-0247-3851](https://orcid.org/0000-0002-0247-3851)

**Katarzyna Siuzdak** – Centre for Plasma and Laser Engineering, The Szevalski Institute of Fluid-Flow Machinery, Polish Academy of Sciences, Gdańsk 80-231, Poland; [orcid.org/0000-0001-7434-6408](https://orcid.org/0000-0001-7434-6408)

Complete contact information is available at: <https://pubs.acs.org/10.1021/acsami.3c11580>

### Notes

The authors declare no competing financial interest.

## ACKNOWLEDGMENTS

This work was financially supported by the National Science Center under PRELUDIUM grant 2022/45/N/ST5/00192 and the Polish Ministry of Science and Education under grant DI2019 017649.

## REFERENCES

- (1) Palladino, P.; Bettazzi, F.; Scarano, S. Polydopamine: Surface Coating, Molecular Imprinting, and Electrochemistry—Successful Applications and Future Perspectives in (Bio)Analysis. *Anal. Bioanal. Chem.* **2019**, *411* (19), 4327–4338.
- (2) Jin, Z.; Yang, L.; Shi, S.; Wang, T.; Duan, G.; Liu, X.; Li, Y. Flexible Polydopamine Bioelectronics. *Adv. Funct. Mater.* **2021**, *31* (30), 2103391.
- (3) Bisht, N.; Dwivedi, N.; Khosla, A.; Mondal, D. P.; Srivastava, A. K.; Dhand, C. Review—Recent Advances in Polydopamine-Based Electrochemical Biosensors. *J. Electrochem. Soc.* **2022**, *169* (10), 107505–107505.
- (4) Liebscher, J.; Mrówczyński, R.; Scheidt, H. A.; Filip, C.; Hädade, N. D.; Turcu, R.; Bende, A.; Beck, S. Structure of Polydopamine: A Never-Ending Story? *Langmuir* **2013**, *29* (33), 10539–10548.
- (5) Alfieri, M.; Panzella, L.; Oscurato, S.; Salvatore, M.; Avolio, R.; Errico, M.; Maddalena, P.; Napolitano, A.; d'Ischia, M. The Chemistry of Polydopamine Film Formation: The Amine-Quinone Interplay. *Biomimetics* **2018**, *3* (3), 26.
- (6) d'Ischia, M.; Napolitano, A.; Ball, V.; Chen, C.-T.; Buehler, M. J. Polydopamine and Eumelanin: From Structure–Property Relationships to a Unified Tailoring Strategy. *Acc. Chem. Res.* **2014**, *47* (12), 3541–3550.
- (7) Delparastan, P.; Malollari, K. G.; Lee, H.; Messersmith, P. B. Direct Evidence for the Polymeric Nature of Polydopamine. *Angew. Chem.* **2019**, *131* (4), 1089–1094.
- (8) Lee, H. A.; Park, E.; Lee, H. Polydopamine and Its Derivative Surface Chemistry in Material Science: A Focused Review for Studies at KAIST. *Adv. Mater.* **2020**, *32* (35), 1907505.
- (9) Li, S.; Wang, H.; Young, M.; Xu, F.; Cheng, G.; Cong, H. Properties of Electropolymerized Dopamine and Its Analogues. *Langmuir* **2019**, *35* (5), 1119–1125.
- (10) Marchesi D'Alvise, T.; Sunder, S.; Hasler, R.; Moser, J.; Knoll, W.; Synatschke, C. V.; Harvey, S.; Weil, T. Preparation of Ultrathin and Degradable Polymeric Films by Electropolymerization of 3-Amino-L-Tyrosine. *Macromol. Rapid Commun.* **2022**, *44*, e2200332.
- (11) Cao, W.; Mao, H.; McCallum, N. C.; Zhou, X.; Sun, H.; Sharpe, C.; Korpanty, J.; Hu, Z.; Ni, Q. Z.; Burkart, M. D.; Shawkey, M. D.; Wasielewski, M. R.; Gianneschi, N. C. Biomimetic Pheomelanin to Unravel the Electronic, Molecular and Supramolecular Structure of the Natural Product. *Chem. Sci.* **2023**, *14*, 4183 DOI: [10.1039/d2sc06418a](https://doi.org/10.1039/d2sc06418a).
- (12) Mrówczyński, R.; Markiewicz, R.; Liebscher, Jürgen; Liebscher, J. Chemistry of Polydopamine Analogues. *Polym. Int.* **2016**, *65* (11), 1288–1299.
- (13) Kim, Y.; You, A.; Kim, D.; Bisht, H.; Heo, Y.; Hong, D.; Kim, M.; Kang, S. M. Effect of N-Methylation on Dopamine Surface Chemistry. *Langmuir* **2022**, *38*, 6404 DOI: [10.1021/acs.langmuir.2c00513](https://doi.org/10.1021/acs.langmuir.2c00513).
- (14) Wang, Z.; Zou, Y.; Li, Y.; Cheng, Y. Metal-Containing Polydopamine Nanomaterials: Catalysis, Energy, and Theranostics. *Small* **2020**, *16* (18), 1907042.
- (15) Han, X.; Tang, F.; Jin, Z. Free-Standing Polydopamine Films Generated in the Presence of Different Metallic Ions: The Comparison of Reaction Process and Film Properties. *RSC Adv.* **2018**, *8* (33), 18347–18354.
- (16) Olejnik, A.; Ficek, M.; Szkodo, M.; Stanisławska, A.; Karczewski, J.; Ryl, J.; Dołęga, A.; Siuzdak, K.; Bogdanowicz, R. Tailoring Diffusional Fields in Zwitterion/Dopamine Copolymer Electropolymerized at Carbon Nanowalls for Sensitive Recognition of Neurotransmitters. *ACS Nano* **2022**, *acsnano.2c06406*. 1613183.
- (17) Chalmers, E.; Lee, H.; Zhu, C.; Liu, X. Increasing the Conductivity and Adhesion of Polypyrrole Hydrogels with Electropolymerized Polydopamine. *Chem. Mater.* **2020**, *32* (1), 234–244.
- (18) Almeida, L. C.; Frade, T.; Correia, R. D.; Niu, Y.; Jin, G.; Correia, J. P.; Viana, A. S. Electrosynthesis of Polydopamine-Ethanolamine Films for the Development of Immunosensing Interfaces. *Sci. Rep.* **2021**, *11* (1), 2237.

- (19) Yang, L.; Guo, X.; Jin, Z.; Guo, W.; Duan, G.; Liu, X.; Li, Y. Emergence of Melanin-Inspired Supercapacitors. *Nano Today* **2021**, 37, 101075.
- (20) Corani, A.; Huijser, A.; Gustavsson, T.; Markovitsi, D.; Malmqvist, P.-Å.; Pezzella, A.; d'Ischia, M.; Sundström, V. Superior Photoprotective Motifs and Mechanisms in Eumelanins Uncovered. *J. Am. Chem. Soc.* **2014**, 136 (33), 11626–11635.
- (21) Yang, P.; Zhang, S.; Chen, X.; Liu, X.; Wang, Z.; Li, Y. Recent Developments in Polydopamine Fluorescent Nanomaterials. *Mater. Horiz.* **2020**, 7 (3), 746–761.
- (22) Almeida, L. C.; Correia, R. D.; Marta, A.; Squillaci, G.; Morana, A.; La Cara, F.; Correia, J. P.; Viana, A. S. Electrosynthesis of Polydopamine Films - Tailored Matrices for Laccase-Based Biosensors. *Appl. Surf. Sci.* **2019**, 480, 979–989.
- (23) Leibl, N.; Duma, L.; Gonzato, C.; Haupt, K. Polydopamine-Based Molecularly Imprinted Thin Films for Electro-Chemical Sensing of Nitro-Explosives in Aqueous Solutions. *Bioelectrochemistry* **2020**, 135, 107541.
- (24) Ren, R.; Cai, G.; Yu, Z.; Zeng, Y.; Tang, D. Metal-Polydopamine Framework: An Innovative Signal-Generation Tag for Colorimetric Immunoassay. *Anal. Chem.* **2018**, 90 (18), 11099–11105.
- (25) Lee, K.; Park, M.; Malollari, K. G.; Shin, J.; Winkler, S. M.; Zheng, Y.; Park, J. H.; Grigoropoulos, C. P.; Messersmith, P. B. Laser-Induced Graphitization of Polydopamine Leads to Enhanced Mechanical Performance While Preserving Multifunctionality. *Nat. Commun.* **2020**, 11 (1), 4848.
- (26) Le, T. D.; Phan, H.; Kwon, S.; Park, S.; Jung, Y.; Min, J.; Chun, B. J.; Yoon, H.; Ko, S. H.; Kim, S.; Kim, Y. Recent Advances in Laser-Induced Graphene: Mechanism, Fabrication, Properties, and Applications in Flexible Electronics. *Adv. Funct. Mater.* **2022**, 32, 2205158–2205158.
- (27) Wang, H.; Zhao, Z.; Liu, P.; Guo, X. Laser-Induced Graphene Based Flexible Electronic Devices. *Biosensors* **2022**, 12 (2), 55–55.
- (28) Shokurov, A. V.; Menon, C. Laser-Induced Graphene Electrodes for Electrochemistry Education and Research. *J. Chem. Educ.* **2023**, 100, 2411 DOI: 10.1021/acs.jchemed.2c01237.
- (29) Vivaldi, F. M.; Dallinger, A.; Bonini, A.; Poma, N.; Sembranti, L.; Biagini, D.; Salvo, P.; Greco, F.; Di Francesco, F. Three-Dimensional (3D) Laser-Induced Graphene: Structure, Properties, and Application to Chemical Sensing. *ACS Appl. Mater. Interfaces* **2021**, 13 (26), 30245–30260.
- (30) Ye, R.; James, D. K.; Tour, J. M. Laser-Induced Graphene: From Discovery to Translation. *Adv. Mater.* **2019**, 31 (1), 1803621.
- (31) Torres, F. G.; Troncoso, O. P.; Rodríguez, L.; De-la-Torre, G. E. Sustainable Synthesis, Reduction and Applications of Graphene Obtained from Renewable Resources. *Sustain. Mater. Technol.* **2021**, 29, No. e00310.
- (32) Shams, S. S.; Zhang, L. S.; Hu, R.; Zhang, R.; Zhu, J. Synthesis of Graphene from Biomass: A Green Chemistry Approach. *Mater. Lett.* **2015**, 161, 476–479.
- (33) Yang, P.; Li, T.; Li, H.; Dang, A.; Yuan, L. Progress in the Graphitization and Applications of Modified Resin Carbons. *New Carbon Mater.* **2023**, 38 (1), 96–108.
- (34) Sukmana, I. F.; Widiatmoko, P.; Nurdin, I.; Devianto; Prakoso, T. Effect of ZnCl<sub>2</sub> on Properties of Graphene Produced from Palm Empty Fruit Bunch. *IOP Conf. Ser. Mater. Sci. Eng.* **2020**, 778 (1), No. 012011.
- (35) Talabi, S. I.; Luz, A. P.; Pandolfelli, V. C.; Lucas, A. A. Structural Evolution during the Catalytic Graphitization of a Thermosetting Refractory Binder and Oxidation Resistance of the Derived Carbons. *Mater. Chem. Phys.* **2018**, 212, 113–121.
- (36) Alizadeh, O.; Hosseini, H. M.; Pourjavadi, A.; Bahramian, A. R. Effect of Graphene Oxide on Morphological and Structural Properties of Graphene Reinforced Novolac-Derived Carbon Aerogels: A Modified Quasi-Percolation Model. *Ceram. Int.* **2020**, 46 (8), 11179–11188.
- (37) Yang, G.; Wang, Y.; Zhou, S.; Jia, S.; Xu, H.; Zang, J. Graphene/Phenolic Resin-Based Porous Carbon Composites with Improved Conductivity Prepared via in Situ Polymerization in Graphene Hydrogels. *J. Mater. Sci.* **2019**, 54 (3), 2222–2230.
- (38) Hunter, R. D.; Ramírez-Rico, J.; Schnepf, Z. Iron-Catalyzed Graphitization for the Synthesis of Nanostructured Graphitic Carbons. *J. Mater. Chem. A* **2022**, 10 (9), 4489–4516.
- (39) Chen, F.; Yang, J.; Bai, T.; Long, B.; Zhou, X. Facile Synthesis of Few-Layer Graphene from Biomass Waste and Its Application in Lithium Ion Batteries. *J. Electroanal. Chem.* **2016**, 768, 18–26.
- (40) Ryu, S.; Chou, J. B.; Lee, K.; Lee, D.; Hong, S. H.; Zhao, R.; Lee, H.; Kim, S. Direct Insulation-to-Conduction Transformation of Adhesive Catecholamine for Simultaneous Increases of Electrical Conductivity and Mechanical Strength of CNT Fibers. *Adv. Mater.* **2015**, 27 (21), 3250–3255.
- (41) Kim, Y.; Kim, J. Carbonization of Polydopamine-Coating Layers on Boron Nitride for Thermal Conductivity Enhancement in Hybrid Polyvinyl Alcohol (PVA) Composites. *Polymers* **2020**, 12 (6), 1410.
- (42) Teng, W.; Zhou, Q.; Wang, X.; Che, H.; Du, Y.; Hu, P.; Li, H.; Wang, J. Biotemplating Preparation of N,O-Codoped Hierarchically Porous Carbon for High-Performance Supercapacitors. *Appl. Surf. Sci.* **2021**, 566, 150613.
- (43) Li, H.; Aulin, Y. V.; Frazer, L.; Borguet, E.; Kakodkar, R.; Feser, J.; Chen, Y.; An, K.; Dikin, D. A.; Ren, F. Structure Evolution and Thermoelectric Properties of Carbonized Polydopamine Thin Films. *ACS Appl. Mater. Interfaces* **2017**, 9 (8), 6655–6660.
- (44) Cen, Y.; Dong, J.; Zhu, T.; Cai, X.; Wang, X.; Hu, B.; Xu, C.; Yu, D.; Liu, Y.; Chen, C. Bi Nanorods Anchored in N-Doped Carbon Shell as Anode for High-Performance Magnesium Ion Batteries. *Electrochim. Acta* **2021**, 397, 139260.
- (45) Zou, R.; Liu, F.; Hu, N.; Ning, H.; Gong, Y.; Wang, S.; Huang, K.; Jiang, X.; Xu, C.; Fu, S.; Li, Y.; Yan, C. Graphene/Graphitized Polydopamine/Carbon Nanotube All-Carbon Ternary Composite Films with Improved Mechanical Properties and Through-Plane Thermal Conductivity. *ACS Appl. Mater. Interfaces* **2020**, 12 (51), 57391–57400.
- (46) Zou, R.; Liu, F.; Hu, N.; Ning, H.; Jiang, X.; Xu, C.; Fu, S.; Li, Y.; Zhou, X.; Yan, C. Carbonized Polydopamine Nanoparticle Reinforced Graphene Films with Superior Thermal Conductivity. *Carbon* **2019**, 149, 173–180.
- (47) Chyan, Y.; Ye, R.; Li, Y.; Singh, S. P.; Arnusch, C. J.; Tour, J. M. Laser-Induced Graphene by Multiple Lasing: Toward Electronics on Cloth, Paper, and Food. *ACS Nano* **2018**, 12 (3), 2176–2183.
- (48) Coy, E.; Iatsunskyi, I.; Colmenares, J. C.; Kim, Y.; Mrówczyński, R. Polydopamine Films with 2D-like Layered Structure and High Mechanical Resilience. *ACS Appl. Mater. Interfaces* **2021**, 13 (19), 23113–23120.
- (49) Zhao, H.; Zeng, Z.; Liu, L.; Chen, J.; Zhou, H.; Huang, L.; Huang, J.; Xu, H.; Xu, Y.; Chen, Z.; Wu, Y.; Guo, W.; Wang, J. H.; Wang, J.; Liu, Z. Polydopamine Nanoparticles for the Treatment of Acute Inflammation-Induced Injury. *Nanoscale* **2018**, 10 (15), 6981–6991.
- (50) Aguilar-Ferrer, D.; Szewczyk, J.; Coy, E. Recent Developments in Polydopamine-Based Photocatalytic Nanocomposites for Energy Production: Physico-Chemical Properties and Perspectives. *Catal. Today* **2021**, 397–399, 316.
- (51) Ahmad, N.; Zhang, X.; Yang, S.; Zhang, D.; Wang, J.; Zafar, S. uz; Li, Y.; Zhang, Y.; Hussain, S.; Cheng, Z.; Kumaresan, A.; Zhou, H. Polydopamine/ZnO Electron Transport Layers Enhance Charge Extraction in Inverted Non-Fullerene Organic Solar Cells. *J. Mater. Chem. C* **2019**, 7 (35), 10795–10801.
- (52) Kim, Y.; Coy, E.; Kim, H.; Mrówczyński, R.; Torruella, P.; Jeong, D.-W.; Choi, K. S.; Jang, J. H.; Song, M. Y.; Jang, D.-J.; Peiro, F.; Jurga, S.; Kim, H. J. Efficient Photocatalytic Production of Hydrogen by Exploiting the Polydopamine-Semiconductor Interface. *Appl. Catal. B Environ.* **2021**, 280, 119423.
- (53) Guan, P.; Bai, H.; Li, C.; Ge, Y.; Xu, D.; Chen, B.; Xia, T.; Fan, W.; Shi, W. Integrated Heterostructure of PDA/Bi-AgIn<sub>5</sub>S<sub>8</sub>/TiO<sub>2</sub> for Photoelectrochemical Hydrogen Production: Understanding the



Synergistic Effect of Multilayer Structure. *Adv. Mater. Interfaces* **2018**, *5* (10), 1701574.

(54) Mao, W.-X.; Lin, X.-J.; Zhang, W.; Chi, Z.-X.; Lyu, R.-W.; Cao, A.-M.; Wan, L.-J. Core–Shell Structured TiO<sub>2</sub>@polydopamine for Highly Active Visible-Light Photocatalysis. *Chem. Commun.* **2016**, *52* (44), 7122–7125.

(55) Damberga, D.; Fedorenko, V.; Grundšteins, K.; Altundal, Ş.; Šutka, A.; Ramanavičius, A.; Coy, E.; Mrówczyński, R.; Iatsunskyi, I.; Viter, R. Influence of PDA Coating on the Structural, Optical and Surface Properties of ZnO Nanostructures. *Nanomaterials* **2020**, *10* (12), 2438.

(56) Olejnik, A.; Olbrys, K.; Karczewski, J.; Ryl, J.; Bogdanowicz, R.; Siuzdak, K. Band Gap Engineering toward Semimetallic Character of Quinone-Rich Polydopamine. *J. Phys. Chem. C* **2023**, *127*, 12662 DOI: 10.1021/acs.jpcc.2c08804.

(57) Sun, X.; Yan, L.; Xu, R.; Xu, M.; Zhu, Y. Surface Modification of TiO<sub>2</sub> with Polydopamine and Its Effect on Photocatalytic Degradation Mechanism. *Colloids Surf. Physicochem. Eng. Asp.* **2019**, *570*, 199–209.

(58) Oliver, W. C.; Pharr, G. M. An Improved Technique for Determining Hardness and Elastic Modulus Using Load and Displacement Sensing Indentation Experiments. *J. Mater. Res.* **1992**, *7* (6), 1564–1583.

(59) Smidstrup, S.; Markussen, T.; Vancraeyveld, P.; Wellendorff, J.; Schneider, J.; Gunst, T.; Verstichel, B.; Stradi, D.; Khomyakov, P. A.; Vej-Hansen, U. G.; Lee, M.-E.; Chill, S. T.; Rasmussen, F.; Penazzi, G.; Corsetti, F.; Ojanperä, A.; Jensen, K.; Palsgaard, M. L. N.; Martinez, U.; Blom, A.; Brandbyge, M.; Stokbro, K. QuantumATK: An Integrated Platform of Electronic and Atomic-Scale Modelling Tools. *J. Phys.: Condens. Matter* **2020**, *32* (1), No. 015901.

(60) van Duin, A. C. T.; Dasgupta, S.; Lorant, F.; Goddard, W. A. ReaxFF: A Reactive Force Field for Hydrocarbons. *J. Phys. Chem. A* **2001**, *105* (41), 9396–9409.

(61) Budzien, J.; Thompson, A. P.; Zybin, S. V. Reactive Molecular Dynamics Simulations of Shock through a Single Crystal of Pentaerythritol Tetranitrate. *J. Phys. Chem. B* **2009**, *113* (40), 13142–13151.

(62) Vashisth, A.; Kowalik, M.; Gerringer, J. C.; Ashraf, C.; van Duin, A. C. T.; Green, M. J. ReaxFF Simulations of Laser-Induced Graphene (LIG) Formation for Multifunctional Polymer Nanocomposites. *ACS Appl. Nano Mater.* **2020**, *3* (2), 1881–1890, DOI: 10.1021/acsanm.9b02524.

(63) Schneider, J.; Hamaekers, J.; Chill, S. T.; Smidstrup, S.; Bulin, J.; Thesen, R.; Blom, A.; Stokbro, K. ATK-ForceField: A New Generation Molecular Dynamics Software Package. *Model. Simul. Mater. Sci. Eng.* **2017**, *25*, 085007 DOI: 10.1088/1361-651x/aa8ff0.

(64) Konieczka, P.; Namieśnik, J. *Quality Assurance and Quality Control in the Analytical Chemical Laboratory: A Practical Approach*, 2nd ed.; CRC Press: Boca Raton, 2018. DOI: 10.1201/9781315295015.

(65) Olejnik, A.; Ficek, M.; Siuzdak, K.; Bogdanowicz, R. Multi-Pathway Mechanism of Polydopamine Film Formation at Vertically Aligned Diamondised Boron-Doped Carbon Nanowalls. *Electrochim. Acta* **2022**, *409*, 140000.

(66) Kund, J.; Daboss, S.; D'Alvise, T. M.; Harvey, S.; Synatschke, C. V.; Weil, T.; Kranz, C. Physicochemical and Electrochemical Characterization of Electropolymerized Polydopamine Films: Influence of the Deposition Process. *Nanomaterials* **2021**, *11* (8), 1964.

(67) Camurri, G.; Ferrarini, P.; Giovanardi, R.; Benassi, R.; Fontanesi, C. Modelling of the Initial Stages of the Electropolymerization Mechanism of O-Phenylenediamine. *J. Electroanal. Chem.* **2005**, *585* (2), 181–190.

(68) Losito, I.; Palmisano, F.; Zamboni, P. G. O-Phenylenediamine Electropolymerization by Cyclic Voltammetry Combined with Electrospray Ionization-Ion Trap Mass Spectrometry. *Anal. Chem.* **2003**, *75* (19), 4988–4995.

(69) Pisarevskaya, E. Yu.; Serdyuk, T. M.; Ovsyannikova, E. V.; Buryak, A. K.; Alpatova, N. M. Electropolymerization Features of O-

Phenylenediamine on Carbon Electrode with Developed Surface. *Synth. Met.* **2010**, *160* (21–22), 2366–2370.

(70) Della Vecchia, N. F.; Luchini, A.; Napolitano, A.; D'Errico, G.; Vitello, G.; Szekely, N.; d'Ischia, M.; Paduano, L. Tris Buffer Modulates Polydopamine Growth, Aggregation, and Paramagnetic Properties. *Langmuir* **2014**, *30* (32), 9811–9818.

(71) Liu, T.; Kim, K. C.; Lee, B.; Chen, Z.; Noda, S.; Jang, S. S.; Lee, S. W. Self-Polymerized Dopamine as an Organic Cathode for Li- and Na-Ion Batteries. *Energy Environ. Sci.* **2017**, *10* (1), 205–215.

(72) Batul, R.; Bhawe, M.; J. Mahon, P.; Yu, A. Polydopamine Nanosphere with In-Situ Loaded Gentamicin and Its Antimicrobial Activity. *Molecules* **2020**, *25* (9), 2090.

(73) Kumari, T. S. D. Catalytic Graphitization: A Bottom-up Approach to Graphene and Quantum Dots Derived Therefrom – A Review. *Mater. Today Proc.* **2021**, *46*, 3069–3074.

(74) Han, X.; Ye, R.; Chyan, Y.; Wang, T.; Zhang, C.; Shi, L.; Zhang, T.; Zhao, Y.; Tour, J. M. Laser-Induced Graphene from Wood Impregnated with Metal Salts and Use in Electrocatalysis. *ACS Appl. Nano Mater.* **2018**, *1* (9), 5053–5061.

(75) Pletikosić, I.; Kralj, M.; Pervan, P.; Brako, R.; Coraux, J.; N'Diaye, A. T.; Busse, C.; Michely, T. Dirac Cones and Minigaps for Graphene on Ir(111). *Phys. Rev. Lett.* **2009**, *102* (5), 056808.

(76) Guo, Z.; Lee, D.; Schaller, R. D.; Zuo, X.; Lee, B.; Luo, T.; Gao, H.; Huang, L. Relationship between Interchain Interaction, Exciton Delocalization, and Charge Separation in Low-Bandgap Copolymer Blends. *J. Am. Chem. Soc.* **2014**, *136* (28), 10024–10032.

(77) Athanasiou, M.; Samartzis, N.; Sygellou, L.; Dracopoulos, V.; Ioannides, T.; Yannopoulos, S. N. High-Quality Laser-Assisted Biomass-Based Turbostratic Graphene for High-Performance Supercapacitors. *Carbon* **2021**, *172*, 750–761.

(78) Wawrzyniak, J.; Karczewski, J.; Kupracz, P.; Grochowska, K.; Zaleski, K.; Pshyk, O.; Coy, E.; Bartmański, M.; Szkodo, M.; Siuzdak, K. Laser-Assisted Modification of Titanium Dioxide Nanotubes in a Tilted Mode as Surface Modification and Patterning Strategy. *Appl. Surf. Sci.* **2020**, *508*, 145143.

(79) Wawrzyniak, J.; Karczewski, J.; Kupracz, P.; Grochowska, K.; Coy, E.; Mazikowski, A.; Ryl, J.; Siuzdak, K. Formation of the Hollow Nanopillar Arrays through the Laser-Induced Transformation of TiO<sub>2</sub> Nanotubes. *Sci. Rep.* **2020**, *10* (1), 20235.

(80) Antuch, M. On the Evolution of the Intensity Modulated Photocurrent Spectroscopy (IMPS) Transfer Function in Quadrants (IV)-(I) or Quadrants (II)-(III). *Curr. Opin. Electrochem.* **2022**, *35*, 101043.

(81) Antuch, M.; Millet, P.; Iwase, A.; Kudo, A. The Role of Surface States during Photocurrent Switching: Intensity Modulated Photocurrent Spectroscopy Analysis of BiVO<sub>4</sub> Photoelectrodes. *Appl. Catal. B Environ.* **2018**, *237*, 401–408.

(82) Da Silva Araújo, M.; Barretto, T. R.; Galvão, J. C. R.; Tarley, C. R. T.; Dall'Antônia, L. H.; De Matos, R.; Medeiros, R. A. Visible Light Photoelectrochemical Sensor for Acetaminophen Determination Using a Glassy Carbon Electrode Modified with BiVO<sub>4</sub> Nanoparticles. *Electroanalysis* **2021**, *33* (3), 663–671.

(83) Petruleviciene, M.; Juodkazyte, J.; Savickaja, I.; Karpicz, R.; Morkvenaite-Vilkonciene, I.; Ramanavičius, A. BiVO<sub>4</sub>-Based Coatings for Non-Enzymatic Photoelectrochemical Glucose Determination. *J. Electroanal. Chem.* **2022**, *918*, 116446.

(84) Wang, Y.; Chen, D.; Zhang, J.; Balogun, M.-S.; Wang, P.; Tong, Y.; Huang, Y. Charge Relays via Dual Carbon-Actions on Nanostructured BiVO<sub>4</sub> for High Performance Photoelectrochemical Water Splitting. *Adv. Funct. Mater.* **2022**, *32* (13), 2112738.

(85) Yang, W.; Prabhakar, R. R.; Tan, J.; Tilley, S. D.; Moon, J. Strategies for Enhancing the Photocurrent, Photovoltage, and Stability of Photoelectrodes for Photoelectrochemical Water Splitting. *Chem. Soc. Rev.* **2019**, *48* (19), 4979–5015.

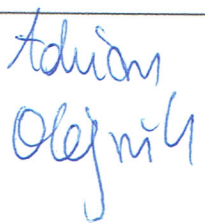
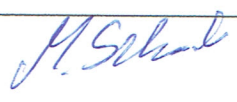


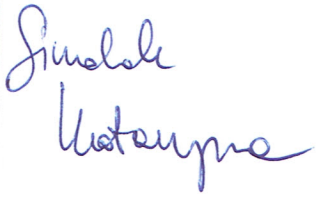
(86) Li, J.; Yuan, H.; Zhang, W.; Jin, B.; Feng, Q.; Huang, J.; Jiao, Z. Advances in Z-scheme Semiconductor Photocatalysts for the Photoelectrochemical Applications: A Review. *Carbon Energy* **2022**, *4* (3), 294–331.



- (87) Shu, J.; Tang, D. Recent Advances in Photoelectrochemical Sensing: From Engineered Photoactive Materials to Sensing Devices and Detection Modes. *Anal. Chem.* **2020**, *92* (1), 363–377.
- (88) Leopold, A. V.; Shcherbakova, D. M.; Verkhusha, V. V. Fluorescent Biosensors for Neurotransmission and Neuromodulation: Engineering and Applications. *Front. Cell. Neurosci.* **2019**, *13*, 474.
- (89) Wang, S.; Li, S.; Wang, W.; Zhao, M.; Liu, J.; Feng, H.; Chen, Y.; Gu, Q.; Du, Y.; Hao, W. A Non-Enzymatic Photoelectrochemical Glucose Sensor Based on BiVO<sub>4</sub> Electrode under Visible Light. *Sens. Actuators B Chem.* **2019**, *291*, 34–41.
- (90) Shang, X.; Weng, Q.; Wang, F.; Wang, J.; Huang, S.; Chen, S.; Han, Z.; Chen, J. Non-Enzymatic Photoelectrochemical Sensors Based on Schiff Base and Chitosan Co-Decorated TiO<sub>2</sub> Nanosheets for Dopamine Detection. *J. Photochem. Photobiol. Chem.* **2021**, *418*, 113426.
- (91) Li, L.; Li, M.; Liu, H.; Li, B.; Wang, B. A Portable Non-Enzyme Photoelectrochemical Ascorbic Acid Sensor Based on BiVO<sub>4</sub> Electrode under 20 W LED Light. *J. Electroanal. Chem.* **2019**, *855*, 113573.
- (92) Sharma, A.; Manna, S.; Kumar, S.; Satpati, A. K. Bismuth Vanadate and 3D Graphene Composite Photoanodes for Enhanced Photoelectrochemical Oxidation of Water. *ACS Omega* **2023**, *8* (37), 33452–33465.
- (93) Khairy, M. A Synergetic Effect of Cerium Oxide Nanocubes and Gold Nanoparticles for Developing a New Photoelectrochemical Sensor of Codeine Drug. *J. Electroanal. Chem.* **2021**, *895*, 115517.
- (94) Liu, F.; Wang, P.; Zhang, Q.; Wang, Z.; Liu, Y.; Zheng, Z.; Qin, X.; Zhang, X.; Dai, Y.; Huang, B.  $\alpha$ -Fe<sub>2</sub>O<sub>3</sub> Film with Highly Photoactivity for Non-enzymatic Photoelectrochemical Detection of Glucose. *Electroanalysis* **2019**, *31* (9), 1809–1814.
- (95) Zhan, W.; Liu, W.; Han, L.; Liang, X.; Chen, R.; Ni, H. GO/Ag<sub>2</sub>S/ZnO Nanorods Coatings for Non-Enzymatic Photoelectrochemical Glycine Determination at Trace Levels. *Phys. B Condens. Matter* **2023**, *665*, 415046.
- (96) Zhang, Y.; Wang, Q.; Liu, D.; Wang, Q.; Li, T.; Wang, Z. Cu<sub>2</sub>O-BiOI Isotype (p-p) Heterojunction: Boosted Visible-Light-Driven Photoelectrochemical Activity for Non-Enzymatic H<sub>2</sub>O<sub>2</sub> Sensing. *Appl. Surf. Sci.* **2020**, *521*, 146434.
- (97) Neven, L.; Shanmugam, S. T.; Rahemi, V.; Trashin, S.; Slegers, N.; Carrión, E. N.; Gorun, S. M.; De Wael, K. Optimized Photoelectrochemical Detection of Essential Drugs Bearing Phenolic Groups. *Anal. Chem.* **2019**, *91* (15), 9962–9969.
- (98) Wu, H.; Zhang, L.; Du, A.; Irani, R.; Van De Krol, R.; Abdi, F. F.; Ng, Y. H. Low-Bias Photoelectrochemical Water Splitting via Mediating Trap States and Small Polaron Hopping. *Nat. Commun.* **2022**, *13* (1), 6231.
- (99) Leau, S.-A.; Lete, C.; Lupu, S. Nanocomposite Materials Based on Metal Nanoparticles for the Electrochemical Sensing of Neurotransmitters. *Chemosensors* **2023**, *11* (3), 179.
- (100) Ashraf, G.; Asif, M.; Aziz, A.; Iftikhar, T.; Liu, H. Rice-Spikelet-like Copper Oxide Decorated with Platinum Stranded in the CNT Network for Electrochemical *In Vitro* Detection of Serotonin. *ACS Appl. Mater. Interfaces* **2021**, *13* (5), 6023–6033.
- (101) Chung, S.; Akhtar, M. H.; Benboudiaf, A.; Park, D.; Shim, Y. A Sensor for Serotonin and Dopamine Detection in Cancer Cells Line Based on the Conducting Polymer–Pd Complex Composite. *Electroanalysis* **2020**, *32* (3), 520–527.
- (102) Sadanandhan, N. K.; Cheriyaathuchenaaramvalli, M.; Devaki, S. J.; Ravindranatha Menon, A. R. PEDOT-Reduced Graphene Oxide-Silver Hybrid Nanocomposite Modified Transducer for the Detection of Serotonin. *J. Electroanal. Chem.* **2017**, *794*, 244–253.
- (103) Selvarajan, S.; Suganthi, A.; Rajarajan, M. A Novel Highly Selective and Sensitive Detection of Serotonin Based on Ag/Polypyrrole/Cu<sub>2</sub>O Nanocomposite Modified Glassy Carbon Electrode. *Ultrason. Sonochem.* **2018**, *44*, 319–330.
- (104) Wang, C.; Chen, J.; Zhang, L.; Yang, Y.; Huang, M.; Chen, C.; Li, C.; Xie, Y.; Zhao, P.; Fei, J. An Ultra-Sensitive Dopamine Photoelectrochemical Sensing Platform Based on Two-Dimensional Zn Carbon Nanosheets, Hollow Cu<sub>2</sub>O and CdTe QDs Composite Films. *Carbon* **2022**, *198*, 101–109.
- (105) Fu, Q.; Wang, C.; Chen, J.; Wang, Y.; Li, C.; Xie, Y.; Zhao, P.; Fei, J. BiPO<sub>4</sub>/BiOCl/g-C<sub>3</sub>N<sub>4</sub> Heterojunction Based Photoelectrochemical Sensing of Dopamine in Serum Samples. *Colloids Surf. Physicochem. Eng. Asp.* **2023**, *656*, 130456.
- (106) Duy, L. X.; Peng, Z.; Li, Y.; Zhang, J.; Ji, Y.; Tour, J. M. Laser-Induced Graphene Fibers. *Carbon* **2018**, *126*, 472–479.
- (107) Lin, J.; Peng, Z.; Liu, Y.; Ruiz-Zepeda, F.; Ye, R.; Samuel, E. L. G.; Yacaman, M. J.; Yakobson, B. I.; Tour, J. M. Laser-Induced Porous Graphene Films from Commercial Polymers. *Nat. Commun.* **2014**, *5* (1), 5714.

**CReditS table for Article 4:**

**Olejn**ik, A., Polaczek, K., Szkodo, M., Stanisławska, A., Ryl, J., & Siuzdak, K. (2023). Laser-induced graphitization of polydopamine on titania nanotubes. *ACS Applied Materials & Interfaces*, 15(45), 52921–52938. <https://doi.org/10.1021/acsami.3c11580>

Author	CRedit author statement	Signature
Adrian Olejnik	<b>Conceptualisation:</b> Full <b>Methodology, Formal analysis, Data curation, Writing Original draft, Writing Review &amp; edit, Visualisation, Project administration, Funding:</b> Leading role, <b>Investigation, Resources, Validation:</b> In part	
Krzysztof Polaczek	<b>Investigation:</b> Leading role <b>Methodology, Validation, Formal analysis, Writing Original draft, Writing Review &amp; edit, Visualisation:</b> In part	
Marek Szkodo	<b>Validation, Methodology, Formal analysis, Investigation, Data curation:</b> In part	
Alicja Stanisławska	<b>Methodology, Formal analysis, Investigation:</b> In part	
Jacek Ryl	<b>Validation, Methodology, Formal analysis, Investigation, Data curation, Writing Original draft, Writing Review &amp; edit:</b> In part	
Katarzyna Siuzdak	<b>Methodology, Validation, Resources, Visualisation, Writing Original draft, Writing Review &amp; edit, Funding, Project administration:</b> In part <b>Supervision:</b> Leading role	

## 6. Conclusions and further research

### 6.1. Conclusions

*Mogłem uczyć się na księdza lub piekarza,  
Duch i ciało zawsze potrzebują stawy,  
Na wojaka mogłem iść I zażyć sławy,  
Co wynosi I przyciąga, bo przeraża...*

*I could have studied to be a priest or a baker,  
Both the spirit and body always need nourishment,  
I could have become a soldier and tasted glory,  
Which elevates and attracts, because it terrifies...*

Przemysław Gintrowski – Syn Marnotrawny (1993)

This work was devoted to the synthesis of PDA and its copolymers on the surface of B:CNW and TNT semiconductors, followed by investigations of the structure and electrochemical properties. From the perspective of a materials scientist, the engineering is performed on the surface morphology and electronic structure by developing electropolymerisation protocols and manipulating the associated synthesis parameters of both the semiconductor substrate and the deposited polymer. Engineering is performed to obtain desired properties, such as high selectivity and sensitivity towards a specific analyte (beneficial in electrochemical sensing) or high charge transfer rates (beneficial in photoelectrochemical applications). The scientific achievements of this thesis can be grouped in several areas: developed synthesis protocols, developed characterisation protocols, and discovered new properties of the PDA-semiconductor junction.

Development of materials synthesis protocols, such as:

- co-electropolymerisation of PDA and PZ on the B:CNW surface;
- hydrogenation-electropolymerisation procedure for obtaining TNT\_PDA materials;
- laser graphitisation of PDA on the surface of TNTs.

Development of materials characterisation protocols and techniques of their analysis, such as:

- protocol for investigating the PDA electropolymerisation mechanism on B:CNWs;
- application of diffusion field description to explain the electrochemical properties of the B:CNW\_PDA\_PZ materials;
- application of novel devices for photoelectrical measurements towards characterisation in terms of photocurrent generation;
- application of the ReaxFF and DFT methodologies to understand the complex phenomena observed experimentally,

Discovered properties of the PDA-semiconductor junctions:

- PDA coupled with PZ can transform highly hydrophobic B:CNW into highly hydrophilic B:CNW\_PDA\_PZ;
- B:CNW\_PDA\_PZ junction exhibits an exceptional distribution of the diffusion field in the vicinity of the electrode during electrochemical measurements;
- Quinone-rich PDA electropolymerised on TNTs enhances the visible photocurrent up to 20x through strong alteration of the surface electronic states of titania;
- TNT\_PDA junctions exhibit semi-metallic properties and nonlinear electric effects;
- Laser treatment of the TNT\_PDA junction increases the charge transfer rate and further boosts the photocurrents, mostly via a reduction of the recombination rates.

Based on the results given in the previous chapter, one could conclude that all three hypotheses were examined and evidenced:

**Hypothesis 1: It will be possible to obtain a homogeneous layer of PDA on the surface of semiconductors via electropolymerisation protocols.**

It was confirmed in **Articles 1–4** that homogeneous PDA coatings can be deposited on the surface of both B:CNW and TNT semiconductors using electropolymerisation protocols. Mechanisms of electropolymerisation were investigated in **Article 1**, voltammetric redox signals were established and assigned to the relevant structural units of the PDA. Depending on the polymerisation pH, potential window and the number of cycles, the thickness and ratio of the PDA structural units can be manipulated. Besides the typical potentiodynamic electropolymerisation investigated and discussed in **Article 1**, a co-electropolymerisation protocol for obtaining a PDA\_PZ coating was developed and described in **Article 2**. Via changes in the synthesis parameters, it is possible to obtain layers with tailorable morphologies and chemistries on the surfaces of both B:CNWs and TNTs.

**Hypothesis 2: Application of the PDA-based coating to B:CNWs will significantly increase the sensitivity and selectivity of the electrode towards sensing catecholamine neurotransmitters.**

The presence of the PDA\_PZ coating on the surface of B:CNWs significantly decreases the water contact angle to 16°, making the surface superhydrophilic. Moreover, it changes the diffusion field geometry in the vicinity of the electrode towards the microelectrode array behaviour. Due to the presence of PDA on the surface, the electrode acquired the ability for dopamine sensing in low concentrations with a sensitivity comparable to the state-of-the-art materials. Due to the presence of PZ, increased antifouling and facilitated transport of the analyte were observed (**Article 2**). Application of the mixed PDA\_PZ coating improved the sensing performance of the B:CNW electrodes, which was shown in **Article 2**. Due to the catalytic effect of the PDA, selectivity towards catecholamine analytes



was achieved, the sensitivity increased 4 times up to  $14.3 \mu\text{A cm}^{-2} \mu\text{M}^{-1}$  and the limit of detection decreased 5 times to 89 nM. Due to the presence of zwitterions, the longevity of the electrode in biofluids environment was extended.

**Hypothesis 3: Application of the PDA-based coating on TNTs will increase their capability towards photocurrent generation in the visible part of the spectrum.**

In **Article 3**, it was shown that quinone-rich PDA synthesised in alkaline conditions can boost the visible photocurrent even 20 times due to significant changes in the electronic structure at the PDA-semiconductor interface. Additionally, the TNT\_PDA coating exhibits a unique, semimetallic behaviour and nonlinear electric effects, as shown in several experiments and DFT computations. Laser graphitisation of the substrate further increased its photocurrents, as well as the charge transfer rate. Moreover, quantum efficiencies of the photocurrent generation in the visible spectrum were also improved. This material possessed a high propensity towards the photoelectrochemical sensing of the neurotransmitter serotonin (**Article 4**).

Overall, on the basis of results in the presented works, it could be stated that research objectives have been fully realised and completed, and the hypotheses were evidenced sufficiently.

## 6.2. Future directions of research

*My vision of the future is so precise that if I had children, I would strangle them immediately.*

*Moja wizja przyszłości jest tak precyzyjna, że gdybym miał dzieci, udusiłbym je natychmiast.*

**Emil Cioran** – ‘The trouble with Being Born’ (1973)

Implementing the B:CNW\_PDA\_PZ electrode into the full sensing device and its field testing would be the next step towards applications. In this context, optimisation of various parameters of both the electrode and the whole device would be required. The target would be achieving a balance between the longevity of the sensor, its cost, sensitivity, and selectivity.

Preparation of other co-electropolymerisation mixtures with PDA is also foreseen as an interesting path for further research. Not only zwitterions, but perhaps other chemistries (e.g. supramolecular structures, metal organic frameworks, molecular crystals, etc.) can be coupled with PDA towards, e.g., photoelectrochemical applications and biosensing.

Considering the extraordinarily high charge transfer rates and electrochemically active surface area of B:CNW electrodes, they exhibit strong potential towards studying the mechanisms of other electrochemical reactions. Not only electropolymerisations, but perhaps various electrosynthesis processes could be studied in various electrolytes and using various potential programs or in the galvanostatic regimes.

Photosensitisation of other semiconductors with PDA would be beneficial towards extending the portfolio of its applications. The interactions of PDA with p-type semiconductors and semi-metals of various origins and associated electronic structures are largely unknown. Comparison of the PDA-semiconductor composites synthesised according to different protocols and high-throughput quantum chemical calculations may be a valuable road in this context. Knowledge in this field could extend the possibilities of bandgap engineering in various fields by either chemical surface modifications or through defect engineering induced by PDA.

Laser graphitisation of various polymers having a similar structure to PDA, such as polyadrenaline, polyserotonin, etc., are also prominent candidates as substrates for LIG. It is also possible to perform LIG-ation with PDA copolymers or the whole composites. Moreover, extensive quantum chemistry and molecular dynamics research into the mechanisms of the PDA synthesis, photosensitisation, and graphitisation could be fruitful research topics, with these not being limited to the electrochemical areas.

## 7. List of Figures

*Conceiving a human into this world is like carrying wood to a burning house.*

*Poczęcie człowieka na ten świat jest jak niesienie drewna do płonącego domu.*

**Peter Wessel Zapfe** – Norwegian pessimistic philosopher; ‘The Last Messiah’ (1933)

<b>Figure 1.</b> Solar energy conversion diagram (left) <sup>1</sup> and scheme of photoelectrochemical cell for water splitting (right) <sup>2</sup> .....	10
<b>Figure 2.</b> Scheme of the dye sensitized solar cell <sup>8</sup> .....	11
<b>Figure 3.</b> Schematic diagram of the electrochemical sensing process <sup>17</sup> .....	12
<b>Figure 4.</b> Two basic routes for the synthesis of polydopamine with proposed reaction mechanism <sup>36</sup> . 14	
<b>Figure 5.</b> Intermolecular interactions of polydopamine <sup>36</sup> .....	15
<b>Figure 6.</b> Doubly staggered band structure of the PDA (reprinted from <sup>53</sup> ) (a) Electronic band structures of ZnS, ZnS <sub>1-x</sub> O <sub>x</sub> (ZnSO), and 5,6-dihydroxyindole (DHI). The black and red lines are the filled and unfilled states, respectively. (b) Schematic representation of the ZnS/PDA heterojunction and photocatalytic process considering charge carrier transfer <sup>53</sup> .....	16
<b>Figure 7.</b> Synthesis and structure of TEMPO-PDA. (A) Schematic illustration of the TEMPO-doped PDA with narrower bandgap and improved light absorption ability compared to conventional PDA. (B) Polymerization of dopamine and TEMPO, together with their molecular structures and powder photographs <sup>54</sup> .....	17
<b>Figure 8.</b> a) Thermogravimetric curve for PDA carbonization; b) SEM image of the carbonized PDA nanoparticles <sup>70</sup> .....	18
<b>Figure 9.</b> HRTEM image of the carbonized PDA nanoparticle and scheme of graphite-like stacking <sup>70</sup> . .....	19
<b>Figure 10.</b> Laser graphitization of the PDA; a) proof-of-concept graphics; b) Raman spectra; c) D/G Raman peaks ratio; d) XPs spectra in the carbon C1s region; e) atomic content as a function of the laser power; f-g) mass spectrometry results of pristine and laser graphitized PDA <sup>71</sup> .....	20
<b>Figure 11.</b> Diagram of applications for the laser induced graphene – based materials <sup>77</sup> . ....	21
<b>Figure 12.</b> Three canonical monomers used for synthesis of polyzwitterions; a) carboxybetaine methacrylate (CBMA), b) sulfobetaine methacrylate (SBMA), c) phosphorylcholine methacrylate (MPC). Value of n lies typically between 1-3 methylene groups <sup>83</sup> .....	22
<b>Figure 13.</b> a) Zwitterions leaving the structure of hydrogen bonding in water unperturbed and b) antifouling mechanism on the molecular level involving lack of counterion release <sup>86</sup> . ....	23
<b>Figure 14.</b> Simplified topologies of the PZ-modified surfaces. ....	24
<b>Figure 15.</b> Covalent attachment of bromoisobutyrate bromide BiBB initiator (top left) to the surface of polydopamine (top right) <sup>83</sup> .....	25
<b>Figure 16.</b> ZI dopamine monomer <sup>93</sup> .....	26

<b>Figure 17.</b> a) Ion migration channels in the PZ-based electrolytes; b) XANES spectrum of the PZ <sup>97</sup> .	27
<b>Figure 18.</b> Morphology of B:CNW (A) nanowall length distribution, (B) top view with the nanowall pattern, (C) cross-sectional image and (D) three-dimensional reconstruction of the nanowall surface <sup>107</sup> .	28
<b>Figure 19.</b> Variations of the bandgap ( $E_g$ ) of boron doped carbon nanowalls. (a) Optical bandgap ( $E_g$ ) and electrical conductivity ( $\sigma$ ) for B:CNW growth at 400 °C, 550 °C, 700 °C, and 850 °C at a ratio of 2000 ppm [B]/[C] ratio; (b) optical band gap and electrical conductivity for B:CNW growth at 0, 2000, 5000, and 7500 ppm [B]/[C] at 700 °C <sup>109</sup> .	29
<b>Figure 20.</b> Comparison of boron-doped diamond (BDD - left) and B:CNW - right in the electrochemical sensing of paracetamol via the difference pulsed voltammetry (DPV) technique <sup>110</sup> .	29
<b>Figure 21.</b> SEM images of the titania nanotube a) top view, b) side view <sup>116</sup> .	30
<b>Figure 22.</b> Influence of anodization voltage on the physiochemical parameters of the loosely spaced titania nanotubes. Dependence of the flat band potential (left panel), charge carrier concentration (right panel) <sup>118</sup> .	31
<b>Figure 23.</b> Influence of anodization voltage on transient photocurrent response <sup>118</sup> .	32
<b>Figure 24.</b> DOS calculations of the pristine and hydrogenated TiO <sub>2</sub> <sup>123</sup> .	33
<b>Figure 25.</b> Photosensitization scheme for example Au <sub>x</sub> – GSH photosensitizer <sup>134</sup> .	33
<b>Figure 26.</b> (Left) Optical absorption spectra and (right) transient photocurrent response of hydrogenated nanotubes modified with PEDOT and different hexacyanometalates <sup>135</sup> .	34
<b>Figure 27.</b> Nanomechanical properties of TNTs modified with the laser beam with varying fluence and indenter angle of incidence <sup>141</sup> .	35
<b>Figure 28.</b> Photoelectrochemical response in UV-vis (left) and vis (right) of TNT modified with various fluence of the Nd:YAG 355 nm laser <sup>142</sup> .	36
<b>Figure 29.</b> Proof-of-concept diagram of the experiments proposed in the thesis.	40
<b>Figure 30.</b> Synthesis of titania nanotubes covered with PDA (TNT_PDA composite) <sup>146</sup> .	43
<b>Figure 31.</b> Schematic diagram of the SEM construction <sup>147</sup> .	45
<b>Figure 32.</b> Interactions of the SEM primary electrons with electrons in the specimen atoms <sup>147</sup> .	46
<b>Figure 33.</b> SEM images of the loosely-spaced titania nanotubes it wo different color palettes a-b) before and c-d) after electropolymerization of the PDA <sup>146</sup> .	47
<b>Figure 34.</b> Schematic of the XPS experimental setup <sup>149</sup> .	48
<b>Figure 35.</b> Interaction of X-Ray photon with inner-shell electrons of the specimen <sup>149</sup> .	48
<b>Figure 36.</b> High-resolution XPS spectra of TNT_PDA with dopamine polymerized in (a) acidic pH (5.7) and (b) alkaline pH (9.1) <sup>146</sup> .	49
<b>Figure 37.</b> Examples of molecular vibrational modes <sup>150</sup> .	50
<b>Figure 38.</b> Experimental setup for IR absorption spectroscopy experiment <sup>151</sup> .	50
<b>Figure 39.</b> Schematic of possible interactions of the light with the sample during the Raman experiment <sup>152</sup> .	51



<b>Figure 40.</b> Experimental setup for Raman spectroscopy experiment <sup>153</sup> .....	52
<b>Figure 41.</b> Example experimental setup for optical absorption spectroscopy experiment; D2 is deuterium lamp emitting UV light and tungsten lamp emits broad spectrum from the UV to IR parts of the electromagnetic spectrum <sup>156</sup> .....	53
<b>Figure 42.</b> Schematic diagram of the integration sphere used in diffuse reflectance measurements <sup>159</sup> . .....	54
<b>Figure 43.</b> Electronic transitions in UV – vis spectroscopy for the molecule <sup>160</sup> .....	54
<b>Figure 44.</b> Optical transitions in UV – vis spectroscopy for the solid semiconductor <sup>161</sup> .....	55
<b>Figure 45.</b> Reflectance (left) and Kubelka-Munk (right) spectra of TNT_PDA materials with variable PDA thickness; inset shows the relation between the number of PDA electropolymerization cycles against the thickness <sup>146</sup> .....	56
<b>Figure 46.</b> a)Schematic of the nanoindentation experimental setup, b) geometry of the example indenter, c) magnification of the indenter tip and its characteristic parameter $d^{165}$ . ....	57
<b>Figure 47.</b> Exemplar load-displacement curve obtained during the nanoindentation process <sup>166</sup> . ....	58
<b>Figure 48.</b> Nanoindentation studies of B:CNW before and after electrodeposition of coatings. (A) Deformation velocity curves; (B) corresponding load–displacement curves; (C) load measured in the scratch test; (D) force of friction measured in the scratch test; (E) load profile applied during impact testing; (F) first, fifth, and 10th impact response of pristine B:CNWs; (G) first, fifth, and 10th impact response of B:CNWs functionalized with a copolymer PDA_PZ coating <sup>167</sup> .....	58
<b>Figure 49.</b> Left: exemplar plot of the CV plot of the redox couple with a single electron transfer reaction; Right: time-potential profile during the forward and backward scan of the CV experiment; $E_2 > E_1$ <sup>169</sup> .....	60
<b>Figure 50.</b> Diffusion field distribution cases with respect to various spacing between microelectrodes in the array <sup>170</sup> . ....	62
<b>Figure 51.</b> Left: simplified diagram illustrating the photocurrent direction and value; Right: exemplar chopped dark/light CA result. ....	63
<b>Figure 52.</b> Diagram of the photocurrent generation in the TiO <sub>2</sub> n-type semiconductor <sup>173</sup> . ....	64
<b>Figure 53.</b> A) Scheme of photoelectrochemical cell; B) Scheme of photoexcitation process utilized for sensing <sup>174</sup> . ....	65
<b>Figure 54.</b> Electrochemical impedance spectroscopy in a nutshell; a) three-electrode system; b) sinusoidal input signal; c) linear approximation; d) Nyquist and Bode plots; e) exemplar Randles equivalent circuit <sup>176</sup> .....	66
<b>Figure 55.</b> A) The general concepts behind electrochemical sensing – recognition, transduction, signal readout; b) sensing signal transduction using various electrochemical techniques <sup>179</sup> .....	69
<b>Figure 56.</b> Multiscale modelling paradigm in materials science. Characteristic length and time correspond to the sizes of the simulation boxes and times of the trajectories for the system investigated with each method <sup>180</sup> . ....	70

<b>Figure 57.</b> Landscape of the quantum chemistry methods <sup>182</sup> .....	72
<b>Figure 58.</b> General concepts of the pseudopotential (left) <sup>183</sup> and the basis set (right) <sup>184</sup> used in quantum chemistry calculations.....	73
<b>Figure 59.</b> Schematic idea differentiating the many-body problem in most quantum chemistry approaches and the electron density problem in DFT <sup>185</sup> .....	73
<b>Figure 60.</b> Hierarchy of the exchange-correlation functionals used in DFT <sup>188</sup> .....	74
<b>Figure 61.</b> Example of two-dimensional potential energy surface <sup>189</sup> .....	75
<b>Figure 62.</b> Example of geometry optimizations to reactants, products and transition state <sup>190</sup> .....	76
<b>Figure 63.</b> Adsorption geometries of two different PDA fragments on the anatase (101) surfaces with electron density maps <sup>146</sup> .....	77
<b>Figure 64.</b> Illustration of the slab model and periodic boundary conditions ideas <sup>191</sup> .....	77
<b>Figure 65.</b> Schematic diagrams of the Density of states plots for several subunits of the PDA. Fermi level is located at 0 eV energy, blue bands are occupied and red are unoccupied <sup>146</sup> .....	78
<b>Figure 66.</b> Example of electrostatic surface potential (ESP) map illustrating interactions between the PDA subunit and zwitterionic molecule <sup>167</sup> .....	79
<b>Figure 67.</b> Left panel: preoptimized geometry of the dopamine adsorbed on the carbon surface coated with PDA_PZ and formation of the molecular pocket for dopamine; Right panel: DFT full optimization of the adsorbed dopamine and geometry illustrating the stabilization of the transition state in the dopamine–dopamine quinone oxidation reaction; the green atom is hydrogen abstracted from the catechol group <sup>167</sup> .....	79
<b>Figure 68.</b> Statistical ensembles used in molecular dynamics <sup>194</sup> .....	80
<b>Figure 69.</b> Components of the typical force field for classical dynamics <sup>196</sup> .....	81
<b>Figure 70.</b> ReaxFF molecular dynamics of the early graphitization stage: (a) initial geometry of the system (4 DHI tetramers); (b, c) geometry of the whole system and the carbon backbone after 250 ps of the annealing at 3000 K; (d) angular distribution function for several periods of the trajectory; (e) evolution of the carbon coordination number; and (f) evolution of the carbon nearest neighbor number projected onto N, O, H, and C atoms (1.8 Å cutoff) <sup>155</sup> .....	82

## 8. List of abbreviations

*A young man becomes an adult when he goes around a puddle instead of stepping into it.*

*Młodzieniec staje się mężczyzną, kiedy obchodzi kałużę zamiast w nią wejść.*

**Plato** – Ancient Philosopher; (V century B.C.)

### 8.1. Compounds and materials:

PDA – polydopamine

PZ – polyzwitterions

ZI – zwitterions

TNT – titania nanotubes

B:CNW – boron-doped carbon nanowalls

DHI – dihydroxyindole

IQ – indolequinone

DA – dopamine

DQ – dopamine-quinone

LDC – leukodopaminechrome

DC – dopaminechrome

SBMA – sulfobetaine methacrylate

CBMA – carboxybetaine methacrylate

MPC – 2-Methacryloyloxyethyl phosphorylcholine

DMSO – dimethylsulfoxide

DEG – diethylene Glycol

PSS – polystyrene sulfonate

PEDOT – poly(3,4-ethylenedioxythiophene)

BiBB – bromoisobutyrate bromide

PPDP – poly(propylsulfonate dimethylammonium propylmethacrylamide)

PEEK – poly(ether ether ketone)

Fc – ferrocene

### 8.2. Techniques:

SAXS – short angle X-ray scattering

EELS – electron energy loss spectroscopy

SEM/TEM – scanning/transmission electron microscopy

XPS – X-ray photoelectron spectroscopy



PE-CVD – plasma enhanced chemical vapor deposition  
 CV – cyclic voltammetry  
 CA – chronoamperometry  
 cCA – cyclic chronoamperometry  
 LSV – linear sweep voltammetry  
 SWV – square wave voltammetry  
 DPV – difference pulsed voltammetry  
 EIS – electrochemical impedance spectroscopy  
 RDE – rotating disk electrode  
 IMPS/IMVS – intensity modulated photocurrent/photovoltage spectroscopy  
 IPCE – incident photon to current efficiency  
 FT-IR – Fourier transform infrared spectroscopy  
 ATR – attenuated total reflection  
 XANES – X-ray absorption near edge spectroscopy  
 ATRP – atom transfer radical polymerization

### **8.3. Computational:**

QM – quantum mechanics  
 DFT – density functional theory  
 MD – molecular dynamics  
 HF – Hartree-Fock  
 MP – Moller-Plesset (perturbation theory)  
 CC – coupled cluster theory  
 CCSC – coupled cluster with Single and Double excitations  
 CI – configuration interaction theory  
 CISD – configuration interaction with Single and Double excitations  
 GGA – generalized gradient approximation  
 LDA – local density approximation  
 RPA – random phase approximation  
 B3LYP – Becke 3 parameter Lee-Yang-Parr functional  
 PBE – Perdew-Burke-Ernzerhof  
 PES – potential energy surface  
 HOMO – highest occupied molecular orbital  
 LUMO – lowest unoccupied molecular orbital  
 DOS – density of states  
 PLDOS – projected local density of states



ESP – electrostatic surface potential

VB/CB – valence band / conduction band

## 8.4. Physical quantities

EASA – electrochemically active surface area [ $\text{m}^2$ ]

$j$  – current or photocurrent density [ $\text{A m}^{-2}$ ]

E and U – potential and voltage [V]

F(R) – Kubelka-Munk function

R – reflectance / resistance [ $\Omega$ ] / universal gas constant or nuclei positions (context dependent)

A – absorbance / arbitrary proportionality constant (context dependent)

T – transmittance [1] / temperature [K] (context dependent)

I or P – light intensity / light power density [ $\text{W m}^{-2}$ ]

Z – impedance [ $\Omega$ ]

$\varphi$  – phase angle

X, Y – real and imaginary parts

C – capacitance [F] / concentration [ $\text{mol dm}^{-3}$ ] (context dependent)

$\hat{H}$  – Hamiltonian

$\hat{T}_n$  – kinetic energy operators

$\hat{V}_n$  – potential energy operators

$\Psi$  – many-body wavefunction

$\phi$  – single-electron Kohn-Sham orbital

G – Gibbs free energy [eV]

## 8.5. Other

DSSC – dye sensitized solar cell

LIG – laser induced graphene

SC – supercapacitor

AOI – angle of incidence

# CRedit definitions (Elsevier's definition)

Term	Definition
Conceptualization	Ideas; formulation or evolution of overarching research goals and aims
Methodology	Development or design of methodology; creation of models
Software	Programming, software development; designing computer programs; implementation of the computer code and supporting algorithms; testing of existing code components
Validation	Verification, whether as a part of the activity or separate, of the overall replication/ reproducibility of results/experiments and other research outputs
Formal analysis	Application of statistical, mathematical, computational, or other formal techniques to analyse or synthesize study data
Investigation	Conducting a research and investigation process, specifically performing the experiments, or data/evidence collection
Resources	Provision of study materials, reagents, materials, patients, laboratory samples, animals, instrumentation, computing resources, or other analysis tools
Data Curation	Management activities to annotate (produce metadata), scrub data and maintain research data (including software code, where it is necessary for interpreting the data itself) for initial use and later reuse
Writing – Original Draft	Preparation, creation and/or presentation of the published work, specifically writing the initial draft (including substantive translation)
Writing – Review & Editing	Preparation, creation and/or presentation of the published work by those from the original research group, specifically critical review, commentary or revision – including pre-or postpublication stages
Visualization	Preparation, creation and/or presentation of the published work, specifically visualization/ data presentation
Supervision	Oversight and leadership responsibility for the research activity planning and execution, including mentorship external to the core team
Project administration	Management and coordination responsibility for the research activity planning and execution
Funding acquisition	Acquisition of the financial support for the project leading to this publication

# Involvement in research projects

*The old man: Now I love God; I do not love men. Man is too imperfect a thing. Love for men would kill me.*

*Zarathustra: What have I spoken of love! I bring men a gift!*

*The old man: Give them nothing! Rather take away a little from them and bear it with them. That will be the most rewarding for them.*

*Starzec: Teraz miłuję Boga, nie kocham ludzi. Człowiek jest rzeczą zbyt niedoskonałą, Miłość ku ludziom zabiłaby mnie.*

*Zarathustra: Cóżem ja o miłości mówił! Niosę ludziom dar!*

*Starzec: Nie dawaj im nic! Raczej ujmij im nieco i dźwigaj z nimi spodem. Tem najbardziej im wynagrodzisz.*

**Friedrich Nietzsche** – ‘Thus Spoke Zarathustra’ (1883)

## List of research projects:

- Principal Investigator of the Ministry of Science and Higher Education project Diamentowy Grant DI2019 017649 ‘Poly(zwitterionic) brushes on titania nanotubes for supercapacitor applications. Characterization of the structure, electrochemistry and nanomechanical properties of heterojunctions’, 217,800 PLN (project duration: 2021 – 2024)
- Principal Investigator of the National Science Center PRELUDIUM 2022/45/N/ST5/00192 project ‘Structure and photoelectrochemistry of the laser graphitized polydopamine on titania nanotubes’, 69,620 PLN (project duration: 2023-2024)
- Investigator in the National Science Center OPUS 2020/37/B/ST7/03262 project: ‘Au-Minecraft – a new approach towards the impedimetric biosensing system’.  
PI: dr hab. eng. Jacek Ryl, prof. PG (duration of my involvement: 2021-2022).  
My tasks in the project included:
  - performing DFT and MD calculations of molecule-surface interactions,
  - participation in the interpretation of the experimental results and tailoring the computational methodology to the project aims,
  - participation in manuscripts preparation.
- Investigator in the National Centre for Research and Development LIDER/2/0003/L-8/16/NCBR/2017 project ‘Innovative, biocompatible sensor for non-invasive glucose monitoring’.  
PI: dr hab. Katarzyna Grochowska (duration of my involvement: 2018-2021).  
My tasks in the project included:
  - fabrication of nanostructured Ti substrates covered with Au nanoparticles using techniques: anodization, magnetron sputtering, laser dewetting
  - development of polymer protective coatings aimed at improving sensor performance
  - electrochemical testing of sensors
  - data analysis, visualization, preparation of research papers

# Conferences and schools

*In solitude, we never waste time, even by doing nothing. We almost always squander it in company.  
W samotności nigdy nie marnujemy czasu, nawet nic nie robiąc. Niemal zawsze trwonimy go w towarzystwie.*

**Emil Cioran** – ‘The Evil Demiurge’ (1967)

*Where solitude ends, there begins the marketplace, and where the marketplace begins,  
there starts the noise of the great actors and the buzzing of the poisonous flies.*

*Gdzie samotność się kończy, tam się zaczyna targ, a gdzie targi się poczynają,  
tam wszczyna się hałas wielkich aktorów i rojne bzykanie much jadowitych.*

**Friedrich Nietzsche** – ‘Thus Spoke Zarathustra’; ‘Tako rzecze Zaratustra’ (1883)

## List of conferences:

- International Workshop on Functional Nanostructured Materials FuNaM – 3  
06-08.10.2021, Kraków  
Oral presentation  
‘Experimental determination of Tauc exponent as a universal tool for investigation of optical transitions in complex semiconductor materials’
- 31<sup>th</sup> International Conference on Diamond and Carbon Materials  
06-09.09.2021, Online  
Poster presentation  
‘Ultra-sensitive Electrochemical Sensing of Dopamine in Neutral pH Using Boron-Doped Carbon Nanowalls’
- Nanotech 2021, 11<sup>th</sup> International Conference.  
09-11.06.2021, Online  
Oral presentation  
‘Electrodeposition of dopamine on the surface of boron doped carbon nanowalls (BCNW) – insights into polymerization mechanism’
- Nanotech 2022, 12<sup>th</sup> International Conference  
Oral presentation  
01-03.06.2022, Poznań  
‘Sensing of neurotransmitters enhanced by the zwitterated polydopamine coating electropolymerized on boron doped carbon nanowalls’
- IEEE 22th Conference on Nanomaterials and Properties (NAP)  
11-16.09.2022, Kraków  
Oral presentation



‘Modification of boron doped carbon nanowalls with electropolymerized dopamine and zwitterions – from intermolecular interactions to enhanced electrochemical sensing’

- Nonlinear phenomena in Electrochemistry and Photovoltaics, Instytut Fotonowy 2022

Invited lecture

16-18.11.2022, Kraków

‘Non-linear response in IMPS/IMVS techniques and spectra of higher harmonics – an introduction’

- 11<sup>th</sup> European Young Engineers Conference (EYEC)

17-19.04.2023, Warszawa

Oral presentation

‘Coupling the Worlds of Theory and Experiment in Materials Science’

- Optomeeting OPTO 2023

17-21.07.2023, Gdańsk

Oral presentation

‘Intensity Modulated Photocurrent/Photovoltage Spectroscopy of Au/Cu Nanoparticle Arrays’

- 244<sup>th</sup> Meeting of the Electrochemical Society (ECS)

8-12.10.2023, Göteborg, Sweden,

Oral presentation

‘Electrochemistry and Electronic Structure of Deuterium-Grown Boron Doped Diamond’

- 11<sup>th</sup> Workshop on Surface Modification for Chemical and Biochemical Sensing (SMCBS)

3-7.11.2023, Łochów, Poland

Oral presentation

‘Laser graphitization of polydopamine on titania nanotubes’

#### **Participation in schools:**

- Summer School on Scattering Theory  
28-30.06.2021 – Integrated Development Program of GUT
- DFT Summer School – Introduction to Density Functional Theory for Experimentalists  
11-17.07.2021 – PARADIM, Cornell University
- PHOTOMOL 2023 Molecular photosensitizers for solar energy conversion in liquid phase  
26.06-07.07.2023 – NAWA Spinaker GUT

# List of Publications

*Teraz masz spokój Hamlecie,  
zrobileś co do ciebie należało I masz spokój.  
Reszta nie jest milczeniem, ale należy do mnie..*

*Now you are at peace, Hamlet,  
you did what you had to do, and you are at peace.  
The rest is not silence, but it belongs to me.*

**Zbigniew Herbert** – polish poet; ‘Tren Fortynbrasa’ (2008)

Total IF = **159.4**

Total ministry points (according to the newest 05.01.2024 criteria) = **3160**

H-index (2024) = **8**

## Publications included as the core of the PHD thesis:

**Article 1: Olejnik, A., Ficek, M., Siuzdak, K., & Bogdanowicz, R. (2022).** Multi-pathway mechanism of polydopamine film formation at vertically aligned diamondised boron-doped carbon nanowalls. *Electrochimica Acta*, 409, 140000. <https://doi.org/10.1016/j.electacta.2022.140000>. (**IF = 7.3, Points = 100**)

**Article 2: Olejnik, A., Ficek, M., Szkodo, M., Stanisławska, A., Karczewski, J., Ryl, J., Dołęga, A., Siuzdak, K. & Bogdanowicz, R. (2022).** Tailoring diffusional fields in zwitterion/dopamine copolymer electropolymerized at carbon nanowalls for sensitive recognition of neurotransmitters. *ACS Nano*, 16(8), 13183-13198. <https://doi.org/10.1021/acsnano.2c06406> (**IF = 17.1, Points = 200**)

**Article 3: Olejnik, A., Olbryś, K., Karczewski, J., Ryl, J., Bogdanowicz, R., & Siuzdak, K. (2023).** Band Gap Engineering toward Semimetallic Character of Quinone-Rich Polydopamine. *The Journal of Physical Chemistry C*. 127(26), 12662–12677. <https://doi.org/10.1021/acs.jpcc.2c08804> (**IF = 4.2, Points = 140**)

**Article 4: Olejnik, A., Polaczek, K., Szkodo, M., Stanisławska, A., Ryl, J., & Siuzdak, K. (2023).** Laser-induced graphitization of polydopamine on titania nanotubes. *ACS Applied Materials & Interfaces*, 15(45), 52921-52938. <https://doi.org/10.1021/acsmi.3c11580> (**IF = 10.4, Points = 200**)

## Other works and results of collaborations:

**Olejnik, A., & Grochowska, K. (2024).** Higher harmonics of the intensity modulated Photocurrent/Photovoltage spectroscopy response-a tool for studying photoelectrochemical nonlinearities. *Measurement*, 224, 113943. <https://doi.org/10.1016/j.measurement.2023.113943> (**IF = 5.1, Points = 200**)

Haryński, Ł., **Olejniki**, A., Grochowska, K., & Siuzdak, K. (2022). A facile method for Tauc exponent and corresponding electronic transitions determination in semiconductors directly from UV–Vis spectroscopy data. *Optical Materials*, 127, 112205. <https://doi.org/10.1016/j.optmat.2022.112205> (**IF = 3.1, Points = 70**)

Haryński, Ł., **Olejniki**, A., Karczewski, J., Ryl, J., Grochowska, K., & Siuzdak, K. (2022). Linking optical and electronic properties to photoresponse of heterojunctions based on titania nanotubes and chromium, molybdenum, and tungsten oxides. *Optical Materials*, 134, 113183. <https://doi.org/10.1016/j.optmat.2022.113183> (**IF = 3.1, Points = 70**)

Lipińska, W., **Olejniki**, A., Karczewski, J., Grochowska, K., & Siuzdak, K. (2023). Annealing Rate as a Crucial Parameter Controlling the Photoelectrochemical Properties of AuCu Mosaic Core–Shell Nanoparticles. *Energy Technology*, 11(1), 2201021. <https://doi.org/10.1002/ente.202201021> (**IF = 4.1, Points = 100**)

Niedzialkowski, P., Koterwa, A., **Olejniki**, A., Zielinski, A., Gornicka, K., Brodowski, M., Bogdanowicz, R., & Ryl, J. (2022). Deciphering the Molecular Mechanism of Substrate-Induced Assembly of Gold Nanocube Arrays toward an Accelerated Electrocatalytic Effect Employing Heterogeneous Diffusion Field Confinement. *Langmuir*, 38(31), 9597-9610. <https://doi.org/10.1021/acs.langmuir.2c01001> (**IF = 3.9, Points = 100**)

Lipińska, W., **Olejniki**, A., Janik, M., Brodowski, M., Sapiega, K., Pierpaoli, M., Siuzdak, K., & Ryl, J. (2023). Texture or Linker? Competitive Patterning of Receptor Assembly toward Ultra-Sensitive Impedimetric Detection of Viral Species at Gold-Nanotextured Titanium Surfaces. *The Journal of Physical Chemistry C*. <https://doi.org/10.1021/acs.jpcc.3c00697> (**IF = 3.7, Points = 140**)

**Olejniki**, A., Dec, B., Goddard III, W. A., & Bogdanowicz, R. (2022). Hopping or tunneling? tailoring the electron transport mechanisms through hydrogen bonding geometry in the boron-doped diamond molecular junctions. *The Journal of Physical Chemistry Letters*, 13(34), 7972-7979. <https://doi.org/10.1021/acs.jpclett.2c01679> (**IF = 5.7, Points = 200**)

Sobaszek, M., Brzhezinskaya, M., **Olejniki**, A., Mortet, V., Alam, M., Sawczak, M., Ficek, M., Gazda, M., Weiss, Z., & Bogdanowicz, R. (2023). Highly Occupied Surface States at Deuterium-Grown Boron-Doped Diamond Interfaces for Efficient Photoelectrochemistry. *Small*, 2208265. <https://doi.org/10.1002/sml.202208265> (**IF = 13.3, Points = 200**)

Pierpaoli, M., Szopińska, M., **Olejniki**, A., Ryl, J., Fudala-Książek, S., Łuczkiwicz, A., & Bogdanowicz, R. (2023). Engineering Boron and Nitrogen Codoped Carbon Nanoarchitectures to Tailor Molecularly Imprinted Polymers for PFOS Determination. *Journal of Hazardous Materials*, 131873. <https://doi.org/10.1016/j.jhazmat.2023.131873> (**IF = 13.6, Points = 200**)

Sain, S., Ficek, M., **Olejnik, A.**, Sawczak, M., Bogdanowicz, R., & Roy, S. S. (2023). Direct determination of paraquat herbicide by square-wave voltammetry by two-step transfer mechanism at heterogeneous boron-doped carbon nanowall electrodes. *Diamond and Related Materials*, 140, 110504. <https://doi.org/10.1016/j.diamond.2023.110504> (IF = 4.1, Points = 100)

Deshmukh, S., Kunuku, S., Jakobczyk, P., **Olejnik, A.**, Chen, C. H., Niu, H., Yang, B., Yang, N., & Bogdanowicz, R. (2023). Diamond-Based Supercapacitors with Ultrahigh Cyclic Stability Through Dual-Phase MnO<sub>2</sub>-Graphitic Transformation Induced by High-Dose Mn-Ion Implantation. *Advanced Functional Materials*, 2308617. <https://doi.org/10.1002/adfm.202308617> (IF = 19.0, Points = 200)

**Olejnik, A.**, Kopec, W., Maskowicz, D., & Sawczak, M. (2023). Spin-Resolved Band Structure of Hoffman Clathrate [Fe (pz) 2Pt (CN) 4] as an Essential Tool to Predict Optical Spectra of Metal–Organic Frameworks. *ACS Applied Materials & Interfaces*, 15(12), 15848-15862. <https://doi.org/10.1021/acsami.2c22626> (IF = 9.5, Points = 200)

**Olejnik, A.**, Siuzdak, K., Karczewski, J., & Grochowska, K. (2020). A flexible Nafion coated enzyme-free glucose sensor based on Au-dimpled Ti structures. *Electroanalysis*, 32(2), 323-332. <https://doi.org/10.1002/elan.201900455> (IF = 3.0, Points = 70)

**Olejnik, A.**, Karczewski, J., Dołęga, A., Siuzdak, K., & Grochowska, K. (2020). Novel approach to interference analysis of glucose sensing materials coated with Nafion. *Bioelectrochemistry*, 135, 107575. <https://doi.org/10.1016/j.bioelechem.2020.107575> (IF = 5.0, Points = 100)

**Olejnik, A.**, Śliwiński, G., Karczewski, J., Ryl, J., Siuzdak, K., & Grochowska, K. (2021). Laser-assisted approach for improved performance of Au-Ti based glucose sensing electrodes. *Applied Surface Science*, 543, 148788. <https://doi.org/10.1016/j.apsusc.2020.148788> (IF = 6.7, Points = 140)

**Olejnik, A.**, Karczewski, J., Dołęga, A., Siuzdak, K., & Grochowska, K. (2020). Insightful analysis of phenomena arising at the metal| polymer interphase of Au-Ti based non-enzymatic glucose sensitive electrodes covered by nafion. *Coatings*, 10(9), 810. <https://doi.org/10.3390/coatings10090810> (IF = 3.4, Points = 100)

**Olejnik, A.**, Karczewski, J., Dołęga, A., Siuzdak, K., Cenian, A., & Grochowska, K. (2022). Simple synthesis route for fabrication of protective photo-crosslinked poly (zwitterionic) membranes for application in non-enzymatic glucose sensing. *Journal of Biomedical Materials Research Part B: Applied Biomaterials*, 110(3), 679-690. <https://doi.org/10.1002/jbm.b.34946> (IF = 3.4, Points = 140)

**Olejnik, A.**, Grochowska, K., & Siuzdak, K. (2021). Synthesis and Characterization of Poly (zwitterionic) Structures for Energy Conversion and Storage. In *Conducting Polymers for Advanced Energy Applications* (pp. 359-382). CRC Press. <https://doi.org/10.1201/9781003150374>



**Olejniak, A.,** Gosz, K., & Piszczczyk, Ł. (2020). Kinetics of cross-linking processes of fast-curing polyurethane system. *Thermochimica Acta*, 683, 178435. **(IF = 3.5, Points = 100)**

**Olejniak, A.,** Kosmela, P., & Piszczczyk, Ł. (2021). Enhancement of PUR/PIR foam thermal stability after addition of *Zostera marina* biomass component investigated via thermal analysis and isoconversional kinetics. *Journal of Polymer Science*, 59(11), 1095-1108. <https://doi.org/10.1002/pol.20210085> **(IF = 3.4, Points = 20)**

Siebert, A., Cholewiński, G., Garwolińska, D., **Olejniak, A.,** Rachoń, J., & Chojnacki, J. (2018). The synthesis and structure of a potential immunosuppressant: N-mycophenoyl malonic acid dimethyl ester. *Journal of Molecular Structure*, 1151, 218-222. <https://doi.org/10.1016/j.molstruc.2017.09.041> **(IF = 3.8, Points = 70)**

# Other achievements

*I teach you the Overman. Man is something that shall be overcome. What have you done to overcome him?*

*Ja was uczyć Nadczłowieka. Człowiek jest czems co pokonanem być powinno. Cóżście uczynili, aby go pokonać?  
[...].*

*Truly, man is a dirty creature. One must be a sea, to receive a dirty stream without becoming unclean.  
Zaprawdę brudnem stworzeniem jest człowiek. Trzeba być morzem, aby brudne strumienie w siebie przyjmować  
i samemu się nie skałać.*

**Fryderyk Nietzsche** – ‘Tako Rzecze Zarathustra’, ‘Thus Spoke Zarathustra’ (1883)

## Stipends:

- IDUB FRANCIUM scholarship for two academic years (second 2022 and third 2023 year of the PhD)
- IDUB NITROGENIUM reward for Article 2
- Polish National Agency for Academic Exchange stipend (NAWA STER – internalization of doctoral schools)

## Patent applications

- Polish patent application P.431086 ‘Electrode material and its modification procedure’
- Polish patent application P.442200 ‘Photoelectrochemically active, conductive material based on titania nanotubes covered with polydopamine’

## Courses:

- Various POWER and InterPhD courses e.g. ‘Mining complex networks’, ‘Computational methods for transport phenomena’, ‘Nutrient removal in municipal water treatment’, ‘Research project management’, ‘Publishing of scientific research’
- Ministry of Science and Higher Education courses eDoktorant 2.0 (2021), e.g. ‘Building and management of effective team’, ‘Become a spiderman: about building a network of relations in academia and business’
- Ministry of Science and Higher Education courses eDoktorant 4.0 (2023), e.g. ‘Mediation in academia’, ‘Scientific communication: from theory to practice’, ‘Effective presentation of scientific results and cooperation with media’

## Article Revisions:

- Revision of the research article in the RSC Analytical Methods Journal

- Revision of the research article in the Elsevier Journal of Photochemistry & Photobiology A: Chemistry

### **Internships:**

- Research internship in the group of prof. Vitezslav Stranak University of South Bohemia, Budweis, Czech Republic under supervision of prof. Zdenek Futera (1 month - 08.2023)  
My tasks:
  - elucidation of the geometry of the plasma – synthesized Nylon using molecular dynamics approaches
  - optimization of MD parameters to obtain the structure the most closely resembling experimental one
  - interactions between the plasma polymer and diamond surface

# List of references

*In the early morning, at the break of day, in all the freshness, at the dawn of one's strength  
to read a book - I call that depravity!*

*Wczesnym rankiem o brzasku dnia, wśród całej świeżości, o jutrzni swej siły  
czytać książkę – to zwę występkiem!*

**Friedrich Nietzsche** – 'Ecce Homo' (1908)

*Die Wissenschaft fragt nicht nach dem Sein.*

*Science does not ask about being.*

*Nauka nie pyta o bycie.*

**Martin Heidegger** – 'Being and Time' (1927)

- (1) Zhang, H.; Lu, Y.; Han, W.; Zhu, J.; Zhang, Y.; Huang, W. Solar Energy Conversion and Utilization: Towards the Emerging Photo-Electrochemical Devices Based on Perovskite Photovoltaics. *Chemical Engineering Journal* **2020**, 393, 124766. <https://doi.org/10.1016/j.cej.2020.124766>.
- (2) Morikawa, T.; Sato, S.; Sekizawa, K.; Arai, T.; Suzuki, T. M. Molecular Catalysts Immobilized on Semiconductor Photosensitizers for Proton Reduction toward Visible-Light-Driven Overall Water Splitting. *ChemSusChem* **2019**, 12 (9), 1807–1824. <https://doi.org/10.1002/cssc.201900441>.
- (3) Lai, W.-F.; Chao, P.-L.; Lin, X.-Y.; Chen, Y.-P.; Liu, J.-H.; Lin, T.-F.; Hsu, W.-C.; Huang, C.-Y. Characteristics of Dye-Sensitized Solar Cells with TiO<sub>2</sub> Stripes. *Materials* **2022**, 15 (12), 4212. <https://doi.org/10.3390/ma15124212>.
- (4) Chiang, Y.-C.; Lee, C.-R.; Huang, C.-Y. Dye-Sensitized Solar Cells Containing Photoelectrodes with TiO<sub>2</sub> Grids. *Phys. Scr.* **2023**, 98 (12), 125965. <https://doi.org/10.1088/1402-4896/ad0d64>.
- (5) Castillo-Robles, J. A.; Rocha-Rangel, E.; Ramírez-de-León, J. A.; Caballero-Rico, F. C.; Armendáriz-Mireles, E. N. Advances on Dye-Sensitized Solar Cells (DSSCs) Nanostructures and Natural Colorants: A Review. *J. Compos. Sci.* **2021**, 5 (11), 288. <https://doi.org/10.3390/jcs5110288>.
- (6) Luo, Y.; Yang, L.; Zhang, J. Photoelectrochemical Polymerization for Solid-State Dye-Sensitized Solar Cells. *Macromol. Rapid Commun.* **2022**, 43 (5), 2100762. <https://doi.org/10.1002/marc.202100762>.
- (7) Javadi, M.; Alizadeh, S.; Khosravi, Y.; Abdi, Y. Electron Transport in Quasi-Two-Dimensional Porous Network of Titania Nanoparticles, Incorporating Electrical and Optical Advantages in Dye-Sensitized Solar Cells. *ChemPhysChem* **2016**, 17 (21), 3542–3547. <https://doi.org/10.1002/cphc.201600609>.
- (8) Klein, M.; Pankiewicz, R.; Zalas, M.; Stampor, W. Magnetic Field Effects in Dye-Sensitized Solar Cells Controlled by Different Cell Architecture. *Sci Rep* **2016**, 6 (1), 30077. <https://doi.org/10.1038/srep30077>.
- (9) Raut, P.; Kishnani, V.; Mondal, K.; Gupta, A.; Jana, S. C. A Review on Gel Polymer Electrolytes for Dye-Sensitized Solar Cells. *Micromachines* **2022**, 13 (5), 680. <https://doi.org/10.3390/mi13050680>.
- (10) Shin, S. S.; Kim, D. W.; Hwang, D.; Suk, J. H.; Oh, L. S.; Han, B. S.; Kim, D. H.; Kim, J. S.; Kim, D.; Kim, J. Y.; Hong, K. S. Controlled Interfacial Electron Dynamics in Highly Efficient Zn<sub>2</sub>SnO<sub>4</sub>-Based Dye-Sensitized Solar Cells. *ChemSusChem* **2014**, 7 (2), 501–509. <https://doi.org/10.1002/cssc.201300915>.
- (11) Chen, C.; Chen, Y.; Nguyen, V. S.; Chen, S.; Tsai, M.; Chen, J.; Lin, S.; Wei, T.; Yeh, C. Double Fence Porphyrins Featuring Indacenodithiophene Group as an Effective Donor for High-Efficiency Dye-Sensitized Solar Cells. *Advanced Energy Materials* **2023**, 13 (20), 2300353. <https://doi.org/10.1002/aenm.202300353>.
- (12) Zhang, L.; Cui, P.; Yang, H.; Chen, J.; Xiao, F.; Guo, Y.; Liu, Y.; Zhang, W.; Huo, F.; Liu, B. Metal–Organic Frameworks as Promising Photosensitizers for Photoelectrochemical Water Splitting. *Advanced Science* **2016**, 3 (1), 1500243. <https://doi.org/10.1002/advs.201500243>.
- (13) Kaushik, R.; Gandhi, S.; Halder, A. Photoelectrochemical Degradation of Organic Pollutants Coupled with Molecular Hydrogen Generation Using Bi<sub>2</sub>O<sub>3</sub>/TiO<sub>2</sub> Nanoparticle Arrays. *ACS Appl. Nano Mater.* **2023**, 6 (6), 4297–4308. <https://doi.org/10.1021/acsanm.2c05406>.
- (14) Wang, J. Electrochemical Glucose Biosensors. *Chem. Rev.* **2008**, 108 (2), 814–825. <https://doi.org/10.1021/cr068123a>.
- (15) Lakard, S.; Pavel, I.-A.; Lakard, B. Electrochemical Biosensing of Dopamine Neurotransmitter: A Review. *Biosensors* **2021**, 11 (6), 179. <https://doi.org/10.3390/bios11060179>.

- (16) Shen, M.; Qu, Z.; DesLaurier, J.; Welle, T. M.; Sweedler, J. V.; Chen, R. Single Synaptic Observation of Cholinergic Neurotransmission on Living Neurons: Concentration and Dynamics. *J. Am. Chem. Soc.* **2018**, *140* (25), 7764–7768. <https://doi.org/10.1021/jacs.8b01989>.
- (17) Chen, K.; Chou, W.; Liu, L.; Cui, Y.; Xue, P.; Jia, M. Electrochemical Sensors Fabricated by Electrospinning Technology: An Overview. *Sensors* **2019**, *19* (17), 3676. <https://doi.org/10.3390/s19173676>.
- (18) Cao, W.; Zhou, X.; McCallum, N. C.; Hu, Z.; Ni, Q. Z.; Kapoor, U.; Heil, C. M.; Cay, K. S.; Zand, T.; Mantanona, A. J.; Jayaraman, A.; Dhinojwala, A.; Deheyn, D. D.; Shawkey, M. D.; Burkart, M. D.; Rinehart, J. D.; Gianneschi, N. C. Unraveling the Structure and Function of Melanin through Synthesis. *J. Am. Chem. Soc.* **2021**, *143* (7), 2622–2637. <https://doi.org/10.1021/jacs.0c12322>.
- (19) Liebscher, J.; Mrówczyński, R.; Scheidt, H. A.; Filip, C.; Hädade, N. D.; Turcu, R.; Bende, A.; Beck, S. Structure of Polydopamine: A Never-Ending Story? *Langmuir* **2013**, *29* (33), 10539–10548. <https://doi.org/10.1021/la4020288>.
- (20) Daboss, S.; Lin, J.; Godejohann, M.; Kranz, C. Redox Switchable Polydopamine-Modified AFM-SECM Probes: A Probe for Electrochemical Force Spectroscopy. *Anal. Chem.* **2020**, *92* (12), 8404–8413. <https://doi.org/10.1021/acs.analchem.0c00995>.
- (21) Yang, L.; Guo, X.; Jin, Z.; Guo, W.; Duan, G.; Liu, X.; Li, Y. Emergence of Melanin-Inspired Supercapacitors. *Nano Today* **2021**, *37*, 101075. <https://doi.org/10.1016/j.nantod.2020.101075>.
- (22) Delparastan, P.; Malollari, K. G.; Lee, H.; Messersmith, P. B. Direct Evidence for the Polymeric Nature of Polydopamine. *Angew. Chem.* **2019**, *131* (4), 1089–1094. <https://doi.org/10.1002/ange.201811763>.
- (23) Almeida, L. C.; Correia, R. D.; Marta, A.; Squillaci, G.; Morana, A.; La Cara, F.; Correia, J. P.; Viana, A. S. Electrosynthesis of Polydopamine Films - Tailored Matrices for Laccase-Based Biosensors. *Applied Surface Science* **2019**, *480*, 979–989. <https://doi.org/10.1016/j.apsusc.2019.03.015>.
- (24) Almeida, L. C.; Frade, T.; Correia, R. D.; Niu, Y.; Jin, G.; Correia, J. P.; Viana, A. S. Electrosynthesis of Polydopamine-Ethanolamine Films for the Development of Immunosensing Interfaces. *Sci Rep* **2021**, *11* (1), 2237. <https://doi.org/10.1038/s41598-021-81816-1>.
- (25) de França, C. C. L.; Meneses, D.; Silva, A. C. A.; Dantas, N. O.; de Abreu, F. C.; Petroni, J. M.; Lucca, B. G. Development of Novel Paper-Based Electrochemical Device Modified with CdSe/CdS Magic-Sized Quantum Dots and Application for the Sensing of Dopamine. *Electrochimica Acta* **2021**, *367*, 137486. <https://doi.org/10.1016/j.electacta.2020.137486>.
- (26) Aguilar, L. E.; Tumurbaatar, B.; Ghavaminejad, A.; Park, C. H.; Kim, C. S. Functionalized Non-Vascular Nitinol Stent via Electropolymerized Polydopamine Thin Film Coating Loaded with Bortezomib Adjunct to Hyperthermia Therapy. *Sci Rep* **2017**, *7* (1), 9432. <https://doi.org/10.1038/s41598-017-08833-x>.
- (27) Marchesi D'Alvise, T.; Harvey, S.; Hueske, L.; Szelwicka, J.; Veith, L.; Knowles, T. P. J.; Kubiczek, D.; Flaig, C.; Port, F.; Gottschalk, K.; Rosenau, F.; Graczykowski, B.; Fytas, G.; Ruggeri, F. S.; Wunderlich, K.; Weil, T. Ultrathin Polydopamine Films with Phospholipid Nanodiscs Containing a Glycophorin A Domain. *Adv. Funct. Mater.* **2020**, *30* (21), 2000378. <https://doi.org/10.1002/adfm.202000378>.
- (28) Ahmad, N.; Zhang, X.; Yang, S.; Zhang, D.; Wang, J.; Zafar, S. uz; Li, Y.; Zhang, Y.; Hussain, S.; Cheng, Z.; Kumaresan, A.; Zhou, H. Polydopamine/ZnO Electron Transport Layers Enhance Charge Extraction in Inverted Non-Fullerene Organic Solar Cells. *J. Mater. Chem. C* **2019**, *7* (35), 10795–10801. <https://doi.org/10.1039/C9TC02781E>.
- (29) Mao, W.-X.; Lin, X.-J.; Zhang, W.; Chi, Z.-X.; Lyu, R.-W.; Cao, A.-M.; Wan, L.-J. Core-Shell Structured TiO<sub>2</sub> @polydopamine for Highly Active Visible-Light Photocatalysis. *Chem. Commun.* **2016**, *52* (44), 7122–7125. <https://doi.org/10.1039/C6CC02041K>.
- (30) Batul, R.; Bhave, M.; J. Mahon, P.; Yu, A. Polydopamine Nanosphere with In-Situ Loaded Gentamicin and Its Antimicrobial Activity. *Molecules* **2020**, *25* (9), 2090. <https://doi.org/10.3390/molecules25092090>.
- (31) Zou, R.; Liu, F.; Hu, N.; Ning, H.; Jiang, X.; Xu, C.; Fu, S.; Li, Y.; Zhou, X.; Yan, C. Carbonized Polydopamine Nanoparticle Reinforced Graphene Films with Superior Thermal Conductivity. *Carbon* **2019**, *149*, 173–180. <https://doi.org/10.1016/j.carbon.2019.04.038>.
- (32) Li, S.; Wang, H.; Young, M.; Xu, F.; Cheng, G.; Cong, H. Properties of Electropolymerized Dopamine and Its Analogues. *Langmuir* **2019**, *35* (5), 1119–1125. <https://doi.org/10.1021/acs.langmuir.8b01444>.
- (33) Wang, J.; Li, B.; Li, Z.; Ren, K.; Jin, L.; Zhang, S.; Chang, H.; Sun, Y.; Ji, J. Electropolymerization of Dopamine for Surface Modification of Complex-Shaped Cardiovascular Stents. *Biomaterials* **2014**, *35* (27), 7679–7689. <https://doi.org/10.1016/j.biomaterials.2014.05.047>.
- (34) Coskun, H.; Aljabour, A.; Uiberlacker, L.; Strobel, M.; Hild, S.; Cobet, C.; Farka, D.; Stadler, P.; Sariciftci, N. S. Chemical Vapor Deposition - Based Synthesis of Conductive Polydopamine Thin-Films. *Thin Solid Films* **2018**, *645*, 320–325. <https://doi.org/10.1016/j.tsf.2017.10.063>.
- (35) Coskun, H.; Aljabour, A.; Greunz, T.; Kehrner, M.; Stifter, D.; Stadler, P. Electrochemical Hydrogen Storage in Amine-Activated Polydopamine. *Adv. Sustainable Syst.* **2021**, *5* (1), 2000176. <https://doi.org/10.1002/adsu.202000176>.



- (36) Lee, H. A.; Park, E.; Lee, H. Polydopamine and Its Derivative Surface Chemistry in Material Science: A Focused Review for Studies at KAIST. *Advanced Materials* **2020**, *32* (35), 1907505. <https://doi.org/10.1002/adma.201907505>.
- (37) Chalmers, E.; Lee, H.; Zhu, C.; Liu, X. Increasing the Conductivity and Adhesion of Polypyrrole Hydrogels with Electropolymerized Polydopamine. *Chem. Mater.* **2020**, *32* (1), 234–244. <https://doi.org/10.1021/acs.chemmater.9b03655>.
- (38) Alfieri, M.; Panzella, L.; Oscurato, S.; Salvatore, M.; Avolio, R.; Errico, M.; Maddalena, P.; Napolitano, A.; d'Ischia, M. The Chemistry of Polydopamine Film Formation: The Amine-Quinone Interplay. *Biomimetics* **2018**, *3* (3), 26. <https://doi.org/10.3390/biomimetics3030026>.
- (39) Wang, Z.; Zou, Y.; Li, Y.; Cheng, Y. Metal-Containing Polydopamine Nanomaterials: Catalysis, Energy, and Theranostics. *Small* **2020**, *16* (18), 1907042. <https://doi.org/10.1002/sml.201907042>.
- (40) El Yakhlifi, S.; Alfieri, M.-L.; Arntz, Y.; Eredia, M.; Ciesielski, A.; Samori, P.; d'Ischia, M.; Ball, V. Oxidant-Dependent Antioxidant Activity of Polydopamine Films: The Chemistry-Morphology Interplay. *Colloids and Surfaces A: Physicochemical and Engineering Aspects* **2021**, *614*, 126134. <https://doi.org/10.1016/j.colsurfa.2021.126134>.
- (41) Kim, Y.; Coy, E.; Kim, H.; Mrówczyński, R.; Torruella, P.; Jeong, D.-W.; Choi, K. S.; Jang, J. H.; Song, M. Y.; Jang, D.-J.; Peiro, F.; Jurga, S.; Kim, H. J. Efficient Photocatalytic Production of Hydrogen by Exploiting the Polydopamine-Semiconductor Interface. *Applied Catalysis B: Environmental* **2021**, *280*, 119423. <https://doi.org/10.1016/j.apcatb.2020.119423>.
- (42) Jastrzebska, M. M.; Isotalo, H.; Paloheimo, J.; Stubb, H. Electrical Conductivity of Synthetic DOPA-Melanin Polymer for Different Hydration States and Temperatures. *Journal of Biomaterials Science, Polymer Edition* **1996**, *7* (7), 577–586. <https://doi.org/10.1163/156856295X00490>.
- (43) Mostert, A. B.; Powell, B. J.; Pratt, F. L.; Hanson, G. R.; Sarna, T.; Gentle, I. R.; Meredith, P. Role of Semiconductivity and Ion Transport in the Electrical Conduction of Melanin. *Proceedings of the National Academy of Sciences* **2012**, *109* (23), 8943–8947. <https://doi.org/10.1073/pnas.1119948109>.
- (44) Matta, M.; Pezzella, A.; Troisi, A. Relation between Local Structure, Electric Dipole, and Charge Carrier Dynamics in DHICA Melanin: A Model for Biocompatible Semiconductors. *J. Phys. Chem. Lett.* **2020**, *11* (3), 1045–1051. <https://doi.org/10.1021/acs.jpcclett.9b03696>.
- (45) Corani, A.; Pezzella, A.; Pascher, T.; Gustavsson, T.; Markovitsi, D.; Huijsers, A.; d'Ischia, M.; Sundström, V. Excited-State Proton-Transfer Processes of DHICA Resolved: From Sub-Picoseconds to Nanoseconds. *J. Phys. Chem. Lett.* **2013**, *4* (9), 1383–1388. <https://doi.org/10.1021/jz400437q>.
- (46) Huijsers, A.; Pezzella, A.; Hannestad, J. K.; Panzella, L.; Napolitano, A.; d'Ischia, M.; Sundström, V. UV-Dissipation Mechanisms in the Eumelanin Building Block DHICA. *Chem. Eur. J. of Chem. Phys.* **2010**, *11* (11), 2424–2431. <https://doi.org/10.1002/cphc.201000257>.
- (47) Li, H.; Marshall, T.; Aulin, Y. V.; Thenuwara, A. C.; Zhao, Y.; Borguet, E.; Strongin, D. R.; Ren, F. Structural Evolution and Electrical Properties of Metal Ion-Containing Polydopamine. *J Mater Sci* **2019**, *54* (8), 6393–6400. <https://doi.org/10.1007/s10853-019-03337-7>.
- (48) Loget, G.; Yoo, J. E.; Mazare, A.; Wang, L.; Schmuki, P. Highly Controlled Coating of a Biomimetic Polymer in TiO<sub>2</sub> Nanotubes. **2016**, *52*, 41–44. <https://doi.org/10.48550/ARXIV.1610.04184>.
- (49) Sun, X.; Yan, L.; Xu, R.; Xu, M.; Zhu, Y. Surface Modification of TiO<sub>2</sub> with Polydopamine and Its Effect on Photocatalytic Degradation Mechanism. *Colloids and Surfaces A: Physicochemical and Engineering Aspects* **2019**, *570*, 199–209. <https://doi.org/10.1016/j.colsurfa.2019.03.018>.
- (50) Guo, Z.; Wang, G.; Fu, H.; Wang, P.; Liao, J.; Wang, A. Photocatalytic Degradation of Methylene Blue by a Cocatalytic PDA/TiO<sub>2</sub> Electrode Produced by Photoelectric Polymerization. *RSC Adv.* **2020**, *10* (44), 26133–26141. <https://doi.org/10.1039/D0RA02076A>.
- (51) Damberga, D.; Fedorenko, V.; Grundšteins, K.; Altundal, Ş.; Šutka, A.; Ramanavičius, A.; Coy, E.; Mrówczyński, R.; Iatsunskyi, I.; Viter, R. Influence of PDA Coating on the Structural, Optical and Surface Properties of ZnO Nanostructures. *Nanomaterials* **2020**, *10* (12), 2438. <https://doi.org/10.3390/nano10122438>.
- (52) Wang, Q.; Jia, F.; Song, S.; Li, Y. Hydrophilic MoS<sub>2</sub>/Polydopamine (PDA) Nanocomposites as the Electrode for Enhanced Capacitive Deionization. *Separation and Purification Technology* **2020**, *236*, 116298. <https://doi.org/10.1016/j.seppur.2019.116298>.
- (53) Kim, Y.; Coy, E.; Kim, H.; Mrówczyński, R.; Torruella, P.; Jeong, D.-W.; Choi, K. S.; Jang, J. H.; Song, M. Y.; Jang, D.-J.; Peiro, F.; Jurga, S.; Kim, H. J. Efficient Photocatalytic Production of Hydrogen by Exploiting the Polydopamine-Semiconductor Interface. *Applied Catalysis B: Environmental* **2021**, *280*, 119423. <https://doi.org/10.1016/j.apcatb.2020.119423>.
- (54) Zou, Y.; Chen, X.; Yang, P.; Liang, G.; Yang, Y.; Gu, Z.; Li, Y. Regulating the Absorption Spectrum of Polydopamine. *Sci. Adv.* **2020**, *6* (36), eabb4696. <https://doi.org/10.1126/sciadv.abb4696>.

- (55) Yu, Z.; Li, F.; Yang, Q.; Shi, H.; Chen, Q.; Xu, M. Nature-Mimic Method To Fabricate Polydopamine/Graphitic Carbon Nitride for Enhancing Photocatalytic Degradation Performance. *ACS Sustainable Chem. Eng.* **2017**, *5* (9), 7840–7850. <https://doi.org/10.1021/acssuschemeng.7b01313>.
- (56) Aguilar-Ferrer, D.; Szewczyk, J.; Coy, E. Recent Developments in Polydopamine-Based Photocatalytic Nanocomposites for Energy Production: Physico-Chemical Properties and Perspectives. *Catalysis Today* **2021**, 397, 316–349. <https://doi.org/10.1016/j.cattod.2021.08.016>.
- (57) Torres, F. G.; Troncoso, O. P.; Rodriguez, L.; De-la-Torre, G. E. Sustainable Synthesis, Reduction and Applications of Graphene Obtained from Renewable Resources. *Sustainable Materials and Technologies* **2021**, 29, e00310. <https://doi.org/10.1016/j.susmat.2021.e00310>.
- (58) Yang, P.; Li, T.; Li, H.; Dang, A.; Yuan, L. Progress in the Graphitization and Applications of Modified Resin Carbons. *New Carbon Materials* **2023**, *38* (1), 96–108. [https://doi.org/10.1016/S1872-5805\(23\)60715-2](https://doi.org/10.1016/S1872-5805(23)60715-2).
- (59) Sukmana, I. F.; Widiatmoko, P.; Nurdin, I.; Devianto; Prakoso, T. Effect of ZnCl<sub>2</sub> on Properties of Graphene Produced from Palm Empty Fruit Bunch. *IOP Conf. Ser.: Mater. Sci. Eng.* **2020**, 778 (1), 012011. <https://doi.org/10.1088/1757-899X/778/1/012011>.
- (60) Talabi, S. I.; Luz, A. P.; Pandolfelli, V. C.; Lucas, A. A. Structural Evolution during the Catalytic Graphitization of a Thermosetting Refractory Binder and Oxidation Resistance of the Derived Carbons. *Materials Chemistry and Physics* **2018**, 212, 113–121. <https://doi.org/10.1016/j.matchemphys.2018.03.029>.
- (61) Alizadeh, O.; Hosseini, H. M.; Pourjavadi, A.; Bahramian, A. R. Effect of Graphene Oxide on Morphological and Structural Properties of Graphene Reinforced Novolac-Derived Carbon Aerogels: A Modified Quasi-Percolation Model. *Ceramics International* **2020**, 46 (8), 11179–11188. <https://doi.org/10.1016/j.ceramint.2020.01.139>.
- (62) Yang, G.; Wang, Y.; Zhou, S.; Jia, S.; Xu, H.; Zang, J. Graphene/Phenolic Resin-Based Porous Carbon Composites with Improved Conductivity Prepared via in Situ Polymerization in Graphene Hydrogels. *J Mater Sci* **2019**, 54 (3), 2222–2230. <https://doi.org/10.1007/s10853-018-2983-z>.
- (63) Chen, F.; Yang, J.; Bai, T.; Long, B.; Zhou, X. Facile Synthesis of Few-Layer Graphene from Biomass Waste and Its Application in Lithium Ion Batteries. *Journal of Electroanalytical Chemistry* **2016**, 768, 18–26. <https://doi.org/10.1016/j.jelechem.2016.02.035>.
- (64) Ryu, S.; Chou, J. B.; Lee, K.; Lee, D.; Hong, S. H.; Zhao, R.; Lee, H.; Kim, S. Direct Insulation-to-Conduction Transformation of Adhesive Catecholamine for Simultaneous Increases of Electrical Conductivity and Mechanical Strength of CNT Fibers. *Adv. Mater.* **2015**, 27 (21), 3250–3255. <https://doi.org/10.1002/adma.201500914>.
- (65) Kim, Y.; Kim, J. Carbonization of Polydopamine-Coating Layers on Boron Nitride for Thermal Conductivity Enhancement in Hybrid Polyvinyl Alcohol (PVA) Composites. *Polymers* **2020**, 12 (6), 1410. <https://doi.org/10.3390/polym12061410>.
- (66) Teng, W.; Zhou, Q.; Wang, X.; Che, H.; Du, Y.; Hu, P.; Li, H.; Wang, J. Biotemplating Preparation of N,O-Codoped Hierarchically Porous Carbon for High-Performance Supercapacitors. *Applied Surface Science* **2021**, 566, 150613. <https://doi.org/10.1016/j.apsusc.2021.150613>.
- (67) Li, H.; Aulin, Y. V.; Frazer, L.; Borguet, E.; Kakodkar, R.; Feser, J.; Chen, Y.; An, K.; Dikin, D. A.; Ren, F. Structure Evolution and Thermoelectric Properties of Carbonized Polydopamine Thin Films. *ACS Appl. Mater. Interfaces* **2017**, 9 (8), 6655–6660. <https://doi.org/10.1021/acsami.6b15601>.
- (68) Cen, Y.; Dong, J.; Zhu, T.; Cai, X.; Wang, X.; Hu, B.; Xu, C.; Yu, D.; Liu, Y.; Chen, C. Bi Nanorods Anchored in N-Doped Carbon Shell as Anode for High-Performance Magnesium Ion Batteries. *Electrochimica Acta* **2021**, 397, 139260. <https://doi.org/10.1016/j.electacta.2021.139260>.
- (69) Zou, R.; Liu, F.; Hu, N.; Ning, H.; Gong, Y.; Wang, S.; Huang, K.; Jiang, X.; Xu, C.; Fu, S.; Li, Y.; Yan, C. Graphene/Graphitized Polydopamine/Carbon Nanotube All-Carbon Ternary Composite Films with Improved Mechanical Properties and Through-Plane Thermal Conductivity. *ACS Appl. Mater. Interfaces* **2020**, 12 (51), 57391–57400. <https://doi.org/10.1021/acsami.0c18373>.
- (70) Yu, X.; Fan, H.; Liu, Y.; Shi, Z.; Jin, Z. Characterization of Carbonized Polydopamine Nanoparticles Suggests Ordered Supramolecular Structure of Polydopamine. *Langmuir* **2014**, 30 (19), 5497–5505. <https://doi.org/10.1021/la500225v>.
- (71) Lee, K.; Park, M.; Malollari, K. G.; Shin, J.; Winkler, S. M.; Zheng, Y.; Park, J. H.; Grigoropoulos, C. P.; Messersmith, P. B. Laser-Induced Graphitization of Polydopamine Leads to Enhanced Mechanical Performance While Preserving Multifunctionality. *Nat Commun* **2020**, 11 (1), 4848. <https://doi.org/10.1038/s41467-020-18654-8>.
- (72) Truong-Son Dinh Le; Hoang-Phuong Phan; Soongeun Kwon; Sangbaek Park; Yeongju Jung; Jinki Min; Byung Jae Chun; Hana Yoon; Seung Hwan Ko; Seung-Woo Kim; Kim, Y.-J. Recent Advances in Laser-Induced Graphene: Mechanism, Fabrication, Properties, and Applications in Flexible Electronics. *Advanced Functional Materials* **2022**, 2205158–2205158. <https://doi.org/10.1002/adfm.202205158>.

- (73) Wang, H.; Zhao, Z.; Liu, P.; Guo, X. Laser-Induced Graphene Based Flexible Electronic Devices. *Biosensors* **2022**, *12* (2), 55–55. <https://doi.org/10.3390/bios12020055>.
- (74) A. Shokurov; Carlo Menon. Laser-Induced Graphene Electrodes for Electrochemistry Education and Research. *Journal of Chemical Education* **2023**, *100* (6), 2411–2417. <https://doi.org/10.1021/acs.jchemed.2c01237>.
- (75) Vivaldi, F. M.; Dallinger, A.; Bonini, A.; Poma, N.; Sembranti, L.; Biagini, D.; Salvo, P.; Greco, F.; Di Francesco, F. Three-Dimensional (3D) Laser-Induced Graphene: Structure, Properties, and Application to Chemical Sensing. *ACS Appl. Mater. Interfaces* **2021**, *13* (26), 30245–30260. <https://doi.org/10.1021/acsami.1c05614>.
- (76) Ye, R.; James, D. K.; Tour, J. M. Laser-Induced Graphene: From Discovery to Translation. *Advanced Materials* **2019**, *31* (1), 1803621. <https://doi.org/10.1002/adma.201803621>.
- (77) Chyan, Y.; Ye, R.; Li, Y.; Singh, S. P.; Arnusch, C. J.; Tour, J. M. Laser-Induced Graphene by Multiple Lasing: Toward Electronics on Cloth, Paper, and Food. *ACS Nano* **2018**, *12* (3), 2176–2183. <https://doi.org/10.1021/acsnano.7b08539>.
- (78) Luong, D. X.; Yang, K.; Yoon, J.; Singh, S. P.; Wang, T.; Arnusch, C. J.; Tour, J. M. Laser-Induced Graphene Composites as Multifunctional Surfaces. *ACS Nano* **2019**, *13* (2), 2579–2586. <https://doi.org/10.1021/acsnano.8b09626>.
- (79) Chemistry (IUPAC), T. I. U. of P. and A. *IUPAC - zwitterionic compounds/zwitterions (Z06752)*. <https://doi.org/10.1351/goldbook.Z06752>.
- (80) Laschewsky, A.; Rosenhahn, A. Molecular Design of Zwitterionic Polymer Interfaces: Searching for the Difference. *Langmuir* **2019**, *35* (5), 1056–1071. <https://doi.org/10.1021/acs.langmuir.8b01789>.
- (81) Laschewsky, A. Structures and Synthesis of Zwitterionic Polymers. *Polymers* **2014**, *6* (5), 1544–1601. <https://doi.org/10.3390/polym6051544>.
- (82) Kharlampieva, E.; Izumrudov, V. A.; Sukhishvili, S. A. Electrostatic Layer-by-Layer Self-Assembly of Poly(Carboxybetaine)s: Role of Zwitterions in Film Growth. *Macromolecules* **2007**, *40* (10), 3663–3668. <https://doi.org/10.1021/ma062811e>.
- (83) Olejnik, A.; Grochowska, K.; Siuzdak, K. Synthesis and Characterization of Poly(Zwitterionic) Structures for Energy Conversion and Storage. In *Conducting Polymers for Advanced Energy Applications*; CRC Press: Boca Raton, 2021; pp 359–382. <https://doi.org/10.1201/9781003150374-20>.
- (84) Li, B.; Jain, P.; Ma, J.; Smith, J. K.; Yuan, Z.; Hung, H.-C.; He, Y.; Lin, X.; Wu, K.; Pfaendtner, J.; Jiang, S. Trimethylamine *N*-Oxide-Derived Zwitterionic Polymers: A New Class of Ultralow Fouling Bioinspired Materials. *Sci. Adv.* **2019**, *5* (6), eaaw9562. <https://doi.org/10.1126/sciadv.aaw9562>.
- (85) Neitzel, A. E.; De Hoe, G. X.; Tirrell, M. V. Expanding the Structural Diversity of Polyelectrolyte Complexes and Polyzwitterions. *Current Opinion in Solid State and Materials Science* **2021**, *25* (2), 100897. <https://doi.org/10.1016/j.cossms.2020.100897>.
- (86) Schlenoff, J. B. Zwitteration: Coating Surfaces with Zwitterionic Functionality to Reduce Nonspecific Adsorption. *Langmuir* **2014**, *30* (32), 9625–9636. <https://doi.org/10.1021/la500057j>.
- (87) Vaterrodt, A.; Thallinger, B.; Daumann, K.; Koch, D.; Guebitz, G. M.; Ulbricht, M. Antifouling and Antibacterial Multifunctional Polyzwitterion/Enzyme Coating on Silicone Catheter Material Prepared by Electrostatic Layer-by-Layer Assembly. *Langmuir* **2016**, *32* (5), 1347–1359. <https://doi.org/10.1021/acs.langmuir.5b04303>.
- (88) Zhou, R.; Ren, P.-F.; Yang, H.-C.; Xu, Z.-K. Fabrication of Antifouling Membrane Surface by Poly(Sulfobetaine Methacrylate)/Polydopamine Co-Deposition. *Journal of Membrane Science* **2014**, *466*, 18–25. <https://doi.org/10.1016/j.memsci.2014.04.032>.
- (89) Yang, W.; Xue, H.; Carr, L. R.; Wang, J.; Jiang, S. Zwitterionic Poly(Carboxybetaine) Hydrogels for Glucose Biosensors in Complex Media. *Biosensors and Bioelectronics* **2011**, *26* (5), 2454–2459. <https://doi.org/10.1016/j.bios.2010.10.031>.
- (90) Olejnik, A.; Karczewski, J.; Dołęga, A.; Siuzdak, K.; Cenian, A.; Grochowska, K. Simple Synthesis Route for Fabrication of Protective Photo-crosslinked Poly(Zwitterionic) Membranes for Application in Non-enzymatic Glucose Sensing. *J Biomed Mater Res* **2022**, *110* (3), 679–690. <https://doi.org/10.1002/jbm.b.34946>.
- (91) Gui, Z.; Qian, J.; An, Q.; Zhao, Q.; Jin, H.; Du, B. Layer-by-Layer Self-Assembly, Controllable Disintegration of Polycarboxybetaine Multilayers and Preparation of Free-Standing Films at Physiological Conditions. *J. Mater. Chem.* **2010**, *20* (8), 1467–1474. <https://doi.org/10.1039/B918170A>.
- (92) Ren, P.-F.; Yang, H.-C.; Liang, H.-Q.; Xu, X.-L.; Wan, L.-S.; Xu, Z.-K. Highly Stable, Protein-Resistant Surfaces via the Layer-by-Layer Assembly of Poly(Sulfobetaine Methacrylate) and Tannic Acid. *Langmuir* **2015**, *31* (21), 5851–5858. <https://doi.org/10.1021/acs.langmuir.5b00920>.
- (93) Yeon, D. K.; Ko, S.; Jeong, S.; Hong, S.-P.; Kang, S. M.; Cho, W. K. Oxidation-Mediated, Zwitterionic Polydopamine Coatings for Marine Antifouling Applications. *Langmuir* **2019**, *35* (5), 1227–1234. <https://doi.org/10.1021/acs.langmuir.8b03454>.



- (94) Byun, J.; Cho, S.; Moon, J.; Kim, H.; Kang, H.; Jung, J.; Lim, E.-K.; Jeong, J.; Park, H. G.; Cho, W. K.; Kang, T. Zwitterionic Polydopamine/Protein G Coating for Antibody Immobilization: Toward Suppression of Nonspecific Binding in Immunoassays. *ACS Appl. Bio Mater.* **2020**, *3* (6), 3631–3639. <https://doi.org/10.1021/acsabm.0c00264>.
- (95) Scott, P. J.; Spiering, G. A.; Wang, Y.; Seibers, Z. D.; Moore, R. B.; Kumar, R.; Lokitz, B. S.; Long, T. E. Phosphonium-Based Polyzwitterions: Influence of Ionic Structure and Association on Mechanical Properties. *Macromolecules* **2020**, *53* (24), 11009–11018. <https://doi.org/10.1021/acs.macromol.0c02166>.
- (96) Afrifah, V. A.; Phiri, I.; Hamenu, L.; Madzvamuse, A.; Lee, K. S.; Ko, J. M. Electrochemical Properties of Poly(2-Acrylamido-2-Methylpropane Sulfonic Acid) Polyelectrolyte Containing Zwitterionic Silica Sulfobetaine for Supercapacitors. *Journal of Power Sources* **2020**, *479*, 228657. <https://doi.org/10.1016/j.jpowsour.2020.228657>.
- (97) Peng, X.; Liu, H.; Yin, Q.; Wu, J.; Chen, P.; Zhang, G.; Liu, G.; Wu, C.; Xie, Y. A Zwitterionic Gel Electrolyte for Efficient Solid-State Supercapacitors. *Nat Commun* **2016**, *7* (1), 11782. <https://doi.org/10.1038/ncomms11782>.
- (98) Ge, K.; Liu, G. Suppression of Self-Discharge in Solid-State Supercapacitors Using a Zwitterionic Gel Electrolyte. *Chem. Commun.* **2019**, *55* (50), 7167–7170. <https://doi.org/10.1039/C9CC02424G>.
- (99) Diao, W.; Wu, L.; Ma, X.; Wang, L.; Bu, X.; Ni, W.; Yang, X.; Fang, Y. Reversibly Highly Stretchable and Self-healable Zwitterion-containing Polyelectrolyte Hydrogel with High Ionic Conductivity for High-performance Flexible and Cold-resistant Supercapacitor. *J Appl Polym Sci* **2020**, *137* (34), 48995. <https://doi.org/10.1002/app.48995>.
- (100) Hyeon, S.-E.; Seo, J. Y.; Bae, J. W.; Kim, W.-J.; Chung, C.-H. Faradaic Reaction of Dual-Redox Additive in Zwitterionic Gel Electrolyte Boosts the Performance of Flexible Supercapacitors. *Electrochimica Acta* **2019**, *319*, 672–681. <https://doi.org/10.1016/j.electacta.2019.07.043>.
- (101) Lu, F.; Li, G.; Yu, Y.; Gao, X.; Zheng, L.; Chen, Z. Zwitterionic Impetus on Single Lithium-Ion Conduction in Solid Polymer Electrolyte for All-Solid-State Lithium-Ion Batteries. *Chemical Engineering Journal* **2020**, *384*, 123237. <https://doi.org/10.1016/j.cej.2019.123237>.
- (102) Lu, F.; Gao, X.; Wu, A.; Sun, N.; Shi, L.; Zheng, L. Lithium-Containing Zwitterionic Poly(Ionic Liquid)s as Polymer Electrolytes for Lithium-Ion Batteries. *J. Phys. Chem. C* **2017**, *121* (33), 17756–17763. <https://doi.org/10.1021/acs.jpcc.7b06242>.
- (103) Yamaguchi, S.; Yoshizawa-Fujita, M.; Takeoka, Y.; Rikukawa, M. Effect of a Pyrrolidinium Zwitterion on Charge/Discharge Cycle Properties of Li/LiCoO<sub>2</sub> and Graphite/Li Cells Containing an Ionic Liquid Electrolyte. *Journal of Power Sources* **2016**, *331*, 308–314. <https://doi.org/10.1016/j.jpowsour.2016.09.058>.
- (104) Wei, X.; Liu, S.; Wang, J.; He, Z.; Zhao, K.; Yang, Y.; Liu, B.; Huang, R.; He, Z. Boosting the Performance of Positive Electrolyte for VRFB by Employing Zwitterion Molecule Containing Sulfonic and Pyridine Groups as the Additive. *Ionics* **2020**, *26* (6), 3147–3159. <https://doi.org/10.1007/s11581-020-03481-0>.
- (105) Leng, K.; Li, G.; Guo, J.; Zhang, X.; Wang, A.; Liu, X.; Luo, J. A Safe Polyzwitterionic Hydrogel Electrolyte for Long-Life Quasi-Solid State Zinc Metal Batteries. *Adv. Funct. Mater.* **2020**, *30* (23), 2001317. <https://doi.org/10.1002/adfm.202001317>.
- (106) Sobaszek, M.; Siuzdak, K.; Ryl, J.; Sawczak, M.; Gupta, S.; Carrizosa, S. B.; Ficek, M.; Dec, B.; Darowicki, K.; Bogdanowicz, R. Diamond Phase (sp<sup>3</sup> - C) Rich Boron-Doped Carbon Nanowalls (sp<sup>2</sup> - C): Physicochemical and Electrochemical Properties. *J. Phys. Chem. C* **2017**, *121* (38), 20821–20833. <https://doi.org/10.1021/acs.jpcc.7b06365>.
- (107) Siuzdak, K.; Ficek, M.; Sobaszek, M.; Ryl, J.; Gnyba, M.; Niedziałkowski, P.; Malinowska, N.; Karczewski, J.; Bogdanowicz, R. Boron-Enhanced Growth of Micron-Scale Carbon-Based Nanowalls: A Route toward High Rates of Electrochemical Biosensing. *ACS Appl. Mater. Interfaces* **2017**, *9* (15), 12982–12992. <https://doi.org/10.1021/acsami.6b16860>.
- (108) Larsson, K. The Combined Influence of Dopant Species and Surface Termination on the Electronic Properties of Diamond Surfaces. *C* **2020**, *6* (2), 22. <https://doi.org/10.3390/c6020022>.
- (109) Pierpaoli, M.; Ficek, M.; Ryciewicz, M.; Sawczak, M.; Karczewski, J.; Ruello, M.; Bogdanowicz, R. Tailoring Electro/Optical Properties of Transparent Boron-Doped Carbon Nanowalls Grown on Quartz. *Materials* **2019**, *12* (3), 547. <https://doi.org/10.3390/ma12030547>.
- (110) Niedziałkowski, P.; Cebula, Z.; Malinowska, N.; Białobrzeska, W.; Sobaszek, M.; Ficek, M.; Bogdanowicz, R.; Anand, J. S.; Ossowski, T. Comparison of the Paracetamol Electrochemical Determination Using Boron-Doped Diamond Electrode and Boron-Doped Carbon Nanowalls. *Biosensors and Bioelectronics* **2019**, *126*, 308–314. <https://doi.org/10.1016/j.bios.2018.10.063>.
- (111) Dettlaff, A.; Jakóbczyk, P.; Ficek, M.; Wilk, B.; Szala, M.; Wojtas, J.; Ossowski, T.; Bogdanowicz, R. Electrochemical Determination of Nitroaromatic Explosives at Boron-Doped Diamond/Graphene

Nanowall Electrodes: 2,4,6-Trinitrotoluene and 2,4,6-Trinitroanisole in Liquid Effluents. *Journal of Hazardous Materials* **2020**, 387, 121672. <https://doi.org/10.1016/j.jhazmat.2019.121672>.

- (112) Pierpaoli, M.; Lewkowicz, A.; Ryciewicz, M.; Szczodrowski, K.; Ruello, M. L.; Bogdanowicz, R. Enhanced Photocatalytic Activity of Transparent Carbon Nanowall/TiO<sub>2</sub> Heterostructures. *Materials Letters* **2020**, 262, 127155. <https://doi.org/10.1016/j.matlet.2019.127155>.
- (113) Patrick, C. E.; Giustino, F. GW Quasiparticle Bandgaps of Anatase TiO<sub>2</sub> Starting from DFT + *U*. *J. Phys.: Condens. Matter* **2012**, 24 (20), 202201. <https://doi.org/10.1088/0953-8984/24/20/202201>.
- (114) Orhan, O. K.; O'Regan, D. D. First-Principles Hubbard *U* and Hund's *J* Corrected Approximate Density Functional Theory Predicts an Accurate Fundamental Gap in Rutile and Anatase TiO<sub>2</sub>. *Phys. Rev. B* **2020**, 101 (24), 245137. <https://doi.org/10.1103/PhysRevB.101.245137>.
- (115) Haryński, Ł.; Grochowska, K.; Karczewski, J.; Ryl, J.; Siuzdak, K. Scalable Route toward Superior Photoresponse of UV-Laser-Treated TiO<sub>2</sub> Nanotubes. *ACS Appl. Mater. Interfaces* **2020**, 12 (2), 3225–3235. <https://doi.org/10.1021/acsami.9b19206>.
- (116) Smith, Y.; Ray, R.; Carlson, K.; Sarma, B.; Misra, M. Self-Ordered Titanium Dioxide Nanotube Arrays: Anodic Synthesis and Their Photo/Electro-Catalytic Applications. *Materials* **2013**, 6 (7), 2892–2957. <https://doi.org/10.3390/ma6072892>.
- (117) Gelderman, K.; Lee, L.; Donne, S. W. Flat-Band Potential of a Semiconductor: Using the Mott–Schottky Equation. *J. Chem. Educ.* **2007**, 84 (4), 685. <https://doi.org/10.1021/ed084p685>.
- (118) Wawrzyniak, J.; Grochowska, K.; Karczewski, J.; Kupracz, P.; Ryl, J.; Dołęga, A.; Siuzdak, K. The Geometry of Free-Standing Titania Nanotubes as a Critical Factor Controlling Their Optical and Photoelectrochemical Performance. *Surface and Coatings Technology* **2020**, 389, 125628. <https://doi.org/10.1016/j.surfcoat.2020.125628>.
- (119) Cui, H.; Zhao, W.; Yang, C.; Yin, H.; Lin, T.; Shan, Y.; Xie, Y.; Gu, H.; Huang, F. Black TiO<sub>2</sub> Nanotube Arrays for High-Efficiency Photoelectrochemical Water-Splitting. *J. Mater. Chem. A* **2014**, 2 (23), 8612–8616. <https://doi.org/10.1039/C4TA00176A>.
- (120) El-Gendy, D. M.; Abdel Ghany, N. A.; Allam, N. K. Black Titania Nanotubes/Spongy Graphene Nanocomposites for High-Performance Supercapacitors. *RSC Adv.* **2019**, 9 (22), 12555–12566. <https://doi.org/10.1039/C9RA01539F>.
- (121) Wang, N.; Ma, Y.; Chen, J.; Chen, C.; San, H.; Chen, J.; Cheng, Z. Defect-Induced Betavoltaic Enhancement in Black Titania Nanotube Arrays. *Nanoscale* **2018**, 10 (27), 13028–13036. <https://doi.org/10.1039/C8NR02824A>.
- (122) Siuzdak, K.; Szkoda, M.; Lisowska-Oleksiak, A.; Karczewski, J.; Ryl, J. Highly Stable Organic–Inorganic Junction Composed of Hydrogenated Titania Nanotubes Infiltrated by a Conducting Polymer. *RSC Adv.* **2016**, 6 (39), 33101–33110. <https://doi.org/10.1039/C6RA01986B>.
- (123) Raghunath, P.; Huang, W. F.; Lin, M. C. Quantum Chemical Elucidation of the Mechanism for Hydrogenation of TiO<sub>2</sub> Anatase Crystals. *The Journal of Chemical Physics* **2013**, 138 (15), 154705. <https://doi.org/10.1063/1.4799800>.
- (124) Will, J.; Wierzbicka, E.; Wu, M.; Götz, K.; Yokosawa, T.; Liu, N.; Tesler, A. B.; Stiller, M.; Unruh, T.; Altomare, M.; Schmuki, P.; Spiecker, E. Hydrogenated Anatase TiO<sub>2</sub> Single Crystals: Defects Formation and Structural Changes as Microscopic Origin of Co-Catalyst Free Photocatalytic H<sub>2</sub> Evolution Activity. *J. Mater. Chem. A* **2021**, 9 (44), 24932–24942. <https://doi.org/10.1039/D1TA04809K>.
- (125) Yoshida, T.; Niimi, S.; Yamamoto, M.; Nomoto, T.; Yagi, S. Effective Nitrogen Doping into TiO<sub>2</sub> (N-TiO<sub>2</sub>) for Visible Light Response Photocatalysis. *Journal of Colloid and Interface Science* **2015**, 447, 278–281. <https://doi.org/10.1016/j.jcis.2014.12.097>.
- (126) Tojo, S.; Tachikawa, T.; Fujitsuka, M.; Majima, T. Iodine-Doped TiO<sub>2</sub> Photocatalysts: Correlation between Band Structure and Mechanism. *J. Phys. Chem. C* **2008**, 112 (38), 14948–14954. <https://doi.org/10.1021/jp804985f>.
- (127) Haryński, Ł.; Grochowska, K.; Karczewski, J.; Ryl, J.; Rysz, J.; Siuzdak, K. Free-Standing TiO<sub>2</sub> Nanotubes Decorated with Spherical Nickel Nanoparticles as a Cost-Efficient Electrocatalyst for Oxygen Evolution Reaction. *RSC Adv.* **2021**, 11 (1), 219–228. <https://doi.org/10.1039/D0RA07563A>.
- (128) Haryński, Ł.; Karczewski, J.; Ryl, J.; Grochowska, K.; Siuzdak, K. Rapid Development of the Photoresponse and Oxygen Evolution of TiO<sub>2</sub> Nanotubes Sputtered with Cr Thin Films Realized via Laser Annealing. *Journal of Alloys and Compounds* **2021**, 877, 160316. <https://doi.org/10.1016/j.jallcom.2021.160316>.
- (129) Park, J. H.; Park, O. O.; Kim, S. Photoelectrochemical Water Splitting at Titanium Dioxide Nanotubes Coated with Tungsten Trioxide. *Appl. Phys. Lett.* **2006**, 89 (16), 163106. <https://doi.org/10.1063/1.2357878>.
- (130) Guan, D.; Gao, X.; Li, J.; Yuan, C. Enhanced Capacitive Performance of TiO<sub>2</sub> Nanotubes with Molybdenum Oxide Coating. *Applied Surface Science* **2014**, 300, 165–170. <https://doi.org/10.1016/j.apsusc.2014.02.029>.



- (131) Trochowski, M.; Kobielski, M.; Pucelik, B.; Dąbrowski, J. M.; Macyk, W. Dihydroxyanthraquinones as Stable and Cost-Effective TiO<sub>2</sub> Photosensitizers for Environmental and Biomedical Applications. *Journal of Photochemistry and Photobiology A: Chemistry* **2023**, *438*, 114517. <https://doi.org/10.1016/j.jphotochem.2022.114517>.
- (132) Hamza, M. A.; Rizk, S. A.; Ezz-Elregal, E.-E. M.; El-Rahman, S. A. A.; Ramadan, S. K.; Abou-Gamra, Z. M. Photosensitization of TiO<sub>2</sub> Microspheres by Novel Quinazoline-Derivative as Visible-Light-Harvesting Antenna for Enhanced Rhodamine B Photodegradation. *Sci Rep* **2023**, *13* (1), 12929. <https://doi.org/10.1038/s41598-023-38497-9>.
- (133) Szkoda, M.; Trzcinski, K.; Rysz, J.; Gazda, M.; Siuzdak, K.; Lisowska-Oleksiak, A. Electrodes Consisting of PEDOT Modified by Prussian Blue Analogues Deposited onto Titania Nanotubes – Their Highly Improved Capacitance. *Solid State Ionics* **2017**, *302*, 197–201. <https://doi.org/10.1016/j.ssi.2016.12.025>.
- (134) Mestre, A. S.; Carvalho, A. P. Photocatalytic Degradation of Pharmaceuticals Carbamazepine, Diclofenac, and Sulfamethoxazole by Semiconductor and Carbon Materials: A Review. *Molecules* **2019**, *24* (20), 3702. <https://doi.org/10.3390/molecules24203702>.
- (135) Szkoda, M.; Rysz, J.; Ryl, J.; Lisowska-Oleksiak, A.; Siuzdak, K. Fabrication and Photoactivity of Organic-Inorganic Systems Based on Titania Nanotubes and PEDOT Containing Redox Centres Formed by Different Prussian Blue Analogues. *Journal of Alloys and Compounds* **2017**, *723*, 498–504. <https://doi.org/10.1016/j.jallcom.2017.06.257>.
- (136) Sopha, H.; Mirza, I.; Turčičova, H.; Pavlinak, D.; Michalicka, J.; Krbal, M.; Rodriguez-Pereira, J.; Hromadko, L.; Novák, O.; Mužík, J.; Smrž, M.; Kolibalova, E.; Goodfriend, N.; Bulgakova, N. M.; Mocek, T.; Macak, J. M. Laser-Induced Crystallization of Anodic TiO<sub>2</sub> Nanotube Layers. *RSC Adv.* **2020**, *10* (37), 22137–22145. <https://doi.org/10.1039/D0RA02929G>.
- (137) Hsu, M.-Y.; Van Thang, N.; Wang, C.; Leu, J. Structural and Morphological Transformations of TiO<sub>2</sub> Nanotube Arrays Induced by Excimer Laser Treatment. *Thin Solid Films* **2012**, *520* (9), 3593–3599. <https://doi.org/10.1016/j.tsf.2011.12.036>.
- (138) Yu, J.; Dai, G.; Cheng, B. Effect of Crystallization Methods on Morphology and Photocatalytic Activity of Anodized TiO<sub>2</sub> Nanotube Array Films. *J. Phys. Chem. C* **2010**, *114* (45), 19378–19385. <https://doi.org/10.1021/jp106324x>.
- (139) Xu, Y.; Melia, M. A.; Tsui, L.; Fitz-Gerald, J. M.; Zangari, G. Laser-Induced Surface Modification at Anatase TiO<sub>2</sub> Nanotube Array Photoanodes for Photoelectrochemical Water Oxidation. *J. Phys. Chem. C* **2017**, *121* (32), 17121–17128. <https://doi.org/10.1021/acs.jpcc.7b05368>.
- (140) Wawrzyniak, J.; Karczewski, J.; Kupracz, P.; Grochowska, K.; Coy, E.; Mazikowski, A.; Ryl, J.; Siuzdak, K. Formation of the Hollow Nanopillar Arrays through the Laser-Induced Transformation of TiO<sub>2</sub> Nanotubes. *Sci Rep* **2020**, *10* (1), 20235. <https://doi.org/10.1038/s41598-020-77309-2>.
- (141) Wawrzyniak, J.; Karczewski, J.; Kupracz, P.; Grochowska, K.; Załęski, K.; Pshyk, O.; Coy, E.; Bartmański, M.; Szkodo, M.; Siuzdak, K. Laser-Assisted Modification of Titanium Dioxide Nanotubes in a Tilted Mode as Surface Modification and Patterning Strategy. *Applied Surface Science* **2020**, *508*, 145143. <https://doi.org/10.1016/j.apsusc.2019.145143>.
- (142) Siuzdak, K.; Wawrzyniak, J.; Haryński, Ł.; Bielan, Z.; Grochowska, K. The Impact of Side-Selective Laser Tailoring of Titania Nanotubes on Changes in Photoelectrocatalytic Activity. *Micromachines* **2023**, *14* (2), 274. <https://doi.org/10.3390/mi14020274>.
- (143) Zhao, Y. Preparation and Characterization of Vertically Columnar Boron Doped Diamond Array Electrode. *Applied Surface Science* **2014**, *301* (1), 419–424. <https://doi.org/10.1016/j.apsusc.2014.03.017>.
- (144) Pierpaoli, M.; Ficek, M.; Jakóbczyk, P.; Karczewski, J.; Bogdanowicz, R. Self-Assembly of Vertically Orientated Graphene Nanostructures: Multivariate Characterisation by Minkowski Functionals and Fractal Geometry. *Acta Materialia* **2021**, *214*, 116989. <https://doi.org/10.1016/j.actamat.2021.116989>.
- (145) Wawrzyniak, J.; Karczewski, J.; Coy, E.; Iatsunskiy, I.; Ryl, J.; Gazda, M.; Grochowska, K.; Siuzdak, K. Spectacular Oxygen Evolution Reaction Enhancement through Laser Processing of the Nickel-Decorated Titania Nanotubes. *Adv. Mater. Interfaces* **2021**, *8* (1), 2001420. <https://doi.org/10.1002/admi.202001420>.
- (146) A. Olejnik; Karol Olbryś; J. Karczewski; J. Ryl; R. Bogdanowicz; K. Siuzdak. Band Gap Engineering toward Semimetallic Character of Quinone-Rich Polydopamine. *Journal of Physical Chemistry C* **2023**, *127* (26), 12662–12677. <https://doi.org/10.1021/acs.jpcc.2c08804>.
- (147) The 2 Main Electron Microscopy Techniques: SEM vs TEM. *Microscopy and Imaging*. April 6, 2022.
- (148) Zadora, G.; Brożek-Mucha, Z. SEM–EDX—a Useful Tool for Forensic Examinations. *Materials Chemistry and Physics* **2003**, *81* (2–3), 345–348. [https://doi.org/10.1016/S0254-0584\(03\)00018-X](https://doi.org/10.1016/S0254-0584(03)00018-X).
- (149) Gurwitz, R.; Cohen, R.; Shalish, I. Interaction of Light with the ZnO Surface: Photon Induced Oxygen “Breathing,” Oxygen Vacancies, Persistent Photoconductivity, and Persistent Photovoltage. *Journal of Applied Physics* **2014**, *115* (3), 033701. <https://doi.org/10.1063/1.4861413>.

- (150) El-Azazy, M. Introductory Chapter: Infrared Spectroscopy - A Synopsis of the Fundamentals and Applications. In *Infrared Spectroscopy - Principles, Advances, and Applications*; El-Azazy, M., Ed.; IntechOpen, 2019. <https://doi.org/10.5772/intechopen.82210>.
- (151) Muthuselvi, C. Vibrational, Optical and Antimicrobial Activity Studies on Diglycine Perchlorate Single Crystal. Master, Devanga Arts College, Aruppukkottai, India, 2020. [https://www.researchgate.net/publication/346718577\\_Vibrational\\_Optical\\_and\\_Antimicrobial\\_Activity\\_Studies\\_on\\_Diglycine\\_Perchlorate\\_Single\\_Crystal](https://www.researchgate.net/publication/346718577_Vibrational_Optical_and_Antimicrobial_Activity_Studies_on_Diglycine_Perchlorate_Single_Crystal).
- (152) Mosca, S.; Conti, C.; Stone, N.; Matousek, P. Spatially Offset Raman Spectroscopy. *Nat Rev Methods Primers* **2021**, *1* (1), 21. <https://doi.org/10.1038/s43586-021-00019-0>.
- (153) Downes, A.; Elfick, A. Raman Spectroscopy and Related Techniques in Biomedicine. *Sensors* **2010**, *10* (3), 1871–1889. <https://doi.org/10.3390/s100301871>.
- (154) Yang, P.; Zhang, S.; Chen, X.; Liu, X.; Wang, Z.; Li, Y. Recent Developments in Polydopamine Fluorescent Nanomaterials. *Mater. Horiz.* **2020**, *7* (3), 746–761. <https://doi.org/10.1039/C9MH01197H>.
- (155) Olejnik, A.; Polaczek, K.; Szkodo, M.; Stanisławska, A.; Ryl, J.; Siuzdak, K. Laser-Induced Graphitization of Polydopamine on Titania Nanotubes. *ACS Appl. Mater. Interfaces* **2023**, *15* (45), 52921–52938. <https://doi.org/10.1021/acsami.3c11580>.
- (156) Rocha, F. S.; Gomes, A. J.; Lunardi, C. N.; Kaliaguine, S.; Patience, G. S. Experimental Methods in Chemical Engineering: Ultraviolet Visible Spectroscopy—UV-Vis. *Can J Chem Eng* **2018**, *96* (12), 2512–2517. <https://doi.org/10.1002/cjce.23344>.
- (157) Vargas, W. E.; Niklasson, G. A. Applicability Conditions of the Kubelka–Munk Theory. *Appl. Opt.* **1997**, *36* (22), 5580. <https://doi.org/10.1364/AO.36.005580>.
- (158) Myrick, M. L.; Simcock, M. N.; Baranowski, M.; Brooke, H.; Morgan, S. L.; McCutcheon, J. N. The Kubelka-Munk Diffuse Reflectance Formula Revisited. *Applied Spectroscopy Reviews* **2011**, *46* (2), 140–165. <https://doi.org/10.1080/05704928.2010.537004>.
- (159) Morozzi, P.; Ballarin, B.; Arcozzi, S.; Brattich, E.; Lucarelli, F.; Nava, S.; Gómez-Cascales, P. J.; Orza, J. A. G.; Tositti, L. Ultraviolet–Visible Diffuse Reflectance Spectroscopy (UV–Vis DRS), a Rapid and Non-Destructive Analytical Tool for the Identification of Saharan Dust Events in Particulate Matter Filters. *Atmospheric Environment* **2021**, *252*, 118297. <https://doi.org/10.1016/j.atmosenv.2021.118297>.
- (160) Sagadevan, S.; Murugasen, P. Studies on Optical, Mechanical and Electrical Properties of Organic Nonlinear Optical p-Toluidine p-Toluenesulfonate Single Crystal. *JCPT* **2014**, *04* (02), 99–110. <https://doi.org/10.4236/jcpt.2014.42013>.
- (161) Schneider, K. Optical Properties and Electronic Structure of V<sub>2</sub>O<sub>5</sub>, V<sub>2</sub>O<sub>3</sub> and VO<sub>2</sub>. *J Mater Sci: Mater Electron* **2020**, *31* (13), 10478–10488. <https://doi.org/10.1007/s10854-020-03596-0>.
- (162) Coulter, J. B.; Birnie, D. P. Assessing Tauc Plot Slope Quantification: ZnO Thin Films as a Model System. *Phys. Status Solidi B* **2018**, *255* (3), 1700393. <https://doi.org/10.1002/pssb.201700393>.
- (163) Dolgonos, A.; Mason, T. O.; Poepelmeier, K. R. Direct Optical Band Gap Measurement in Polycrystalline Semiconductors: A Critical Look at the Tauc Method. *Journal of Solid State Chemistry* **2016**, *240*, 43–48. <https://doi.org/10.1016/j.jssc.2016.05.010>.
- (164) Feng, Y.; Lin, S.; Huang, S.; Shrestha, S.; Conibeer, G. Can Tauc Plot Extrapolation Be Used for Direct-Band-Gap Semiconductor Nanocrystals? *Journal of Applied Physics* **2015**, *117* (12), 125701. <https://doi.org/10.1063/1.4916090>.
- (165) Wang, S.; Zhao, H. Low Temperature Nanoindentation: Development and Applications. *Micromachines* **2020**, *11* (4), 407. <https://doi.org/10.3390/mi11040407>.
- (166) Zhao, S.; Xu, X.; Yang, L.; Qin, K.; Yu, X.; Chao, Q.; Zhou, N.; Zuo, J. Investigation on the Mechanical Properties of Shale Subjected to Different Conditions Based on Nanoindentation Experiments and Numerical Simulation. *Case Studies in Construction Materials* **2022**, *17*, e01438. <https://doi.org/10.1016/j.cscm.2022.e01438>.
- (167) Olejnik, A.; Ficek, M.; Szkodo, M.; Stanisławska, A.; Karczewski, J.; Ryl, J.; Dołęga, A.; Siuzdak, K.; Bogdanowicz, R. Tailoring Diffusional Fields in Zwitterion/Dopamine Copolymer Electropolymerized at Carbon Nanowalls for Sensitive Recognition of Neurotransmitters. *ACS Nano* **2022**, *16* (8), 13183–13198. <https://doi.org/10.1021/acs.nano.2c06406>.
- (168) Compton, R. G.; Kätelhön, E.; Ward, K. R.; Laborda, E. *Understanding Voltammetry: Simulation of Electrode Processes*, 2nd ed.; WORLD SCIENTIFIC (EUROPE), 2020. <https://doi.org/10.1142/q0246>.
- (169) Elgrishi, N.; Rountree, K. J.; McCarthy, B. D.; Rountree, E. S.; Eisenhart, T. T.; Dempsey, J. L. A Practical Beginner's Guide to Cyclic Voltammetry. *J. Chem. Educ.* **2018**, *95* (2), 197–206. <https://doi.org/10.1021/acs.jchemed.7b00361>.
- (170) Davies, T. J.; Compton, R. G. The Cyclic and Linear Sweep Voltammetry of Regular and Random Arrays of Microdisc Electrodes: Theory. *Journal of Electroanalytical Chemistry* **2005**, *585* (1), 63–82. <https://doi.org/10.1016/j.jelechem.2005.07.022>.

- (171) Galus, Zbigniew. *Teoretyczne Podstawy Elektroanalizy Chemicznej: Polarografia, Chronowoltamperometria, Chronopotencjometria, Metoda Wirującego Dysku*; Państwowe Wydawnictwo Naukowe, 1971.
- (172) Bard, A. J.; Faulkner, L. R. *Electrochemical Methods: Fundamentals and Applications*, 2nd ed.; Wiley: New York, 2001.
- (173) Wojtyła, S.; Baran, T. Photosensitization and Photocurrent Switching Effects in Wide Band Gap Semiconductors: CuI and TiO<sub>2</sub> Functionalized with Iron and Nickel Complexes: From Semiconductors to Logic Devices. *J Inorg Organomet Polym* **2017**, 27 (2), 436–445. <https://doi.org/10.1007/s10904-016-0484-6>.
- (174) Shu, J.; Tang, D. Recent Advances in Photoelectrochemical Sensing: From Engineered Photoactive Materials to Sensing Devices and Detection Modes. *Anal. Chem.* **2020**, 92 (1), 363–377. <https://doi.org/10.1021/acs.analchem.9b04199>.
- (175) Lasia, A. *Electrochemical Impedance Spectroscopy and Its Applications*; Springer: New York, 2014.
- (176) Wang, S.; Zhang, J.; Gharbi, O.; Vivier, V.; Gao, M.; Orazem, M. E. Electrochemical Impedance Spectroscopy. *Nat Rev Methods Primers* **2021**, 1 (1), 41. <https://doi.org/10.1038/s43586-021-00039-w>.
- (177) Sivula, K. Mott–Schottky Analysis of Photoelectrodes: Sanity Checks Are Needed. *ACS Energy Lett.* **2021**, 6 (7), 2549–2551. <https://doi.org/10.1021/acsenergylett.1c01245>.
- (178) Hankin, A.; Bedoya-Lora, F. E.; Alexander, J. C.; Regoutz, A.; Kelsall, G. H. Flat Band Potential Determination: Avoiding the Pitfalls. *J. Mater. Chem. A* **2019**, 7 (45), 26162–26176. <https://doi.org/10.1039/C9TA09569A>.
- (179) Lopes, L. C.; Santos, A.; Bueno, P. R. An Outlook on Electrochemical Approaches for Molecular Diagnostics Assays and Discussions on the Limitations of Miniaturized Technologies for Point-of-Care Devices. *Sensors and Actuators Reports* **2022**, 4, 100087. <https://doi.org/10.1016/j.snr.2022.100087>.
- (180) Fermeglia, M.; Mio, A.; Aulic, S.; Marson, D.; Laurini, E.; Pricl, S. Multiscale Molecular Modelling for the Design of Nanostructured Polymer Systems: Industrial Applications. *Mol. Syst. Des. Eng.* **2020**, 5 (9), 1447–1476. <https://doi.org/10.1039/D0ME00109K>.
- (181) Piela, L. *Ideas of Quantum Chemistry*, Second Edition.; Elsevier, 2013.
- (182) Grimme, S.; Schreiner, P. R. Computational Chemistry: The Fate of Current Methods and Future Challenges. *Angew Chem Int Ed* **2018**, 57 (16), 4170–4176. <https://doi.org/10.1002/anie.201709943>.
- (183) Pseudopotential. *Wikipedia*.
- (184) Smidstrup, S.; Markussen, T.; Vancraeyveld, P.; Wellendorff, J.; Schneider, J.; Gunst, T.; Verstichel, B.; Stradi, D.; Khomyakov, P. A.; Vej-Hansen, U. G.; Lee, M.-E.; Chill, S. T.; Rasmussen, F.; Penazzi, G.; Corsetti, F.; Ojanperä, A.; Jensen, K.; Palsgaard, M. L. N.; Martinez, U.; Blom, A.; Brandbyge, M.; Stokbro, K. QuantumATK: An Integrated Platform of Electronic and Atomic-Scale Modelling Tools. *J. Phys.: Condens. Matter* **2020**, 32 (1), 015901. <https://doi.org/10.1088/1361-648X/ab4007>.
- (185) Posysaev Sergei. Applications of Density Functional Theory for Modeling Metal-Semiconductor Contacts, Reaction Pathways, and Calculating Oxidation States. Doctoral, University of Oulu, 2018. <https://www.semanticscholar.org/paper/Applications-of-density-functional-theory-for-and-Posysaev/3262f9f1418d1bcfd6be316fef39103b8b5fbc53>.
- (186) Ghose, K. K.; Brown, J. J.; Frankcombe, T. J.; Page, A.; Bayon, A. Density Functional Theory Modeling of Critical Properties of Perovskite Oxides for Water Splitting Applications. *WIREs Energy & Environment* **2023**, 12 (4), e476. <https://doi.org/10.1002/wene.476>.
- (187) Ferreira, L. G.; Marques, M.; Teles, L. K. Slater Half-Occupation Technique Revisited: The LDA-1/2 and GGA-1/2 Approaches for Atomic Ionization Energies and Band Gaps in Semiconductors. *AIP Advances* **2011**, 1 (3), 032119. <https://doi.org/10.1063/1.3624562>.
- (188) Grimme, S.; Antony, J.; Ehrlich, S.; Krieg, H. A Consistent and Accurate *Ab Initio* Parametrization of Density Functional Dispersion Correction (DFT-D) for the 94 Elements H-Pu. *The Journal of Chemical Physics* **2010**, 132 (15), 154104. <https://doi.org/10.1063/1.3382344>.
- (189) Abad, E.; Lewis, J. P.; Zobač, V.; Hapala, P.; Jelínek, P.; Ortega, J. Calculation of Non-Adiabatic Coupling Vectors in a Local-Orbital Basis Set. *The Journal of Chemical Physics* **2013**, 138 (15), 154106. <https://doi.org/10.1063/1.4801511>.
- (190) R. Rüger, M. Franchini, T. Trnka, A. Yakovlev, E. van Lenthe, P. Philipsen, T. van Vuren, B. Klumbers, T. Soini. AMS 2023.1, SCM, Theoretical Chemistry.
- (191) Heimel, G.; Romaner, L.; Zojer, E.; Brédas, J.-L. A Theoretical View on Self-Assembled Monolayers in Organic Electronic Devices; Heremans, P. L., Muccini, M., Meulenkaamp, E. A., Eds.; Strasbourg, France, 2008; p 699919. <https://doi.org/10.1117/12.785122>.
- (192) Murray, J. S.; Politzer, P. The Electrostatic Potential: An Overview. *WIREs Comput Mol Sci* **2011**, 1 (2), 153–163. <https://doi.org/10.1002/wcms.19>.
- (193) van Setten, M. J.; Giantomassi, M.; Bousquet, E.; Verstraete, M. J.; Hamann, D. R.; Gonze, X.; Rignanese, G.-M. The PseudoDojo: Training and Grading a 85 Element Optimized Norm-Conserving

- Pseudopotential Table. *Computer Physics Communications* **2018**, 226, 39–54.  
<https://doi.org/10.1016/j.cpc.2018.01.012>.
- (194) Nasiri, S. Molecular Simulation of Metal-Carbon Nanoparticle Composites. Doctoral, Friedrich-Alexander-University of Erlangen-Nürnberg, 2021.  
[https://www.researchgate.net/publication/355957515\\_Molecular\\_simulation\\_of\\_metal-carbon\\_nanoparticle\\_composites](https://www.researchgate.net/publication/355957515_Molecular_simulation_of_metal-carbon_nanoparticle_composites).
- (195) Latour, R. A. Perspectives on the Simulation of Protein–Surface Interactions Using Empirical Force Field Methods. *Colloids and Surfaces B: Biointerfaces* **2014**, 124, 25–37.  
<https://doi.org/10.1016/j.colsurfb.2014.06.050>.
- (196) Unke, O. T.; Chmiela, S.; Sauceda, H. E.; Gastegger, M.; Poltavsky, I.; Schütt, K. T.; Tkatchenko, A.; Müller, K.-R. Machine Learning Force Fields. *Chem. Rev.* **2021**, 121 (16), 10142–10186.  
<https://doi.org/10.1021/acs.chemrev.0c01111>.
- (197) Vashisth, A.; Kowalik, M.; Gerringer, J.; Ashraf, C.; van Duin, A. C. T.; Green, M. J. ReaxFF Simulations of Laser-Induced Graphene (LIG) Formation for Multifunctional Polymer Nanocomposites. **2020**, 3 (2), 1881–1890. <https://doi.org/10.1021/acsanm.9b02524>.